

Astrophysics and Space Science Library 417

Margarita Ryutova

# Physics of Magnetic Flux Tubes

AS  
SL

 Springer

# Astrophysics and Space Science Library

---

Volume 417

## Editorial Board

### *Chairman*

W.B. Burton, *National Radio Astronomy Observatory, Charlottesville, VA, USA*  
([bburton@nrao.edu](mailto:bburton@nrao.edu)); *University of Leiden, The Netherlands*  
([burton@strw.leidenuniv.nl](mailto:burton@strw.leidenuniv.nl))

F. Bertola, *University of Padua, Italy*

C.J. Cesarsky, *Commission for Atomic Energy, Saclay, France*

P. Ehrenfreund, *Leiden University, The Netherlands*

O. Engvold, *University of Oslo, Norway*

A. Heck, *Strasbourg Astronomical Observatory, France*

E.P.J. Van Den Heuvel, *University of Amsterdam, The Netherlands*

V.M. Kaspi, *McGill University, Montreal, Canada*

J.M.E. Kuijpers, *University of Nijmegen, The Netherlands*

H. Van Der Laan, *University of Utrecht, The Netherlands*

P.G. Murdin, *Institute of Astronomy, Cambridge, UK*

B.V. Somov, *Astronomical Institute, Moscow State University, Russia*

R.A. Sunyaev, *Space Research Institute, Moscow, Russia*

More information about this series at <http://www.springer.com/series/5664>

Margarita Ryutova

# Physics of Magnetic Flux Tubes

 Springer

Margarita Ryutova  
Lawrence Livermore National Laboratory  
Institute of Geophysics and Planetary  
Physics  
Livermore, CA  
USA

ISSN 0067-0057                      ISSN 2214-7985 (electronic)  
Astrophysics and Space Science Library  
ISBN 978-3-662-45242-4              ISBN 978-3-662-45243-1 (eBook)  
DOI 10.1007/978-3-662-45243-1

Library of Congress Control Number: 2014958576

Springer Heidelberg New York Dordrecht London  
© Springer-Verlag Berlin Heidelberg 2015

This work is subject to copyright. All rights are reserved by the Publisher, whether the whole or part of the material is concerned, specifically the rights of translation, reprinting, reuse of illustrations, recitation, broadcasting, reproduction on microfilms or in any other physical way, and transmission or information storage and retrieval, electronic adaptation, computer software, or by similar or dissimilar methodology now known or hereafter developed.

The use of general descriptive names, registered names, trademarks, service marks, etc. in this publication does not imply, even in the absence of a specific statement, that such names are exempt from the relevant protective laws and regulations and therefore free for general use.

The publisher, the authors and the editors are safe to assume that the advice and information in this book are believed to be true and accurate at the date of publication. Neither the publisher nor the authors or the editors give a warranty, express or implied, with respect to the material contained herein or for any errors or omissions that may have been made.

Cover illustration: The image is a 3-wavelength composite of solenoidal slinky at the coronal temperatures 2 MK (Fe XV 211 A), 1.5 MK (Fe XII 193 A) and 0.6 MK (Fe IX/X 171A) taken by the SDO/AIA on August 31, 2012.

Printed on acid-free paper

Springer-Verlag GmbH Berlin Heidelberg is part of Springer Science+Business Media  
([www.springer.com](http://www.springer.com))

*To Dmitri, Alex and Dmitri, Jr.*

# Preface

The advanced space and ground-based observations show amazing details in the sun's behavior providing us with invaluable information on the sun as a star and as our own energy source. The behavior of the sun is determined by a tremendous variety of physical phenomena acting on a wide range of spatial and temporal scales. Every aspect requires its own specific subject studies, and a lot of work is still needed to understand the inner workings of this fascinating things.

This book addresses one group of the phenomena: those involving finely structured magnetic fields. It has been more than five decades since the small-scale intense magnetic flux tubes were found to cover the huge "magnetic free" surface of the sun outside sunspots and active regions. For the time being, the fact that all the magnetic field of the sun from its visible surface, throughout corona, and further to the interplanetary space has a fine filamentary structure, is well established. This ubiquity of the magnetic flux tubes and their obvious role in a variety of processes affecting the dynamics of the solar atmosphere and of the outflowing plasma calls for detailed study of their properties. And yet, no book on *Physics of Magnetic Flux Tubes* and their role in the dynamics of various magnetized objects has been available.

This book is intended to fill this gap at least partly, offering the first comprehensive account of the *Physics of Magnetic Flux Tubes*. The book provides side-by-side presentation of observations and analytical theory complemented by quantitative analysis. Many problems that are usually treated separately are presented in the book as a coupled phenomena and are treated on the unified basis. In some cases the author takes a risk to point at the effects that have not yet been looked for, or may be used for the predictability of events, and makes suggestions on what the observer should expect and what to search for in huge banks of observational data.

A major feature of the book is the application and observational test of the analytical theories that have not been previously considered in the context of the solar physics. Examples are: negative energy waves that may lead to formation of solitons propagating along flux tubes; explosive instability in the multiwave interactions; energetically open circuit leading to understanding of the observed variety of coronal structure formation, and others. These concepts are discussed

vis-à-vis pertinent observational data. Extremely important is assessment of collective phenomena in the ensembles of magnetic flux tubes randomly distributed in space and over their physical parameters making the rarefied ensembles in the quiet sun, more crowded families in plages, and dense conglomerates in sunspots and active regions.

The book contains also examples where, conversely, the new theory developments were prompted and enabled by the observations. One can mention the observations of continuous fragmentation of flux tubes accompanied by generation of mass flows, which turned out to be consistent with magnetoacoustic streaming—an effect analogous to Faraday's acoustic streaming. Likewise, the flux tube reconnections and post-reconnection processes that occur in high plasma beta environment have clearly demonstrated the need for significant extensions of the existing theory that focused on low beta coronal reconnections.

The reader will also find descriptions of such intriguing and not fully understood phenomena as the bullwhip effect—an explosively growing amplitude of flux tube oscillation; a greenhouse-like effect, where the temperature under the prominences grows much higher than the expected coronal temperatures; and the effects of a spatiotemporal echoes in the series of recurrent flares and microflares.

The work was done in Lawrence Livermore National Laboratory. The Lab's hospitality is greatly acknowledged. I am particularly grateful to Robert Becker, Kem Cook, Jim Sharp, Charles Alcock, John Bradely, and David Dearborn.

I would like to thank my former colleagues from Landau's theoretical department, Kapitza's Institute for Physical Problems in Moscow, where I received my graduate degrees and worked for years on quantum vortices in superfluid Helium and Type II superconductors. My special thanks go to my teachers Isaak Khalatnikov (my Diploma adviser), Lev Pitaevskii, and Alexei Abrikosov, my Ph.D. advisers.

My interest in solar physics dates back to the 1970s, when I once came across an early paper by Howard and Stenflo about small-scale magnetic flux tubes on the sun. I was captivated by this beautiful subject. I am grateful to Jan Stenflo and Robert Howard not only for their excellent paper, which triggered my lifetime interest, but for all the meetings and discussions that I have had with them later.

I would like to thank Henk Spruit, Gene Parker, Bernie Roberts, and Gene Avrett, who happened to be my first foreign correspondents in the field of solar physics. After about a decade and a half of working on magnetic flux tubes (still back in the Soviet Union), I realized that my results were not known in the West. I then chose these outstanding physicists and sent them some of my offprints. All responded. Henk Spruit immediately made me an invited speaker at the IAU Symposium. Gene Parker was also quick, but I found out about it only seven months later when I was summoned by the authorities and presented a huge tattered box full of papers for identification and explanation what it all meant. It meant that Gene Parker sent me all his papers without any note. Berny Roberts together with Eric Priest invited me to the University of St Andrews for several weeks to work together. I visited Gene Avrett in Harvard Smithsonian Center for Astrophysics several times and had wonderful communications with him and other researchers in



the CFA, especially with Shadia Habbal and Wolfgang Kalkofen, whom I also thank a lot.

I am pleased to thank all my collaborators, particularly Toshi Tajima, Barry LaBonte, Jun-ichi Sakai, Shadia Habbal, Richard Woo, Tom Berger, Mandy Hagenaar, and Zoe Frank. I am especially grateful to Dick Shine. Many beautiful results obtained from observations and described in this book would not have been here without his insight and help.

I would like to thank Alan Title, Philip Scherrer, and Ted Tarbell for not only being my collaborators, but also as trusting people who gave me a job at Stanford Lockheed Institute for Space Research. No CV, no references, and no questions were asked.

Finally, I am extremely grateful to my husband Dmitri (Mitya) Ryutov for his patience and encouragement expressed sometimes in my native Georgian.

Livermore, CA

Margarita Ryutova

# Contents

<b>1</b>	<b>The Sun's Magnetic Fields</b> . . . . .	1
1.1	The Sun as a Star . . . . .	1
1.1.1	Legacy of Ancients . . . . .	1
1.1.2	Hidden Interior . . . . .	3
1.1.3	Magnetic Dipole . . . . .	4
1.2	Magnetic Surface . . . . .	6
1.2.1	Quiet Sun . . . . .	7
1.2.2	Sunspots and Active Regions . . . . .	8
1.2.3	Plages . . . . .	10
1.2.4	High Latitudes and Polar Regions . . . . .	11
1.3	Mass Flows . . . . .	12
1.4	Magnetic Skeleton . . . . .	18
	References . . . . .	20
<b>2</b>	<b>A Quick Look on Small Scale Flux Tubes</b> . . . . .	21
2.1	Early Years . . . . .	21
2.1.1	First Direct Observational Signs of Magnetic Flux Tubes . . . . .	22
2.1.2	The Sunspot Dilemma . . . . .	23
2.2	Elements of Theory for de Facto Flux Tubes . . . . .	25
2.3	Numerical Visualization and Observations . . . . .	28
2.4	Filamentary Structures in Laboratory and Universe . . . . .	32
	References . . . . .	37
<b>3</b>	<b>Intrinsic Properties of Flux Tubes—Wave Phenomena</b> . . . . .	39
3.1	Equations of Motion or How Are Tube Waves Excited . . . . .	39
3.1.1	Equation of Motion for a Single Flux Tube . . . . .	41
3.1.2	Macroscopic Motions of an Ensemble of Flux Tubes . . . . .	42
3.2	Absorption of Acoustic Waves—Landau Resonance . . . . .	45
3.3	Effects of Noncollinearity of Flux Tubes . . . . .	48

3.4	Exact Theory of Linear Oscillations of Magnetic Flux Tube . . .	49
3.5	Radiation of Secondary Waves by Oscillating Flux Tubes . . . .	51
3.6	Scattering of Acoustic Waves and Maximum Energy Input . . .	53
3.7	Axisymmetric Oscillations of Flux Tube . . . . .	54
3.7.1	Types of $m = 0$ Mode . . . . .	54
3.7.2	Equation of Motion for Sausage Oscillations . . . . .	56
3.7.3	Dispersion Relation . . . . .	58
3.7.4	Sausage and Fast Oscillations in Homogeneous Flux Tube . . . . .	60
3.7.5	Effects of Radial Inhomogeneities on Sausage Oscillations . . . . .	61
	References . . . . .	66
<b>4</b>	<b>Effects of Flux Tube Inhomogeneities and Weak Nonlinearity . . .</b>	<b>69</b>
4.1	Radially Inhomogeneous Flux Tube—Internal Resonances . . .	69
4.1.1	Anomalous Resonance in Kink Oscillations . . . . .	69
4.1.2	Alfvén Resonance . . . . .	72
4.2	Boundary Value Problem . . . . .	75
4.2.1	Phase-Mixing in Flux Tubes . . . . .	75
4.2.2	Phase-Mixed Torsional Waves . . . . .	76
4.2.3	Phase-Mixed Kink Oscillations . . . . .	78
4.3	Longitudinal Resonances . . . . .	80
4.3.1	Loss of Radial Equilibrium . . . . .	81
4.3.2	Bullwhip Effect . . . . .	83
4.4	Standing Resonances and the Temperature Jump . . . . .	87
4.4.1	Growth of the Oscillation Amplitude—First Resonance . . . . .	88
4.4.2	Spectral Density and Strong Enhancement of the Oscillation Amplitude . . . . .	90
4.5	Weakly Nonlinear Waves in Flux Tubes . . . . .	91
4.5.1	Nonlinear Kink Oscillations—KdV-Bürgers Equation . . . . .	91
4.5.2	Possibility of Solitary Sausage Wave . . . . .	96
	References . . . . .	97
<b>5</b>	<b>Flux Tube Dynamics in the Presence of Mass Flows . . . . .</b>	<b>99</b>
5.1	Kelvin–Helmholtz Instability and Negative-Energy Waves . . . .	99
5.2	Shear Flow Instabilities in Magnetic Flux Tubes . . . . .	103
5.2.1	Specifics of Kelvin–Helmholtz Instability Along Flux Tubes . . . . .	103
5.2.2	Flux Tubes and Negative-Energy Waves (NEWs) . . . .	104
5.3	Basic Equations of Flux Tube Oscillations with Shear Flows . . . . .	106

5.4	Dissipative Instabilities of Negative-Energy Kink Oscillations . . . . .	107
5.5	Radiative Instability of Flux Tube Oscillations in the Presence of Flows . . . . .	110
5.5.1	Sausage Oscillations . . . . .	111
5.5.2	Kink Oscillations . . . . .	112
5.6	Parity of Negative and Positive Energy Waves . . . . .	113
5.7	Explosive Instability of Negative-Energy Waves . . . . .	115
5.8	Subcritical Mass Flows—Absence of Instabilities . . . . .	116
5.8.1	Can the Alfvén Waves Heat the Corona? . . . . .	117
5.8.2	Effect of Mass Flows on the Efficiency of Heating by Alfvén Waves . . . . .	118
5.9	Phase Mixed Alfvén Waves at Sub-alfvénic Mass Flows . . . . .	120
5.9.1	Damping Rate and Height of Energy Release . . . . .	120
5.9.2	Observable Morphological Effects . . . . .	122
5.10	The Asymptotic Behavior of the Total Energy Flux . . . . .	124
5.11	The Wave Extinction in the Presence of Downflows . . . . .	126
	References . . . . .	134
<b>6</b>	<b>Collective Phenomena in Rarefied Ensembles of Flux Tubes . . . . .</b>	<b>137</b>
6.1	Response of Flux Tubes to Propagation of Sound Waves . . . . .	137
6.1.1	Energy Exchange Between the Acoustic Waves and Ensembles of Flux Tubes . . . . .	138
6.1.2	Near-Resonance Condition . . . . .	140
6.2	Nonlinear Estimates of the Maximum Energy Input . . . . .	141
6.3	Axisymmetric Oscillation in Flux Tube Ensembles . . . . .	145
6.3.1	Equations of Motion . . . . .	145
6.3.2	Dispersion Relation—Resonance and Frequency Shift . . . . .	147
6.4	The Interaction of Unsteady Wave Packets with an Ensemble of Flux Tubes . . . . .	151
6.5	Spreading of the Energy Absorption Region—“Clouds of Energy” . . . . .	154
6.5.1	Large Wave Packets . . . . .	155
6.5.2	Short Wave Packets—Energy Absorption and Release . . . . .	157
6.6	The Energy Transfer from Unsteady Wave Packets to the Medium . . . . .	161
	References . . . . .	165

<b>7</b>	<b>Effects of Magnetic Flux Tubes in Helioseismology</b> . . . . .	167
7.1	The Time-Distance Tomography . . . . .	167
7.1.1	Key Points of Time-Distance Analysis with Magnetic Fields . . . . .	168
7.1.2	The Travel Times . . . . .	169
7.2	The Effects of Horizontal Flows . . . . .	171
7.3	Effects of Horizontal Magnetic Field . . . . .	172
7.4	Effects of Background Inhomogeneities . . . . .	174
7.4.1	Weak Inhomogeneities . . . . .	174
7.4.2	Variations of Flow Velocities . . . . .	175
7.5	Practical Use of the Forward–Backward Information . . . . .	176
7.5.1	Symmetry Properties . . . . .	176
7.5.2	Reconstruction of Subsurface Flow and Magnetic Fields from Observations . . . . .	177
7.6	Magnetic Corrections in a Vertically Stratified Atmosphere . . . . .	180
7.7	Estimate of the Energy Flux from Time-Distance Analysis . . . . .	182
7.7.1	Heat and Magnetic Energy Fluxes . . . . .	183
7.7.2	Contribution of Eddy Fluxes . . . . .	185
7.7.3	Reconstruction of Energy Fluxes from Observational Data . . . . .	186
7.8	Raman Spectroscopy of Solar Oscillations . . . . .	186
7.8.1	Stokes and Anti-stokes Satellites . . . . .	187
7.8.2	Using Raman Spectroscopy in Observations . . . . .	190
	References . . . . .	192
<b>8</b>	<b>Wave Phenomena in Dense Conglomerate of Flux Tubes</b> . . . . .	193
8.1	Propagation of MHD Waves in an Ensemble of Closely Packed Flux Tubes . . . . .	193
8.1.1	Basic Equations and Dispersion Relation . . . . .	194
8.1.2	Special Cases . . . . .	199
8.2	Dissipative Processes . . . . .	200
8.2.1	Weakly Inhomogeneous Medium . . . . .	201
8.2.2	Medium with Moderate and Strong Inhomogeneities . . . . .	203
8.2.3	Dissipation by Thermal Conduction . . . . .	204
8.2.4	Dissipation by Viscosity . . . . .	206
8.2.5	Total Dissipation Rate . . . . .	207
8.3	Anomalous Damping at Small Wavevectors . . . . .	209
8.4	Absorption of P-Modes by Sunspots and Active Regions—Observations . . . . .	211
8.5	The Interpolation Formula and Comparison with Observations . . . . .	215
	References . . . . .	220

<b>9</b>	<b>Nonlinear Wave Phenomena in Dense Conglomerate of Flux Tubes</b> . . . . .	221
9.1	Nonlinear Equations in Strongly Inhomogeneous Medium . . . . .	221
9.2	Formation of Shocks Across Small-Scale Inhomogeneities . . . . .	225
9.2.1	Validation of the Overturning Condition . . . . .	227
9.3	Effect of Inhomogeneities on the Dispersion Properties of the System . . . . .	228
9.3.1	Basic Equations . . . . .	228
9.3.2	Dispersion Relation . . . . .	230
9.3.3	KdV—Bürgers’ Equation with Strong Inhomogeneities . . . . .	232
9.4	Numerical Analysis . . . . .	233
9.4.1	The Model . . . . .	233
9.4.2	Formation of Shock Waves . . . . .	234
9.4.3	Energy Dissipation . . . . .	236
	References . . . . .	239
<b>10</b>	<b>Magnetosonic Streaming</b> . . . . .	241
10.1	Secondary Flows—Boundary Layer Effects . . . . .	241
10.1.1	Acoustic Streaming—History and Nature of Faraday’s Effect . . . . .	241
10.1.2	Secondary Flows in Magnetohydrodynamics . . . . .	243
10.2	Magnetosonic Streaming Due to the Action of Ponderomotive Force . . . . .	244
10.3	Process of Filamentation and Diffusive Vanishing of Magnetic Flux Tubes . . . . .	249
10.3.1	Diffusive Broadening of Flux Tube . . . . .	250
10.3.2	Quantitative Estimates—Lifetimes and Spatial Scales of Flux Tubes . . . . .	252
10.4	Generation of Mass Flows Due to the Absorption Mechanisms . . . . .	254
10.5	Numerical Analysis . . . . .	257
10.5.1	Basic Equations and Numerical Method . . . . .	258
10.5.2	Numerical Results . . . . .	259
10.6	Intrinsic Nature of Flux Tube Fragmentation . . . . .	263
	References . . . . .	265
<b>11</b>	<b>Moving Magnetic Features (MMFs)</b> . . . . .	267
11.1	Types of MMFs and Their Observed Properties . . . . .	267
11.2	Impossibility of the Origin of MMF’s in Conservative Systems . . . . .	269
11.2.1	The Mechanism . . . . .	271
11.3	Nonlinear Kink and Its Evolution in the Presence of Shear Flows . . . . .	272

11.4	Soliton and Shocklike Formations Along the Flux Tube—Numerical Studies . . . . .	275
11.5	Observations and Comparison with Theory . . . . .	279
11.6	Quantitative Analysis . . . . .	283
11.7	Unification of Known Types of Moving Magnetic Features . . . . .	287
11.8	Impact of MMFs on the Overlying Atmosphere . . . . .	290
11.9	Anticorrelation Between Population of MMF's and Coronal Loop Formation . . . . .	294
	References. . . . .	298
<b>12</b>	<b>Reconnection of Flux Tubes—Specifics of High Plasma <math>\beta</math></b> . . . . .	<b>299</b>
12.1	Basics of Magnetic Reconnection . . . . .	299
12.2	Photospheric Reconnections—No Immediate Gain in Energy . . . . .	304
12.2.1	Specifics of Photospheric Reconnections . . . . .	305
12.2.2	Flux Tubes Carrying Different Amount of Magnetic Flux . . . . .	308
12.2.3	Number of Events—Importance of Noncollinearity of Flux Tubes. . . . .	311
12.3	Dynamics of Post-reconnection Products . . . . .	312
12.3.1	Self-similarity of Solution . . . . .	313
12.3.2	Energy Analysis . . . . .	315
12.3.3	Transsonic Motion . . . . .	316
12.4	Dynamics of U-shaped Flux Tubes . . . . .	317
12.5	Dynamics of $\cap$ -shaped Flux Tube . . . . .	319
	References. . . . .	323
<b>13</b>	<b>Post-reconnection Processes—Shocks, Jets, and Microflares</b> . . . . .	<b>325</b>
13.1	Key Regularities Observed in the Photosphere/Transition Region . . . . .	325
13.2	Post-reconnection Shocks and Hydromagnetic Cumulation of Energy . . . . .	328
13.2.1	Head-On Convergence of Shock Fronts . . . . .	329
13.2.2	Energy Distribution Between Heat, Jet, and Their Combinations. . . . .	331
13.3	Observation of Photospheric Reconnections and Their Impact on Overlying Atmosphere . . . . .	334
13.3.1	Microflares, Jets, and Their Combinations . . . . .	336
13.3.2	Effects of Converging Supergranular Flows . . . . .	339
13.4	Key Elements of Energy Production and Observation of Shocks . . . . .	341

13.5	Explosive Events . . . . .	344
13.6	Response of the Upper Atmosphere to Reconnection of Unipolar Flux Tubes . . . . .	348
	References. . . . .	350
<b>14</b>	<b>Photospheric Network as Energy Source for Quiet Sun Corona . . .</b>	<b>351</b>
14.1	Post-reconnection Processes in Arbitrarily Magnetized Environment . . . . .	351
14.1.1	Magnetic Loop Arcades in the Chromosphere . . . . .	352
14.1.2	Post-reconnection Shocks in Upper Atmosphere—Types and Characters . . . . .	355
14.2	Heights of Shock Formation. . . . .	358
14.3	Energy Release in the Chromosphere-Transition Region . . . . .	363
14.3.1	Quantitative Analysis . . . . .	363
14.3.2	Total Energy Flux in Quiet Sun Atmosphere . . . . .	367
14.4	Magnetic Energy Avalanche and the Fast Solar Wind . . . . .	368
	References. . . . .	371
<b>15</b>	<b>Response of the Corona to Magnetic Activity in Underlying Plage Regions . . . . .</b>	<b>373</b>
15.1	Magnetic Imprint of Plage Regions in the Corona. . . . .	373
15.2	Coronal Dynamics Above Unipolar and Mixed Polarity Plages . . . . .	375
15.3	Properties of Braidlike Coronal Structures . . . . .	378
15.4	Comparison of Coronal Emission Above Mixed Polarity and Unipolar Plages . . . . .	381
15.5	Energy Extraction Mechanisms from the Ensembles of Photospheric Flux Tubes . . . . .	385
15.5.1	Mixed Polarity Plage. . . . .	385
15.5.2	Unipolar Plage . . . . .	387
15.5.3	N-Solitons . . . . .	389
	References. . . . .	393
<b>16</b>	<b>Electrodynamic Coupling of Active Region Corona with the Photosphere . . . . .</b>	<b>395</b>
16.1	The Problem of Multiface Corona. . . . .	395
16.2	Emerging Magnetic Flux and Structure Formation in Overlying Atmosphere. . . . .	397
16.3	Current Drive Mechanisms Associated with the Emerging Magnetic Flux . . . . .	403
16.3.1	Proper Motion . . . . .	404
16.3.2	Acoustic Waves . . . . .	404
16.3.3	Alfvén Waves . . . . .	406



16.4	Energy Flow Throughout Solar Atmosphere . . . . .	408
16.4.1	An Equivalent Circuit—Earlier Attempts . . . . .	409
16.4.2	LRC Circuit with Mutual Inductance (Transition Region) . . . . .	410
16.5	Energetically Open Circuit . . . . .	413
16.6	Evolution of Current Systems . . . . .	418
16.6.1	Linear Regime . . . . .	418
16.6.2	Nonlinear Regime . . . . .	419
16.7	Quantitative Analysis . . . . .	422
16.7.1	Examples . . . . .	423
16.8	Limiting Currents and Filamentary Structures . . . . .	426
	References . . . . .	432
<b>17</b>	<b>Fine Structure of Penumbrae: Formation and Dynamics . . . . .</b>	<b>433</b>
17.1	Peculiarities of Sunspot Penumbrae—Observations . . . . .	433
17.2	Dynamics of Penumbral Filaments and Ongoing Reconnections . . . . .	437
17.3	Formation of Filamentary Penumbrae . . . . .	441
17.3.1	Phenomenology of Basic Mechanism . . . . .	442
17.3.2	Filamentary Structure of Sunspot . . . . .	443
17.3.3	Properties of Individual Filaments . . . . .	444
17.4	Screw Pinch Instability and Dark Cores . . . . .	446
17.4.1	More on Substructures of Filaments . . . . .	449
17.4.2	Effects of Axial Flows . . . . .	450
	References . . . . .	452
<b>18</b>	<b>Bow Shocks and Plasma Jetting over Penumbrae . . . . .</b>	<b>455</b>
18.1	Response of the Overlying Atmosphere to Penumbral Dynamics . . . . .	455
18.1.1	Penumbral Transients—Double Structures and Jets . . . . .	456
18.1.2	Viewing Under Different Angles . . . . .	459
18.1.3	Brief Summary of Properties . . . . .	464
18.2	Phenomenology and Quantitative Analysis . . . . .	466
18.2.1	Dynamics of U-shaped Filaments . . . . .	467
18.2.2	Nature of Double Structures . . . . .	469
18.3	Bow Shocks . . . . .	470
18.4	Energy Release and Lifetime of Bright Transients . . . . .	473
	References . . . . .	477
<b>19</b>	<b>Self-organization in the Corona and Flare Precursors . . . . .</b>	<b>479</b>
19.1	Well-Organized Multithreaded Coronal Arcades—Slinkies . . . . .	479
19.2	Essential Difference Between “Regular” and Slinky-Producing Flares . . . . .	482
19.3	Precursors and Predictability . . . . .	488

19.4 Exemplary Case of X-Class Flare and Formation of Slinkies . . . . . 491

19.5 Phenomenology of Energy Build Up and Quantitative Analysis . . . . . 495

19.6 Recurrent Flares and Echoes . . . . . 501

    19.6.1 Landau Damping, Memory, and Spatiotemporal Echoes . . . . . 502

    19.6.2 Echo Effects in Slinkies. . . . . 505

    19.6.3 Spatial and Temporal Recurrences in Flares . . . . . 507

References. . . . . 510

**20 Quiescent Prominences . . . . . 513**

    20.1 Background—Problem of Stability . . . . . 513

    20.2 Large-Scale Observed Regularities . . . . . 516

    20.3 Formation of Prominence Cavity and Helical Structures. . . . . 521

        20.3.1 The Case of the 16 August 2007 Prominence. . . . . 525

        20.3.2 Phenomenology of Cavity Formation. . . . . 526

    20.4 Regular Series of Plumes—Multimode Regime of Rayleigh–Taylor Instability . . . . . 529

        20.4.1 Practical Use . . . . . 530

    20.5 Fast-Growing Plumes—Nonlinear Regime . . . . . 533

        20.5.1 Mushroom Formation . . . . . 534

        20.5.2 Two-Bubble Competition. . . . . 537

    20.6 Greenhouse-Like Effect . . . . . 537

References. . . . . 540

**Index . . . . . 543**

# Acronyms

AAS	American Astronomical Society
AIA	Atmospheric Imaging Assembly (on board of SDO)
APS	American Physical Society
BBSO	Big Bear Solar Observatory
CDS	Coronal Diagnostics Spectrometer (on board of SOHO)
DOT	Dutch Open Telescope
EIS	Extreme ultraviolet Imaging Spectrom (on board of Hinode)
EIT	Extreme ultraviolet Imaging Telescope (on board of SOHO)
EOS	Earth Observing System
EPOD	Earth Science Picture of Day
ESO	European Southern Observatory
EUV	Extreme Ultraviolet
GOES	Geostationary Operational Environmental Satellite
HAO	High Altitude Observatory
HEP	High Energy Proton (flux)
HMI	Helioseismic and Magnetic Imager (on board of SDO)
IOP	Institute of Physics
ISP	Institute for Solar Physics
JPL	Jet Propulsion Laboratory
KdV	Korteweg-de Vries equation
KH	Kelvin–Helmholtz (instability)
LASCO	Large Angle and Spectrometric Coronagraph Experiment (on board of SOHO)
MDI	The Michelson Doppler Imager (on board of SOHO)
MMFs	Moving Magnetic Features
NEWS	Negative Energy Waves
NST	New Solar Telescope
OCIW	Observatory of the Carnegie Institute of Washington
RT	Rayleigh–Taylor (instability)
SOHO	The Solar and Heliospheric Observatory

SDO	Solar Dynamics Observatory
SOT	Solar Optical Telescope (on board of Hinode)
SST	Swedish 1-m Solar Telescope (SST) on La Palma
SUMER	Solar Ultraviolet Measurements of Emitted Radiation (on board of SOHO)
SVST	Swedish Vacuum Solar Telescope on La Palma
SXT	Soft X-ray Telescope (on board of Yohkoh)
TRACE	Transition Region and Coronal Explorer
UV	Ultraviolet

# Chapter 1

## The Sun's Magnetic Fields

**Abstract** In this introductory chapter we first briefly describe some overall characteristics of the sun, and then take a closer look at the sun's magnetic surfaces. We shall see that highly advanced space and ground-based observations show various magnetic elements, their clusters, and mass flows in great detail. The chapter is concluded with the description of the magnetic skeleton of the sun showing the well-defined imprint of the photospheric magnetic field pattern at all available temperatures from low chromosphere to the outermost corona.

### 1.1 The Sun as a Star

#### *1.1.1 Legacy of Ancients*

Since ancient times all people on the earth have considered the sun as their own. They knew that they depended on it, and wanted to know why.

Back in 3000 BC the Egyptians believed that the sun is He who is above and has created himself from himself, and the earth and sky, and man was born from his tears.

The Chinese at that time pragmatically built observatories to map out time, record sunspots, flares, prominences, and eclipses. The origin of the sun and the fear to lose it was described along the lines: Of all celestial objects it is the Sun that good heaven put in the China's sky and give it to Chinese people, animals and plants, and when Dark force, the dragon, eats the sun at bad times, inspired brave people of China to scare the dragon with loud gongs. And it always worked. People of China were first to record and predict the solar eclipses.

And, yet, it was Pythagoras (569–475 BC) and his followers who formulated the first mathematical basis of heaven (“Number is within of all things”). They postulated that the universe is in constant circular motions, and that the sun and all the heavenly objects revolve about a single central fire. They declared that the sun is spherical and has a substance similar to glass that collects rays from the central fire, and transmits them to us. Most importantly, they linked the geometry of harmonious motions with its physical nature. Pythagoras said: “from the sun and moon and from the stars in so great number, and of so great size, moving so swiftly, there must necessarily

arise a sound inconceivably great... and the sound of the stars moving on in a circle becomes musical.” Concluding that the universe exists in accordance with musical harmony, so the sun also makes a harmonious period. The Pythagoreans believed that the moon has an earthy appearance, and this is because, “like our earth, it is inhabited throughout by animals and plants, only larger and more beautiful; for the animals on it are fifteen times stronger, not having any sort of excrement, and their day is fifteen times as long as ours.”

The harmonious cosmological model of the Pythagoreans did not receive immediate development.

In the words of Plutarch “Anaxagoras was the first to put in writing, most clearly and most courageously of all men, the explanation of the moon’s illumination and darkness, ... and even his account was not common property but was still a secret, current only among a few and received by them with caution or simply on trust.” Anaxagoras (500–497 BC) declared that “the moon has a light which is not its own but comes from the sun.” Anaxagoras’s cosmology teaches that the world began with a vortex setup, that the rotatory movement began at one point and then gradually spread, taking in wider and wider circles. And then, “in consequence of the violence of the whirling motion stones were torn from the earth and kindled into stars.”

Democritus, who according to his own account “was young when Anaxagoras was old” has in fact reinstated the views of Anaxagoras, but unlike Anaxagoras believed that the earth is flat and rides on the air. Democritus believed that the earth remains where it is because it is in equilibrium and there is no reason why it should move one way rather than another. At the same time Democritus’ vision of heaven was so advanced that it could fit a modern astronomy textbook: “There are worlds infinite in number and differing in size. In some there is neither sun nor moon, in others the sun and moon are greater than with us, in others there are more than one sun and moon. The distances between the worlds are unequal, in some directions there are more of them, in some fewer, some are growing, others are at their prime, and others again declining, in one direction they are coming into being, in other they are waning. Their destruction comes about through collision with one another. Some worlds are destitute of animal and plant life and of all moisture.”

But it was not until Plato that Astronomy became a science comparable to Mathematics as it was prescribed by Pythagoras.

Plato (427 BC) said: “We shall pursue astronomy, as we do geometry, by means of problems, and we shall dispense with the starry heavens, if we propose to obtain a real knowledge of astronomy, and by that means to convert the natural intelligence of the soul from useless to a useful possession.”

And long voyage of theory of harmonious motions with earth at the center continued for centuries. It swallowed the first heliocentric model of the universe by Aristarchus of Samos, who not only hypothesized that “fixed stars and the sun remain unmoved, that the earth revolves about the sun,” but measured sizes of the earth, moon, and sun, and their distances. He described the moon as a satellite of the earth. He declared that the sizes of the earth and the sun are negligible in size compared

to the universe. He radically improved the sun-dial, and regarded time as “quantity expressed by things in motion and at rest.”

The heliocentric system was abandoned for another 1,800 years until the time of Copernicus. With or without Copernicus the time came for putting the sun to where it belonged.

In what follows, the overall characteristic of the sun is briefly described. Then the sun’s magnetic surfaces and its magnetic skeleton sustaining the overlying atmosphere is presented in view of the most recent observations.

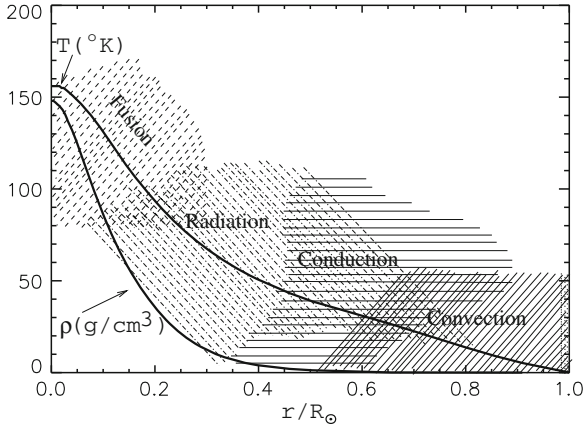
This book is devoted solely to the physics of small-scale magnetic flux tubes, being the first attempt to consolidate problems involving the intermittent magnetic fields per se. There are of course excellent books on all the aspects of solar physics accumulated during the decades of the subject studies (Athay 1976; Moffatt 1978; Parker 1979; Sturrock et al. 1986; Zirin 1988; Cox et al. 1991; Somov 1991; Strong et al. 1999; Dwivedi 2003; Severny 2004; Golub and Pasachoff 2010; Priest 2014). This fairly incomplete list of references which themselves contain rich bibliographies is given in order to direct the reader to valuable information on various solar subjects that are beyond the scope of this book.

### ***1.1.2 Hidden Interior***

The sun today belongs to a family of moderately warm yellow dwarfs, and is in its middle age.

Almost the entire energy of the sun produced by nuclear fusion in the core is transported throughout the rest of the solar interior, its visible atmosphere, and out into space. This process is determined by the composition of the medium, its temperature, density, pressure, and internal energy. In high density and high temperature plasmas under conditions immediately outside the solar core, the energy is transported by radiation. Plasma density here is still so high that photons liberated by nuclear fusion travel a short distance and soon are either scattered or absorbed and reemitted by other particles. At lower temperatures, but still high densities, electrons provide another means of energy transport-conduction. This process occupies the region approximately up to  $0.74 R_{\odot}$ . Farther outward, the plasma density and temperature rapidly drop. Sharp temperature gradient provides conditions for convective instability: a heated plasma element (not a particle!) becomes buoyant and rises some distance, called the mixing length, before it falls back due to releasing its energy into the surrounding plasma. The overall qualitative picture of the stages of energy production and transport in the solar interior are sketched in Fig. 1.1. Regions of action of various mechanisms must obviously overlap.

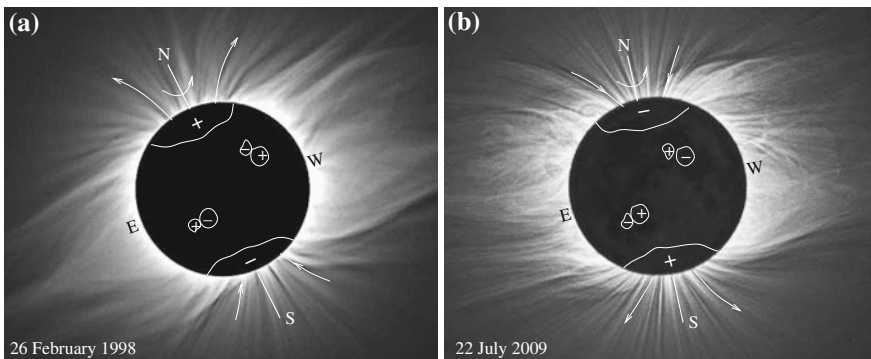
The sun’s interior is hidden from us and its true structure and physical processes are a subject of guessing and modeling. What we see well, however, is that the photosphere, chromosphere, multi-temperature corona, and its extension to interplanetary space. These regions supply us with invaluable information for studying the sun as a star.



**Fig. 1.1** Schematic of the energy production and transport in solar interior. Data for the temperature and density plots are taken from Bahcall and Ulrich (1988)

### 1.1.3 Magnetic Dipole

The sun as a star appears in the form of a modestly magnetized well-shaped dipole with a mean field intensity of about 1 G (Fig. 1.2). What seems however as a neat dipole is in fact a tremendously complicated magnetic body, very inhomogeneous, intermittent, and highly dynamic. And yet, the overall properties of magnetic fields and the general pattern of their behavior are in many ways quite systematic.



**Fig. 1.2** Magnetic dipole. The background cartoons are the images of total solar eclipse: **a** 1998 February eclipse, and **b** 2009 July eclipse photographed by Miloslav Druckmüller. Note that the tilt of the sun's axis is different during the two eclipses. On 26 February 1998 the tilt is near its maximum. This is because when viewed from Earth the tilt is maximum during the first week of March and decreases to minimum toward the first week of June (second maximum and minimum fall in the first week of September and the first week of December, respectively). Reprinted from <http://www.zam.fme.vutbr.cz/~druck/eclipse/>. Courtesy of M. Druckmueller

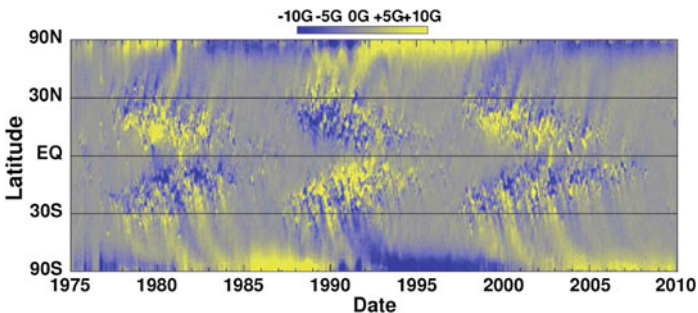


For example, measurements of the magnetic flux of a “dipole” over many solar cycles show that its intensity remains about the same and ranges in the interval of  $1.5\text{--}2.5 \times 10^{22}$  Mx. The axis of magnetic dipole is tilted at about  $\pm 7.23^\circ$  with respect to the ecliptic, and it also remains steady (in the sun’s coordinate system). The magnetic flux of the dipole mainly comprises of the high latitude magnetic fields, where in average it is unipolar and uniquely determines the polarity of a dipole.

An ensemble of polar magnetic fields being quite irregular and variable at short timescales, shows remarkably regular pattern at large timescales: the mean magnetic flux of a dipole periodically weakens and subsequently undergoes a reversal of polarity. This happens roughly every 10–11 years and is directly related to periodic change in sunspot numbers observed during the centuries and known as 11-year solar cycle.

The reversal of a dipole polarity marks the abrupt changes in the configuration of sunspots and active regions over the entire solar surface. Most remarkable is the appearance of new sunspots at latitudes of  $38\text{--}40^\circ$ —this is the highest range of latitudes for sunspots to appear. New sunspot groups in both hemispheres have magnetic polarities opposite to those of previous sunspot groups, i.e., the polarity reversal occurs here as well.

Farther in time, new sunspot groups emerge closer and closer to the equator in both hemispheres. The number of sunspots gradually increases and reaches the maximum in about 3–4 years. After that, fewer and fewer sunspots emerge in locations closer to the equator (Fig. 1.3). Sunspot groups are always organized in such a way that the leading sunspot tends to be closer to the equator, whereas the trailing sunspot is closer to the pole. The polarity of the following sunspot is always opposite to that of the pole. At the end of cycle when the last sunspots appear in the equatorial zone, the polarity reversal of a dipole is about to happen.



**Fig. 1.3** Diagram of the distribution of the sun’s magnetic field over three 11-year solar cycles. *Yellow* represents the magnetic field directed out of the sun. *Blue* represents the magnetic field into the sun. Sunspots themselves produce the “Butterfly” pattern at low latitudes. The sun’s meridional flow from the equator to the poles in each hemisphere carries magnetic remains of the sunspots to the poles. This produces the streaks seen at higher latitudes and reverses the magnetic polarity of the sun’s poles every 11 years. Reprinted from <http://solarscience.msfc.nasa.gov>. Image credit: NASA/ARC/David Hathaway

The time between two consecutive minima (or maxima) in the sunspot numbers and migration of the zone of their emergence, traditionally determined as the 11-year cycle, changes considerably during the centuries, and may range from 7 to 17 years. And, of course, the number of sunspots in every cycle changes considerably as well. There were periods of extremely low solar activity when sunspots were not observed at all. The most striking is the Mounder Minimum that occurred between 1645 and 1715. This period was called the Little Ice Age, during which the Thames and the canals of Venice were covered with ice. Progress in the analysis of radioactive Carbon 14 and Beryllium 10 that trace the influence of solar activity on the Earth provided information about the solar cycles back to hundreds of centuries (see, e.g. Lockwood (2013), and literature therein).

It is only natural to expect that the magnetism of other stars has the same nature. But it was not until the 1980s that this fact was confirmed. Although the magnetic field concentrations are not directly observable on stars, these areas produce strong emission in the Ca II H and K resonance lines in the optical, and the Mg II H and K lines in the ultraviolet diapason. Observing variations in Ca II H and K lines in main sequence stars, Wilson (1978) found that the solar type stars of type G2 and older indeed show cyclic variations. It was also found that the magnitude of these variations is of the same order as that for the sun (Vaughan 1980; White and Livingston 1981).

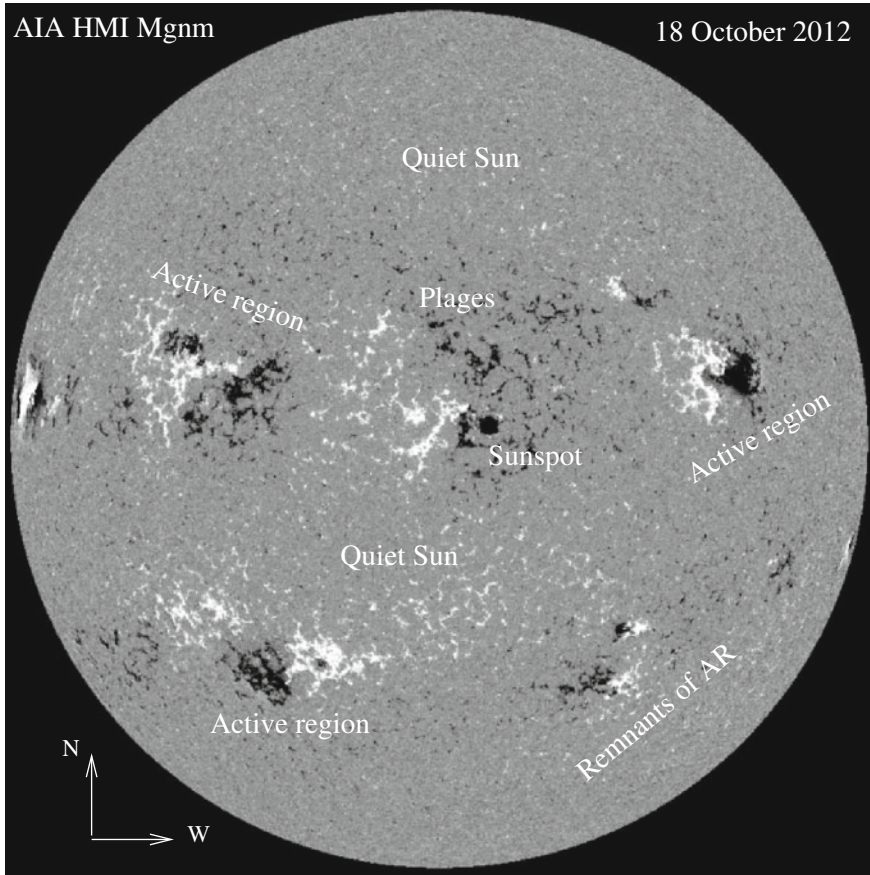
But it is only our sun that provides us with unprecedented details of its magnetism and behavior.

## 1.2 Magnetic Surface

Highly advanced space and ground observations have revealed amazing details of solar magnetism. The surface of the sun is the best source for obtaining information on how the magnetic field emerges and evolves, and how it is distributed over the surface. At any moment of time the solar surface is covered with uneven ensembles of magnetic elements having various spatial sizes, shapes, and lifetimes (Fig. 1.4).

Their distribution over space, so-called magnetic filling factor, also varies over space and time. The magnetic filling factor,  $f_m$  is a convenient parameter defined as  $f_m = S_m/S$ , where  $S$  is the area of interest, and  $S_m$  is the area occupied by the magnetic field. In terms of the filling factor, the solar surface can roughly be categorized as follows.

- Quiet sun—the largest regions of the solar surface covered by small magnetic flux tubes far removed from each other with average filling factor much less than unity,  $f_m \ll 1$ .
- Sunspots with filling factor of the order of unity,  $f_m \simeq 1$ .
- Active regions that are clusters of bipolar sunspots and surrounding them mixed polarity magnetic elements with average magnetic filling factor close to unity,  $f_m \leq 1$ .
- Remnant active regions consisting of mixed polarity elements with magnetic filling factor in the range of  $f_m \sim 0.3-0.6$ .



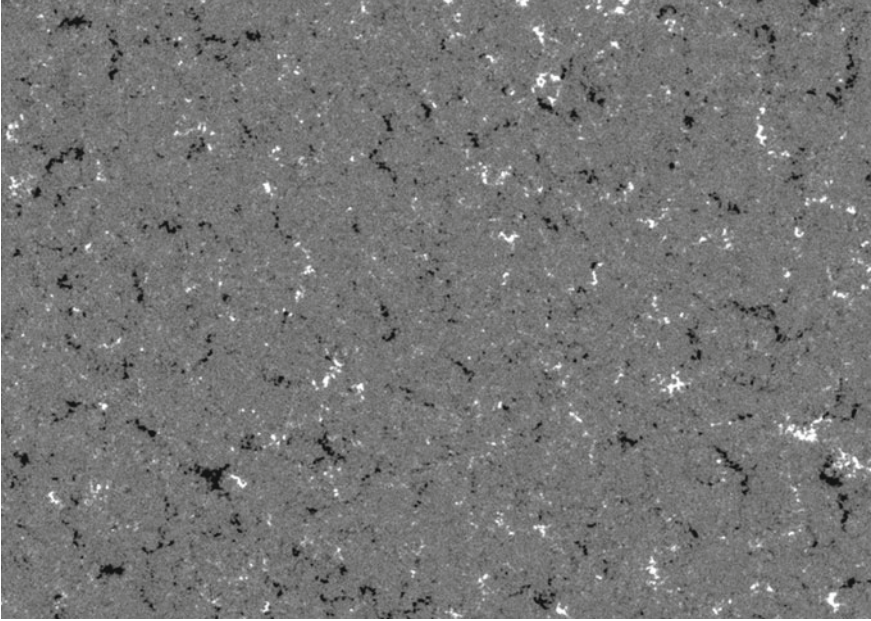
**Fig. 1.4** Full disk magnetogram taken by the AIA/HMI instrument on board of SDO. *White and black patches* represent line-of-sight (*vertical*) magnetic field of positive and negative polarities

- Plages, which are rarefied ensembles of either unipolar or mixed polarity elements with filling factor in the range of  $f_m \sim 0.2-0.35$ .

The magnetic elements that form these ensembles have their own substructures and consist of small-scale flux tubes. Size of the smallest constituents may be well below the resolution, which for the time being has reached a few tens of kilometers.

### 1.2.1 Quiet Sun

Most of the solar surface, in fact 90% of it is covered by small-scale magnetic elements—magnetic flux tubes. They usually trace the convective cell boundaries

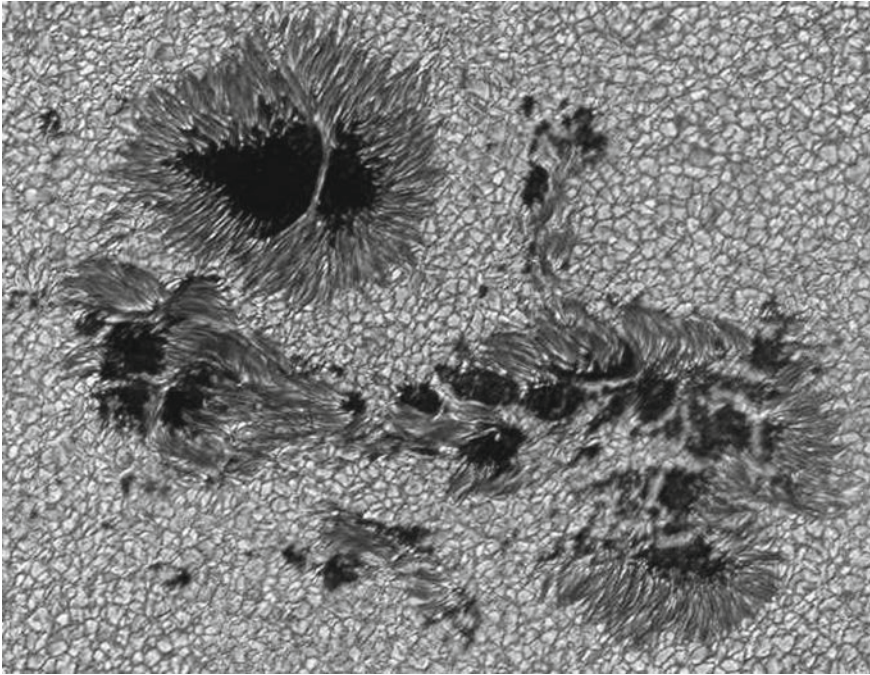


**Fig. 1.5** Fragment of a quiet sun magnetogram taken by HMI/SOT at the disk center. The field of view is  $346 \times 283 \text{ arcsec}^2$

at all scales, the smallest of which is the granulation network. The size of network granules ranges from a few hundred kilometers, to several arcseconds ( $1 \text{ arcsec} = 726 \text{ km}$ ). The network picture is well recognizable in the quiet sun magnetograms, where negative and positive magnetic flux tubes trace the granulation pattern and encircle it (Fig. 1.5). The lifetime of individual magnetic flux tubes ranges from a few minutes to a couple of hours. The entire supply of the “pepper and salt” magnetic flux forming quiet sun “magnetic carpet” is replaced in about 40h (Title and Schrijver 1997), which eventually provides a permanent energy supply to the overlying atmosphere.

### ***1.2.2 Sunspots and Active Regions***

Sunspots are huge conglomerates of magnetic flux concentrations seen as dark spots. Their temperature is about a thousand degrees lower than the average surface temperature. A closer look at sunspots reveals their extremely complex nature. For example, mature sunspots are usually surrounded by the penumbra: strong, almost vertical magnetic field of umbra, becomes more and more horizontal toward the periphery forming an “uncombed” system of thin magnetic filaments arcing radially outward from the umbra and terminating in the photosphere (Fig. 1.6). The inclination of



**Fig. 1.6** Image of the active region (AR 10375) in  $4,320\text{\AA}$  Blue Continuum covering  $100 \times 130$  arcsec area. Both, younger sunspot (*upper left*) and decaying AR (*bottom*) show well-developed filamentary penumbrae. One can see small bright points inside the umbrae, which are signs of their filamentary structure. Image taken by DOT on June 6, 2003. Reprinted from <http://www.staff.science.uu.nl>, courtesy of R. Rutten

the magnetic filaments is found to vary across the penumbra from  $45$  to  $90^\circ$  to the sunspot normal (Title et al. 1993). There are strong intensity inhomogeneities across the penumbra, resulting in a visual effect of interlaced dark and bright filaments.

The Evershed flow (unsteady plasma outflow at the photospheric level) is also found to be structured at the scale of the penumbral filaments. The flow is more horizontal than the mean magnetic field at all radii in the penumbra and has spatial correlation with dark penumbral filaments (Shine et al. 1994). The bright filaments are usually less horizontal thus making some angle with the Evershed flows. Livingston (1991), comparing images of sunspots with different exposures, came to the conclusion that the sunspot umbra also has a filamentary structure, and may exhibit the presence of vertical, diverging, and even horizontal filaments.

Newly emerged young sunspots sometimes do not develop penumbrae, and remain “naked.” These are called pores. Typically, they are  $3,000$ – $6,000$  km in size and live for many hours.

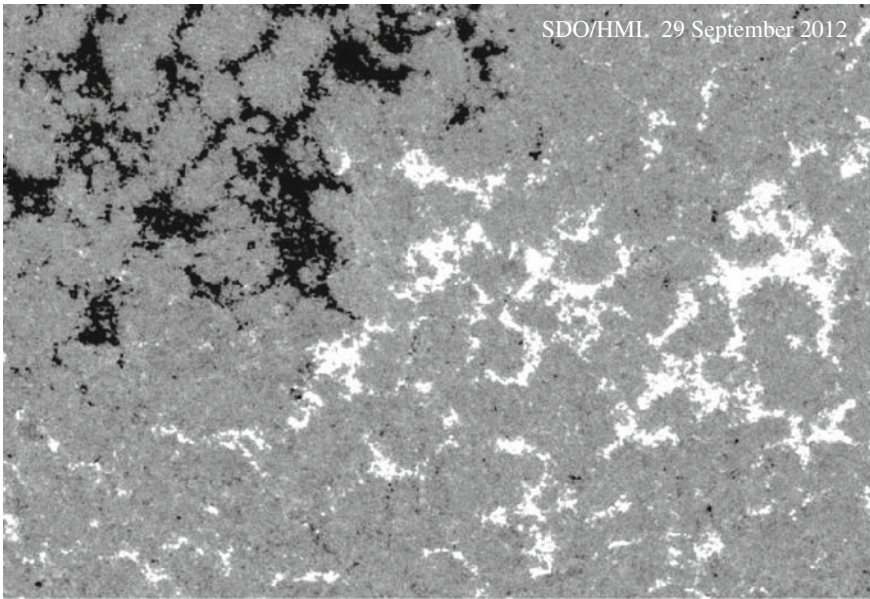
Sunspot formation and their appearance at a visible surface is a gradual process that may take hours and days. A complex conglomerate consisting of several sunspots

and pores, as shown in Fig. 1.6, takes several solar rotations to form, live, and decay. Due to a close neighborhood of opposite polarity formations the active regions harbor a wide range of electromagnetic phenomena that shape the overlying atmosphere: chromosphere, transition region, and corona. The latitudes of a complex active regions are also sites of the origin of a slow solar wind.

### 1.2.3 Plages

Plages are complex conglomerates of magnetic flux concentrations with average magnetic filling factor of about  $f \sim 0.2-0.3$ .

There are two major types of plages: mixed polarity plage, and plage dominated by one polarity magnetic elements. The origin of plages is mainly associated to the decaying active regions, but they may also form due to the subsurface magnetic activity leading to elevated rate of emergence of small-scale magnetic flux tubes. An average magnetic field in magnetic concentrations here is about 100 G. Figure 1.7 shows an example of a typical plage with average magnetic field strength exceeding 100 G, and a filling factor of about  $f \geq 0.3$ . Usually, plages resulting from remnant active regions are bipolar formations. The decaying sunspot leads to formation of



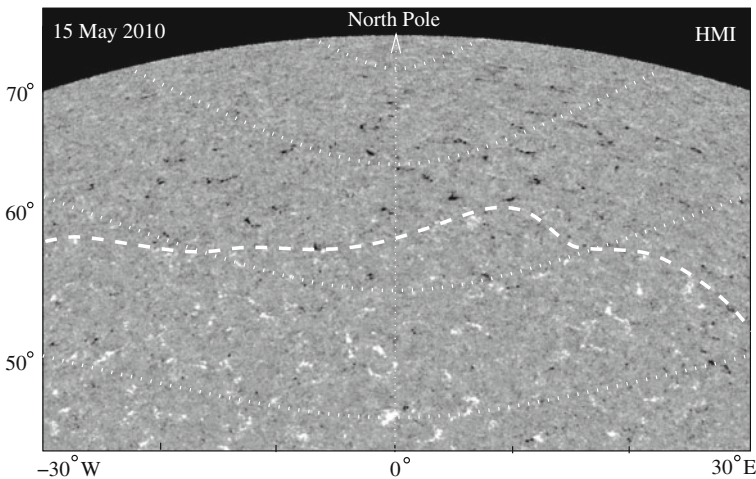
**Fig. 1.7** Image of a plage taken by the HMI/SDO instrument. *White* and *black patches* corresponding to positive and negative magnetic fluxes form typical unipolar plages. Note a well-defined supergranular pattern demarcated by magnetic flux concentrations. Field of view is  $150 \times 200$  arcsec

unipolar plages, which may overlap with the neighboring opposite polarity plage and form a mixed polarity region.

Dynamics of plages and their activity is extremely rich. There are common effects produced by unipolar and bipolar plages, but most importantly, each category has its own unique features.

### 1.2.4 High Latitudes and Polar Regions

As mentioned above, toward the end of the 11-year cycle active latitudes “shrink,” and remaining sunspots and sunspot groups migrate toward the equator, while the 10–11 year-old remnants of the previous cycle have already migrated toward the poles. The polarity of the pole has a polarity of the ending cycle where small-scale magnetic elements occupy the polar and high altitude regions. At the turn of a cycle the opposite polarity sunspots and sunspot groups start to emerge at about  $\pm 40^\circ$  latitudes. Newly emerged sunspots migrate toward the equator while their peripheral magnetic elements migrate toward the polar regions. Thus in the first half of a new cycle one observes the merging of the opposite polarity ensembles of small-scale magnetic elements of the previous cycle with those of a new cycle (Fig. 1.8). The filling factor of ensembles and the location of demarcation line between them plays a crucial role in the dynamics of the overlying atmosphere, the most spectacular of which is formation and evolution of quiescent prominences and polar plumes.



**Fig. 1.8** Magnetogram of high altitude solar region near the North pole shows the encounter of the ensemble of negative polarity network elements of a previous cycle with the ensemble of positive polarity magnetic elements coming from a new cycle. *White dashed line* is the approximate demarcation line between these regions

### 1.3 Mass Flows

The entire solar atmosphere from its visible surface to interplanetary space is pierced by a great variety of mass flows. They are observed in all temperature ranges, and may have steady, unsteady, and explosive character. Their velocities vary from a few tens of  $\text{km s}^{-1}$  to hundreds of  $\text{km s}^{-1}$ . The presence of flows dramatically changes the physical picture of any given event, leading often to formation of energetically open non-conservative systems. We will discuss several special cases associated with the presence of mass flows throughout the book. Here we briefly overview a few general patterns of mass flows.

The surface of the sun exhibits multiple-scale convective motions which traditionally are described as granular, mezogranular and supergranular pattern. Irregularly shaped granules with sizes ranging from a few hundred kilometers to arcseconds, uniformly cover the entire solar surface outside the pores and sunspots. The average lifetime of granules is about 8 min. In the center of granule a warm plume is rising with velocity  $\simeq 0.4 \text{ km s}^{-1}$  diverging and falling down at the edge of a granule. Figure 1.9 shows co-aligned images of a region containing several pores surrounded with unipolar plage and quiet sun patches. The top panels are the magnetogram and Dopplergram taken simultaneously by the SST instrument on Hinode. Line-of-sight magnetic field reaches  $\sim 2,300 \text{ G}$ . Dopplergram measurements give velocities ranging between  $\sim -1.2$  and  $1.6 \text{ km s}^{-1}$ . White dots correspond to downflows, black points to upflows. Note that downflows are usually associated with magnetic flux concentrations. The bottom left of Fig. 1.9 is the same region in G-band. The black box there singles out the region of emerging flux which is enlarged on the right, where the map of horizontal velocities restored from time series of the SST data are shown. The velocities are averaged over 20 min. Arrows indicate the direction of horizontal velocities and their value.

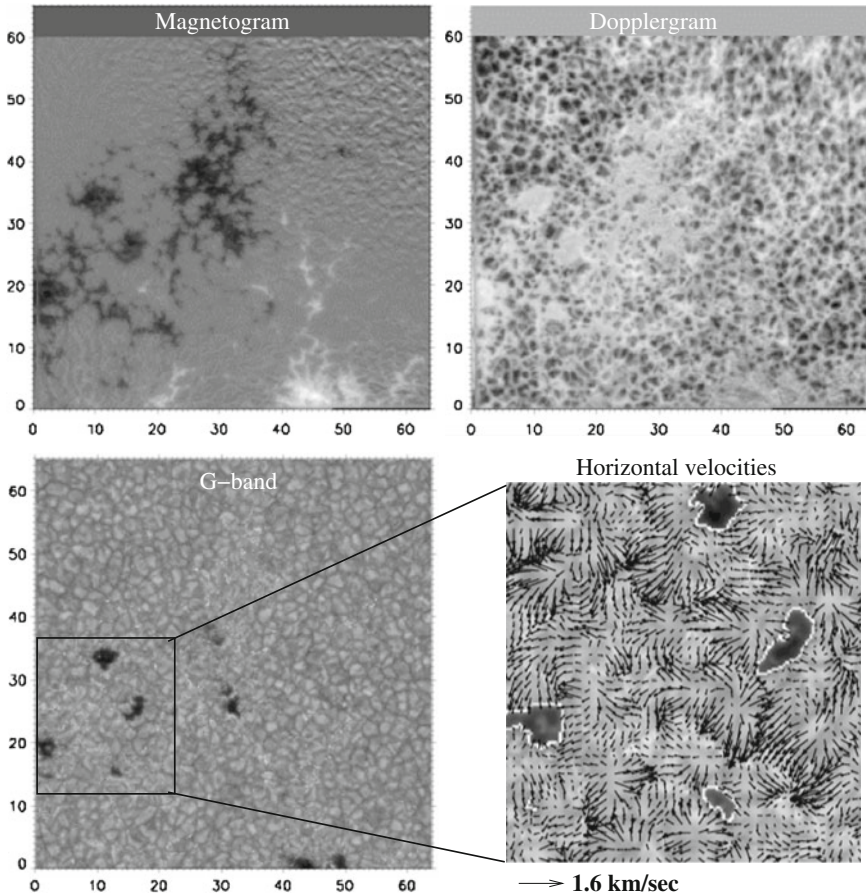
Convective motions are also organized at larger scales. The most systematically observed motions that form cellular patterns are mesogranulation and supergranulation.

Mezogranular pattern of mass flows is characterized by advection of granular convection and associated small-scale magnetic fields. Rising velocities of plasma in a center are usually small, while horizontal velocities of diverging plasma are about  $0.5 \text{ km/s}$ . Horizontal distance between mezogranular centers is  $5,000\text{--}10,000 \text{ km}$  with lifetime of about 2 h.

In case of supergranulation mass flow rising from the center of neighboring cells with velocities of about  $0.1 \text{ km/s}$  diverge horizontally with velocities  $0.3\text{--}0.5 \text{ km/s}$ . Supergranular pattern is closely related to magnetic network consisting of magnetic elements with stronger than average magnetic field. The typical diameter of supergranules is of the order of  $30,000 \text{ km}$ , and lifetime of about 36 h.

A cellular pattern has multi-scale character and at all scales the inter-cellular lanes are filled by magnetic flux tubes. There they emerge, move around, and interact with each other and the surrounding flows, directly affecting the overlying atmosphere.





**Fig. 1.9** Co-temporal and co-spatial set of images of  $50 \times 50$  arcsec region taken by the SST instrument on Hinode on 2007 September 30. *Magnetogram* is scaled to a maximum of  $\sim 2,300$  G. *Dopplergram* velocities range from  $\sim -1.2$  to  $1.6 \text{ km s}^{-1}$ . *White dots* correspond to downflows, *black points* to upflows. The coordinates are expressed in arcsec. *Bottom left* is the same area in the *G-band*. *Black box* shows the region of emerging flux, shown enlarged on the *right* together with the corresponding horizontal flow map. Credit: Vargas Domínguez et al. (2010), reproduced with permission ESO

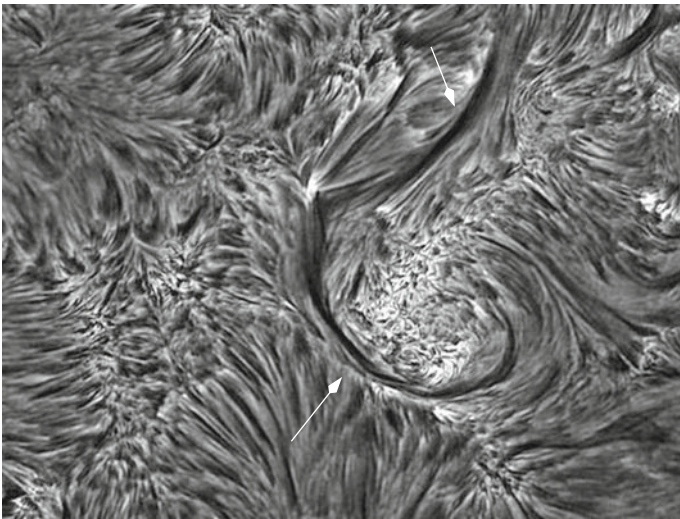
The first to respond is the chromosphere. Here the temperature rises from 4,000 to  $2.5 \times 10^4$  K in about 1,500 km. Extremely dynamic, the chromosphere creates a narrow transition region where in another couple of 100 km the temperature jumps up by a million degrees to set up the corona.

Blocked by strong emission of the photospheric white light, the chromosphere requires narrow bandpass filters around the spectral lines emitted at chromospheric temperatures from the temperature minimum region (4,200 K) to its “upper boundary” ( $2.5 \times 10^4$  K at about 3,000 km above the surface). The middle and low chromosphere are best observed in Ca II K, He II and H $\alpha$  lines.

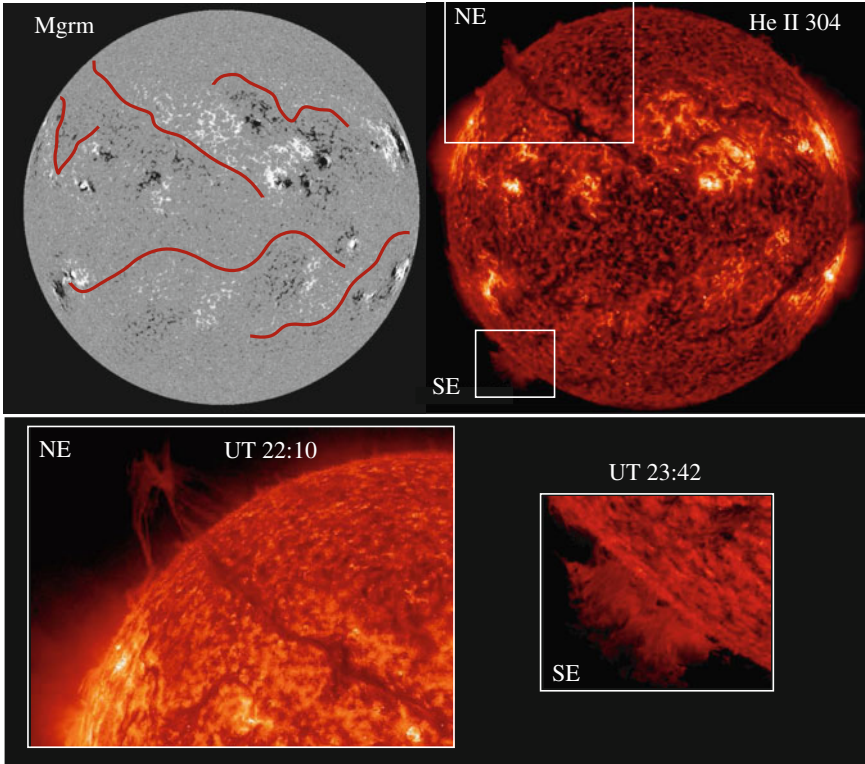
The chromospheric features associated with mass flows are seen especially well in  $H\alpha$  line. Here we give only a few examples of the most pervasive *large-scale* chromospheric flows. These are fibrills, active filaments, quiescent prominences, penumbral jets and spicules. All these features are uniquely associated with and governed by the magnetic field.

Fibrills are elongated dark structures with characteristic sizes of 1,500–7,000 km. Their lifetimes are of the order of network turnover times of about 15–20 h. They overhang the polarity inversion line everywhere, in the quiet sun, in plages, and around the sunspots. Examples of fibrills are shown in Fig. 1.10. The area is located south of the decaying active region which produced a huge active filament (more precisely set of filaments), marked by white arrows. The crescent part of the filament carefully encircles a unipolar plage which is seen in the chromosphere as a milky conglomerate of bright rosettes.

Filaments and prominences form two classes of magnetic structures with very different patterns of mass flows. Filaments are usually associated with the active regions. They are confined mostly in the chromosphere, i.e., their height is about 1,500–2,000 km, and their length is in the range of 50–100 Mm. Magnetic field strength in active filaments may be as high as 500–700 G. Their lifetime ranges from a few hours to days, and is determined by the evolution of parental active region. Plasma streaming along the filament may reach  $30 \text{ km s}^{-1}$ . Some transverse velocities were recorded to be about  $3\text{--}10 \text{ km s}^{-1}$ .



**Fig. 1.10** The  $H\alpha$  image of a relatively quiet sun/plage region taken by DOT on September 23, 2006. The field of view is  $86 \times 65 \text{ Mm}$ . Fibrills of many shapes and sizes bridging the polarity inversion lines and outline the magnetic connections between the opposite magnetic elements. A huge crescent-like dark feature is an active filament (*white arrows*). A milky area surrounded by filament is plage. Reprinted from <http://www.staff.science.uu.nl>, courtesy of R. Rutten



**Fig. 1.11** Full disk images of the sun taken by the HMI and AIA instruments on the SDO on November 13, 2011. The *red strokes* on the HMI magnetogram demarcate the polarity inversion lines that coincide with the chromospheric filaments seen as long dark structures in 304 Å He II line ( $5 \times 10^4$  K). These are quiescent prominences. Their projection on the sky at the northeast and southeast limbs are shown in inlets. Height of a limb portion of both prominences exceeds 50,000 km

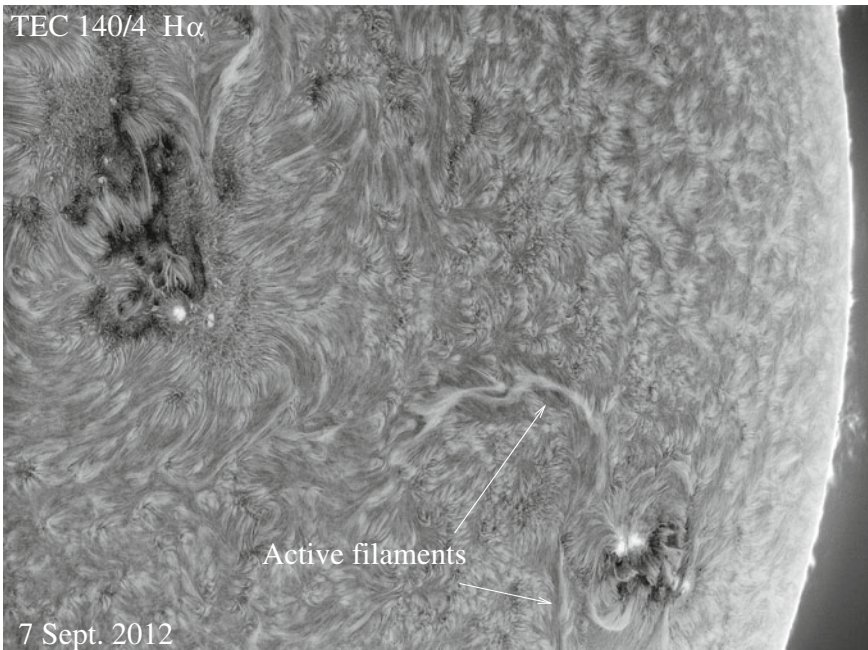
At much larger scales  $H\alpha$  chromosphere exhibits huge dark features that demarcate the *global* polarity inversion lines (Fig. 1.11). These are quiescent prominences. In fact, these complex structures are far from quiescent, and harbor a wide range of plasma instabilities from a regular flow instabilities to explosive mass release. Having lifetimes from a few days to several solar rotations, their name is quite justified by their longevity. Compared to active filaments, the  $H\alpha$  prominences are much longer and much taller structures. Their length may be more than solar radius. Their height *always* exceeds the coronal heights, i.e., the quiescent prominences overhang the corona. At the same time the mass density of prominences is by 2–3 orders of magnitude higher than the coronal plasma density. In other words, a heavy cool material of prominence suspended over rarefied hot gas is like an iron bar floating in thin air.

Figure 1.11 shows the sun in 304 Å He II line ( $5 \times 10^4$  K) taken by the SDO/AIA instrument on November 13, 2011 together with the HMI magnetogram. The red lines on the magnetogram follow the path of prominences suspended above the demar-

cation line dividing the quiet sun magnetic network of opposite polarities. White boxes on the northeast (NE) and southeast (SE) of the chromospheric image contain a projection of a limb portion of prominences. Slightly enlarged, these images are shown at the bottom of Fig. 1.11. Note that the northeast limb shows the projection of a huge prominence whose body crosses the solar disk from its center, whereas the southeast limb shows the projection of prominences hidden from us on the far side of the sun.

Mass flows associated with the quiescent prominences is hard to classify. Whatever shape is taken by the prominences they all have highly intermittent filamentary structure. Small-scale filaments comprising prominence are usually accompanied by mass flows induced by the local magnetic field and electric currents.

Among a huge variety of magnetic structures and flows, the sun has one of the most persistent phenomena: spicules. These are magnetized plasma jets coming out of the magnetic network and outlining supergranular boundaries. They are ubiquitous as large-scale convective patterns forming regular bush-like structures arranged into the rosettes that are mainly anchored in the supergranular lanes. They have self-similar properties practically all over the solar surface. Their lifetime is usually several minutes. The plasma in spicules is ejected with a speed of about  $20\text{--}30\text{ km s}^{-1}$ , and in a few minutes, like a fountain, drops down onto the photosphere. Figure 1.12



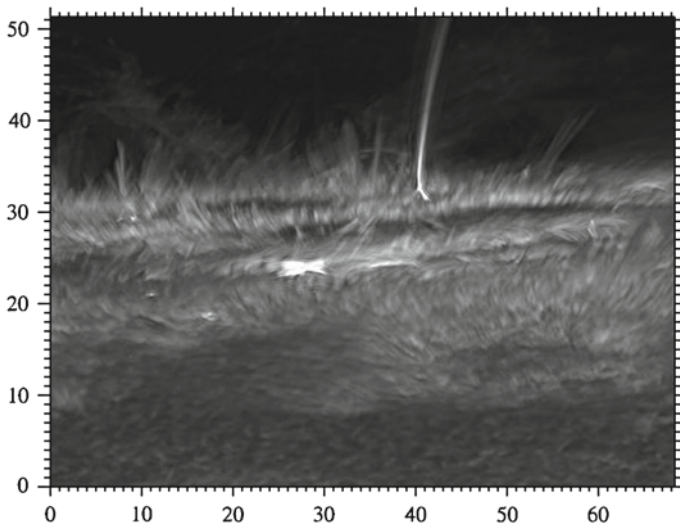
**Fig. 1.12** The amateur picture of the sun in  $H\alpha$  showing the active regions surrounded by filaments and a wonderful prairie of spicules forming extremely regular bushes that outline the chromospheric network. Reprinted from <http://www.stern-fan.de>. Courtesy of Rolf Geissinger

shows a beautiful picture taken by an amateur astronomer in  $H\alpha$  line, showing the solar surface covered by spicules. One can see a regular chromospheric network outlined by the bushes of spicules. Two active regions destroy the regularity of the network and produce characteristic fibrills and filaments around them.

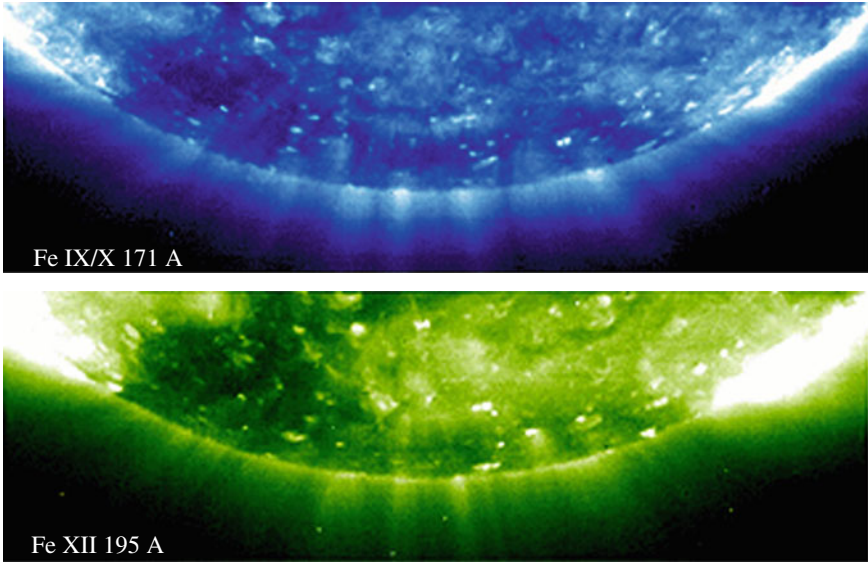
Along with the large-scale streamers accompanying sunspots and active regions, there are specific, always present systematic small-scale jets coming out of the penumbrae with velocities of a few  $\text{km s}^{-1}$ . Their typical length is between 1,000 and 4,000 km, some may reach 10,000 km. Their lifetime ranges from 30 s to several minutes. When at the limb, the sunspot looks like a crowned disk (Fig. 1.13).

We conclude this chapter by mentioning the polar plumes. These are long thin streamers projected in the sky as beams emanating from the north and south poles. These streamers are associated with small-scale magnetic elements and, when visible, their footpoints are seen as bright points. As we know, the polar regions are populated only by small-scale magnetic elements—remnants of dispersed magnetic clusters migrated toward the poles. Figure 1.14 shows a segment of the south pole taken with the EIT instrument on SOHO in the Fe IX/X 171 Å (top) and Fe XII 195 Å (bottom) lines on May 8, 1996. Their temperature is therefore about 1 MK. They extend up to 30 Mm above the photosphere.

Note that we gave above only a few examples of the flow structures. In reality, the filaments, fibrills, and quiescent prominences form a broad class of electromag-



**Fig. 1.13** Image of the active region (AR 10486) just before it rotated out of sight over the west limb to the backside of the sun in Ca II H line. The sunspots appear as *flat dark pancakes* encircled by spikes of penumbral jets and further surrounded by chromospheric fibrills. The foreground shows granulation pattern and spicules. A huge jet exceeding 15 Mm in length stands out between two sunspots. Tickmarks are arc seconds. Courtesy of R. Rutten. Image taken by DOT on November 4, 2003. Reprinted from <http://www.staff.science.uu.nl>



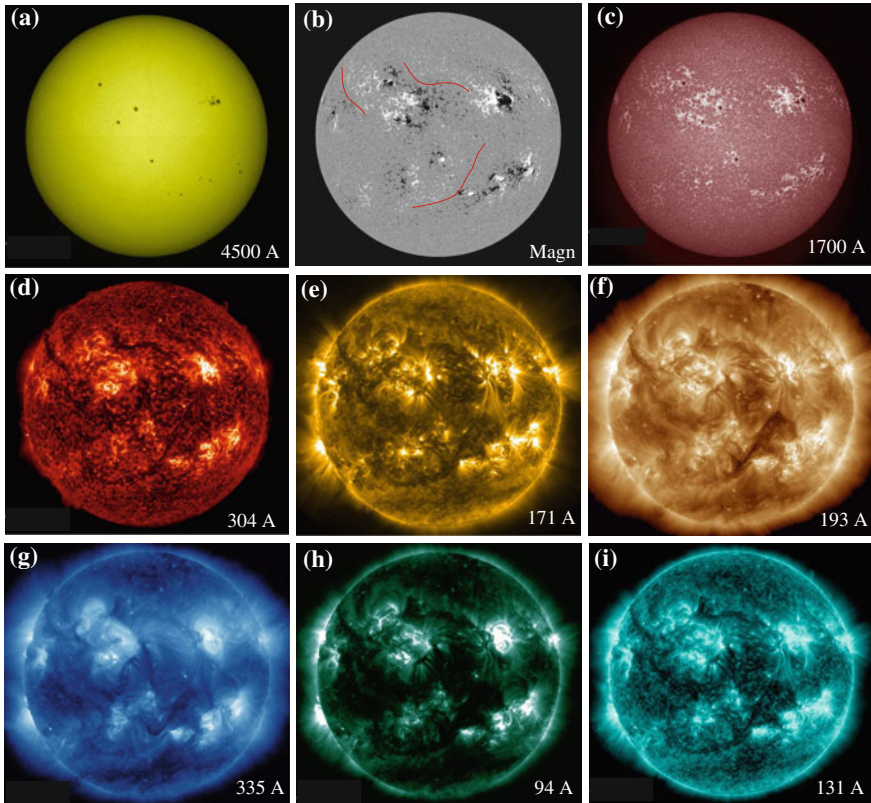
**Fig. 1.14** The EUV images of the south pole with regular arrays of polar plumes emanated radially outward from the solar surface. One can see bright footpoints of plumes associated with small-scale magnetic flux tubes—remnants of dispersed magnetic clusters that migrated in course of the solar cycle toward the poles

netic formations. And each class provides its own unique opportunity to study the fundamental physical processes.

## 1.4 Magnetic Skeleton

In a visible light radiated from the photosphere the sun looks like a smooth ball covered with a few tiny pockmarks (Fig. 1.15a). These tiny pockmarks are caused by the presence of magnetic field where temperature is significantly lower than the surrounding photosphere. In the immediate vicinity to the surface, the solar atmosphere shows “normal” behavior: its temperature and density *drop* with height. But reaching the temperature minimum of  $\simeq 4,400$  K at about 500 km height, the temperature quickly rises, and at about 1,500 km from the temperature minimum reaches  $\simeq 10^4$  K, forming the chromosphere (Fontenla et al. 2006). From that level, just in a narrow transition region of a few hundred kilometers the temperature jumps to a million degrees, forming a vast corona (for contemporary model of solar atmosphere, see e.g. Fontenla et al. 2006 and literature therein).

The problem of energy production, its transfer, and release throughout the solar atmosphere has been and still remains one of the major challenges in solar physics.



**Fig. 1.15** The magnetic surface of the sun and its imprint in the overlying atmosphere: **a** The solar surface in the *white light* showing the atmosphere at 5,500–6,400 K; **b** Line of sight magnetogram with a few *red lines* demarcating the large-scale magnetic shear; the imprint of these lines, as well as the presence of magnetic fields is seen throughout the entire atmosphere; **c** The temperature minimum region in a cool emission line at about 4,500–5,000 K; **d** Upper chromosphere and transition region in He II line formed at  $\simeq 10^5$  K; **e–i** Corona at escalating temperatures of about  $6.3 \times 10^5$ ,  $1.3 \times 10^6$ ,  $2 \times 10^6$  K, **g**  $6.3 \times 10^6$ , and  $2 \times 10^7$  K, respectively. Images taken by the AIA/SDO instrument on November 10, 2011

The obvious platform for approaching this problem is understanding the generation, structure, and evolution of magnetic fields, embedded in a highly dynamic environment and interacting with it.

The overall imprint of the line-of-sight magnetic field in the overlying atmosphere and its outline is illustrated in Fig. 1.15.

The enhanced intensity of a hot plasma at all temperature levels mimics the magnetic field pattern seen at the surface. The very specifics of energy production, its transfer, and release, i.e., electromagnetic coupling of the photosphere with the upper layers of the atmosphere is totally determined by the characteristic features of

local magnetic fields, be it the quiet sun with its rarefied ensembles of small-scale magnetic flux tubes, or dense clusters of magnetic flux tubes forming sunspots and active regions.

Throughout this book we shall study the properties of isolated flux tubes and their interaction with the surrounding medium and each other. We will see that different topologies of flux tube ensembles present in the quiet sun, plages, and active regions, together with various mass flows interacting with them, result in a wide range of phenomena that are observable and may be quite well understood.

## References

- G. Athay, *The Solar Chromosphere and Corona: Quiet Sun* (D. Reidel Publishing Co., Dordrecht, 1976)
- J.N. Bahcall, R.K. Ulrich (1988)
- A.N. Cox, W.C. Livingston, M.S. Matthews, *Solar Interior and Atmosphere* (University of Arizona Press, Tucson, 1991)
- B.N. Dwivedi, *Dynamic Sun* (Cambridge University Press, New York, 2003)
- J.M. Fontenla, E. Avrett, G. Thuillier, J. Harder, *Astrophys. J.* **639**, 441 (2006)
- L. Golub, J.M. Pasachoff, *The Solar Corona* (Cambridge University Press, Cambridge, 2010)
- W. Livingston, *Nature* **350**, 45 (1991)
- M. Lockwood, *Living Rev. Sol. Phys.* **10**, 4 (2013)
- H.K. Moffatt, *Magnetic Field Generation in Electrically Conducting Fluids* (Cambridge University Press, Cambridge, 1978)
- E.N. Parker, *Cosmical Magnetic Fields* (Clarendon Press, Oxford, 1979)
- E.R. Priest, *Magnetohydrodynamics of the Sun* (Cambridge University Press, New York, 2014)
- A. Severny, *Solar Physics* (Press Holdings Int., 2004)
- R.A. Shine, A.M. Title, T.D. Tarbell, K. Smith, Z.A. Frank, *Astrophys. J.* **430**, 413 (1994)
- B.V. Somov, *Physical Processes in Solar Flares* (Kluwer Academic Publishers, Dordrecht, 1991)
- K.T. Strong et al., *The Many Faces of the Sun* (Springer, 1999)
- Sturrock et al., *Physics of the Sun*, vols. 1–3 (D. Reidel Publishing Co., Dordrecht, 1986)
- A.M. Title, C.J. Schrijver, in *Cool Stars, Stellar Systems, and the Sun*, ed. by R. Donahue, J.A. Bookbinder (Astronomical Society of the Pacific Conference Series 1997)
- A. Title et al., *Astrophys. J.* **403**, 780 (1993)
- S. Vargas Domínguez et al., *A&A*, **516**, A91 (2010)
- A.H. Vaughan, *Publ. Astron. Soc. Pac.* **92**, 392 (1980)
- O.R. White, W.C. Livingston, *Astrophys. J.* **249**, 798 (1981)
- O.C. Wilson, *Astrophys. J.* **226**, 379 (1978)
- H. Zirin, *Astrophysics of the Sun* (Cambridge University Press, Cambridge, 1988)



## Chapter 2

# A Quick Look on Small Scale Flux Tubes

**Abstract** In this chapter we recall some basic steps of how magnetic flux tubes were discovered and how they were viewed in their early years. During the decades after their discovery, flux tubes evolved from an interesting novelty into a founding element of solar magnetism. Today, we know that the entire magnetic field of the Sun, from sunspots to coronal loops and solar wind, has a filamentary structure. We briefly discuss the universality of filamentary structures in universe.

### 2.1 Early Years

For ages, solar magnetic fields were associated with sunspots. The existence of magnetic field concentrations outside sunspots has been realized only in the late 1950s. Howard (1959), observing magnetic fields in various active and quiet sun regions, found that existence of magnetic “features” with fields greater than 75 G outside sunspots and far removed from them, is “not uncommon.” Confirming the correspondence between calcium bright points (seen at chromospheric temperatures) and photospheric magnetic fields, described earlier by Babcock and Babcock (1955), Howard writes: “A close correspondence in most small structural details between the calcium plages and magnetic field tends to indicate a real physical relationship between the two,” and finally suggests that “the magnetic field in the solar photosphere and chromosphere is in the form of more or less *vertical columns*.”

Leighton (1959) describing his observations of magnetic field in plage regions also concludes that “relatively strong field, 100 or 200 G in strength are found in extensive areas throughout plage regions, the field pattern being in striking agreement with the pattern of Ca II emission.”

The same year, Severny (1959) reports on the observations of fine structures in *sunspots*!

Such was the birth of small scale magnetic flux tubes. Not only were the existence of small scale magnetic features detected, but they were found uniquely associated with two important phenomena. One was a direct correlation with heating the overlying chromosphere (Ca II emission), and the other was formation of large-scale magnetic shear formed all over the solar surface by small scale “columns” of opposite polarity.

Pikel'ner (1963), well before the small scale flux tubes were directly observed, was the first to predict the existence of flux tubes. He suggested that convective motions acting on the magnetic lines of force, squeeze them and crowd in toward the periphery of the granules, and that the field becomes concentrated into a network covering the sun's surface. He also predicted that the enhanced convection contributes to chromospheric emission, so that the network becomes observable in Ca II and H $\alpha$  lines. Moreover, Pikel'ner found that the motion of plasma entrained in the magnetic field lines is responsible for the observed mottles consisting of granular elements streaming from the center toward the periphery, and concluded that the presence of mottling over the entire solar surface demonstrates that a "weak" field exists everywhere. The direct observation of these suggestions were still to come.

### ***2.1.1 First Direct Observational Signs of Magnetic Flux Tubes***

Using the photographic technique of Leighton for high spatial resolution measurements of photospheric magnetic fields, Sheeley (1966, 1967) finds that as a bipolar magnetic region develops in time and as its magnetic flux spreads over a larger area, the flux density does not decrease smoothly, but is distributed in bits and fragments of progressively smaller sizes until finally, they escape detection below the threshold of photographic measurements. The magnetic field in these small magnetic features was found to range from 200 to 700 G. Sheeley states that "wherever there are adjacent regions of opposite polarity, there are disk filaments in H $\alpha$ ." His conclusion, that "magnetic fields of several hundred gauss occur in tiny areas easily as small as 500 km in regions of the solar surface sometimes well removed from sunspot activity," became the turning point which, despite the predecessors, is a fact of the discovery of small scale flux tubes.

Just at about the same time, observing magnetic fields of small sunspots and pores, Steshenko (1967) finds that the field strength of the smallest pores ( $1'' - 0.5 - 2''$ ) is about 1,400 G. In larger spots he finds very small elements with a field strength of 5,350 G (!), much higher than the average field of the sunspot itself. He also observed an isolated places outside sunspots having field strengths up to 1,000 G.

Beckers and Schröter (1968) performed an extremely detailed study of the small scale magnetic structures *in* and *around* the sunspots. These studies included the measurements of velocity, intensity, and magnetic field strength in the fine elements. By these observations they confirmed and extended Sheeley' findings, providing substantial guideline for future observations. Being quite cautious, they start the discussion as follows: "We presented in this paper evidence that most, and perhaps all, of the photospheric magnetic field around an unipolar sunspot is concentrated in a few thousand small region (1,000 km in diameter) with strong magnetic fields (up to 1,400 G). This, together with the other properties of the magnetic knots, shows that they are an essential part of a solar activity regions. We are, however, not yet able to decide definitely whether they occur only in the dissolution phase or whether they are a permanent constituent of a solar activity region."

Soon, it was found that almost the entire surface outside sunspots is covered by small scale magnetic elements. Howard and Stenflo (1972), analyzing Mount Wilson magnetogram recordings obtained during 26 days with 17 by 17 arcsec aperture, found that more than 90 % of the total flux is channeled through narrow flux tubes with very high field strength in plages and at the boundaries of supergranular cells. The flux tubes occupying a very small region in the photosphere were found rapidly spreading out with height. This spreading of the field lines and decreasing the field strength with height was dubbed the “mushroom effect,” described earlier by Pikel’ner (1963) as chromospheric mottling (Frazier and Stenflo 1972).

### 2.1.2 The Sunspot Dilemma

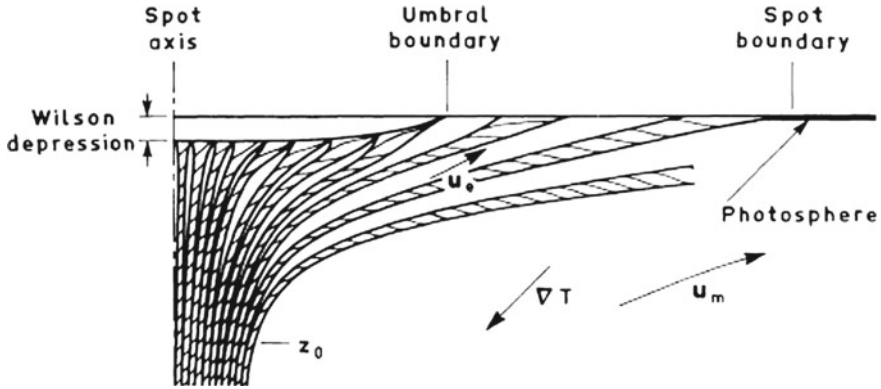
It is interesting that just before these fundamental results establishing the filamentary structure of sun’s magnetic fields outside sunspots, and long before the recent high-resolution observations, Papathanasoglou (1971), along the earlier findings of Crimea group (see e.g. Severny 1959), has observed the filamentary structure of *sunspot umbra*, and showed that the widths of umbral filaments are  $< 1''$ , and that dark spacing between them are about 0.6.” This amazing result was totally ignored, earning only three (!) citations, first of which was given by Livingston (1991) in his Nature article “Radial Filamentary Structure in a Sunspot Umbra,” where he also reports on the direct observations of the filamentary structure of sunspot umbra.

For many years, however, the study of small scale filamentary structure of umbrae was overshadowed by studies of a sunspot as a whole, its stability and its impact on the surrounding and overlying atmosphere. The large-scale observational data clearly indicated that as a whole, the sunspots must be intrinsically unstable. The stability analysis of such a complex and ever changing body requires consideration of many competing effects—the job that yet has to be done. And search for the mechanisms of sunspot stability became an uphill battle. The filamentary structure of the sunspot body has been put aside by the majority of researchers. The most revealing of the acute situation of those days is, probably, an example of Piddington’s research.

The large body of Piddington’s work on solar magnetic fields may be characterized by his own words (1975): “A phenomenological model of solar magnetic fields is developed, which differs drastically from all currently popular (diffuse-field) models. Its acceptance would require a review of a major part of theoretical solar physics.”

Revision of a major part of solar theories and interpretations was not easy, and Piddington’s ideas in many aspects of solar magnetism caused various reactions, from such definitions as “Piddington’s Heresy” (Parker (1976) on role of turbulent diffusion) to a silent dropping off his works from citations. Figure 2.1 shows an example of the Piddington’s model of sunspot consisting of the individual twisted flux tubes.

Meyer et al. (1977) reacted to Piddington’s model of sunspot stability simply: “We shall show, using a simplified model, that a sunspot can be stable in and immediately below the photosphere. This stability can be related to the potential energy associated with the Wilson depression. *There is no need to invoke twisted fields* (e.g. Piddington (1975)), *which have not been observed.*” (!)



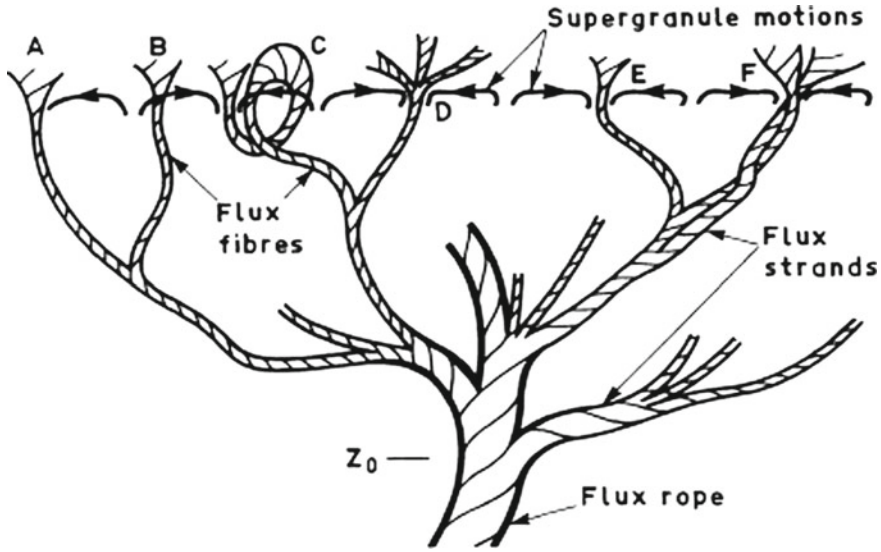
**Fig. 2.1** Section of a sunspot magnetic field with the flux-rope helical twist omitted for simplicity. The individual flux tubes are shown twisted and separated by nonmagnetic plasma regions whose width increases with distance from the axis, thus accounting for the penumbral filaments, the Evershed flow  $u_e$  has different directions and velocities inside and outside the flux tubes. Reprinted from Piddington (1978) by permission from Springer Science and Business Media

By the time of this statement, from a basic plasma theory, supported by laboratory experiments, it was already well known that long magnetic cylinders are intrinsically unstable with respect to so-called screw-pinch instability (Shafranov 1956; Kruskal and Kulsrud 1958; Kadomtsev 1966). A condition for screw-pinch instability, known as Kruskal-Shafranov condition, is simple: flux tube with magnetic field  $\mathbf{B}(0, B_\phi, B_z)$ , radius  $R$  and length  $L$ , will be inevitably twisted if

$$q = \frac{2\pi R B_z}{L B_\phi} \equiv \frac{h}{L} < 1, \quad (2.1)$$

where  $q$  is the safety factor, and  $h$  is the pitch of helical configuration, i.e., the distance in which the field line makes one revolution around the flux tube. In case of solar magnetic flux tubes, the safety factor is always  $< 1$ , which means that any magnetic flux confined in a cylinder with roughly  $R \ll L$  must be twisted. Indeed, high-resolution observation shows that magnetic flux tubes, sunspots, ropes and loops are intrinsically twisted. And Kruskal-Shafranov condition is fulfilled for prevailing majority of solar magnetic structures. We will see throughout the book how well this feature is observed, and what an important role is played by screw-pinch instability in properties and dynamics of various regions of solar atmosphere.

One can say that at those times Piddington's model of solar magnetic fields including sunspots (Fig. 2.1), active regions and their environments, based on the model of twisted flux ropes, was too ahead of time and probably the closest to the goal. More general features of solar magnetic field visualized by Piddington (1978) are shown in Fig. 2.2. All these features, as already mentioned, have been subsequently confirmed (Ryutova et al. 2008; Su et al. 2010; Ruiz Cobo and Puschmann 2012; Stenflo 2013).

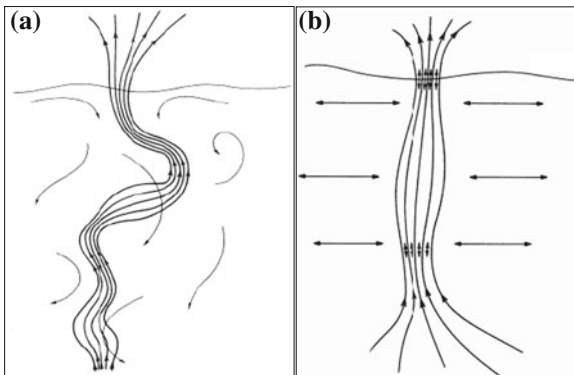


**Fig. 2.2** Schematic of the main magnetic and plasma features of decaying active regions and quiet sun. The flux-rope section acts as the trunk of a tree-like structure whose main branches are flux strands. These, in turn, fray into flux fibres ( $\approx 3 \times 10^{18}$  Mx) which provide the network rosettes (on disk) and bushes (at limb). These tend to be driven to the supergranular boundaries (A), but may be observed piercing the cell interior (B). The kink instability provides a loop (C). A flux fibre frays further (D) into flux threads ( $\approx 3 \times 10^{17}$  Mx) which provide the photospheric filigree and chromospheric mottles. A group of flux fibres (E) and perhaps some flux strands (F) form a boundary and force a convective cell to turn over continuously for several days. Reprinted from Piddington (1978) by permission from Springer Science and Business Media

## 2.2 Elements of Theory for de Facto Flux Tubes

The theoretical approach to the origin and properties of small scale magnetic flux tubes started to flourish only in the middle of 70s. By that time, a decade of efforts of observers prepared a rich ground for these studies.

Parker (1974a, b) proposed a simple hydrodynamic mechanism associated with turbulent pumping to squeeze magnetic field into the slender tube (Fig. 2.3). He writes: “The obvious point of departure for an inquiry into the origin of intense fields in the supergranular boundaries is the well-known effect in which the outflow of fluid from the center of each supergranular sweeps the vertical component of magnetic field to the boundary.” The key element in this scheme is that the turbulent pumping of fluid downward at the supergranular boundary produces a partial vacuum within the flux tubes, just like in the water jet vacuum pump, in which one fluid is forced along by turbulent coupling to another. In this scheme, the field is restricted by energy equipartition,  $B^2/8\pi \simeq (1/2)\rho v^2$ , and limits the value of the magnetic field by a maximum of about 500G. Uncertainty in velocity fields and too low value of the magnetic field leads Parker to add yet another effect that is supposed to further concentrate the



**Fig. 2.3** Sketch of a magnetic flux tube extending up through the photosphere. **a** Turbulent subsiding fluid in a supergranular boundary into the tenuous chromosphere above the visible surface of the sun. **b** The magnetic field lines alternately squeezed and expanded in the turbulent convection beneath the photosphere, causing the surge up and down along the flux tube; the open ends are indicated by the *short double arrows*. Reprinted from Parker (1974a, b) by permission from IOP, AAS

individual flux tubes, namely the Bernoulli effect. Unfortunately, this effect increases the mean magnetic field only to a fraction of the equipartition value. And Parker concludes that “we must look farther” (Parker (1974b), see also Parker (1979)).

The origin of the small scale magnetic flux tube covering the entire solar surface and making up sunspots, plages, and active regions is still an open question.

It is therefore not surprising that the first theoretical works on fundamental properties of flux tubes were based on their de facto existence (Cram and Wilson 1975; Ryutov and Ryutova 1976; Defouw 1976; Ryutova 1977; Roberts and Webb 1978; Spruit 1981).

The basic equations employed in early attempts to study properties of magnetic flux tubes are Maxwell equations mainly in the MHD approximation:

$$\nabla \cdot \mathbf{B} = 0 \quad (2.2)$$

$$\frac{\partial \mathbf{B}}{\partial t} = \nabla \times (\mathbf{v} \times \mathbf{B}) + \eta_D \nabla^2 \mathbf{B} \quad (2.3)$$

$$\rho \frac{d\mathbf{v}}{dt} = -\nabla p + \frac{1}{4\pi} (\nabla \times \mathbf{B}) \times \mathbf{B} - \rho g(z) \quad (2.4)$$

$$\frac{d\rho}{dt} + \rho \nabla \cdot \mathbf{v} = 0 \quad (2.5)$$

$$\frac{\partial(\rho^{-\gamma} p)}{\partial t} + \mathbf{v} \nabla(\rho^{-\gamma} p) = 0 \quad (2.6)$$

where  $d/dt$  designates a full derivative ( $d/dt = \partial/\partial t + \mathbf{v} \cdot \nabla$ ),  $\eta_D = c^2/4\pi\sigma$  is magnetic diffusivity, and  $\sigma = 1.96ne^2/(m_e\nu_{ei})$  is the plasma conductivity.

The magnetic flux tube, in a simple cylindrically symmetric model, may be considered as a set of magnetic field lines through some surface  $S$  bounded by the closed contour  $C$ . The lines of force are defined in terms of  $\mathbf{B}(\mathbf{r})$ , as the solution of equations

$$\frac{dr}{B_r} = \frac{r d\phi}{B_\phi} = \frac{dz}{B_z} \quad (2.7)$$

Applying Gauss's theorem to (2.2) we see that the total magnetic flux across any closed surface  $S$  is zero,

$$\int_S \mathbf{B} \cdot d\mathbf{S} = 0, \quad (2.8)$$

which means that every line of force entering  $S$  must also leave, i.e., the individual lines either extend to infinity or form closed curves. It follows then that the total number of lines, i.e., the total magnetic flux through any closed contour  $C$  is constant and can be written as

$$\Phi = \int_C \mathbf{B} \cdot d\mathbf{S} \quad (2.9)$$

which means, for example, that the strength of a flux tube increases when it narrows and decreases when it widens.

Let us now turn to question what are the requirements for the equilibrium of a flux tube. Consider the simplest case of hydrostatic equilibrium and assume that the magnetic field depends only on coordinate  $r$ ,  $\mathbf{B} = B(0, 0, B_z(r))$ . Equation (2.4), that provides the momentum balance, is then

$$-\nabla p + \frac{1}{4\pi}(\nabla \times \mathbf{B}) \times \mathbf{B} - \rho \mathbf{g} = 0 \quad (2.10)$$

In an absence of gravity from this equation we have

$$p(r) + \frac{B_z^2(r)}{8\pi} = p_e \quad (2.11)$$

$$p(r) + \frac{B_z^2(r)}{8\pi} = p_e + \frac{B_{ze}^2(r)}{8\pi}$$

where the constant of integration,  $p_e$  is obviously a gas pressure outside the flux tube,  $p_e$ , in case if flux tube is embedded in magnetic free environment,  $p_e + B_{ze}^2/8\pi$ , if the magnetic field outside flux tube is nonzero. Equations (2.11) are classical conditions for static equilibrium of magnetic flux tube.

In the presence of gravity, if it acts along the negative direction of  $z$ -axis, (2.10) gives:

$$\frac{dp}{dz} + \rho g(z) = 0 \quad (2.12)$$

Taking into account the ideal gas law,  $\rho = mp/kT$  ( $k$  is Boltzmann constant) we have

$$p = p_0 \exp\left(-\int_0^z \frac{1}{\Lambda(z)} dz\right) \quad (2.13)$$

where

$$\Lambda(z) = \frac{kT}{mg} \quad (2.14)$$

is the pressure scale height. In terms of density, (2.13) becomes

$$\rho = \rho_0 \frac{T_0}{T(z)} \exp\left(-\int_0^z \frac{1}{\Lambda(z)} dz\right) \quad (2.15)$$

It is important to note that MHD equations (2.2)–(2.6) allow to study quite a limited classes of phenomena. Throughout this book, however, we will encounter the problems that will require much more elaborated approach. In each particular case, for example, such as nonlinear unsteady phenomena, dynamics of nonconservative systems, self-organized processes and many others, we will deal with the special technique.

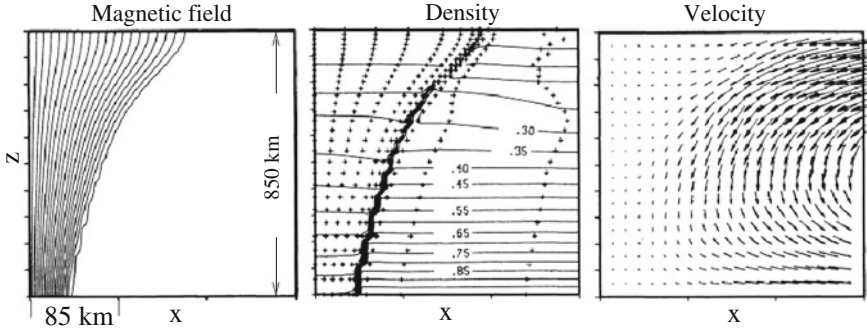
### 2.3 Numerical Visualization and Observations

One of the first exemplary models of a quasi-static flux tube was constructed numerically by Deinzer et al. (1984a, b). The full MHD equations for a compressible medium together with an energy equation were solved in two-dimensional geometry for a slender slab being in the pressure equilibrium with surrounding plasma. It was assumed that all quantities have a barometric dependence on  $z$ ; cf. (2.13).

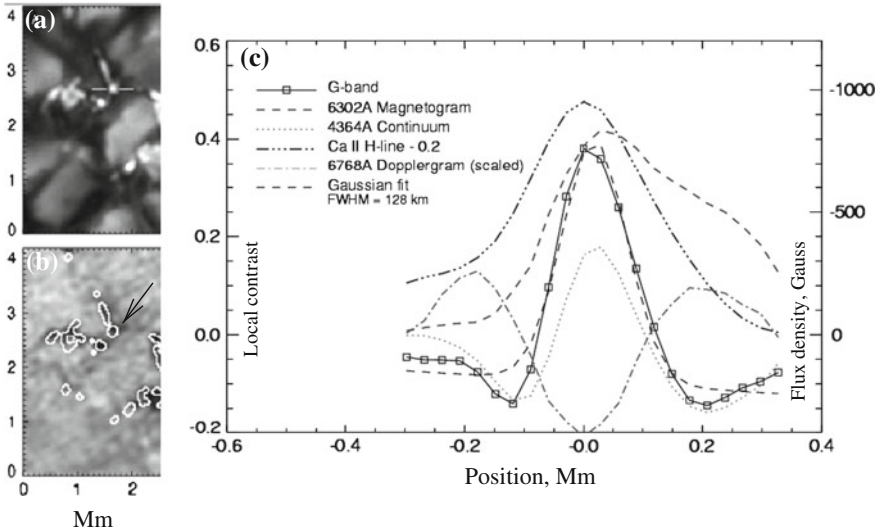
Figure 2.4 shows an example of the numerical solution for density, magnetic field and velocity at a time when stationary state has been evolved (half of the symmetric structure is shown). The important results obtained in this calculation are, for example, that the density is reduced inside the slab to half of the ambient plasma, and appearance of downflows around the magnetic slab caused by noncollinearity of the isotherms and lines of constant gravitational potential (not shown). Even these relatively early modeling (although only two dimensional) quite adequately represent what is to be observed. The results of more advanced numerical simulations of flux tube structures and additional literature can be found, for example, in Steiner (2007).

High-resolution observation with ground-based and space telescopes have allowed to study the inner structure of small scale flux tubes and their chromospheric counterparts seen as bright points.



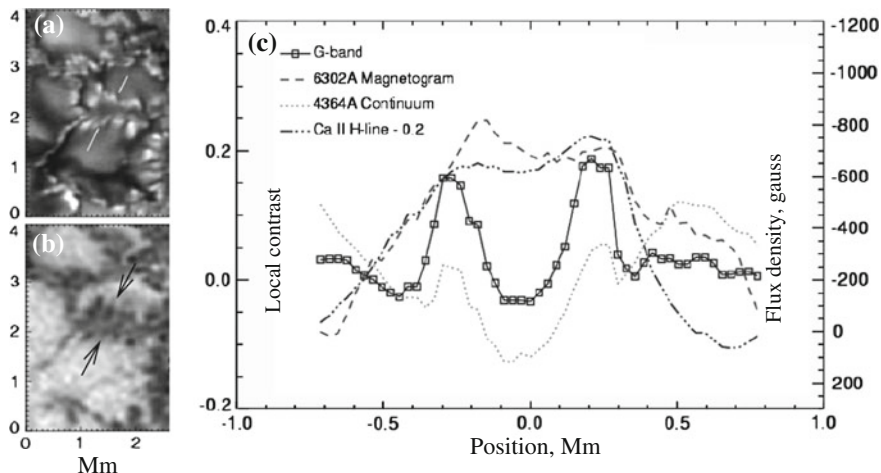


**Fig. 2.4** Results of the slab modeling. **a** Lines of constant density normalized to  $\rho_0 = 1.610^{-6} \text{g cm}^{-3}$ ; the *crosses* indicate the location of the node points, concentrated at the edge of the slab where the steepest gradients appear. **b** Magnetic field lines. **c** Velocity field; maximum velocity is  $\sim 200 \text{m s}^{-1}$ . The horizontal scale is stretched by a factor 10/3 in order to show more details of the structure. Credit: Deinzer et al. (1984a, b), reproduced with permission ESO



**Fig. 2.5** Region containing a closely packed system of small scale magnetic element. *Top left* is G-band 4,305 Å filtergram and *bottom left* is magnetogram. The *white lines* highlight a *bright point* across which a relative intensity profiles are shown in *right panel*. Credit: Berger et al. (2004), reproduced with permission ESO

Figures 2.5 and 2.6 show results of the observations made with the Swedish 1-m Solar Telescope (SST) on La Palma (Scharmer et al. 2003), which may resolve the magnetic structures in the G-band 4,305 Å bandpass with 70 km resolution. Using the SST data, Berger et al. (2004) studied magnetic elements in a plage region near disk center. The SST data were complimented by a co-temporal Ca II H image, showing



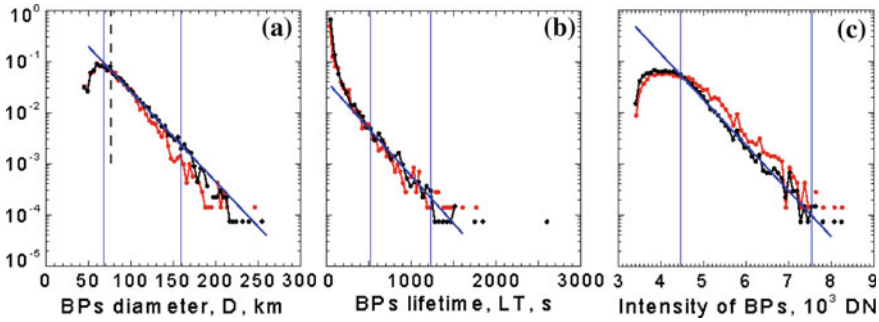
**Fig. 2.6** The same as in Fig. 2.5 but for a region containing very small isolated bright point and elongated dark features. Credit: Berger et al. (2004), reproduced with permission ESO

the network elements in low chromosphere, and high-resolution magnetogram that resolves structures as small as 120 km with a flux sensitivity of  $\approx 130 \text{ Mx cm}^{-2}$ . Figure 2.5 shows a  $2.5 \times 4 \text{ Mm}$  sample region containing small scale magnetic elements which, at any moment of time fill intergranular lanes. Their lifetime is usually on the order of granular time scales ( $\sim 8\text{--}10 \text{ min}$ ) or less. The top left panel shows G-band 4,305 Å filtergram and bottom left is magnetogram of the region. The white lines highlight a bright point across which intensities of several parameters were measured. These are shown in the right panel.

The solid curve with squares is the G-band intensity, duplicated by the Gaussian fit (dark dashed curve). The FWHM is 128 km. Also shown are plots of co-temporal and aligned data in the chromospheric Ca II H-line and 4,364 Å continuum with the corresponding magnetogram and Dopplergram signals. The peak absolute magnetic flux density is  $836 \text{ Mx cm}^{-2}$ . The peak downflow velocity measured in the Dopplergram slice is  $543 \text{ m s}^{-1}$ , displaced from the G-band peak emission by approximately 200 km on either side of the cut. This displacement of downflow velocity relative to the magnetic and bright point agrees well with the numerical models mentioned above (Deinzer et al. 1984a, b). This has been confirmed in later numerical simulations as well (e.g. Steiner et al. (1998)).

Figure 2.6 is another example of the same procedure as above but for the diverging ribbon-like structure which is not resolved into individual flux tubes. The measured magnetic flux density in the ribbon structures ranges from 300 to  $1,500 \text{ Mx cm}^{-2}$ .

As in the previous case, the chromospheric emission closely follows the G-band pattern and the magnetogram signal exhibits more discrete structures. The right panel shows a distinct double-peak shape in all of the emission lines indicating higher intensities and magnetic flux density at the edges of the ribbon structure. The maximum



**Fig. 2.7** Probability distribution functions of small scale magnetic features: **a** diameters, **b** lifetimes and **c** intensities. The data represent two sets of runs corresponding to lowest (*black*) and highest (*red*) threshold of intensity masks. *Straight blue lines* show the exponential fit showing a log-normal distribution of all the parameters. Courtesy of Abramenko, see also Abramenko et al. (2010)

absolute-value flux density in the bright point region is  $1,341 \text{ Mx cm}^{-2}$ . The magnetic flux density in the central region is also quite large,  $\sim -700 \text{ Mx cm}^{-2}$ , indicating that this is a complex but rather symmetric magnetic body with a darkened interior and bright walls.

This kind of structures appeared in various numerical simulations studying formation of photospheric flux tubes, pores and light bridges (see e.g. Steiner (2007), Jafarzadeh et al. (2013) and literature therein). These studies are well facilitated by increasing possibilities of observations which include not only studies of individual flux tubes but their statistical properties as well.

Figure 2.7 shows an example of statistical studies performed with New Solar Telescope (NST) of Big Bear Solar Observatory. Observations were done with adaptive optics correction using TiO 7057 Å line with 10 s time cadence (Abramenko et al. 2010). Figure 2.7 shows the probability distribution functions (PDFs) for the diameter,  $D$ , lifetime,  $LT$ , and maximum intensity,  $I_{\max}$ , of bright points tracked during about 2 h period.

It was found that 98.6% of bright points live less than 120 s. The lifetime distribution function follows a log-normal approximation for all features with lifetime exceeding 100 s. The longest registered life time was 44 min. The size and maximum intensity of BPs were found to be proportional to their lifetimes. A majority of bright points were found to be transient events reflecting the strong dynamics of the quiet sun populated by small scale magnetic flux tubes. The distribution function of their sizes extends to the diffraction limit of instrument, 77 km. The authors conclude that the *real minimum size of magnetic flux tubes has not yet been detected* in observations with modern high resolution telescopes.

As a building block of the solar magnetic fields, flux tubes play a major role in all physical processes in the sun from the energy production, its transfer and release to overall global behavior of the sun. Study of these processes and the flux tubes involvement in them is the subject of this book.

## 2.4 Filamentary Structures in Laboratory and Universe

The universe consisting of ever moving elementary particles and ionized gases is pierced by inborn magnetic fields. Highly advanced observations show their ubiquitous filamentary structure. But long before this fact became evident, in studies of laboratory plasma the *concept* of magnetic flux tubes became a necessity.

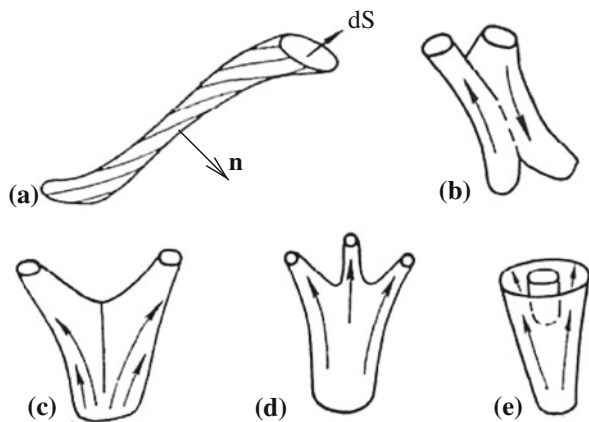
Invention of tokamak, and a possibility that magnetic field of the appropriate configuration could provide plasma confinement brought up the problems of plasma equilibrium and stability. This, in turn, led to the concept of *magnetic flux tubes* (Rosenbluth and Longmire 1957; Spitzer 1958; Kadomtsev 1959). It has been realized that among the properties of the magnetic field that are needed for stable confinement of plasma, the essential role may be played by their filamentary structure (Leontovich 1965; Morozov and Solov'ev 1966; Leontovich 1966). Examples illustrating a possible configuration of flux tubes is shown in Fig. 2.8.

The concept of magnetic flux tube requires that on the surface on the tube  $(\mathbf{n} \cdot \mathbf{B}) = 0$ , where  $\mathbf{n}$  is the normal to tube surface. Given that  $\text{div}\mathbf{B} = 0$ , inside flux tube magnetic flux must be conserved,  $d\Phi = \mathbf{B}d\mathbf{S}$ ; cf. (2.8) and (2.9).

Although magnetic field is divergence free, it was understood, that a flux tube can branch into two or more tubes. If line of force does not branch, then it cannot have a beginning or an end. Hence, it was postulated that there are three classes of nonbranching lines of force:

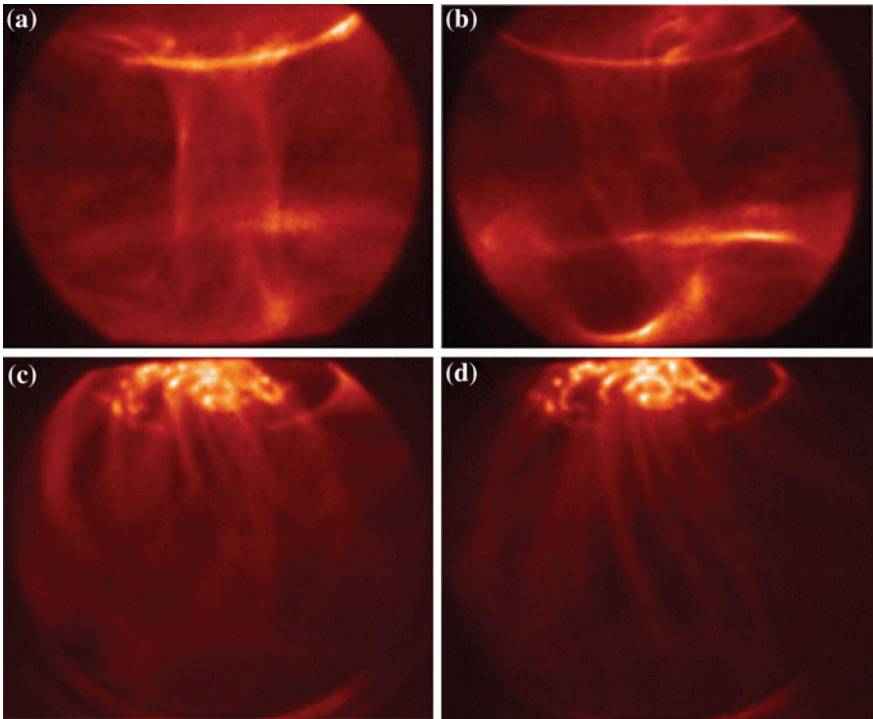
- (1) those that start at infinity and end at infinity;
- (2) those that remain in a bounded volume (closed or nonclosed) and
- (3) field lines that originate at infinity but are trapped within a finite volume. These early studies of various magnetic field configurations and their properties form the basis for the studies of magnetic field structures and their effects on various plasmas. Since then, these studies went far beyond the tokamak devices, and, along the mainstream of creating energy producing devices, brought together laboratory and astrophysical plasmas.

**Fig. 2.8** The concept of magnetic flux tube. **a** The tube of a cross section  $dS$  and the normal to tube surface,  $\mathbf{n}$ ; **b–e** Several possibilities of branching of tube which occurs at singular points having different characters (after Morozov and Solov'ev (1966))



The laboratory experiment allows one to change characteristic parameters of the object and follow a time history of the event during desired time interval. It is remarkable that the laboratory experiments that deal with targets of a spatial scale from several  $\mu\text{m}$  to several cm and timescales of nanoseconds and seconds can reproduce phenomena occurring in stellar coronae, galactic jets, fine structures in supernovae remnants and solar atmosphere. Existence of a broad magnetohydrodynamic similarity (Ryutov et al. 2001; Ryutov and Remington 2007; Drake 2009) allows a direct scaling of laboratory results to astrophysical phenomena.

For the time being, a rich bank of encouraging results from laboratory experiments aimed to study the astrophysical plasma have been accumulated (Romero-Talamas et al. 2006; Lapenta et al. 2006; Bellan 2008; Perrone et al. 2013; Brown et al. 2014). As an example, in Fig. 2.9 we show the spheromak formation and evolution (Romero-Talamas et al. 2006), captured by a high-speed imaging system in the sustained spheromak physics experiment (SSPX) (Hooper et al. 1999; McLean et al. 2001). Spheromak is one of the topologically simplest “long-lived” configuration in the form of a compact toroid. Of many applications, spheromaks can be used, for

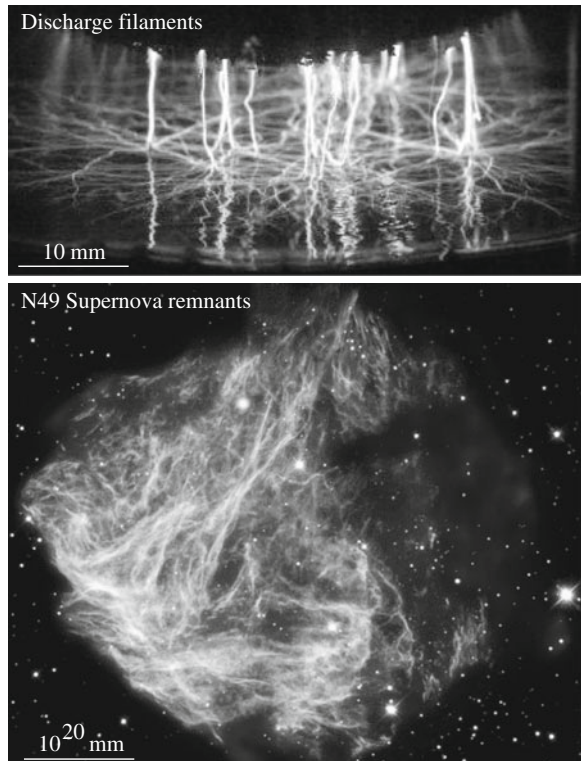


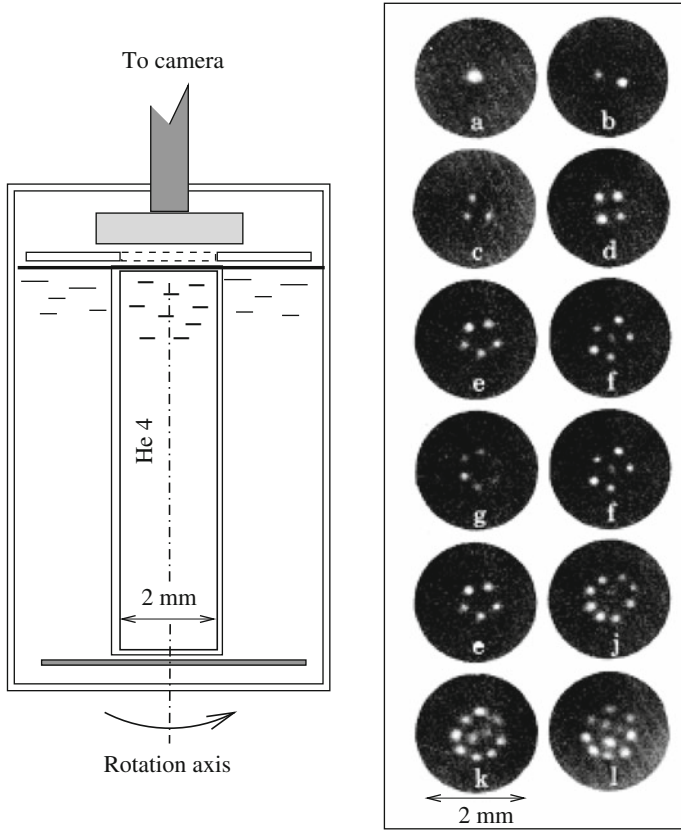
**Fig. 2.9** Formation and evolution of a plasma column inside the spheromak: **a** Regime of a column formation (about  $50\ \mu\text{s}$  after the plasma injection). **b** At  $80\ \mu\text{s}$  the column acquires a *kinked shape*. **c** Regime of filamentation: central column becomes a messy collection of filaments. **d** Possible regimes of selforganization of filamentary structure (Courtesy of Harry McLean, LLNL, see also Romero-Talamas et al. (2006))

example, to study how electric currents in the plasma produce the spheromak, how it evolves and whether it is capable containing hot plasmas. In course of these studies it became clear that the observed regularities are often similar to phenomena observed in astrophysical plasmas, and in particular in the solar corona. Figure 2.9 shows four stages of the spheromak evolution. The plasma enters the high-speed camera field of view a few tens of microseconds after injection, and begins to balloon out of the injector gun. In about  $50\ \mu\text{s}$  the plasma reaches the bottom of the flux conserver and a column forms. This moment is shown in Fig. 2.9a. At  $80\ \mu\text{s}$  the column acquires a kinked shape (Fig. 2.9b). Toward the end of the plasma's lifetime, its central column becomes a collection of thin filaments and then reorganizes itself into a more regular system of filaments.

The process of filamentation and accompanying phenomena have numerous analogies from chemistry and discharge tubes to neutron stars and supernovae. Examples of two extreme objects pierced by “thin” filaments are shown in Fig. 2.10. Top panel shows a pulsed corona discharge in atmospheric air generated between a planar high-voltage electrode and the water surface with an immersed stainless steel plate electrode. During each pulse thin glow-like filaments were formed which then propagate along the gas–liquid interface (Lukes et al. 2011). Bottom panel shows a well-defined hairy structure of # 49 supernova remnant, typical to all the supernovae and their remnants.

**Fig. 2.10** Two extreme scales of filamentary structures. *Top* The gas discharge filaments generated along the water surface (courtesy of Petr Lukes); *Bottom* N49 supernova remnant located in the Large Magellanic Cloud taken by NASA's Chandra X-ray observatory (courtesy of NASA)

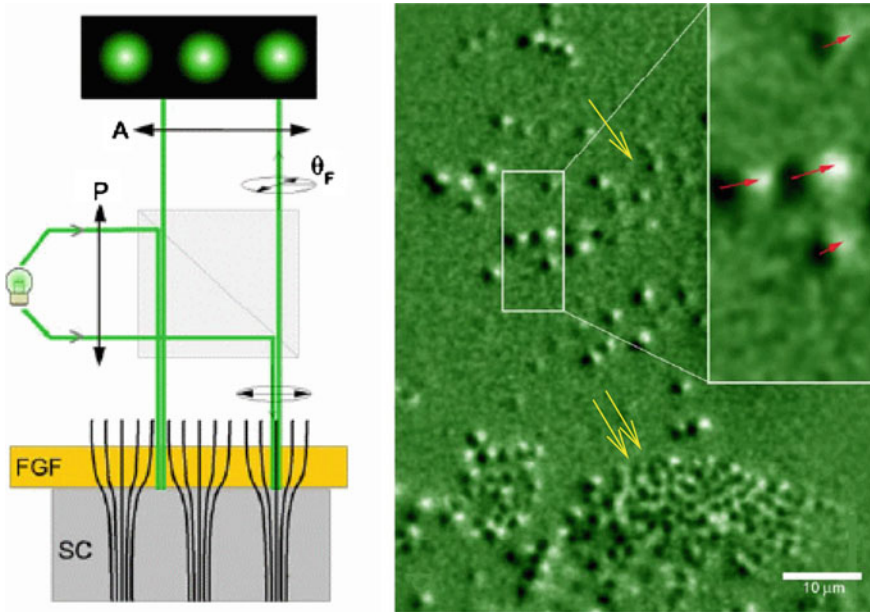




**Fig. 2.11** Photographs of stable vortex arrays. *Left* Schematic of the experiment. *Right* Appearance of quantum vortices at different angular velocities of bucket. The diameter of the dark circles corresponds to the 2mm bucket diameter. The angular velocities range from (a)  $0.30\text{s}^{-1}$  to (l)  $0.59\text{s}^{-1}$  with somewhat uneven intervals. Reprinted with permission from Yarmchuk et al. (1979). Copyright APS

We conclude this chapter by a fascinating and known for a long time examples of filamentary structures that were predicted and discovered as macroscopic quantum phenomena.

Long before the concept of magnetic flux tubes has been introduced in a tokamak plasma, in low temperature physics filamentation of substance became a starting point in studies of amazing phenomena in superfluidity and superconductivity (Landau 1941; Onsager 1949; Feynman 1955; Abrikosov 1957). A He 4 isotope below the 2.17 K (dabbed Helium II) becomes superfluid, but in various situations, such as under action of a heat or placed in a capillary tube, behaves as a mixture of a superfluid and normal components. A dual nature of Helium II is especially prominent when placed in a rotating cylinder. At some critical angular velocity there appear vortices with circulation quantized in units of  $h/m$  ( $h$  being a Planck’s constant and  $m$  is the mass of the Helium atom).



**Fig. 2.12** Visualization of Abrikosov vortices and their dynamics in superconducting  $NbSe_2$ . *Left* Schematic of the experiment setting (see text for details). *Right* Magneto-optical images of vortices and their response to an increase of the applied magnetizing field by 4 mOe. The dark and bright spots represent initial and final vortex positions, respectively. The scale bar represents  $10\ \mu\text{m}$ . Reprinted from Goa et al. (2001) by permission from IOP Publishing

By the nature the vortices are the elements of a condensate: the vortex core consists of the *normal* component, and formation of vortices transforms the superfluid into the normal state. According to the theory, appearance of quantum vortices is energetically favorable. Moreover, in the established state the vortices have a minimal circulation (i.e., just  $h/m$ ) and happen to form a regular lattice.

One of the first experiments demonstrating the formation of quantum vortices is shown in Fig. 2.11. One can see that with increasing the angular velocity of container there appear more and more vortices, just in agreement with theory predicting that in a container rotating at angular velocity  $\omega$ , vortices should appear with a density  $2\omega m/h$  (Feynman 1955). Tkachenko (1966) predicted that in equilibrium the vortices should form a triangular lattice. And they indeed do.

Filamentary processes occur as well in Bose-Einstein condensates (BEC, very cold atomic gases), He-3 isotope below 0.0025, and various types of superconductors.

Metals in superconducting phase having a zero resistivity are known to expel the magnetic field. The transition from superconducting to normal state usually has a discrete quantum nature. In Type-II superconductors, for example, such a transition occurs via formation of an Angstrom size threads that carry quantized magnetic flux, Abrikosov vortices (Abrikosov 1957).



With the improved experimental technique it became possible to observe individual vortices and their dynamics. Figure 2.12 shows a real-time imaging of Abrikosov vortices in superconducting  $NbSe_2$  (Goa et al. 2001).

Left panel in Fig. 2.12 shows a principle of a high-sensitivity magneto-optical (MO) imaging. The maxima of the magnetic field from vortices in a superconducting sample (SC) give maxima in the Faraday rotation  $F$  of incoming plane polarized light, which shows up in a ferrite garnet layer (FGF) near the sample. Vortices appear as bright spots when imaged using a crossed polarizer,  $P$ , and analyzer,  $A$ . Right panel shows resulted vortex dynamics during flux penetration. The image shows the change in flux distribution over a 1 s time interval after a 4 mOe increase in the applied field. The dark and bright spots represent initial and final vortex positions, respectively. Medium brightness corresponds to an unchanged flux distribution, indicating stationary vortices. The insert shows a close-up view of four vortex jumps. The arrows indicate the direction of vortex motion. Note how close is a visual resemblance between the distribution of vortices and distribution of flux tubes over the solar surface: a “filling factor” of vortices changes from very small number where they form a rarefied ensembles (white arrow) to almost unity where vortices form a dense conglomerate (double white arrows).

Vortices in superfluid Helium and superconductors, magnetic flux tubes in solar atmosphere and space, filamentation process in biology and chemistry have probably a common ground, which is to be yet established. One conclusion can be made for sure: *formation of filamentary structures in nature is energetically favorable and fundamental process.*

## References

- V. Abramenko et al., *Astrophys. J.* **725**, L101 (2010)  
 A.A. Abrikosov, *Sov. Phys. JETP* **5**, 1174 (1957)  
 H.W. Babcock, H.D. Babcock, *Astrophys. J.* **121**, 349 (1955)  
 G. Batchelor, *An Introduction to Fluid Dynamics* (Cambridge University Press, Cambridge, 2000)  
 J.M. Beckers, E.H. Schröter, *Sol. Phys.* **4**, 142 (1968)  
 P.M. Bellan, *Fundamentals of Plasma Physics* (Cambridge University Press, Cambridge, 2008)  
 T.E. Berger, L.H.M. Rouppe van der Voort, M.G. Lfdahl et al., *Astron. Astrophys.* **428**, 613 (2004)  
 M.R. Brown et al., *Micro-physics of Cosmic Plasmas: Hierarchies of Plasma Instabilities from MHD to Kinetic* (Springer, Berlin, 2014)  
 L.E. Cram, P.R. Wilson, *Sol. Phys.* **41**, 313 (1975)  
 R.J. Defouw, *Astrophys. J.* **209**, 266 (1976)  
 W. Deinzer, G. Hensler, M. Schuessler, E. Weisshaar, *Astron. Astrophys.* **139**, 426 (1984a)  
 W. Deinzer, G. Hensler, M. Schuessler, E. Weisshaar, *Astron. Astrophys.* **139**, 435 (1984b)  
 R.P. Drake, *Phys. Plasmas* **16**, 5501 (2009)  
 R.P. Feynman, *Progr. Low Temp. Phys.* Chap. 2. **1** (1955)  
 E.N. Frazier, J. Stenflo, *Sol. Phys.* **27**, 330 (1972)  
 P.E. Goa et al., *Supercond. Sci. Technol.* **14**, 729 (2001)  
 R. Howard, *Astrophys. J.* **130**, 193 (1959)  
 R. Howard, J. Stenflo, *Sol. Phys.* **22**, 402 (1972)  
 E.B. Hooper, L.D. Pearlstein, R.H. Bulmer, *Nucl. Fusion* **39**, 863 (1999)  
 S. Jafarzadeh et al., *Astron. Astrophys.* **549**, 116 (2013)

- B.B. Kadomtsev, *Plasma Physics and the Problem of Controlled Thermonuclear Reactions*, vol. IV (Pergamon Press, New York, 1959)
- B.B. Kadomtsev, in *Reviews of Plasma Physics*, vol. 2, ed. by M.A. Leontovich (Consultants Bureau, New York, 1966), p. 153
- M.D. Kruskal, R.M. Kulsrud, *Phys. Fluids* **1**, 265 (1958)
- L.D. Landau, *J. Phys. Mosc.* **5**, 71 (1941)
- G. Lapenta et al., *JGR* **111**, A12S06 (2006)
- R.B. Leighton, *Astrophys. J.* **130**, 366 (1959)
- M.A. Leontovich (ed.), *Reviews of Plasma Physics*, vol. 1 (Consultants Bureau, New York, 1965)
- M.A. Leontovich (ed.), *Reviews of Plasma Physics*, vol. 2 (Consultants Bureau, New York, 1966)
- W. Livingston, *Nature* **350**, 45 (1991)
- P. Lukes, M. Clupek, V. Babicky, *IEEE Trans. Plasma Sci.* **39**, 2644 (2011)
- H.S. McLean et al., *Rev. Sci. Instrum.* **72**, 556 (2001)
- F. Meyer, H.U. Schmidt, N.O. Weiss, *MNRAS* **179**, 741 (1977)
- A.I. Morozov, L.S. Solov'ev, in *Reviews of Plasma Physics*, vol. 2, ed. by M.A. Leontovich (Consultants Bureau, New York, 1966), p. 1
- L. Onsager, *Suppl. Nouvo Cimento* **6**, 249 (1949)
- D. Papathanasoglou, *Sol. Phys.* **21**, 113 (1971)
- E. Parker, *Astrophys. J.* **189**, 563 (1974a)
- E. Parker, *Astrophys. J.* **190**, 429 (1974b)
- E. Parker, in *Basic Mechanisms of Solar Activity*, IAU, ed. by V. Bumba, J. Kleczek (1976), p. 406
- E. Parker, *Cosmical Magnetic Fields* (Oxford University Press, Oxford, 1979)
- J.H. Piddington, *Astrophys. Space Sci.* **34**, 347 (1975)
- J.H. Piddington, *Astrophys. Space Sci.* **55**, 401 (1978)
- S.B. Pikel'ner, *Sov. Astron.* **6**, 757 (1963)
- D. Perrone et al., *SSRv.* **178**, 233 (2013)
- B. Roberts, A.R. Webb, *Sol. Phys.* **56**, 5 (1978)
- C.A. Romero-Talamas et al., *Phys. Plasmas* **13**, 2502 (2006)
- M.N. Rosenbluth, C. Longmire, *Ann. Phys.* **1**, 120 (1957)
- B. Ruiz Cobo, K.G. Puschmann, *Astrophys. J.* **745**, 141 (2012)
- D.D. Ryutov, M.P. Ryutova, *Sov. Phys. - JETP* **43**, 491 (1976)
- D.D. Ryutov, B.A. Remington, H.F. Robey, R.P. Drake, *Phys. Plasmas* **8**, 1804 (2001)
- D.D. Ryutov, B.A. Remington, *Astrophys. Space Sci.* **307**, 291 (2007)
- M.P. Ryutova, in *Proceedings of the XIII-th International Conference on Phenomena in Ionized Gases*, p. 859 (1977)
- M. Ryutova, T. Berger, A. Title, *Astrophys. J.* **676**, 1356 (2008)
- V.D. Shafranov, *At. Energy* **30**, 38 (1956)
- G. Scharmer, K. Bjelksjo, T. Korhonen, B. Lindberg, B. Petterson, in *Proceedings of SPIE in Innovative Telescopes and Instrumentation for Solar Astrophysics*, vol. 4853 ed. by S.L. Keil, S.V. Avakyan, p. 341 (2003)
- A.B. Severny, *Soviet Astronomy* **3**, 214 (1959)
- N.R. Sheeley Jr, *Astrophys. J.* **144**, 723 (1966)
- N.R. Sheeley Jr, *Sol. Phys.* **1**, 171 (1967)
- L. Spitzer in *Proceedings of 2-nd International Conference Atoms for Peace*. (Geneva 1958), p. 40
- H.C. Spruit, *Astron. Astrophys.* **98**, 155 (1981)
- O. Steiner, U. Grossmann-Doerth, M. Knoelker, M. Schuessler, *Astrophys. J.* **495**, 468 (1998)
- O. Steiner, *AIP Conf. Proc.* **919**, 74 (2007)
- J. Stenflo, *Astron. Astrophys. Rev.* **21**, 66 (2013)
- N.V. Steshenko, *Publ. Crime. Astrophys. Obs.* **37**, 21 (1967)
- J.T. Su et al., *Astrophys. J.* **710**, 170 (2010)
- V.K. Tkachenko, *Sov. Phys. JETP* **23**, 1049 (1966)
- E.J. Yarmchuk, M.J.V.R. Gordon, R.E. Packard, *Phys. Rev. Lett.* **43**, 214 (1979)

## Chapter 3

# Intrinsic Properties of Flux Tubes—Wave Phenomena

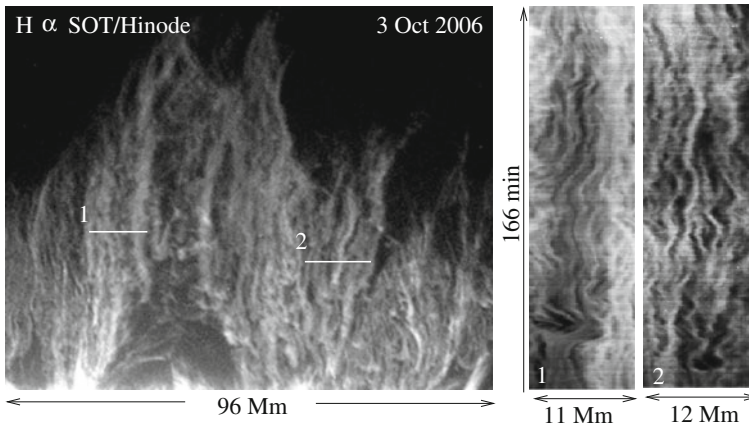
**Abstract** The ensembles of small-scale magnetic elements that cover 90% of the solar surface outside sunspots and active regions are embedded in highly dynamic environment. The individual flux tubes shaken by convective motions and interacting with the various wave trains, such as ubiquitous 5-min oscillations and magnetosonic waves, respond to these actions in various ways. First of all they are set in motion, which in a specific situation may have oscillatory character. In this chapter we shall consider conditions that are necessary for the excitation of waves propagating along the individual flux tubes, and specify their character.

### 3.1 Equations of Motion or How Are Tube Waves Excited

The photospheric flux tubes, constantly buffeted by convective flows and wave trains are brought into motion. The character of these motions is not a trivial question and requires detailed analysis of the flux tube behavior in a given field of flows. As flux tubes are long, slender and cylindrical, it is only natural to expect that generated motions will have an oscillatory character. We will see, however, that to successfully generate and *sustain* the oscillations *propagating* along flux tube require special conditions. If these conditions are not fulfilled the flux tube, just like a simple rope, disturbed on one end and even showing the first signs of wavy motion, quickly loses it. In other words, if not specially arranged, waves excited at one end of the rope damp out in “no time”. We will see, however, that conditions in solar atmosphere are favorable for excitation and maintenance of flux tube oscillations. Before moving to the main subject of this chapter it is tempting to see the oscillating flux tubes in action.

If we choose the photospheric flux tubes for direct illustration of oscillations, the task is challenging because flux tubes in the photosphere are aligned predominantly with the line-of-sight, and detecting their oscillations requires special decoding of the observational data (Ploner and Solanki 1997; Fujimura and Tsuneta 2009; Zlotnik et al. 2011). To see the vertical extent of flux tubes we choose for illustrative purpose the thin magnetic threads comprising prominences that are well observable at the limb.

To study a temporal variability of various small-scale formations, the special procedure called space-time cuts was developed for application to data compiled in



**Fig. 3.1** Image of the October 3, 2006 prominence taken in  $H\alpha$  line by the SOT instrument on Hinode (left). Right panels show space-time images obtained from 166 min movie with 15 s cadence. Kinked oscillatory motions of elemental filaments are ubiquitous phenomena. The scale of the left panel is 1/2 of the right panels

movies. This procedure allows one to follow motions of all the bright and dark patches lying along the cut (straight line or circle) made on the movie snapshot. Throughout the book we will use results of this procedure many times. Figure 3.1 (left) shows a limb portion of the prominence taken in  $H\alpha$  line by the SOT instrument on Hinode (October 3, 2006). Data were compiled in 166 min movie with 15 sec cadence. Examples of two space-time cuts are shown by white lines marked by numbers 1 and 2. Two right panels show the results of the space-time cuts: motions of dark and bright patches lying along the cuts during 166 min time interval. One can see clear oscillatory motion in exemplary magnetic filaments.

It is important to emphasize, however, that although the kinked oscillatory motions are ubiquitous phenomena in systems of magnetic filament, not all the flux tubes are subject to regular oscillatory motions. And there must be a specific mechanism providing the conditions for excitation and, most importantly, for maintenance of propagating wave with a definite frequency and amplitude that must be specific for each individual flux tube.

Thus, the questions are:

- What makes the motion acquired by a flux tube due to its interaction with outer flows or wave trains to be a wave motion with a specific frequency and amplitude?
- Why, on the other hand, do some flux tubes seemingly under the same conditions exhibit non-oscillatory motions?
- How are the physical parameters of individual flux tube and outer motions associated with the final outcome?

To find the answers to these basic questions we need to construct and solve the equation of motion of magnetic flux tubes in the dynamic environment. More precisely, we need to study collective phenomena in the ensembles of flux tubes

interacting with outer motions and having random parameters (radius  $R$ , magnetic field,  $B$ , plasma density  $\rho$ , inclination with respect to solar surface, etc.) to see why some flux tubes are brought to oscillatory motions while others are not.

### 3.1.1 Equation of Motion for a Single Flux Tube

We start with the situation typical to quiet sun, i.e., when magnetic filling factor is much less than unity,  $f_m = R^2/d^2$  ( $d$  is an average distance between the flux tubes), i.e.,

$$R \ll d, \quad (3.1)$$

and consider a long-wavelength limit,

$$\lambda \equiv k^{-1} \gg d. \quad (3.2)$$

As a first step we consider the motion of a separate magnetic flux tube relative to the plasma and find the force of interaction between the flux tube and the plasma. After that, by averaging over a volume containing many flux tubes (but still smaller than the wavelength  $\lambda$ ), we obtain an expression for the volume force acting on the medium due to the ensemble of flux tubes, which subsequently allows us to write macroscopic equations for a plasma containing many magnetic flux tubes.

We take the initial direction of the flux tube as the  $z$ -axis and denote the displacement of the flux tube from its equilibrium position by a vector  $\xi(z, t)$  which is transverse to the  $z$ -axis. Since the relative velocity of the plasma motion and flux tube is a first-order quantity, we can neglect the change in the size and shape of the cross section of the flux tube when evaluating the interaction force.

The equation of motion for the tube having constant circular cross section of radius  $R$  can be written as follows:

$$\rho_i \pi R^2 \frac{\partial^2 \xi}{\partial t^2} = \rho_e \pi R^2 \frac{\partial \mathbf{v}_\perp}{\partial t} + \rho_e \pi R^2 \left( \frac{\partial \mathbf{v}_\perp}{\partial t} - \frac{\partial^2 \xi}{\partial t^2} \right) + \pi R^2 \frac{B^2}{4\pi} \frac{\partial^2 \xi}{\partial z^2} \quad (3.3)$$

where  $\mathbf{v}_\perp$  is the normal component of the macroscopic velocity of the plasma,  $B$  is the magnetic field inside flux tube, and  $\rho_i$  and  $\rho_e$  are the plasma densities inside and outside flux tube respectively. The meaning of the forces given on the right-hand side of the equation is quite simple: the first term corresponds to the Archimedes force (pushing out), acting on the tube moving in a liquid with acceleration; the second term takes into account the effect of the added mass per unit length, namely  $\pi R^2 \rho_e$  (Landau and Lifshitz 1987), also arising due to the acceleration; the third term is the effect of the magnetic tension inside the flux tube.

When using the added mass concept we assumed that the plasma is incompressible. This is valid since the velocities  $\partial \xi / \partial t$  and  $\mathbf{v}_\perp$  are small compared to the sound speed while the period of the long-wave oscillations is large compared to natural

periods of the radial oscillations of the flux tubes. Equation (3.3) can be written in the form

$$\frac{\partial^2 \xi}{\partial t^2} - \frac{B^2}{4\pi(\rho_i + \rho_e)} \frac{\partial^2 \xi}{\partial z^2} = \frac{2}{(1 + \rho_i/\rho_e)} \frac{\partial \mathbf{v}_\perp}{\partial t} \quad (3.4)$$

In the absence of external motions, i.e., when  $\mathbf{v}_\perp = 0$ , this equation describes the natural kink oscillations of the flux tube with phase speed (Ryutov and Ryutova 1976; Spruit 1981)

$$\frac{\omega}{k} = \frac{B}{\sqrt{4\pi(\rho_i + \rho_e)}} \quad (3.5)$$

It is remarkable that (3.4), which is the fundamental equation for kink oscillations of flux tube and corresponding expression for phase velocity (3.5), were first derived in such a simple way just by considering the balance of forces (Ryutov and Ryutova 1976). Of course, (3.4) can be derived from MHD equations as well, which will be discussed later in this chapter. It is important to note however that the equation of motion for individual flux tube only shows that the flux tube may perform the oscillations with frequency determined by its magnetic field and plasma density inside and outside it. But the equation alone does not give an answer to questions of how flux tube oscillations are excited, and what determines whether the flux tube is capable to sustain these oscillations or not. As mentioned above, for this problem we need to consider the motion of an ensemble of flux tubes randomly distributed over their parameters.

### 3.1.2 Macroscopic Motions of an Ensemble of Flux Tubes

To describe an ensemble of flux tubes and collective phenomena in it we have to take into account that each separate tube is characterized by its own physical parameters, magnetic field,  $B$ , radius,  $R$ , an internal plasma density,  $\rho_i$ , and temperature,  $T_i$ . For simplicity, we assume that the matter inside the flux tube is cold,  $T_i \ll T_e$ , and we can neglect the gas-kinetic pressure,  $p_i$ , inside the flux tubes. This assumption is not at all a principal one and can always be taken into account. Then the unperturbed state can be described by the pressure equilibrium condition:

$$\frac{B^2}{8\pi} = p_e \equiv \frac{1}{\gamma} \rho_e c_s^2 \quad (3.6)$$

where  $p_e$  is the pressure outside the flux tubes,  $\gamma$  is the specific heat ratio, and  $c_s$  is the sound speed.

We now introduce the dimensionless parameter

$$\eta = \frac{\rho_i}{\rho_e}, \quad (3.7)$$

which together with the tube radius,  $R$ , describes the individual properties of the flux tube, which obviously may change greatly from one tube to another. So, rewriting the

equation of motion (3.3) for a separate tube and henceforth labeling the displacement vector,  $\xi_{\perp}$  with the index  $\eta$  (emphasizing that the displacement of the tube depends on  $\eta$ ), we have

$$\frac{\partial^2 \xi_{\eta}}{\partial t^2} - \frac{2}{\gamma} \frac{c_s^2}{(1 + \eta)} \frac{\partial^2 \xi_{\eta}}{\partial z^2} = \frac{2}{1 + \eta} \frac{\partial \mathbf{v}_{\perp}}{\partial t} \quad (3.8)$$

Now we proceed to the derivation of the equation for “macroscopic” quantities. By macroscopic we mean the quantities averaged over the volumes with the characteristic dimension  $d$  satisfying the inequalities (3.1) and (3.2):

$$R \ll d \ll \lambda \quad (3.9)$$

In other words, we take averages over the volumes which comprise a large number of flux tubes but are still small compared to the characteristic scale  $\lambda$  of variation of “macroscopic” parameters.

All the flux tubes situated in some averaging volume of the size  $d$  as in (3.9) are subject to the same external conditions (the same  $\mathbf{v}$  in (3.8)). In particular, the motion of the flux tubes with the same  $\eta$  in the averaging volume are identical.

To find the macroscopic equations of motion we introduce the distribution function of flux tubes,  $f$ , with respect to the parameters  $R$  and  $\eta$ , and define it as follows:

$$d\alpha = f(R, \eta) dR d\eta, \quad (3.10)$$

where  $d\alpha$  is the fraction of the volume which is occupied by flux tubes with values of the parameters  $R$  and  $\eta$  in the intervals  $(R, R + dR)$ ,  $(\eta, \eta + d\eta)$ . The normalization of the function  $f$ , defined in such a way, is clearly the following:

$$\alpha = \int_0^{\infty} \int_0^{\infty} dR d\eta f(R, \eta) \quad (3.11)$$

Here  $\alpha$  is simply the total fraction of the volume occupied by flux tubes, which simply corresponds to the magnetic filling factor of the medium. And, according to our assumption (we are considering the case of widely spaced magnetic flux tubes:  $r \ll d$ ),  $\alpha \sim R^2/d^2 \ll 1$ .

It is convenient also to introduce the distribution function only over the parameter  $\eta$ :

$$g(\eta) = \int_0^{\infty} f(R, \eta) dR \quad (3.12)$$

Obviously,

$$\alpha = \int_0^{\infty} g(\eta) d\eta \quad (3.13)$$

From (3.3) it is clear that the force acting on the unit length of the flux tube from the side of the ambient plasma is equal to

$$\mathbf{F}_\eta = \pi R^2 \rho_e \left( 2 \frac{\partial \mathbf{v}_\perp}{\partial t} - \frac{\partial^2 \boldsymbol{\xi}}{\partial t^2} \right). \quad (3.14)$$

Of course, this force is eventually produced by the momentum flux through the surface of the tube. The tube, on the other hand, acts on the ambient medium with the force  $-\mathbf{F}_\eta$ .

The macroscopic force  $\mathbf{F}(\mathbf{r}, t)$  acting on the unit volume of the external fluid can be presented as a result of the summation of the forces  $-\mathbf{F}_\eta$  (see (3.14)) over all the flux tubes occupying the averaging volume:

$$\mathbf{F}(\mathbf{r}, t) = -\rho_e \int \left[ 2 \frac{\partial \mathbf{v}_\perp}{\partial t} - \frac{\partial^2 \boldsymbol{\xi}}{\partial t^2} \right] g(\eta) d\eta, \quad (3.15)$$

where dependence on  $\mathbf{r}$  describes the variation of all the quantities over the volume.

The macroscopic equation of motion of the ambient plasma can now be written as

$$\rho_e \frac{\partial \mathbf{v}}{\partial t} = -c_s^2 \nabla \delta \rho_e + \mathbf{F}(\mathbf{r}, t) \quad (3.16)$$

or

$$\rho_e \frac{\partial \mathbf{v}}{\partial t} = -c_s^2 \nabla \delta \rho_e - \rho_e \int \left[ 2 \frac{\partial \mathbf{v}_\perp}{\partial t} - \frac{\partial^2 \boldsymbol{\xi}}{\partial t^2} \right] g(\eta) d\eta. \quad (3.17)$$

where  $\delta \rho_e$  is the density perturbation of ambient plasma under the adiabatic law

$$\delta p_e = c_s^2 \delta \rho_e, \quad (3.18)$$

satisfying the continuity equation

$$\frac{\partial \rho_e}{\partial t} + \rho_e \operatorname{div} \mathbf{v} = 0 \quad (3.19)$$

In the above equations we skip the averaging sign over the macroscopic fluid velocity  $\mathbf{v}$  and macroscopic pressure perturbation  $\delta p_e$ .

Strictly speaking, there are additional terms of the order of  $\alpha$  in the continuity and momentum equations: the terms which arise from the fact that the part of the averaging volume is occupied by the flux tubes. We neglect these terms because of the assumed smallness of  $\alpha$ . If retained, these terms would give rise to the appearance of a small ( $\sim \alpha$ ) correction of the phase velocity of sound waves. The first term in the integrand of (3.17) which after the integration over  $\eta$  acquires the form  $-2\rho_e \partial \mathbf{v}_\perp / \partial t$ , gives rise to corrections of the same order of smallness.



The role of the terms proportional to  $\alpha$  can be also seen from the energy consideration. Indeed, multiplying (3.17) by  $\mathbf{v}$ , and taking into account (3.19) we obtain for the energy density of a plasma motion:

$$\rho_e \frac{\partial}{\partial t} \int dV \left[ \frac{1}{2} \mathbf{v}^2 + \frac{1}{2} c_s^2 \left( \frac{\delta \rho_e}{\rho_e} \right) + \alpha \mathbf{v}_\perp^2 \right] = \rho_e \int dV \int g(\eta) d\eta \frac{\partial^2 \boldsymbol{\xi}_\eta}{\partial t^2} \cdot \mathbf{v}_\perp \quad (3.20)$$

We see that the term containing  $\alpha$  on the left-hand side which appeared from terms proportional to  $2\partial \mathbf{v}_\perp / \partial t$  on the right-hand side of (3.17) is negligibly small. So that, accounting for this particular and analogous terms, or completely neglecting them, results in only some minor ( $\sim \alpha$ ) redefining of the energy of fluid motion. Accordingly, when we study the energy exchange between the fluid motion and the flux tubes oscillations for the case of widely spaced flux tubes with  $\alpha \ll 1$ , we can omit this, and analogous terms.

On the other hand, taking into account the force  $\mathbf{F}$  in (3.16), which is also of the order of  $\alpha$ , leads to a qualitatively new effect associated with the elasticity of the flux tubes. In other words, the only term of the order of  $\alpha$  which matters in (3.17) is that proportional to  $\partial \boldsymbol{\xi}_\eta^2 / \partial t^2$ , as this term describes the energy exchange between the oscillating flux tubes and the fluid. It is just this term that is responsible for the qualitatively new effect which consists in the Landau-like damping of the acoustic waves and transferring their energy into the energy of flux tube oscillations.

Equations (3.8), and (3.17)–(3.19) form a closet set describing large-scale, macroscopic motions of the fluid containing randomly distributed flux tubes. Note that in these motions the flux tubes behave as an ensemble, and cannot be described as individual elements. In this sense, one can say that (3.8) and (3.17)–(3.19) describe the collective phenomena in the system of flux tubes. On the other hand, as will shall see in the next section, such an approach allows us to reveal some remarkable properties of *individual* flux tube that cannot be found without a macroscopic approach.

## 3.2 Absorption of Acoustic Waves—Landau Resonance

Using (3.8), and (3.17)–(3.19) we can study the interaction of the acoustic waves with an ensemble of flux tubes randomly (and widely) distributed in space and over their parameters,  $R$ ,  $B$ ,  $\rho_i$ , etc. Consider the eigensolutions of this set of equations in the form of traveling waves, i.e., when all perturbed quantities,  $\boldsymbol{\xi}_\eta$ ,  $\mathbf{v}$  and  $\delta \rho$ , change in proportion to  $\exp(-i\omega t + i\mathbf{k}\mathbf{r})$ .

Using (3.8) we first express  $\boldsymbol{\xi}_\eta$  through  $\mathbf{v}_\perp$ :

$$\boldsymbol{\xi}_\eta = \frac{2i\omega \mathbf{v}_\perp}{\omega^2(1 + \eta) - 2\gamma^{-1} c_s^2 k^2 \cos^2 \theta} \quad (3.21)$$

where  $k \cos \theta = k_z$  is the component of the acoustic wave vector along the flux tube, and  $\theta$  is the angle between the direction of propagation of the sound wave

and the flux tube axis. We consider the solution with  $\text{Re } \omega > 0$ . Substituting (3.21) into (3.15) we obtain

$$\mathbf{F} = i\omega\rho_e\mathbf{v}_\perp\mathcal{I}(\omega, \mathbf{k}) \quad (3.22)$$

where

$$\mathcal{I}(\omega, \mathbf{k}) = 2 \int_0^\infty \left[ 1 - \left( \eta + 1 - \frac{2c_s^2 k^2 \cos^2 \theta}{(\omega + i0)^2} \right)^{-1} \right] g(\eta) d\eta \quad (3.23)$$

Obviously, as  $t$  approaches  $-\infty$  the perturbations must vanish, and so we may replace  $\omega$  by  $\omega + i0$  in the denominator of the integrand.

The integral  $\mathcal{I}(\omega, \mathbf{k})$  is of the order of  $\alpha$  and is therefore small compared to unity. This fact allows us to easily obtain a dispersion relation. Using (3.16), (3.19) and (3.22), (3.23), we have

$$\omega \simeq kc_s \left[ 1 - \frac{\sin^2 \theta}{2} \mathcal{I}(\omega, \mathbf{k}) \right] \quad (3.24)$$

The effect of an ensemble of magnetic flux tubes on the oscillations of the medium enters into the problem through the integral  $\mathcal{I}(\omega, \mathbf{k})$ . The form of  $\mathcal{I}(\omega, \mathbf{k})$  containing a resonant denominator indicates the resonance character of the interaction between the medium and the flux tubes. And the resonance condition is

$$c_s = v_{\text{ph}} \cos \theta \quad (3.25)$$

where  $v_{\text{ph}} = \omega/k$  is the phase speed of flux tube oscillations (3.5). The condition (3.25) is analogous to the Cherenkov condition in Landau resonance theory (Landau 1946). The analogy with Landau damping is described in Appendix A.

Thus, when condition (3.25) is satisfied, there occurs a resonant transfer of acoustic wave energy into the energy of flux tube oscillations. Since the plasma density and magnetic field are different inside different flux tubes, the phase velocity, (3.5), varies from tube to tube. Thus, one can find for each angle of propagation,  $\theta$ , the tubes for which the condition (3.25) is satisfied and which, therefore, remove energy from the sound wave, and maintain their own oscillatory motion.

To determine corresponding damping rate we have to evaluate  $\mathcal{I}(\omega, \mathbf{k})$ . To do this we can set the frequency equal to the solution of the dispersion relation for a ‘‘pure’’ plasma (free from flux tubes), namely  $\omega = kc_s$ . We must also note that taking into account the real part of  $\mathcal{I}$  leads only to an insignificant change in the frequency of the oscillations. Thus, it is sufficient to find an imaginary part of  $\mathcal{I}$ . Using the  $\delta$ -function representation

$$\text{Im} \frac{1}{x + i0} = -i\pi\delta(x), \quad (3.26)$$

we find the damping rate,  $\nu \equiv -\text{Im}\omega$ , of the sound wave,

$$\nu = \frac{kc_s \sin^2 \theta}{2} \text{Im}\mathcal{I}(\omega, \mathbf{k}), \quad (3.27)$$

to be

$$\nu = \begin{cases} \pi k c_s \sin^2 \theta g(\eta), & \eta_0 > 0 \\ 0 & \eta_0 < 0 \end{cases} \tag{3.28}$$

where

$$\eta_0 = \frac{2 \cos^2 \theta}{\gamma} - 1 \tag{3.29}$$

One could arrive at the same result by a more formal method, considering the solution of the Cauchy problem for the set (3.8)–(3.19) and using a Laplace transform—exactly in the same way as is done by Landau (1946) studying Langmuir oscillations in a rarefied plasma.

A sketch of the function  $g(\eta)$ , which according to our basic assumptions is a smooth broad function of flux tube parameters, is shown in Fig. 3.2. Here,  $\Delta\eta$  is the width of the distribution function, i.e., the interval of parameters of all flux tubes,  $\Delta\eta \gg \text{Im}\omega/\omega = \nu/\omega$ , and  $\delta\eta$  is the interval of resonant flux tubes, such that  $\delta\eta \sim \alpha \ll \Delta\eta$ . If we make the natural assumption that the plasma density inside the flux tubes,  $\rho_i$ , changes with respect to the surrounding density,  $\rho_e$ , by not more than several times from one tube to another, we can conclude that the width,  $\Delta\eta$ , of that region of  $\eta$ -values where the distribution function is essentially nonzero, is of the order of unity, then we have  $g(\eta_0) \simeq \alpha$ . This allows us to write the following estimate for the damping rate

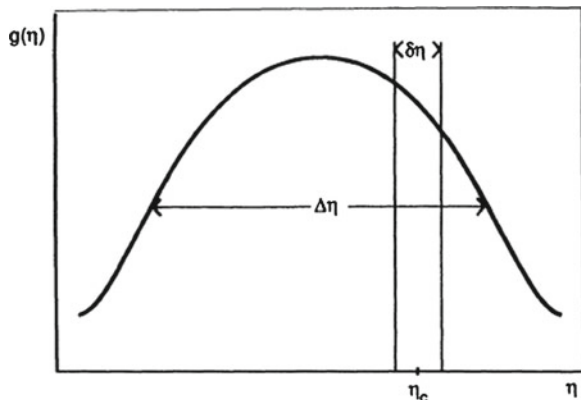
$$\frac{\nu}{k c_s} \simeq \alpha. \tag{3.30}$$

This estimate holds only for a rather narrow range of values of  $\theta$  where  $\eta_0 > 0$ , that is, where

$$\cos^2 \theta > \frac{\gamma}{2} \tag{3.31}$$

For a monatomic gas the corresponding region is about  $\theta \leq \arccos(5/6)^{1/2} \simeq -5^\circ$ . This restriction comes from the condition  $\eta_0 > 0$  merely because of the

**Fig. 3.2** Sketch of the distribution function of flux tubes,  $g(\eta)$ , as a function of the ratio of internal and external densities of the tubes,  $\eta = \rho_i/\rho_e$



approximation (3.6). If we remove this restriction and take into account plasma pressure inside the flux tube, then instead of (3.23), we find

$$\mathcal{I}(\omega, \mathbf{k}) = 2 \int_0^\infty d\eta d v_A g(\eta, v_A) \left[ 1 - \frac{\omega^2}{(1 + \eta)[(\omega + i0)^2 + c_k^2 k^2 \cos^2 \theta]} \right] \quad (3.32)$$

Here  $v_A$  is the Alfvén velocity inside flux tube

$$v_A = \frac{B}{\sqrt{4\pi\rho_i}} \quad (3.33)$$

The essential difference between this result and (3.23) is that now there is no evident restriction on the propagation angle: an integration over the parameter  $\eta$  gives directly the Cherenkov condition for arbitrary values of parameter  $\eta$  and angle  $\theta$ .

### 3.3 Effects of Noncollinearity of Flux Tubes

It is hard to imagine that magnetic flux tubes, embedded in highly dynamic environment, stay parallel to each other. Obviously, each flux tube has its own (and arbitrary) inclination with respect to surface, which means that flux tubes are essentially noncollinear. This fact turned to be very important in their interaction with the ambient atmosphere and leads to some striking effects in their dynamics.

To take into account noncollinearity of the flux tubes let us characterize the direction of a separate flux tube by a single vector  $\mathbf{n}$  directed along the flux tube axis. Denote the distribution function of flux tubes with respect to their directions by  $h(\mathbf{n})$ . To single out the effect of noncollinearity of the flux tubes we assume in these calculations that the parameter  $\eta$  is fixed. The normalization of the function  $h(\mathbf{n})$  is

$$\alpha = \int h(\mathbf{n}) d\omega \quad (3.34)$$

where  $\alpha$  is again the magnetic filling factor and  $d\omega$  is an element of solid angle. The component of the macroscopic velocity at right angles to the vector  $\mathbf{n}$  is equal to  $\mathbf{v} - \mathbf{n}(\mathbf{nv})$ . We have thus instead of (3.21)

$$\boldsymbol{\xi}_{\mathbf{n}} = -\frac{2i\omega[\mathbf{v} - \mathbf{n}(\mathbf{nv})]}{\omega^2(1 + \eta) - 2\gamma^{-1}c_s^2(\mathbf{kn})^2} \quad (3.35)$$

We have labeled here the displacement  $\boldsymbol{\xi}$  by the index  $\mathbf{n}$ , to reflect dependence of  $\boldsymbol{\xi}$  on the orientation of the flux tube.

The volume force acting on the plasma can by analogy with (3.22) be written as

$$F_i = -i\omega\rho_e K_{ij} v_j \quad (3.36)$$

where

$$K_{ij} = -2 \int doh(\mathbf{n})(\delta_{ij} - n_i n_j) \left[ 1 - \left( \eta + 1 - \frac{2c_s^2(\mathbf{kn})^2}{\gamma(\omega + i0)^2} \right)^{-1} \right] \quad (3.37)$$

Once we have the expression for the force we can use (3.16)–(3.19) to write down the dispersion relation

$$\omega = kc_{se} \left[ 1 - \frac{k_i k_j}{k^2} K_{ij}(\omega, \mathbf{k}) \right], \quad (3.38)$$

and, bearing in mind that  $K_{ij}$  is small, find the small imaginary correction to the frequency:

$$\frac{\nu}{kc_s} = \int doh(\mathbf{n}) \left[ 1 - \frac{(\mathbf{kn})^2}{k^2} \right] \delta \left[ \eta + 1 - \frac{2(\mathbf{kn})^2}{\gamma k^2} \right] \quad (3.39)$$

In the particular case of an isotropic distribution of flux tubes we have  $h(\mathbf{n}) = \alpha/4\pi$ , and the expression for the damping rate is especially simple

$$\frac{\nu}{kc_s} = \frac{\sqrt{2}}{8} \frac{\alpha\gamma[2 - \gamma(1 - \eta)]}{\sqrt{\gamma(1 + \eta)}} \quad (3.40)$$

where we assumed that  $\eta < 2/\gamma - 1$ .

Thus, the contribution of noncollinearity of flux tubes into the process of absorption of sound waves and accumulation of their energy is quite essential. The more the tubes deviate from the vertical direction, the more efficient the absorption of sound waves becomes.

The fact that magnetic flux tubes are noncollinear plays an essential role in the interaction of neighboring flux tubes, namely allowing the reconnection between the *same* polarity magnetic flux tubes that leads to farther fragmentation of flux tubes and other macroscopic effects that are observed. These will be addressed in the following chapters.

### 3.4 Exact Theory of Linear Oscillations of Magnetic Flux Tube

Linear oscillations of flux tubes can be described straightforward from the MHD equations. The linearized set of MHD equations for the plasma *inside* the magnetic flux tube is of the form

$$\rho_i \frac{\partial \mathbf{v}}{\partial t} = \frac{1}{4\pi} [[\nabla \times \mathbf{b}] \times \mathbf{B}], \quad \frac{\partial \mathbf{b}}{\partial t} = \nabla[\mathbf{v} \times \mathbf{B}], \quad (3.41)$$

where  $\mathbf{v}$  and  $\mathbf{b}$  are the perturbations of velocity and magnetic field respectively. As the gas kinetic pressure inside the flux tubes vanishes the equation of continuity splits off.

In cylindrical coordinates  $(r, \phi, z)$  with a  $z$ -axis directed along the flux tube, the linearized MHD equations with perturbations proportional to  $\exp(-i\omega t + ik_z z + im\phi)$  imply that the velocity components inside the flux tube are as follows:

$$v_r = -\frac{\partial\psi_i}{\partial r}, \quad v_\phi = -\frac{im\psi_i}{r}, \quad v_z = 0 \quad (3.42)$$

where  $m = 0, \pm 1, \pm 2, \pm 3, \pm 4, \dots$ , and  $\psi_i$  satisfies the equation

$$\frac{1}{r} \frac{\partial}{\partial r} r \frac{\partial\psi_i}{\partial r} + \left( \frac{\omega^2}{v_A^2} - k_z^2 - \frac{m^2}{r^2} \right) \psi_i = 0 \quad (3.43)$$

In the nonmagnetized region outside flux tube the linearized set of equations can also be reduced to a single equation for the velocity potential  $\psi_e$  ( $\mathbf{v}_e = \nabla\psi_e$ ):

$$\frac{1}{r} \frac{\partial}{\partial r} r \frac{\partial\psi_e}{\partial r} + \left( \frac{\omega^2}{c_s^2} - k_z^2 - \frac{m^2}{r^2} \right) \psi_e = 0 \quad (3.44)$$

The perturbation of gas-kinetic pressure in terms of  $\psi_e$  is then

$$\delta p_e = \frac{ic_s^2}{\omega\gamma} \rho_e \Delta\psi_e \quad (3.45)$$

The external sound speed and Alfvén velocity are connected through the relation (cf. (3.6))

$$v_A^2 = \frac{2}{\gamma\eta} c_s^2. \quad (3.46)$$

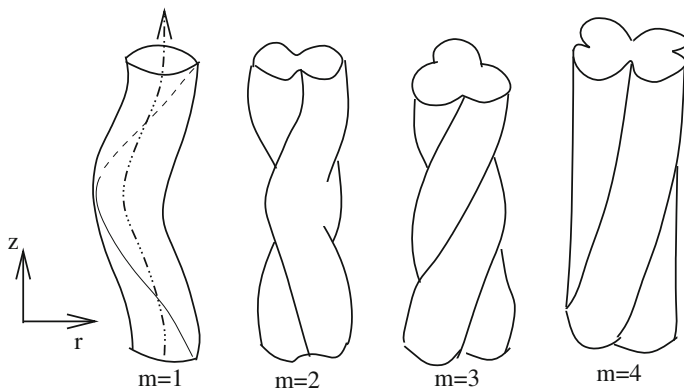
On the surface of flux tube, at  $r = R$ , we must satisfy the conditions for the continuity of the normal components of velocity and total pressure,

$$v_r|_i = v_r|_e, \quad \frac{Bb_z}{4\pi} = \delta p_e \quad (3.47)$$

Using (3.42)–(3.46) we can reduce the set of boundary conditions to a single equation for the logarithmic derivatives of  $\psi_i$  and  $\psi_e$ :

$$\left( \eta - \frac{2k_z^2 c_s^2}{\gamma\omega^2} \right) \frac{\partial \ln \psi_e}{\partial r} = \frac{\partial \ln \psi_i}{\partial r} \quad \text{at } r = R \quad (3.48)$$

Inside the flux tube the solution is proportional to an  $m$ th order Bessel function  $\psi_i \sim J_m(q_i, r)$ , where  $q_i = (\omega^2/v_A^2 - k_z^2)^{1/2}$ . Outside the flux tube the solution has the form of outgoing waves:  $\psi \sim H_m^{(1)}(q_e r)$ , where  $H^{(1)}$  is a first-order Hankel function, and  $q_e = (\omega^2/c_s^2 - k_z^2)^{1/2}$  (we have chosen the branch of the root corresponding to  $\text{Re } q_e > 0$ ).



**Fig. 3.3** Shape of the flux tube for various  $m \neq 0$  modes

Since we are considering long-wave oscillations with  $k_z R \ll 1$ , the arguments of the Bessel and Hankel functions in the boundary condition (3.48) are small compared to unity. If we retain only the first nonvanishing terms in the expansion with respect to this small parameter we obtain the following dispersion relation:

$$\omega_m = \Omega \equiv k_z c_s^2 \sqrt{\frac{2}{\gamma(1+\eta)}} \quad (3.49)$$

for  $m = \pm 1, \pm 2, \pm 3, \pm 4, \dots$ . It is only natural that the oscillations of flux tubes may have multiple azimuthal modes. The first four modes (except  $m = 0$ ) are shown in Fig. 3.3.

The dipole mode,  $m = \pm 1$  corresponds to kink oscillations of flux tube. Note that eigenfrequencies of all the modes are independent of the azimuthal number,  $m$ , and are the same, except for axisymmetric mode  $m = 0$ . This case requires separate consideration and will be addressed in Sect. 3.7.

Although the frequencies of all the modes are the same, their *amplitudes* and *damping rates* are different and strongly depend on the mode number. The oscillation amplitude in the vicinity of flux tube is proportional to  $(kR)^{|m|}$ , and progressively diminishing for higher order modes.

### 3.5 Radiation of Secondary Waves by Oscillating Flux Tubes

So far, considering the equation of motion of a separate flux tube (see 3.8), we have neglected the compressibility of the medium surrounding the flux tube. This was justified by the smallness of the frequency of oscillations  $\omega = kc_s$  as compared to  $c_s/R$ . Taking compressibility into account, i.e., higher-order terms in the parameter

$\omega R/c_s \sim kR$ , leads to the appearance of a new effect, namely to the radiation of secondary acoustic or MHD waves by the oscillating flux tubes.

If we retain in the boundary condition (3.48) the next order term in powers of  $kR$ , it leads, on the one hand to a small change in the real part of the frequency and, on the other hand, to the appearance of radiative damping of oscillations. The resulting damping rate  $\nu_{\text{rad}}^{|m|}$  has the following form:

$$\nu_{\text{rad}}^{|m|} = \frac{\pi\Omega}{|m|!(|m|-1)!(1+\eta)} \left(\frac{Rk_z}{2}\right)^{2|m|} \left[\frac{2}{\gamma(1+\eta)} - 1\right]^{|m|} \quad (3.50)$$

Thus an oscillating flux tube may radiate secondary acoustic waves. The frequency of radiated waves is obviously the same as frequency of natural oscillations of flux tube. The corresponding radial wave number  $k_r$  is determined from the dispersion relation and is

$$k_r = \frac{(\omega^2 - k^2 c_s^2)^{1/2}}{c_s}, \quad (3.51)$$

Radiation of secondary waves occurs only if  $k_r$  is real, that is, if the phase velocity ( $\omega/k$ ) of flux tube oscillations is larger than  $c_s$ . For the kink mode, for example, the radiative damping rate is

$$\nu_{\text{rad}} = \frac{\pi\Omega}{(1+\eta)} \left(\frac{Rk_z}{2}\right)^2 \left[\frac{2}{\gamma(1+\eta)} - 1\right] \quad (3.52)$$

The ability of flux tube to radiate the secondary acoustic or MHD waves provides one of the most important mechanisms of energy transfer from primary acoustic waves and convective motions to overlying atmosphere. Indeed, as was shown in the previous sections the resonant flux tubes absorb the energy of a sound wave in a time

$$\tau_{\text{res}} \simeq \frac{1}{\nu_{\text{res}}}, \quad (3.53)$$

where  $\nu \simeq \alpha k c_s$ , see (3.30) and (3.40).

The absorbed energy is accumulated in flux tubes in the form of their natural oscillations, and then, after a considerably longer time

$$\tau_{\text{rad}} \simeq \frac{1}{\nu_{\text{rad}}}, \quad (3.54)$$

the flux tubes release the accumulated energy in the form of secondary acoustic waves, or secondary MHD waves if the surrounding plasma is magnetized.

The main condition for the above process to take place is as follows:

$$\nu_{\text{res}} > \nu_{\text{rad}}, \quad (3.55)$$

Since  $\nu_{\text{res}} \simeq \omega\alpha$  and  $\nu_{\text{rad}} \simeq \omega k^2 R^2$ , the condition (3.55) is satisfied if  $k^2 R^2 < \alpha$ . Bearing in mind that the distance,  $d$ , between flux tubes is of the order of  $R/\alpha$ , we



can write that  $kd \ll 1$ . In other words, under the conditions when a macroscopic description of widely spaced flux tubes is applicable ( $k \ll d^{-1}$ ), the condition (3.55) is satisfied automatically. Luckily, these are typical conditions for quiet sun regions and rarefied plages.

### 3.6 Scattering of Acoustic Waves and Maximum Energy Input

The process of energy transfer to the medium can also occur without preliminary accumulation of energy in the form of flux tube oscillations. Depending on the parameters of the medium, the interaction between the primary sound wave and an ensemble of flux tubes may have a character of resonant scattering.

Suppose a plane acoustic wave,  $\omega = kc_s$ , is propagating with unit amplitude

$$\chi = -\frac{1}{2}\exp(-i\omega t + i\mathbf{k}\mathbf{r}) + \text{c.c.}, \quad (3.56)$$

c.c. stands for complex conjugate. In the presence of a magnetic flux tube the solution outside flux tube will be superposition of this plane wave and outgoing cylindrical waves:

$$\psi_e = e^{-i\omega t + ik_z z} \left[ -\frac{1}{2}e^{-iq_e r \cos\phi} + \sum_{m=-\infty}^{\infty} A_m H_m^{(1)}(q_e r) e^{im\phi} \right] + \text{c.c.} \quad (3.57)$$

where we have used the relation  $\mathbf{k}\mathbf{r} = k_z z + q_e r \cos\phi$ .

Inside the flux tube the solution has the form

$$\psi_i = e^{-i\omega t + ik_z z} \sum_{m=-\infty}^{\infty} B_m J_m(q_i r) e^{im\phi} + \text{c.c.} \quad (3.58)$$

Using the identity

$$e^{iq_e r \cos\phi} \equiv \sum_{m=-\infty}^{\infty} i^m J_m(q_e r) e^{im\phi} + \text{c.c.} \quad (3.59)$$

and writing down the boundary condition (3.48) for each azimuthal harmonic  $m$  we obtain the following expression for the coefficients  $A_m$ :

$$A_m = -\frac{i^m}{2} \frac{\tilde{\eta} q_i J'_m(q_i R) J_m(q_e R) - q_e J'_m(q_e R) J_m(q_i R)}{\tilde{\eta} q_e H_m^{(1)'}(q_e R) J_m(q_i R) - q_i J'_m(q_i R) H_m^{(1)}(q_i R)} \quad (3.60)$$

where  $\tilde{\eta} = \eta - 2k_z^2 c_s^2 / \gamma \omega^2$ .

For long-wave oscillations with  $kR \ll 1$  and  $m > 0$ ,  $A_m$  reduces to

$$A_m = -\frac{\pi i^{|m|-1}}{|m|!(|m|-1)!(1+\eta)} \left(\frac{kR \sin \theta}{2}\right)^{2|m|} \frac{\Omega}{\omega - \Omega + i\nu_{\text{rad}}^{|m|}} \quad (3.61)$$

where  $\Omega(\eta)$  is given by (3.49).

The power radiated in the  $m$ -th mode per unit length of the flux tube is  $2\pi\rho Q_m$ , where  $Q_m$  is the density of radiated energy flux

$$Q_m = |A_m|^2 \frac{\rho c_s k}{\pi r} \quad (3.62)$$

The energy density,  $W$  in the incident acoustic wave is  $\rho\omega^2 c_s^2/2$ . Now we can find relation between this energy and the energy,  $Q$ , of the secondary waves radiated per unit time and per unit length of the flux tube to be

$$Q = \zeta(\eta, R, \omega) W \quad (3.63)$$

where

$$\zeta = \zeta_0 + 2 \sum_{m=1}^{\infty} \zeta_m \quad (3.64)$$

with the coefficients  $\zeta_0$  and  $\zeta_m$  as

$$\zeta_0 = \frac{c_s^2 \pi^2}{k} \frac{1}{16} (kR)^2 \left(\sin^2 \theta - \frac{\gamma}{2}\right), \quad (3.65)$$

$$\zeta_m = \frac{c_s^2}{k} \left[ \frac{\pi}{|m|!(|m|-1)!(1+\eta)} \right]^2 \left(\frac{kR \sin \theta}{2}\right)^{4|m|} \frac{\Omega^2}{(\omega - \Omega)^2 + (\nu_{\text{rad}}^{|m|})^2} \quad (3.66)$$

In these expressions  $\Omega(\eta)$  and  $\nu_{\text{rad}}^{|m|}$  are determined by (3.49) and (3.50), respectively, and  $\cos \theta = k_z/k$ .

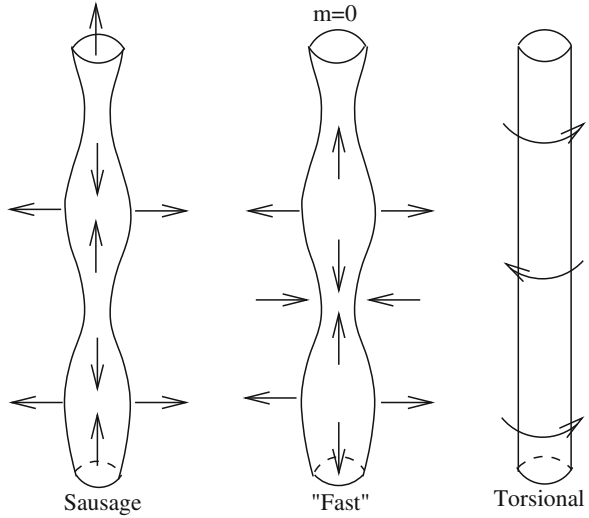
Equations (3.63)–(3.66) solve the problem of energy input to the medium due to the radiation of secondary waves by a single oscillating flux tube.

## 3.7 Axisymmetric Oscillations of Flux Tube

### 3.7.1 Types of $m = 0$ Mode

Axisymmetric oscillations of flux tube have their own peculiarities and should be considered separately (Cram and Wilson 1975; Defouw 1976; Roberts and Webb 1978; Ryutova 1981).

**Fig. 3.4** Types of axisymmetric oscillations of flux tube with azimuthal wave number  $m = 0$



There are three types of axisymmetric modes with  $m = 0$  (Fig. 3.4):

1. The analogue of slow magnetosonic waves, so-called sausage or tube waves with the phase velocity

$$c_T = \frac{\omega}{k} = \frac{c_s v_A}{\sqrt{c_s^2 + v_A^2}}; \tag{3.67}$$

These are quasi-longitudinal waves propagating along the flux tube in such a way that a compression (expansion) of a plasma inside flux tube is compensated by the decrease (increase) in the longitudinal magnetic field due to a corresponding change of the tube cross section. So that the sum of gas-kinetic and magnetic pressure in linear approximation is unperturbed,  $\delta p_i + B \delta B / 4\pi = 0$ ;

2. The high frequency fast oscillations analogous to fast magnetosonic waves with phase velocity  $\sim \sqrt{c_s^2 + v_A^2}$ . Because of high frequency which is of the order of  $v_A/R$ , excitation of this mode is quite difficult. Besides, it experiences strong radiative damping.
3. Torsional oscillations which are actually pure Alfvén waves. These are transverse incompressible waves. In their presence neither the tube boundary nor the surrounding plasma are disturbed. Besides, their amplitude is very small,  $\sim v_{\text{conv}} R / L_{\text{conv}}$ , where  $v_{\text{conv}}$  is characteristic velocity in the convective zone, and  $L$  is the convective cell size. Thus these waves have quite insignificant influence on the dynamics and energy production processes.

Thus the main candidate of these three axisymmetric tube waves is the sausage mode.

### 3.7.2 Equation of Motion for Sausage Oscillations

The main feature of sausage oscillations, as mentioned above, is that the total pressure,  $P = p + B^2/4\pi$ , remains unperturbed, i.e.:

$$\delta P = \delta p + \frac{\mathbf{b}\mathbf{B}}{4\pi} = 0 \tag{3.68}$$

Thus, in linear approximation the compression or expansion of a flux tube and the perturbations of plasma and magnetic pressure are uniform. This fact leads to quite specific features of the sausage oscillations absent in higher mode tube waves.

To observe their features we consider axially symmetric flux tube being uniform along its length, and use cylindrical coordinates  $(r, \phi, z)$  with the  $z$ -axis directed along the unperturbed magnetic field. In other words, we assume that the unperturbed density  $\rho$ , the gas-kinetic pressure  $p$ , and the magnetic field  $\mathbf{B}(0, 0, B)$  depend on  $r$ . As the magnetic field inside flux tube is much stronger than outside, we shall consider the flux tube environment magnetic-free.

We adopt the model of flux tube shown in Fig. 3.5 and assume that the magnetic field decreases smoothly from a maximum value on the axis of the flux tube to zero as  $r \rightarrow \infty$ , and that the plasma density and pressure are also smooth functions of  $r$ .

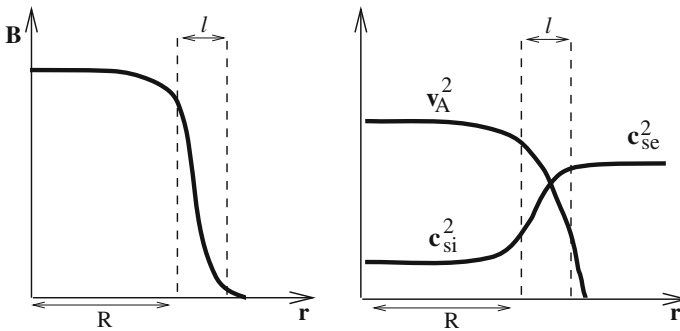
Let us bring again the linearized set of MHD equations written in the form

$$\rho \frac{\partial \mathbf{v}}{\partial t} = -\nabla \delta p + \frac{1}{4\pi} [\nabla \times \mathbf{b}] \times \mathbf{B} \tag{3.69}$$

$$\frac{\partial \mathbf{b}}{\partial t} = \nabla \times [\mathbf{v} \times \mathbf{B}] \tag{3.70}$$

$$\frac{\partial \delta \rho}{\partial t} + \text{div} \rho \mathbf{v} = 0 \tag{3.71}$$

$$\frac{\partial \delta S}{\partial t} + \mathbf{v} \nabla S = 0 \tag{3.72}$$



**Fig. 3.5** Sketch of smooth parameter profiles of inhomogeneous flux tube with the sharp inhomogeneity confined near the tube boundary of the width  $\sim l$

where  $S = \rho^{-\gamma} p$  is the entropy measure, and  $\mathbf{v}$ ,  $\mathbf{b}$ ,  $\delta\rho$ ,  $\delta p$ , and are the perturbed quantities, of the velocity, magnetic field, plasma density, and gas kinetic pressure, and

$$\delta S = \rho^{-\gamma} \delta p + \gamma \rho^{-\gamma-1} S \delta \rho \quad (3.73)$$

is the entropy perturbation.

For perturbations independent of  $\phi$  and proportional to  $\exp(-i\omega t + ikz)$ , (3.69) gives

$$-i\omega\rho\left(1 - \frac{k^2 v_A^2}{\omega^2}\right)v_r = -\frac{\partial}{\partial r}\left(\delta p + \frac{b_z B}{4\pi}\right), \quad (3.74)$$

$$-i\omega\rho v_z = \frac{b_r}{4\pi} \frac{\partial B}{\partial r} - ik\delta p. \quad (3.75)$$

From (3.70),

$$b_r = -\frac{kB}{\omega}v_r, \quad b_z = \frac{1}{i\omega} \frac{1}{r} \frac{\partial}{\partial r}(rv_r B), \quad (3.76)$$

and (3.71)–(3.73) take the form

$$-i\omega\delta\rho + \frac{1}{r} \frac{\partial}{\partial r} r\rho v_r + ik\rho v_z = 0, \quad (3.77)$$

$$\delta p - \gamma \frac{p}{\rho} \delta\rho = \frac{v_r}{i\omega} \left( \frac{\partial p}{\partial r} - \gamma \frac{p}{\rho} \frac{\partial \rho}{\partial r} \right). \quad (3.78)$$

Eliminating from the last two equations  $\delta\rho$  we get the equation for  $\delta p$  expressed through velocity perturbations. Now we substitute the obtained expression for  $\delta p$  into (3.75) to obtain the following equation:

$$-i\omega\rho v_z = -\frac{k}{\omega}v_r \frac{\partial}{\partial r} \left( \frac{B^2}{4\pi} + p \right) - \frac{k}{\omega} \gamma p \left( \frac{1}{r} \frac{\partial}{\partial r} r v_r + i\omega k z \right) \quad (3.79)$$

The first term on the right-hand side vanishes due to the flux tube equilibrium condition, (3.68), and (3.79) takes the form

$$i\omega \left( 1 - \frac{k^2 c_{\text{si}}^2}{\omega^2} \right) v_z = \frac{k c_{\text{si}}^2}{\omega} \frac{1}{r} \frac{\partial}{\partial r} r v_r \quad (3.80)$$

In order to obtain the equation for  $v_r$ , we need to express the right-hand side of (3.74) through velocity perturbations. From (3.68) and (3.76)–(3.78) we have

$$\delta p + \frac{b_z B}{4\pi} = \rho \frac{c_{\text{si}}^2 + v_A^2}{i\omega} \frac{v_r}{r} + \frac{c_{\text{si}}^2}{\omega} k \rho v_z \quad (3.81)$$

Substituting here the expression for  $v_z$  from (3.80) we obtain

$$\delta p + \frac{b_z B}{4\pi} = \frac{\rho}{i\omega} \frac{\omega^2(c_{\text{si}}^2 + v_A^2) - k^2 c_{\text{si}}^2 v_A^2}{\omega^2 - k^2 c_{\text{si}}^2} \frac{1}{r} \frac{\partial}{\partial r} r v_r, \quad (3.82)$$

and finally the equation for radial velocity perturbation takes the form

$$\frac{\partial}{\partial r} \rho \frac{\omega^2(c_{\text{si}}^2 + v_A^2) - k^2 c_{\text{si}}^2 v_A^2}{\omega^2 - k^2 c_{\text{si}}^2} \frac{1}{r} \frac{\partial}{\partial r} r v_r + \rho(\omega^2 - k^2 c_{\text{si}}^2) v_r = 0 \quad (3.83)$$

This equation describes the small axisymmetric oscillations of radially inhomogeneous plasma both inside and outside magnetic flux tube.

Note that (3.83) describes two  $m = 0$  modes, the slow (sausage) and “fast” oscillations. In both cases the flux tube boundary performs the radial displacement  $v_r = \partial \xi_r / \partial t$ . The torsional,  $m = 0$ , oscillations are characterized by the azimuthal component of velocity,  $v_\phi = \partial \xi_\phi / \partial t$ , and will be considered in Chap. 4, Sect. 4.2.1.

### 3.7.3 Dispersion Relation

Outside the flux tube at large enough distances,  $r \gg R$ , where we can assume that the plasma is uniform and the magnetic field is negligibly small, (3.83) turns to be just a second-order Bessel equation. Bearing in mind that in the region  $r \gg R$  there are only outgoing waves, the solution to (3.83) is simply proportional to a second-order Hankel function:

$$v_r = C_1 H_1^{(2)}(qr) \quad (3.84)$$

where

$$q = \sqrt{(\omega^2/c_{\text{se}}^2) - k^2} \quad (3.85)$$

Obviously,  $\text{Re } \omega > 0$ , and we choose the branch of the roots with  $\text{Re } q > 0$ .

At small compared to  $k^{-1}$  distances from the flux tube axis (i.e., inside flux tube and its immediate neighborhood) the second term on the left-hand side of (3.83) is small compared to the first, because  $k^2 R^2 \ll 1$ . Neglecting the second term we have in the zeroth approximation

$$\rho \frac{\omega^2(c_{\text{si}}^2 + v_A^2) - k^2 c_{\text{si}}^2 v_A^2}{\omega^2 - k^2 c_{\text{si}}^2} \frac{1}{r} \frac{\partial}{\partial r} r v_r = C_2 \quad (3.86)$$

where  $C_2$  is a constant.

From the condition that there be no singularities at  $r \rightarrow 0$  we find

$$v_r = \frac{C_2}{r} \int_0^r \frac{(\omega^2 - k^2 c_{\text{si}}^2) r' dr'}{\omega^2(c_{\text{si}}^2 + v_A^2) - k^2 c_{\text{si}}^2 v_A^2} \quad (3.87)$$

This solution is valid for arbitrary  $r$ -dependence of  $\rho(r)$  and  $B(r)$ . In the region  $R \ll r \ll k^{-1}$  (3.84) and (3.87) have overlapping regions of applicability. This means that by matching solutions in these regions we can obtain the dispersion relation.

Consider first the behavior of the solution (3.87) in the region  $r \gg R$ . Here  $v_A = 0$  and  $c_{se} = \text{const.}$ , i.e., the integrand changes in proportion to  $r$ . Hence, the main term in the asymptotic expression of  $v_r$  is proportional to  $r$ . To find the next term in the expansion we add to and subtract from the expression for  $v_r$ , the term

$$\int_0^r \frac{1}{\rho} \frac{(\omega^2 - k^2 c_{se}^2)}{\omega^2 c_{se}^2} r' dr', \quad (3.88)$$

after which we get

$$\begin{aligned} v_r = \frac{C_2}{r} \int_0^r \left[ \frac{1}{\rho \omega^2 (c_{si}^2 + v_A^2)} \frac{\omega^2 - k^2 c_{si}^2}{-k^2 c_{si}^2 v_A^2} - \frac{(\omega^2 - k^2 c_{se}^2)}{\rho_e \omega^2 c_{se}^2} \right] r' dr' \\ + \frac{C_2}{r} \frac{\omega^2 - k^2 c_{se}^2}{\rho_e \omega^2 c_{se}^2} \frac{r^2}{2} \end{aligned} \quad (3.89)$$

The expression inside the square brackets decreases fast at large distances, and for  $r \gg R$  we obtain

$$v_r = C_2 \frac{r}{c_{se}^2} \left[ \frac{1}{\rho_e} \frac{\omega^2 - k^2 c_{se}^2}{2\omega^2} + \frac{D(\omega)}{r^2} \right] \quad (3.90)$$

where function  $D(\omega)$  describes the dispersion and is defined as follows:

$$D(\omega) = c_{se}^2 \int_0^\infty \left[ \frac{1}{\rho(c_{si}^2 + v_A^2)} \frac{\omega^2 - k^2 c_{si}^2}{\omega^2 - k^2 c_T^2} - \frac{1}{\rho_e c_{se}^2} \frac{\omega^2 - k^2 c_{se}^2}{\omega^2} \right] r' dr' \quad (3.91)$$

Here,  $c_T$  is the phase velocity of the axisymmetric tube oscillations; cf. (3.67):

$$c_T^2 = \frac{c_{si}^2 v_A^2}{c_{si}^2 + v_A^2} \quad (3.92)$$

Thus, we found the next term in the asymptotic expression.

Using now expression for the Hankel function for small arguments,

$$H_1^{(2)} = \frac{qr}{2} - \frac{2i}{\pi qr}, \quad (3.93)$$

and equating the expressions obtained from (3.90) and (3.92), we find the dispersion relation:

$$D(\omega) = -\frac{2ic_{se}^2}{\pi\rho_e\omega} \quad (3.94)$$

The integrand in (3.91) for  $D(\omega)$  is nonvanishing only when  $r \leq R$ , i.e.,  $D(\omega) \sim R^2$ .

For the class of solutions related to axisymmetric modes with  $R \ll k^{-1}$ , we have  $\omega/kc_{si} \sim 1$  and  $\omega/kv_A \sim 1$ . In this case the ratio of the left- and right-hand sides of (3.94) is of the order of  $k^2R^2 \ll 1$ . Therefore, for this class of solutions condition (3.94) can be satisfied only by a special choice of  $\omega$ , such that the denominator ( $\omega^2 - k^2c_T^2$ ) be close to zero. This fact by itself shows the great sensitivity of the solution to the inhomogeneity of the plasma and magnetic field inside the flux tube. In other words, the excitation and propagation of the axisymmetric tube waves are very sensitive to radial profiles of plasma and magnetic field inside the flux tube. As in realistic situations inhomogeneities certainly exist, it is necessary to consider their role in any model of the axisymmetric oscillations. We shall discuss this issue in Sect. 3.7.5.

### 3.7.4 Sausage and Fast Oscillations in Homogeneous Flux Tube

Consider first the case of nearly homogeneous flux tube with a stepwise distribution of the plasma parameters, i.e., flux tube with a sharp boundary (i.e.,  $\ell \simeq 0$  in Fig. 3.5). In this case

$$D(\omega) = \frac{c_{se}^2 R^2}{2(c_{si}^2 + v_A^2)} \frac{\omega^2 - k^2 c_{si}^2}{\omega^2 - k^2 c_T^2}, \quad (3.95)$$

and from (3.94) we have

$$z \frac{z - c_{si}^2/c_T^2}{z - 1} = -iQ \frac{1}{k^2 R^2} \quad (3.96)$$

where  $z$  and  $Q$  stand for

$$z = \frac{\omega^2}{k^2 c_T^2}, \quad Q = \frac{4c_{se}^2 v_A^2}{\pi c_T^4} \quad (3.97)$$

The right-hand side of (3.95) is a large quantity, because  $Q \simeq 1$  and  $kR \ll 1$ . This allows us to find both solutions of this equation. We define these solutions for fast and slow oscillations as  $z_F$  and  $z_S$ , respectively.

The  $|z| \gg 1$  solution of (3.95)–(3.97) is obviously

$$z_F \simeq -i \frac{Q}{k^2 R^2}, \quad (3.98)$$



or, for  $\text{Re } \omega > 0$

$$z_F \simeq \frac{1}{\sqrt{2}} \frac{c_T}{R} (1 - i) \quad (3.99)$$

Thus, the frequency of the fast axisymmetric oscillations is very high, and having correspondingly high imaginary part, these oscillations are rapidly damping.

Another solution of the dispersion relation (3.95) corresponding to the case when the denominator on the left-hand side of (3.95) tends to zero, describes the slow oscillations, and is of the form

$$z_S \simeq 1 - i \frac{k^2 R^2}{Q} \left( \frac{c_{\text{si}}^2}{c_T^2} - 1 \right) \quad (3.100)$$

or choosing  $\text{Re } \omega > 0$  and keeping in mind relations (3.97) we have

$$\omega_S \simeq kc_T \left[ 1 - i \frac{k^2 R^2}{2Q} \left( \frac{c_{\text{si}}^2}{c_T^2} - 1 \right) \right]. \quad (3.101)$$

Thus, the real part of (3.101) is a natural eigenfrequency of the sausage oscillations, while the imaginary part describes their radiative damping. One can see that, as far as  $k \ll R$ , radiative damping is small. This fact may play an important role in large-scale dynamics of solar atmosphere. A smallness or radiative damping means that the oscillations excited in the photosphere where the flux tube interacts with the acoustic wave trains, may propagate along the flux tube for a long time without damping.

The main problem with this process, however, is that, as mentioned above, the sausage mode is extremely sensitive to radial inhomogeneities of the plasma and magnetic field inside the flux tube. From this perspective the more slender the flux tube the more chance they have to sustain the sausage oscillations. We will discuss this issue in the next section.

### 3.7.5 Effects of Radial Inhomogeneities on Sausage Oscillations

In order to determine the conditions under which the radial inhomogeneities of flux tube start to show an appreciable effect on the sausage oscillations, we consider a model situation when the phase velocity,  $c_T$ , changes with radius across the flux tube as follows:

$$c_T^2 = \begin{cases} c_{T0}^2 (1 - \epsilon r^2 / R^2), & r < R \\ 0, & r > R \end{cases} \quad (3.102)$$

Clearly, when  $\epsilon \ll 1$ , the quantities in the integral (3.91) for  $D(\omega)$  inside the flux tube are independent of  $r$ . Then, in terms of parameter  $z$ , defined by (3.97), we have for  $D(z)$ :

$$D(z) = \frac{R^2 c_{T0}^2 c_{se}^2 (z - v_{A0}^2/c_{T0}^2)}{2 c_{si}^2 c_{T0}^2} \int_0^1 \frac{d\zeta}{z - 1 + \epsilon\zeta} \quad (3.103)$$

This integral determines an analytical function  $D(z)$  in the complex  $z$ -plane with a cut between the points  $z = 1 - \epsilon$  and  $z = 1$  (Fig. 3.6a):

$$D(z) = \frac{R^2 c_{T0}^2 c_{se}^2}{2 v_{A0}^2 c_{si}^2} \frac{z - v_{A0}^2/c_{T0}^2}{\epsilon} \ln \frac{z - 1 + \epsilon}{z - 1} \quad (3.104)$$

The imaginary part of the logarithm changes in the interval  $(-i\pi, i\pi)$ .

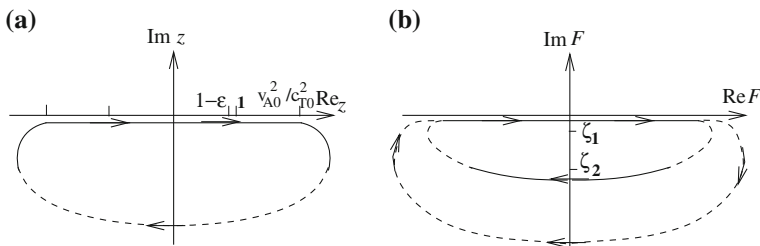
In the framework of this model the dispersion relation has the form

$$z \left( z - \frac{v_{A0}^2}{c_{T0}^2} \right) \ln \frac{z - 1 + \epsilon}{z - 1} = -i Q \frac{\epsilon}{k^2 R^2} \quad (3.105)$$

We can modify the left-hand side of this equation at  $\epsilon \rightarrow 0$  by performing an expansion in powers of  $\epsilon$ . This procedure leads to the dispersion equation (3.96), which has the solution  $z = 1$ . This result is valid when  $\epsilon \ll k^2 R^2$ . Note that the solution corresponding to the sausage mode disappears when  $\epsilon \geq k^2 R^2$ .

In the opposite case, when  $\epsilon \gg k^2 R^2$  but still  $\epsilon \ll 1$ , (3.105) does not have a solution  $z = 1$ . Indeed, as the imaginary part of the logarithm changes from  $-i\pi$  to  $i\pi$ , and the absolute magnitude of the right-hand side of (3.105) is large compared to unity, the absolute value of  $z$  must also be large compared to unity, which is necessary in order to satisfy (3.105). To find the corresponding solution, we take into account that at  $z \gg 1$ ,

$$\ln \left( 1 + \frac{\epsilon}{z - 1} \right) \simeq \frac{\epsilon}{z}, \quad (3.106)$$



**Fig. 3.6** Study of the dispersion relation: **a** the complex  $z$ -plane with a cut between the points  $z = 1 - \epsilon$  and  $z = 1$ ; **b** the hodograph in the complex  $F$ -plane corresponding to the  $z$ -plane contour shown in panel *a*

and (3.105) gives

$$z = -i \frac{\epsilon Q}{k^2 R^2} \quad (3.107)$$

This, on the other hand coincides with (3.99). Thus, the solution with  $z \gg 1$  corresponds to a fast mode.

To find the critical value of  $\epsilon$  for which the solution vanishes, we can use a hodograph method mapping the contour shown in Fig. 3.6b onto the complex  $F$ -plane, which we define as

$$F(z) = z \left( z - \frac{v_{A0}^2}{c_{T0}^2} \right) \ln \frac{z - 1 + \epsilon}{z - 1} \quad (3.108)$$

In accordance with the Nyquist criterion the number of roots of (3.105) lying in the lower  $z$ -half-plane is equal to the number of times the hodograph of  $F$  goes round the point  $-i Q \epsilon / k^2 R^2$ . Note that as the system initially is stable, we are interested only in roots with  $\text{Im } z < 0$ .

The obtained shape of the hodograph and both roots,

$$\zeta_1 = -i \frac{Q \epsilon}{k^2 R^2}, \quad \zeta_2 = i \pi \left( 1 - \frac{\epsilon}{2} \right) \left( 1 - \frac{\epsilon v_{A0}}{2 c_{T0}} \right) \quad (3.109)$$

lying inside it, is shown in Fig. 3.6b. From the figure it is clear that the critical value of  $\epsilon$  is determined by the equation

$$\pi \left( 1 - \frac{\epsilon}{2} \right) \left( \frac{v_{A0}^2}{c_{T0}^2} + \frac{\epsilon}{2} - 1 \right) = Q \frac{\epsilon}{k^2 R^2} \quad (3.110)$$

Given that  $kR \ll 1$  we have for the critical value of  $\epsilon$

$$\epsilon_{\text{cr}} = \frac{\pi k^2 R^2}{Q} \left( \frac{v_{A0}^2}{c_{T0}^2} - 1 \right) \quad (3.111)$$

This is quite a small quantity, which means that for the sausage oscillations to survive and propagate along flux tube, there is a very narrow threshold of physical parameters. On the other hand, radial pulsation of the surface of the tube with inhomogeneous parameters may become large and cause a catastrophic growth of radiative losses, and thus damping of the tube waves.

## Appendix A: Analogy with Landau Damping

Landau damping is a fundamental effect occurring in dispersive and dissipative media sustaining any kind of wave phenomena (Timofeev 1970; Tataronis and Grossmann 1970; Chen and Hasegawa 1974; Ryutov 1999).

A plasma wave of frequency  $\omega$  and wave number  $k$  propagating in a collisionless plasma is subject of Landau damping because the wave distorts the particular distribution function associated with a resonance

$$\omega = kv \quad (3.112)$$

Particles having speed  $v$  are resonant with the wave and so exchange energy with it. Mathematically, the dispersion relation for plasma waves is

$$I = \frac{\omega_p^2}{k^2} \int \frac{\partial f_0 / \partial v}{v - \omega/k} dv, \quad (3.113)$$

where  $\omega$  has a small imaginary part and the imaginary part of the integral gives a  $\delta$ -function, so that

$$I = \frac{\omega_p^2}{k^2} \mathcal{P} \int \frac{\partial f_0 / \partial v}{v - \omega/k} dv + i\pi \frac{\partial f_0}{\partial v}, \quad (3.114)$$

This, in turn, leads to the dispersion relation

$$\omega = \omega_p + i\omega_p \frac{\pi}{2} \frac{\omega_p^2}{k^2} \left( \frac{\partial f_0}{\partial v} \right)_{v=\omega/k} \quad (3.115)$$

In our case the resonant excitation of kink and/or sausage waves produces a Landau-like damping of an incident acoustic wave. Physically, the acoustic wave damps because the wave distorts the distribution function of flux tubes. This, just like in kinetic plasma, is associated with a resonance

$$\omega \cos \theta = kc_s. \quad (3.116)$$

The flux tubes having natural phase speed,  $\omega/k$ , are resonant with the acoustic wave and so exchange energy with it. The dispersion relation (3.24) for the acoustic wave can be written as

$$\omega = kc_s \left[ 1 - \frac{1}{2} \sin^2 \theta \int d\eta g(\eta) \left( 1 - \frac{\omega^2}{\eta + 1 - 2c_s^2 k^2 \cos^2 \theta} \right) \right] \quad (3.117)$$

where  $\omega$  has a small imaginary part, and the imaginary part of the integral gives a  $\delta$ -function. The resulting dispersion relation is

$$\omega = kc_s [1 - i\pi \sin^2 \theta g(\eta_0)], \quad (3.118)$$

where

$$\eta_0 = 2\cos^2(\theta/2) - 1 = kc_s. \quad (3.119)$$

Resonance is where

$$\eta + 1 = \frac{2\cos^2 \theta}{\gamma} \quad (3.120)$$

But

$$\frac{\omega^2}{k^2} = \frac{B^2}{4\pi(\rho_i + \rho_e)} = \frac{B^2}{4\pi\rho_e(\eta + 1)}, \quad (3.121)$$

and

$$\frac{B^2}{8\pi} = p_e = \frac{\rho_e c_s^2}{\gamma}, \quad (3.122)$$

So that the resonance condition (3.116) becomes just expression (3.120).

## Appendix B: Derivation of Equation for Kink Oscillations from MHD

The linearized set of MHD equations in the cylindrical coordinates with  $z$ -axis directed along magnetic field for the perturbations proportional to  $\exp(-i\omega t + ikz + im\phi)$  have a form:

$$\omega\delta P = -i\rho \frac{\omega^2(c_{si}^2 + v_A^2) - k^2 c_{si}^2 v_A^2}{\omega^2 - k^2 c_{si}^2} \left( \frac{1}{r} \frac{\partial}{\partial r} r v_r + \frac{1}{r} \frac{\partial}{\partial \phi} v_\phi \right), \quad (3.123)$$

$$\omega \frac{\partial}{\partial r} \delta P = -i\rho(\omega^2 - k^2 v_A^2) v_r, \quad (3.124)$$

$$\omega \frac{1}{r} \frac{\partial}{\partial \phi} \delta P = -i\rho(\omega^2 - k^2 v_A^2) v_r, \quad (3.125)$$

where  $\delta P = \delta p_i + b_z B/4\pi$  is the total pressure perturbation.

From (3.124) to (3.125) it is obvious that

$$(\omega^2 - k^2 v_A^2) \nabla_z \mathbf{v} = 0 \quad (3.126)$$

Since we are not interested in pure Alfvén wave, (3.126) gives for velocity perturbations  $\nabla_z \mathbf{v} = 0$ , and we can introduce the velocity potential (see (3.42)) which reduces the set (3.123)–(3.125) to the single equation inside flux tube, (3.43), and to (3.44) outside it. Respectively, on the surface of the flux tube, at  $r = R$ , the conditions for the continuity of the normal component of velocity and total pressure have a form

$$(\omega^2 - k^2 v_A^2) \nabla_z \mathbf{v} = 0 \quad (3.127)$$

$$\rho_i \left( 1 - \frac{k^2 v_A^2}{\omega} \right) \psi_i \Big|_R = \rho_e \psi_e \Big|_R \quad (3.128)$$

Consider the motion of a magnetic flux tube in a field of a plane acoustic wave propagating with the amplitude  $\zeta_0$  (see (3.56) where we used a unit amplitude):

$$\Psi_{0e} = \frac{1}{2} \exp(-i\omega t + i\mathbf{kr}) + \text{c.c.} \quad (3.129)$$

where  $\mathbf{kr} = k_z z + q_e r \cos \phi$ , and  $q_e = \omega^2/c_{se}^2 - k_z^2$ .

The solution of MHD equations outside flux tube as a superposition of this plane wave and outgoing cylindrical waves with  $m = \pm 1$ , has a form

$$\Psi_{0e} = \frac{1}{2} \exp(-i\omega t + i\mathbf{kr}) + \text{c.c.} \quad (3.130)$$

We have taken a real part of (3.57) and retained only the first nonvanishing term in the expansion of Hankel function over a small argument. The solution inside flux tube (3.58) can be written as

$$\Psi_{0i} = e^{-i\omega t + ik_z z} B r \cos \phi \quad (3.131)$$

Using now (3.127)–(3.131) we can find coefficients  $A$  and  $B$  expressed through the amplitude of the incident sound wave  $\zeta_0$ . After some algebra we have

$$A = -\zeta_0 q_e R^2 \frac{1 - \eta(1 - k^2 v_A^2/\omega^2)}{1 + \eta(1 - k^2 v_A^2/\omega^2)} \quad (3.132)$$

$$B = 2\zeta_0 q_e \frac{1}{1 + \eta(1 - k^2 v_A^2/\omega^2)} \quad (3.133)$$

Inserting now (3.132) and (3.133) into (3.130) and (3.131) and taking into account (3.42), we can express the velocity inside flux tube  $\mathbf{v}_{i\perp}$  through the velocity in outer region,  $\mathbf{v}_{e\perp}$ :

$$\mathbf{v}_{i\perp} = 2\mathbf{v}_{e\perp} \frac{1}{1 + \eta(1 - k^2 v_A^2/\omega^2)} \quad (3.134)$$

For a plane harmonic dependence this relationship gives the following equation for the flux displacement:

$$(1 + \eta) \frac{\partial^2 \xi_{\perp}}{\partial t^2} - \eta v_A^2 \frac{\partial^2 \xi_{\perp}}{\partial z^2} = 2 \frac{\partial \mathbf{v}_{\perp}}{\partial t} \quad (3.135)$$

Recalling that  $\eta = \rho_i/\rho_e$  we see that (3.135) exactly coincides with (3.4).

## References

- L. Chen, A.A. Hasegawa, *J. Geophys. Res.* **79**, 1033 (1974)  
 L.E. Cram, P. Wilson, *Sol. Phys.* **41**, 313 (1975)  
 R.J. Defouw, *Astrophys. J.* **209**, 266 (1976)

- D. Fujimura, S. Tsuneta, *Astrophys. J.* **702**, 1443 (2009)  
L.D. Landau, E.M. Lifshitz, *Fluid Mechanics* (Pergamon Press, Oxford, 1987)  
L.D. Landau, *Sov. Phys.-JETP* **16**, 574 (1946)  
S.R.O. Ploner, S.K. Solanki, *Astron. Astrophys.* **325**, 1199 (1997)  
B. Roberts, A.R. Webb, *Sol. Phys.* **56**, 5 (1978)  
D.D. Ryutov, M.P. Ryutova, *Sov. Phys.-JETP* **43**, 491 (1976)  
M.P. Ryutova, *Sov. Phys.-JETP* **53**, 529 (1981)  
D.D. Ryutov, *Plasma Phys. Control Fusion* **41**, A1 (1999)  
H.C. Spruit, *Astron. Astrophys.* **98**, 155 (1981)  
J.A. Tataronis, W. Grossmann, *Z. Phys.* **261**, 203 (1970)  
A. Timofeev, *Sov. Phys.-Uspekhi*, **13**, 632. *Astron. Astrophys.* **98**, 155 (1970)  
E.Ya. Zlotnik et al., *AStL*, **37** 508 (2011)

## Chapter 4

# Effects of Flux Tube Inhomogeneities and Weak Nonlinearity

**Abstract** In this chapter we shall consider some special properties of magnetic flux tubes associated with their radial and longitudinal inhomogeneities. Magnetic flux tube embedded in weakly magnetized or nonmagnetic environment and kept in dynamic equilibrium by external pressure, must be intrinsically inhomogeneous. Even if magnetic field and density inside flux tube are radially smooth across the most of its cross section, at the periphery they must have finite gradient to match the physical parameters of surrounding plasma. Besides, flux tubes in the photosphere are subject to longitudinal inhomogeneity because of sharp stratification of low atmosphere. It is remarkable that this intrinsic property of flux tubes to be inhomogeneous plays a crucial role in their ability to absorb the energy of the outer motions, carry it upward, and convert it into the heat or other forms of energy. We shall discuss some macroscopic effects associated with flux tube inhomogeneities, which, in fact, are observable. We shall also study a weakly nonlinear waves in flux tubes and show that they obey a KdV-Bürgers equation and may develop into shocks and solitons.

### 4.1 Radially Inhomogeneous Flux Tube—Internal Resonances

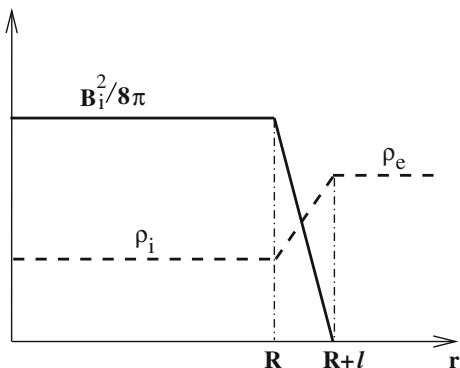
#### 4.1.1 Anomalous Resonance in Kink Oscillations

Consider first the effect of radial inhomogeneity of flux tube, which, in fact, results in a striking property of flux tube: it turns out that even in the absence of any dissipative effects, an additional and strong damping of flux tube oscillations occurs near the singular point where the phase velocity of oscillations becomes equal to the local value of the Alfvén speed (Ryutova 1977; Ionson 1978). Existence of resonant layer inside *any* flux tube makes virtually all the flux tubes responsible for permanently acting mechanism of energy accumulation and its transfer. It is not surprising therefore that enhanced emission in the overlying atmosphere (almost at all temperatures) mimics the pattern of small-scale flux tubes observed in the photosphere.

To demonstrate the action of an *internal resonance* consider the kink oscillations of flux tube with somewhat simplified profile shown in Fig. 4.1, where the solid line



**Fig. 4.1** Sketch of the flux tube parameters with the sharp boundary layer



is the magnetic pressure  $B^2(r)/8\pi$ , and the dashed line is the gas-kinetic pressure  $p(r)$ . Both functions are linear in the interval  $[R, R + l]$ , with  $l \ll R$ . We assume magnetic free environment.

For kink oscillations of flux tube with  $kR \ll 1$  a plasma can be considered incompressible and the MHD system for small oscillations proportional to  $\exp(-i\omega t)$ , are as follows:

$$\begin{aligned} \operatorname{div} \mathbf{v} &= 0 \\ -i\omega \mathbf{b} &= \nabla \times [\mathbf{v} \times \mathbf{b}] \\ -i(\omega + i\nu)\rho \mathbf{v} &= -\nabla p + \frac{1}{4\pi} ([\nabla \times \mathbf{b} \times \mathbf{B}] + [\nabla \times \mathbf{B} \times \mathbf{b}]) \end{aligned} \quad (4.1)$$

with  $\mathbf{v}$  and  $\mathbf{b}$  being perturbed quantities.

In order to provide a proper account for singularity in a matching point of phase velocities, i.e., where  $v_A = \omega/k$ , we have added a small imaginary part,  $\nu$ , to the frequency in the equation of motion. Physically, this addition can be attributed, for example, to the rare collisions between ions and neutrals in plasma.

We use cylindrical coordinates  $(r, \phi, z)$  with  $z$ -axis directed along the flux tube. At  $kR \ll 1$  the kink oscillations of flux tubes can be considered as a plane motion, and we can put  $v_z = 0$ . The other components of velocity can be expressed through the velocity potential  $\psi$ , just as we did in Chap. 3:

$$v_r = -\frac{1}{r} \frac{\partial \psi}{\partial \phi} \quad v_\phi = \frac{\partial \psi}{\partial r} \quad (4.2)$$

and reduce the system (4.1) to a single equation for  $\psi$ :

$$\frac{\partial}{\partial r} \left( \rho - \frac{k^2 B^2}{4\pi\omega^2} \right) r \frac{\partial \psi}{\partial r} - \left( \rho - \frac{k^2 B^2}{4\pi\omega^2} \right) \frac{\psi}{r} = 0 \quad (4.3)$$

The solution of (4.3) in the region  $r < R$  is obviously

$$\psi_i = C_1 r, \quad (4.4)$$

and in the region  $r > R + l$ ,

$$\psi_e = \frac{C_2}{r}. \tag{4.5}$$

To find the solution in the transition layer ( $R, R + l$ ), it is convenient to introduce a new variable

$$x = \frac{r - R}{l}, \quad 0 < x < 1 \tag{4.6}$$

Taking into account that  $l \ll R$ , (4.3) can be written as follows:

$$\frac{d}{dx}(x - x_0 - i\epsilon) \frac{d\psi}{dx} - \frac{l^2}{R^2}(x - x_0 - i\epsilon)\psi = 0 \tag{4.7}$$

where

$$x_0 = \left( \frac{k^2 B_i^2}{4\pi\omega^2} - \rho_i \right) \left( \frac{k^2 B_i^2}{4\pi\omega^2} + \rho_e - \rho_i \right)^{-1}, \tag{4.8}$$

and small imaginary part  $i\epsilon$  is associated with imaginary term  $i\nu$  coming from the system (4.1). The specific value of  $\epsilon$  is not important because it does not enter into the final result. In other words, the kinetic losses present in plasma act “behind the scene.”

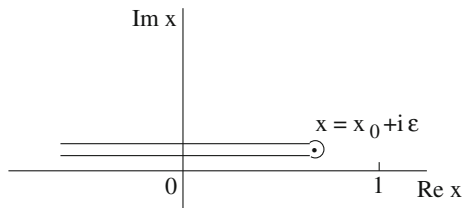
Equation (4.7) has a single-valued solution in the complex plane  $x$  with a cut along the line  $\text{Im } x = i\epsilon$ . This is illustrated in Fig. 4.2. At the same time,  $-\infty < \text{Re } x < x_0$ . Equation (4.7), being of complex arguments, is a modified Bessel equation of zeroth order. Taking into account that  $l \ll R$ , the solution to this equation can be written as follows:

$$\psi = A + D \ln(x - x_0 - i\epsilon) \tag{4.9}$$

At both boundaries,  $r = R$  and  $r = R + l$ , we have to satisfy continuity conditions for the functions  $\psi$  (i.e., for solutions (4.4), (4.5) and (4.9)) and their derivative:

$$\begin{aligned} \psi_i(r) \Big|_R &= \psi(r) \Big|_R, & \frac{d\psi_i(r)}{dr} \Big|_R &= \frac{d\psi(r)}{dr} \Big|_R; \\ \psi(r) \Big|_{R+l} &= \psi_e(r) \Big|_{R+l}, & \frac{d\psi(r)}{dr} \Big|_{R+l} &= \frac{d\psi_e(r)}{dr} \Big|_{R+l} \end{aligned} \tag{4.10}$$

**Fig. 4.2** The complex  $x$ -plane with a cut along the line  $\text{Im } x = i\epsilon$



Now, choosing the logarithm branch single-valued in the region with the cut shown in Fig. 4.2, we obtain the following dispersion relation:

$$\ln \frac{1-x_0}{x_0} + \frac{R}{l} \left( \frac{1}{1-x_0} - \frac{1}{x_0} \right) + i\pi = 0 \quad (4.11)$$

In terms  $\omega$  and  $k$  this expression becomes as follows

$$\omega \simeq \frac{k B_i}{\sqrt{4\pi(\rho_i + \rho_e)}} \left( 1 + \frac{i\pi}{4} \frac{\rho_i}{\rho_i + \rho_e} \frac{l}{R} \right). \quad (4.12)$$

This result shows that kink oscillations of flux tube, with radial dependence of magnetic field and density inside it, are subject to strong resonant damping. At the applicability limit, when  $l$  becomes of the order of radius,  $R$ , we have even  $\text{Im} \omega \sim \text{Re} \omega$ . One can show that this result is also valid in the case when the magnetic field outside the flux tube is nonzero.

Physically, the nature of the damping is due to the pumping of oscillation energy into the resonance point where the dissipation occurs. The effect is similar to the wave phenomena occurring in moving inhomogeneous media (plasma and liquids) that develop at the resonant points where the velocity of the substance coincides with the phase velocity of the oscillations (Timofeev 1970).

As mentioned above, given that flux tubes in nature are always inhomogeneous across their cross section, the existence of anomalous resonance damping becomes a major agent in various processes of energy conversion. In particular, the long waves propagating in plasma with magnetic flux tubes or with any other kind of magnetic field filamentation experience strong resonance absorption resulting in rapid transformation of oscillation energy into heat.

### 4.1.2 Alfvén Resonance

The resonant absorption layer, being a site of the anomalous absorption of the kink oscillation of flux tubes, may also support the resonant absorption of a local kinetic Alfvén waves. By nature kinetic Alfvén waves are MHD waves having short cross-field scales comparable to the ion gyroradius,  $r_i = v_{Ti}/\omega_{ci}$ . For such short waves the resonant layer may be considered “uniform”, which is not too principal, but allows to simplify the analysis (Ionson 1978).

The basic assumption can be summarized as follows:

- (1)  $\mathbf{B} = B(0, 0, B)$ ,
- (2) local values of velocities are  $v_{Ti} < v_A < v_{Te}$ ,
- (3) in harmonic perturbations  $\sim \exp(-i\omega t + \mathbf{k} \cdot \mathbf{r})$ ,  $k_r \gg k_\perp \gg k_z$ .

The MHD equations for a warm ion–electron plasma are as follows:

$$\frac{\partial n_\alpha}{\partial t} + \nabla \cdot (n_\alpha \mathbf{v}_\alpha) = 0 \quad (4.13)$$

$$m_\alpha \frac{d\mathbf{v}_\alpha}{dt} = e_\alpha \mathbf{E} + \frac{1}{c} e_\alpha \mathbf{v}_\alpha \times \mathbf{B} - \frac{1}{n_\alpha} \nabla P_\alpha, \quad (4.14)$$

$$P_\alpha = n_\alpha k_B T_\alpha \quad (4.15)$$

where the subscript  $\alpha$  refers to the particle species. It is also assumed that  $(\nabla \times \mathbf{E}) = 0$  (shear waves). Linearizing the system (4.13)–(4.15) with respect to perturbations  $\sim \exp(-i\omega t + \mathbf{k} \cdot \mathbf{r})$ , one obtains equations for density  $\tilde{n}_\alpha$  and current  $\tilde{j}_{z\alpha}$  fluctuations:

$$\frac{\tilde{n}_\alpha}{n_\alpha} = \left[ \frac{ie_\alpha k_z}{m_\alpha} \tilde{E}_z + \frac{ic\omega^2 k_r}{B\Omega_\alpha} (1 - s_\alpha) \tilde{E}_r \right] \frac{1}{\omega^2 - v_{T\alpha}^2 k_z^2}, \quad (4.16)$$

$$\tilde{j}_{z\alpha} = \frac{in_\alpha e_\alpha^2}{m_\alpha \omega} \tilde{E}_z + \frac{n_\alpha e_\alpha v_{T\alpha}^2 k_z}{\omega} \frac{\tilde{n}_\alpha}{n_\alpha} \quad (4.17)$$

where  $s_\alpha = k_r^2 v_{T\alpha}^2 / \Omega_\alpha^2$ ,  $\Omega_\alpha$  is the cyclotron frequency,  $v_{T\alpha}$  is the thermal velocity, and tilde marks small fluctuations. The term  $(1 - s_\alpha)$  in (4.14) has been externally introduced by letting  $\tilde{\mathbf{E}} \rightarrow (1 - s_\alpha) \tilde{\mathbf{E}}$  and represent finite gyroradius correction, or in other words, it reflects the amount by which the average field felt by the particles deviates from that at the center of their orbit. Since  $v_{Ti} < v_A < v_{Te}$ , and  $\omega \simeq k_z v_A$ , (4.14)–(4.15) reduce to

$$4\pi \tilde{n}_e e = \frac{i\omega_{pe}^2}{v_{Te}^2} \left( 1 + \frac{\omega^2}{k_z^2 v_{Te}^2} \right) \frac{\tilde{E}_z}{k_z}, \quad (4.18)$$

$$4\pi \tilde{j}_{\parallel e} = -\frac{i\omega_{pe}^2 \omega}{v_{Te}^2} \frac{\tilde{E}_z}{k_z} \quad (4.19)$$

for electrons, and

$$4\pi \tilde{n}_i e = \frac{i\omega_{pi}^2 k_z^2}{\omega^2} \frac{\tilde{E}_z}{k_z} - \frac{\omega_{pi}^2 s_i (1 - s_i)}{v_{Ti}^2} \frac{\tilde{E}_r}{k_r} \quad (4.20)$$

$$4\pi \tilde{j}_{zi} = \frac{i\omega_{pi}^2 k_z}{\omega} \frac{\tilde{E}_z}{k_z} \quad (4.21)$$

for ions.

Using now (4.18)–(4.21) and  $z$ -component of

$$\nabla \times (\nabla \times \tilde{\mathbf{E}}) = \frac{4\pi}{c^2} \frac{\partial \tilde{j}}{\partial t} - \frac{1}{c^2} \frac{\partial^2 \tilde{E}}{\partial t^2}, \quad (4.22)$$

one can easily obtain the following dispersion relation for kinetic Alfvén waves:

$$\frac{\omega^2}{k_z^2 v_A^2} = 1 + \beta + k_r^2 r_i^2 \left( 1 + \frac{T_e}{T_i} \right) \quad (4.23)$$

Here  $T_e$  and  $T_i$  are the electron and ion temperatures,  $r_i$  is the ion gyroradius, and  $\beta$  is a local plasma beta. Note that these waves do not have magnetic shear and yet are capable of propagating across the ambient magnetic field. It is important that the existence of such waves largely depends on the inclusion of nonzero electron inertia ensuring the presence of the second term in (4.18) (inertia term), which would otherwise vanish.

Using the dispersion relation (4.23) in Maxwell's equations yields the following useful relationships between  $\tilde{\mathbf{B}}$  and  $\tilde{\mathbf{E}}$ :

$$\frac{\tilde{\mathbf{B}}_{\perp}}{\tilde{E}_r} = \frac{1}{v_A}, \quad \frac{\tilde{B}_r}{\tilde{E}_r} = -\frac{\mathbf{k}_{\perp}}{k_r} \frac{1}{v_A} \quad (4.24)$$

$$\frac{\tilde{\mathbf{E}}_{\perp}}{\tilde{E}_r} = \frac{\mathbf{k}_{\perp}}{k_r}, \quad \frac{\tilde{E}_z}{\tilde{E}_r} = -k_r^2 r_i^2 \frac{k_z T_e}{k_r T_i} (1 - k_r^2 r_i^2) \quad (4.25)$$

The transverse structure of kinetic Alfvén waves (i.e.,  $k_r \neq 0$ ) greatly increases viscous damping and leads to irreversible heating of the ions. Furthermore, because these waves are accompanied by a field-aligned electric field  $\tilde{E}_z$ , Joule dissipation of the field-aligned electric current can heat the electrons.

The rate at which energy is dissipated (per unit volume) due to the ions is

$$q_i = \rho \nu_r \left( \frac{\partial \tilde{v}_{i\perp}}{\partial r} \right)^2 \quad (4.26)$$

where  $\rho$  is the mass density,  $\tilde{v}_{i\perp}$  is the ion velocity, and  $\nu_r$  is the cross-field kinematic viscosity

$$\nu_r = \frac{v_{Ti}^2 \nu_i}{\Omega_i^2} \left( 1 + \frac{\nu_i^2}{\Omega_i^2} \right)^{-1}, \quad (4.27)$$

where  $\nu_i$  is the ion-ion collision frequency. With (4.26) and (4.27) a heating rate for  $\nu_i \ll \Omega_i$  is given by

$$q_i = k_r^2 r_i^2 \nu_i \frac{|\tilde{\mathbf{B}}_{\perp}|^2}{8\pi} \quad (4.28)$$

Here the relation  $\tilde{v}_{i\perp}/v_A \simeq \tilde{B}_{\perp}/B$  has been used. The electron heating rate, which is given by

$$q_e = \frac{1}{2} Re (\tilde{j}_{ez} \tilde{E}_{ez}), \quad (4.29)$$

is related to the ion heating rate as follows:

$$q_e \simeq \frac{\sqrt{m_e/m_i}}{\beta} q_i. \quad (4.30)$$

Since in solar plasma  $\beta \simeq \sqrt{m_e/m_i}$ , electrons and ions are heated at approximately the same rate. The dissipation rates given by (4.28) and (4.30) greatly exceed those inferred by an ideal MHD description.

## 4.2 Boundary Value Problem

Flux tubes embedded in an ever-moving environment may carry a significant amount of energy stored around them. One of the important agents of energy transport is the ability of the *oscillating* flux tubes to respond to the action of surrounding changes, temperature inhomogeneities, atmospheric stratification, etc. (Ryutova and Khijakadze 1990; Solanki et al. 1996; Ploner and Solanki 1997; de Andrade 2007; Penn et al. 2011). In the subsequent sections we discuss some particular effects resulting from the response of oscillating flux tubes to changes in the environmental conditions.

### 4.2.1 Phase-Mixing in Flux Tubes

As in the previous section, here again we consider the radially inhomogeneous flux tubes. Another class of phenomena caused by the inhomogeneity of flux tube parameters is associated with frequency detuning between neighboring oscillating magnetic surfaces inside the flux tube. Even if the waves propagating along the radially inhomogeneous flux tube do not possess local resonances they undergo intense phase-mixing during which the oscillations of neighboring field lines become rapidly out of phase (Tataronis and Grossman 1970; Timofeev 1970; Heyvaerts and Priest 1983). This naturally leads to generation of small-scale motions, at which the dissipative effects turn on and result in strong absorption of flux tube oscillations.

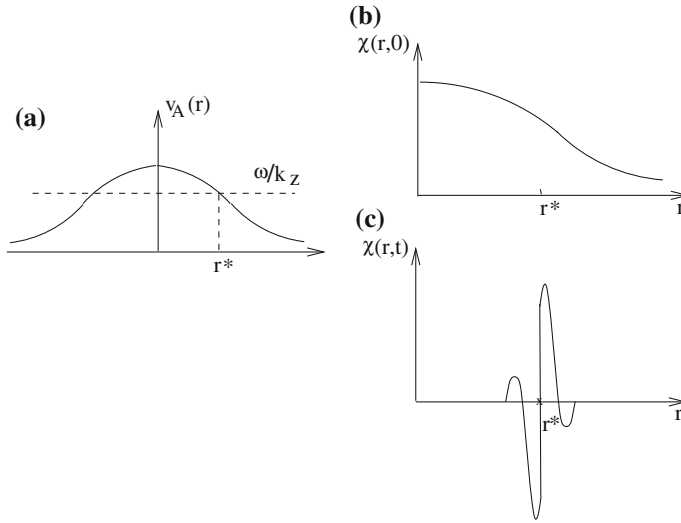
To look into the effect of phase-mixing we need to consider the general case when flux tube parameters vary across the entire cross-section of flux tube, as shown in Fig. 4.3a. In this case, the weakly damped wave which could be described in terms of smoothly varying radial eigenfunction does not exist any more. What happens is that if at the initial moment of time ( $t = 0$ ) the eigenfunction had a smooth radial profile (Fig. 4.3b)

$$\psi(r, z, t)|_{t=0} = \chi(r, 0)e^{ik_z z + i\phi}, \quad (4.31)$$

with time it evolves into a strongly oscillating function concentrated in the resonance point  $r^*$  (Fig. 4.3c).

Further in time and at higher altitudes the eigenfunction becomes multi-spiky, and waves in neighboring magnetic surfaces will have different phases.

The linearized MHD equations, together with the equilibrium condition  $p_i(r) + B^2(r)/8\pi = p_e(r)$ , lead to the following equations for a spatial variation of the tube displacement,  $\xi$ :



**Fig. 4.3** The flux tube with the smooth radial profile across its entire cross section and the evolution of the eigenfunction: **a** The Alfvén velocity,  $r^*$  is the point where the Alfvén velocity coincides with the phase velocity of tube wave. **b** The eigenfunction at the initial moment of time. **c** Strongly oscillating eigenfunction at the resonant point,  $r^*$

$$-\omega^2 \rho \xi = \nabla \delta P + \frac{B^2(r)}{4\pi} \frac{\partial^2 \xi}{\partial z^2} \quad (4.32)$$

where  $\delta P = \delta p + Bb_z/4\pi$  is a perturbation of total pressure (as earlier we use cylindrical coordinates with the  $z$ -axis directed along the tube).

The best way to solve this three-dimensional set of equations with  $r, \phi, z$  variables is to use the Laplace transform over  $z$ , then solve the radial equation, and then apply Laplace inversion. In the next section we shall consider some special cases, namely the case of the Alfvén (torsional) waves, and then address the kink oscillations.

## 4.2.2 Phase-Mixed Torsional Waves

In case of torsional Alfvén waves ( $m = 0$ ),  $\xi_r = \xi_z = 0$ , and the system (4.32) reduces to a single equation for  $\xi_\phi$ :

$$-\omega^2 \xi_\phi(r, z) = v_A^2(r) + \frac{\partial^2 \xi_\phi(r, z)}{\partial z^2} \quad (4.33)$$

Laplace transform of  $\xi_\phi(r, z)$  over  $z$  with  $Re p > 0$  is

$$\xi_{\phi p} = \int_0^\infty e^{-pz} \xi_\phi dz \quad (4.34)$$

With this, (4.34) becomes as follows:

$$\omega^2 \xi_{\phi p}(r) + v_A^2(r) p^2 \xi_{\phi p}(r) = -v_A^2(r) \left[ \xi_\phi(r, 0) + p \frac{\partial \xi_\phi(r, 0)}{\partial z} \right] \quad (4.35)$$

Thus, for  $\xi_{\phi p}(r)$  we have

$$\xi_{\phi p} = -i \frac{v_A(r)}{2\omega} \left[ \xi_\phi(r, 0) + p \frac{\partial \xi_\phi(r, 0)}{\partial z} \right] \left[ \frac{1}{p + i\omega/v_A} - \frac{1}{p - i\omega/v_A(r)} \right] \quad (4.36)$$

Laplace inversion,

$$\xi_\phi(r, z) = - \oint e^{pz} \xi_{\phi p}(r) dp \quad (4.37)$$

requires integration to be performed along the contour which is a vertical line lying on the right of all the poles of the function  $\xi_{\phi p}$ . The poles are obviously at the points  $p = \pm i\omega/v_A(r)$ .

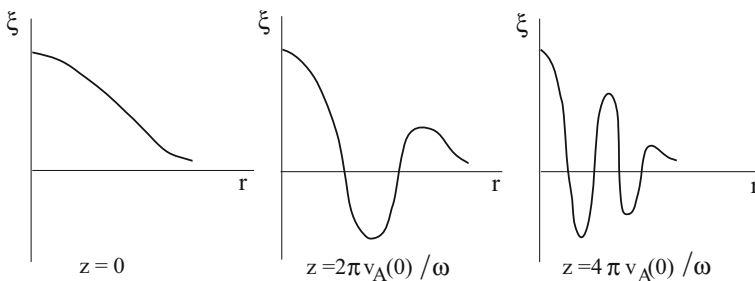
Shifting the contour  $C$  to the left and taking residues, one can arrive at the following solution for displacement  $\xi_\phi(r, z)$ :

$$\xi_\phi(r, z) = \frac{\xi'_\phi(r, 0) v_A(r)}{\omega} \sin \frac{\omega z}{v_A(r)} + \xi_\phi(r, 0) \cos \frac{\omega z}{v_A(r)}. \quad (4.38)$$

Equation (4.38) shows how a profile of function  $\xi_\phi(r, 0)$  changes at higher altitudes in the course of wave propagation. Indeed, if at the base of the flux tube, i.e., at  $z = 0$ ,  $\xi_\phi(r, 0)$  is a smooth function of radius, say,  $\xi_\phi(r, 0) \sim r$  (i.e., a rigid rotation takes place), then at higher altitudes the dependence of  $\xi_\phi$  on  $r$  becomes more and more spiky (Fig. 4.4).

The characteristic radial scale length of perturbations,  $\Delta r$  is of the order of

$$\Delta r \sim \frac{v_A^2(r)}{z\omega v'_A(r)} \sim \frac{v_A(r)r}{\omega z}, \quad (4.39)$$



**Fig. 4.4** Profiles of the eigenfunction with height in phase-mixed Alfvén wave



and diminishes inversely with  $z$ . Respectively, the dissipative processes, like viscosity, Ohmic losses, and/or thermal conductivity, become more and more important at larger  $z$ . At the same time, it is obvious that the energy flux no longer depends on  $z$  exponentially.

To obtain a true picture of the dissipation process one should include the dissipative terms into (4.33). For instance, taking into account viscous losses, the right-hand side of (4.33) acquires additional term (Landau and Lifshitz Hydrodynamics):

$$\nu \frac{1}{r^2} \frac{\partial}{\partial r} \left( r^3 \frac{\partial}{\partial r} \frac{\xi_\phi}{r} \right), \quad (4.40)$$

where  $\nu$  is kinematic viscosity.

Let us assume that for oscillations with a smooth radial profile (on a scale of the order of flux tube radius) which initially are generated by convective motions, dissipation is slow,  $\omega \gg \nu/R^2$ . In this case the oscillations will propagate almost without damping up to the heights where the inverse damping rate  $\Delta r^2/\nu$  (here  $\Delta r \sim v_A R/\omega z$  is the scale-length of perturbations) becomes equal to the propagation time  $z/v_A(r)$ . The corresponding height can be estimated as

$$z = z_* \simeq \frac{v_A(r)}{\omega} \left( \frac{\omega R^2}{\nu} \right)^{1/3}. \quad (4.41)$$

For the volume density of the power  $Q$  released by viscous dissipation we have the following estimate

$$\sim \rho \nu \frac{\omega^2 \xi^2}{(\Delta r)^2}. \quad (4.42)$$

As  $\Delta r$  diminishes with height,  $Q$  is growing with  $z$ . At the altitude given by (4.41),  $Q$  reaches a maximum and then rapidly decreases (see Fig. 4.5). Thus, the heating power has a characteristic shape with a pronounced maximum at a certain altitude  $z$ . For comparison, the dotted line in Fig. 4.5 shows the power for the usual exponentially damping wave.

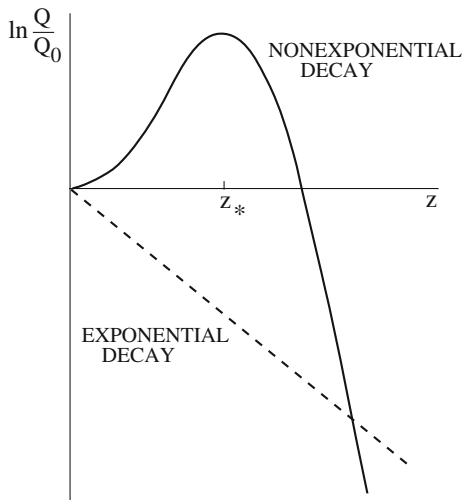
It is therefore obvious that even in the case of a smooth radial profile the flux tube oscillation can transfer energy from the photosphere and the convective zone to the upper well defined heights of the atmosphere.

### 4.2.3 Phase-Mixed Kink Oscillations

Consider now the phase-mixing effect in the kink oscillations of flux tube (Ryutova and Khijakadze 1990). In a low frequency limit,  $\omega \ll v_A/R$ , the linearized MHD equations can be reduced to the following equation for the  $r$ -component of the tube's displacement vector:

$$\frac{\partial^2}{\partial z^2} \left( \frac{B^2}{4\pi} \xi_r + \frac{\partial}{\partial r} \frac{B^2}{4\pi} r \frac{\partial}{\partial r} r \xi_r \right) + \omega^2 \left( \rho \xi_r + \frac{\partial}{\partial r} \rho r \frac{\partial}{\partial r} r \xi_r \right) = 0. \quad (4.43)$$

**Fig. 4.5** The volume density of power released by viscous dissipation; *solid line* with the maximum at the definite altitude  $z_*$  (4.41) represents the phase-mixed wave, while *dashed line* is for the regular exponentially damping wave



The Laplace transform for this equation is of the form:

$$\frac{\partial}{\partial r} \rho(\omega^2 + p^2 v_A^2) r \frac{\partial}{\partial r} r \xi_{rp} + \rho(\omega^2 + p^2 v_A^2) \xi_{rp} = -F(0) - pF(0), \quad (4.44)$$

where  $\xi_{rp}$  is the Laplace transform for the displacement  $\xi_r(z)$ , and

$$F(r) = \frac{B^2}{4\pi} \xi_r + \frac{\partial}{\partial r} \frac{B^2}{4\pi} r \frac{\partial}{\partial r} r \xi_r \quad (4.45)$$

The exact solution of the boundary-value problem in this case is much more difficult than in the previous case of the torsional Alfvén waves. However, some general conclusions on the asymptotic behavior of the solution at  $z \rightarrow \infty$ , can be obtained in a simpler way.

The main contribution to the asymptotic solution comes from singularities of  $\xi_{rp}$  that are nearest to the imaginary axis in the complex plane. In other words, we should consider the solution of (4.44) in the limit of  $Re(p) = \epsilon \rightarrow 0$ . In this limit the solution has a strongly oscillating shape near the point where the following condition is fulfilled:

$$v_A^2(r) = \frac{\omega^2}{(\text{Im } p)^2} \quad (4.46)$$

The solution in this region is of the form:

$$\xi_{rp} = D(r) \ln \frac{1}{r - r_0 + i(\epsilon/\text{Im } p)(v_A(r)/v'_A(r))} \quad (4.47)$$

where  $D(r)$  is a slowly varying function of  $p$ , and  $r_0$  is determined by (4.46). As to the  $v_A(r)$  and  $v'_A(r) = dv_A(r)/dr$ , they are taken at the point  $r = r_0$ .

From (4.41) and (4.47) for  $\xi_{\phi p}$  we have

$$\xi_{\phi p} \sim \frac{1}{r - r_0 + i(\epsilon/\text{Im } p)[v_A(r)/v'_A(r)]} \quad (4.48)$$

One can see that the function  $\xi_{\phi p}$  has poles near the points  $p = \pm v_A/\omega$ , i.e., the solution in this case is similar to that of the Alfvén waves (i.e., for torsional waves). The same holds for the asymptotic behavior of the solution. Again, we may conclude that even for smooth radial profiles of flux tube parameters, the kink oscillations provide an efficient mechanism for energy transfer from the lower to the upper layers of the solar atmosphere.

### 4.3 Longitudinal Resonances

In this section we consider another aspect of the energy accumulation which is associated with longitudinal inhomogeneities of flux tube and/or its environment. In particular, we study here the situation when magnetic flux tubes are pinned at some altitudes. This problem is also related to the coronal loops where both ends of coronal loop threads are pinned at the photosphere and may lead to resonance structure formations.

There are situations when magnetic flux tubes stretched upward from the photosphere get “pinned” at some height (Rytova and Khijakadze 1990). At this height, almost complete reflection of the tube wave may occur, which means that standing waves can be excited and conditions for longitudinal resonances arise. Below, we discuss two examples of such resonant structures.

Consider the flux tube with a stepwise radial profile of density, magnetic field, and pressure. But we will take into account the height dependence of flux tube parameters and the parameters of environment. In this case flux tube sustains weakly damped kink oscillations. It is important to note that the phase-mixing and associated effects are now absent.

For the  $z$ -dependent case the equation for kink oscillations has the form

$$4\pi R^2(\rho_i + \rho_e) \frac{\partial^2 \xi}{\partial t^2} = \frac{\partial}{\partial z} \left( R^2 B^2 \frac{\partial \xi}{\partial z} \right) \quad (4.49)$$

With the condition of flux conservation

$$R^2(z)B(z) = \text{const.} \quad (4.50)$$

Equation (4.49) can be written as follows:

$$4\pi \frac{(\rho_i + \rho_e)}{B} \frac{\partial^2 \xi}{\partial t^2} = \frac{\partial}{\partial z} B \frac{\partial \xi}{\partial z} \quad (4.51)$$

We solve this equation for two types of longitudinal resonances: one is associated with loss of radial equilibrium by flux tube, which may lead to the effect similar to bullwhip effect, and another is caused by the temperature jump at some altitude along the flux tube.

### 4.3.1 Loss of Radial Equilibrium

To demonstrate the effect of gravity let us consider for simplicity an isothermal atmosphere. Then  $z$ -dependence of plasma parameters obeys the simple barometric law, as for example,

$$\rho_i = \rho_{i0} e^{-\kappa_i z}, \quad \rho_e = \rho_{e0} e^{-\kappa_e z}, \quad (4.52)$$

where  $\kappa_i$  and  $\kappa_e$  are inverse pressure scale-height inside and outside flux tube

$$\kappa_{i,e} \equiv \frac{1}{\Lambda_{i,e}} = \frac{mg}{k_B T_{i,e}}. \quad (4.53)$$

At  $\kappa_e > \kappa_i$ , i.e., when the pressure scale-height outside the flux tube is less than that inside ( $T_e < T_i$ ), the flux tube rapidly expands and its mass per unit length becomes very large. Formally, this means that at some height the flux tube gets “dissolved”. Indeed, from (4.52) it follows that when approaching the height (from below)

$$z_* = \frac{\Lambda_i \Lambda_e}{\Lambda_i - \Lambda_e} \ln \frac{p_{i0} + B^2/8\pi}{p_{e0}}, \quad (4.54)$$

the magnetic field tends to zero, and according to magnetic flux conservation,  $R \rightarrow \infty$ . Of course this is a formal statement, since at the point  $z = z_*$ , the equilibrium of the flux tube is no longer one-dimensional, but the qualitative conclusion that in this region the flux tube rapidly expands, or, in other words, its inertia becomes infinitely large, remains valid. Respectively, the amplitude of flux tube oscillations becomes close to zero, and (4.49) should be solved with the boundary condition  $\xi(z_*) = 0$ . This is a typical Sturm-Liouville problem and the corresponding solution has discrete frequency spectrum. Which means the presence of resonances in the system, and if the spectrum of the exciting force is sufficiently narrow, the amplitude of flux tube oscillations can increase at several points (namely at the gulf points) along the tube.

Consider first a quasi-classical problem of forced oscillations of flux tube with  $\xi \sim \exp(-i\omega t)$ . Equation (4.51) takes the form:

$$\frac{\partial}{\partial z} B \frac{\partial \xi}{\partial z} + 4\pi \frac{(\rho_i + \rho_e)}{B} \omega^2 \xi = 0 \quad (4.55)$$

In a quasi-classical approach, a local wave vector,

$$q(z) = \frac{\omega B(z)}{\sqrt{4\pi[\rho_i(z) + \rho_e(z)]}} \equiv \frac{\omega}{c_k(z)} \quad (4.56)$$

is much larger than  $\kappa_i$  and  $\kappa_e$ , i.e., the wave frequency is quite large. In this approximation, the flux tube can be considered “locally homogeneous,” and the energy density flux of tube oscillations takes the simple form

$$S = \pi R^2(\rho_i + \rho_e)\xi^2\omega^2c_k \quad (4.57)$$

It is just a product of phase velocity of kink oscillations (which in this case coincides with the group velocity), and the energy density of oscillations per unit length of the tube. The condition,  $S = \text{const}$ , determines the oscillation amplitude as a function of height. From (4.50) and (4.56) we have

$$\xi(z) = \frac{[\rho_{i0} + \rho_{e0}]^{1/4}}{[\rho_i(z) + \rho_e(z)]^{1/4}}\xi(0) \quad (4.58)$$

As the plasma density drops with height exponentially, the oscillation amplitude grows exponentially as well. This fact has important consequences. For example, at large enough amplitudes, the oscillation energy will be efficiently dissipated due to nonlinear processes, of which, the first to appear is generation of shock waves.

For illustration consider a particular case, when (4.55) can be solved exactly. This can be done if we assume that scale heights inside and outside flux tube are close,  $\kappa_i \simeq \kappa_e$ . Then, from equilibrium conditions we have

$$B(z) = B(0)e^{-\kappa z/2}, \quad \frac{\rho_i(z) + \rho_e(z)}{B(z)} = \frac{\rho_i(0) + \rho_e(0)}{B(0)}e^{-\kappa z/2} \quad (4.59)$$

With these, (4.55) becomes

$$\frac{\partial^2 \xi}{\partial z^2} - \kappa \frac{\partial \xi}{\partial z} + q^2 \xi = 0 \quad (4.60)$$

where  $q$  is given by (4.56).

A secular equation for the solution of (4.60) of the form  $\sim \exp(i\mu z)$  is as follows:

$$\mu^2 + i\mu\kappa - q^2 = 0 \quad (4.61)$$

To choose a correct root of (4.61), we need to add a small imaginary part to the frequency,  $\omega = \omega_0 + i\epsilon$ , such that at  $\omega_0 > 0$ ,  $\epsilon \rightarrow +0$ . The sign of  $\epsilon$  corresponds to a slow adiabatic excitation of perturbation at  $t \rightarrow -\infty$ . Out of two solutions of (4.58), we need to choose one that has  $\text{Re } \mu > 0$ , which corresponds to the assumption that at  $t \rightarrow -\infty$  the flux tube was at rest, and that the oscillations excited at  $z = 0$  propagate from the origin of coordinate system to infinity, i.e.,

$$\mu = -\frac{i\kappa}{2} + \sqrt{q^2 - \frac{\kappa^2}{4}} \quad (4.62)$$

After choosing the root, we put  $\epsilon = 0$ . Finally,

$$\xi \sim e^{\kappa z/2} \exp(iz\sqrt{q^2 - \kappa^2/4}) \quad (4.63)$$

This solution has two slightly different branches determined by the frequency. One branch corresponds to relatively high frequencies, when  $q > \kappa/2$ , i.e., when

$$\omega > c_k/4\Lambda, \quad (4.64)$$

In this case the flux tube oscillations represent running waves propagating upward along the flux tube with exponentially growing amplitude.

In the opposite case, when  $q < \kappa/2$  and, i.e., for lower frequencies such that

$$\omega < c_k/4\Lambda \quad (4.65)$$

the solution of (4.55) has pure exponential dependence on height

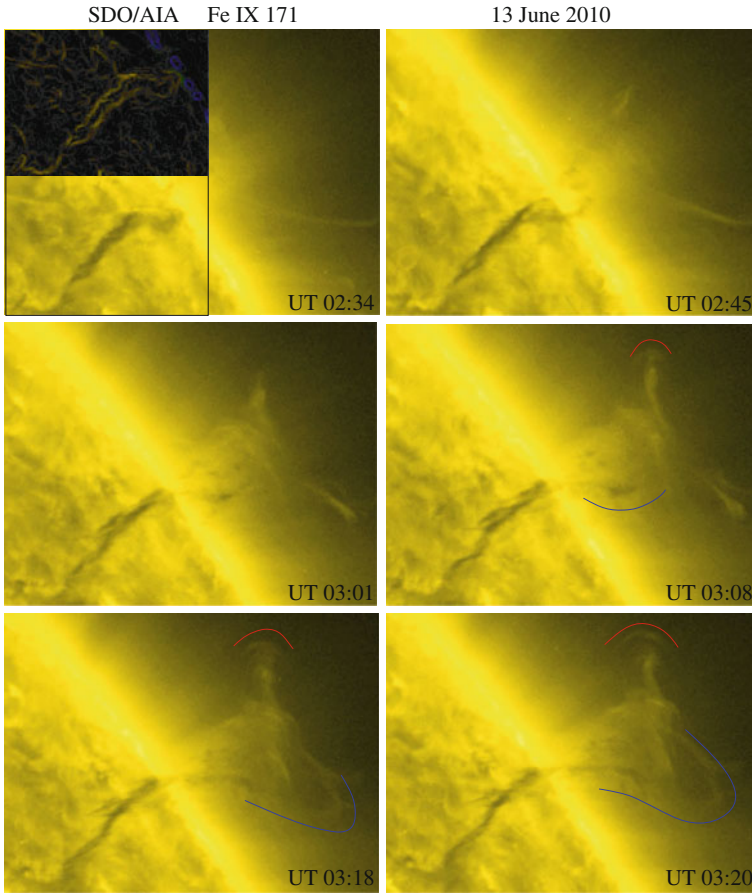
$$\xi \sim e^{(\kappa/2 - \sqrt{\kappa^2/4 - q^2})z} \quad (4.66)$$

In both cases ( $q > \kappa/2$  and  $q < \kappa/2$ ), the exponential growth of oscillation amplitude will be eventually limited by some physical processes determined by specific properties of a system. First to act are nonlinear processes and, in particular, formation of shocks and solitons.

### 4.3.2 Bullwhip Effect

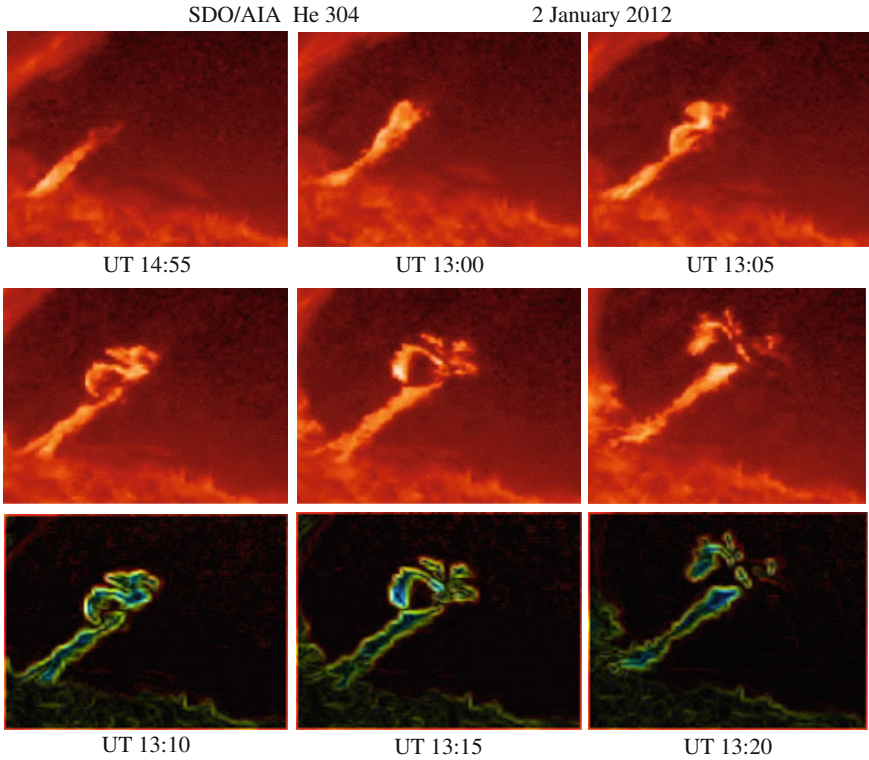
By its nature, an unlimited growth of the amplitude of flux tube oscillations is similar to the effect of bullwhip: in both cases the growth of the oscillation amplitude is associated with *longitudinal* inhomogeneity of the object. Note that the final stage, i.e., exponentially growing amplitude of flux tube, and shock formation may occur at different heights for two branches, (4.64) and (4.65). One may expect that in case of  $\omega > c_k/4\Lambda$  with accompanying running waves, shock formation occurs at higher altitudes and hence, at higher temperatures, than in case of  $\omega < c_k/4\Lambda$ .

From the observational point of view such a process may be easily recognizable, especially now when high resolution and high cadence observations show great details in dynamics of various formations throughout the solar atmosphere. Examples of such events taken by the AIA instrument on SDO are shown in Figs. 4.6 and 4.7.



**Fig. 4.6** A bullwhip behavior of a flux tube at coronal temperatures,  $T \simeq 6.3 \times 10^5$  K shown at six instances of time. The *dark inlet* on the image at UT 02:34 is produced by the Edge Detect procedure of the area marked by *box* in the *left lower corner* clearly reveals the flux tube oscillations well seen in all subsequent snapshots. *Blue curves* at the final stages outline the exponentially growing amplitude. The *red arcs* at three last snapshots outline the growing shock front. Field of view is  $153 \times 114$  Mm

Figure 4.6 shows a bullwhip behavior of a flux rope captured by the AIA instrument at coronal temperatures in Fe IX 171 line. Shown is the formation and evolution of growing loop curvature at the “end” of the rope (marked by blue curves) accompanied in the final stage by shock formation and its farther growth (marked by the red curves). The dark inlet on the image at UT 02:34 is produced by the Edge Detect procedure of the area marked by a box in the left lower corner of that snapshot. The inlet reveals quite regular oscillations of flux tube, which farther in time (seen in the subsequent snapshots) evolves into the exponentially growing swing.



**Fig. 4.7** Bullwhip behavior of a compact magnetic flux at the chromospheric temperatures,  $T \simeq 6.3 \times 10^5$  K, shown at six instances of time. The last three snapshots (*middle row*) are reproduced in the *bottom* with application of the Edge Detect procedure, which reveals clearly the oscillatory pattern throughout the process. Field of view is  $68 \times 51$  Mm

Another example of bullwhip behavior seen at lower chromospheric temperatures is shown in Fig. 4.7. In this case explosive growth of the flux tube amplitude and shock formation occurs already at the chromospheric temperatures. The upper six images show a compact energized magnetic flux tube in the chromosphere taken by AIA instrument on the SDO in 304 emission line on January 2, 2012. The Edge Detect procedure applied to all three images in the middle row reveals both the oscillatory pattern of the body of flux tube and the formation of a swing at the end of flux tube. One should bear in mind that the end of flux tube and its oscillation amplitude are governed by (4.58) and (4.63).

The bullwhip effect in solar flux tubes is a regular phenomenon and may be observed at all temperatures from the chromospheres to the outer corona. All it requires, actually, is the longitudinal inhomogeneity of a flux tube and its ability to sustain the oscillatory motion. As mentioned above, these are in fact the same requirements that are needed to excite the growing oscillations along the bullwhip



and produce a crack, i.e., shock wave or exploding soliton, as different theories of bullwhip predict (Bernstein et al. 1958; Krehl et al. 1998; McMillen and Goriely 2003).

Since antiquity man used to practice whip cracking for various reasons. The fact that the crack is associated with acceleration of the wave that reaches the supersonic velocity at the tip, and generates shock wave, was realized only at the beginning of the twentieth century.

And yet, the first obvious experiment and mathematical illustration of the effect were done only in Bernstein et al. (1958). They studied a bullwhip operated by an expert whip cracker, using a movie camera and still photographs. They found that the crack is produced by the tip of the whip exceeding the sound speed and producing the shock wave. In their words, “in order to produce a crack it is necessary to start a sharp loop near the handle and cause this loop to propagate down toward the tip by investing the system with sufficient momentum or kinetic energy. Apparently this energy becomes concentrated near the tip end, and when the tip tries to negotiate the sharp turn around the loop, it does so with sufficient velocity to cause a shock wave in air.”

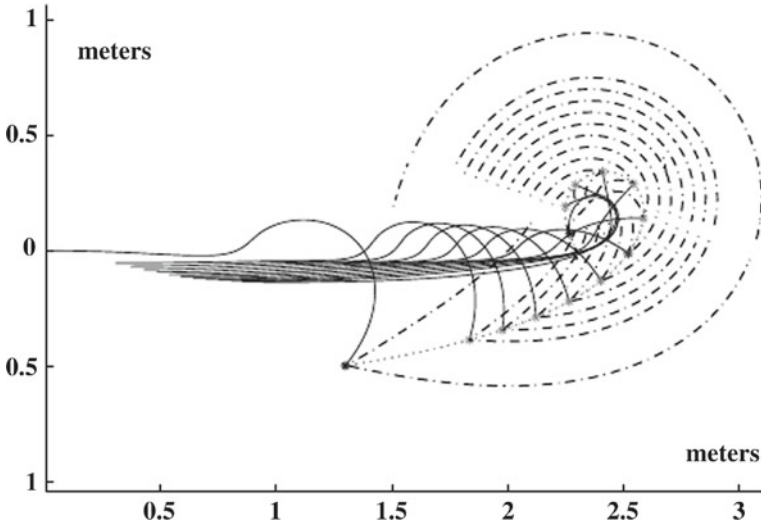
They also gave a mathematical solution for idealized whip assuming that a discontinuity in tension propagates down the whip reaching infinite values associated with decreasing of the mass of the whip. For example, they arrived at a solution for the speed of a kink in the form:

$$\frac{ds}{dt} = k + \frac{c}{\sqrt{L-s}} \quad (4.67)$$

Here  $s$  is the coordinate of a kink along the whip,  $L$  is the length of the whip, and  $k$  and  $c$  are constants of integration. Calculated tension, which is proportional to  $(ds/dt)^2$ , also turns out to be inverse proportional to  $1/\sqrt{L-s}$ . This means that in finite time, the speed of the tip and the tension increase without limit as  $s \rightarrow L$ , i.e., as the kink reaches the tip.

Figure 4.8 shows a numerical solution for the wave propagating along the whip. The whip is modeled as an inhomogeneous planar elastic rod with a tapered end (McMillen and Goriely 2003). It was found that an impulse applied to the handle of the whip travels to the end and accelerates the tip to supersonic speed. A crack is produced when a section of the whip breaks the sound barrier. Dash-dotted curves in Fig. 4.8 are the shock waves emitted by a material point on the rod.

In the solar atmosphere, the open structures that reach the height that no longer sustains conditions of  $\omega\xi_0 < c_{se}$  are all subject to explosively growing amplitude and exhibition of bullwhip effect. It is important to note that in this particular case the fact of the exponential growth of amplitude is not at all associated with the instability of a system, but rather is a consequence of the atmospheric stratification, i.e., an exponential drop of density inside the flux tube.



**Fig. 4.8** Numerical solution for time sequence of the whip behavior. The *solid curves* are the rod; the *dashed curve* is the path the tip of the whip travels; the *dash-dotted curves* are the shock waves. Reprinted from McMillen and Goriely (2003) by permission from Elsevier

### 4.4 Standing Resonances and the Temperature Jump

Consider now another mechanism for the formation of longitudinal resonant structures associated with temperature jump (Ryutova and Khijakadze 1990). Take for example,

$$T = \begin{cases} T_1, & 0 < z < L \\ T_2, & z > L \end{cases} \tag{4.68}$$

We assume for simplicity that temperatures inside and outside the flux tube are about the same.

In the particular case considered in this section, the presence of a sharp discontinuity in the vertical temperature, leads to formation of standing resonances along the oscillating flux tube. To avoid possibility of shock formation, we assume that the initial amplitude of flux tube oscillations is small enough to satisfy condition  $\omega \xi_0 < c_{se}$ , where  $c_{se}$  is sound speed outside flux tube.

The solution of (4.60) in the region below the temperature jump,  $0 < z < L$ , is as follows:

$$\xi = e^{(\kappa z/2)} \left[ \xi_0 \cos(z\sqrt{q^2 - \kappa^2/4}) + A \sin(z\sqrt{\kappa^2/4 - q^2}) \right] \tag{4.69}$$

Here, we took into account that boundary condition at the base of the flux tube,  $z = 0$ , with a given amplitude of oscillations  $\xi_0$ , i.e.,  $\xi|_{z=0} = \xi_0$ , provides expressions for the coefficient in front of the first term, which obviously is  $\xi_0$ .

In the region above the temperature jump,  $z > L$ , with  $1/\Lambda_2 = (mg)/(kT_2)$ , (4.49) is of form:

$$\frac{\partial^2 \xi}{\partial z^2} - \kappa \frac{T_1}{T_2} \frac{\partial \xi}{\partial z} + q^2 \frac{T_1}{T_2} \xi = 0 \quad (4.70)$$

Here we took into account that  $1/\Lambda_2 = \kappa(T_1/T_2)$ . The solution to this equation for the open end of flux tube is as follows:

$$\xi = C e^{(\sigma kz/2)} \exp\left(i\sqrt{q^2\sigma - \kappa^2\sigma^2/4}\right), \quad \sigma = \frac{T_1}{T_2} \quad (4.71)$$

Two other arbitrary constants  $A$  and  $C$  are determined from the boundary conditions at the point  $z = L$ :

$$\xi \Big|_{z=L} = 0; \quad \frac{d\xi}{dz} \Big|_{z=L} = 0 \quad (4.72)$$

After a simple algebra, we get for  $A$ , describing the behavior of flux tube in region  $0 < z < L$ :

$$A = -\xi_0 \frac{\kappa L \cos \alpha - 2\alpha \sin \alpha - \left(\sigma \kappa L + 2i\sqrt{4\sigma q^2 L^2 - \sigma^2 \kappa^2 L^2}\right) \cos \alpha}{\kappa L \sin \alpha + 2\alpha \cos \alpha - \left(\sigma \kappa L + i\sqrt{4\sigma q^2 L^2 - \sigma^2 \kappa^2 L^2}\right) \sin \alpha} \quad (4.73)$$

where the coefficient  $C$  is included in  $A$ , and

$$\alpha = L\sqrt{q^2 - \frac{\kappa^2}{4}} \quad (4.74)$$

From the expression (4.73) it is clear that at  $\sigma = T_1/T_2 \ll 1$  there appear narrow resonances in the system. Indeed, the imaginary part in the denominator is small, and when the real part of denominator tends to zero, the amplitude of oscillations becomes infinitely large.

#### 4.4.1 Growth of the Oscillation Amplitude—First Resonance

To consider this effect in detail, let us simplify the analysis by neglecting the terms of the order of  $\sqrt{T_1/T_2}$  (and higher) in the numerator, and terms of the order of  $T_1/T_2$  in the denominator. In this approximation we then have

$$A = -\xi_0 \frac{\kappa L \cos \alpha - 2\alpha \sin \alpha}{\kappa L \sin \alpha + 2\alpha \cos \alpha - 2iqL\sqrt{\sigma} \sin \alpha} \quad (4.75)$$

The denominator here tends to zero at  $\operatorname{tg} \alpha = (2qL\sigma - 2\alpha)/\kappa L$ . Taking into account the smallness of parameter  $\sigma = T_1/T_2 \ll 1$ , we find that the resonance condition is determined by the equation

$$\operatorname{tg} \alpha = -\frac{2\alpha}{\kappa L} \quad (4.76)$$

Respectively, for the set of resonance frequencies we have

$$\omega_n^2 = c_k(0) \sqrt{\frac{\alpha_n}{L^2} + \frac{\kappa^2}{4}} \quad (4.77)$$

where  $\alpha_n$  are the roots of (4.76),  $n = 1, 2, 3, \dots$

Near the resonance frequency  $\omega_n$ , i.e., at  $|\omega - \omega_n| \ll 0$ , one can replace the numerator in (4.75) by its value at the resonance point and expand the denominator over  $(\omega - \omega_n)$ . This gives

$$A_n = -\xi_0 \frac{2\alpha_n(\kappa^2 L^2 - 4\alpha_n^2)}{[2\kappa L + \kappa^2 L^2 + 4\alpha_n^2] \sqrt{4\alpha_n^2 + \kappa^2 L^2}} \frac{\omega_n}{\omega - \omega_n + i\nu_n/2} \quad (4.78)$$

where

$$\nu_n = 16\omega_n \sqrt{\sigma} \frac{\alpha_n^3}{[2\kappa L + \kappa^2 L^2 + 4\alpha_n^2] \sqrt{4\alpha_n^2 + \kappa^2 L^2}} \quad (4.79)$$

are the damping rates.

As an example, let us consider the first resonance,  $n = 1$ , which lies in the interval  $\pi/2 < \alpha_1 < \pi$ . Assume that the wavelength of oscillations are comparable with  $L$ , i.e.,  $\kappa L \simeq 1$ . Then,  $\alpha_1 = 1.9$ , and

$$A_1 = 5\xi_0 \left( \omega - \omega_1 + i \frac{\nu_1}{2} \right); \quad \frac{\nu_1}{\omega_1} = 1.4\sqrt{\sigma} \quad (4.80)$$

The oscillation amplitude can be found from (4.59). Near the resonance we can neglect the first term, thus obtaining

$$\xi(L) = A_1 \exp(\kappa L/2) \sin \alpha_1, \quad (4.81)$$

and for  $\kappa L \simeq 1$ ,

$$\xi(L) = 6\xi_0 \frac{\omega_1}{\omega - \omega_1 + 0.7i\omega_1 \sqrt{T_1/T_2}} \quad (4.82)$$

Now, if, for example,  $T_2 = 10T_1$ , the width of the resonance is 20 % of the frequency. This is quite well measurable quantity in the solar atmosphere.

#### 4.4.2 Spectral Density and Strong Enhancement of the Oscillation Amplitude

We have considered the above harmonic oscillations excited at the base of the flux tube. Actually, in the region where flux tubes are rooted, they experience random displacements caused by the convective motions. Therefore, more adequate would be the description of these displacements in terms of the spectral density of oscillations, which can be represented in the form

$$(\xi_n^2)_\omega = \frac{|F|^2(\xi_0^2)_\omega}{(\omega - \omega_n)^2 + \nu_n^2/4} \quad (4.83)$$

where  $(\xi_n^2)_\omega$  is the spectral density of flux tube oscillations averaged over the “length” of the flux tube,  $\omega_n$  and  $\nu_n$  are, as before, the  $n$ th order eigenfrequency and corresponding damping rate. The function  $F$  has a meaning of a form-factor which is of the order of unity and depends on the particular longitudinal structure of the eigenfunction.

To get the square average of flux tube displacement, we have to integrate (4.83) over frequencies. For narrow resonances,  $\nu_n \ll \omega_n$ , one can replace  $(\xi_0^2)_\omega$  by the constant,  $(\xi_0^2)_{\omega_n}$ , to obtain

$$\overline{\xi_r^2} - \int (\xi_r^2)_\omega d\omega = \frac{1}{\nu_n} 2|F|^2(\xi_0^2)_{\omega_n} \quad (4.84)$$

Thus, the displacement of a flux tube at some height can be much larger than at its footpoint. In other words, if somewhere the resonance structure is formed, one can expect quite a large oscillation level and with some probability the amplitude of oscillations can be substantially larger than its time-averaged value. This means that in this region nonlinear dissipation can occur. Note that these effects may exist along the resonances described above and occurrence of a bullwhip effect.

The probability distribution function  $P(\xi)$  depends on the properties of a random process  $\xi_0(t)$ . For example, for a Gaussian process the probability has a standard exponential form

$$P(\xi) \sim \exp\left(-\xi^2/2\overline{\xi^2}\right), \quad (4.85)$$

which gives considerable probability for fluctuations during which  $\xi^2$  is about 6 times larger than its average value  $\overline{\xi^2}$ , while  $\overline{\xi^2}$  itself is already enhanced and is quite large; see (4.84):

$$\xi^2 \simeq 6 \overline{\xi^2}. \quad (4.86)$$

In the observations such events will manifest themselves in a range of phenomena, from a temporal brightening of a flux tube region at a given height to explosive events and violent mass ejections.

Note that we did not make any assumptions regarding the properties of spectral density of exciting oscillations, so that it can be arbitrary. The results therefore are quite general.

## 4.5 Weakly Nonlinear Waves in Flux Tubes

In this section we address the problem of weakly nonlinear oscillations of flux tubes. Besides nonlinearity, the flux tube oscillations are a subject of the dispersion associated in the first place with inhomogeneity of the flux tube parameters and its environment. As in many other natural environments, if the wave amplitude steepens, the competition between nonlinearity and dispersion may lead to stabilization of the amplitude and, thus to formation of a dynamically stable kink, propagating as a solitary wave. We will see below that both nonlinear kink and sausage oscillations may produce the solitary kink and sustain its longevity.

### 4.5.1 Nonlinear Kink Oscillations—KdV-Bürgers Equation

In this section we follow studies of weakly nonlinear long wavelength kink oscillations of flux tube performed by Ryutova and Sakai (1993). We adopt, as earlier, the model of cylindrical flux tube of radius  $R$ , directed along the  $z$ -axis. Radius of the flux tubes are assumed to be much less than the wavelength  $\lambda = k^{-1}$ :  $kR \ll 1$ . The analysis is based on the ideal MHD equations which we write here for convenience:

$$\rho \frac{\partial \mathbf{v}}{\partial t} + (\mathbf{v} \nabla) \mathbf{v} = -\nabla \delta p + \frac{1}{4\pi} [\nabla \times \mathbf{B}] \times \mathbf{B} \quad (4.87)$$

$$\frac{\partial \mathbf{B}}{\partial t} = \nabla \times [\mathbf{v} \times \mathbf{B}]$$

$$\frac{\partial \rho}{\partial t} + \text{div} \rho \mathbf{v} = 0 \quad (4.88)$$

$$p = p_0 \left( \frac{\rho}{\rho_0} \right)^\gamma$$

The set is completed by the pressure equilibrium condition.

At the surface of flux tube the boundary conditions of continuity of the normal component of velocity,

$$v_{ri}|_{r=R} = v_{re}|_{r=R}, \quad (4.89)$$

and the normal component of the momentum flux

$$p_i + \frac{B^2}{8\pi} \Big|_{r=R} = p_e \Big|_{r=R} \quad (4.90)$$

should be satisfied. These conditions lead to the following dispersion relation (see (3.47)–(3.48)):

$$\eta \frac{\omega^2 - k^2 v_A^2}{\omega^2} \frac{\partial \ln \psi_e}{\partial r} \Big|_{r=R} = \frac{\partial \ln \psi_i}{\partial r} \Big|_{r=R} \quad (4.91)$$

In the long-wavelength limit the expression (4.91) is subject to expansion in powers of a small parameter ( $kR$ ). The first term in this expansion gives the phase velocity of a kink mode,  $c_k = B/\sqrt{4\pi(\rho_i + \rho_e)}$ .

Retaining the next order terms we obtain

$$\omega = c_k k + \beta_k k^3 + i\mu k^3, \quad (4.92)$$

where

$$\beta_k = -\frac{c_k R^2}{8(1+\eta)^2}, \quad \mu = \frac{\pi c_k R^2}{4} \frac{c_k^2 - c_s^2}{9(1+\eta)c_s^2} \quad (4.93)$$

Here  $c_s$  is the sound speed *outside* flux tube.

The second term in the dispersion relation (4.92) describes a weak dispersion of the kink mode associated with the flux tube inertia, and the third term corresponds to radiative damping of flux tube oscillations.

Now we need to determine the character of the nonlinearity of the kink oscillations. Analyzing the next terms we arrive at a simple conclusion that the first nonlinear term that can affect the finite-amplitude kink oscillations is a cubic term, since the azimuthal dependence of the quadratic nonlinearity contains only terms with  $m = 0$  and  $m = 2$ . Thus, the character of nonlinearity of a kink mode appears to be cubic.

To find the equation of kink mode corresponding to the dispersion relation (4.92) and containing a cubic nonlinearity we use the method of the stretched variables

$$\zeta = \epsilon(z - c_k t), \quad \tau = \epsilon^2 t \quad (4.94)$$

where  $\epsilon$  is a key small parameter.

To carry out the adequate perturbation analysis we perform expansion of the MHD equations by representing the velocity, magnetic field, and other plasma parameters in power series with respect to  $\epsilon$ . For simplicity we assume that plasma inside flux tube is cold,  $p_i \ll p_e$ , and respectively, neglect the gas-kinetic pressure inside flux tube. This assumption is not principal but allows to simplify algebra. Thus inside the flux tube we may write

$$\begin{aligned}
\mathbf{v}_\perp &= \epsilon^{1/2} \mathbf{v}_{1\perp} + \epsilon^{3/2} \mathbf{v}_{2\perp} + \dots \\
v_z &= \epsilon v_{1z} + \epsilon^2 v_{2z} + \dots \\
\mathbf{B}_\perp &= \epsilon^{1/2} \mathbf{B}_{1\perp} + \epsilon^{3/2} \mathbf{B}_{2\perp} + \dots \\
B_z &= B_0 + \epsilon^{3/2} B_{1z} + \epsilon^{5/2} B_{2z} + \dots \\
\rho &= \rho_0 + \epsilon \rho_1 + \epsilon^2 \rho_2 + \dots
\end{aligned} \tag{4.95}$$

Respectively, outside the flux tube we have

$$\begin{aligned}
\mathbf{v}_{e\perp} &= \epsilon^{1/2} \mathbf{v}_{e1\perp} + \epsilon^{3/2} \mathbf{v}_{e2\perp} + \dots \\
v_{ez} &= \epsilon v_{e1z} + \epsilon^2 v_{e2z} + \dots \\
p_e &= p_{e0} + \epsilon^{3/2} p_{e1} + \epsilon^{5/2} p_{e2} + \dots \\
\rho_e &= \rho_{e0} + \epsilon^{3/2} \rho_{e1} + \epsilon^{5/2} \rho_{e2} + \dots
\end{aligned} \tag{4.96}$$

where  $\mathbf{v}_\perp$  and  $\mathbf{B}_\perp$  are the transverse ( $r$  and  $\phi$ ) components of velocity and magnetic field.

The expansions (4.95) and (4.96), along the exact representation of a linear stage of flux tubes oscillations, describe the dispersion properties of a system that includes the oscillating flux tube and its environment. Besides, the above choice of variables allows one to specify the nature of the nonlinearity independently of the dispersive properties of a system.

Substituting (4.95) and (4.96) in the MHD equations, and equating terms of each order in  $\epsilon$ , we obtain sequence of equations up to the desired order.

First, in the order of  $\epsilon^{3/2}$  for a flux tube interior we have from (4.87) and (4.88)

$$-c_k \rho_0 \frac{\partial \mathbf{v}_{1\perp}}{\partial \zeta} = -\frac{B_0}{4\pi} \nabla_\perp B_z + \frac{B_0}{4\pi} \frac{\partial \mathbf{B}_{1\perp}}{\partial \zeta} \tag{4.97}$$

$$-c_k \frac{\partial \mathbf{B}_{1\perp}}{\partial \zeta} = B_0 \frac{\partial \mathbf{v}_{1\perp}}{\partial \zeta} \tag{4.98}$$

and for outer region

$$-c_k \rho_{e0} \frac{\partial \mathbf{v}_{e1\perp}}{\partial \zeta} = -\nabla_\perp p_1 \tag{4.99}$$

$$p_1 = c_s^2 \rho_1 \tag{4.100}$$

Substituting  $\mathbf{B}_{1\perp} = -(B_0/c_k) \mathbf{v}_{1\perp}$  which follows directly from (4.98), into (4.97) we have

$$\left( -c_k \rho_0 + \frac{B_0}{4\pi c_k} \right) \frac{\partial \mathbf{v}_{1\perp}}{\partial \zeta} = -\nabla_\perp \frac{B_0 B_{1z}}{4\pi}, \tag{4.101}$$

and, respectively,

$$\left( -c_k \rho_0 + \frac{B_0}{4\pi c_k} \right) \frac{\partial \mathbf{v}_{1\perp}}{\partial \zeta} = -c_k \rho_{e0} \frac{\partial \mathbf{v}_{1\perp}}{\partial \zeta} \tag{4.102}$$



This equation coincides naturally with the basic equation for linear oscillations which gives the phase velocity of kink mode.

Now we proceed to the next,  $\epsilon^2$ , order approximation. At this order from  $z$ -component of (4.87) and the second equation in (4.88) we have

$$\rho_1 = \frac{\rho_0}{c_k} v_{1z}, \quad \rho_0 c_k v_{1z} = \frac{c_k^2}{v_A^2} \frac{\mathbf{B}_{1\perp}^2}{8\pi} \quad (4.103)$$

Here we used the relationship

$$\nabla_{\perp} B_{1z} = \frac{v_A^2 - c_k^2}{v_A^2} \frac{\partial \mathbf{B}_{1\perp}}{\partial \zeta}. \quad (4.104)$$

Now, in the next,  $\epsilon^{5/2}$  order, the transverse components of (4.87) and the first equation in (4.88) for the flux tube interior take the forms

$$\rho_0 c_k \frac{\partial \mathbf{v}_{2\perp}}{\partial \zeta} + \frac{B_0}{4\pi} \left( \frac{\partial \mathbf{B}_{2\perp}}{\partial \zeta} - \nabla_{\perp} B_{2z} \right) = \rho_0 \frac{\partial \mathbf{v}_{1\perp}}{\partial \tau} - (\rho_1 c_k - \rho_0 v_{1z}) \frac{\partial \mathbf{v}_{1\perp}}{\partial \zeta} \quad (4.105)$$

$$c_k \frac{\partial \mathbf{B}_{2\perp}}{\partial \zeta} + B_0 \frac{\partial \mathbf{v}_{2\perp}}{\partial \zeta} = \frac{\partial \mathbf{B}_{1\perp}}{\partial \tau} + \frac{\partial}{\partial \zeta} (v_{1z} \mathbf{B}_{1\perp}) \quad (4.106)$$

In the outer region of this order we have

$$\rho_{e0} c_k \frac{\partial \mathbf{v}_{e2\perp}}{\partial \zeta} - \nabla_{\perp} p_2 = \rho_{e0} \frac{\partial \mathbf{v}_{e1\perp}}{\partial \tau} + \frac{\rho_{e1}}{2} \nabla_{\perp} \mathbf{v}_{e1\perp}^2, \quad (4.107)$$

$$\rho_{e0} c_k \frac{\partial v_{e1z}}{\partial \zeta} = \frac{\partial p_1}{\partial \zeta} \quad (4.108)$$

Using  $p_1 = c_s^2 \rho_{e1}$  in (4.108) and taking into account that

$$\nabla \rho_{e1} = \frac{\rho_{e0} c_k}{c_s^2} \frac{\partial \mathbf{v}_{e1\perp}}{\partial \zeta} \quad (4.109)$$

we can write (4.107) in the form:

$$\rho_{e0} c_k \frac{\partial \mathbf{v}_{e2\perp}}{\partial \zeta} - \nabla_{\perp} \left( p_2 + \frac{\rho_{e1} \mathbf{v}_{e1\perp}^2}{2} \right) = \rho_{e0} \frac{\partial \mathbf{v}_{e1\perp}}{\partial \tau} - \frac{c_k \rho_{e0}}{c_s^2} \mathbf{v}_{e1\perp}^2 \frac{\partial \mathbf{v}_{e1\perp}}{\partial \zeta} \quad (4.110)$$

Matching (4.105) and (4.110) through the boundary conditions, we obtain

$$(\rho_{i0} + \rho_{e0})c_k \frac{\partial \mathbf{v}_{2\perp}}{\partial \zeta} + \frac{B_0}{4\pi} \frac{\partial \mathbf{B}_{2\perp}}{\partial \zeta} = (\rho_{i0} + \rho_{e0})c_k \frac{\partial \mathbf{v}_{1\perp}}{\partial \tau} - \frac{c_k \rho_{e0}}{c_s^2} \mathbf{v}_{1\perp}^2 \frac{\partial \mathbf{v}_{1\perp}}{\partial \zeta} \quad (4.111)$$

Eliminating the second-order terms in (4.111) and (4.106) we arrive straightforwardly to nonlinear equations for kink mode written in the stretched variables:

$$2 \frac{\partial \mathbf{B}_{1\perp}}{\partial \tau} + \frac{c_k}{\rho_{i0} v_A^2} \frac{\partial}{\partial \zeta} \left( \mathbf{B}_{1\perp} \frac{\mathbf{B}_{1\perp}^2}{8\pi} \right) - \frac{c_k^2}{c_s^2} \frac{\rho_{e0} c_k}{B_0^2 (\rho_{i0} + \rho_{e0})} \frac{\mathbf{B}_{1\perp}^2}{2} \frac{\partial \mathbf{B}_{1\perp}}{\partial \zeta} = 0 \quad (4.112)$$

It is convenient to introduce instead of the transverse components  $\mathbf{B}_\perp$  the complex quantity  $H = B_r - iB_\phi$ , and normalize it by the unperturbed magnetic field,  $B_0$ . Finally, the nonlinear equation for a kink mode acquires the form:

$$\frac{\partial H}{\partial \tau} + \frac{c_k}{4} \frac{\partial}{\partial \zeta} (|H|^2 H) - \frac{c_k^3}{4(1+\eta)c_s^2} |H|^2 \frac{\partial H}{\partial \zeta} = 0. \quad (4.113)$$

Equation (4.113) is a fundamental equation describing nonlinear kink oscillations of magnetic flux tubes. We see that, as expected, the character of nonlinearity is cubic.

It is interesting that the first two terms in (4.113) formally are similar to those describing hydromagnetic waves propagating along the magnetic field in a cold plasma (Mjølhus 1976). Note however that the similarity is only formal, because in cold plasma the MHD waves propagate in an unbounded plasma, whereas in case of magnetic flux tubes, we deal with an oscillating “magnetic string” which interacts with the nonmagnetic environment. The influence of the magnetic free region is represented by the last term in (4.113), and is reflected in the propagation velocity of the kink mode.

It should be emphasized that the entire procedure developed above (starting from stretched variables (4.113)) was aimed to find the character of nonlinearity. To construct the full equation describing the nonlinear kink oscillations in weakly dispersive and dissipative media, (4.113) should be supplemented with the dispersion terms obtained in the analysis of radiative damping.

Applying a standard procedure to the dispersion relation (4.92) we obtain the evolutionary equation describing a weakly nonlinear kink oscillations in weakly dispersive medium, which includes the intrinsic dissipative process associated with radiation of secondary MHD waves by oscillating flux tube

$$\begin{aligned} \frac{\partial H}{\partial \tau} + \frac{c_k}{4} \frac{\partial}{\partial \zeta} (|H|^2 H) - \frac{c_k^3}{4(1+\eta)c_s^2} |H|^2 \frac{\partial H}{\partial \zeta} + \beta_k \frac{\partial^3 H}{\partial \zeta^3} \\ + \frac{\mu}{\pi} v.p. \int_{-\infty}^{\infty} \frac{\partial^3 H}{\partial s^3} \frac{ds}{s - \zeta} = 0 \end{aligned} \quad (4.114)$$

where  $\beta_k$  and  $\mu$  are given by expressions (4.93).

Equation (4.114) fully describes a nonlinear oscillations of flux in a dissipative and weakly dispersive media. The equation is obviously of a type of KdV-Bürgers equation (see e.g. Karpman 1975). The final outcome depends on the interplay between the nonlinearity, dispersion, and dissipation processes. If, for example, nonlinearity prevails dispersion and dissipation, kink oscillations evolve into shock waves. In case of competitive dispersion effect, a kinked flux tube will sustain a solitary kink for a long time. The effect of radiative damping (last term in (4.114)) plays an important role in development of strong plasma instabilities which will be addressed later. Here we must add that kink solitons proved to be ubiquitous in solar atmosphere, and are well observed, especially in sunspot and plage regions. This will be studied in Chaps. 11 and 15.

### 4.5.2 Possibility of Solitary Sausage Wave

On the possibility of symmetric,  $m = 0$  mode, soliton solution in a magnetic slab was first pointed out by Roberts and Mangeney (1982). They considered a uniform, two-dimensional slab of magnetic field  $B$ , with width  $2d$ , embedded in a gravity-free, nonmagnetic atmosphere. Earlier, Roberts (1981) studied a long wavelength symmetric pulsations of such a slab and obtained their dispersion relation up to nonlinear terms with respect to wavenumber,  $k$ . It was found that there are two possible symmetric waves propagating along the magnetic field depending on the phase velocity,  $c_T = c_{si}v_A/\sqrt{c_{si}^2 + v_A^2}$  and the sound speed outside the slab,  $c_{se}$ .

If  $c_T < c_{se}$ , then the dispersion relation is of form

$$\omega \simeq kc_T(1 - \alpha|k|), \quad (4.115)$$

where the constant  $\alpha$  is a measure of the environment's inertia,

$$\alpha = \frac{1}{2} \frac{\rho_e}{\rho_i} \frac{c_T^2 c_{se}}{c_{si}^2 v_A^2} \frac{c_{si}^2 - c_T^2}{\sqrt{c_{se}^2 - c_T^2}} d \quad (4.116)$$

If  $c_T > c_{se}$  or  $c_{si} < c_{se}$ , then the dispersion relation for slab oscillations takes the form

$$\omega \simeq kc_{se}(1 - \alpha_e k^2), \quad (4.117)$$

where

$$\alpha_e = \frac{1}{2} \frac{\rho_e}{\rho_i} \frac{c_{se}^2}{c_{si}^2 + v_A^2} \frac{c_{se}^2 - c_{si}^2}{c_{se}^2 - c_T^2} d^2 \quad (4.118)$$

Dispersion relation (4.115) corresponds to wave propagating inside the slab, and (4.117) to those outside the slab.

Using the method of stretched variables for magnetic slab oscillations, Roberts (1985) derived nonlinear equation for sausage mode:

$$\frac{\partial v}{\partial t} + c_T \frac{\partial v}{\partial z} + \beta_T v \frac{\partial v}{\partial z} + \alpha \frac{1}{\pi} \frac{\partial^2}{\partial z^2} \int_{-\infty}^{\infty} \frac{v(z', t) dz'}{z' - z} \quad (4.119)$$

where  $v$  is the wave propagation velocity, and  $\beta_T$  is a coefficient of nonlinearity

$$\beta_T = \frac{1}{2} \frac{v_A^2 [3c_{si}^2 + (\gamma + 1)v_A^2]}{(c_{si}^2 + v_A^2)^2} \quad (4.120)$$

Thus, for a slab, weakly nonlinear sausage oscillations are governed by the equation similar to one-dimensional integro-differential equation obtained by Benjamin (1967) and Ono (1975) for internal waves in deep water.

One should bear in mind, however, that there are several problems with sausage oscillations. One is that they are very sensitive to radial inhomogeneity across their cross section, and can survive only if the flux tube is highly homogeneous which, under real conditions of solar atmosphere, is quite unlikely. The same fact also works “against” nonlinearity of sausage oscillations. One of the obvious mechanisms for steepening the waves in the solar flux tubes, is gravity: the waves propagating upward against gravity quickly grow, so does the cross section of flux tubes, and, sausage waves damp away earlier than they become nonlinear.

## References

- T.B. Benjamin, *J. Fluid Mech.* **29**, 559 (1967)  
 B. Bernstein, D.A. Hall, H.M. Trent, *J. Acoust. Soc. Am.* **30**, 1112 (1958)  
 J. Boussinesq, *Comptes Rendus de l'Academie des Sciences* **72**, 755 (1871)  
 L.C.G. de Andrade, *Astrophys. Space Sci.* **310**, 25 (2007)  
 J. Heyvaerts, E.R. Priest, *A&A* **117**, 220 (1983)  
 J.A. Ionson, *Astrophys. J.* **226**, 650 (1978)  
 V.I. Karpman, *Nonlinear Waves in Dispersive Media* (Pergamon Press, London, 1975)  
 D.J. Korteweg, G. de Vries, *Phil. Mag. Ser. 5* **39**, 422 (1895)  
 P. Krehl, S. Engemann, D. Schwenke, *Shock Waves* **8**, 1 (1998)  
 L. Rayleigh, *Philos. Mag., Ser. 5* **1**(4), 257 (1876)  
 T. McMillen, A. Goriely, *Physica D* **184**, 192 (2003)  
 E. Mjølhus, *J. Plasma Phys.* **16**, 321 (1976)  
 H. Ono, *Phys. Soc. Jpn.* **39**, 1082 (1975)  
 M.J. Penn et al., *Astrophys. J.* **734**, 47 (2011)  
 S.R.O. Ploner, S.K. Solanki, *Astron. Astrophys.* **325**, 1199 (1997)  
 B. Roberts, *Solar. Phys.* **69**, 39 (1981)  
 B. Roberts, A. Mangeney, *Mon. Not. Roy. Astron. Soc.* **198**, 7 (1982)  
 B. Roberts, *Phys. Fluids* **28**, 3280 (1985)  
 B. Roberts, A.R. Webb, *Solar. Phys.* **56**, 5 (1978)

- M.P. Ryutova, in *Proceedings of the XIII-th International Conference on Phenomena in Ionized Gases, Part: II*, p. 859 (1977)
- M.P. Ryutova, L.G. Khijakadze, *Geophys. Monogr.* **58**, 99 (1990)
- M.P. Ryutova, J.I. Sakai, *JETP Lett.* **58**, 507 (1993)
- S.K. Solanki et al., *Astron. Astrophys.* **315**, 303 (1996)
- J.A. Tataronis, W. Grossman, Decay of MHD waves by phase mixing. *Z. Phys.* **261**, 203 (1970)
- A. Timofeev, *Sov. Phys.-Uspekhi* **13**, 632 (1970)

# Chapter 5

## Flux Tube Dynamics in the Presence of Mass Flows

**Abstract** Mass flows observed throughout the solar atmosphere exhibit many patterns. They are observed in a wide temperature range of  $3 \times 10^4$ – $10^7$  K, and can have a steady, unsteady, or explosive character. Their amplitudes vary from a few tenths of  $\text{km s}^{-1}$  at the photosphere up to hundreds of  $\text{km s}^{-1}$  in the transition region and corona. The presence of mass flows drastically changes the dynamics of magnetic structures, and most importantly, plays a crucial role in the processes of the energy production, transfer, and release. Depending on the geometry and intensity of the flow, the system of magnetic flux tubes exhibits a number of unusual phenomena that are directly observed. In this chapter, we consider mainly two effects associated with the presence of mass flows. One is the instability of negative-energy waves (NEWs) and other lies in the range of velocities beyond the instability threshold, namely the effect of mass flows on the energy transfer by the phase mixed Alfvén waves.

### 5.1 Kelvin–Helmholtz Instability and Negative-Energy Waves

The mass flows observed in the solar atmosphere and beyond are as ubiquitous as the magnetic structures. They are predominantly collinear with the magnetic structures, with some differences between downflows, upward mass flows, and vortical motions. For example, in the chromospheres/transition region strong *downflows* are usually associated with complex dynamical structures with multiple velocities (Kjeldseth-Moe et al. 1994). Upward mass flows, also seen at chromospheres/transition region temperatures, apart the “well behaved” spicules, may be adjacent to downflows and often exhibit explosive character ejecting plasma with velocities ranging from 100 to  $400 \text{ km s}^{-1}$  (Dere et al. 1989). Nonisotropic and unsteady high-velocity events often having a twisted character, such as macrospicules, are observed to move outward into the corona at velocities of  $10$ – $150 \text{ km s}^{-1}$ . Mass flows in macrospicules often follow a ballistic trajectories (Withbroe et al. 1976; Habbal and Gonzalez 1991). Quiet prominences and active chromospheric filaments are in fact ever-moving magnetized plasma with all kinds of shapes and energetics. We shall discuss the effect of various flows throughout the book. Here we concentrate on some basic and at the same time nontrivial features of the system of flux tubes and flows.

To understand the basic dynamic processes associated with flows, we need to study their interaction with the structured magnetic fields.

One of the well-known effects of mass flow on the magnetic and nonmagnetic interface is the Kelvin–Helmholtz (KH) instability (see e.g. Chandrasekhar 1961).

In the atmosphere, for example, the condition for KH instability is simple

$$u \geq \sqrt{2gd \frac{\rho_2 - \rho_1}{\rho_2 + \rho_1}} \quad (5.1)$$

Here  $g$  is the gravitational acceleration,  $d$  is the thickness of a narrow mixing layer,  $\rho_2$  and  $\rho_1$  are the gas densities in lower and upper layers of atmosphere,  $\rho_2 > \rho_1$ , and  $u = u_2 - u_1$  is the shear flow associated with different velocities of a wind below and above some layer of the clouds. The consequences of condition (5.1) are observed from its simplest manifestation on our sky and waters to quantum world and biology.

Figure 5.1 shows a typical example of KH instability often seen on our sky as a result of interaction between the clouds and the wind with sheared velocities.



**Fig. 5.1** Two different regimes of shear flow instabilities. The *upper panel* is a typical KH instability caused by interaction of wind with layered clouds. *Bottom panel* shows another regime of flow instability leading to creation of a powerful rogue wave similar to the ocean rogue waves exhibiting explosively growing “amplitude.” In both cases, the energy of a system locally is not conserved: “unaccounted energy comes from the wind.” The upper picture is taken by Henrik Bondo in Denmark on December 30, 2006, reprinted from <http://epod.usra.edu>, credit EPOD at NASA’s Earth Science Division and the EOS (GSFC); the lower picture, the rogue wave over Alabama, is courtesy of Xinhua photo agency, reprinted from <http://news.xinhuanet.com/english/photo>

The choice of this picture (although the oceans and large water surfaces are even more favorite objects) has been motivated by interesting fact: note that higher in the atmosphere the size and regularity of KH rolls change significantly (upper panel). One can see from condition (5.2) that with height, i.e., with the drop of the atmospheric density condition for the instability changes, so does the amplitude of the KH rolls. At some point the velocity of the wind may no longer be higher than the required threshold. In this case, two different scenarios may develop. One corresponds to such low shear velocities that system is stable with respect to any drastic changes. Another scenario may develop under some special conditions determined by system parameters, when the system becomes a subject of explosively growing amplitude KH rolls. Example of such a situation may be illustrated by “the rogue wave over Alabama” shown in bottom panel of Fig. 5.1. Such an extreme situation, that often occurs in the solar atmosphere as well, is the main subject of this chapter.

In our case of magnetic flux tube KH instability develops when the plasma flow exceeds some threshold  $u_{KH}$ . This threshold is supersonic for any tangential discontinuity in the absence of magnetic field, and becomes super-Alfvénic when the magnetic field is involved.

Much more intriguing turned out to be the range of flow velocities below the KH threshold, i.e., when the system is stable with respect to a regular KH instability. What happens is, that at the sheared mass flows having velocities less than  $u_{KH}$  but larger than some threshold, the nonlinear dissipative instabilities may develop, which lead to the appearance of negative-energy waves (NEWs) (Ryutova 1988). The characteristic feature of negative-energy waves is that any interaction of these waves with the medium, i.e., any mechanism of subtraction of their energy (dissipative effects, interaction with other waves, etc.) leads to fast growth of their amplitudes. Accordingly, the damping rate becomes the growth rate. This in turn results in the onset of strongly nonlinear processes and the widening of the classes of instabilities, most important of which is the explosive instability when the amplitudes of the perturbations in a system ( $A$ ) reach infinitely large values in a finite time:  $A \sim 1/(t - t_0)$ ,  $t_0$  is the “explosion” time, and it is completely determined by the physical properties of the medium (Kadomtzev et al. 1964; Dikasov et al. 1965; Sturrock 1966; Coppi et al. 1969; Weiland and Wilhelmsson 1977; Ostrovskii et al. 1964, 1986). It is important to emphasize that NEWs may appear only in energetically open systems, i.e., systems with “unaccounted” energy source and sink of energy. In the system of atmospheric clouds, for example, the source is a wind energy, and the dissipation is any viscous or thermal losses.

Analytically, to recognize the negative-energy waves and distinguish them from usual, positive energy waves, is very simple. *Any wave will have a negative energy* if, for example, at a positive eigenfrequency the derivative of the corresponding dispersion function,  $D(\omega, k) = 0$ , with respect to  $\omega$  becomes negative, i.e., if

$$\frac{\partial D(\omega, k)}{\partial \omega} < 0 \quad (5.2)$$

The location where this derivative becomes zero is the bifurcation point that corresponds to the upper threshold for NEW and lower threshold for classical KH



instability. Hence, if along the magnetic flux tube the amplitude of the mass flow is in the interval,  $u_{\text{NEW}} \leq u \leq u_{\text{KH}}$ , the system is able to maintain vigorous dynamics characteristic to the presence of negative-energy waves.

The properties and existence of negative-energy waves are largely determined by the dispersion properties of the system. To demonstrate their nature in a simple way, consider longitudinal electromagnetic wave with frequency  $\omega$  propagating in a dispersive medium. The energy of such wave is given by the expression (Landau and Lifshitz 1984):

$$U = \frac{1}{8\pi} \frac{\partial \epsilon(\omega, k)}{\partial \omega} \omega \langle E^2 \rangle \quad (5.3)$$

where  $\epsilon(\omega, k)$  is the dielectric function and serves as linear dispersion relation for a system

$$\epsilon(\omega, k) = 0 \quad (5.4)$$

We see that the wave energy is proportional to the derivative  $d\epsilon/d\omega$ , so that the sign of energy depends on whether the medium exhibits normal dispersion,  $\partial\epsilon/\partial\omega > 0$  or anomalous dispersion  $\partial\epsilon/\partial\omega < 0$ .

Similarly, for any other system with the dispersion function

$$D(\omega, k) = 0, \quad (5.5)$$

the energy of the wave  $\sim A \exp(-i\omega t)$  is

$$W = \frac{1}{4} \omega \frac{\partial D(\omega, k)}{\partial \omega} A^2 \quad (5.6)$$

Consider now the system with any kind of dissipation, e.g., Landau damping, Ohmic, thermal conductivity, viscosity, etc., which causes appearance of small imaginary part,  $i\alpha$ , in the dispersion relation

$$D(\omega + i\nu, k) + i\alpha = 0 \quad (5.7)$$

This adds a small imaginary part in the wave frequency whose amplitude now is  $\sim A \exp[-i(\omega + i\nu)t]$ . Expanding the dispersion function with respect to the small imaginary term,  $\nu$ , we obtain

$$D_0(\omega_0) + i\nu \left. \frac{\partial D}{\partial \omega} \right|_{\omega_0} + i\alpha = 0, \quad (5.8)$$

which gives

$$\nu = -\frac{\alpha}{\partial D / \partial \omega|_{\omega_0}}. \quad (5.9)$$

Equations (5.6) and (5.9) show that at the normal dispersion, i.e., when  $\partial D / \partial \omega > 0$ , the parameter  $\nu < 0$  is a damping rate and dissipative effects lead to the absorption of

wave energy. In the opposite case of anomalous dispersion, i.e., when  $\partial D/\partial\omega < 0$ ,  $\nu > 0$  becomes the growth rate and any subtraction of wave energy leads to growing of the wave amplitude. It must be understood that the system which may possess the anomalous dispersion must be energetically open system, i.e., locally the energy of a system is not conserved. In this particular case, the system loses the energy on the expense of growing the wave amplitude. This leads to the strong dissipative instabilities which will be considered below, and which play an essential role in the dynamics of solar atmosphere.

## 5.2 Shear Flow Instabilities in Magnetic Flux Tubes

### 5.2.1 Specifics of Kelvin–Helmholtz Instability Along Flux Tubes

Consider a homogeneous magnetic flux tube of circular cross section in the presence of a flow directed along the tube axis. We adopt for a coordinate system in which the matter inside the flux tube is at rest, while the flow velocity outside the tube has a value  $u$  and is directed toward increasing  $z$ .

We begin with the kink oscillations, and describe the displacement of the tube with respect to its unperturbed position by the vector  $\xi(z, t)$ , which lies in the plane perpendicular to the axis of the tube. The equation for kink oscillations in the presence of shear flow can be written as follows:

$$\rho_i \frac{\partial^2 \xi_{\perp}}{\partial t^2} = -\rho_e \left( \frac{\partial}{\partial t} + u \frac{\partial}{\partial z} \right)^2 \xi_{\perp} + \frac{B^2}{4\pi} \frac{\partial^2 \xi_{\perp}}{\partial z^2} \quad (5.10)$$

Equation (5.10) has an energy integral, which has the form

$$I = \int dz \frac{\pi R^2}{2} \left[ (\rho_i + \rho_e) \left( \frac{\partial \xi_{\perp}}{\partial t} \right)^2 + \left( \frac{B^2}{4\pi} - \rho_e u^2 \right) \left( \frac{\partial \xi_{\perp}}{\partial z} \right)^2 \right] = \text{const.} \quad (5.11)$$

The integrand has the meaning of the energy of the oscillations per unit length along the tube.

For sinusoidal traveling waves  $\sim \exp(-i\omega t + ikz)$  the dispersion relation obtained from (5.10) has the form

$$D(\omega) = \omega^2 + \frac{1}{\eta} (\omega - ku)^2 - k^2 v_A^2 = 0 \quad (5.12)$$

where as earlier,  $\eta = \rho_i/\rho_e$ . From (5.12) we have

$$\omega_{\pm} = \frac{k}{1 + \eta} \left[ u \pm \sqrt{\eta [v_A^2 (1 + \eta) - u^2]} \right] \quad (5.13)$$

This dispersion relation describes two different kinds of instabilities, and accordingly, two branches and different thresholds for the onset of these instabilities.

One instability is analogous to a usual Kelvin–Helmholtz instability, and the other one is the instability of NEWs.

The condition for Kelvin–Helmholtz instability follows from (5.13) immediately, and corresponds to the appearance of an imaginary part in frequency, i.e., when the integrand in (5.13) becomes negative:

$$u > u_c^{\text{KH}} = v_A \sqrt{(1 + \eta)} \quad (5.14)$$

Thus at  $u > v_A \sqrt{(1 + \eta)}$ , mass flows directed along the flux tube cause the excitation of natural oscillations flux tube, just like a strong wind causes appearance of KH rolls at the ocean surface or along the layered clouds.

By nature the KH instability develops at a linear stage, although its threshold in hydro- and gas dynamics is supersonic. In our case, when magnetic field is involved, the threshold becomes supereffvénic.

It follows from dispersion relation (5.13) that unstable perturbations propagate upstream:  $\text{Re}(\omega/k) = u/(1 + \eta) > 0$ . Consequently, if an upstream flow of surrounding plasma “blows over” a certain length of flux tube, the kink oscillations excited here will also propagate upstream.

This instability is remarkable in that it may be considered as an important agent for exciting oscillations in the regions far from a convection zone. It is usually assumed that the excitation of oscillations of magnetic tubes requires an oscillatory motion of their point where it is shaken by an unsteady convection. Oscillations of magnetic flux tubes excited by convective motions have the frequencies of the order of the inverse timescale of the granular or supergranular motions, i.e., on the order of  $l/\tau \sim 10^{-2} - 3 \times 10^{-3} \text{ s}^{-1}$ . These low-frequency oscillations indeed cover entire solar surface and are well observed in lower atmosphere. In the upper atmosphere, however, the oscillations of filamentary structures are observed to have wide range of frequencies which is hard to explain by the involvement of the convective motions.

The KH instability, on the other hand, provides another mechanism, which does not require motions at the base of the flux tube, and not just any motions but such that the resonance conditions must hold. The KH instability may act anywhere in the solar atmosphere from photosphere to corona and solar wind. The frequencies of oscillations in this case, being totally unrelated to the timescales of convection, may be arbitrary. They are determined by the local physical parameters of a system, and may be used for diagnostic goals.

### 5.2.2 Flux Tubes and Negative-Energy Waves (NEWs)

At a flow velocity which is less than  $u_c^{\text{KH}}$ , i.e., when the system is stable with respect to classical KH instability, the system may become subject of instability

of negative-energy waves. It is important to emphasize, that the instability of NEW is *below* the hydrodynamic instability, and requires weaker, as we will see below, sub-alfvénic, flows to trigger an exchange of energy and momentum between the magnetic flux and outer motions. Besides, as discussed above, any loss of energy by NEWs leads to the growing of their amplitude. Along the usual dissipative processes, the nondissipative mechanisms of energy loss typical to flux tube per se, naturally contribute to growing of their amplitude. These are radiation of secondary waves by oscillating flux tube and the resonance damping (Rytova 1977; Ionson 1978). In later chapters we shall see the negative-energy waves in action and study various consequences of their instabilities observed throughout the solar atmosphere. Now, to understand the nature of NEWs, and find out the range of velocities for their existence let us employ the energy analysis.

Using the energy integral (5.11) and dispersion relation (5.13), we can find for traveling waves the energy density per unit length of the tube

$$W = \frac{\pi R^2}{2} \rho_e \xi_{\perp}^2 k^2 \left[ (1 + \eta) \frac{\omega^2}{k^2} + \eta v_A^2 - u^2 \right] \quad (5.15)$$

or

$$W = \frac{1}{(1 + \eta)} \pi R^2 k^2 \rho_e \xi_{\perp}^2 (w^2 \pm uw), \quad (5.16)$$

where we have introduced notation

$$w = \sqrt{\eta[v_A^2(1 + \eta) - u^2]} \quad (5.17)$$

One should keep in mind that the radicand here is *positive*, i.e., we consider the velocities  $u < v_A \sqrt{(1 + \eta)}$ , i.e., the system is stable with respect to KH instability.

For  $u > 0$ , the only wave which can have a negative energy is one that corresponds to the minus sign in dispersion relation (5.13), i.e., the wave which would propagate in the negative  $z$  direction in the absence of a flow. For this wave a lower branch of (5.16) gives

$$W = \pi R^2 k^2 \rho_e \xi_{\perp}^2 (\eta v_A^2 - u^2) \frac{w}{w + u}, \quad (5.18)$$

One can see that the energy of the wave becomes negative at

$$u > u_c^{\text{NEW}} = \sqrt{\eta} v_A \quad (5.19)$$

where the superscript “NEW” specifies that the threshold corresponds to the appearance of negative-energy waves. Comparing conditions (5.14) and (5.19), we see that the relation  $u_c^{\text{NEW}} < u_c^{\text{KH}}$  holds with a good margin, i.e., that negative-energy waves have an appreciate range of parameters where they can be generated.

Thus, in the interval of sheared flow velocities

$$u_c^{\text{NEW}} < u < u_c^{\text{KH}} \quad (5.20)$$

an instability of negative-energy waves occurs and action of any dissipative effects, or nondissipative damping result in their enhancement and thus an increase of their amplitude.

As mentioned above, a remarkable property that magnetic tubes exhibit, is that even in the absence of dissipative processes, the development and enhancement of this instability may be facilitated by the mechanism of a collisionless dissipation of kink oscillations. The most important of which are associated with two intrinsic features of flux tubes:

- (1) The resonant absorption of the oscillations in an Alfvén resonance layer, and
- (2) Loss of the energy due to the radiation of secondary waves, both acoustic or MHD. In the next section we consider several examples.

### 5.3 Basic Equations of Flux Tube Oscillations with Shear Flows

The linearized system of MHD equations in the presence of mass flow with an unperturbed velocity  $\mathbf{u}$ , is follows:

$$\rho \frac{\partial \mathbf{v}}{\partial t} + (\mathbf{u} \nabla) \mathbf{v} + (\mathbf{v} \nabla) \mathbf{u} = -\nabla \delta p + \frac{1}{4\pi} ([\nabla \times \mathbf{b}] \times \mathbf{B} + [\nabla \times \mathbf{B}] \times \mathbf{b}) \quad (5.21)$$

$$\frac{\partial \mathbf{b}}{\partial t} = \nabla \times [\mathbf{v} \times \mathbf{B}] + \nabla \times [\mathbf{u} \times \mathbf{b}] \quad (5.22)$$

$$\frac{\partial \delta \rho}{\partial t} + \text{div } \rho \mathbf{v} + \text{div } \delta \rho \mathbf{u} = 0 \quad (5.23)$$

$$\frac{\partial \delta S}{\partial t} + \mathbf{v} \nabla S + \mathbf{v} \nabla \delta S = 0 \quad (5.24)$$

where  $\mathbf{v}$ ,  $\mathbf{b}$ ,  $\delta \rho$ , and  $\delta p$  are perturbed parameters, and  $\mathbf{u} = u(0, 0, u(r))$ . All the flux tube parameters are assumed to be functions only of the radius. For the perturbations proportional to  $\exp(-i\omega t + im\phi + ikz)$  from (5.21) we have

$$\begin{aligned} -i(\omega - ku)\rho v_r &= -\frac{\partial}{\partial r} \left( \delta p + \frac{b_z B}{4\pi} \right) + ik \frac{B}{4\pi} b_r \\ -i(\omega - ku)\rho v_\phi &= \frac{1}{r} \frac{\partial}{\partial \phi} \left( \delta p + \frac{b_z B}{4\pi} \right) + ik \frac{B}{4\pi} b_\phi \\ -i(\omega - ku)\rho v_z &= -ik\delta p - \rho v_r \frac{\partial u}{\partial r} - \frac{kB}{4\pi(\omega - ku)} v_r \frac{\partial B}{\partial r} \end{aligned} \quad (5.25)$$

Equation (5.22) gives

$$\begin{aligned}
b_r &= -\frac{kB}{\omega - ku} v_r, \\
b_\phi &= -\frac{kB}{\omega - ku} v_\phi, \\
-i(\omega - ku)b_z &= -\frac{1}{r} \frac{\partial}{\partial r} r B v_r - \frac{imB}{r} v_\phi + b_r \frac{\partial u}{\partial r}
\end{aligned} \tag{5.26}$$

Note that  $\text{div } \mathbf{b} = 0$ .

Equations (5.23) and (5.24) become respectively, as follows:

$$-i(\omega - ku)\delta\rho + \frac{1}{r} \frac{\partial}{\partial r} r \rho v_r + \frac{im}{R} \rho v_\phi + ik\rho v_z = 0, \tag{5.27}$$

$$-i(\omega - ku)(\delta p - c_s^2 \delta\rho) + v_r \left( \frac{\partial p}{\partial r} - c_s^2 \frac{\partial \rho}{\partial r} \right) = 0 \tag{5.28}$$

To put system of (5.25)–(5.28) in a compact form, we express all the perturbed quantities in terms of  $v_r$ ,  $v_\phi$  and the perturbation of the total pressure,  $\delta P = \delta p + b_z B/4\pi$ . After some algebra we obtain the following system:

$$\begin{aligned}
i\delta P &= \rho \frac{\Omega^2(c_s^2 + v_A^2) - k^2 c_s^2 v_A^2}{\Omega^2 - k^2 c_s^2} \left[ \frac{1}{r} \frac{\partial}{\partial r} r v_r \frac{v_r}{\Omega} + \frac{im}{r} \frac{v_\phi}{\Omega} \right] \\
\frac{\partial \delta P}{\partial r} &= i\rho(\Omega^2 - k^2 v_A^2) \frac{v_r}{\Omega}, \\
\frac{im}{r} \delta P &= i\rho(\Omega^2 - k^2 v_A^2) \frac{v_\phi}{\Omega}
\end{aligned} \tag{5.29}$$

where

$$\Omega = \omega - ku. \tag{5.30}$$

System (5.29) describes all types of small oscillations of a magnetic tube in the presence of field aligned shear flows.

## 5.4 Dissipative Instabilities of Negative-Energy Kink Oscillations

Consider first the kink oscillations. In the long wave limit, and with assumption that the fluid is incompressible, i.e., that  $\text{div } \mathbf{v} = 0$ , we can replace the velocity by a stream function  $\psi$  (cf. Chap.3):

$$v_r = -\frac{1}{r} \frac{\partial \psi}{\partial \phi} \quad v_\phi = \frac{\partial \psi}{\partial r} \tag{5.31}$$

then, instead of the system (5.29) we have a single equation for kink oscillation in the presence of shear flow:

$$\frac{1}{r} \frac{\partial}{\partial r} \left[ \left( \rho \Omega - \frac{k^2 B^2}{4\pi \Omega} \right) r \frac{\partial \psi}{\partial r} \right] - \left( \rho \Omega - \frac{k^2 B^2}{4\pi \Omega} \right) \frac{\psi}{r^2} = 0 \quad (5.32)$$

We are assuming that  $\omega$  contains a small imaginary part  $i\nu$ , introduced in order to bypass the singular point at  $\rho \Omega = k^2 B^2 / 4\pi \Omega$  correctly. Physically, the appearance of this correction can be explained in terms of any dissipative processes present in the system, i.e., for example caused by collisions between the plasma particles. We use the model of flux tube which is homogeneous nearly throughout entire radius, except a narrow diffuse boundary layer where the plasma density and the magnetic pressure are linear functions of the radius (cf. Fig. 3.6):

$$\begin{aligned} \rho \Omega^2 &= \rho_i \omega^2 \frac{R - r + l}{l} + \rho_e \Omega^2 \frac{r - R}{l} \\ B^2(r) &= B^2 \frac{R - r + l}{l} \end{aligned} \quad (5.33)$$

where thickness of boundary layer  $l \ll R$ .

Solutions of (5.32) at constant values of the density, magnetic field, and flow velocity are Bessel functions in the flux tube interior and Hankel functions outside it. To first order in  $kR \ll 1$ , these solutions are, respectively,

$$\psi = \begin{cases} C_1 r, & r < R \\ C_2 / r, & r > R + l \end{cases} \quad (5.34)$$

To find solutions in the transition region  $R < r < R + l$  (as we did in Chap. 3, Sect. 3.8), we introduce the variable

$$x = \frac{r - R}{l}, \quad 0 < x < 1, \quad (5.35)$$

and using the smallness of parameter  $l/R$ , rewrite (5.32) in the form (which is identical to (3.118)):

$$\frac{d}{dx} (x - x_0 - i\epsilon) \frac{d\psi}{dx} - \frac{l^2}{R^2} (x - x_0 - i\epsilon) \psi = 0, \quad (5.36)$$

where small imaginary part  $i\epsilon$  comes from taking into account the dissipative properties of a system, and  $x_0$  now includes the shear flow velocity:

$$x_0 = (k^2 v_A^2 - \omega^2) \left( k^2 v_A^2 + \frac{\rho_e}{\rho_i} \Omega^2 - \omega^2 \right)^{-1} \quad (5.37)$$

Just like in Chap. 3 (Sect. 3.8) we can find a single-valued solution of (5.35) in the complex plane  $x$  with a cut along the line  $\text{Im}x = i\epsilon$  (see Fig. 3.7):

$$\psi = A + D \ln(x - x_0 - i\epsilon) \quad (5.38)$$

At the same time,  $-\infty < \text{Re}x < x_0$ . Using now continuity of  $\psi$  and  $d\psi/dx$  at both boundaries,  $r = R$  and  $r = R + l$ , we find the dispersion relation

$$\ln \frac{1 - x_0}{x_0} + \frac{R}{l} \left( \frac{1}{1 - x_0} - \frac{1}{x_0} \right) + i\pi = 0 \quad (5.39)$$

The real part of (5.39) yields

$$1 - x_0 = x_0 \quad (5.40)$$

It is easy to verify that this expression is precisely the same as the dispersion relation (5.13).

For imaginary part of the frequency (5.39) gives following expression:

$$\frac{\gamma}{\omega} = -\frac{\pi l}{4 R} \frac{\eta}{(1 + \eta)^2} \frac{(\eta u \mp w)^2}{\pm w} \quad (5.41)$$

Equations (5.40) and (5.41) solve the problem of kink oscillations of flux tube with smooth radial profile and in the presence of shear flows. One can see that for waves with a positive energy (the upper sign) the quantity  $\gamma$  corresponds to a damping rate, while for waves with a negative energy (the lower sign),  $\gamma$  becomes positive, and thus corresponds to a growth rate.

Finally, the growth rate of the instability of NEW supported by the anomalous absorption (Alfvén resonance) is as follows:

$$\frac{\gamma_{\text{res}}}{\omega} = \frac{\pi l}{4 R} \frac{\eta}{(1 + \eta)^2} \frac{\left\{ \eta u + \sqrt{\eta[v_A^2(1 + \eta) - u^2]} \right\}^2}{\sqrt{\eta[v_A^2(1 + \eta) - u^2]}} \quad (5.42)$$

Note that the anomalous absorption effect which is responsible here for the instability of negative-energy waves may also occur in the case of a homogeneous magnetic flux tube if the shear flow has the coordinate dependence. Since under real conditions of solar atmosphere both the magnetic flux tube and mass flows along them are inhomogeneous, the instability of negative energy waves may be considered as one of the most natural occurrence triggering a violent phenomena in systems with filamentary magnetic fields.



## 5.5 Radiative Instability of Flux Tube Oscillations in the Presence of Flows

In this Section we address the problem of radiative damping of flux tube oscillations in the presence of sheared mass flows. We focus here on the kink and sausage modes and find the damping rates of these modes and their energy content.

We start with the density perturbations written in the form

$$\delta\rho = \cos(m\phi) \left[ \frac{1}{2} f(r) \exp(-i\omega t + ikz) + \text{c.c.} \right] \quad (5.43)$$

The function  $f$  satisfies the equation

$$\frac{1}{r} \frac{d}{dr} \left( r \frac{df}{dr} \right) \frac{m^2}{r^2} - k^2 f + \frac{(\omega - ku)^2}{c_{se}^2} f = 0 \quad (5.44)$$

A solution to this equation corresponding to acoustic waves which propagate away from the tube is

$$f_e(r) = A H_m^{(1)}(k_{\perp} r), \quad (5.45)$$

where

$$k_{\perp} = \sqrt{\frac{(\omega - ku)^2}{c_{se}^2} - k^2} = \frac{k}{c_{se}} \sqrt{(v_{\phi} - u)^2 - c_{se}^2} \quad (5.46)$$

The radiation of secondary acoustic waves by flux tube is possible only if the radicand here is *non-negative*.

At large distances from the flux tube ( $k_{\perp} r \gg 1$ ), solution (5.45) has the asymptotic behavior

$$f = a \left( \frac{2}{\pi k_{\perp} r} \right)^{1/2} \exp \left( ik_{\perp} r - \frac{im\pi}{2} - i\frac{\pi}{4} \right). \quad (5.47)$$

For  $k_{\perp} r \gg 1$ , solution for  $\delta\rho$  (5.43) will still be a plane wave,

$$\delta\rho = \frac{1}{2} \rho_0 \cos(m\phi) \exp(-i\omega t + ikz + ik_{\perp} r) + \text{c.c.} \quad (5.48)$$

With this we can calculate the energy density of a radiated wave to obtain

$$W_{se} = \frac{\rho_e c_{se}^2}{2} \left| \frac{\delta\rho_0}{\rho_e} \right|^2 \frac{c_{se} \sqrt{k^2 + k_{\perp}^2} - ku}{c_{se} \sqrt{k^2 + k_{\perp}^2}} \cos^2 m\phi. \quad (5.49)$$

Under condition (5.67) (see below),  $W_{se}$  is negative. Using relation (5.47), we find

$$W_{se} = \frac{c_{se}}{\pi k_{\perp} r} \frac{|A|^2}{\rho_e} \frac{\chi c_{se} - ku}{\chi} \cos^2(m\phi) \quad (5.50)$$

here  $\chi = \sqrt{k^2 + k_{\perp}^2}$ .

The energy flux from a unit length of the flux tube,

$$Q = 2\pi r \langle W_{se} \rangle k_{\perp} c_{se} / \chi \quad (5.51)$$

is

$$Q = \frac{2c_{se}^2 |A|^2}{\rho_e} \frac{\chi c_{se} - ku}{\chi^2} \begin{cases} 1, & m = 0 \\ 1/2, & m = 1 \end{cases} \quad (5.52)$$

Now we need to express the coefficient  $A$  in terms of the flux tube oscillation amplitude. To do this, we shall consider the solution of (5.45) near the flux tube boundary at  $k_{\perp} r \ll 1$ . Corresponding analysis is presented in the next two sections separately for sausage and kink oscillations.

### 5.5.1 Sausage Oscillations

For sausage oscillations we have

$$f = \left( 1 + \frac{2i}{\pi} \ln \frac{C k_{\perp} r}{2} \right), \quad (5.53)$$

where  $C$  is Euler's constant. Using the system (5.21), one can see that for nonmagnetic environment, the density perturbation is related to the radial component of the displacement of the fluid,  $\xi_r$ , as follows:

$$\xi_r = \frac{c_{se}^2}{\rho_e (\omega - ku)^2} \frac{\partial \delta \rho}{\partial r}. \quad (5.54)$$

Accordingly, for the displacement of the tube boundary in the sausage oscillations of the form  $\xi_r = (1/2)\xi_0 \exp(-i\omega t + ikz) + \text{c.c.}$ , from (5.43), (5.53), and (5.54), we get

$$A = -\frac{i\pi R \rho_e (\omega - ku)^2}{2 c_{se}^2} \xi_0 \quad (5.55)$$

Finally, for sausage oscillations, the energy flux,  $Q_T$ , radiated from a unit length of the flux tube is

$$Q_T = \frac{\pi^2 \rho_e}{2} v_{\phi} (v_{\phi} - u)^2 k^3 R^2 |\xi_0|^2. \quad (5.56)$$

### 5.5.2 Kink Oscillations

Now we turn to kink oscillations. Using the expansion of the Hankel function  $H_m^{(1)}(k_{\perp}r)$  at  $k_{\perp}r \ll 1$ , we find from (5.45):

$$f \simeq -\frac{2iA}{\pi k_{\perp}r} \quad (5.57)$$

The radial component of the flux tube displacement in the kink oscillations,  $\xi_r = \cos\phi[(1/2)\xi_0 \exp(-i\omega t + ikz) + \text{c.c.}]$ , follows from (5.43), (5.54), and (5.57):

$$A = -\frac{i\pi k_{\perp}R^2 \rho_e (\omega - ku)^2}{2 c_{se}^2} \xi_0 \quad (5.58)$$

Note that for long wavelength kink oscillations  $\xi_0$  is, in fact, the amplitude of the tube axis displacement from its unperturbed position.

The energy flux,  $Q_k$ , radiated from a unit length of the flux tube performing kink oscillations, is

$$Q_k = \frac{\pi^2 \rho_e}{4} v_{\phi} (v_{\phi} - u)^2 [(v_{\phi} - u)^2 - c_{se}^2] \frac{k^5 R^4 |\xi_0|^2}{c_{se}^2} \quad (5.59)$$

Let us now find the energy of the sausage and kink oscillations for a unit length of the tube. For the kink oscillations, the result follows directly from (5.11) and acquires the following form

$$W_k = \frac{\pi R^2}{4} |\xi_0|^2 k^2 \left[ (\rho_i + \rho_e) \frac{\omega^2}{k^2} + \rho_i v_A^2 - \rho_e u^2 \right] \quad (5.60)$$

In the case of the sausage oscillations, we need to carry out some calculations. First note that for these oscillations we have

$$W_T = \left\langle \frac{\rho \delta v_{\parallel}^2}{2} + \frac{\gamma \rho}{2} \left( \frac{\delta \rho}{\rho} \right)^2 + \frac{\delta B^2}{8\pi} \right\rangle \pi R^2 \quad (5.61)$$

where the averaging is done over a wavelength. When writing this expression we have assumed that the transverse velocity of the plasma motion inside the flux tube is small compared to the velocity of a shear flow. From the equations of motion, the continuity equations, and the frozen-in condition we find the following relations inside the tube:

$$\delta v_{\parallel} = \frac{c_{si}}{\rho} \delta \rho, \quad \delta B = B \frac{\xi}{2R}, \quad \delta \rho = \frac{v_A^2}{2c_{si}^2} \frac{\xi}{R} \quad (5.62)$$

using for  $\xi$  the expression (5.54), we obtain

$$W_T = \frac{\pi |\xi_0|^2}{8} \frac{\rho_i v_A^2 (v_A^2 + c_{si}^2)}{c_{si}^2} \quad (5.63)$$

Having the expressions for the energy flux,  $Q$ , radiated from a unit length of the flux tube and the energy of flux tube oscillations  $W$ , we can directly find the instability growth rates,  $\gamma^{\text{rad}} = Q/2W$ . Indeed, for the kink oscillations we have

$$\frac{\gamma_b^{\text{rad}}}{\omega} = \frac{\pi k^2 R^2}{2} \frac{(v_\phi - u)^2 [(v_\phi - u)^2 - c_{se}^2]}{c_{se}^2 v_\phi [(1 + \eta)v_\phi - u]} \quad (5.64)$$

and for the sausage oscillations,

$$\frac{\gamma_T^{\text{rad}}}{\omega} = \frac{\pi k^2 R^2}{4} \frac{\rho_e c_T^2 (c_T - u)^2}{\rho_i v_A^4}. \quad (5.65)$$

All the quantities entering into the both expressions are directly or indirectly measurable. The obtained results, therefore allow to infer physical parameters that are not directly observable, and to develop the predictability tools.

## 5.6 Parity of Negative and Positive Energy Waves

The radiative damping of primary flux tube oscillations in the presence of shear flows may lead to strong enhancement of the oscillations. This is possible in two cases:

- (1) If the flux tube oscillations have a negative energy, and the radiated wave has a positive energy, and
- (2) If the flux tube oscillations have a positive energy, and the radiated wave has a negative energy.

The dispersion relation for plane sound waves far from the flux tube is as follows:

$$\left. \frac{\omega}{k} \right|_{\text{se}} = u \pm c_{\text{se}} \sqrt{1 + \frac{k_\perp^2}{k^2}}, \quad (5.66)$$

where  $k_\perp$  is the component of the wave vector perpendicular to the  $z$ -axis, and  $k$  is the component of the wave vector along the  $z$ -axis. The subscript *se* specifies sound waves.

It is easy to verify that the sound wave which in the absence of a flow propagates in the negative  $z$  direction may have a negative energy. This corresponds to the lower sign in dispersion relation (5.66). The condition for the flow velocity under which the energy of radiated acoustic wave becomes negative is

$$u \geq c_{\text{se}} \sqrt{1 + k_\perp^2/k^2} \quad (5.67)$$

The transverse component of the wave vector of this wave is found from the condition

$$(\omega/k)|_k = (\omega/k)|_s \quad (5.68)$$

Let us first find the conditions under which the kink oscillations with a positive energy radiate sound waves with a negative energy, i.e., the conditions under which the following relations hold:

$$\frac{1}{1+\eta}(u+w) = u - c_{se} \sqrt{1 + \frac{k_{\perp}^2}{k^2}} > 0 \quad (5.69)$$

where, as earlier,  $w = \sqrt{\eta[v_A^2(1+\eta) - u^2]}$ .

Simple calculations show that these relations can hold under following conditions:

$$v_A > c_{se}/\sqrt{\eta}, \quad u > c_{se} + \sqrt{\frac{v_A^2 - c_{se}^2}{\eta}} \quad (5.70)$$

It follows from the equilibrium condition of the unperturbed tube,  $p_i + B^2/8\pi = p_e$ , that

$$c_{se} > v_A \sqrt{\gamma\eta/2}, \quad (5.71)$$

where  $\gamma$  is the adiabatic index. Consequently, conditions (5.70) can be satisfied only if  $\gamma < 2$ , which holds very well for the most of the solar atmosphere.

The question is, can a negative-energy kink oscillation radiate a wave with a positive energy? In other words, can the condition

$$\frac{1}{1+\eta}(u-w) = u + c_{se} \sqrt{1 + \frac{k_{\perp}^2}{k^2}} \quad (5.72)$$

be satisfied? the answer is negative: this condition cannot be satisfied since it reduces to the equation

$$-w = \eta u + (1+\eta)c_{se} \sqrt{1 + \frac{k_{\perp}^2}{k^2}} \quad (5.73)$$

whose left side is negative, and right side is positive. Thus, we may conclude that the kink oscillations with a positive energy traveling “downstream” will become unstable due to the radiation of secondary acoustic waves with a negative energy. The growth rate of this instability is given by (5.64). We have to bear in mind, of course that the primary condition for this instability is that the shear flow velocity must be in the interval given by conditions (5.70).

The mechanism of the negative energy instability associated with the radiative damping operates for sausage oscillations as well. Although a flow has essentially no effect on the axisymmetric oscillations, and their energy remains positive even in

the presence a flow, the NEW instability may develop due to the radiation of negative-energy waves. The sound waves having negative energy are those which propagate against the flow in the coordinate system of the fluid; their energy becomes negative under condition (5.67), i.e., if they are traveling downstream in the laboratory system. Now, taking into account the phase matching condition we obtain an instability condition; cf. (5.69):

$$c_T = u - c_{se} \sqrt{1 + k_{\perp}^2/k^2} > 0 \quad (5.74)$$

This condition can hold if

$$u > c_T + c_{se} \quad (5.75)$$

A slow wave propagating downstream may thus be unstable with respect to radiation of negative-energy waves. The growth rate of this instability is given by (5.65).

## 5.7 Explosive Instability of Negative-Energy Waves

A specific nonlinear instability, an explosive instability, occurs in a system which contains waves with energies of different signs. This instability was first studied by Dikasov et al. (1965) in the particular case of waves with random phases. Coppi et al. (1969) described the explosive instability for a “triplet” of coherent positive and negative-energy waves, and introduced the term “explosive instability.” A distinctive feature of an explosive instability is that the amplitudes of *all* the interacting waves reach infinitely large values in a finite time. This statement is of course formal, because at large enough, but finite amplitudes higher order nonlinear processes turn on and limit the growth of the amplitude to a certain level. A very good account of the negative-energy waves and associated explosive instability is given in the book by Weiland and Wilhelmsson (1977).

Analyzing nonlinear processes, in particular, three-wave processes, it is convenient to assume that the sign of the frequency corresponds to the sign of the energy. When this approach is taken, the condition for the explosive instability of a three-wave process can be written as follows:

$$\begin{aligned} \omega_1 + \omega_2 + \omega_3 &= 0 \\ k_1 + k_2 + k_3 &= 0 \\ |m_1| \pm |m_2| \pm |m_3| &= 0 \end{aligned} \quad (5.76)$$

where the indices 1, 2, 3, mark the three interacting waves. Since we are considering oscillations with  $m = 0, \pm 1$ , it follows from the last relation in (5.76) that either all three waves are axisymmetric,  $m = 0$ , or two of them have  $m = \pm 1$ , and the third  $m = 0$ .

In case of flux tube oscillations, conditions (5.76) indeed hold, providing thus development of explosive instability. We may consider, for example, the interaction

of one sausage mode ( $m = 0$ ) and two kink modes ( $m = \pm 1$ ). Condition (5.76) in this case reduce to the following:

$$\omega_T + \omega_{k+} + \omega_{k-} = 0, \quad k_T + k_{k+} + k_{k-} = 0 \quad (5.77)$$

The  $k+$  and  $k-$  subscripts correspond to waves traveling downstream and upstream respectively.

It is simple to verify that conditions (5.77) are compatible if  $k_T > 0$ , and if the following inequality holds:

$$u > \frac{c_T}{1 + \eta} + \sqrt{v_A^2 \eta - c_T^2 \frac{\eta(\eta^2 + 3\eta + 3)}{1 + \eta^2}}, \quad (5.78)$$

which is exactly the condition for an explosive instability.

It is important to emphasize that condition (5.78) is quite powerful: even if only a single wave, e.g., a sausage wave with  $k_T > 0$ , has been excited in the system, and the amplitudes of the two other waves are on the level of thermal noise, then the amplitudes of these two waves will grow exponentially reaching finally the explosive phase. From dimensionality considerations it is clear that the typical growth rate is on the order of magnitude  $k_T c_T$ . After a time of several inverse growth rates, at which the amplitudes of all three waves become comparable, the amplitudes begin a power-law growth in accordance with (Dikasov et al. 1965; Coppi et al. 1969):

$$v_T \sim \frac{1}{t_0 - t} \quad (5.79)$$

where  $t_0$  is the time of the “explosion.” In our case,  $t_0 \simeq (k_T, v_T)^{-1}$ . In later chapters we consider the practical use and observational evidences of the explosive instability in flux tubes.

## 5.8 Subcritical Mass Flows—Absence of Instabilities

In this section we shall consider the effects of *subcritical mass flows* when a system is stable with respect to both, the KH and NEW instabilities. In particular, we will study the influence of mass flows on the propagation of shear Alfvén waves.

We will see that even in a simple case of regular mass flows directed along the magnetic field, their presence considerably modifies the dissipation of shear Alfvén waves, affecting both the magnitude and the height of maximum dissipation. The strongest effect occurs in the case of downflows when the flow velocity at a certain height becomes equal to the Alfvén velocity. Near that point the wave comes to extinction and gives off its energy completely. This effect can be directly associated

with observed high-velocity downflows in the transition region, and, in particular, can serve as a qualitative explanation for the high variability of the emission observed around  $10^5$  K. In the presence of upward mass flows and moderate downflows, the dissipation of Alfvén waves is accompanied by the radial redistribution of the energy input across the magnetic structure thus creating a mosaic pattern in the emitting regions that are also well observed. Note again, that the flow velocities are assumed to be below the thresholds which correspond to the onset of hydrodynamic and dissipative instabilities.

### 5.8.1 Can the Alfvén Waves Heat the Corona?

The specific mechanism of the dissipation of the Alfvén waves is an important agent in the problem of the energy transfer and release in the solar atmosphere. One of the major mechanisms by which Alfvén waves may heat the plasma is their dissipation due to the phase mixing effect (Heyvaerts and Priest 1983). The origin of this effect, as discussed earlier, is associated with the strong distortion of the wave front which occurs at the propagation of Alfvén waves upward in the solar atmosphere (see Sect. 4.2). The absorption of the wave reaches a maximum at the height where the dissipation time becomes comparable to the propagation time ( $z/v_A$ ). The estimate for this characteristic damping length is:

$$z_{\max} \sim L_d \sim \frac{v_A}{\omega} \left( \frac{R^2 \omega}{\nu} \right)^{1/3} \quad (5.80)$$

where  $\nu$  is the kinematic viscosity coefficient. In the higher layers of the solar atmosphere where the plasma is typically collisionless, the Reynolds number  $Re = (R^2 \omega)/\nu$  is very large,  $\sim 10^{10}$ . Therefore, the damping length, (5.80), greatly exceeds the typical length of magnetic structures in the solar atmosphere. Parker (1991) gave a detailed analysis of difficulties connected with the efficiency of phase mixing effect, which under solar conditions, occurs far beyond the corona. And the search began for the effects that would make the phase mixing process to work at reasonable (e.g., coronal) heights.

Important advances were obtained by Similon and Sudan (1989) who treated the propagation of Alfvén waves in a three-dimensional geometry propagating in a complex magnetic field made up of stochastic field lines: the irregular motions at the footpoints of an inhomogeneous magnetic structure and the stochastization of the magnetic field lines lead to shortening of the damping length down to  $L_d \sim \ln Re$ .

Still too high. There are various models based on different physical factors, such as plasma turbulence, relaxation effects, and others, which can affect the efficiency of heating by the Alfvén waves and especially its location (Hood et al. 1997; De Moortel et al. 2000; Voitenko and Goossens 2000; Rogava et al. 2000; Walsh and Ireland 2003).



### 5.8.2 *Effect of Mass Flows on the Efficiency of Heating by Alfvén Waves*

We consider one more aspect, namely, the influence of background mass flows on the propagation of the Alfvén waves and their possible influence on the phase mixing effect. We shall see that the presence of shear flows not only reduces height of energy release but leads to important topological effects that are observable.

To visualize these effects we assume that Alfvén waves excited by convective motions are subject to slow dissipation. That is, for oscillations with initially smooth radial profile over a scale on the order of flux tube radius  $R$ , the frequency

$$\omega \gg \nu/R^2 \quad (5.81)$$

In this case for pure cylindrical geometry with  $z$ -axis directed along the magnetic field, the oscillations with velocity

$$v = v_0 \cos \frac{\omega z}{v_A(r)} \quad (5.82)$$

will propagate almost without damping up to the heights  $z_*$  where the inverse damping rate  $\Delta r^2(z)/\nu$  becomes equal to the propagation time  $z/v_A(r)$ :

$$\Delta r^2(z)/\nu \simeq z/v_A \quad (5.83)$$

Here  $\Delta r$  is the scale length of the perturbation at a height  $z$  estimated as

$$\Delta r(z) \sim \frac{v_A(r)}{|dv_A/dr|} \frac{v_A(r)}{\omega z} \quad (5.84)$$

If  $R$  is the characteristic radius of the magnetic structure, then

$$\frac{v_A(r)}{|dv_A/dr|} \sim R, \quad (5.85)$$

and at a height of a few wavelengths ( $z \gg \frac{v_A}{\omega}$ ), the scale length,  $\Delta r$ , becomes smaller and smaller:

$$\Delta r(z) \sim R \frac{v_A}{\omega z} \ll R \quad (5.86)$$

Note that relationships (5.83) and (5.86) give straightforward the estimate (5.80).

At a small scale ( $\sim \Delta r$ ) the dissipative effects turn on and ultimately result in the strong damping of a wave at a certain altitude. The dissipative terms link the perturbations at the field lines separated by a distance not exceeding a generalized skin depth

$$\delta = \sqrt{\nu_* \frac{z}{v_A}} \quad (5.87)$$

where

$$\nu_* = \frac{\eta}{\rho} + \nu_m \quad (5.88)$$

At the height  $z_{\max}$  where the main dissipation occurs (cf. (5.80)), the skin depth is given by

$$\delta = R \frac{1}{Re^{1/3}} \ll R \quad (5.89)$$

This means that considering the wave propagation and dissipation at a certain magnetic surface, we need to know the coefficients of the equation of motion only in the vicinity of this surface. In other words, after the formation of narrow spikes, the analysis becomes local (across the magnetic field), and it can be applied essentially to any field and velocity profile. In the case of an arbitrary magnetic field geometry, the velocity perturbation in the Alfvén wave is

$$\mathbf{v}(\ell, \mathbf{r}) = \mathbf{v}(\ell) e^{iS(\mathbf{r})} \quad (5.90)$$

where  $S(\mathbf{r})$  is an eikonal:

$$S(\mathbf{r}) = \int_{L_0}^L \frac{\omega}{v_A(\mathbf{r}) + u(\mathbf{r})} d\ell \quad (5.91)$$

The integration is carried out along the ray trajectory from the flux tube footpoint.

The dependence of the velocity  $\mathbf{v}$  on the coordinates transverse to the magnetic field  $\mathbf{B}$  as in geometrical acoustics is determined by the gradient of the eikonal across the magnetic structure

$$\mathbf{v}(\ell, \mathbf{r}) = \tilde{\mathbf{v}}(\ell) e^{i\boldsymbol{\tau} \nabla_{\perp} S} \quad (5.92)$$

where  $\boldsymbol{\tau}$  is a two-dimensional vector in the plane perpendicular to  $\mathbf{B}$ .

The dissipation per unit volume is

$$q \simeq \frac{1}{2} \rho \nu_* (\nabla_{\perp} S)^2 \tilde{\mathbf{v}}^2(\ell) \quad (5.93)$$

where the dependence of  $\tilde{\mathbf{v}}(\ell)$  on the coordinate  $\ell$  along the ray trajectory is determined by the conservation of the energy flux

$$B \frac{d}{d\ell} \left( \frac{\rho \tilde{\mathbf{v}}^2}{2} \frac{1}{B} (v_A + u) \right) = -\frac{1}{2} \rho \nu_* (\nabla_{\perp} S)^2 \tilde{\mathbf{v}}^2(\ell) \quad (5.94)$$

Here  $B$  is the absolute value of the magnetic field and the operator

$$B \frac{d}{d\ell} \left( \frac{1}{B} \dots \right)$$

in the left-hand side of (5.94) takes into account the change of the cross section of the magnetic flux.

For a given magnetic field  $\mathbf{B}(\mathbf{r})$  (5.94) solves the problem of the wave dissipation and yields the dissipation rate at any point in the magnetic structure.

Let us define the expression in brackets in the left-hand side of (5.94) as a function  $f(\ell)$ :

$$f(\ell) = \frac{v_A + u}{B(\ell)} \frac{\rho \tilde{v}^2}{2} \quad (5.95)$$

With this function, (5.94) can be rearranged as follows:

$$\frac{df}{d\ell} = -\nu_* \frac{(\nabla_{\perp} S)^2}{v_A + u} f(\ell) \quad (5.96)$$

The integration of this equation is straightforward and yields:

$$f = f_0 e^{-\int \nu_* [(\nabla_{\perp} S)^2 / (v_A + u)] d\ell} \quad (5.97)$$

The dissipation rate, (5.17), is then

$$q \simeq \nu_* (\nabla_{\perp} S)^2 \frac{B}{v_A + u} f_0 \exp \left( - \int \nu_* \frac{(\nabla_{\perp} S)^2}{v_A + u} d\ell \right) \quad (5.98)$$

This expression describes the propagation of an Alfvén wave in an arbitrary magnetic field and flow velocity directed along the same ray trajectory.

In the next section we derive the maximum energy release and the characteristic damping length for some chosen geometry of the magnetic field and aligned mass flow.

## 5.9 Phase Mixed Alfvén Waves at Sub-alfvénic Mass Flows

### 5.9.1 Damping Rate and Height of Energy Release

Let us consider the two-dimensional magnetic field  $\mathbf{B} = \mathbf{B}(0, B_{\phi}, B_z)$  with  $B_{\phi} = B_{\phi}(r)$  and  $B_z = B_0 = \text{const.}$  We will assume that the plasma flow is directed

along the magnetic field. Consequently, the phase velocity  $\mathbf{v}_{\text{ph}} = \mathbf{v}_A + \mathbf{u}$  will be  $\mathbf{v}_{\text{ph}} = \mathbf{v}_{\text{ph}}(0, v_{\text{ph}\phi}(r), v_{\text{ph}z})$ . The eikonal (5.91), can be written as

$$S(\mathbf{r}) = \int^L \frac{\omega}{\sqrt{v_{\text{ph}\phi}^2 + v_{\text{ph}z}^2}} d\ell \quad (5.99)$$

For the chosen geometry

$$d\ell = \sqrt{r^2 d\phi^2 + dz^2} \quad (5.100)$$

and

$$\frac{v_{\text{ph}\phi}}{v_{\text{ph}z}} = \frac{B_\phi}{B_z} \quad (5.101)$$

$$\frac{dz}{B_z} = \frac{r d\phi}{B_\phi(r)} \quad (5.102)$$

With the help of relationships (5.101) and (5.102) we can rearrange the expressions for the arc element (5.100), and phase velocity as follows:

$$d\ell = \sqrt{1 + \frac{B_\phi^2}{B_z^2}} dz \quad (5.103)$$

$$|\mathbf{v}| = \sqrt{v_{\text{ph}\phi}^2 + v_{\text{ph}z}^2} = v_{\text{ph}z} \sqrt{1 + \frac{B_\phi^2}{B_z^2}} \quad (5.104)$$

Substituting (5.103) and (5.104) into (5.99) yields

$$S(\mathbf{r}) = \int^z \frac{\omega}{v_{\text{ph}z}(\mathbf{r})} dz \quad (5.105)$$

For the transverse gradient of the eikonal, we have then

$$\nabla_\perp S(\mathbf{r}) = \frac{\partial}{\partial \mathbf{r}} \int^z \frac{\omega}{v_{\text{ph}z}(\mathbf{r})} dz = -\frac{v'_{\text{ph}z}(\mathbf{r})\omega}{v_{\text{ph}z}^2(\mathbf{r})} z. \quad (5.106)$$

With this expression, the dissipation rate (5.98) becomes as follows:

$$q = \nu_* \frac{\rho |v_0|^2}{2} \frac{\omega^2 v_{\text{ph}}^2}{v_{\text{ph}}^4} z^2 \exp\left(-\frac{2}{3} \nu_* \frac{\omega^2 v_{\text{ph}}^2}{v_{\text{ph}}^5} z^3\right) \quad (5.107)$$

We took into account here the relationships (5.101) and (5.102) and integrated the exponent over  $z$ . For convenience, we dropped the index “ $z$ ” of the phase velocity and will keep in mind below that  $v_{\text{ph}}$  is the  $z$ -component of  $\mathbf{v}_{\text{ph}} = \mathbf{v}_A + \mathbf{u}$ .

The function  $f(\zeta) = \zeta^2 e^{-(2/3)\zeta^3}$  has a maximum at  $\zeta = 1$  which from (5.107) gives a height where the maximum absorption of Alfvén waves occurs:

$$z_{\text{max}}(r_0) = \frac{v_{A0} + u_0}{\omega} \left[ \frac{\omega(v_{A0}^2 + u_0^2)}{\nu_*(v'_{A0} + u'_0)^2} \right]^{1/3} \quad (5.108)$$

Here  $r_0$  is the radius of some arbitrary magnetic surface. The subscript “0” introduced in (5.108) reflects the fact that the height of the maximum energy input depends on the radius of the magnetic surface. Thus, for the particular magnetic surface the maximum damping rate is

$$q_m = \nu_* \frac{\rho |v_0|^2}{2} \left[ \frac{[v'_A(r_0) + u'(r_0)]\omega}{\nu_* [v_A(r_0) + u(r_0)]} \right]^{2/3} e^{-2/3} \quad (5.109)$$

### 5.9.2 Observable Morphological Effects

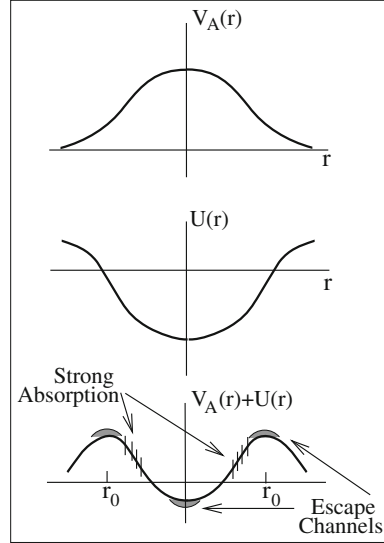
The presence of mass flows considerably modifies the picture of the energy release contributed by Alfvén waves. First of all, since the profiles of the Alfvén velocity and flow speed are different functions of radius, the phase velocity  $v_A(r) + u(r)$  can have more than one extremum across the magnetic structure. Obviously, the maximum heating occurs at those radii where the gradients of the Alfvén velocity and plasma flows are strongest. The height of maximum absorption, given by (5.108), can be quite adequate for those regions of the atmosphere where observational evidence for an extreme fine structure is found (see, e.g., Kjeldseth-Moe et al. 1994, p. 89).

According to observations, multiple velocities in the transition region are the result of the simultaneous existence of distinctly different velocities associated with separate magnetic filaments with individual sizes of 4–40 km. Taking the magnetic field as 10 G, the temperature as  $10^5$  K, and the scale of the magnetic filament and mass flow as  $R_1 = 10$  km and  $R_2 = 40$  km (see, e.g., Dere 1994; Kjeldseth-Moe et al. 1994), we can estimate the height (5.108). For this choice of parameters, the combined kinetic coefficient is  $\nu_* \simeq 2.1 \cdot 10^{10} \text{ cm}^2 \text{ s}^{-1}$ , and the estimate for the height of maximum dissipation is 6,300 km for the thinner filaments, and 16,000 km for the filaments with a 40 km radius. Using the observational data one can calculate the contribution of shear Alfvén waves in patchy brightenings.

One more morphological effect caused by the presence of mass flows, which can be observed, is appearance of an *escape channels* across the magnetic structure carrying energy into upper layers of atmosphere. Indeed, at those radii where

$$v'_A(r_0) + u'(r_0) \Rightarrow 0 \quad (5.110)$$

**Fig. 5.2** Schematic example of slightly different magnetic field and flow profiles. The extrema of the phase velocity correspond to the energy escape channels, and the regions of steepest gradients are those where the strongest energy absorption occurs

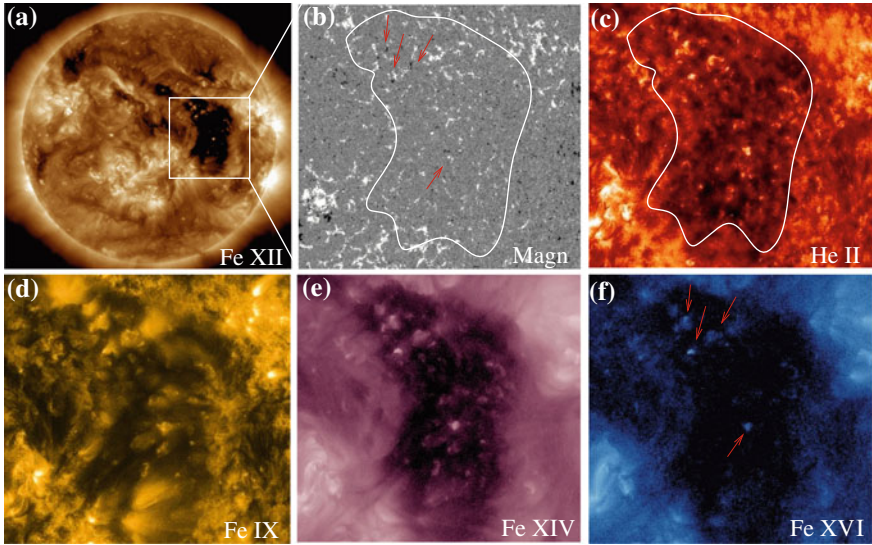


the damping of the Alfvén waves becomes negligibly small and the wave energy is carried out along these radii to higher altitudes. Thereby, along the magnetic structure, these radii form the escape channels for the energy of Alfvén waves (Fig. 5.2).

Habbal et al. (1990) comparing the morphological structure and temporal behavior of the emission from coronal bright points in a coronal hole and a quiet sun region, found that the peaks of emission in the six different wavelengths from the chromosphere to corona, are not always co-spatial, implying that bright points, consist of a bunch of small-scale loops of different temperatures.

It is important to note that the patchy brightenings associated with magnetic structures may be observed in a wide range of spatial and timescales. For example, the energy escape channels may be associated with the ensembles of unipolar magnetic flux tubes typical to the photosphere underlying the coronal holes (Harvey and Sheeley 1979; Tian et al. 2008). The energy transfer via *unipolar* flux tubes most probably is associated with the Alfvén waves, and being the subject of ever present mass flows, will exhibit the effect described above. In other words, the energy carried by flux tubes, depending on their parameters and associated mass flows may be deposited at different heights and at different temperatures, determined by the realization of escape channels. This may be illustrated by Fig. 5.3. The first panel here shows a snapshot of the sun in Fe XII 193 Å line at  $1.26 \times 10^6$  K with a huge coronal hole region outlined by the white box. The subsequent snapshots show the coronal hole region at increasing temperatures, starting with magnetogram (Fig. 5.3b).

One can see that the chromospheric bright points (Fig. 5.3c) closely mimic the ensemble of magnetic flux tubes, i.e., almost every flux tubes “delivers” the energy at  $5 \times 10^4$  K. Higher in the atmosphere, at  $6.3 \times 10^5$  K (Fig. 5.3d) there are noticeably less number of bright points, although they still fill the region quite densely. At



**Fig. 5.3** Image of coronal hole taken on May 31, 2013 with the AIA and HMI instruments on the SDO. **a** A whole disk image in Fe XII line at  $1.3 \times 10^6$  K with well-defined coronal hole; an area in *white box* containing coronal hole is shown in subsequent images; **b** the magnetogram under the coronal hole is dominated by a rarefied ensemble of mostly unipolar flux tubes; *white curve* is an approximate border of coronal hole, *red arrows* show some of the most prominent opposite polarity inclusions; **c–f** coronal hole at the increasing temperatures,  $5 \times 10^4$  K (He II),  $6.3 \times 10^5$  K (Fe IX),  $2 \times 10^6$  K (Fe XIV),  $2.5 \times 10^6$  K (Fe XVI). *Red arrows* on the Fe XVI image show the only surviving bright points inside the coronal hole at highest temperatures shown here

million degree temperatures (Fig. 5.3e) we see significantly less bright points, which actually disappear at  $2.5 \times 10^6$  K (Fig. 5.3f). At this temperature there are only a few survivors (marked by red arrows). These bright points have different origin: as seen on the magnetogram they are associated with the opposite polarity flux tubes, and the energy transfer here is associated with interaction between the opposite polarity flux tubes through the reconnection and post-reconnection processes. This subject will be discussed in detail in Chaps. 12–14.

The next important question associated with effect of mass flows is that of the asymptotic behavior of the total power flux in the phase mixed wave and its distribution across the magnetic structure. We proceed to this problem in the next section. This effect as well can be observed and measured.

## 5.10 The Asymptotic Behavior of the Total Energy Flux

The total energy flux  $\mathcal{P}$  in the wave, integrated over the cross section of the magnetic structure in the absence of a background plasma flow is

$$\mathcal{P} = \frac{\pi}{2} \int \rho |v|^2 v_A r dr \quad (5.111)$$

From the expression for the damping rate, (5.109), it is clear that the slowest damping occurs near the axis of the flux tube where for a monotonic dependence of  $B(r)$  and  $\rho(r)$  on  $r$ , the derivative of the Alfvén speed tends to zero. Near the axis the derivative of the Alfvén speed can be represented by

$$v'_A \simeq v''_A(0) r, \quad (5.112)$$

where by the order of magnitude

$$v_A''(0) \simeq \frac{v_A}{R^2} \quad (5.113)$$

From (5.92) and (5.106) in the absence of mass flows we have for  $|v|^2$

$$|v|^2 = |v_0|^2 \exp \left[ -\frac{1}{3} \frac{\omega^2 \nu_* (v''_A)^2 r^2}{v_A^5} z^3 \right] \quad (5.114)$$

Since  $v$  is a function of radius,  $v = \Omega r$ , we should take into account that

$$v_0 = \Omega(0)r \quad (5.115)$$

Substituting (5.114) and (5.115) into (5.111), we find that asymptotically, at a height  $z \gg (v_A/\omega)(1/Re^{1/3})$  the total power flux has a power-law dependence on  $z$ :

$$\mathcal{P} = \pi \rho(0) v_A(0) \Omega^2(0) \int_0^\infty \exp \left[ -\frac{2}{3} \frac{\omega^2 \nu_* (v''_A)^2 z^3 r^2}{v_A^5} \right] r^3 dr \quad (5.116)$$

Indeed, the integration gives

$$\mathcal{P} = \frac{1}{2} \pi \rho(0) v_A(0) \Omega^2(0) \left( \frac{3v_A^5}{2\omega^3 \nu_* (v''_A)^2} \right)^2 \frac{1}{z^6} \quad (5.117)$$

or

$$\mathcal{P} = \pi \rho(0) v_A(0) \Omega^2(0) R^4 \left( \frac{z_{\max}}{z} \right)^6 \quad (5.118)$$

This energy flux is produced within the central part of a magnetic structure limited by the radius

$$R_* \simeq R \left( \frac{z_{\max}}{z} \right)^{3/2} \quad (5.119)$$



The situation changes when the background plasma flows are taken into account. In this case, the maximum and/or minimum energy input is redistributed across the magnetic structure and the location of the corresponding regions is determined by those radii where the sum,  $v_A(r) + u(r)$ , has an extremum. With different profiles of Alfvén speed and flow velocity, as observed, there might be several points where this sum has an extremum. Therefore, the picture of a heated area across the magnetic field, as already discussed, should have quite a patchy and mosaic form. For example, in the simplest case when there is only one point, say,  $r = r_0$ , instead of (5.112) we will have

$$v_A' + u' \simeq (v_A'' + u'')(r - r_0) \quad (5.120)$$

Respectively, the total power flux is

$$\begin{aligned} \mathcal{P} \simeq & \pi \rho(0) [v_A(r_0) + u(r_0)] \Omega^2(r_0) r_0^3 \\ & \times \int_0^\infty \exp \left[ -\frac{1}{3} \frac{\omega^2 (v_A'' + u'')(r - r_0)^2 \nu_*}{v_A^5} z^3 \right] dr \end{aligned} \quad (5.121)$$

this gives the following law for the  $z$ -dependence of the total power flux:

$$\mathcal{P} \sim \left( \frac{z_{\max}}{z} \right)^{3/2} \quad (5.122)$$

while in the absence of plasma flows the  $z$ -dependence of the total power flux, (5.118) is proportional to  $(z_{\max}/z)^6$ . Therefore, the presence of plasma flows significantly changes the distribution of energy input with height. First of all, the total energy input occurs at much lower altitudes in the presence of flows than without them. Second, the energy release and its manifestation must have a patchy character. This result seems quite natural and can be easily understood: in the absence of plasma flows the energy flux is concentrated near the center of the magnetic structure, now it is redistributed across the magnetic field, and occurs in some annular channel with a width which has a height dependence of the form:

$$|r - r_0| \sim r_0 \left( \frac{z_{\max}}{z} \right)^{3/2} \quad (5.123)$$

From observational point of view this effect seems to be ubiquitous.

## 5.11 The Wave Extinction in the Presence of Downflows

In the case of downflows, if at some point the flow velocity becomes equal to the Alfvén speed, the phase velocity (the denominator in (5.98)) becomes zero and the damping becomes infinite. The physical reason for this effect is quite simple: when the

flow speed becomes comparable to Alfvén speed, the wave flux undergoes stagnation (in the laboratory frame), dissipating all its energy as it approaches the stagnation point. As both Alfvén and flow velocities have some radial profiles, the stagnation occurs at a height which depends on radius. This fact gives rise to a peculiar spatial distribution of the dissipated power which must be observable.

Let us consider a flux tube in which the flow is directed toward the surface of the Sun. Denote the cross section of the flux tube by  $A$ . Then from the magnetic flux conservation  $BA = \text{const.}$  and the mass conservation  $\rho u A = \text{const.}$  we find that the Alfvén velocity scales as

$$v_A \sim \frac{B}{\sqrt{\rho}} \quad (5.124)$$

or

$$\frac{v_A}{u} = \text{const.} \sqrt{\rho} \quad (5.125)$$

We see that the ratio of the Alfvén velocity and flow speed,  $v_A/u$ , decreases with height as the density decreases (Fig. 5.4). Thus simple consideration shows that the condition  $v_A \simeq u$  can most easily be met at higher altitudes in the chromosphere and corona.

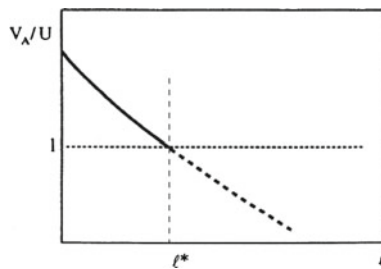
Near the point  $v_A(r) = u(r)$  where the phase velocity of the wave  $\mathbf{v}_{\text{ph}} = \mathbf{v}_A + \mathbf{u}$  becomes zero, the wave comes to extinction, and Alfvén waves propagating upward will release all their energy.

Near the point  $v_A = u$  at the axis of the magnetic structure, we have

$$v_{\text{ph}}(r, l) = \frac{\partial v_{\text{ph}}}{\partial l} (l - l_0) + \frac{1}{2} \frac{\partial^2 v_{\text{ph}}}{\partial r^2} r^2 \quad (5.126)$$

As earlier, we consider an example of a simple profile for the Alfvén velocity and the mass flow and assume that they have an extremum at the center of a magnetic flux tube. Let us introduce the notations

$$\Omega_l = \frac{\partial v_{\text{ph}}}{\partial l}, \quad (5.127)$$



**Fig. 5.4** Possible behavior of the ratio of the Alfvén and flow speeds with height

$$\Omega_r = R \frac{\partial^2 v_{\text{ph}}}{\partial r^2} \quad (5.128)$$

For a given field line (at a distance  $r$  from axis) the condition  $v_{\text{ph}} = 0$  holds at the height

$$l^*(r) = l_0 - \frac{\Omega_r}{\Omega_l} \frac{r^2}{2R} \quad (5.129)$$

When approaching the point  $l^*$ , the eikonal diverges logarithmically; therefore, it depends weakly on the lower integration limit  $l_0$ . Substituting the expansion (5.126) into the expression (5.91) and retaining only the first term in this expansion yields

$$S(l) = \int_{l_0}^l \frac{\omega dl}{\Omega_l |l - l^*|} = \frac{\omega}{\Omega_l} \ln \left| \frac{l - l^*}{l} \right| \quad (5.130)$$

The radial derivative of the eikonal is then

$$\frac{\partial S}{\partial r} = \frac{\omega}{\Omega_l |l - l^*|} \frac{\partial l^*}{\partial r} \quad (5.131)$$

Using now expression (5.129) we have

$$\frac{\partial S}{\partial r} = -\frac{\omega^2}{\Omega_l} \frac{r \Omega_r}{R |l - l^*|} \quad (5.132)$$

This expression allows us to find how the energy flux, or actually, the function  $f$  determined by (5.95), damps out near  $l = l^*$ . From (5.97) and (5.132) we have

$$f \propto \exp \left[ -\nu_* \frac{\omega^2 \Omega_r^2 r^2}{|\Omega_l^5| R^2} \int_{\mathcal{L}_0}^l \frac{dl}{|l - l^*|^3} \right]. \quad (5.133)$$

The integration gives

$$f \propto \exp \left[ -\nu_* \frac{\omega^2 \Omega_r^2 r^2}{2 |\Omega_l^5| R^2} \frac{1}{(l - l^*)^2} \right]. \quad (5.134)$$

We see that near the point  $l^*$  the damping is very strong: *nothing propagates beyond this point.*

Before the wave comes to extinction at the point  $l = l^*$ , the strong damping occurs at the height,  $l_d$ , which is determined by the condition (for  $r \sim R$ )

$$\nu_* \frac{\omega^2 \Omega_r^2}{|\Omega_l^5| (l^* - l_d)^2} \sim 1 \quad (5.135)$$

We took into account here that at  $r \sim R$ ,  $l^* = l_d$ ; see (5.129). Using the estimates

$$\Omega_l \sim \frac{v_A}{l^*}, \quad \Omega_r \sim \frac{v_A}{R}, \quad (5.136)$$

we have from (5.135)

$$(l^* - l_d)^2 \sim \nu_* \frac{\omega^2 l^{*5}}{R^2 v_A^3}. \quad (5.137)$$

This expression gives the distance  $\Delta = l^* - l_d$  at which the strong damping of the wave increases dramatically and ends up with the complete absorption of the wave power at the point  $l^*$ :

$$\Delta \sim l^* \left( \frac{l^*}{z_{\max}} \right)^{3/2}; \quad (5.138)$$

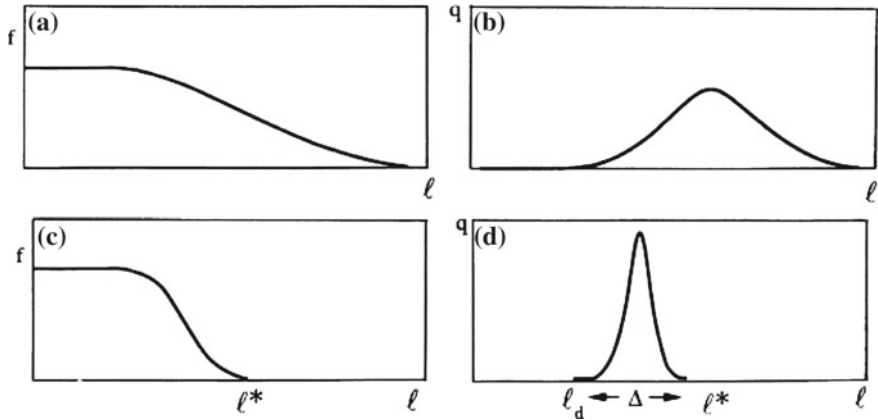
$z_{\max}$  here is the characteristic damping length of the shear Alfvén waves provided by the phase mixing effect in the absence of plasma flows (5.80). To estimate the axial extent of the total energy release, we take the parameters corresponding to the transition region, at  $10^5$  K, where the largest downflows are observed. For a magnetic field strength  $B = 4$  G, a density  $10^{10} \text{ cm}^{-3}$ ,  $R = 40$  km, an Alfvén wave period of 100 s, the characteristic damping length in the absence of flows is  $z_{\max} = 9 \times 10^4$  km. Taking the height of the transition region to be  $l^* = 10^4$  km, we get the axial extent of the absorption region to be  $\Delta = 370$  km.

In Fig. 5.5 we sketch the qualitative behavior of the amplitude and damping rate of the Alfvén wave with height. The amplitude (Fig. 5.5a) and the damping rate (Fig. 5.5b) in the absence of plasma flows are shown. In this case the amplitude of the Alfvén wave drops gradually with height until it reaches the height where the eigenfunction of perturbations becomes highly oscillatory so that the wave damps out due to the regular phase mixing effect. At this height, the amplitude drops rapidly and the damping rate has a maximum determined by (5.108) and (5.109) with  $u = 0$ .

In the presence of downflows the process of the wave damping has an entirely different character: at lower altitudes the behavior of the wave amplitude Fig. 5.5c and the damping rate Fig. 5.5d are similar to those without mass flows. At the point  $l = l_d$  the strong damping occurs and at a short distance  $\Delta = l^* - l_d$  the wave damps out completely, so that no portion of it propagates farther.

Note that the same consideration is applicable also to the other modes of flux tube oscillations, in particular kink,  $m = \pm 1$ , and sausage,  $m = 0$  oscillations.

Hence, the physical parameters of the magnetic field and plasma flows determine the morphology of a heated area: the geometrical height where the maximum heating



**Fig. 5.5** Qualitative behavior of the amplitude and the damping rate both in the absence and in the presence of downflows. In the absence of mass flows the amplitude of the Alfvén wave, **a** drops gradually with height until it reaches the height where the eigenfunction of perturbations becomes highly oscillatory so that the wave damps out due to the phase mixing effect. Near that region the damping rate, **b** has a maximum. In the presence of downflows at lower altitudes the behavior of the wave amplitude, **c** and the damping rate, **d** are similar to those without mass flows. At the point  $l = l_d$  the strong damping occurs and at a short distance of  $\Delta = l^* - l_d$  the wave damps out completely, so that no portion of it propagates farther

occurs now is not restricted by the phase mixing effect and can be much lower than  $z_{\max}$ .

## Appendix A: Equation for Alfvén Waves in the Presence of Parallel Mass Flows

In this section we derive the general equation for Alfvén waves in the presence of mass flows which can be used for solving problems other than those considered in the previous sections.

In particular, this equation will allow one to study the influence of mass flows on the resonance absorption of Alfvén waves and to explore the development of different kinds of hydrodynamic instabilities.

Consider for simplicity a magnetic field having only a  $z$ -component,  $\mathbf{B}_0(0, 0, B(r))$ . The background mass flow with the velocity  $\vec{u}(r)$  is assumed to be directed along the magnetic field. All the plasma parameters are monotonic functions of radius. The perturbation of the velocity  $\mathbf{v}(0, v_\varphi(r, z, t), 0)$  and the magnetic field  $\mathbf{b}(0, b_\varphi(r, z, t), 0)$  are axisymmetric, and we will drop the index  $\varphi$  further. The MHD equations for a given geometry which include the viscous losses have the form

$$\rho \left( \frac{\partial v}{\partial t} + u \frac{\partial v}{\partial z} \right) = \frac{B}{4\pi} \frac{\partial b}{\partial z} + \frac{1}{r^2} \frac{\partial}{\partial r} \eta r^3 \frac{\partial v}{\partial r} \quad (5.139)$$

$$\frac{\partial b}{\partial t} + u \frac{\partial b}{\partial z} = B \frac{\partial v}{\partial z} + \frac{\partial}{\partial r} \frac{1}{r} \nu_m \frac{\partial}{\partial r} r b \quad (5.140)$$

All notations are standard;  $\eta$  is ion viscosity ( $\omega_i \tau_i \gg 1$ ) and  $\nu_m$  is magnetic diffusivity. Since the dissipation is weak, we have neglected in the dissipative terms the derivatives  $\partial/\partial z$ .

Taking the derivative ( $\partial/\partial t + u\partial/\partial z$ ) of (5.139) and using (5.140) we have

$$\begin{aligned} \rho \left( \frac{\partial}{\partial t} + u \frac{\partial}{\partial z} \right)^2 v &= \frac{B}{4\pi} \frac{\partial}{\partial z} \left[ B \frac{\partial v}{\partial z} + \frac{\partial}{\partial r} \frac{1}{r} \nu_m \frac{\partial}{\partial r} r b \right] \\ &+ \left( \frac{\partial}{\partial t} + \frac{\partial}{\partial z} \right) \frac{1}{r^2} \frac{\partial}{\partial r} \eta r^3 \frac{\partial v}{\partial r} \end{aligned} \quad (5.141)$$

At weak dissipation, one can use in the second term in right-hand side of (5.141), the following expression for  $\partial b/\partial z$ :

$$\frac{B}{4\pi} \frac{\partial b}{\partial z} \simeq \rho \left( \frac{\partial v}{\partial t} + u \frac{\partial v}{\partial z} \right), \quad (5.142)$$

Now we can write a single equation for  $v$ :

$$\begin{aligned} \rho \left( \frac{\partial}{\partial t} + u \frac{\partial}{\partial z} \right)^2 v &= \frac{B^2}{4\pi} \frac{\partial^2 v}{\partial z^2} + \frac{B}{4\pi} \frac{\partial}{\partial r} \frac{1}{r} \nu_m \frac{\partial}{\partial r} r \frac{4\pi\rho}{B} \left( \frac{\partial v}{\partial t} + u \frac{\partial v}{\partial z} \right) \\ &+ \left( \frac{\partial}{\partial t} + u \frac{\partial}{\partial z} \right) \frac{1}{r^2} \frac{\partial}{\partial r} \eta r^3 \frac{\partial v}{\partial r} \end{aligned} \quad (5.143)$$

For the boundary value problem with

$$v|_{z=0} = v_0 e^{i\omega t} \quad (5.144)$$

and without the dissipation we have from (5.143); see (5.82):

$$v = v_0 \cos \frac{\omega z}{v_A(r)} \quad (5.145)$$

As discussed in Sect. 5.8, the velocity profile becomes spiky with height, and its scale (5.86), at the heights  $z \gg v_A/\omega$  becomes much less than  $R$ :

$$\Delta r \ll R \quad (5.146)$$

This condition allows us to simplify the (5.141). Namely, in the dissipative terms we can neglect the radial derivatives of all the functions except  $v$ . Note that the background plasma parameters,  $B(r)$ ,  $\rho(r)$ , and  $u(r)$  change at the scale  $R$ , and from to condition (5.146) we have

$$\frac{db}{dr}, \frac{d\rho}{dr}, \frac{du}{dr} \ll \frac{\partial v}{\partial r} \quad (5.147)$$

Furthermore,

$$\frac{\partial^2}{\partial r^2} \gg \frac{1}{r} \frac{\partial}{\partial r}, \frac{1}{r^2} \quad (5.148)$$

Under these conditions (5.143) becomes:

$$\left( \frac{\partial}{\partial t} + u \frac{\partial}{\partial z} \right)^2 v = v_A^2(r) \frac{\partial^2 v}{\partial z^2} + \nu_* \left( \frac{\partial}{\partial t} + u \frac{\partial}{\partial z} \right) \frac{\partial^2 v}{\partial r^2} \quad (5.149)$$

where  $\nu_* = \eta/\rho + \nu_m$ .

One can see, that in the absence of dissipation, different radii do not communicate with each other as is clearly seen from (5.149): The Alfvén waves along each cylindrical surface propagate with the speed determined only by the surface radius  $r$ , i.e., at a speed  $v_A(r)$ .

The dissipative term links the perturbations at the field lines separated by the distance not exceeding a generalized skin depth (5.89), which means that considering the wave propagation and dissipation at a certain magnetic surface, we need to know the coefficients of (5.149) only in the vicinity of this surface. We denote the radius of some arbitrary surface by  $r_0$ , and for

$$r = r_0 + x, \quad (5.150)$$

use the approximations

$$v_A(r) \cong v_A(r_0) + \frac{dv_A(r)}{dx} \Big|_{r_0} \quad (5.151)$$

$$u(r) \cong u(r_0) + \frac{du(r)}{dx} \Big|_{r_0} \quad (5.152)$$

$$\nu_* \cong \nu_*(r_0) \quad (5.153)$$

We drop the index “0” below, and will keep in mind that these quantities have a local meaning at a certain radius  $r_0$ .

For perturbations  $\sim \exp(-i\omega t)$ , (5.149) reduces to

$$[u^2(r) - v_A^2(r)] \frac{\partial^2 v}{\partial z^2} - 2i\omega u(r) \frac{\partial v}{\partial z} - \omega^2 v = \nu_* \frac{\partial^2}{\partial r^2} \left( -i\omega v + u(r) \frac{\partial v}{\partial z} \right) \quad (5.154)$$

It is convenient to represent the velocity perturbations in a form

$$v = w(r, z, t) \exp\left(i \frac{\omega}{v_{A0} + u_0} z\right) \quad (5.155)$$

where  $v_{A0} = v_A(r_0)$  and  $u_0 = u(r_0)$ . Simple algebra gives the following equation for  $w$  (the analogue of parabolic equation in diffraction theory):

$$\begin{aligned} \frac{\partial w}{\partial z} + i\omega \frac{v'_{A0} + u'_0}{(v_{A0} + u_0)^2} x w \\ - \nu_* \left[ \frac{1}{2(v_{A0} + u_0)} \frac{\partial^2 w}{\partial^2 x} - \frac{u'(r)}{v_{A0}(v_{A0} + u_0)} \frac{\partial w}{\partial x} - \frac{u''(r)}{2v_{A0}(v_{A0} + u_0)} w \right] = 0 \end{aligned} \quad (5.156)$$

Prime means the derivative over radius.

Equation (5.156) is the basic equation describing the Alfvén wave propagation in the presence of plasma flows. Magnetic field and plasma parameters have a smooth dependence on radius. This equation can be written in especially convenient form using a function  $Q$  which we define as follows:

$$w = Q(x, z, t) \exp\left(\frac{u'(x)}{v_{A0}} x\right), \quad (5.157)$$

and in the variables:

$$\xi = x \left[ \frac{\omega(v'_{A0} + u'_0)}{\nu_*(v_{A0} + u_0)} \right]^{1/3} \quad (5.158)$$

$$\zeta = z \frac{\omega(v'_{A0} + u'_0)}{(v_{A0} + u_0)^2} \left[ \frac{\omega(v'_{A0} + u'_0)}{\nu_*(v_{A0} + u_0)} \right]^{-1/3} \quad (5.159)$$

With (5.157)–(5.159), the basic parabolic equation (5.156) takes a form:

$$\frac{\partial Q}{\partial \zeta} + i\xi Q - \frac{\partial^2 Q}{\partial \xi^2} + \alpha(\xi) \cdot Q = 0 \quad (5.160)$$



with

$$\alpha(\xi) \sim \left[ \frac{(u')^2(\xi)}{v_{A0}^2} + \frac{u'(\xi)}{v_{A0}} \right] \quad (5.161)$$

Equation (5.160) allows one to study the various instabilities in the presence of mass flows.

It is important to note that the asymptotic behavior of the total power flux of the wave varies much more slowly with height in the presence of mass flows than without them. Namely, the total power flux  $\mathcal{P}$  in the presence of flows scales with height as  $\mathcal{P} \sim z^{(-3/2)}$ , while it scales as  $\mathcal{P} \sim z^{-6}$  in their absence.

Thus, a regular *subsonic* upward and downward mass flows modify considerably the propagation of phase mixed Alfvén waves. First of all, the radial redistribution of the energy input occurs, which is determined by the fact that the extrema of the Alfvén speed and flow velocity are not spatially coincident. In this case, the strongest absorption occurs at those radii at which the gradients of the phase velocity are steepest, while those radii at which the phase velocity has extrema form an escape channel for the wave energy. Therefore, even for moderate flow velocities (compared with the magnitude of the Alfvén speed), both upward and downward flows lead to the creation of a complex mosaic of highly localized bright regions with varying heights. These effects can be considered as a reasonable explanation for understanding the complex intermittent emission such as observed in coronal bright points (Huang et al. 2012; Alexander et al. 2011; Habbal and Withbroe 1981; Habbal et al. 1990).

Note also that the strongest effect occurs in the case of downflows: if at some geometrical height the Alfvén speed and flow velocity become equal, the wave comes to extinction and gives off its energy completely. This process is independent of the heating due to phase mixing and can occur much earlier and at lower altitudes than the onset of the latter. Near this region the absorption length  $\Delta = l^* - l_d$  along the direction of the magnetic field becomes very small. Since both the Alfvén speed  $v_A$  and flow velocity  $u$  depend on  $r$  and  $l$ , the points where  $v_A = u$  constitute a surface  $l = l(r)$  in which essentially all the wave energy is released. This effect, as mentioned earlier, should manifest itself as a complex picture of localized bright regions, as complex as the topology of the magnetic fields and plasma flows throughout the solar atmosphere.

## References

- C.E. Alexander, G. Del Zanna, R.C. Maclean, *Astron. Astrophys.* **526**, 134 (2011)  
 S. Chandrasekhar, *Hydrodynamic and Hydromagnetic Stability* (Dover Publications Inc., New York, 1961)  
 B. Coppi, M.N. Rosenbluth, R. Sudan, *Ann. Phys.* **55**, 201 (1969)  
 I. De Moortel, A.W. Hood, T.D. Arber, *Astron. Astrophys.* **354**, 334 (2000)  
 K.P. Dere, J.-D.F. Bartoe, G.E. Brueckner, *Sol. Phys.* **123**, 41 (1989)

- K.P. Dere, *Space Science Rev.* **70**, 21 (1994)
- V.M. Dikasov, L.I. Rudakov, D.D. Ryutov, *Sov. Phys. JETP* **21**, 1965 (1965)
- S.R. Habbal, G.L. Withbroe, *Sol. Phys.* **69**, 77 (1981)
- S.R. Habbal, G.L. Withbroe, J.F. Dowdy Jr, *Astrophys. J.* **352**, 333 (1990)
- S.R. Habbal, R.D. Gonzalez, *Astrophys. J.* **326**, L25 (1991)
- J.W. Harvey, N.R. Sheeley Jr, *Space Sci. Rev.* **23**, 139 (1979)
- J. Heyvaerts, E.R. Priest, *Astron. Astrophys.* **117**, 220 (1983)
- A.W. Hood, J. Ireland, E.R. Priest, *Astron. Astrophys.* **318**, 957 (1997)
- Z. Huang, M.S. Madjarska, J.G. Doyle, D.A. Lamb, *Astron. Astrophys.* **548**, 62 (2012)
- J.A. Isonson, *Astrophys. J.* **226**, 650 (1978)
- B.B. Kadomtzev, A.B. Mikhailovski, A.V. Timofeev, *Sov. Phys. JETP* **20**, 1517 (1964)
- O. Kjeldseth-Moe, N. Brynildsen, P. Brekke, P. Maltby, *Space Sci. Rev.* **70**, 89 (1994)
- L. Landau, M. Lifshitz, *Fluid Mechanics* (Pergamon Press, Oxford)
- L.A. Ostrovskii, S.A. Rybak, LSh Tsimring, *Phys. Uspekhi* **29**, 1040 (1964)
- L.A. Ostrovskii, S.A. Rybak, LSh Tsimring, *Phys. Uspekhi* **29**, 1040 (1986)
- E.N. Parker, *Astrophys. J.* **376**, 355 (1991)
- A.D. Rogava, S. Poedts, S.M. Mahajan, *Astron. Astrophys.* **354**, 749 (2000)
- M.P. Ryutova, in *Proceedings of XIII International Conference on Ionized Gases* (Berlin, 1977), p. 859
- M.P. Ryutova, *Sov. Phys. JETP* **67**(8), 1594 (1988)
- P.L. Similon, R.N. Sudan, *Astrophys. J.* **336**, 442 (1989)
- P.A. Sturrock, *Phys. Rev. Lett.* **16**, 270 (1966)
- H. Tian, W. Curdt, M. Eckart, *Astrophys. J.* **681L**, 121 (2008)
- Yu. Voitenko, M. Goossens, *Astron. Astrophys.* **357**, 1073 (2000)
- R.W. Walsh, J. Ireland, *Astron. Astrophys. Rev.* **12**, 1 (2003)
- G.L. Withbroe, D.T. Jaffe, P.V. Foukal, M.C.E. Huber, R.W. Noyes, E.M. Reeves, E.J. Schmahl, J.G. Timothy, J.E. Vernazza, *Astrophys. J.* **203**, 528 (1976)
- J. Weiland, H. Wilhelmsson, *Coherent Nonlinear Interaction of Waves in Plasmas* (Pergamon Press, Oxford, 1977)

## Chapter 6

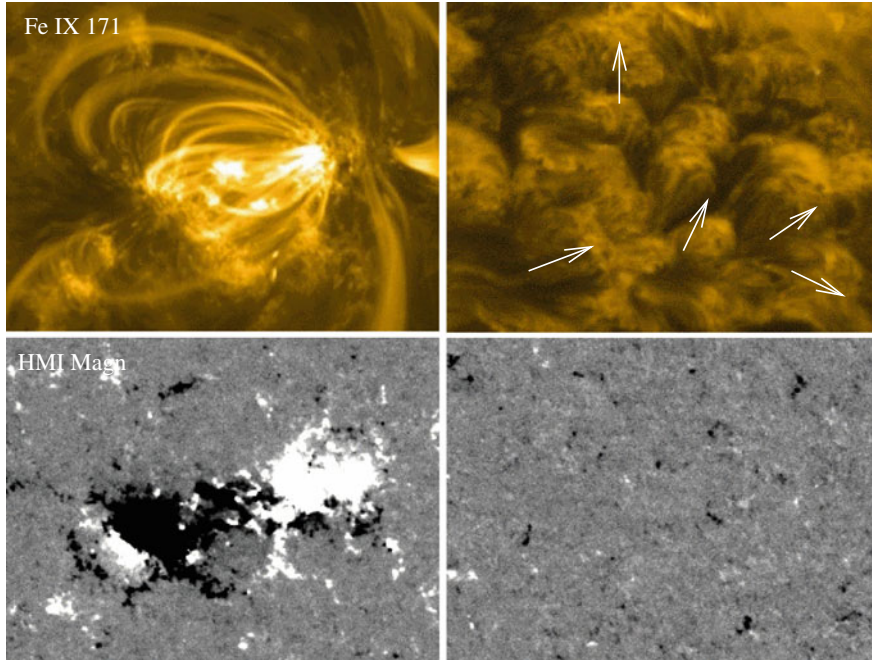
# Collective Phenomena in Rarefied Ensembles of Flux Tubes

**Abstract** In the previous chapters we have considered the properties of individual flux tubes and their dynamics due to interaction with the surrounding medium. The solar atmosphere, however, consists of ensembles of flux tubes randomly distributed in space and over their parameters. In this chapter we shall consider the time-dependent response of a randomly magnetized medium to propagation of acoustic waves and unsteady wave packets. We will see that the collective phenomena resulted from these interactions lead to clear morphological effects that are observable. The character of these effects, and the associated energy input and distribution, crucially depend on the magnetic filling factor of the medium and several other factors that will be specified.

### 6.1 Response of Flux Tubes to Propagation of Sound Waves

The response of a randomly magnetized medium to propagation of acoustic waves and unsteady wave packets strongly depends on the distribution of magnetic elements and their individual properties (Ryutova and Priest 1993a, b). Obviously, the wave packets and other motions near the surface carry a significant amount of energy, which, by various means, may be absorbed by the magnetic flux tubes and carried upward into higher layers of the atmosphere. The outcome depends not only on the properties of an individual flux tube, but strongly depends on the set of neighboring flux tubes. For illustrative purpose we show in Fig. 6.1 examples of the corona overlying two different ensembles of magnetic flux tubes. The left panels show a dense conglomerate of magnetic elements forming a small active region with magnetic filling factor of the order of unity. Hot compact loops are “customary” and overly the dense mixed polarity region. The right panels show a quiet sun region with rarefied ensemble of flux tubes with small filling factor. One can see *clouds of energy*, at the same,  $0.5 \times 10^5$  K temperature, as active region coronal loops, but spread diffusively over the ensembles of far removed flux tubes. Later in this chapter we shall see that the appearance of hot large clouds of plasma is a natural consequence of the collective phenomena in rarefied ensembles of flux tubes.

SDO 2 June 2012



**Fig. 6.1** Snapshots of two typical ensembles of magnetic elements and their overlying corona in Fe IX 171 Å line at  $6.3 \times 10^5$  K. *Left* The magnetogram of a compact active region forming well-defined hot loops; *Right* a quiet sun region magnetogram and hot cloudy corona above it. *White arrows* show an approximate direction of the propagation of clouds. Field of view of each snapshot is  $130 \times 100$  Mm

### 6.1.1 Energy Exchange Between the Acoustic Waves and Ensembles of Flux Tubes

We start with consideration of rarefied ensembles of flux tubes and their interaction with acoustic waves and unsteady wave packets. The subject of dense conglomerate will be studied in Chaps. 8 and 9.

The most important role here is played by resonant interaction, both absorption and scattering of the sound wave by flux tubes. Recall that in the case of resonant absorption the acoustic waves (of frequency  $\omega$ ) energy of the incident acoustic wave is accumulated in the system of magnetic flux tubes. The acoustic wave first damps out at a rate  $\nu_L \sim (R^2/d^2)\omega$ , and remains for a long time in the form of flux tube oscillations. Then, in a time  $\nu_{\text{rad}}^{-1}$  which is much longer than the damping time of the sound wave, the resonant flux tubes radiate their energy as secondary acoustic (or MHD) waves, where  $\nu_{\text{rad}} \sim \omega k^2 R^2$ . The incident acoustic wave can also be resonantly scattered with the main contribution coming from the kink mode; it leads to a linear frequency shift and to the appearance

of incoherent noise without a preliminary buildup of wave energy in flux tube oscillations.

When the distribution of flux tube natural frequencies is broader than  $\nu_L$  the Landau-like resonant absorption process is more important than resonant scattering, but when the distribution is narrow the tubes are almost identical and resonant scattering may dominate.

Figure 6.2 illustrates these two cases of distribution function over the flux tube parameters. Obviously, the case of broad distribution function is much more realistic than the case of almost identical flux tubes (Bogdan and Zweibel 1987). Thus, the damping of long-wavelength acoustic oscillations in the rarefied plasma ( $R \ll d$ ) with

$$\lambda = k^{-1} \gg d, \tag{6.1}$$

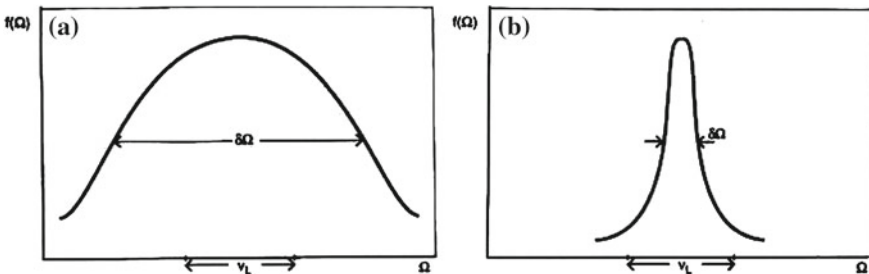
is largely determined by Landau damping (Landau 1946; Timofeev 1970; Chen and Hasegawa 1974; Ryutov and Ryutova 1976; Lontano et al. 2000).

To look into the problem in-depth we need to make nonlinear estimates, and consider the damping of monochromatic sound wave of finite amplitude. This will allow us to solve several problems. In particular, to find the maximum energy that can be transferred to the medium from the acoustic wave packets, and a frequency shift of the propagating waves, which is of measurable quantity.

Let a periodic acoustic wave be excited at the initial moment of time,  $t = 0$ , with amplitude  $\zeta_0$  and frequency  $\omega_0$ . The displacement amplitude  $\xi_\eta(t)$  of a flux tube in the field of this sound wave is described by the equation:

$$\frac{\partial \xi_\eta}{\partial t^2} + \Omega^2(\eta)\xi_\eta = A\Omega^2(\eta)\zeta_0 e^{-i\omega t} \tag{6.2}$$

where  $\Omega(\eta)$  is the eigenfrequency of flux tube oscillations and  $A$  is a numerical factor of order unity.



**Fig. 6.2** Distribution function  $f(\Omega)$  of the flux tubes as a function of their frequencies,  $\Omega$ , for **a** a broad distribution with  $\delta\Omega \gg \nu_L$ ; **b** a narrow distribution with  $\delta\Omega \ll \nu_L$  where  $\delta\Omega$  is the spread in eigenfrequencies and  $\nu_L$  is the damping rate of the acoustic wave due to Landau resonance

### 6.1.2 Near-Resonance Condition

Let us first consider the energy exchange between the acoustic wave and the flux tube in conditions close to resonance, i.e., in a region of small  $(\eta - \eta_0)$ . We assume that the frequency shift  $\Delta$  is small:

$$|\Delta| - |\omega - \Omega| \ll \omega \quad (6.3)$$

Under this condition, for those values of  $\eta$  that are sufficiently close to  $\eta_0$  the amplitude of the flux tube oscillations increases linearly in time, so that very rapidly, just in a few periods, it becomes much larger than  $\zeta_0$ , and we can neglect the initial amplitude  $\xi_0$  ( $\simeq \zeta_0$ ).

The solution of (6.2) corresponding to the initial conditions  $\xi = 0$  and  $d\xi/dt = 0$  at  $t = 0$  is

$$\xi = A\zeta_0 \left[ -\frac{\Omega e^{i\Omega t}}{2(\Omega + \omega)} - \frac{\Omega e^{-i\Omega t}}{2(\Omega - \omega)} + \frac{\Omega^2 e^{-i\omega t}}{\Omega^2 - \omega^2} \right] \quad (6.4)$$

The first term on the right has a nonresonant character and can be neglected. The last two terms can be combined, and using again the condition (6.3) we find

$$\xi \simeq \frac{A\zeta_0\omega}{2\Delta} e^{-i\omega t} (1 - e^{-i\Delta t}). \quad (6.5)$$

The energy density of flux tube oscillations which is proportional to  $|\xi|^2$  is then estimated as

$$W \simeq \frac{|1 - e^{-i\Delta t}|^2}{\Delta^2} = \frac{\sin^2(\Delta t/2)}{\Delta^2}. \quad (6.6)$$

Let us denote the distribution function of flux tubes over their eigenfrequencies  $\Omega$  by  $f(\Omega)$ . Then the total energy transfer to the flux tubes within time  $t$  is proportional to

$$I = \int f(\Omega) \frac{\sin^2(\Delta t/2)}{\Delta^2} d\Omega. \quad (6.7)$$

At a time  $t \gg 1/\omega$ , the interval of frequencies  $\Omega$  that gives a significant contribution to the integral (6.7) is of the order of  $(1/t) \ll \Omega$ . Respectively, for a broad enough distribution function  $f(\Omega)$  can be replaced by its value at  $\Omega = \omega$ :

$$I \simeq \frac{1}{2} f(\omega) t \int_{-\infty}^{\infty} \frac{\sin^2(x)}{x^2} dx = \frac{\pi}{2} f(\omega) t \quad (6.8)$$

Then the power absorbed by the flux tubes is proportional to  $|\zeta_0|^2 f(\omega)$ .

By retaining all the numerical factors one can obtain in this way the damping rate,  $\nu_L$ , of the acoustic wave due to the Landau resonance, which is given by (3.28) of

Chap. 3. Thus in order of magnitude,

$$\nu_L (\equiv \text{Im } \omega) \simeq \alpha \omega \quad (6.9)$$

Note that this estimate holds for a broad distribution function  $f(\Omega)$  with  $\Delta \sim \Omega$  (Fig. 6.2).

Equation (6.7) shows that, when the damping rate of the acoustic wave equals  $\nu_L$ , the wave is absorbed by flux tubes whose

$$|\Delta| \equiv |\omega - \Omega| \leq \nu_L \quad (6.10)$$

Within a time  $t_L = 1/\nu_L$  the energy of the acoustic wave is transferred to the resonant flux tubes. The oscillations of the flux tubes, in principle, are gradually dissipated in two ways: first, by radiative damping through the radiation of secondary acoustic or MHD waves with damping rate  $\nu_{\text{rad}} \sim (kR)^2 \Omega$  (see 3.50); and, second, by the usual dissipative effects (e.g., viscosity, thermal losses, etc.), with corresponding damping rate  $\nu_{\text{diss}}$ .

The Landau damping mechanism corresponds to the case when

$$\nu_L \gg \nu_{\text{rad}} + \nu_{\text{diss}} \quad (6.11)$$

In this case the sequence of energy transfer phenomena is as follows:

- (1) Within a time  $t_L = 1/\nu_L$  the energy of the acoustic wave is transferred to the flux tubes with eigenfrequencies in the range  $|\omega - \Omega| \sim \nu_L$ ;
- (2) Within a time of a few inverse damping rates  $|\omega - \Omega|^{-1} \sim \nu_L^{-1}$  the flux tube oscillations become phase-mixed and their oscillations become completely incoherent;
- (3) Within a time proportional to  $(\nu_{\text{rad}} + \nu_{\text{diss}})^{-1}$  the flux tube oscillations damp away due to either, or both mechanisms mentioned above, i.e., radiation and dissipative processes.

The flux tube oscillation energy is converted into heat if  $\nu_{\text{rad}} > \nu_{\text{diss}}$ , or into the energy of incoherent secondary acoustic noise if  $\nu_{\text{rad}} < \nu_{\text{diss}}$ .

It is important that if  $\nu_L \gg \nu_{\text{rad}} + \nu_{\text{diss}}$ , absorption of the acoustic wave occurs neither by resonant absorption nor by resonance scattering: the initial energy of the acoustic wave is instead stored for a long time,  $\sim (\nu_{\text{rad}} + \nu_{\text{diss}})^{-1}$ , in the form of incoherent flux tube oscillations.

## 6.2 Nonlinear Estimates of the Maximum Energy Input

Let us return to (6.2) and for definiteness rewrite it for the kink mode with eigenfrequency  $\Omega = kc_s/\sqrt{2/\gamma(1+\eta)}$

$$\frac{\partial^2 \xi_\eta}{\partial t^2} + \Omega^2(\eta) \xi_\eta = -\omega^2 \zeta_\perp e^{-I\omega t} \quad (6.12)$$

As was already mentioned, near the resonance, in a few periods, the flux tube oscillation amplitude,  $\xi$ , far exceeds the amplitude  $\zeta_{\perp}$  of the initial sound wave, and the oscillations become nonlinear. The first effect which saturates the growth of the amplitude is a nonlinear frequency shift, which we denote as  $\Delta\omega_{\text{nl}}(\xi_{\eta})$ . Now the frequency of flux tube oscillations can be written as

$$\Omega_{\text{nl}} = \Omega + \Delta\omega_{\text{nl}}(\xi_{\eta}) \quad (6.13)$$

The first nonvanishing term in the expansion of  $\Delta\omega_{\text{nl}}(\xi_{\eta})$  in powers of  $\xi_{\eta}$  has the form

$$\Delta\omega_{\text{nl}}(\xi_{\eta}) = \Omega(k_z\xi_{\eta})^2 \quad (6.14)$$

For values  $\eta$  that are sufficiently close to resonance value  $\eta_0$  (condition (6.3)), the stationary value of the amplitude can be estimated directly from (6.12):

$$\xi(\eta) \left| \frac{d\Omega}{d\eta}(\eta - \eta_0) - \Omega k_z^2 \xi_{\eta}^2 \right| \sim \zeta_{\perp} \omega \quad (6.15)$$

Since  $d\Omega/d\eta \sim \omega$ , it follows from (6.14) and (6.15) that  $\xi_{\eta}$  depends on  $\eta$  as follows:

$$\nu \simeq \left\{ \begin{array}{ll} \zeta_{\perp}/|\eta - \eta_0|, & |\eta - \eta_0| \gg (\zeta_{\perp} k_z)^{2/3} \\ \zeta_{\perp} (\zeta_{\perp} k_z)^{-2/3}, & |\eta - \eta_0| \leq (\zeta_{\perp} k_z)^{2/3} \end{array} \right\} \quad (6.16)$$

This expression allows us to estimate the energy which will be transferred by an ensemble of flux tubes to the medium when the amplitude of flux tube oscillations reaches saturation. Since the energy of flux tube oscillations per unit length is of the order of magnitude of  $\rho_e R^2 \xi_{\eta}^2 \omega^2$ , the energy per unit volume transferred to the medium can be estimated as

$$W^* \simeq \rho_e \omega^2 \int g(\eta) \xi_{\eta}^2 d\eta \quad (6.17)$$

Near the resonance we have

$$W^* \simeq \rho_e \omega^2 \zeta_{\perp}^2 (\zeta_{\perp} k_z)^{-2/3} g(\eta_0) \quad (6.18)$$

or

$$\frac{W^*}{W} \simeq \alpha \left( \frac{\rho_e c_{\text{se}}^2}{W} \right)^{1/3} \quad (6.19)$$

Here  $W \sim \rho_e \omega^2 \zeta^2$  is the energy density of the incident sound wave. We used here the estimate  $g(\eta_0) \sim \alpha$ .

This result solves the problem of damping of a finite-amplitude wave, which may proceed in two major ways:

1. When  $W/c_{\text{se}}^2 > \alpha^3$  the maximum energy which can be transferred by the flux tube is small compared to the energy of the sound wave, that is, the wave transfers only an insignificant fraction of its initial energy to flux tubes, after which the damping stops.



2. At  $W/c_{se}^2 < \alpha^3$ , the energy of flux tubes remains small even when the sound wave is completely absorbed; in this case, nonlinear effects, and in particular, a nonlinear frequency shift, are unimportant, and damping is determined by the linear theory.

The condition for the applicability of the linear approximation in the problem of damping of a monochromatic sound wave with initial amplitude  $\zeta$  thus has the form

$$k\zeta < \alpha^{3/2}. \quad (6.20)$$

Consider now the example of the case opposite to (6.20), i.e., when

$$k\zeta > \alpha^{3/2} \quad (6.21)$$

In this case the sound wave is ultimately damped to extinction due to radiation damping of the flux tube oscillations. The damping time turns out to be much larger than  $\nu_L^{-1}$ . In this case the dissipation rate of the acoustic energy can be estimated as  $-Q \sim \nu_{\text{rad}} W^*$ , where  $W^*$  is given by (6.19) and  $\nu_{\text{rad}}$  is the radiative damping rate. Now, instead of the estimate (6.19) we have

$$-\frac{\partial W}{\partial t} \simeq \nu_{\text{rad}} W \alpha \left( \frac{\rho_e c_{se}^2}{W} \right)^{1/3}, \quad (6.22)$$

which gives the characteristic damping time of the acoustic wave as

$$\tau \simeq \frac{1}{\nu_{\text{rad}} W \alpha} \left( \frac{\rho_e c_{se}^2}{W} \right)^{-1/3} \gg \nu_{\text{rad}}^{-1} \quad (6.23)$$

Note that we have kept the assumption that  $\nu_{\text{rad}} \ll \Delta\omega_{\text{nl}}$ , otherwise the nonlinear effects become unimportant.

To compare the contribution of linear and nonlinear processes let us directly find the dependence of the flux tube oscillation amplitude on the initial amplitude of the sound wave in both cases.

In the linear case we have

$$\xi_\eta \sim \frac{\zeta_\perp}{k_z^2 R^2} \quad (6.24)$$

A nonlinear estimate of the oscillation amplitude can be obtained from (6.15)

$$\xi_\eta \simeq \left| \frac{\zeta_\perp}{\Delta - \Omega k_z^2 \xi_\eta^2 - i\nu_{\text{rad}}} \right|, \quad (6.25)$$

where  $\nu_{\text{rad}}$  is the small imaginary part of the radiative damping of tube oscillations, and instead of the expansion of  $\Omega$  in powers of  $|\eta - \eta_0|$  we have retained  $\Delta = |\omega - \Omega|$ . Now with (6.14) we can rewrite (6.25) in the form

$$\xi_\eta \simeq \left| \frac{\zeta_\perp}{\Delta - \Delta\omega_{nl} - i\nu_{\text{rad}}} \right|. \quad (6.26)$$

In the case of an exact linear resonance we have

$$|\Delta| - |\omega - \Omega| = 0 \quad (6.27)$$

Which, in fact, is the basic Cherenkov condition in Landau resonance,  $c_s = v_{\text{ph}} \cos \theta$ . Indeed, since  $\omega = c_s k_z$  and  $\Omega = c_{\text{ph}} k_z \cos \theta$ , the condition  $\omega - \Omega = 0$  gives  $c_s = v_{\text{ph}} \cos \theta$ .

Now, from (6.26), (6.14), and (3.50, Sect. 3.5) we find

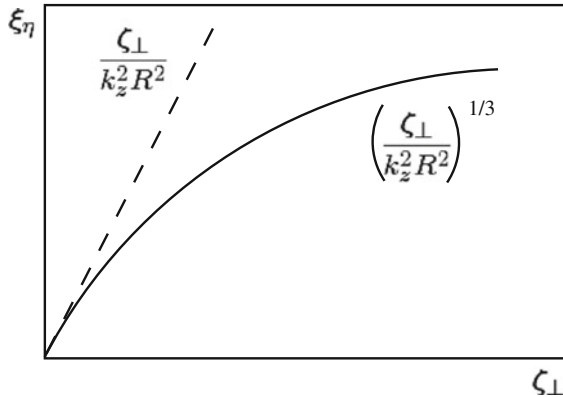
$$\xi_\eta \simeq \left| \frac{\zeta_\perp \omega}{\omega(k_z \xi_\eta)^2 + i\omega(k_z R)^2} \right|. \quad (6.28)$$

This gives the simple dependence of  $\xi_\eta$  on the initial amplitude of the sound wave

$$\xi_\eta \sim \zeta_\perp \frac{1}{k_z^2 \sqrt{\xi_\eta^4 + R^4}} \quad (6.29)$$

Figure 6.3 shows plots of the function  $\xi_\eta(\zeta_\perp)$  for both cases, the linear, dashed line (6.24) and nonlinear, solid line (6.29).

These plots show that, for large amplitudes,  $\zeta_\perp$ , i.e., in nonlinear regime the scattering cross section considerably decreases with respect to the linear case. Thus the process of the energy transfer to the medium and its efficiency is totally governed by the wave packet parameters, the properties of individual flux tubes, and on their



**Fig. 6.3** Plots of the amplitude of flux tube displacement,  $\xi_\eta$ , as a function of the initial sound wave amplitude,  $\zeta_\perp$ : *dashed line* for the linear case, and *solid line* for nonlinear case

relationship. In other words on the character of oscillations excited in the flux tube ensembles.

Although the most contribution comes from the kink modes, the axisymmetric oscillations may also contribute to the dynamics and energy exchange in an ensemble of magnetic flux tubes (Komm et al. 2000; Tirry 2000; Fujimura and Tsuneta 2009). In the next section we describe the collective phenomena associated with the excitation of the  $m = 0$  mode.

## 6.3 Axisymmetric Oscillation in Flux Tube Ensembles

### 6.3.1 Equations of Motion

Of three types of axisymmetric modes the most efficient is a sausage mode with phase velocity ((3.67), Chap. 3):

$$c_T = \frac{\omega}{k} = \frac{c_{si} v_A}{\sqrt{c_{si}^2 + v_A^2}} \quad (6.30)$$

The fact that the total pressure in the sausage oscillations, remains unperturbed,  $\delta P = \delta p + B\delta B/(4\pi) = 0$ , allows us to write down the  $r$ -component of the displacement vector as

$$\xi_r = \xi_0 \frac{r}{R} \quad (6.31)$$

Note that expression (6.31) is, in fact, a solution of the linearized MHD equations for  $m = 0$ , namely the first term in the expansion of the resulting Bessel function.

In terms of displacement vector the linearized MHD equations for perturbations of the form  $\exp(-i\omega t + im\phi + ikz)$  with  $m = 0$  then are

$$\begin{aligned} -\rho_i \omega^2 \xi_z &= -ik_z \delta p \\ b_r &= ik_z \xi_r B_0, \quad b_z = -B_0 \frac{1}{r} \frac{\partial}{\partial r} r \xi_r \\ \delta \rho + \rho_i \frac{1}{r} \frac{\partial}{\partial r} r \xi_r + ik_z \xi_z & \\ \delta p_i &= c_{si}^2 \delta \rho \end{aligned} \quad (6.32)$$

From this set and expression (6.31) for  $\xi_r$  we can find the total pressure perturbation

$$\delta P = -2\rho_i \frac{\xi_0}{R} \left( \frac{2\rho_i c_{si}^2}{1 - c_{si}^2 k_z^2 / \omega^2} + v_A^2 \right) \quad (6.33)$$

Each flux tube that performs such oscillations pushes the surrounding plasma with a force proportional to  $\delta P$ . The boundary condition

$$\delta P = -\delta p \quad (6.34)$$

gives a connection between the response of the external bulk plasma and the volume force with which the ensemble of flux tubes act on the plasma.

Let us find this connection. First of all, note that (6.34) gives the dependence of the flux tube displacement on the external pressure. Indeed, substituting (6.33) into (6.34) we have

$$2\rho_i \frac{\xi_0}{R} \left( \frac{c_{si}^2}{1 - c_{si}^2 k_z^2 / \omega^2} + v_A^2 \right) = \delta p_e, \quad (6.35)$$

which gives for  $\xi_0$  the following expression:

$$\xi_0 = R \frac{\delta p_e}{\rho_i v_A^2} \frac{\omega^2 - k_z^2 c_{si}^2 c_T^2}{\omega^2 - k_z^2 c_T^2 c_{si}^2} \quad (6.36)$$

Now we have to write the equation describing the propagation of sound waves in the medium containing the ensemble of random flux tubes. We assume that outside the flux tubes plasma is unmagnetized. Then the continuity equations become as

$$\rho_e \omega^2 \xi = -ik \delta p \quad (6.37)$$

$$\delta p_e = c_{si}^2 \delta \rho_e \quad (6.38)$$

and, instead of  $\delta \rho_e = -\rho_e \operatorname{div} \xi$ , we have

$$\delta \rho_e = -\rho_e \operatorname{div} \xi + \rho_e \frac{\langle \delta V \rangle}{L^3}, \quad (6.39)$$

where  $V$  is the volume occupied by flux tubes within the large volume  $L^3$ , such that  $V \ll L^3$ , i.e., the flux tubes form a rarefied ensemble with small filling factor,  $\alpha \ll 1$ .

The presence of the second term on the right-hand side of (6.39) is important and its meaning can be easily understood: this is the natural contribution of the expansion and compression of the oscillating flux tubes to the density perturbation of the surrounding plasma.

For flux tubes that are collinear but random in their other parameters the volume  $V$  can be written as  $V = L \sum_j \pi R_j^2$ , and for its perturbation we have

$$\delta V = 2v \sum_j \pi R_j \delta R_j, \quad (6.40)$$

It is obvious that

$$\delta R_j = \xi_{0j} \quad (6.41)$$

Where the displacement  $\xi_{0j}$  of the individual flux tube's boundary is defined by (6.36). Thus, we have

$$\delta R_j = \xi_{0j} = R_j \frac{\delta p_{ej}}{2\rho_i v_{Aj}^2} \frac{\omega^2 - k_z^2 c_{sj}^2}{\omega^2 - k_z^2 c_{Tj}^2} \frac{c_{Tj}^2}{c_{sj}^2} \quad (6.42)$$

When considering kink oscillations of flux tubes we neglected the plasma pressure inside the flux tubes. This assumption does not affect the phenomenological results. For sausage oscillations, however, we cannot neglect  $p_i$ , and unlike the previous case, the distribution function now contains one more parameter.

### 6.3.2 Dispersion Relation—Resonance and Frequency Shift

Let us introduce a broad distribution function of flux tubes  $f(\Xi)$  over the set  $\Xi$  of all their parameters, radius  $R$ , gas-kinetic pressure inside,  $p_i$ , and outside flux tube,  $p_e$ , density ratio,  $\eta = \rho_i/\rho_e$ , and magnetic field  $B$ . Normalization of the distribution function gives the magnetic filling factor of the medium:

$$\int f(\Xi) d\Xi dR = \alpha \quad (6.43)$$

where  $d\Xi = d\eta dp_i dp_e dB$ , and  $\alpha \ll 1$ .

With the help of the distribution function we can find the average of the perturbed value  $\langle \delta V \rangle$  in (6.39), which allows one to find the volume force with which oscillating flux tubes act on the medium. To do this, we use first the traditional procedure and suppose that we have large number  $N \gg 1$  of flux tubes occupying the volume  $V$ . The volume  $dV$  occupied by flux tubes whose parameters are in the intervals  $\Xi + d\Xi$ ,  $R + dR$  in a total volume  $L^3$ , is

$$dV = L^3 f(\Xi) d\Xi dR \quad (6.44)$$

The corresponding number of flux tubes in a volume  $L^3$  is then

$$dN = \frac{L^3}{\pi R^2} f(\Xi) d\Xi \quad (6.45)$$

The contribution of  $dN$  flux tubes in the perturbation  $\delta V$  of the volume (6.40) equals

$$\frac{\delta V}{L^3} = \frac{2}{L^2} \pi R \delta R dN \quad (6.46)$$

Integrating this expression and, taking into account (6.45), we find

$$\frac{\delta V}{L^3} = 2 \int \frac{\delta R(\Xi)}{R(\Xi)} f(\Xi) d\Xi. \quad (6.47)$$

Substituting (6.42) for  $\delta R$  into (6.47), we obtain the perturbed volume averaged over the flux tube ensemble:

$$\frac{\delta V}{L^3} = \delta p_e \int \frac{1}{\rho_i v_A^2} \frac{\omega^2 - k_z^2 c_{si}^2}{\omega^2 - k_z^2 c_T^2} \frac{c_T^2}{c_{si}^2} f(\Xi) d\Xi. \quad (6.48)$$

With this expression (6.39) becomes

$$\delta \rho_e = -\rho_e \operatorname{div} \xi + \frac{\delta p_e}{c_{se}^2} I(\omega, \mathbf{k}), \quad (6.49)$$

where

$$I(\omega, \mathbf{k}) = \gamma p_e \int \frac{1}{\rho_i v_A^2} \frac{\omega^2 - k_z^2 c_{si}^2}{\omega^2 - k_z^2 c_T^2} \frac{c_T^2}{c_{si}^2} f(\Xi) d\Xi. \quad (6.50)$$

Equations (6.37), (6.38), (6.49), and (6.50) form a closed set which describes the response of the medium containing a random ensemble of flux tubes to the propagation of sound waves provided by the resonant excitation of sausage oscillations of the flux tubes.

For plane wave propagating in an arbitrary direction (6.37) and (6.49) give the straightforward dispersion relation:

$$\omega^2 [1 - I(\omega, \mathbf{k})] = kc_{se}^2. \quad (6.51)$$

Since  $I(\omega, \mathbf{k}) \sim \alpha \ll 1$ , we can rewrite (6.51) as

$$\omega = kc_{se} [1 + \frac{1}{2} I(\omega, \mathbf{k})]. \quad (6.52)$$

To perform the integration in (6.50) we have to specify the set of parameters  $\Xi$ . In the whole set of parameters there are only a few independent ones. We will show that by adequate transformation and choice we can reduce their number to two. We will choose as independent variables the sound speed inside flux tube,  $c_{si}$ , and sausage oscillation phase velocity,  $c_T$ . Let us write the pressure equilibrium for a flux tube in the form

$$\rho_i c_{si}^2 + \frac{\gamma}{2} \rho_i v_A^2 = \rho_e c_{se}^2 \quad (6.53)$$

This gives for the plasma density inside the flux tube

$$\rho_i = \frac{\rho_e c_{se}^2}{c_{si}^2 + (\gamma/2)v_A^2}. \quad (6.54)$$

Using the expression for phase velocity (6.30) and (6.54), we can express  $(\rho_i v_A^2)^{-1}$  in terms of  $c_{si}$  and  $c_T$  as

$$\frac{1}{\rho_i v_A^2} = \frac{1}{c_{se}^2} \left( \frac{c_{si}^2}{c_T^2} - 1 + \frac{\gamma}{2} \right). \quad (6.55)$$

Substituting this expression into the integral (6.50) we have

$$I(\omega, \mathbf{k}) = \gamma p_e \int \frac{1}{c_{se}^2} \left( \frac{c_{si}^2}{c_T^2} - 1 + \frac{\gamma}{2} \right) \frac{\omega^2 - k_z^2 c_{si}^2 c_T^2}{\omega^2 - k_z^2 c_T^2 c_{si}^2} f(\Xi) d\Xi. \quad (6.56)$$

Here  $\gamma p_e$  cancels with  $\rho_e c_{se}^2$ , and so the integrand becomes a function of only  $c_{si}$  and  $c_T$ . Now putting  $d\Xi = d\tilde{c}_{si} d\tilde{c}_T$ , where  $\tilde{c}_{si}$  and  $\tilde{c}_T$  are nondimensionalized in terms of the sound speed outside the flux tubes ( $\tilde{c}_T = c_T/c_{se}$  and  $\tilde{c}_{si} = c_{si}/c_{se}$ ), with the use of (6.52) we arrive at the dispersion relation:

$$\omega = kc_{se} \left[ 1 + \frac{1}{2} \int \left( 1 - \frac{2 - \gamma c_T^2}{2 c_{si}^2} \right) \frac{\omega^2 - k_z^2 c_{se}^2 \tilde{c}_{si}^2}{\omega^2 - k_z^2 c_{se}^2 \tilde{c}_T^2} f(\tilde{c}_{si}, \tilde{c}_T) d\tilde{c}_{si} d\tilde{c}_T \right]. \quad (6.57)$$

The real part of the integral gives a linear frequency shift for the acoustic waves interacting with the ensemble of flux tubes, while the imaginary part reflects the resonant absorption of sound waves due to the excitation of flux tube oscillations. The corresponding damping rate and frequency shift are

$$\nu = -\text{Im} \omega = -\frac{kc_{se}}{2} \text{Im} I(\omega, \mathbf{k}), \quad (6.58)$$

and

$$\Delta\omega = \frac{kc_{se}}{2} \text{Re} I(\omega, \mathbf{k}). \quad (6.59)$$

For illustrative purposes let us calculate the damping rate. To find  $\text{Im} I(\omega, \mathbf{k})$  it is useful to rewrite the integral (6.56) in the form

$$\text{Im} I(\omega, \mathbf{k}) = \text{Im} \int \left( 1 - \frac{2 - \gamma c_T^2}{2 c_{si}^2} \right) \frac{[\omega^2 - k_z^2 c_{se}^2 \tilde{c}_{si}^2] f(\tilde{c}_{si}, \tilde{c}_T) d\tilde{c}_{si} d\tilde{c}_T}{(\omega - k_z c_{se} \tilde{c}_T + i0)(\omega + k_z c_{se} \tilde{c}_T)}. \quad (6.60)$$

where we have added a vanishing imaginary part in the resonance denominator in order to choose the correct integration path. Using the standard identity we can write

$$\text{Im} \frac{1}{\omega - k_z c_{se} \tilde{c}_T + i0} = -i\pi\delta(\omega - k_z c_{se} \tilde{c}_T), \quad (6.61)$$

The resonance condition is  $\omega = k_z \tilde{c}_T$ , has the form of the usual Cherenkov condition. Indeed, as  $k = k_z \cos \theta$ , and  $\tilde{c}_T = c_T/c_{se}$ , we have

$$c_{se} = c_T \cos \theta. \quad (6.62)$$

Now, integrating (6.60) over  $d\tilde{c}_T$  we obtain

$$\text{Im} I(\omega, \mathbf{k}) = \frac{\pi}{k_z c_{se}} \int_0^\infty \left[ 1 - \frac{2 - \gamma (\omega/k_z c_{se})^2}{2 \tilde{c}_{si}^2} \right] f(\omega/k_z, \tilde{c}_{si}) d\tilde{c}_{si} \quad (6.63)$$

Bearing in mind that  $\omega/(k_z c_{se}) = 1/\cos \theta$ , we can rewrite (6.63) in the form

$$\text{Im } I(\omega, \mathbf{k}) = \frac{\pi}{2\cos^2\theta} \int_0^\infty \left[ 1 - \frac{2-\gamma}{2} \frac{1}{x^2} \right] (1-x^2) f(x) dx, \quad (6.64)$$

where we have introduced the variable

$$x = \tilde{c}_{se} \cos \theta \quad (6.65)$$

The integral (6.64) for a given distribution function is equal in order of magnitude to the magnetic filling factor of the medium. Thus, an estimate for the Landau damping rate is

$$\nu \simeq \alpha \frac{\pi k c_{se}}{4\cos^2\theta} \quad (6.66)$$

Note that the integrand contains a product of two terms  $(1-x^2)$  and  $[1 - (2-\gamma)/2x^2]$ , which for a proper sign of the damping rate have to be positive. Since always  $(1-x^2) > 0$  (because  $\tilde{c}_{si} = c_{si}/c_{se} < 1$ , from (6.53)), we have to satisfy also the condition

$$\left( 1 - \frac{2-\gamma}{2} \frac{1}{x^2} \right) > 0 \quad (6.67)$$

which is automatically satisfied since  $1/x^2 < 2/(2-\gamma)$ . Using the definition of  $x$ , and the resonance condition (6.62), we have

$$c_T^2 < \frac{2}{2-\gamma} c_{si}^2, \quad (6.68)$$

which also always holds ( $c_T < c_{si}$  and  $2/(2-\gamma) > 1$ ).

In the same way one can find the frequency shift (6.59). Given that  $I(\omega, \mathbf{k}) \sim \alpha$ , it is obvious that

$$\Delta\omega \simeq \alpha \frac{kc_{se}}{2} \quad (6.69)$$

Thus, under the resonance condition (6.62), the flux tubes absorb the energy of sound waves which remains in the form of natural oscillations of the flux tubes until it turns into one or the other form of energy depending on the particular dissipation mechanism.

The first effect which turns on is the radiative damping of sausage oscillations. The corresponding damping rate is (cf. 3.101, Chap. 3):

$$\nu_{\text{rad}}^{m=0} = \frac{\pi\omega}{2} \frac{k^2 R^2}{2} \frac{c_{si}^6}{c_{se}^2 (c_{ci}^2 + v_A^2)^2} \quad (6.70)$$

In this case the energy transfer scenario can be described as follows. If the Landau damping rate determined by (6.66),



$$\nu_{\text{L}} \equiv \nu > \nu_{\text{rad}}^{m=0}, \quad (6.71)$$

the resonant flux tubes absorb the energy of the sound wave in a time  $t_{\text{L}} = \nu_{\text{L}}^{-1}$ , and accumulate it during a time  $\nu_{\text{rad}}^{-1}$ , after which the oscillating flux tubes radiate secondary acoustic or MHD waves. In the case opposite to (6.71) when

$$\nu_{\text{L}} \equiv \nu < \nu_{\text{rad}}^{m=0}, \quad (6.72)$$

the energy of the incident acoustic waves goes directly to the energy of secondary waves, that is, a direct resonance scattering of sound waves takes place.

## 6.4 The Interaction of Unsteady Wave Packets with an Ensemble of Flux Tubes

In this section we consider the interaction of an unsteady wave packets of acoustic waves with plasma containing random ensembles of magnetic flux tubes. We focus mainly on the physical mechanisms of energy transfer to the plasma. We shall see, for example, that the propagation of an acoustic wave packets in randomly magnetized solar atmosphere is accompanied by clear morphological effects, which include the spreading of the energy absorption region over scales much larger than the size of the initial wave packet. From observational point of view this is one of the ordinary events observed in the chromosphere and corona above the quiet sun regions (see Fig. 6.1 right panels).

The regions of an efficient energy input and their localization depend on the distribution of magnetic flux tubes in space and over their physical parameters, including their noncollinearity, which plays important role here. The appearance of clouds of energy above the rarefied ensembles of flux tubes is determined by the fact that the solar atmosphere is *randomly* magnetized, and magnetic flux tubes covering the solar surface are essentially nonidentical.

We start with a brief summary of the acoustic wave propagation through the random ensembles of magnetic flux tubes. As was shown, the interaction of an acoustic wave with an ensemble of flux tubes results in the excitation of oscillations propagating along those *particular* flux tubes for which the Cherenkov resonance condition is satisfied:

$$\omega = (\mathbf{k} \cdot \mathbf{n})v_{\text{ph}} \quad (6.73)$$

where  $v_{\text{ph}}$  is the phase speed either of a kink mode ( $m = \pm 1$ ) or an axisymmetric mode ( $m = 0$ ). It is important that  $v_{\text{ph}}$  carries the required information on flux tube parameters and completely determines its individuality.

We shall operate again with a broad distribution function over flux tube parameters with the mean width  $\Delta\eta \gg \alpha$ , where  $\alpha$  is the total fraction of the volume occupied by flux tubes in given area (see Fig. 3.2, Chap. 3). At the same time, it is only natural that the interval  $\delta\eta$  of the parameters of those tubes that are close to resonance with a particular sound wave is small:

$$\delta\eta \simeq \alpha \ll \Delta\eta \quad (6.74)$$

The width of the interval of phase velocities of excited flux tube oscillations is  $\delta v_{\text{ph}} \simeq \text{Im } \omega/k \simeq \alpha\omega/k$ , so that

$$\delta v_{\text{ph}}/v_{\text{ph}} \simeq \alpha \quad (6.75)$$

The Landau damping rates due to the excitation of kink and sausage modes are respectively

$$\nu^{m=\pm 1} = g(\eta_0)\pi k c_{\text{se}} \sin^2\theta, \quad \eta_0 = \frac{2\cos^2\theta}{\gamma} - 1, \quad (6.76)$$

and

$$\nu^{m=0} \simeq \alpha \frac{\pi k c_{\text{se}}}{4\cos^2\theta} \quad (6.77)$$

Hereafter we will denote the damping rates (6.76) and (6.77) by  $\nu_{\text{L}}$ , remembering that a Landau resonance occurs for both kinds of modes; which mode should be considered in a particular case is determined by the Cherenkov condition (6.73).

Once excited the flux tube oscillations are subject to radiative damping with the following damping rates:

$$\nu_{\text{rad}}^{m=\pm 1} = \frac{\pi\omega}{1+\gamma} \left( \frac{k_z R}{2} \right)^2 \left[ \frac{2}{\gamma(1+\gamma)} - 1 \right] \quad (6.78)$$

and

$$\nu_{\text{rad}}^{m=0} = \frac{\pi\omega}{2} \frac{(kR)^2}{2} \frac{c_{\text{si}}^6}{c_{\text{se}}^2 (c_{\text{si}}^2 + v_{\text{A}}^2)^2} \quad (6.79)$$

For convenience let us overview the major steps in the process of the interaction of a sound wave with the magnetic flux tubes.

Under the Cherenkov condition (6.73) the resonant flux tubes absorb the energy of the sound wave in a time

$$\tau_{\text{L}} = \nu_{\text{L}}^{-1} \quad (6.80)$$

Excited oscillations then propagate along the flux tubes (Fig. 6.4). In a time

$$\tau_{\text{rad}} = \nu_{\text{rad}}^{-1} \quad (6.81)$$

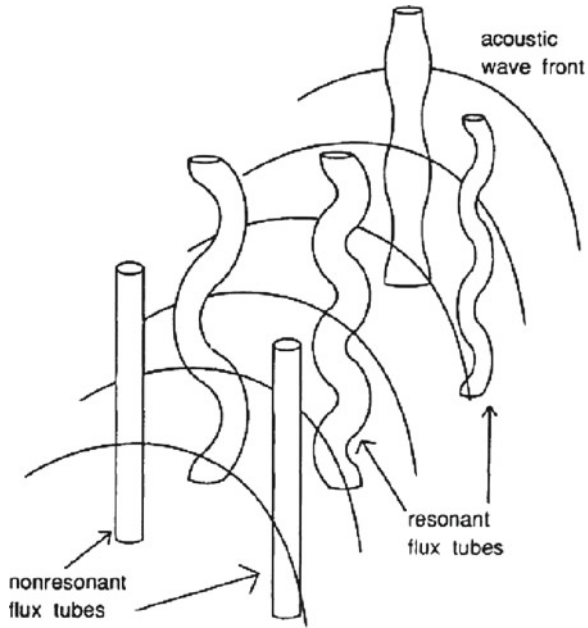
the absorbed energy is re-radiated as secondary acoustic or MHD waves. The time for radiation of secondary waves is estimated as

$$\tau_{\text{rad}} \simeq \frac{1}{\omega(kR)^2}, \quad (6.82)$$

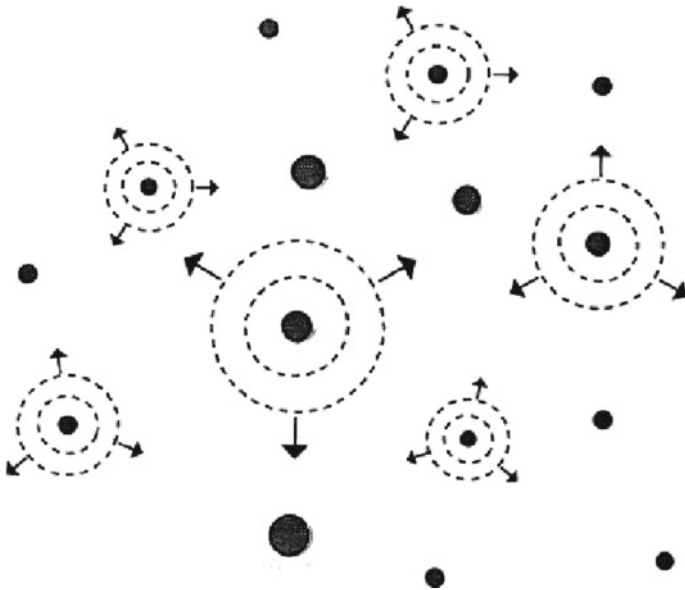
For those regions of the solar atmosphere where the magnetic filling factor,  $\alpha$ , is small, i.e.,  $R \ll l \ll k^{-1}$ , expression (6.82) is much larger than the Landau damping time:

$$\tau_{\text{rad}} \gg \tau_{\text{L}} \quad (6.83)$$

Thus the energy of the incident acoustic wave remains for a long time in the form of flux tube oscillation energy.



**Fig. 6.4** Propagation of an acoustic wave through an ensemble of flux tubes, some of which are nonresonant, while others are resonant with respect to kink or sausage modes



**Fig. 6.5** Radiation of secondary acoustic or MHD waves by resonant flux tubes. Different flux tubes radiate secondary waves in different times and at different heights

From expression (6.82) it is obvious that the different flux tubes radiate secondary waves over different times and at different heights: thicker flux tubes, for example, radiate sooner than the thinner ones; and, of course, the radiated waves have random phases

$$\Delta\omega \simeq \nu_L \quad (6.84)$$

This process is illustrated in Fig. 6.5. These phenomena manifest themselves in clear morphological effects, namely in the appearance of clouds of energy overlying the rarefied ensembles of flux tubes. In other words, the energy absorption region spreads over the area that is much larger than the size of the initial wave packet. The amount of the energy input and its location determined by physical parameters of a system will be discussed in the next section.

## 6.5 Spreading of the Energy Absorption Region—“Clouds of Energy”

The processes described above by (6.78)–(6.83) and illustrated in Figs. 6.4 and 6.5, represent the initial stage of the interaction between acoustic wave-trains and ensembles of flux tubes. The process may continue farther due to the fact that the secondary acoustic or MHD waves are also subject to absorption or scattering by the randomly magnetized medium.

Specifically, the secondary waves are again reabsorbed after a length scale  $L_L$  which is of the order of  $c_{se}/\nu_L$ , or

$$L_L = \frac{c_{se}}{\nu_L} \simeq \frac{\lambda}{\alpha}, \quad (6.85)$$

This process cascades farther until a reradiated waves get finally absorbed due to the action of some dissipative effects. In other words, process of the resonant absorption and re-radiation of the waves proceeds until final extinction of the wave energy. The duration and character of these processes depend, again, on the parameters of the acoustic wave packets and the properties flux tube ensembles.

To visualize clearly these effects let us start with the following criteria:

$$\nu_L \gg \nu_{rad} \gg \nu_{diss}, \quad (6.86)$$

where  $\nu_{diss}$  is a damping rate due to the usual dissipative mechanisms, thermal conductivity, viscosity, Ohmic losses. These conditions are appropriate for the solar atmosphere, but the analysis can be reproduced with minor changes for other relationships between the acting damping rates.

Let us introduce the damping lengths corresponding to Landau damping,  $L_L$ , radiation,  $L_{rad}$  and dissipative processes  $L_{diss}$ :

$$L_L = \frac{c_{se}}{\nu_L}, \quad L_{rad} = \frac{v_{ph}}{\nu_{rad}}, \quad L_{diss} = \frac{v_{ph}}{\nu_{diss}}, \quad (6.87)$$

In accordance with criteria (6.86) we have

$$L_L \ll L_{rad} \ll L_{diss}. \tag{6.88}$$

Consider two limiting cases:

- (1) The case of a large wave packet, whose size  $D$  is larger than the Landau damping length  $L_L$ 

$$D \gg L_L, \tag{6.89}$$

- (2) The case of a short wave packet when  $D$  is much smaller than  $L_L$ 

$$D \ll L_L, \tag{6.90}$$

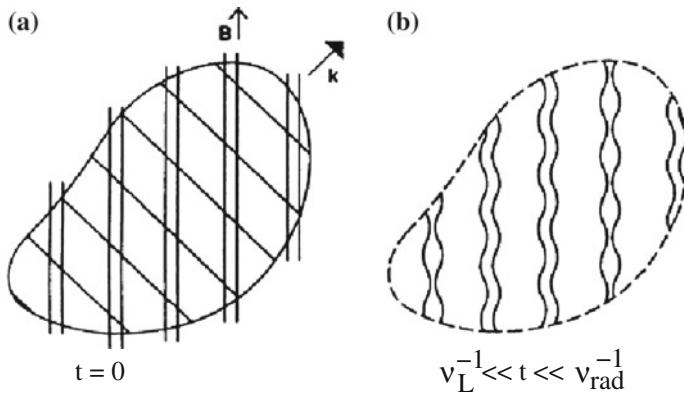
At the same time for both cases the following inequality holds with a good margin:

$$D \gg \lambda \gg d, \tag{6.91}$$

where  $d$ , as earlier, is the mean distance between flux tubes.

### 6.5.1 Large Wave Packets

Under the condition (6.89) a wave packet interacting with an ensemble of flux tubes is damped away without considerable displacement: since the Landau damping length is much less than the size of the wave packet, all the resonant flux tubes are excited in the initial area of the wave packet. In Fig. 6.6 a schematic of a large wave packet which covers the space containing the ensemble of widely spaced flux tubes is shown. At the initial moment of time  $t = 0$  flux tubes are not excited.



**Fig. 6.6** Propagation of a large wave packet through an ensemble of flux tubes: **a** Initial location of a wave packet with no flux tubes yet excited; **b** At an intermediate time,  $\nu_L^{-1} \ll t \ll \nu_{rad}^{-1}$ , the wave packet has damped away, but the energy remains in the form of natural oscillations of flux tubes that have not yet radiated secondary waves.  $\mathbf{k}$  is the direction of the propagation of the wave packet

At a time which is larger than the Landau damping time but less than the time of the radiation of secondary waves

$$\frac{L_L}{c_{se}} \ll t \ll \frac{L_{rad}}{v_{ph}}, \quad (6.92)$$

the wave packet is already damped away, but the excited flux tubes have not yet radiated secondary waves. In other words, at the time  $t$  such that

$$\nu_L^{-1} \ll t \ll \nu_{rad}^{-1}, \quad (6.93)$$

the wave packet is damped away, but its energy remains in the form of natural oscillations of resonant flux tubes *imitating* the initial area of the wave packet. This stage is shown in Fig. 6.6b.

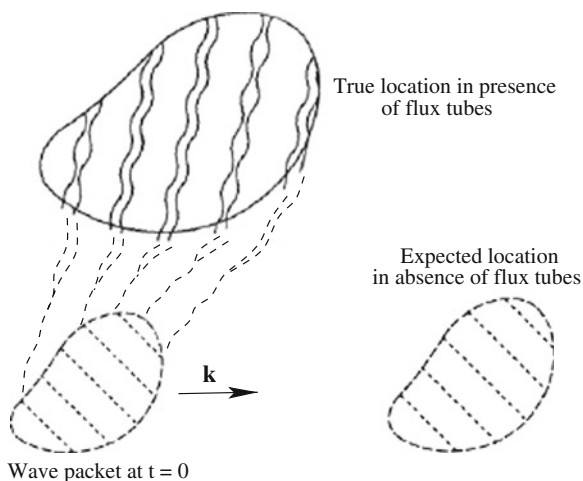
The excited perturbations, kink or sausage modes, propagate along the flux tubes carrying the accumulated energy of wave packet to higher layers of the atmosphere with a speed whose projection on the direction of the wave packet propagation is approximately  $c_{se}$ .

After a time

$$t \simeq \nu_{rad}^{-1}, \quad (6.94)$$

secondary waves are radiated. Since  $\nu_{rad}$  depends on the radius of the flux tube (6.78) and (6.79), different flux tubes radiate in different times. Respectively, the height of the energy input is different for different flux tubes. This fact leads to a significant spreading of the region where the energy of the initial wave packet is transferred to the medium, so that the region of energy input becomes much larger than the initial size of the wave packet. Note that noncollinearity of flux tubes enhances the spreading of energy input region. It is also important that the location of energy input, or in other words, the location of reappearance of the wave packet image

**Fig. 6.7** Initial location and size of a wave packet shown at  $t = 0$ . In a time  $t = \nu_{rad}^{-1}$  the final location of wave packet carrying the energy will be observed at the expected location if there are no magnetic flux tubes, and on a true location when passing through the ensemble of flux tubes



differs from the expected position of the wave packet in the absence of random flux tubes.

The sketch of the process is shown in Fig. 6.7. In the absence of flux tubes the wave packet would travel along its initial direction spreading out diffusively. On the other hand, when passing through the random ensembles of flux tubes, the wave packet loses in fact its identity and reappears as a product of flux tube oscillations in different location and of different sizes. The most typical coronal emission above the rarefied ensembles of flux tubes forming quiet sun regions shown in Fig. 6.1 is in striking agreement with the process described above.

### 6.5.2 Short Wave Packets—Energy Absorption and Release

For a short wave packet, with size  $D \ll L_L$ , we have

$$D \ll \frac{c_{se}}{\alpha\omega} \simeq \frac{\lambda}{\alpha} \quad (6.95)$$

where we have taken into account that  $L_L \simeq c_{se}/\nu_L$ , see (6.87), and thus

$$\nu_L \simeq \alpha\omega. \quad (6.96)$$

The condition (6.95) means that, during the traveling of the wave packet through the ensemble of flux tubes, both excited and non-excited flux tubes exist simultaneously.

Indeed, the wave packet traverses any particular flux tube within a time

$$T \simeq D/c_{se} \ll \nu_L^{-1} \quad (6.97)$$

which is short compared to Landau damping time. Thus the wave packet excites resonant flux tubes on its way and propagates further, leaving a trace of excited flux tubes, which in turn radiate secondary waves. In principle, the first excited flux tubes can already radiate their energy before the wave packet is finally damped away. In this case secondary acoustic waves coexist with the initial wave packet.

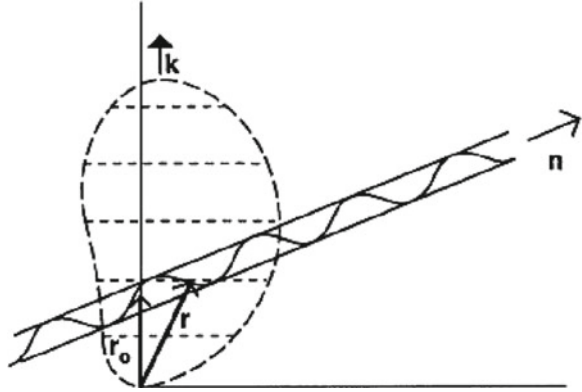
The particular scenario of wave packet dynamics and the final region of the energy input depend on the specifics of the flux tube distribution. In other words, the shape of the “new image” of the wave packet is determined by the memory of the system.

Now we proceed to quantitative analysis. Conditions (6.97) allow to write the pressure perturbation, and other perturbed quantities, through the slowly varying envelope:

$$\delta p_e = \frac{1}{2} \delta p_0 F \left( \mathbf{r} - \frac{\mathbf{k}}{k} c_{se} t \right) e^{-i\omega t + i\mathbf{k}\mathbf{r}} + c.c. \quad (6.98)$$

where  $\omega = c_{se}k$ , and  $F(\mathbf{r} - (\mathbf{k}/kc_{se})t)$  is the slowly varying envelope. No damping is taken into account in this expression because of the condition (6.97). For definiteness, we consider  $\delta p_0$  and  $F$  as real functions, i.e.,  $\delta p_0 = \delta p_0^*$  and  $F = F^*$ .

**Fig. 6.8** A wave packet moving in the direction  $\mathbf{k}$ .  $\mathbf{n}$  is the direction of a flux tube and  $\mathbf{r}$  is the coordinate of a point on the flux tube surface



Let us first consider the response of a certain flux tube to the action of the external perturbation in the form (6.98). Consider as an example the kink oscillations of flux tube and recall the equation for the displacement vector  $\xi$  of a flux tube ((3.8), Chap. 3):

$$\frac{\partial^2 \xi_\eta}{\partial t^2} - v_{\text{ph}}^2 \frac{\partial^2 \xi_\eta}{\partial \zeta^2} = \frac{2}{1 + \eta} \frac{\partial v_\perp}{\partial t} \quad (6.99)$$

where  $v_\perp$  is the normal component of the macroscopic velocity of plasma outside the flux tubes, and  $\zeta$  is the coordinate along the flux tubes.

Without the external motions, when  $v_\perp = 0$ , (6.99) describes the  $m = \pm 1$  eigenoscillations of a flux tube, whereas the right-hand side of (6.99) with nonzero  $v_\perp \neq 0$ , represents the interaction force between flux tube and its environment.

Consider the wave packet traveling in the  $\mathbf{k}$  direction as sketched in Fig. 6.8, and let  $\mathbf{n}$  be a unit vector along the flux tube. The coordinate of any point at the flux tube surface can be written as  $\mathbf{r} = \mathbf{r}_0 + \mathbf{n}\zeta$ .

The absolute value of the macroscopic plasma velocity outside the flux tube,  $\mathbf{v}$ , can be written as  $\mathbf{v} = (\mathbf{k}/k)v$ , so that its component, normal to the vector  $\mathbf{n}$  is

$$\mathbf{v}_\perp = v \frac{\mathbf{k} - \mathbf{n}(\mathbf{k} \cdot \mathbf{n})}{k} \quad (6.100)$$

In the external region, which we assume to be magnetic free, we have

$$-i\omega\rho_e v = -ik\delta p_e \quad (6.101)$$

which gives  $v = k\delta p_e/\omega\rho_e$  or  $v = \delta p_e/(c_{se}\rho_e)$ , so that

$$\frac{\partial v}{\partial t} = \frac{1}{c_{se}\rho_e} \frac{\partial \delta p_e}{\partial t} \quad (6.102)$$

For the slowly varying envelope, given by (6.98), we therefore have



$$\frac{\partial v}{\partial t} \simeq -i\omega \frac{\delta p_0}{c_{se}\rho_e} F\left(\mathbf{r} - \frac{\mathbf{k}}{k} c_{se} t\right) e^{-i\omega t + i\mathbf{k}\mathbf{r}} + \text{c.c.} \quad (6.103)$$

and the force on the right-hand side of (6.99) can be written as

$$\frac{\partial \mathbf{v}_\perp}{\partial t} = -\frac{\mathbf{k} - \mathbf{n}(\mathbf{k} \cdot \mathbf{n})}{k} \left[ \omega \frac{\delta p_0}{c_{se}\rho_e} F\left(\mathbf{r} - \frac{\mathbf{k}}{k} c_{se} t\right) e^{-i\omega t + i\mathbf{k}\mathbf{r}} + \text{c.c.} \right] \quad (6.104)$$

Introducing the notations

$$\tilde{v} \equiv \frac{2\delta p_0}{(1 + \eta)c_{se}\rho_e}, \quad \boldsymbol{\xi}_\perp = \tilde{\boldsymbol{\xi}} \frac{\mathbf{k} - \mathbf{n}(\mathbf{k} \cdot \mathbf{n})}{k}, \quad (6.105)$$

and using expression (6.104) for the interaction force we have instead of (6.99):

$$\frac{\partial^2 \tilde{\xi}_\eta}{\partial t^2} - v_{ph}^2 \frac{\partial^2 \tilde{\xi}_\eta}{\partial \zeta^2} = -i\omega \tilde{v} F\left(\mathbf{r} - \frac{\mathbf{k}}{k} c_{se} t\right) e^{-i\omega t + i\mathbf{k}\mathbf{r}} + \text{c.c.} \quad (6.106)$$

Since  $F$  is slowly varying function, we seek the solution of (6.106) in the form

$$\tilde{\xi} = \frac{1}{2} \xi_0(\zeta, t) e^{-i\omega t + ik_\parallel \zeta} + \text{c.c.} \quad (6.107)$$

where  $\xi_0(\zeta, t)$  is also slowly varying function, and  $k_\parallel = (\mathbf{k} \cdot \mathbf{n}) \equiv k \cos \theta$ .

Taking second derivatives of function (6.107) over time and coordinate, substituting them into (6.106) we obtain

$$\frac{1}{2} (\omega^2 - k_\parallel^2 v_{ph}^2) \xi_0(\zeta, t) + i\omega \xi_{0t} + ik_\parallel v_{ph}^2 \xi_{0\zeta} = i\omega \tilde{v} F. \quad (6.108)$$

For flux tubes that are close to resonance the following conditions are fulfilled:

$$|\omega - k_\parallel v_{ph}| \ll \omega \quad (6.109)$$

For exact resonance we have the Cherenkov condition:  $\omega = k_\parallel v_{ph}$ . Denote the deviation from exact resonance by

$$\delta\omega = |\omega - k_\parallel v_{ph}| \quad (6.110)$$

Then the coefficient of the first term on the left of (6.108) can be written as

$$\frac{1}{2} (\omega^2 - k_\parallel^2 v_{ph}^2) = \frac{1}{2} (\omega + k_\parallel v_{ph})(\omega - k_\parallel v_{ph}) \simeq \omega \delta\omega \quad (6.111)$$

With this we can rewrite (6.108) in the form

$$\xi_{0t} + v_{ph} \xi_{0\zeta} - i\delta\omega \xi_0 = \tilde{v} F(\zeta, t), \quad (6.112)$$

and for the complex conjugate

$$\xi_{0t}^* + v_{\text{ph}} \xi_{0\zeta}^* + i \delta \omega \xi_0^* = \tilde{v} F(\zeta, t), \quad (6.113)$$

Multiplying (6.112) by  $\xi_{0t}^*$ , (6.113) by  $\xi_{0t}$ , and integrating the sum we get the energy density of flux tube oscillations:

$$\frac{\partial}{\partial t} \int_{-\infty}^{\infty} |\xi_0|^2 d\zeta' = \tilde{v} \int_{-\infty}^{\infty} F(\zeta', t) [\xi_0(\zeta', t) + \xi_0^*(\zeta', t)] d\zeta' \quad (6.114)$$

The next important step is to average expression (6.114) over the large volume containing many tubes. In this way we can find the energy input in this volume provided by the interaction of the acoustic wave packet with the ensemble of flux tubes.

Let us first find the energy density of a single magnetic flux tube. The energy of a flux tube per unit length is

$$\langle W \rangle = \left\langle \pi R^2 (\rho_i + \rho_e) \sin^2 \theta \left( \frac{\partial \tilde{\xi}_{\perp}}{\partial t} \right)^2 \right\rangle \quad (6.115)$$

Taking into account (6.107) we have for the averaged energy per unit length:

$$\langle W \rangle = \pi R^2 (\rho_i + \rho_e) \sin^2 \theta \omega^2 |\xi_0|^2. \quad (6.116)$$

The total energy of the flux tube is then,

$$W = \int_{-\infty}^{\infty} \langle W \rangle d\zeta' = \pi R^2 (\rho_i + \rho_e) \sin^2 \theta \omega^2 \int_{-\infty}^{\infty} |\xi_0|^2 d\zeta'. \quad (6.117)$$

Taking the time derivative of (6.117) and comparing it with (6.114) we get an expression for the temporal variation of the flux tube energy:

$$\frac{\partial W}{\partial t} = \tilde{v} \pi \omega^2 R^2 (\rho_i + \rho_e) \sin^2 \theta \int_{-\infty}^{\infty} F(\zeta', t) \text{Re} \xi_0(\zeta', t) d\zeta'. \quad (6.118)$$

where we took into account that  $\xi_0 + \xi_0^* = 2 \text{Re} \xi_0$ ;  $\xi_0(\zeta, t)$  is governed by (6.112).

To solve the problem qualitatively we have to find an explicit expression for  $\xi_0(\zeta, t)$ , that is, to solve (6.106). To do so we introduce new variables

$$s \equiv \zeta - v_{\text{ph}} t, \quad x \equiv \zeta \quad (6.119)$$

such that

$$\frac{\partial}{\partial t} \equiv -v_{\text{ph}} \frac{\partial}{\partial s}, \quad \frac{\partial}{\partial \zeta} \equiv \frac{\partial}{\partial s} + \frac{\partial}{\partial x}. \quad (6.120)$$

In these variables (6.112) becomes

$$-v_{\text{ph}} \frac{\partial \xi_0}{\partial s} + v_{\text{ph}} \left( \frac{\partial \xi_0}{\partial s} + \frac{\partial \xi_0}{\partial x} \right) - i\delta\omega \xi_0 = \tilde{v} F \left( x, \frac{x-s}{v_{\text{ph}}} \right) \quad (6.121)$$

or, finally,

$$\frac{\partial \xi_0}{\partial s} - i\delta\omega \xi_0 = \frac{\tilde{v}}{v_{\text{ph}}} F \left( x, \frac{x-s}{v_{\text{ph}}} \right). \quad (6.122)$$

The solution of this equation is of the form

$$\xi_0 = \frac{\tilde{v}}{v_{\text{ph}}} \exp \left( i \frac{\delta\omega}{v_{\text{ph}}} x \right) \int_{-\infty}^x \exp \left( -i \frac{\delta\omega}{v_{\text{ph}}} x' \right) F \left( x', \frac{x'-s}{v_{\text{ph}}} \right) dx'. \quad (6.123)$$

In the original variables see (6.119) this solution is

$$\xi_0(\zeta, t) = \frac{\tilde{v}}{v_{\text{ph}}} \int_{-\infty}^{\zeta} \exp \left[ -i \frac{\delta\omega}{v_{\text{ph}}} (\zeta - \zeta') \right] F \left( \zeta', \frac{\zeta' - \zeta}{v_{\text{ph}}} + t \right) d\zeta', \quad (6.124)$$

and for temporal variation of the energy of flux tube oscillations (6.118) we have

$$\frac{\partial W}{\partial t} = \tilde{v} \pi \omega^2 R^2 (\rho_i + \rho_e) \sin^2 \theta \text{Re} \int_{-\infty}^{\infty} F(\zeta, t) d\zeta \cdot \xi_0(\zeta, t) \quad (6.125)$$

where  $\xi_0(\zeta, t)$  is given by (6.124).

Averaging this expression over the large volume containing many flux tubes we can find the energy deposition to the medium from the ensemble of flux tubes interacting with the acoustic wave packets. This will be done in the next section.

## 6.6 The Energy Transfer from Unsteady Wave Packets to the Medium

Let us consider a large volume with a cross section of dimensions  $\mathcal{L}$  by  $\mathcal{L}$ , such that  $d \ll \mathcal{L} \ll \lambda$ , where  $d$  is, as earlier, a mean distance between the flux tubes.

The energy deposition into the volume with the cross section  $\mathcal{L} \times \mathcal{L}$  has the form

$$\begin{aligned} \frac{1}{\mathcal{L}^2} \frac{\partial W_{\mathcal{L}}}{\partial t} &= \text{Re} \frac{\omega^2 \tilde{v}^2}{v_{\text{ph}}} \sin^2 \theta \int_0^{\infty} (\rho_i + \rho_e) g(\eta) d\eta \int_{-\infty}^{\infty} F(\zeta, t) d\zeta \\ &\times \int_{-\infty}^{\zeta} \exp \left[ -i \frac{\delta\omega}{v_{\text{ph}}} (\zeta - \zeta') \right] F \left( \zeta', \frac{\zeta' - \zeta}{v_{\text{ph}}} + t \right) d\zeta' \end{aligned} \quad (6.126)$$

As discussed, for a broad distribution function the estimate for the parameter range of resonance is quite small  $\delta\eta \simeq \alpha \ll 1$ . This condition implies that the main contribution in the expression (6.126) comes from a narrow resonance region of width  $\delta\eta$  near the resonance value of  $\eta = \eta_0$ , ( $\eta_0 = 2\cos^2\theta/\gamma - 1$ ).

The first integral in (6.126) can be written as

$$\int_{\eta}^{\infty} (\rho_i + \rho_e)g(\eta)d(\eta - \eta_0) \quad (6.127)$$

Since the function  $g(\eta)$  is strongly peaked near the  $\eta_0$ , the lower limit in this integral can be replaced by  $-\infty$  and  $(\rho_i + \rho_e)g(\eta)$  by its value at exact resonance,  $[(\rho_i + \rho_e)g(\eta)]_{\eta_0}$ . Then the triple integral in (6.126) can be written as

$$I_3 = \int_{-\infty}^{\infty} F(\zeta, t)d\zeta \cdot I_2(\zeta), \quad (6.128)$$

where

$$I_2 = (\rho_i + \rho_e)g(\eta)|_{\eta_0} \times \int_{-\infty}^{\zeta} \int_{-\infty}^{\infty} \exp \left[ -i \frac{\delta\omega}{v_{ph}} (\zeta - \zeta') \right] F \left( \zeta', \frac{\zeta' - \zeta}{v_{ph}} + t \right) d\zeta' d(\eta - \eta_0) \quad (6.129)$$

The real part of (6.129) determines the energy dissipation (6.126) in the medium. After performing the double integration in (6.129) we find

$$\text{Re } I_2(\zeta) = \pi \frac{1}{|(d/d\eta)(\delta\omega/v_{ph})|_{\eta_0}} (\rho_i + \rho_e)g(\eta)|_{\eta_0} F(\zeta, t). \quad (6.130)$$

The evaluation of this double integral is detailed in the Appendix.

Using now (6.126) and (6.130) we can write the energy deposition into the ensemble of flux tubes from the acoustic wave packet as

$$\frac{\partial W_{\mathcal{L}}}{\partial t} = \frac{2\pi\mathcal{L}^2\omega^2 v^2 \sin^2\theta}{v_{ph} |(d/d\eta)(\delta\omega/v_{ph})|_{\eta_0}} [(\rho_i + \rho_e)g(\eta)]_{\eta_0} \int_{-\infty}^{\infty} F^2(\zeta, t)d\zeta. \quad (6.131)$$

This gives the value of the energy dissipation in a volume with cross section  $\mathcal{L} \times \mathcal{L}$  containing the ensemble of flux tubes with distribution function  $g(\eta)$ .

The energy dissipation per unit volume according to (6.131) will be

$$\frac{\partial W_{\mathcal{L}}}{\partial t} = \frac{2\pi\rho_e\omega^2 \tilde{v}^2 \sin^2\theta}{v_{ph} |(d/d\eta)(\delta\omega/v_{ph})|_{\eta_0}} (1 + \eta)g(\eta)|_{\eta_0} F^2(\zeta, t), \quad (6.132)$$

or, after substituting here  $\tilde{v}$  from (6.105),

$$\frac{\partial W_{\mathcal{L}}}{\partial t} = \frac{8\pi\omega^2 g(\eta_0) \sin^2\theta}{v_{\text{ph}} |(d/d\eta)(\delta\omega/v_{\text{ph}})|_{\eta_0} (1 + \eta_0)} \frac{\delta p_0^2}{\rho_e c_{\text{se}}^2} F^2. \quad (6.133)$$

From this equation we can find the damping rate of the acoustic packet. To do so, we first find the energy density of the acoustic wave packet itself, namely,  $W = \overline{\rho v^2}$ , where the velocity  $v$  is

$$\overline{v^2} = \frac{\overline{\delta p_e^2}}{\rho_e^2 c_{\text{se}}^2} F^2. \quad (6.134)$$

Averaging the expression (6.98) representing the form of the wave packet we obtain

$$\overline{v^2} = \frac{1}{2\rho_e^2 c_{\text{se}}^2} \delta p_0^2 F^2, \quad (6.135)$$

and for the energy density of the acoustic wave packet we have:

$$W_{ac} = \frac{\delta p_0^2}{2\rho_e c_{\text{se}}^2} F^2. \quad (6.136)$$

Comparing (6.133) and (6.136) one can see that (6.133) can be written as follows:

$$\frac{\partial W_{\mathcal{L}}}{\partial t} = \frac{16\pi\omega^2 g(\eta_0)}{v_{\text{ph}} |(d/d\eta)(\delta\omega/v_{\text{ph}})|_{\eta_0}} \frac{\sin^2\theta}{1 + \eta_0} W_{ac}, \quad (6.137)$$

which implies the damping rate of

$$\Gamma = \frac{16\pi\omega^2 g(\eta_0)}{v_{\text{ph}} |(d/d\eta)(\delta\omega/v_{\text{ph}})|_{\eta_0}} \frac{\sin^2\theta}{1 + \eta_0}. \quad (6.138)$$

Now recall that  $v_{\text{ph}}$  is the phase velocity of the kink mode in the flux tube, and  $\delta\omega$  is determined by (6.110). Then for the derivative in the denominator of (6.138) we have

$$\frac{d}{d\eta} \frac{\delta\omega}{v_{\text{ph}}} = \frac{d}{d\eta} \frac{\omega - k_{\parallel} v_{\text{ph}}}{v_{\text{ph}}} = -\frac{\omega}{v_{\text{ph}}^2} \frac{dv_{\text{ph}}}{d\eta} \quad (6.139)$$

And so

$$v_{\text{ph}} \left| \frac{d}{d\eta} \frac{\delta\omega}{v_{\text{ph}}} \right|_{\eta_0} = \frac{1}{2} \cdot \frac{\omega}{1 + \eta_0} \quad (6.140)$$

After substituting (6.140) into (6.138) we have for the damping rate

$$\Gamma = 32\pi\omega g(\eta_0) \sin^2\theta. \quad (6.141)$$

Comparing (6.141) with the damping rate of a monochromatic wave, (6.76), we see that qualitatively the damping rate of an unsteady wave packet is determined exactly by the same physical parameters, but it is almost an order of magnitude larger than that of a monochromatic wave. It is important to note, however, that the essential difference between these two cases is that the propagation of unsteady wave packet is accompanied by spreading of energy input region and its specific location.

Modern space instruments allow nowadays to observe and measure large-scale disturbances, like, e.g., so-called ‘‘EIT’’ waves (Delaboudiniere et al. 1995; Chen et al. 2005; Gopalswamy et al. 2009; Chen and Wu 2011; Long et al. 2013). Obviously these waves are hardly a local phenomena and are directly connected with the energy absorbed by the ensembles of photospheric flux tubes and transferred in form of various clouds of energy and high frequency waves into the corona.

## Appendix

To perform the integration in (6.129) we introduce the function

$$\kappa(\eta) = \frac{\delta\omega}{v_{\text{ph}}} \quad (6.142)$$

and change the variable  $\zeta - \zeta' = x$ . Then the double integral in (6.129) becomes (we need only its real part):

$$\text{Re } I(\zeta) = \text{Re} \int_0^{\infty} \int_{-\infty}^{\infty} d(\eta - \eta_0) e^{i\kappa(\eta)x} F\left(\zeta - x, t - \frac{x}{v_{\text{ph}}}\right) dx. \quad (6.143)$$

Now, the shortest way to integrate (6.143) is to use the definition of the  $\delta$ -function, namely

$$\delta(x) = \frac{1}{2\pi} \int_{-\infty}^{\infty} e^{ikx} dk, \quad \delta[f(x)] = \frac{1}{|df/dx|_0} \delta(x). \quad (6.144)$$

Therefore, (6.143) can be written as

$$\text{Re } I(\zeta) = \text{Re} \int_0^{\infty} 2\pi \frac{1}{|df/dx|_0} \delta(x) F\left(\zeta - x, t - \frac{x}{v_{\text{ph}}}\right) dx. \quad (6.145)$$

which gives immediately

$$\text{Re } I(\zeta) = \frac{\pi}{|df/dx|_0} F(\zeta, t). \quad (6.146)$$

Substituting (6.146) into (6.143) we come to expression (6.130)

$$\operatorname{Re} I_2(\zeta) = (\rho_i + \rho_e)g(\eta)|_{\eta_0} \frac{\pi}{|(d/d\eta)(\delta\omega/v_{\text{ph}})|_{\eta_0}} F(\zeta, t). \quad (6.147)$$

## References

- T. Bogdan, E. Zweibel, *Astrophys. J.* **676**, L89 (1987)  
 L. Chen, A.A. Hasegawa, *J. Geophys. Res.* **79**, 1033 (1974)  
 P.F. Chen, Y. Wu, *Astrophys. J.* **732**, L20 (2011)  
 P.F. Chen, C. Fang, K. Shibata, *Astrophys. J.* **622**, 1202 (2005)  
 J.P. Delaboudiniere et al., *Sol. Phys.* **162**, 291 (1995)  
 D. Fujimura, S. Tsuneta, *Astrophys. J.* **702**, 1443 (2009)  
 N. Gopalswamy et al., *Astrophys. J.* **691**, L123 (2009)  
 R.W. Komm, R. Howe, F. Hill, *Astrophys. J.* **543**, 472 (2000)  
 L.D. Landau, *Sov. Phys. JETP* **16**, 574 (1946)  
 D.M. Long et al., *Sol. Phys.* **288**, 567 (2013)  
 M. Lontano, E. Lazzaro, D. Ryutov, *Physica Scripta* **T84**, 52 (2000)  
 D.D. Ryutov, M.P. Ryutova, *Sov. Phys. JETP* **43**, 491 (1976)  
 M.P. Ryutova, E.R. Priest, *Astrophys. J.* **419**, 349 (1993a)  
 M.P. Ryutova, E.R. Priest, *Astrophys. J.* **419**, 371 (1993b)  
 A. Timofeev, *Sov. Phys. Uspekhi* **13**, 632 (1970)  
 W.J. Tirry, *Astrophys. J.* **528**, 493 (2000)

## Chapter 7

# Effects of Magnetic Flux Tubes in Helioseismology

**Abstract** In the previous chapter we studied the response of rarefied ensembles of random magnetic flux tubes to the propagation of acoustic waves and unsteady wave packets. In this chapter we shall study how the properties of acoustic wave packets at the photospheric level, modified by presence of magnetic flux tubes flux tube, can be used for diagnostics goals. In particular, we shall study effects of flux tubes on local helioseismology based on the time-distance analysis (Duvall et al. 1993, 1996). We shall see that flux tubes strongly affect the standard methods of time-distance tomography, and allow more realistic inference of physical parameters, including flows, magnetic fields and their nonuniformities. Besides, one can study the structure of solar atmosphere by spectral features of acoustic waves using an approach in the data analysis called “Raman spectroscopy of p-modes”.

### 7.1 The Time-Distance Tomography

The time-distance tomography is based on the measurement of travel time of an acoustic wave between any point on the solar surface and a surrounding annulus (Duvall et al. 1993, 1996). An acoustic wave propagating through the near-surface envelope interacts with its random magnetic fields and mass flows and is exposed to the density and temperature perturbations. The alterations in travel time of acoustic waves due to these interactions carry the information on the surface and subsurface structures. In the original approach the travel times were measured by calculating the temporal cross-correlation function between the data at some point of given area and the data within an annulus at large distance from the point. For each of the chosen annuli the travel times were measured for both forward and backward propagation, i.e., from the central point of the annulus, ( $\tau^{(+)}$ ), and back ( $\tau^{(-)}$ ). However, this approach, even though later extended to measurements of travel times in the north–south and east–west directions separately (Duvall et al. 1997) did not allow to detect the presence of magnetic fields.

The situation has changed with development of the procedure based on the angular dependence of travel times (Ryutova and Scherrer 1998). An advantage of such an approach is in its intrinsic invariance with respect to the choice of the coordinate frame and sensitivity to the presence of magnetic elements. The method provides an automatic rule of assigning proper weights to every observational points and its magnetic status.



### 7.1.1 Key Points of Time-Distance Analysis with Magnetic Fields

Consider a typical geometry of time-distance analysis in local helioseismology, but let the magnetic field be present (Ryutova and Scherrer 1998). Figure 7.1 shows the geometry of the problem: acoustic wave propagating from the point  $A$  on the solar surface downward is reflected at the depth of  $h$  and propagates back to a certain point  $C$  on the surface. Flow velocity is denoted by  $u$ , its direction is characterized by the angle  $\theta_u$ ; the magnetic field,  $B$  forms the angle  $\theta_B$  with the axis  $x$ . The angle  $\theta$  is counted, say, from west at the solar surface.

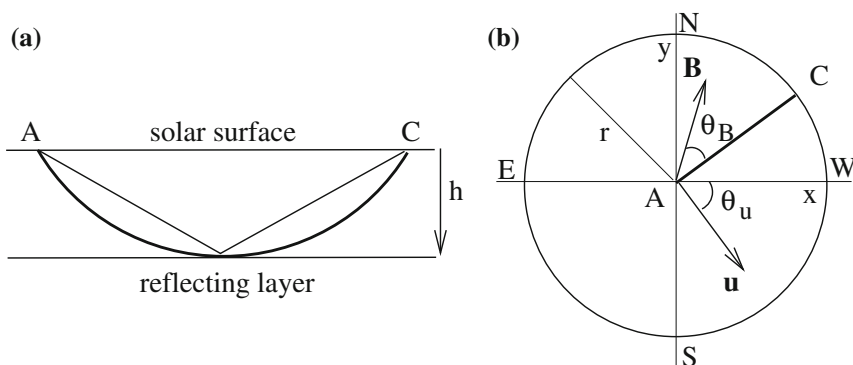
In ray approximation the averaged value of the propagation time can be expressed as

$$\bar{\tau} = \frac{1}{2\pi} \int_0^{2\pi} \tau(\theta) d\theta \quad (7.1)$$

The key point of the approach that reflects the presence of magnetic flux tubes is that in addition to the average (7.1) one must also take  $\sin n\theta$  and  $\cos n\theta$  transforms of the propagation time

$$\bar{\tau}_c^{(n)} = \frac{1}{2\pi} \int_0^{2\pi} \tau(\theta) \cos n\theta d\theta \quad (7.2)$$

$$\bar{\tau}_s^{(n)} = \frac{1}{2\pi} \int_0^{2\pi} \tau(\theta) \sin n\theta d\theta \quad (7.3)$$



**Fig. 7.1** Geometry of the problem: **a** ray trajectory in the model of uniform slab;  $AC = r$  **b** annulus on the solar surface; the  $x$ -axis is parallel to solar equator, while the  $y$ -axis is directed along the local meridian

We will use the approximation of geometrical acoustics and assume that the magnetic effects are small. We will discuss only averages corresponding to the first two harmonics,  $n = 1, 2$ . It is remarkable that the first harmonics and their various combinations give amazingly rich information when used with the observational data. In particular, the first harmonics alone ( $n = 1$ ) give information on the direction and absolute value of the horizontal flow velocity.

Combinations of the second harmonics ( $n = 2$ ) of the inward ( $\tau^{(-)}$ ) and outward ( $\tau^{(+)}$ ) times give information on the orientation and absolute value of horizontal magnetic fields and the spatial gradients of flow velocity. Namely the sum of forward and backward propagating times,  $\tau^{(+)} + \tau^{(-)}$  carries information on the magnetic field distribution, while the difference,  $\tau^{(+)} - \tau^{(-)}$ , on the magnitude and orientation of shear flows.

Besides, the method allows to separate the contributions of mass flows from the contribution of the magnetic fields and find the alteration of the travel time provided by flow field and magnetic field independently. One can also single out the horizontal components from vertical components of the magnetic field and mass flows. Higher order harmonics carry information on the finer structures of the medium, and require high resolution data.

To illustrate the kind of information that is contained in  $\bar{\tau}_{c,s}^{(1,2)}$ , first we consider a simple model of acoustic wave propagation: we assume that “unperturbed” plasma parameters (i.e., parameters in the absence of flows and magnetic field) are uniform in the slab of thickness  $h$  corresponding to the lower reflection point for the acoustic wave. Then we present the corrections to the propagation time in a vertically stratified atmosphere and show that in this much more general case the alterations in the travel time still manifest the same  $\cos n\theta - \sin n\theta$  dependence on the azimuthal angle.

We assume that the wavelength of acoustic waves is small compared to all other spatial scales and use the ray approximation. Typically, near the surface flow velocities,  $u$ , and Alfvén speed,  $v_A$  are much less than the sound speed,  $c_s$

$$u, v_A \ll c_s, \quad (7.4)$$

Thus effects of flow and magnetic field enter into the propagation time  $\tau(\theta)$  as small additions proportional to  $u/c_s$ , and  $v_A^2/c_s^2$ , respectively. Since the conditions (7.4) are believed to be held for subsurface layers, one can consider the effects of flow and magnetic field separately. We will follow this line of reasoning throughout the chapter.

### 7.1.2 The Travel Times

The travel time of the wave propagating with the group velocity  $\mathbf{v}_{gr} = \partial\omega/\partial\mathbf{k}$  in the ray approximation is

$$\tau = \int_l \frac{1}{v_{gr}} dl \quad (7.5)$$

where  $d\mathbf{l}$  is an element of a ray trajectory. The dispersion relation for acoustic waves in the first approximation with respect to magnetic effects and mass flow,  $\mathbf{u}$ , has the form

$$\omega = kc_s + \mathbf{k}\mathbf{u} + \frac{v_A^2}{2kc_s}[\mathbf{k} - (\mathbf{k}\mathbf{b})\mathbf{b}]^2 \quad (7.6)$$

where  $\mathbf{b}$  is a unit vector along the magnetic field, and  $k = \sqrt{k_x^2 + k_y^2 + k_z^2}$ . The group velocity is

$$\mathbf{v}_{\text{gr}} = \frac{\partial\omega}{\partial\mathbf{k}} = \frac{\mathbf{k}}{k}c_s + \mathbf{u} + \frac{v_A^2}{2c_s} \frac{\mathbf{k}}{k} - \frac{v_A^2}{c_s} \frac{\mathbf{b}(\mathbf{k}\mathbf{b})}{k} + \frac{v_A^2}{2c_s} \frac{\mathbf{k}(\mathbf{k}\mathbf{b})^2}{k^2} \quad (7.7)$$

The absolute value of the group velocity up to the terms linear in  $\mathbf{u}$  and quadratic in  $v_A$  is

$$v_{\text{gr}} = c_s + \mathbf{n}\mathbf{u} + \frac{v_A^2}{2c_s}[1 - (\mathbf{n}\mathbf{b})^2] \quad (7.8)$$

where  $\mathbf{n} = \mathbf{k}/k$ .

Note that in the presence of a weak ( $v_A \ll c_s$ ) magnetic field, in addition to the modified acoustic mode (fast-mode solution of the wave equation) that we have considered, there appear two more modes, the pure Alfvén mode, with

$$\omega = \mathbf{k}\mathbf{u} + (\mathbf{k}\mathbf{b})v_A \quad (7.9)$$

and a slow magnetoacoustic mode with

$$\omega = \mathbf{k}\mathbf{u} + (\mathbf{k}\mathbf{b})v_A - (\mathbf{n}\mathbf{b})^2 \frac{kv_A^2}{2c_s} \quad (7.10)$$

Modes (7.9) and (7.10) have much slower group and phase velocities than the modified acoustic mode (7.6). These modes would correspond to much longer propagation times ( $c_s/v_A$  times longer) and may give large errors in the frame of the time-distance analysis.

It must be noted that in the future one can study a domain of much longer propagation times. Despite some difficulties that may appear at small enough flow speed when group velocity of low-frequency modes (7.9) and (7.10) closely follows the direction of the magnetic field, extension of the time-distance analysis to the domain of the propagation times

$$\tau \simeq \frac{r}{v_A} \quad (7.11)$$

may prove to be feasible and will then provide direct information about sub-surface magnetic fields.

In the first approximation with respect to magnetic and flow effects (cf. the conditions (7.4)) travel time can be written as follows:

$$\tau = \int_l \left( \frac{1}{c_s} - \frac{\delta c_s}{c_s^2} - \frac{\mathbf{n}\mathbf{u}}{c_s^2} - \frac{v_A^2}{2c_s^3}[1 - (\mathbf{n}\mathbf{b})^2] \right) dl \quad (7.12)$$

Thus, the variation in sound speed, flows, and magnetic field have different angular dependence. Therefore, taking Fourier sine and cosine transforms (different harmonics!) of travel time one can see that the parity properties of the contribution of mass flows, magnetic effects, and variation of sound speed with respect to forward and backward propagation are different.

Additional and rich information can be obtained from the analysis of parity properties (with respect to forward and backward propagation) of the various contributions, including the spatial inhomogeneities of background parameters of medium, which can be distinguished by the Fourier sine and cosine transforms of the propagation time (7.12). The Fourier transform should be performed for the forward and backward propagation times, and also for some combinations of their differences. Finally, applying an inversion procedure to the transformed times one can reconstruct the depth-dependent flow and magnetic fields below the solar surface.

## 7.2 The Effects of Horizontal Flows

In the unperturbed state the propagation time from point  $A$  to the point  $C$  (Fig. 7.1) on the ring of radius  $r$  is obviously

$$\tau = \tau_0 = \frac{\sqrt{r^2 + 4h^2}}{c_s}, \quad (7.13)$$

and is the same for the waves traveling in the “forward” (from the point  $A$  to point  $C$ ) and “backward” directions (from  $C$  to  $A$ ). In the presence of plasma flows, these times are different: the “upstream” group velocity of the acoustic wave is greater than that of “downstream.”

Let the direction of flow  $u$  form an angle  $\theta_u$  with the axis  $x$  as shown in Fig. 7.1a. Then from (7.12) elementary calculations (in the linear approximation) show that

$$\tau = \tau_0 - \frac{ur}{c_s^2} \cos(\theta - \theta_u) \quad (7.14)$$

Integrating these expressions with  $\cos \theta$  and  $\sin \theta$  we obtain

$$\tau_s^{(1)} = -\frac{ur}{2c_s^2} \sin \theta_u, \quad \tau_c^{(1)} = -\frac{ur}{2c_s^2} \cos \theta_u \quad (7.15)$$

while  $\tau_s^{(2)} = \tau_c^{(2)} = 0$ .

The absolute value of the velocity can be found from the relationship

$$u = \frac{2c_s^2}{r} \sqrt{[\tau_s^{(1)}]^2 + [\tau_c^{(1)}]^2} \quad (7.16)$$

and the direction of propagation may be determined from

$$\sin \theta_u = -\frac{\tau_s^{(1)}}{\sqrt{[\tau_s^{(1)}]^2 + [\tau_c^{(1)}]^2}}, \quad \cos \theta_u = -\frac{\tau_c^{(1)}}{\sqrt{[\tau_s^{(1)}]^2 + [\tau_c^{(1)}]^2}} \quad (7.17)$$

or

$$u_x = \frac{2c_s^2}{r}\tau_c^{(1)}, \quad u_y = \frac{2c_s^2}{r}\tau_s^{(1)} \quad (7.18)$$

Note that the presence of a uniform vertical flow does not affect (7.16) and (7.17). As for the forward ( $\tau_{s,c}^{(1)+}$ ) and backward ( $\tau_{s,c}^{(1)-}$ ) propagation times, in the case of the uniform flow we have

$$\tau_{s,c}^{(1)+} = -\tau_{s,c}^{(1)-}. \quad (7.19)$$

Therefore, the ‘‘homogeneous’’ flow field may be found through the (7.16) and (7.18), using for  $\tau_{s,c}^{(1)}$  either of the transforms, forward propagation times,  $\tau_{s,c}^{(1)+}$ , backward propagation times,  $\tau_{s,c}^{(1)-}$ , or their average,  $[\tau_{s,c}^{(1)+} + (-\tau_{s,c}^{(1)-})]/2$ . For pure homogeneous flows all three results should be identical. Obviously such situation is far from reality. The stronger the inhomogeneities, the larger will be the discrepancies between the three velocity maps. The main discrepancies will be caused by those effects that have the opposite parity properties, i.e., nonuniformities in sound speed and horizontal magnetic field.

### 7.3 Effects of Horizontal Magnetic Field

First we derive expression for the propagation time  $\tau(\theta)$  in the case when a magnetic field is parallel to  $x$ -axis, and then, we take into account the fact that  $\theta_B$  is a finite angle.

For a simple model of the magnetic field parallel to the  $x$ -axis the dispersion relation (7.6) in the first approximation with respect to magnetic effects has the form:

$$\omega = kc_s + \frac{v_A^2}{2kc_s}(k_y^2 + k_z^2) \quad (7.20)$$

Using the equation for the ray trajectory, (7.5) yields:

$$\tau = \tau_0 - \frac{\tau_0 v_A^2}{2c_s^2} \left(1 - \frac{r^2}{2(4h^2 + r^2)}\right) + \frac{\tau_0 v_A^2}{4c_s^2} \frac{r^2}{4h^2 + r^2} \cos 2(\theta - \theta_B) \quad (7.21)$$

In this case,  $\tau_s^{(1)} = \tau_c^{(1)} = 0$ , while

$$\tau_s^{(2)} = \tau_0 \frac{v_A^2}{4c_s^2} \frac{r^2}{4h^2 + r^2} \sin 2\theta_B \quad (7.22)$$

and

$$\tau_c^{(2)} = \tau_0 \frac{v_A^2}{4c_s^2} \frac{r^2}{4h^2 + r^2} \cos 2\theta_B \quad (7.23)$$

The magnetic field strength (actually, the inverse plasma beta) can be easily determined from the expressions (7.22) and (7.23):

$$\frac{v_A^2}{c_s^2} = 4 \frac{4h^2 + r^2}{r^2} \frac{\sqrt{[\tau_s^{(2)}]^2 + [\tau_c^{(2)}]^2}}{\tau_0} \quad (7.24)$$

The orientation of the magnetic field can be determined from the following relations:

$$\sin 2\theta_B = \frac{\tau_s^{(2)}}{\sqrt{[\tau_s^{(2)}]^2 + [\tau_c^{(2)}]^2}}, \quad \cos 2\theta_B = \frac{\tau_c^{(2)}}{\sqrt{[\tau_s^{(2)}]^2 + [\tau_c^{(2)}]^2}} \quad (7.25)$$

Now, using (7.24) and (7.25) we have for  $B_x = B \cos \theta_B$  and  $B_y = B \sin \theta_B$ :

$$B_{x,y} = \left( \frac{8\pi\rho c_s^2 \sqrt{[\tau_s^{(2)}]^2 + [\tau_c^{(2)}]^2}}{\tau_0 r^2 / (4h^2 + r^2)} \right)^{1/2} \left( 1 \pm \frac{\tau_c^{(2)}}{\sqrt{[\tau_s^{(2)}]^2 + [\tau_c^{(2)}]^2}} \right)^{1/2} \quad (7.26)$$

It is important to note that forward ( $\tau_{s,c}^{(2)+}$ ) and backward ( $\tau_{s,c}^{(1)-}$ ) propagation times are the same

$$\tau_{s,c}^{(2)+} = \tau_{s,c}^{(2)-}. \quad (7.27)$$

This means that the half-sum of measured values of forward and backward propagation times,  $(1/2)(\tau_{s,c}^{(2)+} + \tau_{s,c}^{(2)-})_{\text{obs}}$  will determine the orientation and magnitude of magnetic field (see (7.32)); while the difference in these values carries the information about the gradients of mass flows. Thus,  $\tau_{s,c}^{(2)}$  in (7.24) should be taken as

$$\tau_{s,c}^{(2)} = (1/2) \left( \tau_{s,c}^{(2)+} + \tau_{s,c}^{(2)-} \right)_{\text{obs}} \quad (7.28)$$

The presence of vertical component of a uniform magnetic field will not give a contribution to  $\tau_s^{(2)}$  and  $\tau_c^{(2)}$  (as well as to  $\tau_s^{(1)}$  and  $\tau_c^{(1)}$ ). This fact is one of the merits of this approach that allows to single out the influence of plasma flows from those of magnetic field, on one hand, and explore the orientation and magnitude of horizontal components independently from the vertical projection, on the other. Note that technique described above and throughout this chapter operates with directly measurable parameters, thus representing a diagnostic tool.

## 7.4 Effects of Background Inhomogeneities

### 7.4.1 Weak Inhomogeneities

So far we were considering the simplest situation when the sound speed  $c_s$ , the flow velocity  $\mathbf{u}$ , and magnetic field  $\mathbf{B}$  do not depend on coordinates over the space comparable with radii of annuli where the measurements are taken.

Now we discuss a modification of the earlier results in a case when  $c_s$ ,  $\mathbf{u}$  and  $\mathbf{B}$  weakly depend on coordinates  $x$  and  $y$ , such that they change insignificantly over the radius of annulus; then they can be described linearly over  $x$  and  $y$  additions to otherwise constant  $c_s$ ,  $\mathbf{u}$  and  $\mathbf{B}$ .

As corrections to the propagation times caused by the presence of mass flow, magnetic field, and inhomogeneity of sound speed are small, they can be taken into account separately, i.e., cross terms can be neglected.

Now, instead of a uniform slab of thickness  $h$  with a bottom perfectly reflecting acoustic waves, we consider linear corrections (in  $x$ ,  $y$ ,  $z$ ) to  $c_s$ ,  $\mathbf{u}$  and  $\mathbf{B}$ , in other words, we assume that,

$$c_s = c_{s0} + \vec{\sigma} \cdot \mathbf{r}, \quad (7.29)$$

$$u_\alpha = u_{0\alpha} + \nu_{\alpha\beta} \cdot r_\beta, \quad (7.30)$$

$$B_\alpha = B_{0\alpha} + b_{\alpha\beta} \cdot r_\beta \quad (7.31)$$

where  $\sigma$  is a constant (independent of coordinates) vector and  $\nu_{\alpha\beta}$  and  $b_{\alpha\beta}$  are constant tensors.

Let us consider the effects of the inhomogeneities of these three physical parameters on the sine and cosine transforms of the propagation times.

*Nonuniformities of  $c_s$ :* The vertical nonuniformity (dependence on  $z$ ) does not break the cylindrical symmetry of the problem and does not contribute to  $\tau_{s,c}^{(n)}$  ( $n = 1, 2, \dots$ ) at all. The horizontal nonuniformity (nonvanishing  $\sigma_x$  and/or  $\sigma_y$ ) gives rise to the appearance of finite contributions to  $\tau_{s,c}^{(1)}$ . These contributions, obviously, will be identical for  $\tau_{s,c}^{(1)+}$  and  $\tau_{s,c}^{(1)-}$ .

*Variation of horizontal magnetic field:* The contribution of magnetic field effects to the group velocity scales as  $B^2$  and, therefore, magnetic contributions to  $\tau^{(n)}$  are even ( $\tau^{(n)+} = \tau^{(n)-}$ ). The nonuniformity causes the appearance of the term of the type  $B_{0x}b_{xy}yn_x^2$ ,  $B_{0x}b_{xy}yn_y^2$  and  $B_{0y}b_{yx}xn_y^2$ . As  $n_x^2$  and  $n_y^2$  contain terms proportional to  $\sin 2\theta$ ,  $\cos 2\theta$ , the propagation time will now contain terms proportional to  $\sin \theta$ ,  $\cos \theta$  and  $\sin 3\theta$ ,  $\cos 3\theta$ .

*Variation of horizontal velocity:* The presence of the terms linear in  $x$  and  $y$  gives rise to a contribution to  $\tau_{s,c}^{(2)}$ . The change of the sign in  $\mathbf{u}$  is equivalent to mutual replacement of the emission source and detection points. On the other hand, the change of sign in velocity changes the sign in  $\tau_{s,c}^{(2)}$ . Therefore, we conclude that

$$\tau_{s,c}^{(2)+} = -\tau_{s,c}^{(2)-} \quad (7.32)$$

This particular case is considered in the next section, where we use (7.32) to find the spatial distribution of mass flows through the observed propagation times.

### 7.4.2 Variations of Flow Velocities

We use the model described by (7.30). Denoting the variable part of the velocity vector by  $\Delta \mathbf{u}$ , we can write:

$$\Delta u_x = u_{xx}x + u_{xy}y, \quad (7.33)$$

$$\Delta u_y = u_{yx}x + u_{yy}y \quad (7.34)$$

The horizontal component of the group velocity in the case shown in Fig. 7.1, for the ray propagating in the direction forming an angle  $\theta$  with  $x$ -axis, is

$$\frac{c_s r}{\sqrt{r^2 + 4h^2}} + \Delta u_x \cos \theta + \Delta u_y \sin \theta, \quad (7.35)$$

or

$$\frac{c_s r}{\sqrt{r^2 + 4h^2}} + \rho \left( \frac{u_{xx} - u_{yy}}{2} \cos 2\theta + \frac{u_{xy} + u_{yx}}{2} \sin 2\theta \right) \quad (7.36)$$

where  $\rho$  is a polar radius,  $x = \rho \cos \theta$ ,  $y = \rho \sin \theta$ .

The propagation time up to the terms linear in  $u_{\alpha\beta}$ , is then [see (7.14)],

$$\tau = \tau_0 - \frac{ur \cos \theta}{c_s^2} - \frac{1}{c_s^2} \left( \frac{u_{xx} - u_{yy}}{2} \cos 2\theta + \frac{u_{xy} + u_{yx}}{2} \sin 2\theta \right) \int_0^r \rho d\rho \quad (7.37)$$

or

$$\tau = \tau_0 - \frac{ur \cos \theta}{c_s^2} - \frac{r^2}{2c_s^2} \left( \frac{u_{xx} - u_{yy}}{2} \cos 2\theta + \frac{u_{xy} + u_{yx}}{2} \sin 2\theta \right) \quad (7.38)$$

The first harmonics give the expressions for the horizontal components of uniform flow, while the second harmonics include the effects of possible shear flows in the horizontal plane:

$$\tau_s^{(2)} = -\frac{u_{xy} + u_{yx}}{8c_s^2} r^2 \quad (7.39)$$

$$\tau_c^{(2)} = -\frac{u_{xx} - u_{yy}}{8c_s^2} r^2 \quad (7.40)$$



## 7.5 Practical Use of the Forward–Backward Information

We summarize here the symmetry properties of various contributions to the propagation time and use the results to find the general pattern of magnetic field and flow distribution at two different layers using the observational data.

### 7.5.1 Symmetry Properties

The symmetry properties and in particular, parities of the forward–backward propagation times are shown in Table 7.1. As mentioned earlier, the parity properties give an additional mean to split various effects.

For example, if we take a half-sum of measured times,  $\tau_{s,c}^{(2)+}$  and  $\tau_{s,c}^{(2)-}$ , we obtain the quantity that eliminates the contribution of the flow and by (7.24)–(7.28) gives directly the magnetic field strength. At the same time, the difference,  $(1/2)(\tau_{s,c}^{(2)+} - \tau_{s,c}^{(2)-})$ , gives the flow nonuniformities. Thus, when computing, for example  $u_{xy} + u_{yx}$ , we use the expression (7.39) in a form:

$$\frac{\partial u_x}{\partial y} + \frac{\partial u_y}{\partial x} = -\frac{4c_s^2}{r^2}(\tau_s^{(2)+} - \tau_s^{(2)-}) \quad (7.41)$$

Note that although the *variation* in the horizontal magnetic fields contribute to the first harmonics (last row in Table 7.1), the alteration in travel time would be masked by the effects of a uniform mass flows (second row in Table 7.1) and may be ignored.

**Table 7.1** Symmetry properties of various contributions to the propagation times

Effect	$\tau_{s,c}^{(1)}$	$\tau_{s,c}^{(2)}$	Parity property
Horizontal variation of sound speed	Yes	No	$\tau_{s,c}^{(1)+} = \tau_{s,c}^{(1)-}$
Uniform horizontal flow	Yes	No	$\tau_{s,c}^{(1)+} = -\tau_{s,c}^{(1)-}$
Variation in horizontal mass flow ( $\nu_{\alpha\beta} \neq 0$ )	No	Yes	$\tau_{s,c}^{(2)+} = -\tau_{s,c}^{(2)-}$
Uniform horizontal magnetic field	No	Yes	$\tau_{s,c}^{(2)+} = \tau_{s,c}^{(2)-}$
Variation in horizontal magnetic field ( $b_{\alpha\beta} \neq 0$ )	Yes	No	$\tau_{s,c}^{(1)+} = \tau_{s,c}^{(1)-}$
Uniform vertical flow	No	No	–
Variation in vertical flow	Yes	No	$\tau_{s,c}^{(1)+} = -\tau_{s,c}^{(1)-}$
Variation in vertical magnetic field ( $b_{z\alpha}$ )	Yes	No	$\tau_{s,c}^{(1)+} = \tau_{s,c}^{(1)-}$

### 7.5.2 Reconstruction of Subsurface Flow and Magnetic Fields from Observations

For illustrative purposes we use here results of travel-time measurements obtained from the data sets taken by the MDI instrument on SOHO, and perform their sine and cosine transforms for reconstruction the subsurface flow and magnetic fields. The data were taken from the 8 h observation of line-of-sight velocity in the MDI high resolution field on January 27, 1996. The object of the observation is very quiet sun region. In other words, we deal with the helioseismology effects in the rarefied ensemble of flux tubes.

Figure 7.2 (top) shows magnetogram of the region with magnetic field shown in *blue*. The travel times have been measured for sets of ray paths on a grid of  $30 \times 40$  points on the observed area of  $175 \times 130$  Mm. The sine and cosine transforms have been made for two sets of short distance ray paths. Each set contains the data averaged over the three sets of annuli with the radial distance ranges of  $\Delta = 0.225^\circ$ – $0.625^\circ$  and  $\Delta = 0.625^\circ$ – $1.025^\circ$ .

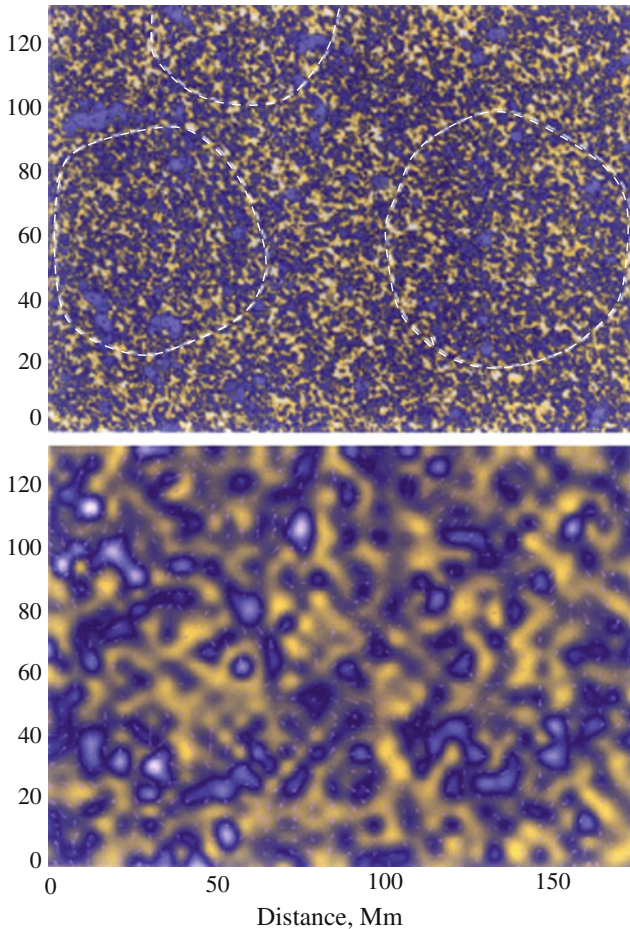
For the reconstructed flow and magnetic fields the mean depths drop at  $h_1 \simeq 1.2$  Mm and  $h_2 \simeq 2.8$  Mm below the solar surface. Thus, for the first set of measured travel times and their sine and cosine transforms we prescribe the mean depth  $h = 1.2$  Mm and mean annulus radius  $r = 5.2$  Mm, respectively, for the second set of measured travel times we have  $h = 2.8$  Mm and  $r = 10$  Mm.

Figure 7.2 (bottom) shows a pattern of the reconstructed magnetic field, more precisely,  $v_A^2/c_s^2$  at the depth  $h = 1.2$  Mm (blue color). One can see a strong correlation between the measured magnetic field on the solar surface and the underlying horizontal field. Note that although the procedure does not allow to resolve the scale less than the ray path, much larger scale of reconstructed local elements compared to elements on magnetogram is consistent with both ray approximation and observational data, which also are restricted by the size of annuli. It is remarkable how well the reconstructed magnetic field pattern mimics a supergranular geometry (marked by white dashed circles in Fig. 7.2).

Figure 7.3 shows the computed map of velocity field for the depths of 1.2 Mm. This map also clearly shows the supergranular pattern in the flow field. Maximum velocity at this depth is  $v_{\max} = 2.3 \text{ km s}^{-1}$ . The flow map reconstructed at 2.8 Mm depth (not shown) also mimics the magnetic pattern, but the velocities are lower, e.g.,  $v_{\max} = 1.7 \text{ km s}^{-1}$ .

In the absence of local inhomogeneities, the velocity field reconstructed from the measurements of backward propagation times and forward propagation times should be the same. However, the presence of the local inhomogeneities of medium violates the exact relationship (7.32) and causes discrepancies in the maps obtained from  $\tau_{s,c}^{(1)+}$  and  $\tau_{s,c}^{(1)-}$ . These discrepancies are associated with those effects that have different parity properties, such as the variation in sound speed and nonuniform magnetic fields

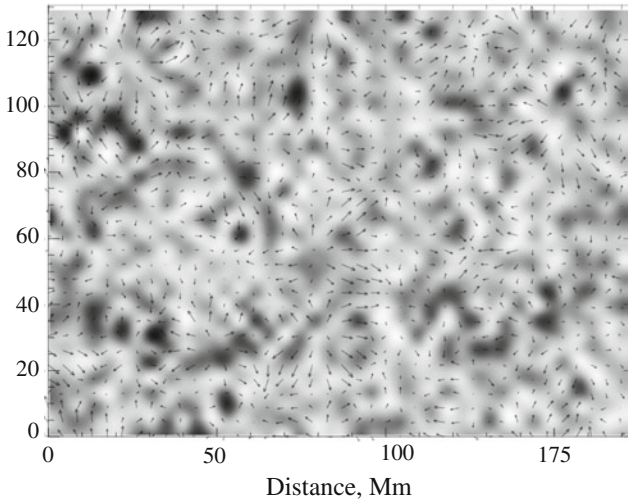
It is important that, although the effect of “uniform” mass flows in  $\tau_{s,c}$  is much stronger than that of the magnetic field inhomogeneities, there is a significant differ-



**Fig. 7.2** *Top* high-resolution magnetogram of a quiet sun region, taken by the MDI/SOHO instruments on January 27, 1996. *Bottom* the reconstructed subsurface horizontal magnetic field in terms of inverse plasma beta,  $v_A^2/c_s^2$  at 1.2Mm below the visible surface,  $(v_A^2/c_s^2)_{\max} = 0.11$ . *Arrows* show the subsurface velocity field. *White dashed circles* outline supergranular pattern populated by the magnetic field concentrations, which are especially well recognizable on the reconstructed map below the surface

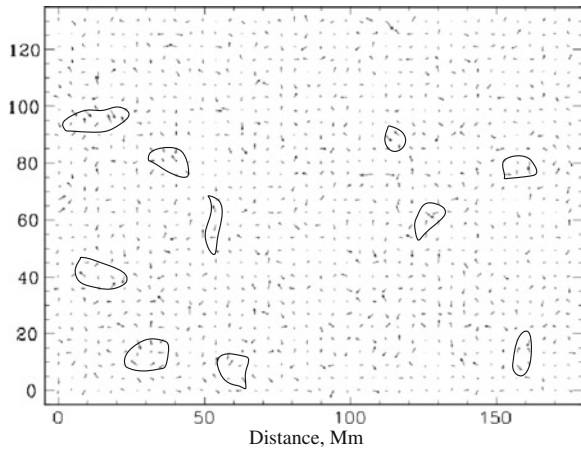
ence between the velocity field reconstructed from the forward and backward propagation times. This difference shows the location of magnetic field inhomogeneities or/and variation in sound speed. Figure 7.4 shows the map of velocity vectors which represent the difference between the velocities obtained from  $\tau_{s,c}^{(1)+}$  and  $\tau_{s,c}^{(1)-}$ . One can see a clear correlation between the location of largest discrepancies in reconstructed velocity field and the locations of strongest magnetic field (cf. Fig. 7.2).

For quantitative estimates of the magnetic field strength we need to adopt some model parameters for plasma density below the surface. Let us try, e.g., the para-



**Fig. 7.3** The reconstructed velocity field at 1.2 Mm below the visible surface,  $v_{\max} = 2.3 \text{ km s}^{-1}$ . One can see that at the location of strong magnetic field the mass flows are inhibited

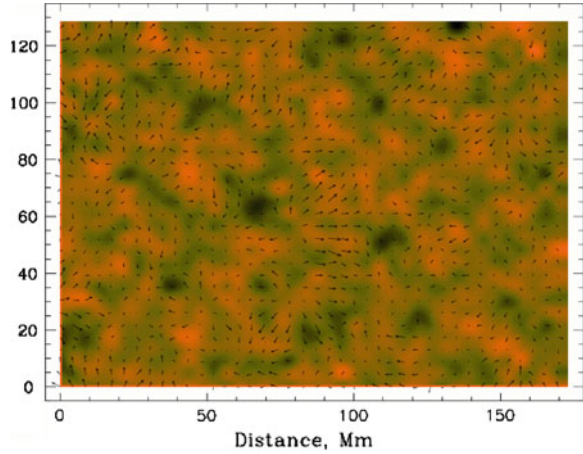
**Fig. 7.4** Discrepancies between the velocity maps obtained from forward and backward propagation times at 1.2 Mm below the visible surface. Some of the largest discrepancies are outlined to show their correlation with strongest magnetic field concentrations



meters given in the model of the convection zone by Spruit (1974): at the depth  $h = 1.2 \text{ Mm}$ ,  $\rho = 0.38 \times 10^{-5} \text{ g cm}^{-3}$ , which gives the estimate for sound speed  $c_s = 14.8 \text{ km s}^{-1}$ ; at  $h = 2.8 \text{ Mm}$ ,  $\rho = 0.36 \times 10^{-4} \text{ g/cm}^3$ , and  $c_s = 18.4 \text{ km s}^{-1}$  (see also Hill 1995, and references therein). For these parameters at  $h = 1.2 \text{ Mm}$ , the upper bound value of magnetic field strength is  $B_{\max} = 3,480 \text{ G}$ ; at  $h = 2.8 \text{ Mm}$ ,  $B_{\max} = 10,760 \text{ G}$ .

As already mentioned, the method allows to obtain the information about the velocity gradients and construct the velocity shear maps. The example of such computation, i.e., the maps of velocity field and the intensity of shear flows,

**Fig. 7.5** The velocity field and the velocity shear at the depth 2.8 Mm,  $D_{\text{hz,max}} \simeq 0.29 \times 10^{-3} \text{s}^{-1}$



$D_{\text{hz}} = \partial u_x / \partial x - \partial u_y / \partial y$ , at the depth 2.8 Mm is shown in Fig. 7.5. Note that at the depth 1.2 Mm, the maximum velocity shear is even higher,  $D_{\text{hz,max}} \simeq 0.67 \times 10^{-3} \text{s}^{-1}$ .

So far we were computing the velocity and magnetic field maps assuming that sound speed and other parameters depend on vertical coordinate in a stepwise manner. In the next section we consider the more general case and take into account the effects of gravity.

## 7.6 Magnetic Corrections in a Vertically Stratified Atmosphere

In this section we generalize the method to the case of a vertically stratified atmosphere. We start from the expression for correction to the propagation time:

$$\delta\tau = - \int_l \frac{dl}{v_{\text{gr}}} \frac{\delta v_g}{v_g} \quad (7.42)$$

where integration is carried out along the unperturbed ray trajectory. From (7.8) we have  $v_g = c_s$ ,  $\delta v_{\text{gr}} = v_A^2 / (2c_s) [1 - (\mathbf{nb})^2]$ . By noting that  $ds/v_g = dz/v_{gz}$ , where  $v_{gz}$  is the vertical component of the group velocity, one finds that

$$\delta\tau = -2 \int_0^h \frac{dz}{v_{gz}} \frac{\delta v_g}{v_g} = - \int_0^h \frac{v_A^2 [1 - (\mathbf{nb})^2] dz}{c_s^3 n_z} \quad (7.43)$$

As earlier,  $h$  is the depth of a layer where reflection of the ray occurs ( $k_z = 0$ ). The factor “2” in (7.43) takes into account two branches of the ray trajectory, descending

and ascending. From the condition  $\omega = \text{const.}$  we have:

$$c_s^2(h)(k_x^2 + k_y^2) = c_s^2(z)(k_x^2 + k_y^2 + k_z^2) \quad (7.44)$$

In the system where  $x$  and  $y$  are ignorable coordinates,  $k_x$  and  $k_y$  are conserved quantities. We have therefore,

$$k_z = \sqrt{k_x^2 + k_y^2} \sqrt{1 - \frac{c_s^2(z)}{c_s^2(h)}} \quad (7.45)$$

and

$$n_z = \sqrt{1 - \frac{c_s^2(z)}{c_s^2(h)}}; \quad n_x = \frac{c_s(z)}{c_s(h)} \cos \theta; \quad n_y = \frac{c_s(z)}{c_s(h)} \sin \theta \quad (7.46)$$

We will take into account both vertical variation of the Alfvén velocity,  $v_A = v_A(z)$ , and the direction of the horizontal magnetic field,  $\theta_B = \theta_B(z)$ . We have:

$$(\mathbf{nb})^2 = \cos^2(\theta - \theta_B) \frac{c_s^2(z)}{c_s^2(h)} \quad (7.47)$$

Taking into account relations (7.43), (7.46) and (7.47) one finds that

$$\delta\tau = - \int_0^h \frac{v_A^2(z) c_s^2(h) [1 - \cos^2(\theta - \theta_B(z))]}{c_s^4(z) \sqrt{c_s^2(h) - c_s^2(z)}} dz \quad (7.48)$$

or

$$\delta\tau = - \int_0^h \frac{v_A^2(z) c_s^2(h) [1 - \cos 2\theta \cos 2\theta_B(z) - \sin 2\theta \sin 2\theta_B(z)]}{c_s^4(z) \sqrt{c_s^2(h) - c_s^2(z)}} dz \quad (7.49)$$

Remarkably, in this much more general case,  $\delta\tau$  still manifests the same  $\cos 2\theta$  and  $\sin 2\theta$  dependence on the azimuthal angle as in the model of a uniform slab.

Recall that in the case of a uniform slab  $(\mathbf{nb})^2 = (r^2/4h^2r^+) \cos^2(\theta - \theta_B)$ ,  $n_z = 2h/\sqrt{4h^2r^+}$ , and one recovers (7.21).

For cosine and sine transforms now, instead of (7.22) and (7.23), we have:

$$\tau_s^{(2)} = \frac{1}{4} \int_0^h \frac{v_A^2(z) c_s^2(h) \sin 2\theta_B(z)}{c_s^4(z) \sqrt{c_s^2(h) - c_s^2(z)}} dz \quad (7.50)$$

$$\tau_c^{(2)} = \frac{1}{4} \int_0^h \frac{v_A^2(z) c_s^2(h) \cos 2\theta_B(z)}{c_s^4(z) \sqrt{c_s^2(h) - c_s^2(z)}} dz \quad (7.51)$$

Probing different annuli, i.e., different reflection depths, and using a standard inversion procedure, one can find by virtue of (7.21) and (7.22) distribution of horizontal magnetic field and its depth dependence.

For known  $c_s(z)$  one can apply Abel inversion to  $\tau_s^{(2)}$  and  $\tau_c^{(2)}$  and obtain in this way both magnitude and direction of the horizontal magnetic field.

Note that one can also solve the problem of the accuracy of reconstruction of sub-surface flows over annular distances which become comparable with characteristic scale of convective motions, granular, mezogranular, and supergranular (Ryutova and Scherrer 1998).

## 7.7 Estimate of the Energy Flux from Time-Distance Analysis

Time-distance measurements in helioseismology can be used to estimate the energy flux on the solar surface (Ryutova 1997). Nonreciprocity of travel times along the ray path and different parity properties of sound speed, flow velocity, and magnetic field allow one to obtain information on large-scale distribution of plasma flows and magnetic fields and their energetics. We shall see that the covariance of sum and difference of the reciprocal travel times is a measure of large-scale, climatological heat flux and that the covariance of sum and difference of their departures from the mean gives an estimate for the magnetic energy flux. Using the reciprocal travel times measured in north–south and west–east directions, one can estimate the latitude- and longitude-dependent energy fluxes.

The procedure is based on the fact that the space-time average of the products,  $\overline{\langle \mathbf{u}c_s^2 \rangle}$  and  $\overline{\langle \mathbf{u}v_A^2 \rangle}$ , which are related, respectively, to large-scale heat flux and magnetic energy flux, can be directly found from time-distance measurements. Indeed, the covariance of sum,  $s = \tau^{(+)} + \tau^{(-)}$  and difference,  $d = \tau^{(+)} - \tau^{(-)}$  is related to the heat flux, while covariance of their departure from the mean,  $(\overline{\Delta s})^2 - (\overline{\Delta d})^2$  is a measure of the magnetic energy flux.

We shall consider large-scale energy fluxes associated with the motions and magnetic field transport over spatial scales comparable to the size of annuli where the measurements are taken and over a time period that is much larger than the characteristic time of magnetic field fluctuations. This is somewhat similar to climatological heat flux measured in ocean tomography (see, e.g., Munk 1986). As in the acoustic monitoring of ocean gyres, solar tomographic measurements can be also used to measure the eddy fluxes: the heat and magnetic energy transport associated with the small-scale flux tubes and rapid motion.

### 7.7.1 Heat and Magnetic Energy Fluxes

Recall that in the approximation of geometrical acoustics the group velocity (7.5) has the form

$$v_{\text{gr}} = c_s + \mathbf{n}\mathbf{u} + \frac{v_A^2}{2kc_s} [1 - (\mathbf{n}\mathbf{b})^2] \quad (7.52)$$

We have already mentioned that the flow velocity and Alfvén speed are much less than the sound speed (7.4), and enter the propagation time  $\tau(\theta)$  as small additions proportional to  $u/c_s$ , and  $v_A^2/c_s^2$ , respectively.

If the duration of observations,  $T$ , is much larger than the period of measured oscillations,  $2\pi/\omega$ , i.e., if

$$\omega T \gg 1, \quad (7.53)$$

one can define the averages over  $T$ , as

$$\begin{aligned} c_s(\mathbf{r}, t) &= \overline{c_{s0}(\mathbf{r})} + \delta c_s(\mathbf{r}, t) \\ u(\mathbf{r}, t) &= \overline{u_0(\mathbf{r})} + \delta u(\mathbf{r}, t) \\ B(\mathbf{r}, t) &= \overline{B_0(\mathbf{r})} + \delta B(\mathbf{r}, t) \end{aligned} \quad (7.54)$$

Time average of the fluctuating parts,  $\delta c_s$ ,  $\delta u$  and  $\delta B$  are zero:

$$\overline{\delta c_s} = 0, \quad \overline{\delta u} = 0, \quad \overline{\delta B} = 0 \quad (7.55)$$

In the first approximation with respect to magnetic and flow effects, the travel time is given by

$$\tau(t) = \int_l \left( \frac{1}{c_{s0}(l)} - \frac{\delta c_s(l, t)}{c_{s0}^2} - \frac{\mathbf{n}[\mathbf{u}_0(l) + \delta \mathbf{u}(l, t)]}{c_{s0}^2} - \frac{v_{A0}^2}{2c_{s0}^3} [1 - (\mathbf{n}\mathbf{b})^2] \right) dl \quad (7.56)$$

To separate the contribution of magnetic field from the velocity, one needs to perform the inversion of the difference,  $d = \tau^+ - \tau^-$ , which yields the simulation of the flow field, and the sum,  $s = \tau^+ + \tau^-$ , that gives the distribution of the temperature. In principle, heat fluxes can be determined through point-by-point multiplication of the inverted flow and temperature fields with the subsequent averaging in space and time, which would be exactly the same as calculating a covariance of  $d$  and  $s$ :  $sd = (\tau^+)^2 - (\tau^-)^2$ , just like in the reconstruction of the flow field by using the first Fourier harmonics of travel times measured as a function of direction and distribution magnetic field patterns using the second harmonics.

Point-by-point multiplication of the two fields would give the average magnetic energy flux. This simply means that if one uses the measured travel times to calculate the covariance of sum and difference of reciprocal travel times and their departures from the mean, one obtains the estimate of heat and magnetic energy fluxes.



To illustrate how the method works, we assume that unperturbed plasma parameters are uniform along the ray path and that the measured ray averages may be considered the range averages. Then travel times in the forward and backward directions can be written as

$$\tau^\pm(t) = \frac{l}{c_{s0}} \left( 1 \mp \frac{u_0}{c_{s0}} - \frac{v_{A0}^2}{2c_{s0}^2} [1 - (\mathbf{nb})^2] + \left\langle -\frac{\delta c_s(l, t)}{c_{s0}} \mp \frac{\delta u}{c_{s0}} \right\rangle \right) \quad (7.57)$$

Taking into account that the mean travel time is  $\tau_0 = l/c_{s0}$ , the deviation of the travel time from the mean value due to the temperature inhomogeneities and presence of mass flows and magnetic fields is obviously

$$\Delta\tau^\pm(t) = \frac{l}{c_{s0}} \left( \mp \frac{u_0}{c_{s0}} - \frac{v_{A0}^2}{2c_{s0}^2} [1 - (\mathbf{nb})^2] + \left\langle -\frac{\delta c_s(l, t)}{c_{s0}} \mp \frac{\delta u}{c_{s0}} \right\rangle \right) \quad (7.58)$$

The time average  $F_B = \overline{uv_A^2}$  is then the measure of the magnetic energy flux over the region where measurements are taken. Bearing in mind that  $c_s^2$  is almost a linear function of temperature, the average  $F_T = \overline{uc_s^2}$  may be considered a measure of the heat flux,  $\overline{uT}$ .

The time average of the above expression is

$$\overline{\Delta\tau^\pm(t)} = \frac{l}{c_{s0}^2} \left( \mp u_0 - \frac{v_{A0}^2}{2c_{s0}^2} [1 - (\mathbf{nb})^2] \right) \quad (7.59)$$

Note that  $\overline{\delta c_s}$  and  $\overline{\delta u}$  vanish due to (7.55). Now we can find the expression for the measure of the magnetic energy flux:

$$F_B = u_0 v_A^2 [1 - (\mathbf{nb})^2] = \frac{c_{s0}^3}{2\tau_0^2} (\overline{\Delta\tau^+}^2 - \overline{\Delta\tau^-}^2) \quad (7.60)$$

Similarly, from (7.57) we obtain the expression for the measure of a heat flux. The time average of (7.57) is:

$$\overline{\tau^\pm(t)} = \frac{l}{c_{s0}^2} \left( c_{s0} \mp u_0 - \frac{v_{A0}^2}{2c_{s0}^2} [1 - (\mathbf{nb})^2] \right), \quad (7.61)$$

The difference in squares of the forward and backward propagation times is then

$$\overline{\tau^+(t)}^2 - \overline{\tau^-(t)}^2 = \tau_0^2 \left( -4 \frac{u_0 c_{s0}}{c_{s0}^2} + 2 \frac{u_0 v_A^2}{c_{s0}^3} \right) \quad (7.62)$$

The last term on right-hand side is a measure of the magnetic energy flux. Using (7.60), we obtain the expression for a heat flux:

$$F_T = \overline{uc_s^2} = -\frac{c_{s0}^3}{4} \frac{(\overline{\tau^{+2}} - \overline{\Delta\tau^{+2}}) - (\overline{\tau^{-2}} - \overline{\Delta\tau^{-2}})}{\tau_0^2} \quad (7.63)$$

Data averaged over the time of observations should represent the natural spatial scales of energy transport over the time comparable to the time of observations. There is, though, the limitation “from below”: the spatial scales cannot be less than the characteristic scale of annuli where measurements are taken. This restriction stems from the ray approximation. The method, however is quite universal and can be used in future improved observational techniques.

### 7.7.2 Contribution of Eddy Fluxes

The eddy fluxes, which are related to the dynamics of the energy transport at small scales, can be calculated by constructing the spatial mean product  $\langle \delta u \delta c_s^2 \rangle$ . For this we use the departure from the time mean:

$$\delta\tau^\pm(t) = \int_l \left( -\frac{\delta c_s^2(l, t)}{2c_{s0}^3} \mp \frac{\delta u}{c_{s0}^2} \right) dl \quad (7.64)$$

The mean square is

$$\overline{(\delta\tau^\pm)^2} = \frac{1}{4c_{s0}^4} \int dl \int ds [\overline{\delta f(l)}][\overline{\delta f(l+s)}] \quad (7.65)$$

where  $f(l) = \delta c_s^2(l) \pm 2c_{s0}\delta u(l)$ . Introducing a correlation length,  $r = \int_{-\infty}^{\infty} ds \rho(s)$ , where  $\rho(s) = \overline{f(l)f(l+s)}/f^2$  we obtain for the mean square

$$\overline{(\delta\tau^\pm)^2} = \frac{[\overline{\delta c_s^2 \pm 2c_{s0}\delta u}]^2}{4c_{s0}^6} lr \quad (7.66)$$

The estimate for the eddy heat flux along a particular ray is then

$$F_{\text{eddy}} = \overline{\langle \delta u \delta c_s^2 \rangle} = \frac{c_s^5}{lr} [(\overline{\delta\tau^+})^2 - (\overline{\delta\tau^-})^2]. \quad (7.67)$$

The same approach can be applied to the travel times measured as a function of direction. In this case, taking sine and cosine convolutions of travel time, we can find the magnetic energy flux provided by small-scale motions,  $F_{\text{eddy}}^B = \langle \delta u \delta v_A^2 \rangle$ , as well.

The merit of this application is that although small-scale granular and mezogranular motions are beyond the resolution of time-distance analysis, their contribution to heat flux can be determined.

### 7.7.3 Reconstruction of Energy Fluxes from Observational Data

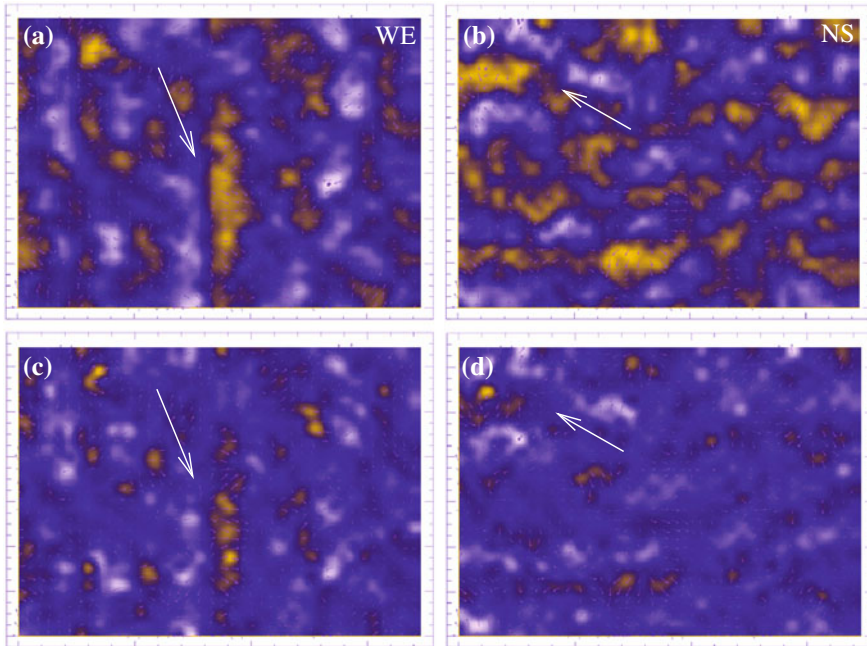
In this section we estimate magnetic energy and heat fluxes (7.60)–(7.63) using the observational data described in the previous section. For the estimate of the energy flux, we use the data sets for westward–eastward (WE) and north–south (NS) times (for observational details, see Duvall et al. 1997). It is important to note that these time sets that are measured in quadrants, cannot be used directly for detecting magnetic fields: according to their parity properties, magnetic fields contribute to the second Fourier harmonics of travel times, and nonconvoluted times are not directly related to magnetic field topology. So that for magnetic field and velocity field measurement one should apply the method described in the previous section. However, although WE and NS times do not give the distribution of the magnetic field, they can be directly used for estimating magnetic energy flux. The result is shown in Fig. 7.6. The two upper panels show the intensity of a heat flux in the west–east (a) and north–south (b) directions. Two lower panels are the intensity of the magnetic energy flux in the west–east (c) and north–south (d) directions. The small arrows on all four panels correspond to the computed velocity field for the depths of 1.2 Mm obtained in Sect. 7.5.

One can see strong correlation between the intensity of a convective heat flux and magnetic energy transport with the direction of mass flows. Note that travel time measurements used for the reconstructed velocity fields and for the energy fluxes are different: the heat and magnetic energy fluxes are computed using both backward and forward propagation times and their departures from the mean; the velocity map is reconstructed from sine and cosine convolutions of travel times measured as a function of direction.

There is also good correlation between the magnetic energy flux and reconstructed magnetic field shown in Fig. 7.2. In all four panels, the brightest yellow patches correspond to the highest flux in the west–east/north–south direction, while the white areas correspond to the strongest flux in the east–west/south–north direction. The white arrows in Fig. 7.6 highlight the essential difference between heat flux (top panels) and magnetic energy flux (bottom panels). Note that the mean of the maximum heat flux,  $\langle F_T \rangle = 1.7 \times 10^{12} \text{ erg cm}^{-2} \text{ s}$ , is larger by an order of magnitude than the magnetic energy flux,  $\langle F_B \rangle = 10^{11} \text{ erg cm}^{-2} \text{ s}$ .

## 7.8 Raman Spectroscopy of Solar Oscillations

Presence of magnetic flux tubes and their interaction with the acoustic waves can form a basis for a new approach in the analysis of helioseismic data. This quite useful analysis can be called “Raman spectroscopy of solar p-modes” (Ryutova 1998). It is based on the fact that interference of oscillating flux tubes with the incoming acoustic wave may result in the generation of beat wave with combination frequency:



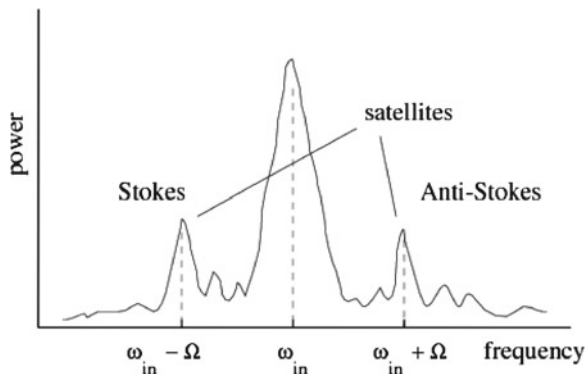
**Fig. 7.6** Reconstruction of the energy flux from observations. **a** Heat flux in the west–east direction,  $|F_T| = 1.84 \times 10^{12} \text{ erg/cm}^2 \text{ s}$ . **b** Heat flux in the north–south direction,  $|F_T| = 1.6 \times 10^{12} \text{ erg cm}^{-2} \text{ s}$ . **c** Magnetic energy flux in the west–east direction,  $|F_B| = 9.5 \times 10^{10} \text{ erg cm}^{-2} \text{ s}$ . **d** Magnetic energy flux in the north–south direction,  $|F_B| = 10.5 \times 10^{10} \text{ erg cm}^{-2} \text{ s}$ . Field of view is the same as in Fig. 7.2

the power spectra of scattered waves in addition to main peak will have Stokes and anti-Stokes satellites (Fig. 7.7). The amplitude and frequency shift of these satellites reflect the properties and the structure of the observed region.

### 7.8.1 Stokes and Anti-stokes Satellites

The presence of the constant level of the solar p-mode fluctuations is a reflection of the dynamic balance between two processes: generation of p-modes by turbulent motions, and their damping by classical and/or anomalous dissipation mechanisms. Observational studies of the acoustic wave properties show that the sources and sinks are distributed nonuniformly over the solar surface. The sources exciting the p-modes (on the average level) are more likely connected with the turbulent motions in the convective zone and, according to the conjecture that was put forward by Brown (1991), may be isolated and thus sources and sinks may well be separated from one another in space and time.

**Fig. 7.7** Sketch of a power spectrum for outgoing wave in Raman scattering. In addition to main peak at the incident frequency, there appear equidistant Stokes and anti-Stokes satellites



Localized sources of the acoustic waves and excess of the acoustic emission compared to the average were observed in the quiet sun regions with the enhanced network of small-scale magnetic flux tubes (Brown 1991; Braun et al. 1992; Braun 1995).

A physical mechanism that may explain the excess of the emission in the quiet Sun is associated with the interaction of p-modes with nonsteady motions, and in particular with the oscillating magnetic flux tubes (see Chap. 3). Note that only nonsteady motions can give rise to the increase in the energy of outgoing waves: the steady-state nonuniformities may cause scattering but not a significant energy increase.

As discussed in Chap. 3, there are two major effects that contribute to this process. One is a *resonance scattering*, when the energy of p-modes propagating in the random ensembles of flux tubes damps out due to the resonance excitation of natural oscillations of magnetic flux tubes. As already discussed transformed energy of p-modes remains for a “long time” in a form of flux tube oscillations. Then, in a time  $\tau_{\text{rad}} \simeq 1/\omega(kR)^2$  the resonant flux tubes radiate the accumulated energy into surrounding plasma. The radiation occurs only if the phase velocity of flux tubes oscillations exceeds the sound speed in the ambient plasma:  $v_{\text{gr}} > c_{\text{se}}$  (Chap. 6).

Another effect works in the opposite case when  $v_{\text{gr}} < c_{\text{s}}$ , and is connected with nonlinear coupling of flux tubes oscillations and acoustic waves, which in turn, leads to generation of beat waves with combination frequencies and wavenumbers:

$$\omega_{\text{out}} = \omega_{\text{in}} \pm \Omega, \quad k_{\text{out}} = k_{\text{in}} \pm K \quad (7.68)$$

The frequency shift,  $\Omega$ , does not necessarily correspond to any of the eigenfrequencies of the p-modes. Both,  $\Omega$  and  $K$  are perturbations determined by local properties of medium, and may correspond, for example, to eigenfrequency (and eigenvector) of a “scattering centers.” It is just this process that facilitates appearance of Stokes and anti-Stokes satellites.

The effective distance at which acoustic waves interact with a particular flux tube is of the order of flux tube radius,  $R$ . The main component of pressure perturbation in the vicinity of the magnetic flux is axisymmetric:

$$\delta p \simeq k\xi_{\text{ac}}p; \quad \delta v \simeq \xi_{\text{ac}}kR; \quad \frac{\delta R}{R} \simeq \frac{\delta p}{p} \quad (7.69)$$

This is coupled with  $m = \pm 1$  flux tube motions. The resulting nonlinear drive exists at the scale  $\simeq R$ , has  $m = \pm 1$  symmetry, and can be expressed as the following equivalent displacement:

$$\delta x \simeq \xi_{\text{kink}} k\xi_{\text{ac}} \quad (7.70)$$

Here  $\delta x$  can be conceived as a forcing term for generating the secondary emission.

Assuming that  $\omega = \omega_{\text{in}} \simeq \Omega$ ,  $k_z^{\text{in}} \simeq K_z$ , one finds the following estimate for the power radiated per unit length of flux tube:

$$P_{\text{Raman}} \simeq \frac{\rho c_{\text{se}}^2}{\omega} \left( \frac{R\omega}{c_{\text{se}}} \right)^4 \xi_{\text{kink}}^2 \omega^2 (k\xi_{\text{ac}})^2 \quad (7.71)$$

If the filling factor of the area is  $f$ , then the power scattered by the volume of the size  $L \times L^2$ , is  $f P_{\text{Raman}} L^3$ . Incident acoustic energy flow into the same volume is  $\xi_{\text{ac}}^2 k^2 \rho c_{\text{se}}^3 L^2$ . The ratio of the two is a measure of the excess of the emitted acoustic power:

$$\zeta = fL \left( \frac{R\omega}{c_{\text{se}}} \right)^5 \frac{\xi_{\text{kink}}^2}{R} \quad (7.72)$$

Obviously, a quantity  $\zeta$  has a meaning of the optical depth with respect to the scattering process. Even more power may be emitted by the Raman scattering of acoustic waves in association with the sausage oscillations. In this case the equivalent displacement is

$$\delta x \simeq \frac{R\omega}{c_{\text{se}}} \xi_{\text{sausg}} \xi_{\text{ac}} \quad (7.73)$$

Energy radiated per unit length is

$$P_{\text{Raman}} \simeq \frac{\rho c_{\text{se}}^2}{\omega} \left( \frac{R\omega}{c_{\text{se}}} \right)^2 \xi_{\text{sausg}}^2 \xi_{\text{ac}}^2 \omega^2 \quad (7.74)$$

and the optical depth is

$$\zeta = \sigma L \left( \frac{R\omega}{c_{\text{se}}} \right)^3 \frac{\xi_{\text{sausg}}^2}{R} \quad (7.75)$$

Using the amplitude of satellites and frequency shift one can infer a typical physical parameters of “scattering centers”, and, generally speaking, develop the analysis for the study of the structure of atmosphere through the spectroscopic features of p-modes.

### 7.8.2 Using Raman Spectroscopy in Observations

In this section we give some examples of measured power spectra of incoming and outgoing waves and their possible interpretation, only to demonstrate the principle of the method.

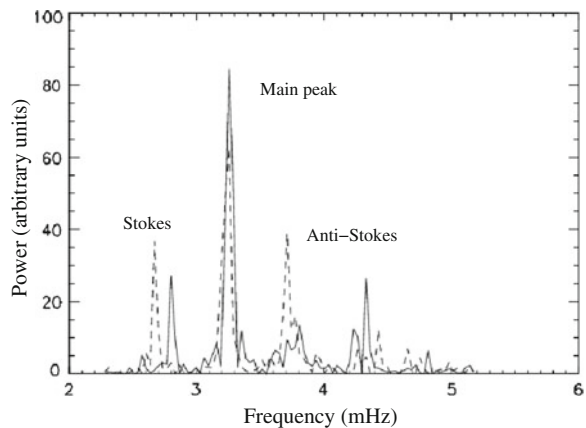
The MDI/SOHO high resolution data were used to compute the series of incoming and outgoing acoustic power for different spherical harmonics employing the Hankel decomposition method (Braun 1995). Some 512 Dopplergrams contributed to this series. The target region was a very quiet sun on the disk center. The annulus had inner and outer radii of 2.5 and 11.25 heliocentric degrees ( $1^\circ = 12.151$  Mm length-of-arc). The power was computed up to  $L = \sqrt{l(l+1)} = 2,016$ .

Figure 7.8 shows example of measured power spectra for incoming (solid line) and outgoing (dashed line) wave for the spherical degree  $l = 452.6$ . The equidistant Stokes and anti-Stokes satellites clearly exceed their counterparts in the incoming power spectrum.

To distinguish a true Stokes and anti-Stokes peaks from closely situated neighboring p-mode ridges, one needs, except fulfillment of equality  $\nu_0 - \nu_- = \nu_0 - \nu_+$ , additional facts which are associated *only* with the Raman scattering and are not related to neighboring acoustic ridges. Most important here is that Stokes frequency shift is determined by physical parameters of a local “scattering centers,” and, in particular is directly associated with an eigenfrequency of oscillating flux tubes. This means that the frequency shifts must not only be equidistant, but should give a reasonable estimate for the Alfvén velocity. For given spherical degree  $\ell$  and frequency  $\nu$  the local sound speed is roughly estimated as (e.g., Hill 1995)

$$c_s(l, \nu) = 2\pi R_\odot \frac{\nu}{l} \quad (7.76)$$

**Fig. 7.8** The measured power spectra for incoming (solid line) and outgoing (dashed line) wave for the spherical degree  $l = 452.6$ . The equidistant Stokes and anti-Stokes satellites clearly exceed their counterparts in the incoming power spectrum



**Table 7.2** The parameters of power spectra and estimates for inferred Alfvén speed

	$P_{\text{in}}$	$P_{\text{out}}$	$\nu$ (MHz)	$\nu_0 - \nu_-$	$\nu_0 - \nu_+$	$c_s$	$v_A$
$\ell = 452.6$	$2.14 \times 10^3$	$1.44 \times 10^4$	$\nu_- = 2.67$	0.55	-0.55	31.1	5.30
	$3.46 \times 10^4$	$2.72 \times 10^4$	$\nu_0 = 3.22$				
	$1.31 \times 10^4$	$3.1 \times 10^4$	$\nu_+ = 3.77$				
$\ell = 699.4$	$4.96 \times 10^3$	$9.9 \times 10^3$	$\nu_- = 2.6$	0.60	-0.60	20.0	3.75
	$3.52 \times 10^4$	$3.51 \times 10^4$	$\nu_0 = 3.20$				
	$2.75 \times 10^4$	$4.48 \times 10^4$	$\nu_+ = 3.8$				
$\ell = 740.6$	$1.54 \times 10^4$	$1.69 \times 10^4$	$\nu_- = 2.7$	0.62	-0.62	19.6	3.66
	$2.32 \times 10^4$	$5.9 \times 10^4$	$\nu_0 = 3.32$				
	$2.78 \times 10^4$	$3.25 \times 10^4$	$\nu_+ = 3.94$				

In conclusion we may summarize some rules in practical use of Raman spectroscopy. The power spectrum of outgoing waves in addition to main

In the subsurface layers Alfvén velocity is small compared to sound speed, therefore the phase velocities of both kink and sausage mode of flux tube oscillations, is close to the Alfvén speed, i.e.,

$$v_{\text{gr}} = \frac{\Omega}{k} \simeq v_A \quad (7.77)$$

Assuming that the wave number is approximately the same as that of incident acoustic wave we can express it through sound speed from (7.76):

$$v_A \simeq \frac{\Omega}{\omega_{\text{in}}} c_s(l, \nu) \quad (7.78)$$

Examples of the parameters of power spectra, calculated sound speed and inferred Alfvén velocity are given in Table 7.2.  $P_{\text{in}}$  and  $P_{\text{out}}$  are values of net averaged powers (in arbitrary units). The averaging is done over a narrow frequency interval (0.23 MHz) near the peaks in outgoing power spectrum for first three cases,  $\ell = 452.6$ ; 699.4 and 740.6. In all three cases the satellite peaks in outgoing power spectra which exceed their counterparts in the incoming power spectra, are shifted, as it must be, equally from the central peak. Peak at incident frequency, must contain *equidistant* Stokes and anti-Stokes satellites. The emitted power is proportional to magnetic filling factor and *size* of the observed area. It is more sensitive to small parameter  $(kR)^2$  than the power radiated, for example, by resonant flux tubes, which, in addition may have incoherent character. Besides, in contrast to the resonance case where the condition  $(kR)^2 \ll 1$  is required, here the parameter  $(kR)^2$  may be finite. Therefore, large regions of flux tubes, comparable with the acoustic wavelength, will contribute to Raman scattering most readily, and will be easier to analyze. Good candidates here are the quiet photospheric network near plages and regions containing small pores.

Finally, it must be noted that the methods of time-distance analysis have proved to be very useful instrument in reconstructing the observational data to test the con-



ditions under the solar surface, and, as we discussed above, to perform additional analysis of the atmospheric structure.

During the last decades the helioseismic approach has been generalized in many ways (Gizon and Birch 2005; Couvidat et al. 2006; Schad et al. 2013). One can apply its methods to various problems from probing the subsurface filamentary structure of sunspots and field inclination (Schunker et al. 2005; Cameron et al. 2011; Felipe et al. 2014) to testing the far-side helioseismic maps (Lindsey and Braun 2000; Zhao 2007; Gonzalez-Hernandez et al. 2013).

It must be noted again that this chapter deals only with the role of small-scale magnetic flux tubes in helioseismology.

## References

- D.C. Braun, *Astrophys. J.* **451**, 859 (1995)  
 D.C. Braun, C. Lindsey, Y. Fan, S.M. Jefferies, *Astrophys. J.* **392**, 739 (1992)  
 T.M. Brown, *Astrophys. J.* **371**, 396 (1991)  
 T.M. Brown, T.J. Bogdan, B.W. Lites, J.H. Thomas, *Astrophys. J.* **394L**, 65 (1992)  
 R.H. Cameron, L. Gizon, H. Schunker, A. Pietarila, *Sol. Phys.* **268**, 293 (2011)  
 S. Couvidat, A.C. Birch, A.G. Kosovichev, *Astrophys. J.* **640**, 516 (2006)  
 T.L. Duvall Jr., S.M. Jefferies, J.W. Harvey, M.A. Pomerantz, *Nature* **362**, 430 (1993)  
 T.L. Duvall Jr., S. D'Silva, S.M. Jefferies, J.W. Harvey, J. Schou, *Nature* **379**, 235 (1996)  
 T.L. Duvall Jr et al., *Sol. Phys.* **170**, 63 (1997)  
 T. Felipe, A.D. Crouch, A.C. Birch, *Astrophys. J.* **788**, 136 (2014)  
 L. Gizon, A.C. Birch, *Local helioseismology. LRSP* (2005)  
 I. Gonzalez-Hernandez et al., *J. Phys. Conf. Ser.* **440a**, 2029 (2013)  
 F. Hill, *Helioseismology, in 4th SOHO Workshop, ESA, vol. 63* (1995)  
 C. Lindsey, D.C. Braun, *Science* **287**, 1799 (2000)  
 W. Munk, *J. Fluid Mech.* **173**, 43 (1986)  
 M. Ryutova, *Astrophys. J.* **490L**, 111 (1997)  
 M. Ryutova, *IAUS* **185**, 213 (1998)  
 M. Ryutova, P. Scherrer, *Astrophys. J.* **494**, 438 (1998)  
 A. Schad, J. Timmer, M. Roth, *Astrophys. J.* **78**, L38 (2013)  
 H. Schunker et al., *Astrophys. J.* **621**, L149 (2005)  
 H.C. Spruit, *Sol. Phys.* **34**, 277 (1974)  
 J. Zhao, *Astrophys. J.* **664**, L139 (2007)

# Chapter 8

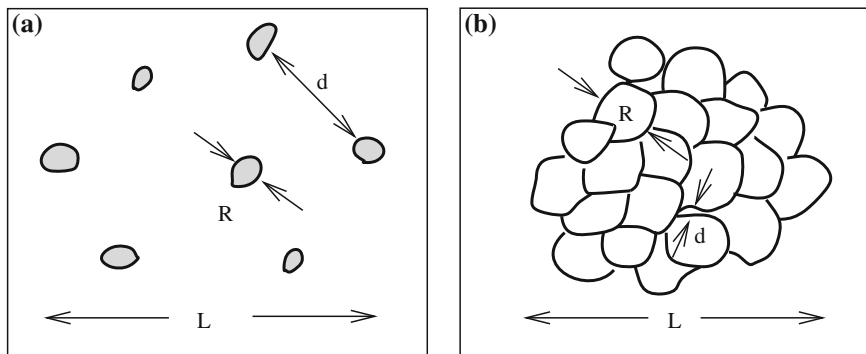
## Wave Phenomena in Dense Conglomerate of Flux Tubes

**Abstract** In this chapter, we shall consider the properties of strongly magnetized regions of the sun such as sunspots, pores, and active regions, where random magnetic flux tubes form a dense conglomerates. Physical processes and, in particular, the wave phenomena in closely packed flux tubes exhibit some distinct features that are observable and can be used for testing the structure and energetics of these regions. One of the most pronounced effects is the strong enhancement of the dissipation of the incoming wave energy, caused by large local gradients of velocity, temperature, and pressure arising at borders of neighboring small-scale inhomogeneities.

### 8.1 Propagation of MHD Waves in an Ensemble of Closely Packed Flux Tubes

In the previous chapters, we studied the response of a rarefied ensembles of random magnetic flux tubes to the propagation of acoustic waves and unsteady wave packets, typical to quiet sun areas (Fig. 8.1a). Unlike quiet photosphere, sunspots and active regions represent a dense conglomerate of flux tubes (Fig. 8.1b) where all the parameters of the medium (magnetic field, plasma density, temperature, etc.) change from one domain to another by an order of magnitude (see e.g. Livingston 1991). The dynamics of these two different types of ensembles, and, in particular, their response to propagation of acoustic and MHD waves, are very different. The dispersion properties and the observational spectroscopy of these regions, as well as the mechanisms of energy transfer from the photosphere to the upper layers of the atmosphere are also very different.

The most striking effect here is that sunspots, pores, and active regions act as a sink of incoming wave energy. This phenomenon is similar to the enhanced dissipation in polycrystals considered many years ago by Zener (1937) and Isakovich (1948), and widely used in modern buildings by use of porous materials in order to reduce the noise. For sunspots and other densely magnetized regions, the effect of enhanced absorption of incoming wave power was first described by Ryutova and Persson (1984) and measured independently by Braun et al. (1987, 1988, 1990). The theory later was extended and complemented by numerical analysis (Ryutova et al. 1991).



**Fig. 8.1** Classes of ensembles of magnetic flux tubes: **a** Widely spaced flux tubes with small magnetic filling factor typical to quiet sun. **b** Dense conglomerate of random flux tubes with magnetic filling factor of the order of unity typical to sunspots

Strong enhancement of the wave dissipation occurs due to the presence of closely packed random flux tubes with characteristic radius,  $R$ , much smaller than the wavelength:

$$d \ll R \ll \lambda \quad (8.1)$$

where  $d$  is a small gap between the flux tube comprising the sunspot. The efficiency of enhanced dissipation is of the order of  $\lambda/R \gg 1$ .

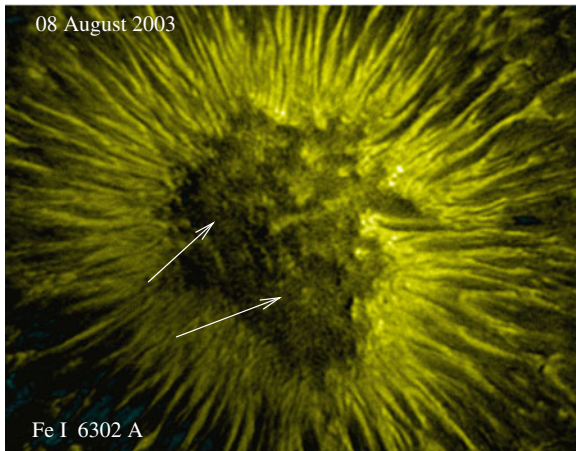
The physical reason for this effect can be easily understood. Since all the plasma parameters change from tube to tube, and tubes have common boundaries, the velocity amplitude of perturbations as well as all other perturbed quantities are different in different flux tubes. This results in appearance of *strong local gradients* of all the plasma parameters at much smaller scales. In other words, the MHD equations now contain a *Vortex part* of these parameters leading to much stronger dissipation of the wave energy compared to homogeneous medium.

The characteristic scale of *local gradients* is naturally of the order of the tube radius—the scale of the inhomogeneities at which the dissipative effects are enhanced. The damping rate, and the very process of absorption, can be quite different in different regions, and is largely determined by the level of the fluctuations of the background plasma parameters and their time and spatial scales. Inside the sunspot physical parameters, as already mentioned, change from one small domain to another by the order of unity. Figure 8.2 shows high-resolution image of a typical well-shaped sunspot. Excellent contrast achieved in Fe I 6302 Å line shows densely packed individual flux tubes inside the umbra (white arrows) surrounded by a beautiful penumbra.

### 8.1.1 Basic Equations and Dispersion Relation

We begin with the linear theory following the original approach by Ryutova and Persson (1984), and describe a formalism that allows to study the propagation of long

**Fig. 8.2** Sunspot umbra densely packed by small-scale magnetic flux tubes (*white arrows*) is surrounded by filamentary penumbra. Magnetogram of the sunspot AR 425 is taken with the Swedish 1-m Solar Telescope (SST) in Fe I 6302 Å line. Reprinted from <http://www.isf.astro.su.se>. Credit G. Scharmer and K. Langhans, ISP, Sweden



MHD waves in an inhomogeneous plasma. We consider the case where unperturbed magnetic field is concentrated in vertical flux tubes with  $z$ -axis directed along the field, and consider the MHD waves propagating *across* the system of magnetic flux tubes.

The unperturbed parameters of plasma,  $B_0(x, y)$ , and  $\rho_0(x, y)$   $p_0(x, y)$  are assumed to be stationary. This means that the inhomogeneities belong to the class of the so-called entropy inhomogeneities, in which the total pressure  $P_0$  is constant

$$P_0 = p_0(x, y) + \frac{B_0^2(x, y)}{8\pi} = \text{const.} \quad (8.2)$$

But local temperature, density, and magnetic field vary each by the order of unity.

The lifetime of such inhomogeneities is determined by the thermal conductivity and the diffusion, which are quite slow varying quantities in a photospheric plasma.

Consider small linear perturbations of all physical parameters, including the entropy,  $S(x, y, t)$ , i.e., assume that

$$\begin{aligned} p &= p_0(x, y) + \delta p(x, y, t) \\ B &= B_0(x, y) + \delta B(x, y, t) \\ \rho &= \rho_0(x, y) + \delta \rho(x, y, t) \\ S &= S_0(x, y) + \delta S(x, y, t) \\ \mathbf{v} &= \delta \mathbf{v}(x, y, t) \end{aligned} \quad (8.3)$$

It is convenient to introduce the displacement vector:

$$\mathbf{v} = \frac{\partial \boldsymbol{\xi}}{\partial t} \quad (8.4)$$

Substituting these into the 2D ideal MHD system and neglecting terms higher than the first order perturbations we obtain

$$\rho_0 \frac{\partial^2 \delta \xi}{\partial t^2} = -\nabla \left( \delta p + \frac{B_0 \delta B}{4\pi} \right) \tag{8.5}$$

$$\delta \rho + \text{div}(\rho_0 \xi) = 0 \tag{8.6}$$

$$\delta B + \text{div}(B_0 \xi) = 0 \tag{8.7}$$

$$\frac{\delta p}{p_0} - \gamma \frac{\delta \rho}{\rho_0} + \xi \left( \frac{\nabla p_0}{p_0} - \gamma \frac{\nabla \rho_0}{\rho_0} \right) = 0 \tag{8.8}$$

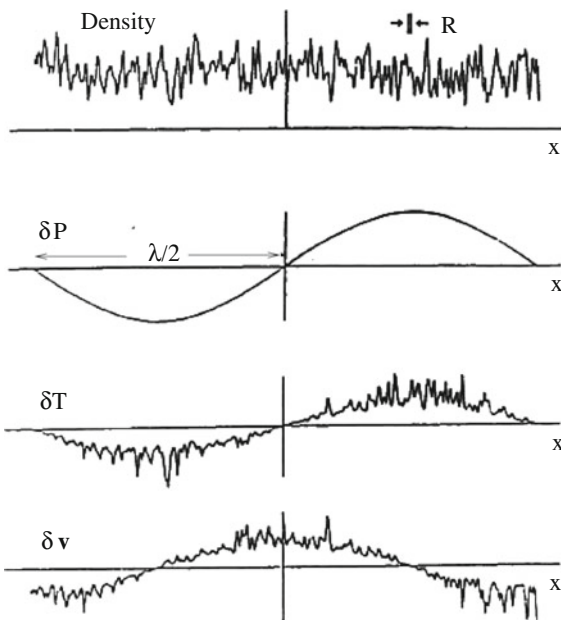
The last equation describes the entropy perturbations. We consider harmonic oscillations, proportional to  $\exp(-i\omega t)$ , and replace  $\partial/\partial t$  by  $-i\omega$ .

We are considering a motion with a scale  $\lambda \gg R$ . At the same time, the scale over which we average the equations of motion,  $l$ , is much larger than  $R$ , i.e.,

$$R \ll l \ll \lambda. \tag{8.9}$$

This means that at the scale  $l$  the compression of the plasma may be considered as a quasi-stationary one, that is,  $\delta P$  is almost a constant, even though  $\rho_0$  and  $\xi$  change by the order of unity at even smaller scale  $R \ll l$ . Figure 8.3 shows the basic approach in spatial variations of plasma parameters in field of wave with  $\lambda \gg R$ . Indeed, as

**Fig. 8.3** Sketch of the spatial variation of plasma parameters in the presence of the long wave. The initial state of the sunspot (or any other dense conglomerate of magnetic elements) has large amplitude density and magnetic field variation on the scale of flux tubes,  $R$ . The incident wave sets up a total pressure perturbations  $\delta P$  on the much larger scale  $\lambda$ . The temperature and velocity respond to the wave with amplitude  $\delta T$  and  $\delta v$  that depend on small-scale structure and thus have many small regions of high gradients (cf. Fig. 8.2)



one can see from (8.5), the change of  $\delta P$  at the scale  $l$  is of the order of  $\rho_0|\xi|\omega^2 l$ , where  $\omega \sim c_s \lambda$  is characteristic frequency of oscillations,  $c_s$  being the sound speed. In other words, the change of  $\delta P$  at the smallest possible averaging scale  $l \sim R$  is as small as  $\rho_0|\xi|\omega^2 R$ , while the change of  $\delta P$  at a scale  $\lambda$  is much larger:

$$\delta P \sim \rho_0|\xi|\omega^2 \lambda. \quad (8.10)$$

Using the equilibrium condition (8.2), from (8.5)–(8.8) we have

$$\delta p = \gamma p_0 \operatorname{div} \xi - \xi \nabla p_0 \quad (8.11)$$

$$\delta B = -B_0 \operatorname{div} \xi - \xi \nabla B_0 \quad (8.12)$$

$$\delta P = -2 \left[ \left( \frac{\gamma}{2} - 1 \right) p_0 + P_0 \right] \operatorname{div} \xi \quad (8.13)$$

Taking into account estimate (8.10), it is obvious from (8.13) that

$$\operatorname{div} \xi \sim \frac{|\xi|}{\lambda} \quad (8.14)$$

and there are *no large terms* of the order of  $|\xi|/R$  in  $\operatorname{div} \xi$ .

It is, however, important that from (8.13) one cannot say anything about the magnitude of the divergence-free part of  $\xi$ . On the other hand, from (8.5) we have

$$\nabla \times \xi = \frac{1}{\omega^2 \rho_0^2} [\nabla \rho_0 \times \nabla \delta P] \quad (8.15)$$

For  $\nabla \delta P$ , (8.10) gives the estimate  $|\nabla \delta P| \sim \omega^2 |\xi| \rho_0$ . As for an inhomogeneous plasma  $|\nabla \rho_0| \sim \rho_0/R$ , we find from (8.15) that

$$|\nabla \times \xi| \simeq \frac{|\xi|}{R}, \quad (8.16)$$

This estimate shows that, unlike the case of a homogeneous plasma, in the dense conglomerate of flux tubes the *divergence-free part* (vortex) is very important.

Let us now proceed to the derivation of averaged equations. By expressing  $\operatorname{div} \xi$  in terms of  $\delta P$  from (8.13), and taking the average, we obtain:

$$\operatorname{div} \langle \xi \rangle = \frac{\langle \delta P \rangle}{2} \left\langle \frac{1}{(\gamma/2 - 1)p_0 + P_0} \right\rangle, \quad (8.17)$$

where angular brackets denote averaging over the volume with characteristic size  $l$  ( $R \ll l \ll \lambda$ ). While deriving (8.17) we have taken into account that, up to the small terms of order  $R\lambda$ , we can put  $\langle \delta P \rangle = \delta P$ .

In order to obtain a closed system of equations describing self-consistently large-scale oscillations in an inhomogeneous plasma, in addition to (8.17) we need to add another equation expressing  $\langle \xi \rangle$  in terms of  $\langle \delta P \rangle$ . From (8.5) we have

$$\xi = \frac{1}{\omega^2 \rho_0} \nabla \delta P \quad (8.18)$$

As shown above,  $\text{div} \xi \ll |\nabla \times \xi|$ . This means, that taking the divergence of (8.18), we can neglect the left-hand side of resulting equation and write the following approximate relation:

$$\text{div} \left( \frac{\nabla \delta P}{\rho_0} \right) \simeq 0 \quad (8.19)$$

Let us introduce the notations:

$$\delta \tilde{P} = \delta P - \langle \delta P \rangle, \quad \tilde{q} = q - \langle q \rangle \quad (8.20)$$

where  $q = 1/\rho$ . It follows from (8.19) that

$$\text{div}(q \delta \tilde{P}) = \nabla \langle \delta P \rangle \cdot \nabla q \quad (8.21)$$

This equation together with the condition  $\langle \delta \tilde{P} \rangle = 0$  uniquely determines  $\delta \tilde{P}$ .

By averaging (8.18), we obtain:

$$\langle \xi \rangle = \frac{1}{\omega^2} \left[ \langle q \nabla \delta P \rangle + \langle \tilde{q} \rangle \langle \nabla \delta \tilde{P} \rangle \right]. \quad (8.22)$$

Since in (8.21), which is linear, the right-hand side is proportional to  $\nabla \langle \delta P \rangle$ , we can write

$$\langle \tilde{q} \nabla \delta \tilde{P} \rangle_\alpha = Q_{\alpha\beta} \nabla_\beta \langle \delta P \rangle \quad (8.23)$$

where  $Q_{\alpha\beta}$  is a tensor whose symmetry is determined by the symmetry of the fluctuations of  $q = 1/\rho_0$ . For example, if statically, there is not any selected direction in the  $xy$ -plane, then obviously,  $Q_{\alpha\beta} = q \delta_{\alpha\beta}$ , where  $Q$  is constant. If the level of fluctuations is of the order of unity, i.e.,  $\langle \tilde{q}^2 \rangle \sim \langle q \rangle^2$ , then  $Q$  is of the order  $\langle q \rangle$ .

Finally, using (8.22) and (8.23) we obtain

$$\langle \xi \rangle_\alpha = \frac{1}{\omega^2} \left[ \langle q \rangle \delta_{\alpha\beta} + Q_{\alpha\beta} \right] \cdot \nabla_\beta \langle \delta P \rangle. \quad (8.24)$$

Equation (8.24), together with (8.17), form a closed system which defines all the properties of the linear long-wave oscillations propagating through the dense conglomerate of random flux tubes. For spatially harmonic wave proportional to  $\exp(i\mathbf{k} \cdot \mathbf{r})$ , these equations lead directly to the dispersion relation:

$$\omega^2 = 2 \left\langle \frac{1}{(\gamma/2 - 1)p_0 + P_0} \right\rangle^{-1} \left[ \left\langle \frac{1}{\rho_0} \right\rangle k^2 + Q_{\alpha\beta} k_\alpha k_\beta \right]. \quad (8.25)$$

It must be noted that this dispersion relation can be directly used for the diagnostic goals when measuring  $\omega(k_x, k_y)$  diagrams, which allows to reconstruct the morphological map of studied region.

The normalized phase velocity corresponding to this dispersion relation (8.25) can be represented as follows:

$$v_{\text{ph}} = \frac{\omega}{k} = \left\langle \frac{1}{\rho(c_s^2 + v_A^2)} \right\rangle^{-1/2} \left( \left\langle \frac{1}{\rho} \right\rangle + Q_{\alpha\beta} \frac{k_\alpha k_\beta}{k^2} \right)^{1/2} \quad (8.26)$$

To find  $Q_{\alpha\beta}$ , one needs to solve (8.21), which, in most cases, cannot be done analytically. Example of two-dimensional case where analytical solution is possible, is given in the next section.

### 8.1.2 Spacial Cases

In a two-dimensional case (8.21) can be analytically solved if we assume that density inhomogeneities are small, i.e.,  $\tilde{q} \ll q$ . Then (8.21) can be written as

$$\langle q \rangle \Delta \delta \tilde{P} = -\nabla \langle \delta P \rangle \cdot \nabla \tilde{q} \quad (8.27)$$

where we have neglected the term  $\langle \tilde{q} \nabla \delta \tilde{P} \rangle \sim \tilde{q}^2$ .

Using the Fourier transformation

$$\tilde{q} = \frac{1}{2\pi} \int e^{i\mathbf{k}\cdot\mathbf{x}} \tilde{q}_{\mathbf{k}} d^2\mathbf{k}, \quad (8.28)$$

we find that

$$\delta \tilde{P}_{\mathbf{k}} = \frac{i\mathbf{k}}{\langle q \rangle k^2} \nabla \langle \delta P \rangle \cdot \tilde{q}_{\mathbf{k}}, \quad (8.29)$$

then

$$\langle \tilde{q} \nabla \delta \tilde{P} \rangle = \frac{1}{(2\pi)^2} \left\langle \iint d^2\mathbf{k}_1 d^2\mathbf{k}_2 e^{i(\mathbf{k}_1+\mathbf{k}_2)\cdot\mathbf{r}} \cdot \tilde{q}_{\mathbf{k}_1} \tilde{q}_{\mathbf{k}_2} \frac{\mathbf{k}_2(\mathbf{k}_2 \cdot \nabla \langle \delta P \rangle)}{\langle q \rangle \mathbf{k}_2} \right\rangle \quad (8.30)$$

Using the formula

$$\langle e^{i(\mathbf{k}_1+\mathbf{k}_2)\cdot\mathbf{r}} \rangle = \frac{4\pi^2}{L^2} \delta(\mathbf{k}_1 + \mathbf{k}_2) \quad (8.31)$$

where  $L$  is normalization length, we obtain

$$\langle \tilde{q} \nabla \delta \tilde{P} \rangle = - \int d^2\mathbf{k} (\tilde{q}^2)_{\mathbf{k}} \frac{\mathbf{k}(\mathbf{k} \cdot \nabla \langle \delta P \rangle)}{\langle q \rangle \mathbf{k}} \quad (8.32)$$



here

$$\langle \tilde{q}^2 \rangle_{\mathbf{k}} \equiv \frac{1}{L^2} |\tilde{q}_{\mathbf{k}}|^2 \quad (8.33)$$

is the spectral density of fluctuations. We used here the identity  $q_{\mathbf{k}} \equiv q_{-\mathbf{k}}^*$ , as  $q(\mathbf{r})$  is a real function.

Using now relation  $\langle \tilde{q}^2 \rangle_{\mathbf{k}} \simeq [(\tilde{\rho}^2)_{\mathbf{k}} / \langle \rho_0 \rangle^4]$ , we obtain the following expression for the correlation function

$$\langle \tilde{q} \nabla \delta \tilde{P} \rangle = -\frac{1}{\langle \rho_0 \rangle^4} \int d^2 \mathbf{k} (\tilde{\rho}_0^2)_{\mathbf{k}} \frac{\mathbf{k}(\mathbf{k} \cdot \nabla \langle \delta P \rangle)}{\langle q \rangle_{\mathbf{k}^2}} \quad (8.34)$$

Thus, up to the terms of the order of  $\tilde{\rho}_0^2$ ,

$$Q_{\alpha\beta} = -\frac{1}{\langle \rho_0 \rangle^3} \int d^2 \mathbf{k} (\tilde{\rho}_0^2)_{\mathbf{k}} k_{\alpha} k_{\beta} \quad (8.35)$$

Finally, we need an expression for the fluctuating part of the displacement vector  $\tilde{\xi} = \xi - \langle \xi \rangle$ . With accuracy up to the terms linear in  $\tilde{\rho}$  we have; see (8.18):

$$\tilde{\xi} = \frac{1}{\omega^2 \tilde{\rho}_0} \left[ \nabla \delta \tilde{P} - \frac{\tilde{\rho}_0}{\langle \rho_0 \rangle} \nabla \langle \delta P \rangle \right], \quad (8.36)$$

where  $\delta \tilde{P}$  is related to  $\tilde{\rho}_0$  by (8.29).

For isotropic fluctuations  $Q_{\alpha\beta} = 0$ , and the dispersion relation (8.25) acquires an especially simple form:

$$\omega^2 = 2 \left\langle \frac{1}{(\gamma/2 - 1)p_0 + P_0} \right\rangle^{-1} \left\langle \frac{1}{\rho_0} \right\rangle k^2. \quad (8.37)$$

## 8.2 Dissipative Processes

In the MHD approximation, there are three major sources of damping of magnetoacoustic waves in plasma: viscosity, thermal conductivity, and Ohmic losses. In most cases the damping is slow, i.e., the damping rate  $\Gamma$  is much smaller than the frequency of oscillations. Thus, we can write

$$\Gamma = \frac{\bar{Q}_{\text{visc}} + \bar{Q}_{\text{therm}} + \bar{Q}_{\text{ohm}}}{2W} \quad (8.38)$$

where  $W$  is the energy density of oscillations and  $\bar{Q}$  is the energy dissipated per unit time and averaged over the space period of the wave.

To be more specific, we will perform the calculations for the case, which is characteristic to solar atmosphere, where  $\omega_i \tau_i \gg 1$ ,  $\tau_i$  and  $\omega_i = eB/m_i c$  being ion collision time and ion gyrofrequency.

We therefore can use standard relations (Braginskii 1965):

$$Q_{\text{visc}} = Q_{\text{visc}}^{(1)} + Q_{\text{visc}}^{(2)} \quad (8.39)$$

with

$$Q_{\text{visc}}^{(1)} = \left( \frac{1}{3} \eta_0 - \eta_1 \right) (\text{div } \delta \mathbf{v})^2 \quad (8.40)$$

$$Q_{\text{visc}}^{(2)} = \frac{1}{2} \eta_1 \left( \frac{\partial v_\alpha}{\partial x_\beta} + \frac{\partial v_\beta}{\partial x_\alpha} \right)^2 \quad (8.41)$$

where

$$\eta_0 = 0.96 n T \tau_i, \quad \eta_1 = \frac{\eta_0}{3} \frac{1}{2(\omega_i \tau_i)^2}, \quad \tau_i = \frac{3}{4} \sqrt{\frac{m_i}{\pi}} \frac{T^{3/2}}{\Lambda e^4 n} \quad (8.42)$$

and  $\Lambda$  is a Coulomb logarithm. Further

$$Q_{\text{therm}} = \frac{\chi}{T} (\nabla \delta T)^2; \quad \chi = \frac{2nT}{m_i \omega_i^2 \tau_i} \quad (8.43)$$

with  $\chi$  being the thermal conductivity. Here, we have assumed that in an unperturbed state the temperature is homogeneous and one can neglect terms of the type  $(\delta \chi / T) \nabla \delta T \cdot \nabla T_0$  in  $Q_{\text{therm}}$ .

### 8.2.1 Weakly Inhomogeneous Medium

We start with the estimate of the damping rate for a homogeneous plasma. We shall see that the terms with small or no effect on the damping rate in homogeneous plasma become very large in the presence of closely packed flux tubes.

The main contribution to damping rate  $\Gamma$  in homogeneous plasma comes from the first term in (8.40), since it does not contain a small parameter  $(\omega_i \tau_i)^{-2}$ , and can be estimated as

$$Q_{\text{visc}}^{(1)} \simeq n T \tau_i \frac{\delta v^2}{\lambda^2} \quad (8.44)$$

while the contribution from the second term in (8.40) is  $(\omega_i \tau_i)^2$  times smaller:

$$Q_{\text{visc}}^{(2)} \simeq \frac{n T \tau_i}{(\omega_i \tau_i)^2} \frac{\delta v^2}{\lambda^2} \quad (8.45)$$

Since  $\delta T$  is of the order of  $T_0(\delta v/\omega\lambda)$ ,  $Q_{\text{therm}}$  is of the same order as  $Q_{\text{visc}}^{(2)}$ , i.e.,  $(\omega_i\tau_i)^2$  times smaller than the viscous dissipation due to  $\eta_0$ , and also can be ignored.

The Ohmic dissipation is estimated as follows:

$$Q_{\text{ohm}} \simeq \left(\frac{c}{4\pi}\right)^2 \frac{\delta B^2}{\sigma\lambda^2} \quad (8.46)$$

where  $\sigma \sim \omega_{\text{pe}}^2\tau_e/4\pi$  is the plasma conductivity.

Now we can estimate the ratio of  $Q_{\text{ohm}}$  to  $Q_{\text{visc}}^{(2)}$ , bearing in mind that  $\delta B$  is of the order of  $(B_0/\omega\lambda)$ :

$$\frac{Q_{\text{ohm}}}{Q_{\text{visc}}^{(2)}} \simeq \sqrt{\frac{m_e}{m_i}} \frac{1}{\beta_0} \quad (8.47)$$

where  $\beta_0 = 8\pi p_0/B_0^2$  is plasma beta in the unperturbed state. That is, for not too small  $\beta_0$ ,  $Q_{\text{ohm}}$  is much smaller than  $Q_{\text{visc}}^{(2)}$  and  $Q_{\text{therm}}$ , and even more so with respect to  $Q_{\text{visc}}^{(1)}$ .

Consequently, the damping rate is essentially determined only by  $Q_{\text{visc}}^{(1)}$ :

$$\Gamma \simeq \frac{Q_{\text{visc}}^{(1)}}{W} \quad (8.48)$$

As the estimate for the energy density is

$$W \simeq m_i n \delta v^2, \quad (8.49)$$

we obtain the following estimate for  $\Gamma$ :

$$\Gamma \simeq \frac{T\tau_i}{m_i\lambda}. \quad (8.50)$$

The reason why the damping rate in a plasma with small-scale inhomogeneities may become much larger than that given by (8.50), is that in such a case all perturbed quantities ( $\delta\tilde{v}$ ,  $\delta\tilde{B}$ ,  $\delta\tilde{T}$  etc.) have a component that changes *not at a scale*  $\lambda$ , but at a scale  $R$ , so that all the spatial derivatives in (8.39)–(8.43) become much larger than for waves traveling in a homogeneous plasma.

Assuming that inhomogeneities are of the order of unity,  $\tilde{\rho} \simeq \rho$ , one can expect that all dissipative terms increase by the factor  $(\lambda/R)^2 \gg 1$ .

Note, however, that the main dissipative term,  $Q_{\text{visc}}^{(1)}$ , does not increase in the inhomogeneous case. This happens because it is proportional to  $(\text{div } \delta v)^2$  and, as it has been shown in Sect. 5.1,  $(\text{div } \delta v)$  is of the order of  $\delta v/\lambda$  even in the case of an inhomogeneous plasma. Therefore, the enhancement of dissipation comes only from terms  $Q_{\text{visc}}^{(2)}$  and  $Q_{\text{therm}}^{(1)}$ .

Although the dissipation in homogeneous case, caused by  $Q_{\text{visc}}^{(2)}$  and  $Q_{\text{therm}}^{(1)}$  is much less than by  $Q_{\text{visc}}^{(1)}$ , in some cases of an inhomogeneous plasma it can be quite large, resulting in a much faster damping than that determined by (8.50). This will be discussed in the next section.

### 8.2.2 Medium with Moderate and Strong Inhomogeneities

Even though the main dissipation term does not increase, the terms  $Q_{\text{visc}}^{(2)}$  and  $Q_{\text{therm}}^{(1)}$  increase by a factor  $(\lambda/R)^2 \tilde{\rho}_0/\rho_0$ , where  $\tilde{\rho}_0$  is the characteristic amplitude of the inhomogeneities; see (8.20). Thus, if

$$\frac{\lambda}{R} \frac{\tilde{\rho}_0}{\rho_0} > \omega_i \tau_i, \quad (8.51)$$

$Q_{\text{visc}}^{(2)}$  and  $Q_{\text{therm}}^{(1)}$  become much larger than  $Q_{\text{visc}}^{(1)}$ , resulting in the significant enhanced dissipation of an incoming wave power.

Thus, under condition (8.51), the energy dissipation is determined by the sum  $Q_{\text{visc}}^{(2)} + Q_{\text{therm}}$ , and can be estimated as

$$Q_{\text{visc}}^{(2)} + Q_{\text{therm}} \simeq \frac{nT\tau_i}{(\omega_i\tau_i)^2} \frac{\delta v^2}{R^2} \left(\frac{\tilde{\rho}_0}{\rho_0}\right)^2 \quad (8.52)$$

$Q_{\text{ohm}}$  remains related to  $Q_{\text{visc}}^{(2)}$  by the estimate (8.47) and is thus much smaller than  $Q_{\text{visc}}^{(2)}$ . The damping rate can be found from (8.49) and (8.52):

$$\Gamma \simeq \frac{T\tau_i}{m_i R^2} \frac{1}{(\omega_i\tau_i)^2} \left(\frac{\tilde{\rho}_0}{\rho_0}\right)^2 \quad (8.53)$$

In previous calculations we assumed that initially the plasma was stationary. However, in an inhomogeneous plasma there are processes of thermal conductivity and magnetic field diffusion that tend to reduce inhomogeneities. The shorter of the two is the thermal conductivity time,

$$\tau_{\text{therm}} \simeq \frac{R^2 n}{\chi} \simeq \left[ \frac{T\tau_i}{m_i R^2} \frac{1}{(\omega_i\tau_i)^2} \right]^{-1} \quad (8.54)$$

Consideration of a stationary background in the problem of the absorption of the wave power requires the condition  $\Gamma\tau_{\text{therm}} \gg 1$  to be satisfied. However, from (8.53) and (8.54) it is obvious that  $\tau_{\text{therm}}$  is always much smaller than  $\Gamma^{-1}$ , which means that the background temperature becomes homogeneous much earlier than the wave is damped. This is just the reason why we assumed that the plasma in the initial state has a homogeneous temperature; see discussion following (8.43).

The diffusion of the magnetic field occurs over a time scale

$$\tau_{\text{diff}} \simeq \frac{4\pi R^2 \sigma}{c^2} \simeq \tau_{\text{therm}} \sqrt{\frac{m_i}{m_e}}, \quad (8.55)$$

(we consider the case when plasma  $\beta \simeq 1$ ).

From the condition  $\Gamma_{\text{diff}} \gg 1$ , we obtain the following restriction on plasma parameters:

$$\left(\frac{\tilde{\rho}_0}{\rho_0}\right)^2 \gg \sqrt{\frac{m_e}{m_i}}. \quad (8.56)$$

Assuming that the condition (8.56) is satisfied, we calculate the enhanced damping rate for the plasma with a moderate level of inhomogeneities,  $\tilde{\rho}_0/\langle\rho_0\rangle < 1$ . In the initial stationary state we have a regular equation of state  $p_0(x, y) = (2/m_p)\rho_0(x, y) \cdot T_0(x, y)$ .

Using (8.6)–(8.8) we can express  $\delta T$  through the displacement vector

$$\delta T = -T_0(\gamma - 1)\text{div}\xi \quad (8.57)$$

Now from (8.11)–(8.13) we have:

$$\frac{\delta T}{T} = (\gamma - 1)\frac{\delta\rho}{\rho} = \frac{\delta P}{P} \frac{\gamma - 1}{\gamma + (2 - \gamma)(P_m/P)}, \quad (8.58)$$

and, using the adiabatic relation, we have for  $\delta\rho$ :

$$\frac{\delta\rho}{\rho} = \frac{\delta P}{P} \frac{1}{\gamma + (2 - \gamma)(P_m/P)}. \quad (8.59)$$

Thus, when the acoustic or MHD waves propagate in the dense conglomerate of flux tubes, there are always temperature and density perturbation with a scale  $R$  which is much less than  $\lambda$ . The enhanced dissipation of incoming waves is caused just by these steep temperature and density gradients.

### 8.2.3 Dissipation by Thermal Conduction

The dissipation caused by thermal conductivity is described by the expression

$$Q_{\text{therm}} = \frac{\chi}{T} \langle (\nabla\delta T)^2 \rangle \quad (8.60)$$

The average is taken over a scale which is much larger than  $R$ . For  $\delta T$  given by (8.58) we obtain

$$Q_{\text{therm}} = \frac{\chi}{T} \left(\frac{\gamma - 1}{\gamma}\right)^2 \frac{\delta P_0^2}{[P + (2/\gamma - 1)P_m]^2} \times \left\{ k^2 + \left\langle \frac{(2/\gamma - 1)^2 (\nabla P_m)^2}{[P + (2/\gamma - 1)P_m]^2} \right\rangle \right\} \quad (8.61)$$

where we have taken into account that  $k \ll 1/R$  and have assumed the sinusoidal dependence of  $\delta P$  on  $x$ :  $\delta P = \delta P_0 \sin(kx - \omega t)$ .

The first term in the curly brackets corresponds to the usual dissipation of p-modes in a homogeneous medium while the second term describes the additional damping associated with strong inhomogeneities.

The spatial damping rate  $\text{Im } k_T$  caused by thermal dissipation (see, e.g., Landau and Lifshitz 1984) is

$$\text{Im } k_T = \frac{Q_{\text{therm}}}{2c_s E_0} \quad (8.62)$$

where  $E_0 = \rho(\delta v)^2/2$  is the energy density of the initial acoustic wave.

Let us express now the velocity perturbations in terms of the total pressure perturbations

$$\delta v = \frac{\delta P}{\rho v_{\text{ph}}} \quad (8.63)$$

where  $v_{\text{ph}}$  is determined by (8.26).

As an example, let us choose an isotropic distribution of inhomogeneities. In this case in (8.26),  $Q_{\alpha\beta} = 0$  and

$$v_{\text{ph}}^2 = \frac{\gamma}{\rho} \left[ P + \left( \frac{\gamma}{2} - 1 \right) P_m \right]. \quad (8.64)$$

Using (8.26) and (8.61)–(8.64) we can write for the damping rate

$$\text{Im } k_T = \frac{\chi}{2c_s} \frac{T(\gamma - 1)^2}{\gamma [P + (2/\gamma - 1)P_m]} \left\{ k^2 + \left\langle \frac{(2/\gamma - 1)^2 (\nabla P_m)^2}{[P + (2/\gamma - 1)P_m]^2} \right\rangle \right\} \quad (8.65)$$

From (8.58)

$$\frac{T(\gamma - 1)^2}{\gamma [P + (2/\gamma - 1)P_m]} = \frac{\delta T}{\delta P}. \quad (8.66)$$

The equation of state and an adiabatic relation of the temperature and gas pressure give

$$\frac{\delta T}{\delta p} \simeq \frac{\delta T}{\delta P} = \frac{1}{\gamma c_V}, \quad (8.67)$$

where instead of the number density  $n$  we used the specific heat at constant volume,  $c_V = n/(\gamma - 1)$ . Combining (8.64), (8.65), and (8.67), for the spatial damping rate we obtain

$$\text{Im } k_T = \frac{\kappa}{2c_s} \frac{\gamma - 1}{\gamma} \left\{ k^2 + \left\langle \frac{(2/\gamma - 1)^2 (\nabla P_m)^2}{[P + (2/\gamma - 1)P_m]^2} \right\rangle \right\} \quad (8.68)$$

where  $\kappa = \chi/c_V$  is the thermal diffusivity.

Note that in denominator of the second term in (8.68) the last term is numerically small compared to the first term; for  $\gamma = 5/3$  it is only 0.2 of the first term even when  $p/P = 1$  (i.e., in nonmagnetic medium, while in sunspots  $p/P < 1$  always). This allows us to use the expansion

$$\frac{1}{[P + (2/\gamma - 1)P_m]^2} \simeq \frac{1}{P^2} \left[ P - 2 \left( \frac{2}{\gamma} - 1 \right) \frac{P_m}{P} \right], \quad (8.69)$$

and write

$$\text{Im } k_T = \frac{\kappa}{2c_s} \frac{\gamma - 1}{\gamma} \left\{ k^2 + \left\langle \frac{(2/\gamma - 1)^2 (\nabla P_m)^2}{P^2} \right\rangle \right\}. \quad (8.70)$$

For flux tubes with known internal structure we can easily take the average of  $\langle (\nabla P)^2 \rangle$ . As an example, suppose the magnetic field decreases from axis according to, say, a Gaussian law,

$$B = B_{\max} \exp(-r^2/R^2). \quad (8.71)$$

With the characteristic distance between flux tubes' centers  $d$  and the flux tube areal filling factor to be  $f = R^2/d^2$ , we have

$$\left\langle \frac{(\nabla P_m)^2}{P^2} \right\rangle = \frac{f}{R^2} \left\langle \frac{P_{m,\max}^2}{P^2} \right\rangle \quad (8.72)$$

In what follows we omit the angle brackets and bear in mind that the ratio  $P_{m,\max}^2/P^2$  is averaged over the ensemble of flux tubes. Note that we use here adiabatic approach which is valid for wavenumbers

$$k > k_T \equiv \frac{\kappa}{R^2 c_s} \quad (8.73)$$

Finally, for the spatial damping rate caused by thermal losses we have:

$$\text{Im } k_T = \frac{\kappa}{2c_s} \frac{\gamma - 1}{\gamma} \left[ k^2 + \left( \frac{2}{\gamma} - 1 \right)^2 \frac{f}{R^2} \frac{P_{m,\max}^2}{P^2} \right] \quad (8.74)$$

For Gaussian magnetic field profile in a flux tube, the average magnetic pressure of the flux tube is  $\langle P_m \rangle = f P_{m,\max}^2/2$ . Even in the case of closely packed flux tubes, with  $f \simeq 1$ , the average magnetic pressure will be reduced below its maximum value, which should be taken into account in constructing equilibrium sunspot models.

### 8.2.4 Dissipation by Viscosity

A very similar mechanism leads to enhancement of the viscous dissipation. The plasma densities inside and outside the individual flux tube are usually different and the total pressure perturbation  $\delta P$  gives rise to a relative motion of flux tube and the external plasma. The characteristic scale of these motions is of the order of  $R$ . The viscous dissipation

$$Q_\nu = \frac{\eta}{2} \left( \frac{\partial v_i}{\partial x_k} + \frac{\partial v_k}{\partial x_i} - \frac{2}{3} \delta_{ik} \text{div } \mathbf{v} \right)^2 + \zeta (\text{div } \mathbf{v})^2 \quad (8.75)$$

can greatly exceed its homogeneous value. Calculations similar to those made in previous section, give

$$Q_\nu = \frac{c_s^2}{2} \left( \frac{4}{3}\eta + \zeta \right) \frac{\delta P^2}{P^2} \left\{ k^2 + \frac{\eta}{(4/3)\eta + \zeta} \left\langle \left[ \nabla \left( 1 - \frac{\rho}{\langle \rho \rangle} \right) \right]^2 \right\rangle \right\} \quad (8.76)$$

Assuming that the temperature of the plasma in the unperturbed state (in absence of the wave) is more or less uniform, we can write that  $[1 - \rho/\langle \rho \rangle] = p + p_m/P$ . With this, for the spatial damping rate  $\text{Im } k_\nu$ , caused by viscous dissipation, we obtain

$$\text{Im } k_\nu = \frac{7}{6} \frac{\nu}{c_s} \left( k^2 + \frac{3}{7} \frac{f}{R^2} \frac{P_{m,\max}^2}{P^2} \right), \quad (8.77)$$

where we assumed that  $\zeta \sim \eta$  and have introduced a kinematic viscosity  $\nu = \eta/\rho$ .

Equation (8.76) has been obtained under the assumption that the viscous forces have a weak influence on the velocity field which is determined by the inertial forces. This is true for time scales  $\omega^{-1}$  of the perturbations less than the time of establishing of viscous flows over the scale  $R$ ,  $\omega^{-1} \leq R^2\nu$ . Thus, the damping rate (8.77) is valid if the condition analogous to condition (8.73) is satisfied, that is, if

$$k > k_{c\nu} \equiv \frac{\nu}{R^2 c_s}. \quad (8.78)$$

### 8.2.5 Total Dissipation Rate

The total damping rate which includes both thermal and viscous losses is simply the sum of expressions (8.74) and (8.77). Both these expressions contain two parts: the usual absorption of sound waves in medium with finite viscosity and thermal conductivity, and the absorption caused by the presence of small-scale inhomogeneities.

Let us denote the spatial damping rate corresponding to the usual losses (i.e., in homogeneous medium) as  $\text{Im } k_1$  and the damping rate caused by the strong local gradients by  $\text{Im } k_2$ . Then the total damping rate is

$$\text{Im } k = \text{Im } k_1 + \text{Im } k_2, \quad (8.79)$$

where

$$\text{Im } k_1 = \frac{k^2}{2c_s} \left[ \frac{7}{3}\nu + \left( 1 - \frac{1}{\gamma} \right) \kappa \right] \quad (8.80)$$

and

$$\text{Im } k_2 = \frac{f}{2c_s R^2} \frac{P_{m,\max}^2}{P^2} \left[ \nu + \left( 1 - \frac{1}{\gamma} \right) \left( 1 - \frac{2}{\gamma} \right)^2 \kappa \right]. \quad (8.81)$$



For pure molecular transport, the kinematic viscosity  $\nu$  and the thermal diffusivity  $\kappa$  are of the same order of magnitude. In this case, because of the small numerical factor in the second term in (8.81), the enhanced dissipation is dominated by viscosity. The same conclusion holds in the case of a turbulent viscosity and thermal conductivity, when

$$\nu \sim \kappa \sim \tilde{\nu} \tilde{l} \quad (8.82)$$

with  $\tilde{\nu}$  being a characteristic velocity of turbulent elements and  $\tilde{l}$  their characteristic scale. Thermal dissipation may become more important in the case of a large radiative heat transfer where  $\kappa \gg \nu$ .

It is important that, although formally  $\text{Im } k$  contains  $k^2$  through  $\text{Im } k_1$ , the damping rate does not depend on  $k$ : according to our basic assumption the scale of inhomogeneities  $R$  is much less than the acoustic wavelength,  $k^2 R^2 \ll 1$ , and, respectively,

$$\text{Im } k_1 \ll \text{Im } k_2. \quad (8.83)$$

So that the absorption is completely determined by the anomalous damping rate  $\text{Im } k_2$ :

$$\text{Im } k_2 = \frac{1}{2} \frac{f P_{\text{m,max}}^2}{P^2} \frac{\nu}{c_s R^2}. \quad (8.84)$$

We neglected here the second term in square brackets in (8.81), and have taken into account the condition (8.82).

Respectively, the enhancement factor

$$EF = \text{Im } k_1 / \text{Im } k_2 \quad (8.85)$$

is

$$EF = \frac{3f}{7k^2 R^2} \frac{P_{\text{m,max}}^2}{P^2}, \quad (8.86)$$

which, because of  $k^2 R^2 \ll 1$  is quite large.

We see, that the expression for  $\text{Im } k_2$  contains the critical wavenumber:

$$k_{\text{cr}} = \frac{\nu}{R^2 c_s}. \quad (8.87)$$

This quantity plays a significant role in the interaction of the wave with the inhomogeneous medium.

Finally, taking into account the condition (8.81) we can neglect  $\text{Im } k_1$  in (8.79) and represent the total damping rate as follows:

$$\text{Im } k = \frac{1}{2} \frac{f P_{\text{m,max}}^2}{P^2} k_{\text{cr}} \quad (8.88)$$

This expression shows, first of all, that the damping of acoustic waves does not depend on the wavenumber and is determined by the physical properties of absorption region: magnetic filling factor, the scale of inhomogeneities, dissipative coefficients, sound speed, and the average magnetic field.

The dependence of the absorption on the magnetic field is quite specific and needs the separate comments. Namely, according to (8.88) the damping rate is proportional to  $B^4$ . At large values of magnetic field, when  $P_{m,\max}^2$  becomes the order of  $P^2$  the damping rate does not depend on magnetic field any more and there occurs a saturation of the absorption enhancement over the magnetic field strength.

So that, for high enough magnetic field, such that  $P_{m,\max}^2 \simeq P^2$  we have

$$\text{Im } k = \frac{f}{2} k_{\text{cr}}. \quad (8.89)$$

The other important meaning which carries the expression (8.88) is that it allows us to introduce the specific parameter  $\mu$  which actually determines the ‘‘acoustic opacity’’ of the region:

$$\mu = \frac{\text{Im } k}{k} = \frac{1}{2} \frac{f P_{m,\max}^2}{P^2}. \quad (8.90)$$

An important feature of the parameter  $\mu$  is that it does not depend on the assumptions on the particular value of viscosity  $\nu$  and, in this respect, is independent on the particular model of viscous transport.

It is also important that the local damping rate has no dependence on the sunspot size; the total absorption of a spot then scales simply with the path length through the spot, that is, the sunspot dimension  $L$ . We will see below that these features are totally consistent with the observations.

If  $\alpha$  is the total absorption of the wave propagating through the sunspot, the spatial damping rate can be evaluated as

$$\text{Im } k = \frac{1}{L} \ln \left( \frac{1}{1 - \alpha} \right). \quad (8.91)$$

So that the total damping coefficient,  $\alpha = 1 - \exp(-\text{Im } kL)$  depends only on the size of sunspot (or/and plage) and, on the physical parameters of medium:

$$\alpha = 1 - \exp \left( -\frac{1}{2} \frac{f P_{m,\max}^2}{P^2} k_{\text{cr}} L \right). \quad (8.92)$$

### 8.3 Anomalous Damping at Small Wavevectors

In the previous sections, to find the dissipation rate of p-modes, we concentrated on the region of wave vectors higher than some critical value  $k_{\text{cr}}$ . In this section, we extend the analysis to the region of low wavenumbers (low frequencies) when

conditions (8.73) and (8.78) break, and

$$k < k_{\text{cr}} \quad (8.93)$$

We will see that the picture of anomalous damping of p-modes described above considerably changes at smaller wave vectors. First of all, the viscous forces inhibit the relative motions of the flux tubes and the ambient gas (“sloshing mode”), thus reducing the dissipation enhancement: there appears a strong dependence of the damping rate on the wavevector (and frequency), and  $\text{Im } k$  decreases with decreasing wave number. The same happens with the damping process provided by thermoconductivity. In what follows, we, as before, assume that  $\nu \sim \kappa$ .

We start from the description of the dissipation caused by the thermal losses. At  $k < \kappa/(R^2 c_s)$ , the temperature and density perturbations become nonadiabatic and their relation should be estimated from the full thermoconductivity equation:

$$\frac{d}{dt} \left[ \delta T - (\gamma - 1) \frac{T \delta \rho}{\rho} \right] = \kappa \Delta \delta T. \quad (8.94)$$

Evaluating for estimation  $d\delta T/dt$  as  $\omega\delta T$ , and  $\kappa\Delta\delta T$  as  $\kappa\delta T/R^2$ , we obtain that, at  $k < k_{\text{cr}}$  the first term in the left-hand side of (8.94) becomes negligibly small as compared to the right-hand side. Hence, the relation between the temperature and density perturbation is determined by the expression

$$\left| \frac{\delta T}{T} \right| \simeq k c_s (\gamma - 1) \frac{R^2 \delta \rho}{\kappa \rho} \quad (8.95)$$

Using here the definition for  $k_{\text{cr}}$  analogous to (8.87), instead of (8.58), we have

$$\left| \frac{\delta T}{T} \right| \simeq \frac{k}{k_{\text{cr}}} (\gamma - 1) \frac{\delta \rho}{\rho} = \frac{k}{k_{\text{cr}}} \left| \frac{\delta P}{P} \right| \frac{\gamma - 1}{\gamma + (2 - \gamma)(P_{\text{m}}/P)}. \quad (8.96)$$

The factor  $k/k_{\text{cr}}$  that appears in (8.96) obviously gives rise to the dependence of the dissipation rate on the wavenumber, and, respectively, on frequency. After the substitution of (8.96) in (8.60) the same procedure described in Sect. 8.2.2, leads to the following expression for damping rate at  $k < k_{\text{cr}}$ ; cf. (8.74):

$$\text{Im } k_T \simeq \frac{k_{\text{cr}}}{2} \frac{\gamma - 1}{\gamma} \left[ k^2 R^2 + \left( \frac{2}{\gamma} - 1 \right)^2 \frac{k^2}{k_{\text{cr}}^2} \frac{f}{P^2} \frac{P_{\text{m,max}}^2}{P^2} \right] \quad (8.97)$$

We see that the contribution provided by the presence of small-scale inhomogeneities of magnetic field (the second term in square brackets) is still larger than the homogeneous one:

$$f \frac{P_{\text{m,max}}^2}{P^2} > k_{\text{cr}}^2 R^2. \quad (8.98)$$

As was mentioned above, at  $k < \nu/(R^2 c_s)$  the relative motions of flux tubes and ambient plasma are inhibited by viscous forces. Indeed, one can see from Navier–Stokes equation that the Archimedian force is now balanced by the viscous friction and the velocity  $\delta v$  of relative motions of fluid elements with different unperturbed densities should be determined from the condition

$$\frac{\nu}{R^2} \left| \frac{\delta v}{v} \right| \simeq \omega \frac{\delta \rho}{\rho} \quad (8.99)$$

with  $\omega = k c_s$ , this estimate becomes as

$$\left| \frac{\delta v}{v} \right| \simeq \frac{k}{k_{\text{cr}}}, \frac{\delta \rho}{\rho} \quad (8.100)$$

and, finally, the damping rate for  $k < k_{\text{cr}}$  becomes as follows; cf. (8.77):

$$\text{Im } k_\nu \simeq k_{\text{cr}} \left( \frac{7}{6} k^2 R^2 + \frac{1}{2} \frac{k^2}{k_{\text{cr}}^2} \frac{f P_{\text{m,max}}^2}{P^2} \right), \quad (8.101)$$

Exactly as in the case of thermal losses, here we have that the anomalous damping caused by the presence of small-scale inhomogeneities even at small wavenumbers is still larger than the dissipation in a uniform medium. Although, both expressions, (8.77) and (8.101), are the order-of-magnitude estimates, they allow us to perform qualitative, and at some degree, quantitative analysis of observational data of p-mode absorption by sunspots. This is done in the next section.

## 8.4 Absorption of P-Modes by Sunspots and Active Regions—Observations

By analyzing the velocity field inside and outside a sunspot, one can directly detect the difference between the radially propagating components of the incident and outgoing waves. The most natural way to perform this analysis is to use a polar coordinate system centered on the sunspot (Braun et al. 1987). The general procedure is analogous to the partial wave analysis in classical mechanics.

The general solution of the two-dimensional wave equation in polar coordinates,  $(r, \phi)$ , is given by the two kinds of Hankel functions, representing incoming,  $H_{\text{m}}^{(1)}(k, r)$ , and outgoing,  $H_{\text{m}}^{(2)}(k, r)$ , waves

$$\Psi_{\text{m}}(r, \theta, t) = e^{(i\omega t + im\phi)} [A_{\text{m}}(\omega, k) H_{\text{m}}^{(1)}(k, r) + B_{\text{m}}(\omega, k) H_{\text{m}}^{(2)}(k, r)] \quad (8.102)$$

Here,  $m$  is the azimuthal wave number,  $k$  is the horizontal wavenumber, and  $A_{\text{m}}$  and  $B_{\text{m}}$  are complex coefficients. Both are determined by power and phase of the waves;  $A_{\text{m}}$  corresponds to the wave traveling radially inward and  $B_{\text{m}}$  to outward wave.

**Table 8.1** 1983, 1986 observing parameters

Date	Activity	Duration (h)	Time interval	Size (arcsec)	Resolution (arcsec)
1983 Jan 18	Spot	4.1	90.8	512 × 240	1 × 1
1983 Feb 23	Spot	6.0	90.8	512 × 240	1 × 1
1983 Apr 26	Quiet	6.4	91.0	512 × 240	1 × 1
1986 Oct 24	Spot	7.8	96.1	512 × 480	1 × 2
1986 Oct 25	Spot	5.8	96.3	512 × 480	1 × 2
1986 Nov 20	Pore	8.4	93.1	512 × 460	1 × 2

If there is no absorption of incoming waves, then  $A_m = B_m$ , and radial component of the wave amplitude can be expressed by Bessel function of the first kind. If, however, there is a sink of wave power, then  $|A_m| \neq |B_m|$ , and there appears a net flow of power either toward or away from the center of sunspot.

Long-run temporal sequences of two-dimensional longitudinal velocity fields were recorded in the vicinity of several sunspots, pore, and a region of quiet sun. A summary of the observational parameters is given in Table 8.1. First column is the date of the observation. The second column is the object of the observation. Following columns list the total duration of the run, the interval between the successive scans, the spatial extent of the object of the observation, and resolution of each scan.

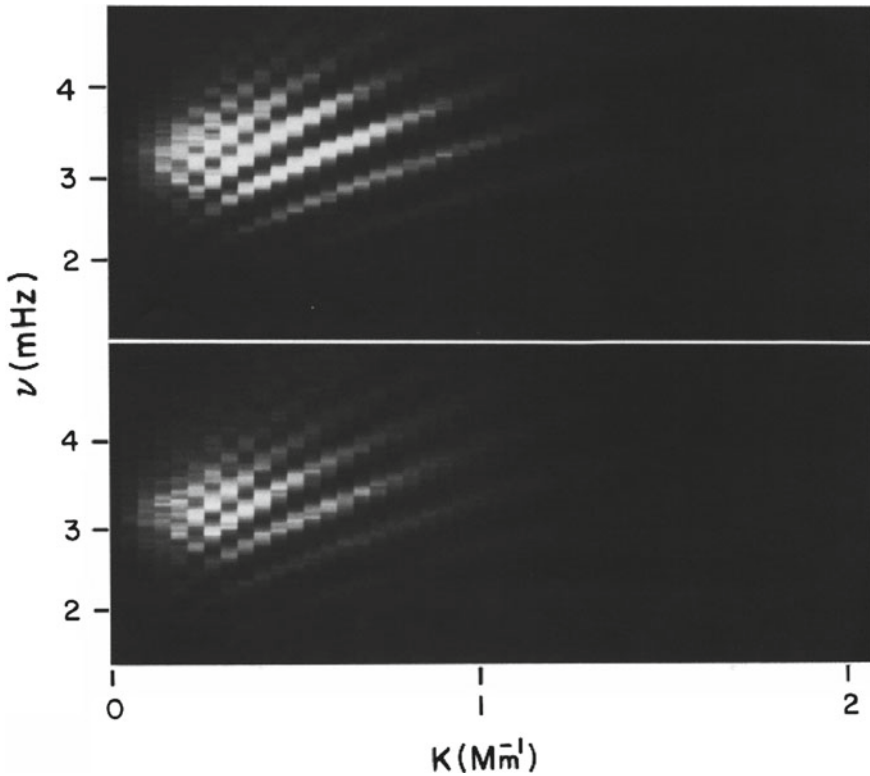
A refined data reduction method which was employed by Braun et al. (1987, 1988) for the analysis of each time series showed that unlike quiet sun region, for each studied sunspot, there was a significant deficit of outgoing power in comparison with incoming power.

Figure 8.4 shows example of the 1986 October run.  $|A_m|^2$  and  $|B_m|^2$ , i.e., power of incoming and outgoing waves summed over all computed azimuthal orders are plotted in the  $k - \omega$  plane. The structure of the p-mode ridges in this diagram is identical to that determined by analysis of quiet sun oscillations with difference that instead of, e.g., spherical harmonic degree  $\ell$ , the radial wavenumber has been used in the present analysis. The top and bottom panels show the amplitude of incoming and outgoing waves, respectively. Note that both,  $|A_m|$  and  $|B_m|$ , are each summed over the interval of azimuthal wavenumbers of  $-5 \leq m \leq 5$ . A deficit of outward traveling waves is clearly seen in all of the p-mode ridges.

In all studies, it was found that for each of the sunspot observations there was a substantial deficit of outgoing power relative to incoming power. This power deficit can be characterized by an absorption coefficient defined as

$$\alpha = \frac{\mathcal{P}_{\text{in}} - \mathcal{P}_{\text{out}}}{\mathcal{P}_{\text{in}}} \quad (8.103)$$

where  $\mathcal{P}_{\text{in}}$  and  $\mathcal{P}_{\text{out}}$  are the total power in the incoming and outgoing p-modes summed over all azimuthal orders and over the frequency interval of  $1.5 \text{ mHz} \leq \nu \leq 5 \text{ mHz}$ .

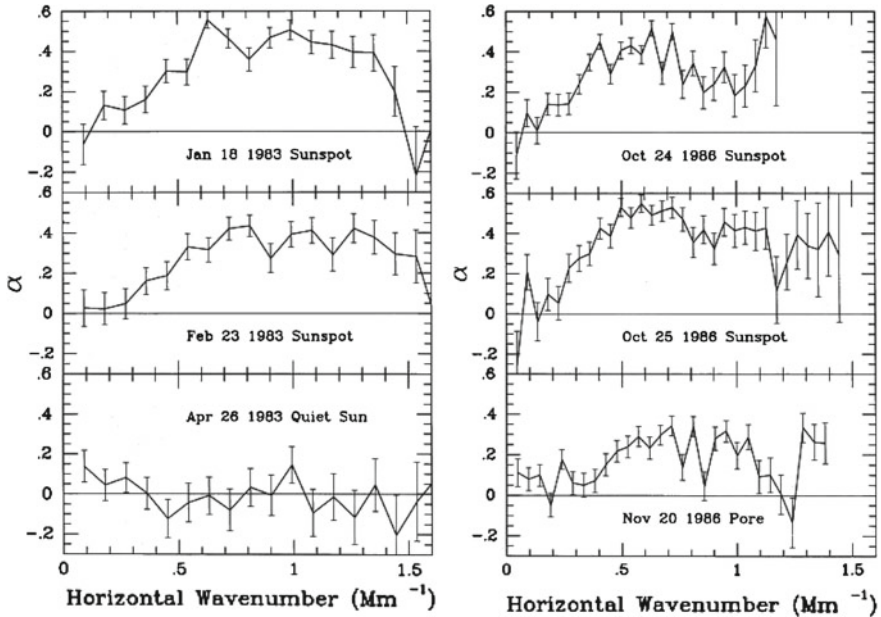


**Fig. 8.4** The power spectrum computed in the  $k-\omega$  plane for the 1986 October time series, summed over all azimuthal orders. Power spectra were computed individually for the October 24 and 25 observing runs and combined for the purposes of this illustration. The *top* and *bottom* halves of the diagram indicate the power present in inward and outward propagating waves, respectively. A deficit of outward traveling waves is clearly seen in all of the ridges. Reprinted from Braun et al. (1988) by permission from IOP copyright AAS

The background noise visible outside of the p-mode ridges has been estimated and subtracted from the total power before calculating  $\alpha$ .

Figure 8.5 shows the dependence of  $\alpha$  on horizontal wavenumber where the incoming and outgoing wave power has been summed over azimuthal orders  $-5 \leq m \leq 5$ . Every sunspot and even a pore show significant absorption of p-mode oscillations. In the case of the January 1983 and October 1986 sunspots as much as 50% of incoming power has been absorbed. It is important to note that the amount of absorption is constant at the higher wavenumbers ( $k \geq 0.5 \text{ Mm}^{-1}$ ), but noticeably drops as  $k$  approaches 0. For comparison with sunspot behavior the measurements were performed over the quiet sun region (see panel marked April 26, 1983). One can see that the quiet sun observations, as expected, shows no significant difference between incoming and outgoing power.

In the subsequent studies, a significant improvement in the measurements of p-mode absorption and scattering amplitudes, and in particular, the increased temporal



**Fig. 8.5** The absorption coefficient  $\alpha$  versus horizontal wavenumber for sunspots, pore, and the quiet sun. In all cases  $\alpha$  is shown up to the horizontal wavenumber where p-mode power could still be discerned from the background noise. The errors were calculated from the statistical properties of the power spectra and a standard treatment of the error propagation. Reprinted from Braun et al. (1988) by permission from IOP copyright AAS

frequency resolution, provided greater details in the interaction of p-modes with sunspots, active regions, and quiet sun (see, e.g., Gizon et al. 2009 and literature therein).

The observed regularities can be summarized as follows:

1. The absorbing regions are spatial coincident with sunspots and plages seen on the solar surface, with some differences in detail.
2. The fraction of the incident p-mode power absorbed is zero at low wavenumbers,  $k \leq 0.1 \text{ Mm}^{-1}$ , then rises to a high value at higher wavenumbers,  $k > 0.4 \text{ Mm}^{-1}$ . The absorbed fraction remains constant at the high value to the observational limit at  $k \sim 1 \text{ Mm}^{-1}$ .
3. The onset of absorption occurs at lower wavenumbers and the absorbed fraction is higher in larger sunspots than in smaller sunspots and pores. Typical isolated sunspots absorb 40 % of p-mode power at high wavenumber ( $k > 0.4 \text{ Mm}^{-1}$ ). Giant sunspots absorb up to 70 %, while small ones absorb only 20 %.
4. The absorbed fraction is larger in sunspots than in plages, but the “acoustic opacity”, the absorption per unit magnetic field, appears to be saturated in sunspots, whereas in plages this effect was not observed.
5. The dependence on the temporal frequency shows a broad peak in p-mode absorption centered approximately at 3 mHz.

Understanding the direct interaction of p-modes with sunspots and plages is a powerful tool in probing inhomogeneities in sunspot interior and for developing the helioseismology methods. It is remarkable that the mechanism of the enhanced absorption of acoustic wave power by sunspots, described earlier in this chapter has been developed before the observational data became available (Ryutova and Persson 1984). The comparison of theory and observations turned out to be remarkably good (LaBonte and Ryutova 1993). In the next section we overview these results.

## 8.5 The Interpolation Formula and Comparison with Observations

The qualitative analysis of the p-mode absorption (LaBonte and Ryutova 1993) shows that at low wavenumbers the damping rate depends on the magnitude of wavenumbers and increases quadratically with the increasing wavenumbers. The total damping rate provided by both, viscosity and thermal conductivity (in sunspot environment  $\nu \simeq \kappa$ ) according to (8.97) and (8.101), is

$$\begin{aligned} \frac{\text{Im } k}{k_{\text{cr}}} &\simeq \left( \frac{7}{6} + \frac{\gamma - 1}{2\gamma} \right) k^2 R^2 \\ &+ \left[ 1 + \left( 1 - \frac{1}{\gamma} \right) \left( 1 - \frac{2}{\gamma} \right)^2 \right] \frac{k^2}{k_{\text{cr}}^2} \frac{f P_{\text{m,max}}^2}{2P^2} \end{aligned} \quad (8.104)$$

This expression for the damping rate is valid up to the critical values of  $k \simeq k_{\text{cr}}$ , above which the enhancement of the absorption becomes more efficient and reaches its saturation.

The damping rate corresponding to the saturation regime is given by (8.88), and, obviously, does not depend on the wavenumber any more.

To unify the description of both limiting cases,  $k < k_{\text{cr}}$ , (8.104), and  $k \geq k_{\text{cr}}$ , (8.88), we will use the following interpolation formula

$$\text{Im } k = q_0 \frac{k^2}{k^2 + k_{\text{cr}}^2}, \quad (8.105)$$

where according to (8.88),  $q_0$  is the damping rate corresponding to the saturation over the wavenumber

$$q_0 = \frac{1}{2} \frac{f P_{\text{m,max}}^2}{2P^2} k_{\text{cr}}. \quad (8.106)$$

The interpolation formula for the total absorption coefficient (8.92) then is

$$\alpha = 1 - \exp \left( -q_0 L \frac{k^2}{k^2 + k_{\text{cr}}^2} \right). \quad (8.107)$$



**Table 8.2** Comparison of the observed and calculated absorption coefficients for 6 different sunspots

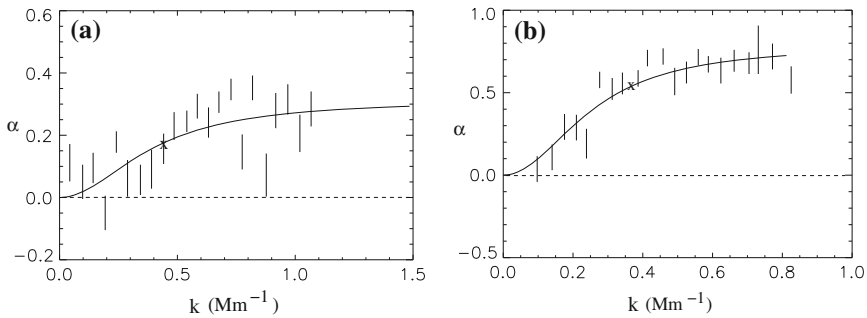
Date	Diameter (Mm)	$q_0$	$k_{cr}$ ( $Mm^{-1}$ )	$\mu = Im k / k_{cr}$	$\alpha_{max}$ observed	$\alpha_{max}$ calculated
1983 Jan 18	40	0.017	0.44	0.0386	0.50	0.44
1988 Feb 23	30	0.02	0.516	0.0387	0.45	0.40
1986 Oct 25	32	0.022	0.33	0.066	0.50	0.45
1986 Nov 20	8	0.047	0.43	0.11	0.31	0.30
1989 Mar 10	120	0.013	0.37	0.35	0.78	0.70
1988 Nov 29	36	0.024	0.445	0.054	0.58	0.45

Using the least squares approximation we can match the curve (8.107) with the observational dependence of the total damping rate  $\alpha$  on  $k$ .

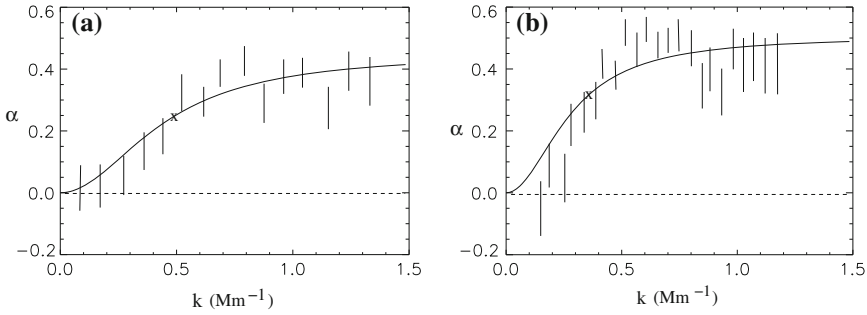
To do this, we choose six sunspots observed in different times (Braun and Duvall 1989; Braun et al. 1988, 1992). Dates and parameters of the observed objects are shown in Table 8.2. These examples cover the cases from the very small sunspot of November 20, up to the giant active region of March 10.

Using the observational data for  $\alpha$  and  $k$  in (8.107) we obtain the values of  $q_0$  and  $k_{cr}$  for chosen sunspots. The observed and calculated values of  $\alpha_{max}$  are shown in two last columns in Table 8.2.

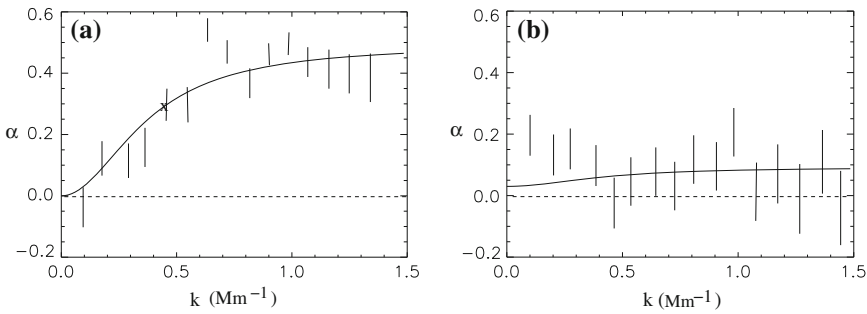
The interpolation curves calculated with (8.107) together with the observed absorption seen in all six sunspots are shown in Figs. 8.6, 8.7, and 8.8. The cross indicates the values of critical wave number  $k_{cr}$ . Note a remarkably good *qualitative* and *quantitative* matching of observations and theory in *all cases*. This includes the theoretical dependence of the absorption on the wave number and size of sunspot.



**Fig. 8.6** The absorption coefficient  $\alpha$  versus horizontal wavenumber  $k$  calculated from theoretical model (solid lines) are compared with the observational data: **a** The 1986 November 20 pore (8 Mm), and **b** the 1989 March 10 giant active region (120 Mm)



**Fig. 8.7** The same as in Fig. 8.6, but two other similar sunspots that are similar in size and properties: **a** the 1983 February 23 sunspot (30 Mm), and **b** the 1986 October 25 sunspot (32 Mm)



**Fig. 8.8** Comparison of the absorption coefficients for **a** a regular sunspot of 1983 January 18 **a** and **b** the quiet sun region taken on 1983 April 26

Recall that at large wavenumbers,

$$k_{cr} \leq k < 1/\ell, \tag{8.108}$$

where  $k_{cr}$  (for  $\nu \simeq \kappa$ ) is given by (8.87), the damping rate is almost constant and by the enhancement factor (EF) larger than in uniformly magnetized plasma; see (8.86). Note that in this regime (i.e.,  $k > k_{cr}$ ), the viscous effects and thermal conductivity have less influence on the sloshing mode, and the enhancement of the wave dissipation becomes more efficient, which is reflected in steepening of the theoretical curve in agreement with observational points.

At smaller wavenumbers,

$$k < k_{cr}, \tag{8.109}$$

the viscosity and thermal conductivity reduce the velocity and temperature fluctuations, and the damping rate  $\text{Im}k$  gets proportional to  $k^2$  (and respectively, to  $\omega^2$ ). The enhancement factor in this interval of wave numbers is

$$EF = \frac{3}{7} \frac{1}{k_{cr}^2 R^2} \frac{f P_{m, \max}^2}{2 P^2}. \tag{8.110}$$

The saturation regime, the very fact of its natural appearance in theory, and the corresponding maximum value of the total absorption coefficient are also in good agreement with observations.

In conclusion, we overview the basic points of agreements between the theory and the observed properties of the p-mode absorption. For the general estimates we adopt the following typical values: flux tube radius,  $R = 50 \text{ km}$ ; p-mode frequency  $\omega = 2\pi \times 3$ ; p-mode wavenumber  $k = 0.5 \text{ Mm}^{-1}$ ; sunspot radius  $L = 25 \text{ Mm}$ ; sound speed  $c_s = 10 \text{ km s}^{-1}$ .

1. Acoustic absorption is co-spatial with magnetic field locations. In the situation where viscous processes are dominant, we conclude that  $\text{Im}k$  in a nonuniform medium increases with respect to the uniform medium by the enhancement factor  $EF$ , given by (8.86) at  $k \geq k_{\text{cr}}$ , and by (8.110) at  $k < k_{\text{cr}}$ .

For a quantitative estimate, we use the observed quantities for  $k$  and  $R$ , take the filling factor  $f \simeq 1$  as appropriate to a sunspot, and assume that  $P_{\text{m,max}}^2/2P^2 = 1/2$ , a value consistent with the models of Maltby et al. (1986) for a sunspot with a photospheric magnetic field of  $\simeq 2 \text{ kG}$ . This gives an enhancement factor of

$$EF \simeq 3 \times 10^2 \quad (8.111)$$

Thus, the enhancement of absorption is quite large. The absorbing regions should be distinct from the background. The lower filling factor  $f$  in plages compared to sunspots explains the reduced absorption seen in the observations, despite the larger size of the plage.

2. The absorbed fraction of the acoustic power rises with increasing wavenumber at low wavenumbers but then levels off and remains constant at high wavenumbers. From (8.104) we see that at wavenumbers below the critical value  $k_{\text{cr}}$  which is determined by the thermal and viscous diffusion time scales, (8.73) and (8.78),  $\text{Im}k$  is proportional to  $k^2$ . Soon above the critical value, the absorption saturates and at large enough wavenumbers ( $k \simeq 1 \text{ Mm}^{-1}$ ) becomes constant.

A plot of absorption coefficient versus wavenumber  $k$  as calculated from theory for six different sunspots is compared with the observational data (Figs. 8.6, 8.7, and 8.8). The calculated curves adequately describe the observed behavior; this includes the saturation regime, the corresponding maximum values of the total absorption coefficient for each sunspot, and the region of wavenumbers below  $k_{\text{cr}}$ . The theory clearly indicates that soon after  $k_{\text{cr}}$  the plot must steepen because at  $k \geq k_{\text{cr}}$ , and the enhancement of wave dissipation becomes more efficient, which is also in agreement with observational points.

3. The absorption level increases with sunspot size. Theoretically indeed the local damping rate, (8.88) has no dependence on sunspot size, and the total absorption of the wave power by a spot scales simply with the path length of the wave through the spot(8.91).

Table 8.2 shows calculated values for the local damping rate  $q_0 = \text{Im } k$ , critical wavenumber  $k_{\text{cr}}$ , and the total absorption coefficient  $\alpha$ , covering the case of a small sunspot saturating at 30 % (1986 November 20) to the giant active region of 1989 March 10 saturating at 70 %. The typical isolated sunspots absorb 40–50 % of incident acoustic wave power (e.g., 1983 January 18, 1983 February 23), in agreement with observations.

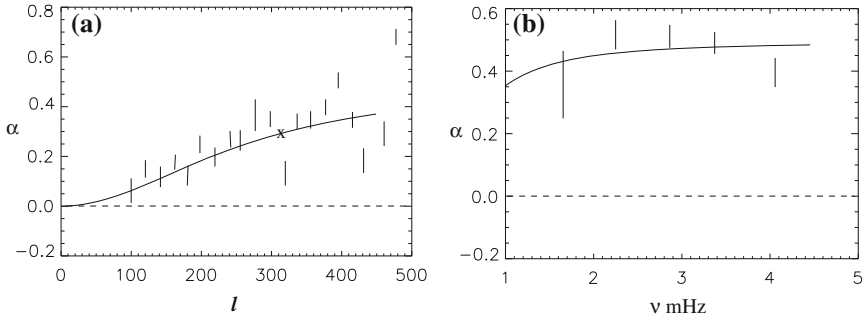
Note that the deviation of critical wavenumbers for different spots from the mean value of  $k_{\text{cr}} = 0.4 \text{ Mm}^{-1}$ , both in theory and observations, is quite small. This means that, generally speaking, the physical parameters of the medium (mean viscosity  $\nu$ , sound speed  $c_s$ , and scale of inhomogeneities  $R$ ) are quite similar in different sunspots. In order to explain the typical value of  $k_{\text{cr}}$ , the kinematic viscosity (neglecting the thermal conductivity contribution) should be of the order of  $10 \text{ km}^2 \text{ s}^{-1}$ . This is much larger than the kinematic viscosity caused by “molecular” transport (the thermal diffusivity would also be larger than that provided by radiative transport). Therefore, we have to assume that within the sunspot some turbulent viscosity is present, which is only natural. If one uses (8.82), then, to fit the calculated value  $\nu$ , one can use the observed limit on turbulent velocities in sunspots (Beckers 1976) of  $\tilde{v} = 2 \text{ km s}^{-1}$  to find the length scale of the turbulence  $\tilde{l} \sim 5 \text{ km}$ , much smaller than flux tube radius but consistent with Becker’s observed limit on turbulent scales.

A very important parameter for future diagnostic goals is the “acoustic opacity coefficient”  $\mu$ , (8.90), the parameter which is determined only by the magnetic field and plasma density distribution over the region and is independent on the particular model of viscous transport.

4. The absorption per unit magnetic field (acoustic opacity) appears to saturate in sunspots compared to plages. The dependence of the enhancement factor, (8.86), on the magnetic field strength is  $EF \sim B^4$  for weak magnetic fields; at large values of  $B$ , when  $P_{\text{m,max}}^2$  becomes the order of  $P^2$ , the enhancement factor saturates. The same holds with the acoustic opacity, (8.90).

There is no observed saturation over magnetic fields in plages, which is quite natural from theoretical point of view: the average magnetic field strength in plages is hundreds of Gauss (and less); the magnetic filling factor is less than unity ( $\simeq 0.3$ ) which means that magnetic elements are separated by almost magnetic free plasma, and the condition  $P_{\text{m,max}}^2 \simeq P^2$  can hardly be reached.

5. In a frame of linear theory, frequency scales linearly with the wavenumber, and we should expect the dependence of the absorption on frequency similar to those on wavenumber. Example of the dependence of the absorption coefficient on frequency is given in Fig. 8.9. Shown are the theoretical curve and the observed absorption coefficient for the November 1988 spot. Left panel is dependence on the absorption coefficient of spherical harmonic degree of the mode 1, and right panel is dependence on the wave frequency. The theoretical curve is calculated for the saturation regime over the wavenumber which corresponds to the critical wavenumber  $k_{\text{cr}} = 0.44 \text{ Mm}^{-1}$ , or  $\ell_{\text{cr}} = 309.73$ . The observational points correspond to  $\ell_{\text{cr}} = 308$  (Braun et al. 1992). Thus for frequency dependence comparison of theory with observations shows good qualitative and the order-of-



**Fig. 8.9** The theoretical curve and the observed absorption coefficient for the 1988 November sunspot (November 27–30 run): **a** versus spherical harmonic degree of the mode 1, and **b** versus the wave frequency

magnitude quantitative agreement, and as we are dealing here with the saturation regime, the calculated curve is smooth.

It must be noted finally, that the dispersion relation (8.26) contains much more information on the structure of medium than those inferred above. In particular, it carries information on the statistical properties of the medium providing the dependence of the phase velocities on the angle of the propagation in a plane perpendicular to the magnetic field. At the same time, there is always the dependence on the angle between the magnetic field and the direction of the wave propagation, i.e.,  $v_{\text{ph}} = v_{\text{ph}}^{\parallel} / \cos\theta$ . These and other details give wider opportunity for topographical studies of randomly magnetized atmosphere.

## References

- S.I. Braginskii, in *Reviews of Plasma Physics* vol. 1, ed. by M.A. Leontovich (Consultants Bureau, New York, 1965)
- D.C. Braun, T.L. Duvall Jr, *Sol. Phys.* **129**, 83 (1989)
- D.C. Braun, T.L. Duvall Jr., B.J. LaBonte, *Astrophys. J.* **319**, L27 (1987)
- D.C. Braun, T.L. Duvall Jr., B.J. LaBonte, *Astrophys. J.* **335**, 1017 (1988)
- D.C. Braun, B.J. LaBonte, T.J. Duvall Jr., *Astrophys. J.* **354**, 372 (1990)
- D.C. Braun et al., *Astrophys. J.* **391**, L113 (1992)
- L. Gizon Jr. et al., *Astrophys. J.* **354**, 372 (1990)
- L. Gizon Jr. et al., *SSRv* **144**, 249 (2009)
- M.A. Isakovich, *Sov. Phys. JETP* **18**, 386 (1948)
- B. LaBonte, R. Ryutova, *Astrophys. J.* **419**, 388 (1993)
- L. Landau, M. Lifshitz, *Fluid Mechanics* (Pergamon Press, Oxford, 1959)
- W. Livingston, *Nature* **350**, 45 (1991)
- P. Maltby, E.H. Avrett, M. Carlsson, O. Kjeldseth-Moe, R.L. Kurucz, R. Loeser, *Astrophys. J.* **306**, 284 (1986)
- M. Ryutova, M. Persson, *Phys. Scr.* **29**, 353 (1984)
- M. Ryutova, M. Kaisig, T. Tajima, *Astrophys. J.* **380**, 268 (1991)
- C. Zener, *Phys. Rev.* **52**, 230 (1937)

## Chapter 9

# Nonlinear Wave Phenomena in Dense Conglomerate of Flux Tubes

**Abstract** Nonlinear wave phenomena in strongly inhomogeneous media have a number of specific features that are important for various physical objects where the parameters of medium change by an order of unity over scales that are small compared to the wavelength. Generally, one would expect that the presence of strong inhomogeneities may “cut” the steepening of the wave front, and thus prevent formation of shocks. We shall see that this is not always the case. In this chapter we address this problem based on properties of sunspots, and describe the procedure that allows one to obtain nonlinear equations in the presence of strong inhomogeneities. The approach involves dispersion properties of a system, and dissipative effects. The equation itself takes a form similar to KdV-Bürgers equation, and thus describes corresponding scenarios of the system evolution. For example, the predominance of dissipative effects leads to damping of the primary wave at linear stage causing direct heating, or, depending on the interplay between nonlinear and dispersion effects, the process of heating may proceed either through the formation of shocks or through the storing of wave energy in a system of solitons which are later damped away. In any case, the presence of inhomogeneities results in strongly enhanced heating compared to that in homogeneous medium.

### 9.1 Nonlinear Equations in Strongly Inhomogeneous Medium

In the previous chapter we saw that strongly inhomogeneous areas such as sunspots and active region consisting of tightly settled flux tubes with varying parameters behave as a sink of incoming wave energy. There are however the observed effects, such as strong local brightenings in sunspots, light bridges, explosive events, and others that cannot be described in the frame of linear theory. Besides, the analysis of the enhanced dissipation of the incoming wave energy by dense conglomerate of magnetic domains becomes more complete in nonlinear studies. First of all we will see that even in the presence of small-scale inhomogeneities the magnetosonic waves of arbitrary (and finite) amplitude can split into two simple (Riemann) waves traveling in the opposite directions. Each wave has a tendency of steepening and overturning with the subsequent formation of shocks.

The presence of inhomogeneities leads also to the finite dispersion of the wave, having the cubic dependence on wavenumber, and thus to the frequency shift of incident wave.

$$\omega = v_{\text{ph}} \cdot k(1 + \delta^2 k^2) \quad (9.1)$$

The final form of the averaged equations for the finite amplitude wave acquire the form of KdV-Bürgers' type equations containing the nonlinear, dispersive and dissipative terms. These terms along their "direct functions" carry the information on statistical properties of the system.

To illustrate small-scale energetic events in magnetic cluster we show in Fig. 9.1 a captivating image of the active region (AR 09169) in G-band taken by the DOT. One can see ubiquitous small-scale brightenings all over the active region, and, as expected, highly filamentary structure of umbrae (seen as faint white dots in darkest areas corresponding to sunspot interior).

We start with a semi-two-dimensional analysis and assume that all plasma parameters are random functions of coordinate  $x$ :  $\rho_0(x)$ ,  $p_0(x)$ ,  $B_0(x)$ ,  $T_0(x)$ . The dependence on coordinate  $y$  is assumed to be weak so that  $\partial/\partial y \ll \partial/\partial x$ , and the magnetic field is directed along the  $z$ -axis.

The lifetime of such inhomogeneities is determined by the thermal conductivity and diffusion which are small in a strongly magnetized plasma in the direction  $x$  perpendicular to the flux tube direction. The inhomogeneities can be considered as stationary, providing at the same time the total pressure being constant

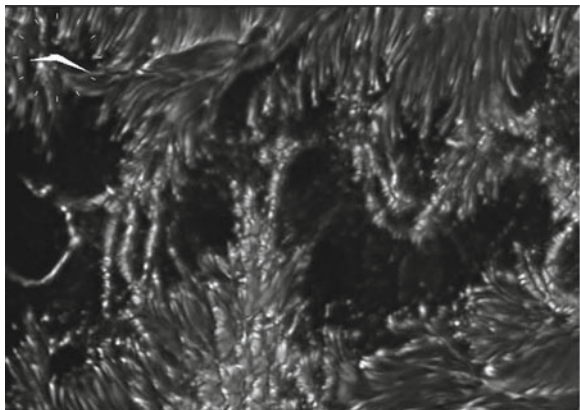
$$P_0 = p_0(x) + \frac{B_0^2(x)}{8\pi} = \text{const.} \quad (9.2)$$

It is important that we make *no* assumption that inhomogeneities are small: all parameters can change from one domain to another by an order of magnitude.

To describe the magnetosonic wave, we use the ideal MHD equations

$$\rho \frac{dv}{dt} = -\frac{\partial P}{\partial x}, \quad \frac{d\rho}{dt} + \rho \frac{\partial v}{\partial x} = 0, \quad \frac{dB}{dt} + B \frac{\partial v}{\partial x} = 0, \quad \frac{dp}{dt} + \frac{p}{\gamma} \frac{\partial v}{\partial x} = 0, \quad (9.3)$$

**Fig. 9.1** Image of the active region (AR 10375) in G-band covering  $80 \times 56$  Mm area. One can see spectacular families of local brightenings all over the active region. The image was taken by the DOT on September 9, 2000. Reprinted from <http://www.staff.science.uu.nl>, courtesy of Rob Rutten



where  $d/dt = \partial/\partial t + v(\partial/\partial x)$ . From the second and third equations of the system (9.3) there follows the frozen flux condition

$$\frac{B(x)}{\rho} = \frac{B_0(x)}{\rho_0(x)}, \quad (9.4)$$

where  $B(x)_0$  and  $\rho(x)_0$  are the values of  $B(x)$  and  $\rho(x)$  at the point where a given element of the medium was located at the initial moment of time,  $t = 0$ . Similarly, from the entropy equation

$$p(x)\rho(x)^{-\gamma} = p_0\rho_0^{-\gamma}. \quad (9.5)$$

We average the first and second equations of the system (9.3) over the scale  $L$  that is much larger than the size of inhomogeneities  $R$ , but much smaller than the length of magnetosonic wave  $\lambda$ :  $R \ll L \ll \lambda$ . Denoting this averaging by angular brackets, we have

$$\left\langle \rho \frac{dv}{dt} \right\rangle = -\frac{\partial}{\partial x} \langle P \rangle \quad (9.6)$$

and

$$\frac{d\langle \rho \rangle}{dt} + \frac{\partial}{\partial x} \langle \rho v \rangle \frac{\partial v}{\partial x} = 0 \quad (9.7)$$

Now, because of the averages  $\langle \rho dv/dt \rangle$  and  $\langle \rho v \rangle$ , the system (9.6) and (9.7) is not a closed one any more. This means that one needs to find a way to split the averages and bring the system of equations to the closed form.

To do this, we use the following considerations, which are valid for large-scale slow motions with a timescale  $T \equiv (2\pi/\omega) \gg R/c_s$  ( $c_s$  being the sound speed) and spatial scale  $\lambda \gg R$ . For these kinds of motions, changes in any characteristics of the system (density, pressure, frozen-in magnetic field, etc.) in the frame moving with the fluid element are slow, for example, within the time of the order of  $T$ . To avoid misunderstanding, it must be emphasized that at the same time, the *partial* derivative  $\partial/\partial t$  can be large,  $\partial/\partial t \sim v/R$ . Now we can rewrite the continuity equations from the system (9.3) in the form

$$\frac{\partial v}{\partial x} = -\frac{d \ln \rho}{dt}, \quad \frac{\partial v}{\partial x} = -\frac{d \ln B}{dt}, \quad \frac{\partial v}{\partial x} = -\frac{1}{\gamma} \frac{d \ln p}{dt} \quad (9.8)$$

It is clear that  $\partial v/\partial x$  is a small quantity estimated as

$$\frac{\partial v}{\partial x} \sim \frac{1}{T} \sim \frac{v}{\lambda} \ll \frac{v}{R} \quad (9.9)$$

That is, despite the presence of inhomogeneities of density, pressure, and magnetic field which have the scale  $R$ , velocity is a “smooth” function, changing only over the scale  $\lambda \gg R$ . This allows us to write the following relations:

$$\left\langle \rho \frac{dv}{dt} \right\rangle \simeq \langle \rho \rangle \frac{d\langle v \rangle}{dt}, \quad \langle \rho v \rangle \simeq \langle \rho \rangle \langle v \rangle \quad (9.10)$$



these relations are valid with the accuracy of the order  $R/\lambda \ll 1$ . Recall that the scale  $L$  over which the averaging is made is small compared to  $\lambda$  and large compared to  $R$ . As a result we obtain instead of (9.6) and (9.7) the following equations:

$$\langle \rho \rangle \frac{d\langle v \rangle}{dt} = -\frac{\partial}{\partial x} \langle P \rangle, \quad (9.11)$$

$$\frac{\partial \langle \rho \rangle}{\partial t} + \left( \frac{\partial}{\partial x} \langle \rho \rangle \right) \langle v \rangle = 0 \quad (9.12)$$

The form of (9.11) and (9.12) is similar to the equations for one-dimensional gas-dynamics. The analogy will become complete when we find the closure relationship between the averaged quantities  $\langle \rho \rangle$  and  $\langle P \rangle$ .

Note that the density  $\rho$  of each plasma element can be expressed in terms of its initial density  $\rho_0(x)$ , pressure  $p_0(x)$ , and total pressure  $P$  at a given point. Thus, by using the definition of  $P$  and relationships (9.2), (9.4) and (9.5), we obtain

$$P = p_0 \left( \frac{\rho}{\rho_0} \right)^\gamma + \frac{P_0 - p_0}{\rho_0^2} \rho^2. \quad (9.13)$$

This relationship determines implicitly the dependence of  $\rho$  on  $P$ ,  $\rho_0$  and  $p_0$  ( $P_0$  is assumed to be known),

$$\rho = \rho(P, \rho_0, p_0). \quad (9.14)$$

In what follows, it is convenient to introduce the distribution function  $f(\rho_0, p_0)$  of the random quantities  $\rho_0$  and  $p_0$ , which we define as follows: the fraction of those segments of the axis  $x$ , where  $\rho_0$  and  $p_0$  take the values in the intervals  $(\rho_0, \rho_0 + d\rho_0)$ ,  $(p_0, p_0 + dp_0)$ , is proportional to  $f(\rho_0, p_0)d\rho_0 dp_0$ :

$$dx_0 \sim f(\rho_0, p_0)d\rho_0 dp_0. \quad (9.15)$$

Let us choose now two Lagrangian planes with the distance  $L$  ( $R \ll L \ll \lambda$ ). The amount of the matter between the Lagrangian planes, which by definition are “affixed” to plasma particles, is constant:

$$M = \int_L \rho(x)dx = \int_{L_0} \rho_0(x_0)dx_0 = \text{const}. \quad (9.16)$$

This condition leads to the connection of the segment  $dx$  in MHD wave with its initial value  $dx_0$

$$dx = dx_0 \frac{\rho_0(x_0)}{\rho(P, p_0, \rho_0)} \quad (9.17)$$

Note that the total pressure  $P$  is slowly varying function with the characteristic scale of the order of  $\lambda$ . Since the distance  $L$  is much less than  $\lambda$ , the change in  $P$  between Lagrangian planes is small, and we can substitute  $P$  by its average value  $\langle P \rangle$ .

With the help of (9.14) we can find the density of each element of plasma, which can be written as  $\rho = \rho(\langle P \rangle, \rho_0, p_0)$ . Then, instead of (9.17) we have

$$dx = dx_0 \frac{\rho_0(x_0)}{\rho(\langle P \rangle, p_0, \rho_0)}. \quad (9.18)$$

Taking into account that  $dx_0 \sim L_0 f(p_0, \rho_0) dp_0 d\rho_0$ , from (9.18) we obtain

$$L = L_0 \frac{1}{\int f(p_0, \rho_0) dp_0 d\rho_0} \int \frac{\rho_0(x_0)}{\rho(\langle P \rangle, p_0, \rho_0)} f(p_0, \rho_0) dp_0 d\rho_0. \quad (9.19)$$

The whole mass of substance between the Lagrangian planes is obviously the following:

$$M = L_0 \frac{\int \rho_0 f(p_0, \rho_0) dp_0 d\rho_0}{\int f(p_0, \rho_0) dp_0 d\rho_0} \quad (9.20)$$

Dividing this mass by the distance defined by (9.19), we obtain the expression for the average density,

$$\begin{aligned} \langle \rho \rangle &= \int \rho_0 f(p_0, \rho_0) dp_0 d\rho_0 \left[ \int \frac{\rho_0(x_0)}{\rho(\langle P \rangle, p_0, \rho_0)} f(p_0, \rho_0) dp_0 d\rho_0 \right]^{-1} \\ &\equiv F(\langle P \rangle). \end{aligned} \quad (9.21)$$

In this way one can find the relationship between  $\langle \rho \rangle$  and  $\langle P \rangle$  for any distribution function  $f(p_0, \rho_0)$ . Now, together with (9.21), equations (9.11) and (9.12), form a closed system of dynamical equations describing self-consistently the propagation of long-wave magnetosonic oscillations of a finite amplitude in an inhomogeneous plasma. The specific features of the system are determined by its statistical properties, and in particular, by the function  $f(p_0, \rho_0)$ .

## 9.2 Formation of Shocks Across Small-Scale Inhomogeneities

The problem of the finite amplitude wave propagation, and in particular the process of the steepening of a wave front and its overturning is largely determined by the dependence of  $\rho$  on  $P$ , i.e., by the specific form of a function  $\rho = F(P)$ .

For ordinary gas the  $\rho = F(P)$  dependence, which is  $\rho \sim P^{1/\gamma}$  (and  $\gamma > 1$ ), automatically satisfies the condition of overturning (see e.g., Landau and Lifshitz 1987):

$$\frac{du}{d\rho} > 0 \quad (9.22)$$

where  $u = v + c_s$ , and  $v = \int (c_s/\rho) d\rho$ .

It must be noted that the analysis of the shock formation in case of a strongly inhomogeneous plasma requires several clarifying steps. First of all, we have to represent the condition (9.22) in a more general form, namely through the relationship (9.21), and then verify whether a particular  $\rho = F(P)$  satisfies the overturning condition or not.

Let us rewrite the (9.11) and (9.12) in the form

$$\rho \frac{dv}{dt} = - \frac{dP}{d\rho} \frac{d\rho}{dv} \frac{dv}{dx}, \quad (9.23)$$

$$\frac{d\rho}{dv} \frac{dv}{dt} = -\rho \frac{\partial v}{\partial x}. \quad (9.24)$$

We omit herewith the averaging brackets and bear in mind that we deal with the averaged quantities. Eliminating  $dv/dt$  in these equations, we find

$$\frac{dP}{d\rho} \frac{d\rho}{dv} \frac{dv}{dx} = \rho^2 \frac{\partial v / \partial x}{d\rho / dv}. \quad (9.25)$$

Substituting this expression in the right-hand side of (9.23), we obtain the general form of nonlinear equation

$$\frac{\partial v}{\partial t} + \left( v + \rho \frac{dv}{d\rho} \right) \frac{\partial v}{\partial x} = 0. \quad (9.26)$$

If we introduce the notation  $u = v + c_s$ , the analogy with an ideal compressible gas becomes complete, and the condition for overturning of the wave front, (9.22), remains the same:

$$\frac{dv}{d\rho} + \frac{d}{d\rho} \left( \rho \frac{dv}{d\rho} \right) > 0. \quad (9.27)$$

We now have to express all terms in this condition through the function  $\rho = \rho(P)$ . From (9.25) it follows that

$$\rho \frac{dv}{d\rho} = \frac{1}{\sqrt{d\rho/dP}} \quad (9.28)$$

For the first term in condition (9.27) this expression yields simply

$$\frac{dv}{d\rho} = \frac{1}{\rho(P) \sqrt{d\rho/dP}} \quad (9.29)$$

The second term in (9.27) can be written as

$$\frac{d}{d\rho} \left( \rho \frac{dv}{d\rho} \right) = \frac{dP}{d\rho} \frac{\partial}{\partial P} \frac{1}{\sqrt{d\rho/dP}}, \quad (9.30)$$

or, performing the differentiation, we have

$$\frac{d}{d\rho} \left( \rho \frac{dv}{d\rho} \right) = - \frac{1}{2} \frac{d^2 \rho / dP^2}{(d\rho/dP)^{5/2}}, \quad (9.31)$$

Using now (9.27), (9.29) and (9.31) we obtain the most general form of the condition for steepening of a wave front in a medium with an arbitrary relationship between the density and pressure:

$$2 \left( \frac{d\rho}{dP} \right)^2 > \rho(P) \frac{d^2\rho}{dP^2}. \quad (9.32)$$

### 9.2.1 Validation of the Overtaking Condition

We need to clarify now that the condition (9.32) is indeed satisfied when the dependence  $\rho = F(\langle P \rangle)$  is defined by the expression (9.21):

$$F(\langle P \rangle) = \int \rho_0 d\Gamma \left[ \int \frac{\rho_0(x_0)}{\rho(\langle P \rangle, p_0, \rho_0)} d\Gamma \right]^{-1} \quad (9.33)$$

where  $d\Gamma = f(\rho_0, p_0) d\rho_0$ .

The first and second derivatives of this function are:

$$\frac{dF}{d\langle P \rangle} = \int \rho_0 d\Gamma \int \frac{\rho_0}{\rho^2} \frac{d\rho}{d\langle P \rangle} d\Gamma \left[ \int \frac{\rho_0}{\rho(\langle P \rangle)} d\Gamma \right]^{-2} \quad (9.34)$$

and

$$\begin{aligned} \frac{d^2F}{d\langle P \rangle^2} &= \frac{2 \int \rho_0 d\Gamma}{\left( \int (\rho_0/\rho) d\Gamma \right)^{-3}} \left( \int \frac{\rho_0}{\rho^2} \frac{d\rho}{d\langle P \rangle} d\Gamma \right)^2 \\ &+ \frac{\int \rho_0 d\Gamma}{\left( \int (\rho_0/\rho) d\Gamma \right)^{-2}} \int \left[ \frac{\rho_0}{\rho^2} \frac{d^2\rho}{d\langle P \rangle^2} - 2 \frac{\rho_0}{\rho^3} \left( \frac{d\rho}{d\langle P \rangle} \right)^2 \right] d\Gamma \end{aligned} \quad (9.35)$$

Combining the condition (9.32) with (9.21), (9.34) and (9.35) after some algebra, we obtain

$$\left( \int \rho_0 d\Gamma \right)^2 \left( \int \frac{\rho_0}{\rho} d\Gamma \right)^{-3} \int \left[ \frac{\rho_0}{\rho^2} \frac{d^2\rho}{d\langle P \rangle^2} - 2 \frac{\rho_0}{\rho^3} \left( \frac{d\rho}{d\langle P \rangle} \right)^2 \right] d\Gamma < 0 \quad (9.36)$$

It is obvious that  $\int \rho_0 d\Gamma > 0$  and  $\int \rho_0/\rho d\Gamma > 0$ .

The first and second derivatives in (9.36) can be easily found from (9.13) where  $P$  is substituted by its average value  $\langle P \rangle$  (see the explanations after (9.17)):

$$\frac{d\rho}{d\langle P \rangle} = \frac{\rho}{\gamma \langle P \rangle + (2 - \gamma)(P_0 - p_0)(\rho^2/\rho_0^2)}, \quad (9.37)$$

$$\frac{d^2\rho}{d\langle P \rangle^2} = \frac{(d\rho/d\langle P \rangle)[\gamma \langle P \rangle - (2 - \gamma)(P_0 - p_0)\rho^2/\rho_0^2] - \gamma\rho}{[\gamma \langle P \rangle + (2 - \gamma)(P_0 - p_0)(\rho^2/\rho_0^2)]^2}, \quad (9.38)$$

these derivatives, taken in the point  $\langle P \rangle = P_0$  become

$$\left. \frac{d\rho}{d\langle P \rangle} \right|_{P_0, \rho_0} = \frac{\rho_0}{\gamma p_0 + 2(P_0 - p_0)}, \quad (9.39)$$

$$\left. \frac{d^2\rho}{d\langle P \rangle^2} \right|_{P_0, \rho_0} = \frac{\rho_0[\gamma p_0 - \gamma^2 p_0 - 2(P_0 - p_0)]}{[\gamma p_0 + 2(P_0 - p_0)]^3}. \quad (9.40)$$

Substituting expressions (9.39) and (9.40) into the condition (9.36) we obtain

$$\int f(p_0, \rho_0) \frac{\gamma(\gamma + 1)p_0 + 6(P_0 - p_0)}{[\gamma p_0 + 2(P_0 - p_0)]^3} d\rho_0 dp_0 > 0. \quad (9.41)$$

In accordance with the equilibrium condition, the magnitude  $P_0 - p_0$  is always positive,  $P_0 - p_0 = B^2/8\pi > 0$ . This means that the integrand in expression (9.41) is positive definite.

Thus the condition (9.41) as well as its general form, (9.32) is satisfied for any distribution function  $f(p_0, \rho_0)$ . It is therefore only natural that the magnetosonic wave of finite amplitude propagating in a plasma with random inhomogeneities can split into two simple waves with subsequent steepening and overturning.

Note however that when the width of the wave front becomes comparable with the characteristic scale of inhomogeneities, this conclusion becomes invalid. In this case the dispersion effects play an essential role; since at  $\lambda \sim R$  the dispersion of MHD waves becomes nonlinear, a steepening of the wave front may be inhibited.

### 9.3 Effect of Inhomogeneities on the Dispersion Properties of the System

In this section we consider the dispersion properties of a dense conglomerate of flux tubes, and find nonlinear dependence of the frequency on the wavenumber.

#### 9.3.1 Basic Equations

Consider again the one-dimensional problem and start with the linearizing of the MHD equations. Let us introduce into system (9.3) small perturbations, remembering that unperturbed quantities are random functions of coordinate  $x$ :

$$\begin{aligned} p &= p_0(x) + \delta p(x, t), & \rho &= \rho_0(x) + \delta \rho(x, t), \\ p &= B_0(x) + \delta B(x, t), & v &= \delta v(x, t). \end{aligned} \quad (9.42)$$

Using the resulted equations and equilibrium condition  $\delta P = \delta p + (B_0 \delta B)/4\pi$  we can write for  $\delta P$ :

$$\frac{\partial \delta P}{\partial t} = -2 \left[ \left( \frac{\gamma}{2} - 1 \right) p_0 + P_0 \right] \frac{\partial \delta v}{\partial x}. \quad (9.43)$$

This equation together with the momentum equation,

$$\rho(x) \frac{\partial \delta v}{\partial t} = - \frac{\partial \delta P}{\partial x}, \quad (9.44)$$

forms a closed set describing linear perturbations in an inhomogeneous plasma.

All perturbed quantities can be represented in the following way:

$$\delta P = \langle \delta P^{(0)} \rangle + \delta P^{(1)}, \quad \delta v = \langle \delta v^{(0)} \rangle + \delta v^{(1)}, \quad \text{etc.}, \quad (9.45)$$

where  $\langle \delta P^{(0)} \rangle$ ,  $\langle \delta v^{(0)} \rangle$ , etc., are linear perturbations averaged over the distance  $L$ :  $R \ll L \ll \lambda$ , and  $\delta P^{(1)}$ ,  $\delta v^{(1)}$ , etc., are fluctuating parts of perturbations caused by the presence of inhomogeneities.

For slow motions,  $\partial/\partial t \sim \epsilon \ll 1$ , we have from (9.43) and (9.44)

$$\frac{\partial \delta v^{(0)}}{\partial x} \sim \epsilon \ll 1, \quad \frac{\partial \delta P^{(0)}}{\partial x} \sim \epsilon \ll 1, \quad (9.46)$$

therefore,  $\delta P^{(0)} \simeq \langle \delta P^{(0)} \rangle$  and  $\delta v^{(0)} \simeq \langle \delta v^{(0)} \rangle$ . At the same time, by definition  $\langle \delta P^{(1)} \rangle = 0$  and  $\langle \delta v^{(1)} \rangle = 0$ .

Since we deal with inhomogeneities that are initially stationary, we can consider a harmonic wave in time and replace  $\partial/\partial t$  by  $-i\omega$ . It is convenient to introduce the notation

$$\phi_0(x) = \frac{1}{2} \left[ \left( \frac{\gamma}{2} - 1 \right) p_0(x) + P_0 \right]^{-1} \quad (9.47)$$

Now (9.43) and (9.44) acquire a form

$$i\omega \rho_0(x) \delta v = \frac{\partial \delta P}{\partial x}, \quad i\omega \phi_0(x) \delta P = \frac{\partial \delta v}{\partial x}. \quad (9.48)$$

Let us represent  $\rho_0(x)$  and  $\phi_0(x)$  as follows:

$$\rho_0(x) = \langle \rho_0(x) \rangle + \rho_1(x), \quad \phi_0(x) = \langle \phi_0(x) \rangle + \phi_1(x) \quad (9.49)$$

Note that the fluctuations of plasma parameters of the background medium and the average values of these parameters are of the same order:  $\rho_1(x) \sim \langle \rho_0(x) \rangle$  and  $\phi_1(x) \sim \langle \phi_0(x) \rangle$ , which reflects the fact that the inhomogeneities are strong, and in particular that all unperturbed quantities change from one flux tube to another by an order of magnitude. At the same time  $\langle \rho_1(x) \rangle = 0$  and  $\langle \phi_1(x) \rangle = 0$ .

Introducing into the system (9.48) a fluctuating part of perturbations and of background inhomogeneities, we have

$$\begin{aligned} i\omega(\langle\rho_0(x)\rangle + \rho_1)(\delta v^{(0)} + \delta v^{(1)}) &= \frac{\partial}{\partial x}[\delta P^{(0)} + \delta P^{(1)}], \\ i\omega(\langle\phi_0(x)\rangle + \phi_1)(\delta P^{(0)} + \delta P^{(1)}) &= \frac{\partial}{\partial x}[\delta v^{(0)} + \delta v^{(1)}] \end{aligned} \quad (9.50)$$

After averaging, (9.50) becomes

$$\begin{aligned} i\omega[\langle\rho_0(x)\rangle\delta v^{(0)} + \langle\rho_1\delta v^{(1)}\rangle] &= \frac{\partial\delta P^{(0)}}{\partial x}, \\ i\omega[\langle\phi_0(x)\rangle\delta P^{(0)} + \langle\phi_1\delta P^{(1)}\rangle] &= \frac{\partial\delta v^{(0)}}{\partial x} \end{aligned} \quad (9.51)$$

The second terms on the left-hand side of (9.51) are those that determine the dispersion of the wave due to the presence of inhomogeneities.

### 9.3.2 Dispersion Relation

To solve the system (9.51), we have to express  $\delta v^{(1)}$  and  $\delta P^{(1)}$  through unperturbed quantities. The equations describing  $\delta v^{(1)}$  and  $\delta P^{(1)}$  can be obtained by subtraction from the system (9.50) of the corresponding equations of system (9.51):

$$\begin{aligned} i\omega[\rho_1\delta v^{(0)} + \langle\rho_0(x)\rangle\delta v^{(1)} + \langle\rho_1\delta v^{(1)}\rangle] &= \frac{\partial\delta P^{(1)}}{\partial x}, \\ i\omega[\phi_1\delta P^{(0)} + \langle\phi_0(x)\rangle\delta P^{(1)} + \langle\phi_1\delta P^{(1)}\rangle] &= \frac{\partial\delta v^{(1)}}{\partial x} \end{aligned} \quad (9.52)$$

Since we are looking for the first-order corrections, we can omit in (9.52) the second and third terms on the left-hand side; these terms give the next order of corrections in  $\delta P^{(1)}$  and  $\delta v^{(1)}$ . Then the system (9.52) becomes

$$i\omega\rho_1\delta v^{(0)} = \frac{\partial\delta P^{(1)}}{\partial x}, \quad i\omega\phi_1\delta P^{(0)} = \frac{\partial\delta v^{(1)}}{\partial x}. \quad (9.53)$$

Now we introduce the following definitions:

$$\rho_1(x) = \frac{d\psi(x)}{dx}, \quad \phi_1(x) = \frac{d\zeta(x)}{dx}. \quad (9.54)$$

Naturally  $\langle\psi\rangle = 0$  and  $\langle\zeta\rangle = 0$ . With these definitions the (9.53) are

$$\delta P^{(1)} \equiv i\omega\psi(x)\delta v^{(0)}, \quad \delta v^{(1)} \equiv i\omega\zeta(x)\delta P^{(0)}. \quad (9.55)$$

Substituting (9.55) into (9.51) we obtain the final set of equations containing the corrections that determine the dispersion of the wave due to the presence of inhomogeneities:

$$\begin{aligned} i\omega[\langle\rho_0(x)\rangle\delta v^{(0)} + i\omega\langle\rho_1\zeta\rangle\delta P^{(0)}] &= \frac{\partial\delta P^{(0)}}{\partial x}, \\ i\omega[\langle\phi_0(x)\rangle\delta P^{(0)} + i\omega\langle\phi_1\psi\rangle\delta v^{(0)}] &= \frac{\partial\delta v^{(0)}}{\partial x} \end{aligned} \quad (9.56)$$

Since the coefficients in the system (9.56) do not depend on coordinates, we can put  $\partial/\partial x = ik$  and obtain the dispersion relation:

$$\langle\phi_0\rangle\langle\rho_0\rangle\omega^2 + \langle\rho_1\zeta\rangle\langle\phi_1\psi\rangle\omega^4 + ik\omega^2[\langle\rho_1\zeta\rangle + \langle\phi_1\psi\rangle] = k^2. \quad (9.57)$$

Using the definitions (9.55), we see that the third term on the left-hand side of (9.57) is a full derivative whose average is evidently zero

$$\langle\rho_1\zeta\rangle + \langle\phi_1\psi\rangle = \left\langle \frac{d\psi}{dx}\zeta + \frac{d\zeta}{dx}\psi \right\rangle = \left\langle \frac{d\zeta\psi}{dx} \right\rangle \equiv 0 \quad (9.58)$$

On the other hand, the square of this expression,  $\langle\rho_1\zeta\rangle + \langle\phi_1\psi\rangle$ , determines the coefficient of  $\omega^4$  in the dispersion relation, and, because of (9.58), evidently has a negative definite quadratic form

$$\langle\rho_1\zeta\rangle\langle\phi_1\psi\rangle = -\frac{1}{2} \left[ \left\langle \frac{d\psi}{dx}\zeta \right\rangle^2 + \left\langle \psi \frac{d\zeta}{dx} \right\rangle^2 \right] \equiv -a^2 \quad (9.59)$$

Taking this into account the dispersion relation (9.57) becomes

$$\langle\phi_0\rangle\langle\rho_0\rangle\omega^2 - a^2\omega^4 = k^2 \quad (9.60)$$

In the zeroth order approximation (neglecting the dispersion of the wave),  $\omega$  scales linearly with  $k$ :

$$\omega = \tilde{c}_s(\rho_0, p_0, B_0)k \quad (9.61)$$

where modified sound speed  $\tilde{c}_s(\rho_0, p_0, B_0)$  has a form:

$$\tilde{c}_s(\rho_0, p_0, B_0) = \frac{1}{\sqrt{\langle\phi_0\rangle\langle\rho_0\rangle}} = \frac{1}{\sqrt{\langle\phi_0\rangle}} \left\langle \frac{1}{\gamma p_0 + B^2/4\pi} \right\rangle^{-1/2}. \quad (9.62)$$

Using linear approximation (9.61), from (9.60) we obtain the next approximation in the wave vector

$$\omega^2 = k^2\tilde{c}_s^2 + a^2k^4\tilde{c}_s^6 \quad (9.63)$$

or, finally,

$$\omega = k\tilde{c}_s(1 + \delta^2k^2). \quad (9.64)$$



Here  $\delta^2$  is a coefficient that determines the dispersion of the wave due to the presence of inhomogeneities:

$$\delta^2 = \frac{1}{2}a^2\tilde{c}_s^4. \quad (9.65)$$

### 9.3.3 KdV—Bürgers' Equation with Strong Inhomogeneities

For a wave of a small but finite amplitude, along a finite dispersion, one should take into account the effects of a weak nonlinearity described by (9.26). Note first that the dispersion relation (9.64), if written in the velocity frame moving with the modified sound speed  $\tilde{c}_s$ , corresponds to the dynamic equation of the form

$$\frac{\partial v}{\partial t} = \tilde{c}_s \delta^2 \frac{\partial^3 v}{\partial x^3}. \quad (9.66)$$

Respectively, the desired nonlinear equation, in the reference frame moving with  $\tilde{c}_s$ , can be written in the form:

$$\frac{\partial v}{\partial t} + \alpha v \frac{\partial v}{\partial x} = \tilde{c}_s \delta^2 \frac{\partial^3 v}{\partial x^3}. \quad (9.67)$$

where  $\alpha$  is coefficient of nonlinearity. This is a typical KdV equation.

Now we can conclude that the evolution of the initial magnetosonic perturbation in a plasma with random density and magnetic field inhomogeneities can be described by a KdV equation whose coefficients are uniquely determined by the statistical properties of these inhomogeneities; (see (9.21) and (9.59)). It must be noted that the coefficient  $\delta$  which determines the dispersion, differs from zero only in an inhomogeneous plasma, whereas in homogeneous case  $\delta = 0$ .

Obviously, (9.67) implies that depending on the interplay between the dispersion and nonlinearity, the system is subject to a soliton formation. In this case the width  $\Delta X$  of leading (the largest) soliton may be estimated in a standard way as

$$\Delta X \sim \sqrt{\frac{\tilde{c}_s \delta^2}{\alpha \tilde{v}_0}}, \quad (9.68)$$

where  $\tilde{v}_0$  is the amplitude of the initial perturbation. In order for the soliton to be formed (and the approach to be valid), the width  $\Delta X$  must be larger than the characteristic scale of inhomogeneities  $R$ . Since, according to (9.59), at large enough inhomogeneities ( $\rho_1 \sim \rho$ ,  $p_1 \sim p_0$ ),  $\delta$  is of the order  $R$ , and  $\alpha$  is of the order of unity, we conclude that the above description is adequate under the condition when  $\tilde{v}_0 \ll \tilde{c}_s$ , which is relatively weak constraint.

As already mentioned, a plasma with strong inhomogeneities exhibits an important feature: dissipative effects caused by thermal conductivity and viscosity are

significantly enhanced. For the complete description of nonlinear wave propagation in such a media, (9.67) has to contain the dissipative terms as well. This leads to KdV-Bürgers' equation (Ryutova et al. 1991)

$$\frac{\partial v}{\partial t} + \alpha v \frac{\partial v}{\partial x} = \tilde{c}_s \delta^2 \frac{\partial^3 v}{\partial t^3} + \mu \frac{\partial^2 v}{\partial x^2} \quad (9.69)$$

where coefficients  $\mu(\rho, p_0, B_0) = \mu_{\text{visc}} + \mu_{\text{therm}}$  are again determined by statistical properties of inhomogeneities and contain parts connected with viscous and thermal losses (Ohmic losses as already discussed, remain the same as in homogeneous medium and are much less than those two). The procedure that allows to find  $\mu$  is described in the previous chapter (Sect. 8.2, (8.53), see also Ryutova and Persson 1984). By the order of magnitude,  $\mu$  can be estimated as follows:

$$\mu \simeq \lambda^2 \Gamma = \lambda^2 \frac{T \tau_i}{m_i R^2} \frac{1}{(\omega_i \tau_i)^2} \left( \frac{\tilde{\rho}_0}{\rho_0} \right)^2 \quad (9.70)$$

where  $\Gamma$  is the damping rate, (8.53), determined by the level of inhomogeneities and mainly by the viscous losses ( $\tau_i$  and  $\omega_i = eB/m_i c$  being ion collision time and ion gyro-frequency).

Equation (9.69) allows us to make general comments. This equation describes the evolution of the arbitrary initial perturbation: depending on the interplay of the nonlinear, dissipative, and dispersive effects, it can evolve either to weak shocks or be split into a train of some number of independent solitons which then will be damped away, or in the case of predominance of dissipative effects, the primary perturbation can be damped away in a linear stage (Karpman 1975).

## 9.4 Numerical Analysis

In this section we study numerically the influence of strong background inhomogeneities with small-scale spatial on the propagation and evolution of long-wavelength perturbations using a one-dimensional code of ideal magnetohydrodynamics. The set of the ideal MHD (9.3) is solved by numerical simulations as given in Ryutova et al. (1991).

### 9.4.1 The Model

As the initial state, consider an isothermal plasma with temperature  $T$  and assume the gas to be a polytrope of index  $\gamma = 1.5$ . The distribution of magnetic field is given by

$$B(x) = \sqrt{\frac{8\pi p(x)}{\beta(x)}} \quad (9.71)$$

where plasma beta

$$\beta(x) = \beta_0 f(x) \quad (9.72)$$

and  $\beta_0$  is the maximum value of the plasma beta,  $f(x) = f(\rho_0, p_0)$  describes the randomly distributed small-scale inhomogeneities of the background. In what follows we use  $\beta_0 = 1.0$ .

The initial density and pressure distributions are calculated using the equation of state  $p(x) = \rho(x)T$ , and the equation of magnetostatic equilibrium (9.2).

Long-wavelength perturbations of the form

$$\delta v_x(x) = A \sin\left(2\pi \frac{x}{\lambda}\right), \quad \delta \rho(x) = \frac{\rho_0}{c_s} \delta v_x, \quad \delta p(x) = \rho_0 c \delta v_x, \quad (9.73)$$

are initially imposed, where  $A$  is the amplitude of the initial perturbation and  $\lambda$  is its wavelength.

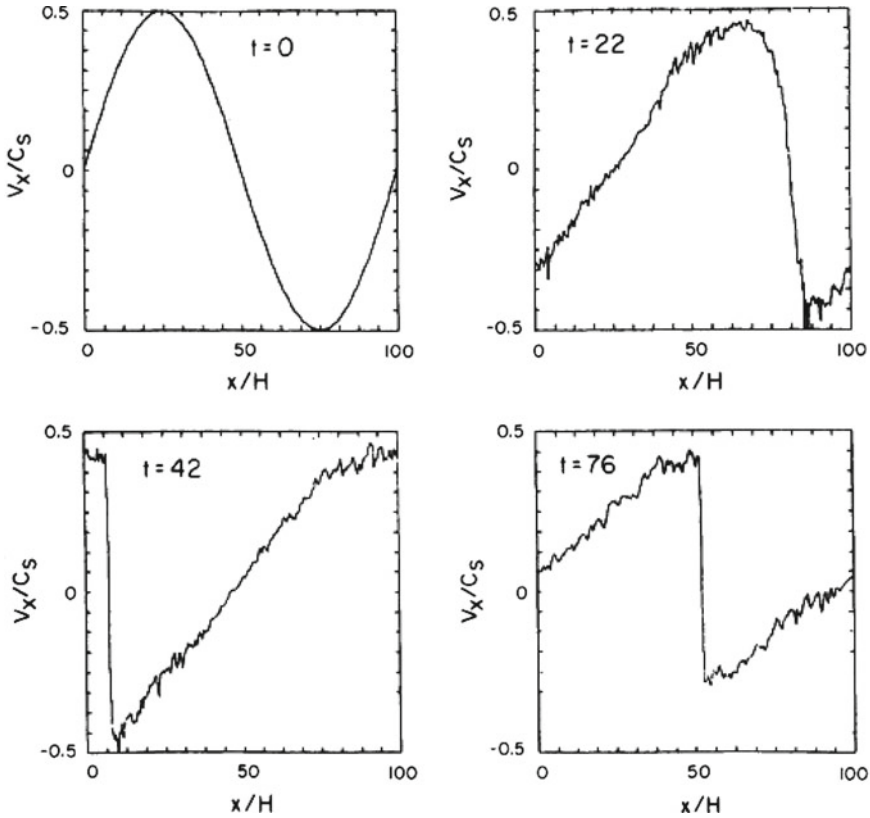
We assume periodic boundaries for  $x = 0$  and  $x = X_{\max}$ , where  $X_{\max}$  is the size of computational domain. The set of MHD equations (9.3) is nondimensionalized using the following normalizing constants: the atmospheric scale height  $H$ , sound speed  $c_s$ , and density  $\rho_0$ .

Equation (9.3) are solved numerically using a modified Lax-Wendroff scheme (Rubin and Burstein 1967) with an artificial viscosity according to Richtmyer and Morton (1967). The test and accuracy of MHD code in such a scheme were described by Shibata (1983), Matsumoto et al. (1988), and Tajima (1989). The mesh size is  $\Delta x = X_{\max}/(N_x - 1)$ , where  $N_x$  is the number of mesh points in the  $x$  direction.

We shall see that the numerical analysis presented below supports the theoretical results derived in the previous sections and extends the studies to the case when  $\lambda \sim R$ . In particular, it will be shown that long-wavelength perturbations steepen and form shock waves even in the presence of small-scale background fluctuations of basic physical parameters, and that the energy dissipation due to the small-scale inhomogeneities is strongly enhanced with respect to the case of a homogeneous medium. Although theory assumes the characteristic wavelength is greater than the characteristic scale of inhomogeneities,  $\lambda \gg R$ , numerical computation allows us to remove such a restriction and generalize the dissipation effect regardless of the characteristic wavelength.

### 9.4.2 Formation of Shock Waves

Assume that  $A = 0.5$ ,  $N_x = 1,001$ ,  $X_{\max} = 100$ , and  $\lambda = X_{\max}$ . Since the length scale of the background fluctuations is  $\Delta x$ , our theoretical assumption  $\lambda \gg R$  is amply fulfilled. The magnitude  $A$  of the initial pressure perturbation is too large to be realistic. However, our simulations with different values of  $A$  show that the amplitude of the perturbation within the regime of  $0.1 < A < 0.5$  does not qualitatively affect the overall evolution. Since the timescale for the steepening of the initial wave with wavelength  $\lambda$  is of the order of  $\lambda/v$ , its quantitative effect is that the smaller  $A$  is,



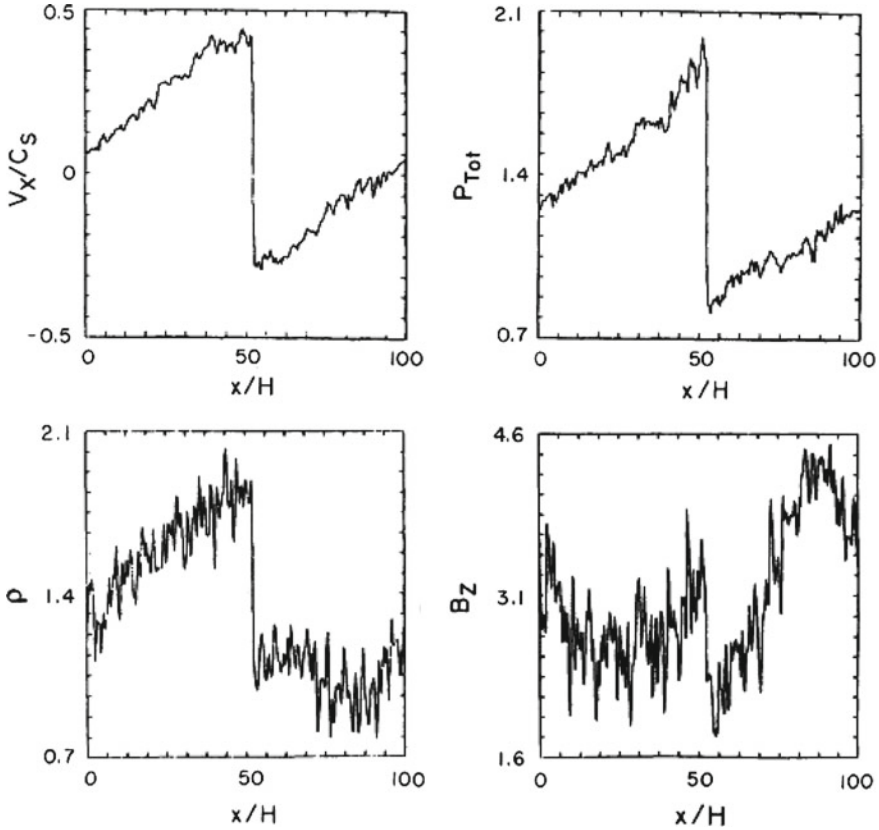
**Fig. 9.2** The case of small-scale inhomogeneities: distribution in  $x$  of the velocity  $V_x$  at  $t = 0$  (upper left panel), and its evolution at  $t = 22$ ,  $42$ , and  $t = 76$

the larger is the computational time. Thus, this high value of the initial perturbation is chosen simply for computational convenience.

Figure 9.2 shows the time variation of the velocity field  $V_x$  in the strongly nonuniform plasma. The initially sinusoidal perturbation becomes more and more asymmetric ( $t \sim 22$ ), steepens, and forms strong shock waves at  $t \sim 42$ . The characteristic Burgers’ sawtooth shock formation is apparent. Note that the “discontinuities” of shocks are more than several grid spacings so that they are not beyond the numerical resolution.

Figure 9.3 contains the velocity  $V_x$ , the total pressure  $P_{tot}$ , the plasma density  $\rho$ , and the vertical magnetic field  $B_z$  in the final state at  $t = 76$ . The shocks are best resolved in  $V_x$ ,  $\rho$ , and  $P_{tot}$ . The profiles of the density and magnetic field are strongly modulated by the small-scale background fluctuations.

At this point, we summarize that even in the presence of strong, small-scale background inhomogeneities the propagation of acoustic waves with wavelengths  $\lambda \gg R$  is characterized by steepening of the wave front and the formations of shocks.



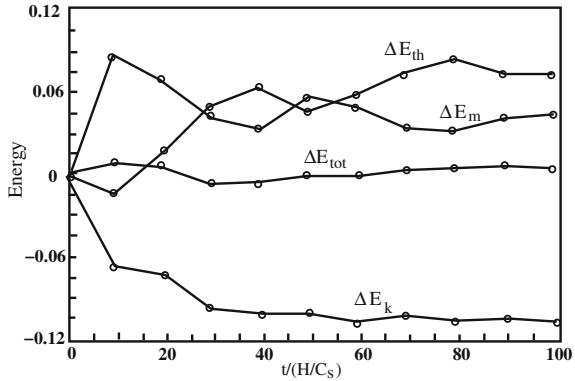
**Fig. 9.3** Plots of the velocity  $V_x$ , the total pressure  $P = p + B^2/8\pi$ , the density  $\rho$  and the magnetic field strength  $B_z$  at  $t = 76$  for the case shown in Fig. 9.2

### 9.4.3 Energy Dissipation

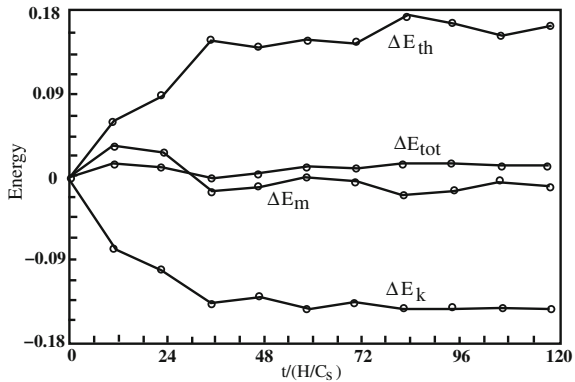
We now discuss the energetics of the system and compare the case of inhomogeneous background fluctuations with that of a homogeneous medium. We assume the same amplitude of the initial perturbation,  $A = 0.5$ , as in the previous calculations, but use  $X_{\max} = 20$ . The smaller wavelength of the initial perturbation reduces the timescale for steepening of the wave front by a factor of 5 compared to the case of  $X_{\max} = 100$ .

Consider first the case of a homogeneous medium. Figure 9.4 shows the time variation of magnetic, thermal, and kinetic energies in a system. It should be noted that  $\Delta E = E(t) - E(0)$ . The kinetic energy  $E_k$  strongly decreases within the first 10 time intervals. In this period the waves steepen and form shocks. Within the next 30 time intervals 10% of the kinetic energy dissipates and is converted mostly

**Fig. 9.4** Time variation of magnetic ( $\Delta E_m$ ), thermal ( $\Delta E_{th}$ ), kinetic ( $\Delta E_k$ ), and total ( $\Delta E_{Tot}$ ) energies, where  $\Delta E = E(t) - E(0)$ , for the case of homogeneous background



**Fig. 9.5** Time variation of magnetic ( $\Delta E_m$ ), thermal ( $\Delta E_{th}$ ), kinetic ( $\Delta E_k$ ), and total ( $\Delta E_{Tot}$ ) energies for the case of dense conglomerate of inhomogeneities

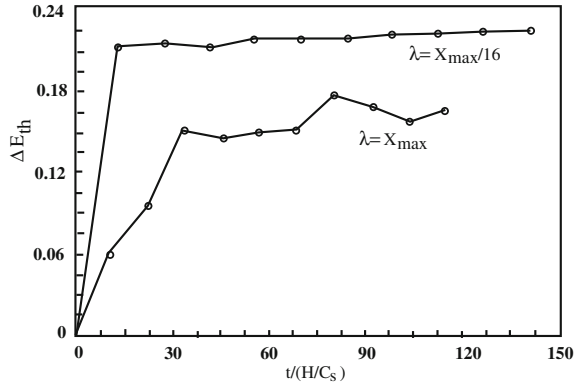


into thermal energy through compressional shock heating, and partly into magnetic energy. The total energy in this numerical analysis is conserved within less than 1 % of its initial value.

Figure 9.5 shows the evolution of the energy flow for the case of an inhomogeneous plasma. The kinetic energy decreases more drastically compared to homogeneous cases. Within the first period ( $t \sim 30$ ) the thermal energy strongly increases partly due to damping of the kinetic energy and partly due to dissipation of the magnetic energy. The heating effect is gauged by the increase in thermal energy  $\Delta E_{th}$ , or lack of it. For example,  $\Delta E_{th}$  in Fig. 9.5 in the inhomogeneous case is  $\sim 0.18$ , while  $\Delta E_{th}$  shown in Fig. 9.4, for homogeneous case is  $\sim 0.09$ .

An interesting difference between the homogeneous and inhomogeneous cases is that in the latter the magnetic field also releases its energy which is converted into thermal energy of medium through formation and dissipation of compressional shocks.

**Fig. 9.6** Time variation of thermal energy,  $\Delta E_{\text{th}}$ , for different wavelengths of the initial perturbation in the case of inhomogeneous medium



Very useful are results of the limiting case when  $\lambda \sim R$ , in which the wavelength of the initial perturbation is of the same order as the length scale of the inhomogeneities (characteristic scale of flux tube). This case is beyond the reach of analytical studies that do not allow to make any predictions.

In solving this problem, the following set of parameters are taken:  $A = 0.5$ ,  $X_{\text{max}} = 20$ , and  $\lambda = X_{\text{max}}/16$ . Results of the calculation show again the strong dissipation of kinetic and magnetic energies in the early stage of the wave front evolution.

Figure 9.6 shows the time evolution of the thermal energy  $\Delta E_{\text{th}}$ . Compared to the case when  $\lambda \simeq X_{\text{max}}$ , which is also shown in Fig. 9.6, the heating of the plasma is even more efficient. Due to strong dissipation from the very beginning, the initial perturbations are rapidly damped before the wave steepens and reaches the shock regime.

Thus, the presence of small-scale background inhomogeneities, in case a dense conglomerate of random flux tubes, results in a much stronger dissipation of incoming wave power and a stronger heating of the medium compared to the case of homogeneous plasma. Qualitatively, this result is independent of the amplitude  $A$  of the initial wave, but the higher is the amplitude the larger the amount of heating. In the limiting case of  $\lambda \sim R$  the numerical analysis indicates that the waves *do not steepen* to form shocks, but rather are rapidly damped out. Compared to the case of long-wave perturbations the heating in this case is more efficient.

It is important to note again that energy deposition due to the generation of shocks and solitons should manifest itself in strong *local* brightenings, chains of bright points, and light bridges (if solitons are involved). The size of bright points is naturally comparable with the thickness of wavefront. Thus, possibility of shock and soliton formation may play an essential role in the widespread appearance of local brightenings and their chains observed in sunspots and active regions (Aballe Villero et al. 1993; Anastasiadis and Vlahos 1994; Berger and Berdyugina 2003; Schleicher et al. 2003; Lagg et al. 2014).

## References

- M.A. Aballe Villero et al., *Astron. Astrophys.* **267**, 275 (1993)
- A. Anastasiadis, L. Vlahos, *Astrophys. J.* **428**, 819 (1994)
- T.E. Berger, S.V. Berdyugina, *Astrophys. J.* **589L**, 117 (2003)
- V.I. Karpman, *Nonlinear Waves in Dispersive Media* (Pergamon Press, London, 1975)
- A. Lagg et al., *Astron. Astrophys.* **568**, 60 (2014)
- L. Landau, E. Lifshitz, *Fluid Mechanics* (Pergamon Press, Oxford, 1987)
- R. Matsumoto et al., *PASJ* **40**, 171 (1988)
- R.D. Richtmayer, K.W. Morton, *Difference Methods for Initial Value Problems*, 2nd edn. (Interscience, New York, 1967)
- E. Rubin, S.Z. Burstein, *J. Comput. Phys.* **2**, 178 (1967)
- M. Ryutova, M. Persson, *Phys. Scr.* **29**, 353 (1984)
- M. Ryutova, M. Kaisig, T. Tajima, *Astrophys. J.* **380**, 268 (1991)
- K. Shibata, *PASJ.* **35**, 263 (1983)
- H. Schleicher et al., *Sol. Phys.* **215**, 261 (2003)
- T. Tajima, *Computational Plasma Physics* (Addison-Wesley, Redwood City, 1989)



# Chapter 10

## Magnetosonic Streaming

**Abstract** The Faraday effect in gas dynamics called acoustic streaming and its accompanying nonlinear phenomena is found to have analogies in plasma magnetohydrodynamics. A natural place where these effects occur is the solar atmosphere covered by random ensembles of magnetic flux tubes. Unlike acoustic streaming, magnetosonic streaming consisting of the generation of plasma flows by an oscillating flux tube, is accompanied by a current drive and results in a specific evolution of magnetic structures. Depending on the physical parameters of a system, a single magnetic flux tube may be either split into thinner flux tubes or be diffusively dissolved into the ambient plasma. The effect of the magnetosonic streaming on one hand, is an obvious candidate for the generation of electric currents and mass flows at magnetic flux tube sites, and, on the other hand, it determines the evolution of magnetic structures, like, e.g., their fragmentation processes, and ultimately their lifetimes. In this chapter, we shall describe the nature and origin of the magnetosonic streaming and then use the theory to explain observed regularities in the evolution of photospheric flux tubes. Some regimes will be also verified in numerical simulation. Application of these results to observed properties of photospheric flux tubes will be given both in the qualitative and quantitative analysis.

### 10.1 Secondary Flows—Boundary Layer Effects

#### *10.1.1 Acoustic Streaming—History and Nature of Faraday's Effect*

The effect of the acoustic streaming was first observed by Faraday in one of his simple trials while assisting the lectures of Professor Devi. Young Faraday found that above the oscillating membrane there appears a well directed, perpendicular to the face of membrane, air streaming. Much later, Lord Rayleigh was involved in the problem of a musical organ seemingly out of tune without an evident reason. He found that for each tube there must be a threshold with respect to the intensity of sound above which some physical effects turn on and lead to discord of organ. Soon he found that these effects are related to viscosity of an air in the vicinity of solid surface of the tube and gave an analytical description (Rayleigh 1884) considering the stationary sound waves in a space between two plain parallel

walls. He found that gas flows must appear due to the viscosity of medium in a thin boundary layer along the tube walls. Moreover, he found these effects similar to the air streaming generated by the vibrating membrane. Lord Rayleigh wrote in his paper:

“Experiments in acoustics have discovered more than one set of phenomena, apparently depending for their explanation upon existence of regular currents of air resulting from vibratory motion...Such currents, involving as they do *circulation* of the fluid, could not arise in the absence of friction...

...The more important of the problems relates to flows generated over vibrating plate ...This was traced by Faraday (1831) to the action of currents of air, rising from the plate at the place of maximum vibration, and falling back to it at the nodes.”

The acoustic streaming is connected with the viscosity of the medium and with the presence of a solid obstacle or solid boundary walls in a field of sound wave, or other kind of oscillations: near the obstacle or a boundary sound waves result in the tangential motion and in additional stresses that give rise due the absorption of the energy of oscillations in a thin boundary layer; this energy is transformed into the energy of stationary mass flows. The effect is nonlinear and appears in the second order in the wave amplitude. Although the effect is provided by presence of viscosity, the velocity of established stationary flows actually does not depend on the viscosity coefficient. However, the time required to set up the steady flows is inversely proportional to coefficients of viscosity.

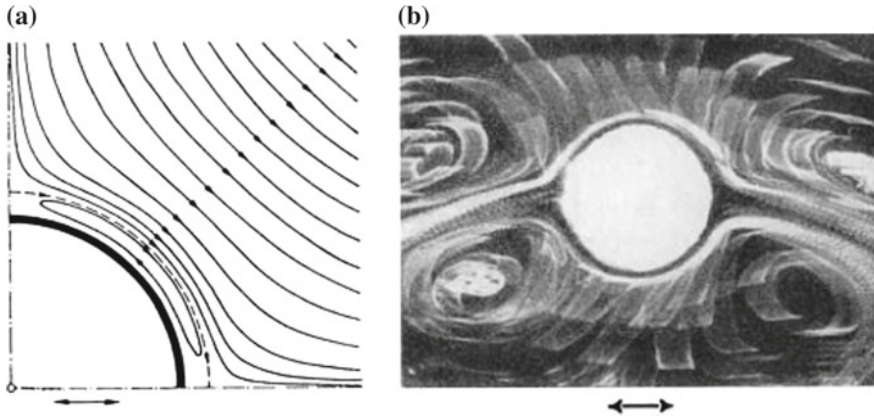
Fascinated by the effect, Rayleigh tried to perform different experiments to further explore it. For example, he found strong air streaming as a result of the oscillation of a fork at the mouth of Helmholtz resonator. After the studies of Lord Rayleigh, almost half of a century passed before the renewal of the problem of the acoustic streaming.

Acoustic streaming was rediscovered in the experiments on piezoelectric generators and named “Quartz wind”: a strong mass flow was observed in front of an oscillating surface of quartz crystal in liquid (Meissner 1926). The flows of liquid generated by an ultrasonic source turned out to be so strong that they were enough to disturb the crystal face.

Soon a new manifestation of acoustic streaming was found. Andrade (1931) experimentally studied flows generated by induced *standing sound waves* about a circular cylinder and found four stationary vortices visible by injection of smoke.

Similar results were obtained by Schlichting (1932), who performed also the calculation of the boundary layer on the cylinder oscillating in viscid fluid. In Fig. 10.1, calculated streamlines of secondary flow and an experiment by Schlichting visualizing the four vortices generated by the oscillating (solid) cylinder are shown.

However, understanding that Andrade’s and Schlichting’s experiments demonstrate the same effect as quartz wind was reached only when a complete theory of acoustic streaming was built up by Eckart (1948). Since then acoustic streaming is often referred to as “Eckart flows.” These studies invoked an activity exploring the acoustic streaming in a wide range of media including the cell membrane in biology (Nyborg 1965). It is interesting that Faraday’s effect explains creation of fountains in Tibetan singing bowls.



**Fig. 10.1** Schlichting's results: **a** Flow portrait of the secondary flow (streaming) close to an oscillating circular cylinder. **b** Experimental result on generation of secondary flow (streaming) close to an oscillating circular cylinder. After Schlichting (1932). See also Schlichting and Gersten 2000, Copyright Springer Science and Business Media

### 10.1.2 Secondary Flows in Magnetohydrodynamics

Especially rich effects analogous to the acoustics streaming were found in studies of nonlinear effects in the interaction of magnetic flux tubes with acoustic wave ( $p$ -modes) in solar atmosphere (Ryutova 1986). It was found that at the site of an oscillating magnetic flux tube, there appear qualitatively new effects that are absent in usual gas- and hydrodynamics. These are briefly described below.

- I. First of all, the Reynolds stresses that appear only *outside* the solid-body cylinder, in case of a magnetic cylinder, the additional magnetic stresses appear both *outside* and *inside* of the flux tube. This causes generation of plasma flows *outside* as well as *inside* magnetic structure. Of these two, the *inner flow* (that is absent in case of a solid obstacles) plays a crucial role in the evolution of flux tube and its dynamics.

As a result, the magnetic field and plasma density are leveled along the field lines of the induced flow. Depending on the ratio of the duration of wave train (in particular  $p$ -modes) to the time of establishing viscous flow, the magnetic flux tube may be either split into smaller flux tubes (in case of coherent wave train, e.g.,) or be diffusively dissolved into the ambient plasma (the case of convective motions or incoherent wave train).

If in the splitting regime the same conditions are fulfilled for newborn flux tubes, each of the newborn flux tube experiences further splitting. This process of filamentation of magnetic structure proceeds until fragmentation products meet conditions corresponding to diffusive dissolution. Outer fragments are dissolved first. Note that higher order nonlinear effects can also stop the fragmentation process.

The very process of fragmentation obviously determines the lifetime of magnetic structure.

- II. Unlike the acoustic streaming, the magnetosonic streaming is accompanied by the generation of electric currents: if the absorption of oscillation energy is provided mostly by one of the plasma species electron or ion (the specific situation depends on the damping mechanism), current drive occurs along the plasma flow. This current leads to distortion and redistribution of the initial magnetic field, and thus, to changing of the equilibrium. Geometry of the currents corresponds to that of the generated mass flows.
- III. The most remarkable feature of the effect in a case of magnetic flux tube is that there are two different mechanisms leading to magnetosonic streaming, while for the acoustic streaming *only the absorption* of oscillation energy in a thin boundary layer is responsible:
  - (a) One mechanism is associated with the ponderomotive force which naturally arises if the force acting on plasma contains a nonzero vortex part. This mechanism is not connected with the direct absorption of oscillations, i.e., dissipative process, but requires radial inhomogeneity of magnetic field and plasma density across the magnetic flux tube. This condition holds always for solar flux tubes. In hydrodynamics it is quite problematic, as it would require the inhomogeneous compressibility of medium.
  - (b) The other mechanism is similar to those in gas dynamics and is connected with the absorption of the momentum and angular momentum of flux tube oscillations.

Absorption of the momentum leads to the generation of *upward* and *downward* mass flows. Absorption of angular momentum causes the rotational mass flows across the flux tube axis.

- IV. In solar magnetic flux tubes there are two major *nondissipative* mechanisms of the absorption of flux tube oscillations (see Chaps. 3 and 4). One is the anomalous damping in the resonance point, where the phase velocity of oscillations becomes equal to local meaning of Alfvén velocity. The second is the radiative damping of flux tube oscillations due to the radiation of secondary acoustic waves. This means that even in the absence of dissipative effects, the flux tube itself is able to provide and sustain the generation of plasma streaming and current drive inside and outside it.

## 10.2 Magnetosonic Streaming Due to the Action of Ponderomotive Force

We start with the generation of plasma streaming in and around magnetic flux tube resulted by action of ponderomotive force which naturally arises in the oscillating electromagnetic field at nonlinear stage.

Consider the flux tube performing a kink oscillations (with  $z$ -axis directed along the magnetic field)

$$m = \pm 1 \quad (10.1)$$

and having a long wavelength:

$$\lambda \gg R \quad (10.2)$$

To visualize the nature of magnetosonic streaming, we choose the kink mode as it is an exact analogue to periodic vibration of a solid cylinder in Schlichting's experiment shown in Fig. 10.1. The analogy is especially complete with the experiment of Andrade who placed a circular cylinder in a field of acoustic waves.

We will see that there are conditions under which an oscillating magnetic flux tube generates four vortices similar to those in the experiments of Andrade and Schlichting. Furthermore, as mentioned above, the force responsible for the generation of vortices *outside* the flux tube affects the plasma *inside* the flux tube as well and leads to generation of *inner plasma flows* and electric currents.

Plasma density and magnetic field are leveled along the streamlines of the induced motions and initially smooth magnetic flux tube splits into four independent flux tubes. The process of splitting continues until "newborn" flux tubes reach the regime when they diffusively dissolve.

The linearized system of MHD equations describing kink oscillations of a flux tube with radial dependence of background parameters has a form

$$\rho \frac{\partial \tilde{\mathbf{v}}}{\partial t} = -\nabla \tilde{p} + \frac{1}{4\pi} (\nabla \times \tilde{\mathbf{B}}) \times \mathbf{B} + \frac{1}{4\pi} (\nabla \times \mathbf{B}) \times \tilde{\mathbf{B}} \quad (10.3)$$

$$\frac{\partial \tilde{\mathbf{B}}}{\partial t} = \nabla \times (\tilde{\mathbf{v}} \times \mathbf{B}) \quad (10.4)$$

where tilde marks perturbed quantities.

For long-wavelength oscillations under the condition (10.2), incompressibility is maintained with good accuracy:

$$\operatorname{div} \tilde{\mathbf{v}} = 0. \quad (10.5)$$

Since in the linear regime the  $z$ -component of velocity of kink oscillations is negligibly small (flux tube performs a periodic transverse motion), velocity perturbations  $\tilde{\mathbf{v}}(\tilde{v}_r, \tilde{v}_\phi, 0)$  can be expressed through the stream function  $\psi$ :

$$\tilde{v}_r = -\frac{1}{r} \frac{\partial \psi}{\partial \phi}, \quad \tilde{v}_\phi = \frac{\partial \psi}{\partial r}. \quad (10.6)$$

Obviously, the ponderomotive force appearing in the second order has only components in the plane perpendicular to the  $z$ -axis, and the problem becomes two-dimensional. Then the equation of motion for plasma in the second order has a form

$$\rho(r) \frac{\partial \mathbf{V}}{\partial t} = -\nabla \left[ p(r) + \frac{B^2(r)}{8\pi} \right] + \mathbf{f} + \nu \Delta \mathbf{V} \quad (10.7)$$

All quantities here have a standard meaning;  $\nu$  is the kinematic viscosity, and  $\mathbf{f}$  is the ponderomotive force acting on a unit volume of plasma:

$$\mathbf{f} = -\left\langle \tilde{\rho} \frac{d\tilde{\mathbf{v}}}{dt} \right\rangle + \frac{1}{c} \langle (\tilde{\mathbf{j}} \times \tilde{\mathbf{B}}) \rangle \quad (10.8)$$

The averaging is performed over the wave period. Under the condition that the inertial term, the first term in left-hand side of (10.7), is small, the (10.7) becomes stationary, describing a velocity field of steady flow:

$$\rho\nu\Delta\mathbf{V} = -\nabla \left[ p + \frac{B^2}{8\pi} \right] + \mathbf{f} \quad (10.9)$$

This equation determines *existence* or *nonexistence* of magnetosonic streaming: the streaming can be generated by the oscillation flux tube only if *the force is nonpotential*. In other words, for generation of secondary flows it is necessary that

$$\nabla \times \mathbf{f} \neq 0. \quad (10.10)$$

Otherwise, the ponderomotive force leads to an insignificant redistribution of the plasma and magnetic field.

We will see below that the nonzero vortex part in the ponderomotive force is provided by the radial dependence of magnetic field and plasma density across the flux tube. The magnitude of the force is, therefore, determined by the gradient of magnetic field and plasma density.

The magnitude of  $\mathbf{f}$  becomes large in the resonance layer where the phase velocity of kink oscillations becomes close to the local Alfvén velocity. Although the generated flow is of the second-order effect, a strong plasma streaming can arise in a thin resonance layer.

Let us rewrite (10.9) through the angular velocity  $\boldsymbol{\Omega} = \nabla \times \mathbf{V}$ :

$$\rho\nu\Delta\boldsymbol{\Omega} = \nabla \times \mathbf{f} \quad (10.11)$$

Equation (10.11) uniquely describes the velocity field of generated steady flows.

To carry out a quantitative analysis, we solve linear equations for kink oscillations and through linear solution find the ponderomotive force.

We assume that all perturbed quantities are proportional to  $\exp(i\omega t - ikz)$  and their dependence on  $\phi$  has a form (linearly polarized wave)

$$\psi(r, \phi) = \chi(r) \cos \phi \quad (10.12)$$

With (10.6) and (10.12), the linearized system of MHD equations for the kink mode is reduced to a single equation for  $\chi$ :

$$\frac{\partial}{\partial r} \left[ \rho(r) - \frac{k^2 B^2(r)}{4\pi\omega^2} \right] r \frac{\partial \chi}{\partial r} - \left[ \rho(r) - \frac{k^2 B^2(r)}{4\pi\omega^2} \right] \chi(r) = 0 \quad (10.13)$$

The important feature of (10.13) is that it has the classical form of the Rayleigh equation with a singularity: the coefficient of higher derivative at some point across the tube becomes zero. In our case, this is just the same point where the phase velocity of kink oscillations ( $\omega/k$ ) becomes equal to the local Alfvén velocity. As considered in Chap. 4 strong absorption of oscillations, the anomalous damping, takes place at this point. The analytical solution of (10.13) and corresponding damping rate are given in Sect. 4.1.

Having solutions of (10.13),

$$\tilde{v}_r = \frac{\chi(r)}{r} \sin \phi, \quad \tilde{v}_\phi = \frac{\partial \chi(r)}{\partial r} \cos \phi \quad (10.14)$$

and

$$\tilde{B}_r = -\frac{kB}{\omega} \frac{\chi(r)}{r} \sin \phi, \quad \tilde{B}_\phi = -\frac{kB}{\omega} \frac{\chi(r)}{r} \cos \phi \quad (10.15)$$

we can find the expression for ponderomotive (nonlinear) force, (10.8).

The averaged force has only stationary terms and can be written as follows:

$$\mathbf{f} = -\langle [\tilde{\mathbf{v}} \operatorname{div}(\rho \tilde{\mathbf{v}}) + \rho(\tilde{\mathbf{v}} \nabla) \tilde{\mathbf{v}}] \rangle + \frac{1}{4\pi} \langle (\nabla \times \tilde{\mathbf{B}}) \times \tilde{\mathbf{B}} \rangle \quad (10.16)$$

After some algebra, we get the following expressions for components of the ponderomotive force:

$$f_r = G(r) \cos 2\phi, \quad f_\phi = H(r) \sin 2\phi \quad (10.17)$$

where

$$f_r = \frac{\rho}{2} \cos 2\phi \left\{ \frac{\chi^2}{r^3} - \frac{\chi'^2}{r} - \frac{\chi^2}{r^2} \frac{\partial \ln \rho}{\partial r} - \frac{k^2 v_A^2}{\omega^2} \left[ \chi' \left( \frac{1}{r} \frac{\partial}{\partial r} r \chi' - \frac{\chi}{r^2} \right) + \chi'^2 \frac{\partial \ln B}{\partial r} \right] \right\} \quad (10.18)$$

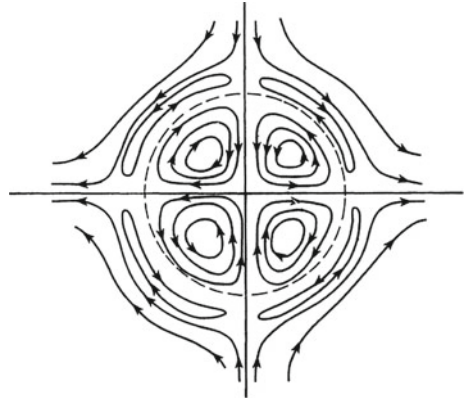
and

$$f_\phi = \frac{\rho}{2} \sin 2\phi \left\{ \frac{\chi}{r} \chi'' + \frac{\chi}{r^2} \chi' - \frac{\chi'^2}{r} + \frac{\chi \chi'}{r} \frac{\partial \ln \rho}{\partial r} - \frac{k^2 v_A^2}{\omega^2} \left[ \frac{\chi}{r} \left( \frac{\chi}{r^2} - \frac{1}{r} \frac{\partial}{\partial r} r \chi' \right) + \frac{\chi \chi'}{r} \frac{\partial \ln B}{\partial r} \right] \right\} \quad (10.19)$$

Here  $\chi(r)$  is the solution of (10.13) and the prime stands for derivative over  $r$ .

Equations (10.17)–(10.19) immediately show that streamlines of the field of ponderomotive force are closed in each quarter of the circle at a given radius of the magnetic flux tube. Sketch of streamlines of generated flow is shown in Fig. 10.2. It is important that plasma particles frozen in magnetic field follow the streamlines and ultimately end up with the same geometry as the generated flows Fig. 10.2. It must be emphasized that the flow is generated *inside* the flux tube as well as *outside* it.

**Fig. 10.2** Field of ponderomotive forces. The *dashed line* is an effective radius of flux tube



It is interesting to compare (10.11) with the classical equation describing the streaming generated by sound waves in a liquid (Equation (25) in Eckart 1948):

$$\frac{\partial \mathbf{R}_1}{\partial t} - \nu_0 \nabla^2 \mathbf{R}_1 = b \frac{\nu_0}{\rho_0} \nabla \rho_1 \times \nabla \left( \frac{\partial \rho_1}{\partial t} \right) \quad (10.20)$$

where  $\mathbf{R}_1 = \nabla \times \mathbf{u}$  is rotation of the secondary flow, and the coefficient  $b = 4/3 + \nu'/\nu_0$  is the abbreviation containing  $\nu$ , which is the ordinary coefficient of shear viscosity measured in  $\text{cm}^2/\text{s}$ , and  $\nu'$  which is the bulk viscosity. Although in fluid dynamics the generation of flow is provided by the viscous stresses and thus by the *absorption* of oscillation energy, the velocity amplitude of secondary flow turns out to be *independent* of the magnitude of viscous coefficients unless the bulk viscosity is nonzero.

There is a principal difference between the amplitude of generated flow in the case of acoustic streaming and that in the magnetosonic streaming. As already mentioned, in the case of flux tube oscillations we have two different means for generation of secondary flows and electric currents. One is associated with the *dissipative effects*. In this case the amplitude of plasma flow is proportional to the ratio of the damping rate to the coefficient of plasma viscosity. The magnitude of the damping rate is determined by the specific mechanism of absorption, which can be provided by the resonance absorption, by radiation of secondary acoustic waves, or by the usual dissipative mechanisms of absorption such as viscosity, thermoconductivity, and Ohmic losses. And yet, like in the acoustic streaming, the amplitude of secondary flow also turns out to be *independent* of the dissipative coefficients. But the time required to set up the steady state depends on the plasma resistance and is inversely proportional to the coefficient of viscosity or other dissipative coefficients. This is discussed in Sect. 10.4.

Another cause of secondary flows is the action of ponderomotive force, considered above. Here the situation is quite different because ponderomotive force is not dissipative and the amplitude of generated flow is no longer *independent* of the viscous



coefficient (or other dissipative coefficients) but is inversely proportional to it. This means that, at the applicability limit, flow generated by the action of ponderomotive force can reach a significant value.

In the following sections, we discuss a qualitative picture of the effect of ponderomotive force, and thus, of the induced flow on the evolution of magnetic flux tubes with the initially smooth radial profile of background parameters.

### 10.3 Process of Filamentation and Diffusive Vanishing of Magnetic Flux Tubes

The evolution of a flux tube due to the generated plasma flow strongly depends on the physical parameters of the flux tube and surrounding plasma. In particular, on the initial size (radius) of the tube, and on the relationship between the time of establishing of viscous flows and the duration of acoustic wave trains interacting with the flux tube. One can see from (10.7) that for large enough flux tubes the viscous term is small and its evolution is determined by the inertial term  $\rho \partial V / \partial t$ .

In this section, we give qualitative analysis of the case when the viscous term is essential and secondary streaming can be described by the averaged stationary equation (10.9). In the end of this section, we compare these results with an estimate of the lifetime of flux tube for which viscous effects are negligible.

We start with qualitative analysis of the field of forces defined by (10.18) and (10.19).

Denote the amplitude of flux tube displacement in kink oscillations by  $\xi = \sqrt{\xi_r^2 + \xi_\phi^2}$  ( $\tilde{\mathbf{v}} = \partial \xi / \partial t$ ). From (10.3) and (10.4), we can estimate the magnitude of magnetic field perturbation  $\tilde{B}$  as

$$\tilde{B} \sim B \frac{\xi \omega}{v_A} \quad (10.21)$$

The magnitude of ponderomotive force is of the order of  $(\tilde{B}^2/R)$ , i.e.,

$$f \sim \frac{B^2 \xi^2 \omega^2}{8\pi v_A^2 R} \quad (10.22)$$

The velocity amplitude of generated flow is estimated from (10.11):

$$\rho \nu V \frac{1}{R} \sim f \quad (10.23)$$

or

$$V \sim \frac{f R^2}{\rho \nu} \quad (10.24)$$

As discussed above, the amplitude of plasma streaming under the action of ponderomotive force does *depend* on the coefficient of viscosity and is inversely proportional

to it. This assertion is valid until the last term in (10.18) is larger than the inertial term.

The quantity  $(R^2/\rho)$  entering estimate (10.24) is proportional to the time of establishing of viscous flow:

$$\tau_\nu \sim \frac{R^2}{\nu}, \quad (10.25)$$

and determines the time required for magnetic structure to reach a new state provided by generated plasma flows.

The field of forces and, therefore, the character of generated flows, depend on the relation between  $\tau_\nu$  and the duration,  $T$ , of the acoustic wave train interacting with the flux tube.

We discuss here two cases, those of “coherent” and “incoherent” wave trains.

In the case of a long “coherent” wave train when

$$T > \tau_\nu, \quad (10.26)$$

the estimate (10.24) becomes as follows:

$$V \sim \frac{f\tau_\nu}{\rho} \quad (10.27)$$

The plasma density and magnetic field are gradually equilibrating along the streamlines of induced flow and obtain the same symmetry as those of ponderomotive force. This process leads to the splitting of magnetic flux into four independent flux tubes. This symmetry is a result of the specific of kink oscillations whose azimuthal number, (10.1) provides the corresponding symmetry of the force:

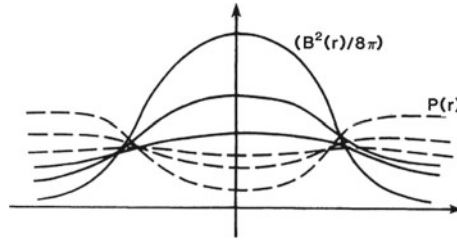
$$\mathbf{f} = \mathbf{i} G(r) \cos 2\phi + \mathbf{j} H(r) \sin 2\phi \quad (10.28)$$

Farther evolution of the system depends on the behavior of newborn flux tubes. Analytical description of the next stage is difficult, because newborn flux tubes form an ensemble of closely spaced structures with complicated flows inside them. They can interact with each other or/and be influenced by acoustic waves as their predecessors. If newborn flux tubes (or some of them) are influenced mostly by coherent acoustic waves, the filamentation process goes further, and those flux tubes experience further splitting. The behavior in this regime is confirmed by numerical simulation (Sect. 10.5). In this case, the lifetime of the magnetic structure is determined by the length of the time required to complete the filamentation process and by the subsequent diffusive vanishing of the smallest flux tubes.

### 10.3.1 Diffusive Broadening of Flux Tube

In the opposite case of short “incoherent” wave train or convective motions, when

$$T < \tau_\nu \quad (10.29)$$



**Fig. 10.3** Schematic change in time of squared magnetic field and gas kinetic pressure: the decreasing of magnetic field and the leveling of gas kinetic pressures inside and outside flux tube ends up by diffusive dissolving of flux tube

the generated flows have a character of stochastic motions. These motions result in a diffusive broadening of a flux tube: the plasma density and magnetic field are smoothed out gradually until the flux tube disappears.

In Fig. 10.3 the schematic change in time of squared magnetic field squared and gas kinetic pressure is shown: the decrease of magnetic field and the leveling of gas kinetic pressures inside and outside flux tube lead ultimately to complete dissolving of a flux tube.

The “diffusion coefficient,” defining a speed of this process, is

$$D \sim \frac{\Delta x^2}{T} \tag{10.30}$$

where  $\Delta x$  is the displacement of an element of a tube estimated as

$$\Delta x \sim VT \tag{10.31}$$

The velocity amplitude of generated flow in this case is of the order of

$$V \sim \frac{f}{\rho} T, \tag{10.32}$$

and for the diffusion coefficient, we have

$$D \sim \frac{\xi^4 \omega^4}{R^2} T^3 \tag{10.33}$$

The lifetime of a magnetic flux tube can be estimated in terms of the diffusion coefficient as

$$t_D \sim \frac{R^4}{\xi^4 \omega^4 T^3} \tag{10.34}$$

This estimate is valid for flux tubes that interact with the acoustic waves with the period  $T$  less than  $\tau_\nu$ , or with the convective motions with turnout time  $T < \tau_\nu$ . At the

same time, the radius of flux tubes should be small enough to satisfy the condition when the inertial term is small compared with the viscous term:

$$\rho \left| \frac{\partial \mathbf{V}}{\partial t} \right| < |\nu \Delta \mathbf{V}| \quad (10.35)$$

As mentioned above for thick flux tubes, the term  $|\nu \Delta \mathbf{V}|$  is negligibly small and their evolution is determined by the inertial term. In this case, the generated flow is estimated as

$$V \sim \frac{f t_V}{\rho}, \quad (10.36)$$

where  $t_V$  is the time of the establishing of the generated flow. If this time is less or comparable with the duration of acoustic wave trains, the flux tube experiences the splitting into thinner tubes. The time of splitting is of the order of  $t_V$ :

$$t_{\text{split}} \sim t_V \sim \frac{R}{V} \sim \frac{\rho R}{f t_{\text{split}}} \quad (10.37)$$

or

$$t_{\text{split}} \sim \sqrt{\frac{\rho R}{f}} \sim \frac{R}{\omega \xi} \quad (10.38)$$

Transition from the case (10.34) to (10.38) occurs when these time scales become comparable, i.e., for a tube radius exceeding the estimate

$$R \sim \xi \omega T. \quad (10.39)$$

In the next section, we give order-of-magnitude estimate of generated flows and corresponding lifetimes for photospheric flux tubes interacting with the convective motions and acoustic wave trains.

### 10.3.2 Quantitative Estimates—Lifetimes and Spatial Scales of Flux Tubes

For quantitative estimates, we adopt the following typical values: the period of acoustic waves  $T_p = 300\text{--}180$  s, duration of acoustic wave train  $T_{\text{wtr}} = 25$  min, and lifetime of convective granule  $T_{\text{conv}} = 8$  min. Consider flux tubes with  $R = 100$  km and less. For the effective viscosity at magnetic flux site, we use the observed limit on turbulent velocities,  $\tilde{v}$ , and characteristic length scale of the turbulence,  $\tilde{l}$ , consistent with observations (Beckers 1976; Title et al. 1992; Yi and Engvold 1993):  $\tilde{v} = 0.4$  km s<sup>-1</sup> and  $\tilde{l} = 20$  km. This gives for the effective viscosity  $\nu = 8$  km<sup>2</sup>/s.

For the chosen parameters  $\tau_\nu = R^2/\nu \simeq 21$  min, and the necessary condition (10.26) is fulfilled. Obviously, the duration of the splitting process is comparable with the time of the establishing of viscous flows, e.g.,  $\tau_\nu$ . So that in time  $t_{\text{split}} \simeq 21$  min

flux tube with radius  $R = 100$  km splits into four newborn flux tubes each with radius roughly of  $R = 50$  km.

To estimate the amplitude of corresponding flows generated across the flux tube, we use (10.24) which with (10.22) becomes as follows:

$$V \simeq \frac{1}{2} \frac{\xi^2 \omega^2}{\nu} R \quad (10.40)$$

We assume that transverse displacement of a flux tube  $\xi$  is not less than  $R/2\pi$ . This assumption may be justified from the condition (10.39) where, for periodic motions replacing  $\omega T$  by  $2\pi$  we come to above estimate.

For the velocity of transverse displacement of a flux tube,  $\tilde{v} = \omega \xi$ , this estimate gives  $\tilde{v} = \omega \xi = R/T_p$ . And for tubes of radius  $R = 100$  km we have  $\tilde{v} = 0.33 \text{ km s}^{-1}$  which is consistent with the observed values. From (10.40) we find the amplitude of generated flows:  $V = 0.7 \text{ km s}^{-1}$ .

Newborn flux tubes having radius 50 km may experience farther splitting. This time either again due to the interaction with the acoustic wave trains or, more likely, due to the action of convective motions: for these flux tubes  $\tau_\nu = 5.21 \text{ min} < T_{\text{conv}}$ . Duration of this process is of the order of 5.21 min. The amplitude of generated flows is  $V \simeq 0.1 \text{ km s}^{-1}$ . In the third generation, flux tubes whose radius is now about 25 km are too thin to experience farther splitting and should vanish diffusively in time  $\simeq 1.3$  min. The total lifetime of a flux tube with  $R = 100$  km is thus roughly 27 min.

It is important to note that the condition (10.39) determines the lower limit of flux tube size (its radius) below which flux tubes do not experience fragmentation and vanish diffusively. To estimate the critical radius given by (10.39), note that diffusive regime requires the condition (10.29). This means that at given timescale  $T$ , flux tubes with radius  $R \leq \sqrt{\nu T}$  are subject to diffusive vanishing with  $t_D \simeq T$  (with  $T \leq \tau_\nu$ !). If we assume that the minimum effective timescale is that of 3 min oscillations, the minimum critical radius is then  $R_{\text{min}} = \sqrt{\nu T_p} = 38 \text{ km}$ . Of course, this estimate is the order-of-magnitude one, and the value of critical radius may be smaller or larger than 40 km. For example, convective motions also can terminate the fragmentation process in flux tubes with radius about 60–70 km. In this case, the flux tube vanishes diffusively in time of  $\simeq 7$ –9 min.

The estimated timescales, the range of velocities, and the dynamics of photospheric flux tubes are in a good agreement with the observed regularities found in sub-arcsecond measurements (Berger et al. 1995; Schrijver et al. 1997; Kubo et al. 2010).

It is important to note that plasma flows are also generated *outside* flux tube. In a case of kink oscillations under the conditions close to (10.26), four stationary vortices are generated outside a flux tube. These vortices, shown in Fig. 10.2 outside dotted line (representing the flux tube radius), are similar to those generated in the experiments of Andrade and Schlichting shown in Fig. 10.1 (see also Holtzmark et al. 1954). In these experiments, as well as in any manifestation of an acoustic streaming, the only mechanism leading to the generation of flows is the *absorption* of the energy of oscillation in a thin boundary layer. Whereas the mechanism of generation of mass flows inside and outside oscillating magnetic flux tubes is associated with “always present” intrinsic properties of flux tubes.

## 10.4 Generation of Mass Flows Due to the Absorption Mechanisms

In presence of dissipative effects just like in the case of acoustic streaming, the energy of oscillating flux tube may be converted into secondary flows within a thin boundary layer. This mechanism leads to additional and much richer effects in magnetohydrodynamics of flux tubes which in some aspects have no analogy in hydrodynamics.

As discussed throughout the book, along with the usual dissipative effects, the energy of flux tube oscillations is intrinsically damped out due to the nondissipative damping mechanisms:

- (1) Radiative damping when an oscillating flux tube gives off its energy through emission of secondary acoustic or MHD waves; and
- (2) Anomalous damping in the resonance layer, where the phase velocity of flux tube oscillations becomes close to the local meaning of Alfvén velocity.

In particular, the anomalous damping of kink oscillations in the resonant layer leads to especially strong effect of magnetosonic streaming.

Recall that physically, the nature of this mechanism is the pumping of oscillation energy into the resonance layer where the dissipation occurs. The whole *momentum* or/and *angular momentum* of flux tube oscillations is transferred to the plasma in a thin layer, causing in nonlinear stage generation of a strong mass flows.

Formally, the expression for the force inducing the secondary streaming has the same form as (10.8), but now the terms that are directly connected with the resonant absorption are taken into account.

Absorption of the *momentum* of oscillations leads to the generation of *upward* or *downward* mass flows. Absorption of *angular momentum* of oscillations causes the rotational mass flows in a plane perpendicular to tube axis. Nonzero angular momentum can be transmitted, for example, by circularly polarized kind oscillations.

The solution of (10.13) for a smooth dependence of plasma density and magnetic field on the tube radius (4.12) leads to the following dispersion relation:

$$\omega \simeq \frac{kB}{\sqrt{4\pi(\rho + \rho_e)}} \left( 1 + \frac{i\pi}{4} \frac{\rho}{\rho + \rho_e} \frac{l}{R} \right) \quad (10.41)$$

One can see that it contains a large imaginary part corresponding to strong absorption of kink oscillations in the resonance layer. For smooth radial profile of magnetic field and density, when  $l \simeq R$ , the damping rate becomes comparable with eigenfrequency  $\gamma = \text{Im } \omega \sim \text{Re } \omega$ , and the effect is quite strong.

From (10.41) we have for the spatial damping rate  $\alpha = \text{Im } k$ :

$$\alpha = \frac{\pi}{4} \frac{\omega}{v_A} \sqrt{\frac{\rho}{\rho + \rho_e}} \frac{l}{R} \quad (10.42)$$

The energy of kink oscillations per unit length of a tube is  $W = \rho \tilde{v}^2 \pi R^2$ ;  $\tilde{v}$  is the magnitude of linear velocity perturbation (see (10.6)). The momentum of oscillation is

$$\mathcal{P} = \frac{k_z}{\omega} W \quad (10.43)$$

The force  $F_z$  appearing due to the absorption of momentum  $\mathcal{P}$  is proportional to

$$F_z \sim \alpha \frac{k_z}{\omega} \mathcal{P} \quad (10.44)$$

The force acting on a unit volume of a tube is then

$$f_z = \frac{F_z}{2\pi Rl} \quad (10.45)$$

From (10.42) and (10.44)–(10.45) we have

$$f_z \simeq \frac{\pi}{8} \frac{\omega}{v_A} \sqrt{\frac{\rho}{\rho + \rho_e}} \rho \tilde{v}^2 \quad (10.46)$$

As we see, the “model” parameter ( $l/R$ ) does not enter in the final expression for the force responsible for the generation of mass flows. The magnitude of generated flows which is proportional to  $f_z$  is completely determined by the basic physical parameters and assumes arbitrary radial dependence of flux tube parameters.

Let us now estimate the flow velocities generated along magnetic flux tubes under a real conditions typical to solar atmosphere. In particular, we consider two examples, flux tubes in the chromosphere and low corona.

For these estimates it is convenient to rewrite expression (10.46) through plasma beta. The pressure equilibrium condition gives that  $\rho/\rho_e = \beta/(1 + \beta)$ , and (10.46) becomes

$$f_z \simeq \frac{\pi}{8} \frac{\omega}{v_A} \sqrt{\frac{\beta}{1 + 2\beta}} \rho \tilde{v}^2 \quad (10.47)$$

The amplitude of generated flows, (10.24), is then

$$V_z \simeq \frac{\pi}{8} \frac{\omega}{v_A} \sqrt{\frac{\beta}{1 + 2\beta}} \tilde{v}^2 \frac{R^2}{\nu} \quad (10.48)$$

In chromosphere and corona, i.e., in the magnetic dominant case ( $\beta \ll 1$ ), viscosity is estimated by Braginsky’s kinetic coefficients:

$$\rho\nu = 2.21 \times 10^{-15} \frac{T^{5/2}}{\ln \Lambda} \text{g cm}^{-1} \text{s}^{-1} \quad (10.49)$$

For quantitative estimate, we use following parameters.

For chromosphere: temperature  $T = 10^4$  K, Coulomb logarithm  $\Lambda = 10$ , density  $n = 10^{11} \text{ cm}^{-3}$  ( $\rho = 1.67 \times 10^{-13} \text{ g cm}^{-3}$ ), magnetic field  $B = 50$  G (Alfvén velocity is then  $v_A = 345 \text{ km/s}$ ), characteristic radius of magnetic structure  $R = 100 \text{ km}$ , and wave period  $T_p = 180 \text{ s}$ .

For low corona: temperature  $T = 10^5$  K,  $\Lambda = 20$ , density  $n = 3 \times 10^9 \text{ cm}^{-3}$  ( $\rho = 5 \times 10^{-15} \text{ g cm}^{-3}$ ), weaker magnetic field of  $B = 10$  G (Alfvén velocity  $v_A = 399 \text{ km/s}$ ), and wider structure of radius  $R = 200 \text{ km}$ ; for the wave period we accept a typical period of Alfvén waves  $T_p = 100 \text{ s}$ .

We assume that the velocity of transverse displacement of a flux tube in chromosphere and corona is proportional to the radius of the structure and wave frequency. This gives in chromosphere  $\tilde{v} \simeq 3 \text{ km/s}$ , and in corona  $\tilde{v} \simeq 12 \text{ km/s}$ .

For chosen set of parameters (10.48) gives the following estimates for the amplitude of mass flows generated along the flux tube: in chromosphere  $V_z \simeq 23 \text{ km/s}$  and in corona  $V_z \simeq 2.5 \text{ km/s}$ . It is remarkable that the range of velocities in the chromosphere are close to those observed in spicules.

Thus in the application to chromospheric magnetic structures, “magnetosonic streaming” can be considered as a promising candidate for more detailed studies of the origin of spicules and their dynamics. It is important to note that the secondary flows generated along and/or across the magnetic flux tube should no be confused with short-living strong sporadic jets observed throughout the solar atmosphere. The secondary flows belong rather to the flux tubes themselves, the feature that is “always there.”

In the same way as above, we can estimate the magnitude of the force appearing due to the absorption of angular momentum of oscillations which is responsible for generation of azimuthal flows and electric currents. The angular momentum directed along the tube axis is estimated as

$$M_z \sim \frac{W}{\omega} \quad (10.50)$$

The angular momentum absorbed per unit length of a tube is proportional to  $(\alpha k_z / \omega) M_z$ . An estimate for force acting on plasma in the azimuthal direction may be obtained from the following relation

$$2\pi Rl \sim \frac{\alpha k_z}{\omega} M_z \omega \quad (10.51)$$

or

$$f_\phi \sim \frac{\alpha k_z}{\omega} \frac{W}{2\pi Rl}, \quad (10.52)$$

These are the same order of magnitude force as in the case of the absorption of the momentum of oscillation.

As mentioned above, if the oscillation energy is mostly absorbed by one of the plasma components (electron or ion), mass flows are accompanied by current drive. In this case, imaginary part of (10.41) contains additional terms connected with the specific damping mechanism.



If the absorption is associated mostly with the electron component of plasma, the damping may be a result of one of the two major damping mechanisms:

(1) Electron-ion collision with collisional damping rate

$$\delta_e \sim \nu_{ei} \frac{v_A}{k_z v_{Te}^2} \quad (10.53)$$

(2) Landau damping with

$$\delta_L \sim \frac{\omega}{k_z v_{Te}}, \quad (10.54)$$

$v_{Te}$  being the electron thermal speed.

For example, in a case of Landau damping for spatial damping rate  $\alpha_L$ , we have

$$\alpha_L \sim \frac{\sqrt{\pi} r_i^2 T_e k v_A}{2 l^2 T_i v_{Te}} \quad (10.55)$$

Here  $r_i$  is the ion Larmor radius,  $T_e$  and  $T_i$  are the electron and ion temperatures, respectively.

Let us estimate, for example, the magnitude of the azimuthal electric current generated by the absorption of angular momentum. The force (10.52) causes the motion of electrons with the velocity

$$u_{e\phi} \sim \frac{f_\phi \tau}{n_e m_e}, \quad (10.56)$$

and thus, leads to the appearance of azimuthal current  $j_\phi = en_e u_\phi$  of the order of

$$j_\phi \sim \frac{\alpha_L}{\nu_{ei}} \frac{e}{m_e} \frac{\rho \tilde{v}^2}{2} \frac{R}{l} \quad (10.57)$$

In the same way, we can estimate the currents generated along the magnetic field due to the action of the  $z$ -component of the force (10.46).

## 10.5 Numerical Analysis

In this section, numerical simulations of magnetosonic streaming and current drive are performed for the regime corresponding to the filamentation process, i.e., to the generation of the azimuthal flows and electric currents.

### 10.5.1 Basic Equations and Numerical Method

For numerical simulations, the following assumptions are adopted:

- (1) the medium is an ideal gas,
- (2) the gas is a polytrope of index  $\gamma = 1.5$ ,
- (3) the magnetic field is frozen in the gas and is vertical, and
- (4) gravity is neglected. Cartesian coordinates  $(x, y, z)$  are adopted so that the  $z$ -direction is parallel to the magnetic field. It is assumed that the evolution is two-dimensional with  $\partial/\partial z = 0$ . Thus the basic equations are as follows:

$$\frac{\partial \rho}{\partial t} + \frac{\partial}{\partial x}(\rho V_x) + \frac{\partial}{\partial y}(\rho V_y) = 0, \quad (10.58)$$

$$\frac{\partial}{\partial t}(\rho V_x) + \frac{\partial}{\partial y}(\rho V_x V_y) + \frac{\partial}{\partial x} \left( \rho V_x^2 + p + \frac{B_z^2}{8\pi} \right) = \delta_x, \quad (10.59)$$

$$\frac{\partial}{\partial t}(\rho V_y) + \frac{\partial}{\partial x}(\rho V_x V_y) + \frac{\partial}{\partial y} \left( \rho V_y^2 + p + \frac{B_z^2}{8\pi} \right) = \delta_y, \quad (10.60)$$

$$\frac{\partial B_z}{\partial t} + \frac{\partial}{\partial x}(V_x B_z) + \frac{\partial}{\partial y}(V_y B_z) = 0, \quad (10.61)$$

$$\begin{aligned} & \frac{\partial}{\partial t} \left[ \frac{p}{\gamma - 1} + \frac{1}{2} \rho (V_x^2 + V_y^2) + \frac{B_z^2}{8\pi} \right] \\ & + \frac{\partial}{\partial x} \left[ \frac{\gamma}{\gamma - 1} p V_x + \frac{1}{2} \rho V_x (V_x^2 + V_y^2) + \frac{B_z^2}{4\pi} V_x \right] \\ & + \frac{\partial}{\partial y} \left[ \frac{\gamma}{\gamma - 1} p V_y + \frac{1}{2} \rho V_y (V_x^2 + V_y^2) + \frac{B_z^2}{4\pi} V_y \right] = \delta_x V_x + \delta_y V_y, \end{aligned} \quad (10.62)$$

where  $\delta_x$  and  $\delta_y$  describe the interaction of a flux tube with acoustic waves. All other symbols have their standard meaning.

The distribution of the initial magnetic field strength  $B_z(x, y)$  is given by

$$B_z(x, y) = [8\pi p(x, y)/\beta(x, y)]^{1/2} \quad (10.63)$$

where

$$\beta(x, y) = \beta_0/f(x, y), \quad (10.64)$$

$$f(x, y) = \frac{1}{2} \left[ -\tanh \left( \frac{r - r_0}{w_0} \right) + 1 \right], \quad (10.65)$$

$$r = [(x - x_0)^2 + (y - y_0)^2]^{1/2}, \quad (10.66)$$

and where  $\beta_0$  is the plasma beta at the center of the flux tube,  $x_0$  and  $y_0$  are the coordinates of the center of the flux tube,  $r_0$  is its radius, and  $w_0$  is the width of the

boundary layer between the flux tube and the unmagnetized plasma. In these calculations, we use  $\beta_0 = 0.2$  and  $w_0 = 1.0 H$ , where  $H$  is the characteristic length scale.

The initial density and pressure distributions are calculated by using (10.63)–(10.66), the equation of the state and the equation of magnetostatic equilibrium

$$p(x, y) + \frac{B_z^2}{8\pi} = \text{const.} \quad (10.67)$$

An incompressible velocity field is initially imposed on the magnetic flux tube. We assume a velocity potential of the form

$$\Phi(x, y) = A \sin \pi x \cdot \sin \pi y, \quad (10.68)$$

and consider resulting velocity field

$$V_x = -f(x, y) \frac{\partial \Phi}{\partial y}, \quad V_y = -f(x, y) \frac{\partial \Phi}{\partial x}, \quad (10.69)$$

Time-dependent acoustic perturbations are imposed on the magnetic flux tube via interaction terms in the equations of motion (10.59) and (10.60) of the following form:

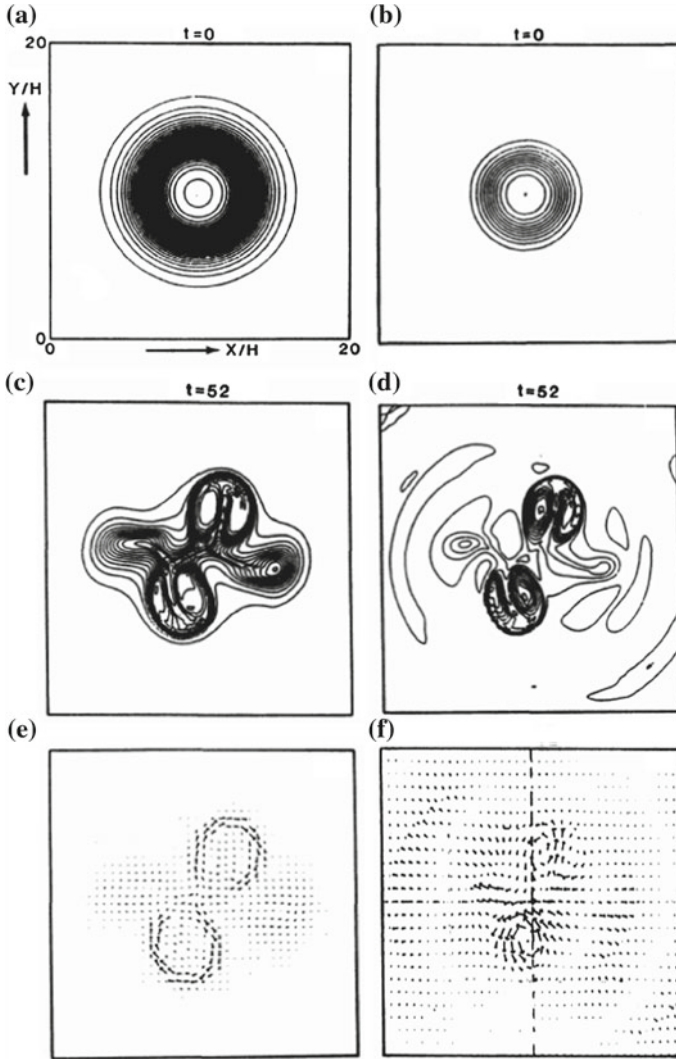
$$\delta_x = Af(x, y) \cdot \sin \omega t, \quad \delta_y = Af(x, y) \cdot \cos \omega t. \quad (10.70)$$

We assume free boundaries for  $x = 0$ ,  $x = X_{\max}$ ,  $y = 0$ , and  $y = Y_{\max}$ . Equations (10.58)–(10.65) are nondimensionalized by using a characteristic length scale  $H$ , the sound speed  $c_s$  and the density  $\rho_0$  outside the flux tube. The system is solved numerically by using a modified Lax–Wendroff scheme with an artificial viscosity according to Richtmyer and Morton (1967). The tests and accuracy of such an MHD code have been described for example in Tajima (1989). The mesh sizes are  $\Delta x = X_{\max}/(N_x - 1)$  and  $\Delta y = Y_{\max}/(N_y - 1)$ , where  $N_x$  and  $N_y$  are the numbers of mesh points in the  $x$ - and  $y$ -directions. The total number of mesh points is  $(N_x \times N_y) = (203 \times 203)$ , the total area is  $(X_{\max} \times Y_{\max}) = (20 \times 20)$  in a typical model in units of the characteristic length scale.

## 10.5.2 Numerical Results

We will present here four examples (models 1–4) of numerical simulation of the filamentation process in the interaction of magnetic flux tube with acoustic waves. The main parameters of simulation models are the interaction terms,  $\delta_x$  and  $\delta_y$ , the initial radius of flux tube,  $r_0$ , the frequency,  $\omega$ , and the artificial viscosity parameter,  $q$ . Models 1–3 represent the case where the interaction term has only an  $x$ -component,  $\delta_x = 0.05$ . In model 4, we allow a nonzero  $y$ -component of the interaction term,  $\delta_y = 0.05$ . The artificial viscosity is  $q = 3.0$ . By varying radius and frequency, we also study the dependence of the evolution of flux tube on these parameters.

Figure 10.4 shows the initial ( $t = 1$ ) and final ( $t = 52$ ) states of the contour lines of the magnetic field  $B_z$ , the density distribution ( $\log \rho$ ), the velocity field  $\mathbf{V} = (V_x, V_y)$ ,



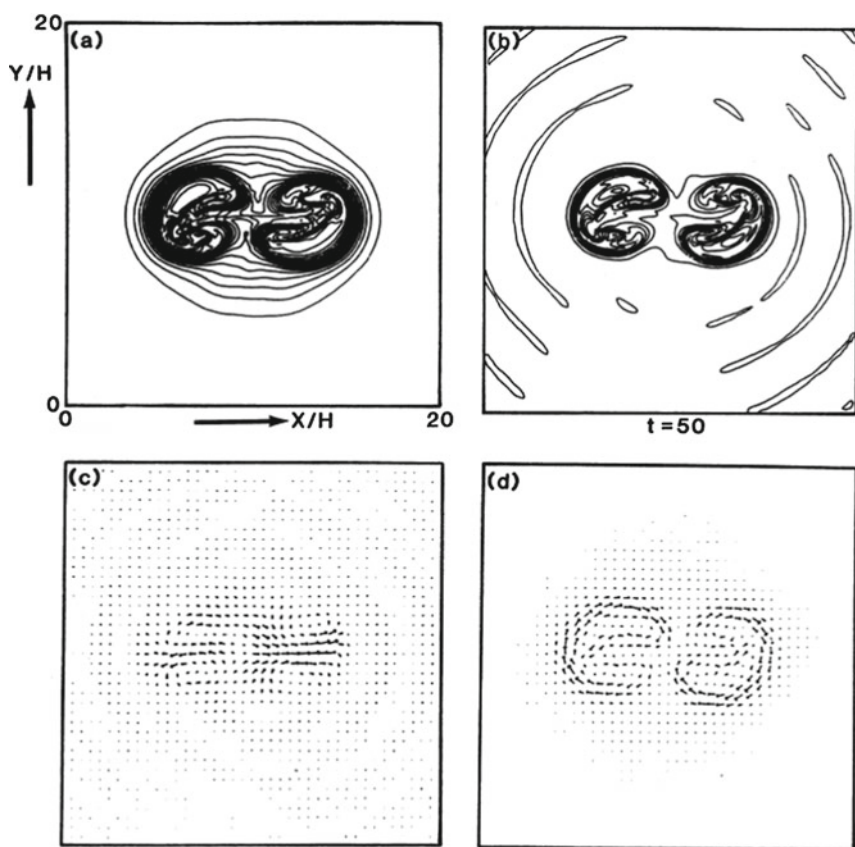
**Fig. 10.4** Results for model 1. Shown are **a** the contour lines of  $B_z$  and **b** the density contours ( $\log \rho$ ) of undisturbed flux tube. **c-f** Results at  $t = 52$ : **c** the contour lines of magnetic field, **d** the density contours, **e** the current density  $\mathbf{j} = (j_x, j_y)$ , and **f** the velocity field  $\mathbf{V} = (V_x, V_y)$ . Total illustrated area is  $(20 \times 20)$  in units of  $H$ . The contour level step width is 1.5 for **a** in the unit of linear scale and 0.2 for **b** in the unit of logarithmic scale. The maximum values of the current density and velocity vectors shown in *panels* (e) and (f) are in units of  $(\rho c_s^2/H)^{1/2}$  and sound speed  $c_s$ , respectively. Numbers on top of each frame represent the time in units of  $H/c_s$

and the current density  $\mathbf{j} = (j_x, j_y)$  for model 1. The radius of unperturbed flux tube in this model is  $r_0 = 2H$ , temporal frequency of the wave is  $\omega = 2\pi/5$ . Initially, the vertical magnetic field with a smooth radial profile is concentrated in a flux tube with radius  $r_0$ , the plasma density inside the flux tube (also having a smooth radial

dependence) is lower than outside for pressure equilibrium (isothermal plasma), and the velocity field shows the potential, incompressible flow imposed on magnetic flux tube according to (10.69). In the course of the evolution, the magnetic flux tube breaks down into four different magnetic structures ( $t = 52$ ).

The magnetic field of the final configuration is distributed into two major and two minor, nearly symmetrical, tubes. The density distribution and generated current density show the filamentation process as well. It is remarkable that magnetic field lines and plasma density lines in the “final” state are no longer collinear—a fact important for further evolution of a conglomerate of newborn flux tubes, as well as for observed properties of magnetic structures.

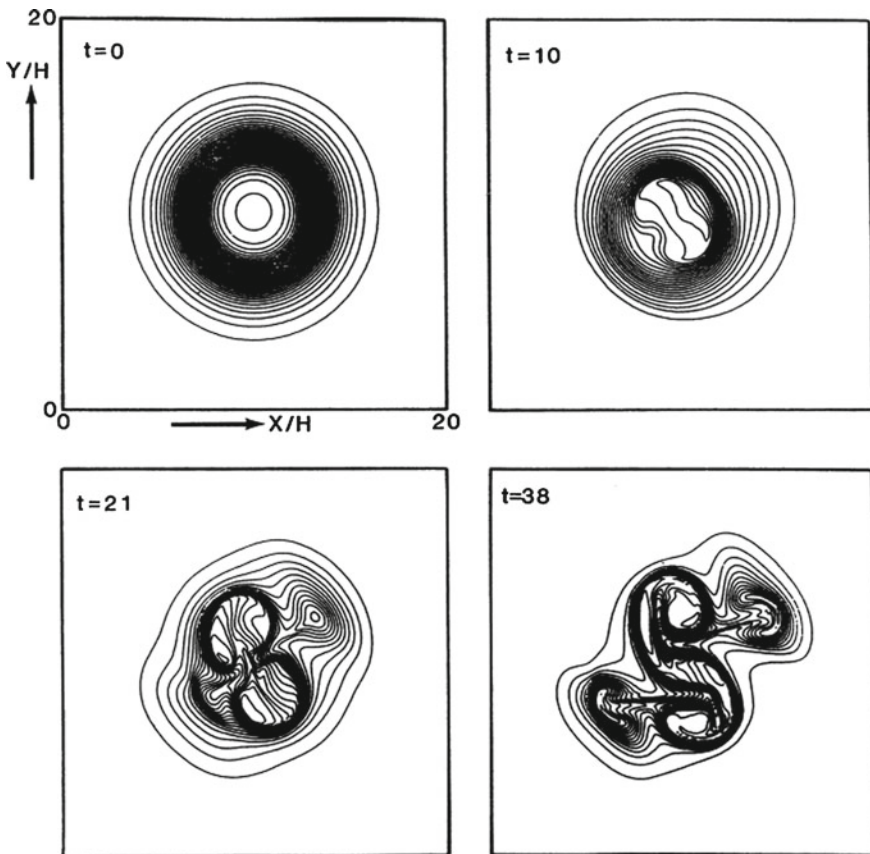
It is important to emphasize that in all cases the generation of flows and fragmentation of magnetic flux tubes accompanied redistribution of electric currents, occurs according to a newly acquired topology determined by system parameters. Results for model 2 are shown in Fig. 10.5. The frequency of acoustic perturbation is twice



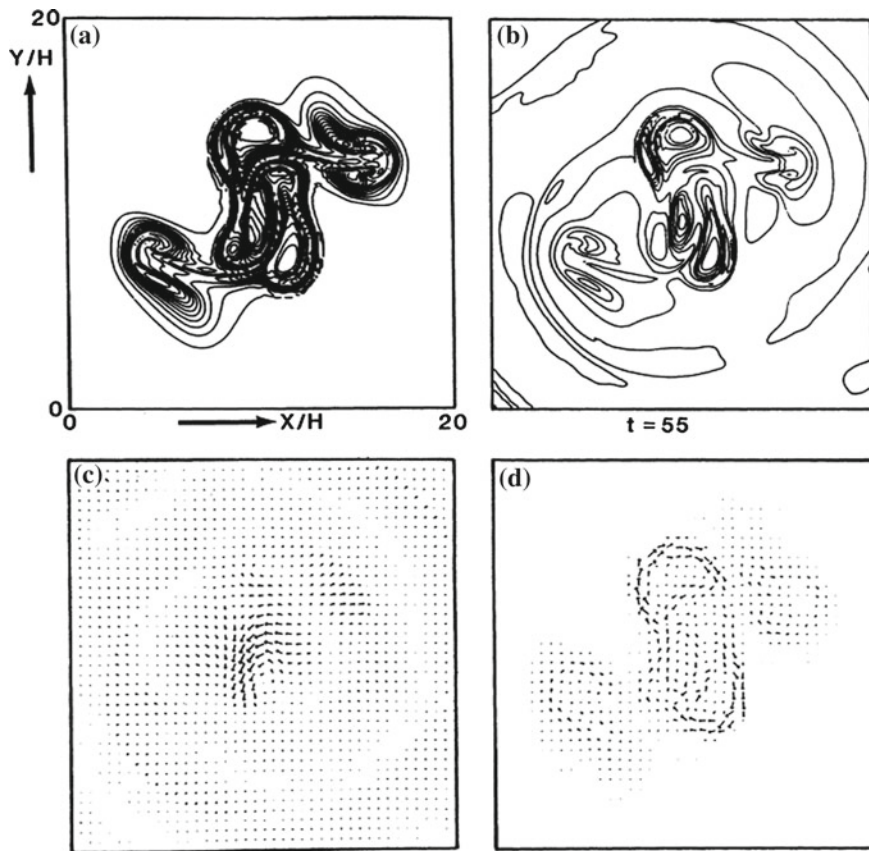
**Fig. 10.5** Results at  $t = 50$  for model 2. Shown is only the final state: **a** the contour lines of  $B_z$ , **b** the density contours ( $\log \rho$ ), **c** the velocity field  $\mathbf{V} = (V_x, V_y)$ , and **d** the current density  $\mathbf{j} = (j_x, j_y)$ . Other remarks are the same as in Fig. 10.4

as high as in model 1. We again witness the splitting of the initial flux tubes, but this time into two identical satellites, while in previous case along two major newborn flux tubes there were two weaker elements. The appearance of two major flux tubes in both cases is provided by the fact that the interaction force has only one component; the lower frequency (longer duration time) in previous case provided the formation of two smaller satellites. In model 3 we study the dependence on the artificial viscosity in the numerical code (Fig. 10.6). The simulations show that within the regime of  $q = 3$  to  $q = 6$ , the evolution of flux tube is not sensitive to the magnitude of the artificial viscosity, except may be for the fact that higher viscosity, as predicted by theory, leads to more a pronounced effect of filamentation.

Finally, we investigate the case where the interaction terms have nonzero  $x$  and  $y$  components (model 4). This case is close to the theoretical analysis with the difference that theory assumes both components of the force equal to each other. The advantage of the numerical result compared with the analytical one is that here



**Fig. 10.6** Results for model 3. Time evolution of flux tube in the interval  $t = 0-38$  with higher artificial viscosity

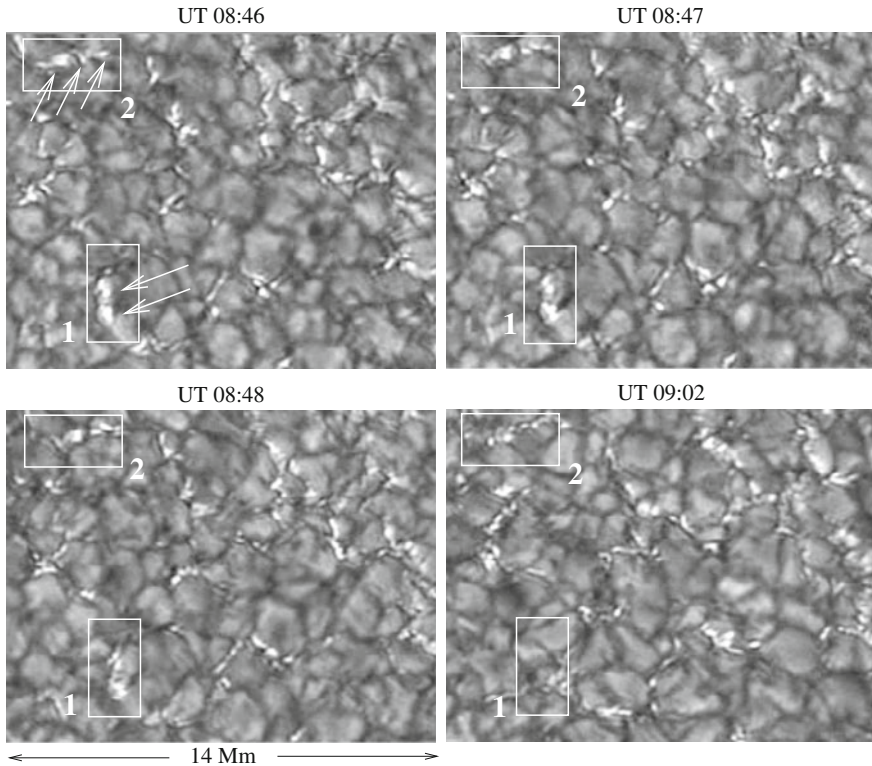


**Fig. 10.7** Results at  $t = 55$  for model 4, where the generated force has both,  $x$ - and  $y$ - components. The formation of a complex structure with many magnetic elements of different strength and size is shown

the evolution of the flux tube can be traced further into later stages: the filamentation process does not stop at the formation of the first four newborn flux tubes but goes further, showing the formation of a complex structure with many magnetic elements of different strength and size (Fig. 10.7).

## 10.6 Intrinsic Nature of Flux Tube Fragmentation

Time series of high-resolution observations show that continuous fragmentation, merging, and dissolution of small-scale magnetic flux tubes is the fundamental process in the photosphere and overlying atmosphere (Yi and Engvold 1993; Berger et al. 1995; Berger and Title 1996; de Wijn et al. 2009; Bellot Rubio et al. 2001). The



**Fig. 10.8** Snapshots of quiet sun region in G-band showing evolution of small-scale magnetic elements buffeted by convective motions. Examples of breaking of magnetic flux tubes in smaller and smaller satellites are highlighted by *boxes 1* and *2*. The image is taken by the DOT on 13 April, 2005. Reprinted from <http://www.staff.science.uu.nl>, courtesy of Rob Rutten

timescale of splitting and merging processes spans from tens of second to minutes. In each individual case, the process persists to the limit of resolution. The resolved elements vary in shape from circular points as small in diameter as 70 km to elongated filaments with lengths of the order of 500–1,000 km which in high resolution consist of *chains of circular flux tubes*. They are located predominantly in the intergranular lanes constantly buffeted by convective motions and wave trains.

The flux tubes are associated with intergranular bright points whose intensity structure consists of a bright core with a dark surroundings. The best proxy of the small-scale flux tubes are G-band images taken through a  $12 \text{ \AA}$  bandpass filter centered at  $4,305 \text{ \AA}$  line. Example of the G-band image of a small quiet sun area is shown at 4 instances of time in Fig. 10.8.

Boxes 1 and 2 highlight examples of two groups of small-scale flux tubes that quickly break into smaller and smaller elements. First three snapshots show the evolution of flux tubes with 1 min interval. The group in the box 1 consisting roughly of four elements in two minutes breaks into about 7–8 smaller elements.



In another four minutes shown at UT 09:02 every flux tubes has been “dissolved.” The fragmentation of flux tubes in box 2 is longer process: at UT 09:02 a beautiful chain of tiny flux tubes have been spread along the intergranular lane. The average cross-section of these elements is less than 100km. In a few minutes, they will be dissolved as well.

It is interesting that the fragmentation process even in the case of photospheric magnetic flux tubes can end up with quite vigorous nonlinear dynamics. In other words, diffusive vanishing is only one possibility of the final stage of life of flux tube. Given that generated flows are accompanied by current drive with quite complicated geometry, strong distortion of the topology of magnetic field takes place. This may lead to such a situation that is favorable for local *reconnections*. This process will manifest itself in a strong localized brightening and plasma jets well above the photosphere, i.e., in the chromosphere/transition region and even in corona. These effects will be considered in Chaps. 12 and 13.

## References

- E.N. Andrade, Proc. R. Soc. **A134**, 445 (1931)  
 J.M. Beckers, *Astrophys. J.* **203**, 739 (1976)  
 L. Bellot Rubio et al., *Astrophys. J.* **560**, 101 (2001)  
 T. Berger et al., *Astrophys. J.* **454**, 531 (1995)  
 T. Berger, A. Title, *Astrophys. J.* **463**, 365 (1996)  
 A.G. de Wijn et al., *SSRv* **144**, 275 (2009)  
 C. Eckart, *Phys. Rev.* **73**, 68 (1948)  
 M. Faraday, *Philos. Trans. R. Soc. Lond.* **121**, 229 (1831)  
 J. Holtzmark et al., *J. Acoust. Soc. Am.* **26**, 26 (1954)  
 M. Kubo, B.C. Low, B.W. Lites, *Astrophys. J.* **712**, 1321 (2010)  
 A. Meissner, *Zs. Tech. Phys.* **7**, 585 (1926)  
 W.L. Nyborg, in *Physical Acoustics, Part B, Properties of Polymers and Nonlinear Acoustics*. vol. 2 (Academic Press, New York, 1965)  
 L. Rayleigh, *Philos. Trans. R. Soc. Lond.* **175**, 1 (1884)  
 R.O. Richtmyer, K.W. Morton, *Difference Methods for Initial Value Problems*, 2nd edn. (Interscience, New York, 1967), Chap 13  
 M.P. Ryutova, in *Proceedings of the Joint Varenna-Abastumani International School on Plasma Astrophysics* (Noordwijk: ESA, 1986), p. 71  
 H. Schlichting, *Phys. Zs.* **33**, 327 (1932)  
 H. Schlichting, K. Gersten, *Boundary-Layer Theory* (Springer, 2000)  
 C.J. Schrijver et al., *Sol. Phys.* **175**, 329 (1997)  
 T. Tajima, *Computational Plasma Physics* (Addison-Wesley, Redwood City, 1989)  
 A.M. Title et al., *Astrophys. J.* **393**, 782–794 (1992)  
 Z. Yi, O. Engvold, *Sol. Phys.* **144**, 1 (1993)

# Chapter 11

## Moving Magnetic Features (MMFs)

**Abstract** In highly dynamic environment of sunspot areas with various sources and sink of energy, small-scale flux tubes do not in general obey the local conservation laws, nor do the ensembles of flux tubes that exhibit a complex collective phenomena. Some of the most spectacular phenomena are associated with the so-called Moving Magnetic Features, MMFs, small bipoles streaming radially outward the sunspot penumbra and exhibiting various mysterious properties. For example, they are observed to propagate faster than background mass flows and sometimes even upstream. Altogether, the properties of the MMFs are inconsistent with the energy and momentum conservation laws and require the approach of a nonconservative, energetically open systems. In this chapter we shall study these amazing features, their observed characteristics, and their impact on the overlying atmosphere. We shall apply the methods of nonconservative systems to understand their behavior. We will also see the negative energy waves in action, and associated formation of shocks and solitons.

### 11.1 Types of MMFs and Their Observed Properties

The regular outward motions of bright points around sunspots observed by Sheeley (1967) and Vrabc (1971), were named by Harvey and Harvey (1973) moving magnetic features, MMFs. They were the first to give detailed description of the MMF properties by using simultaneous magnetic and  $H\alpha$  observations of 37 sunspots (during about 1 year time span). Since then the MMFs were extensively studied both with ground-based and space observations (Brickhouse and LaBonte 1988; Lee 1992; Ryutova et al. 1998; Yurchyshyn et al. 2001; Bernasconi et al. 2003; Ryutova and Hagennar 2007; Ryutova et al. 2007; Zuccarello et al. 2009).

It was found that on the very edge of the penumbra along the systematic outflow of  $0.5\text{--}1\text{ km s}^{-1}$ , the small magnetic features,  $1''\text{--}2''$  in size, are observed to move outward from the penumbra with velocities higher than the background flows. They eventually form the outer boundary of the moat where they vanish or begin to reside

in the network. During their lifetime MMFs exhibit some clear and well established properties that are listed below:

1. MMFs tend to appear in opposite polarity pairs. The pairs may not be equally visible.
2. The emerging phase takes about 10 min.
3. Pairs can emerge anywhere in the moat but most are near the outer edge of the penumbra.
4. They frequently appear along the continuation of dark filaments; a substantial fraction of the magnetic field is horizontal from the mid to outer penumbra and is confined to dark filaments; the Evershed flow occurs in the regions of horizontal fields.
5. MMFs move with (almost) the constant velocity, and may slow down gradually; nearby MMFs may have quite different speeds.
6. The inner foot predominantly shares the sunspots polarity for pair emergence; there are also opposite polarity structures, some might appear nonpaired, emitted from the edge.
7. There is a trend for the shorter-lived MMFs to have higher than average velocities.
8. Shorter-lived MMFs seem to be smaller in size.
9. The outer foot moves slightly faster than the inner one; the opposite polarity footpoints are gradually separating at perhaps  $100 \text{ m s}^{-1}$ .
10. There are other structures that move faster than  $2 \text{ km s}^{-1}$ .
11. Several MMFs seen at the very moment of emergence have initial velocities up to  $8 \text{ km s}^{-1}$ .
12. After the emerging phase, MMFs appear as bright areas in the upper photosphere and chromosphere with excess emission in the Ca II K-line.
13. They appear to carry a total magnetic flux several times larger than the total flux of the sunspot.
14. There are bipolar features that move *inward*, i.e., from the edge of penumbra toward the sunspot umbra.

Having some common properties, MMFs are quite distinct from each other. As a result, they were formally divided into classes (Shine and Title 2001).

Type I MMFs are opposite polarity pairs seen as compact bipoles. Their initial velocities (at the moment of emergence) may be quite high,  $3\text{--}8 \text{ km s}^{-1}$ . Moving outward from the sunspot, they gradually slow down; at this stage the separation between the footpoints gradually increases at about  $100 \text{ m s}^{-1}$ . During their lifetime, which may be hours, they still move with velocities higher than background plasma flows. Nearby MMFs may have quite different speeds. The inner footpoint shares the sunspot's polarity.

Type II MMFs appear as seemingly unipolar features emitted from the edge of a sunspot and having another footpoint partially or totally hidden. They share the sunspot's polarity, and have properties similar to those of the inner footpoint of the Type I MMFs. Footpoints of type I MMFs are often not equally visible with well pronounced inner footpoint and diffuse outer footpoint.

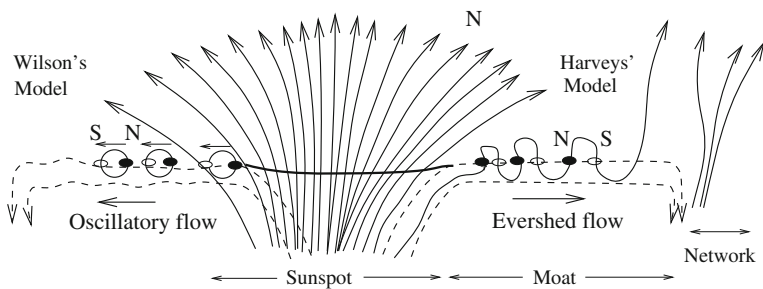
Type III MMFs also appear either as unipolar features, or opposite polarity pairs with one footpoint barely visible. Unlike type II, these MMFs have the polarity (of a strong footpoint) opposite to parental sunspot. They are of smaller size, travel with higher velocities than the other MMFs ( $2\text{--}3\text{ km s}^{-1}$ ), and are associated with bright points in the continuum.

Type I\* MMFs are outflowing opposite polarity pairs with the inner footpoint having the polarity opposite to the sunspot (Yurchyshyn et al. 2001; Zhang et al. 2003). To distinguish them from regular type I MMFs, we use the notation of a “complex conjugate”.

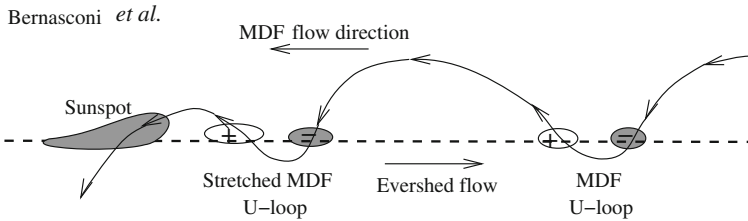
Type IV MMFs, called MDFs, moving dipolar features, were found in an emerging sunspot region (Bernasconi et al. 2003). They have the remarkable property of moving *inward*, i.e., toward the sunspot umbra. These are slowly migrating bipoles ( $0.3\text{--}0.8\text{ km s}^{-1}$ ) with the inner footpoint having a polarity opposite to the sunspot.

### 11.2 Impossibility of the Origin of MMF’s in Conservative Systems

Harvey and Harvey in their original observational paper proposed a graphic scenario in which some flux tube becomes detached (!) from the sunspot trunk at the surface where it is nearly horizontal. The supergranular or granular motions then twist this detached part of flux tube into kinks that are then carried outward by the systematic Evershed outflow. This “sea-serpent” sketch by Harvey and Harvey became the basis for subsequent models. Copy of the original Harvey and Harvey’s cartoon is incorporated in the combined sketch shown in Fig. 11.1, right. Left side of the cartoon shows the sketch of Wilson’s (1986) model. Figure 11.2 is a sketch by



**Fig. 11.1** Cartoon visualizing a possible creation and motion of MMFs: *right side* of the cartoon shows a sketch given by Harvey and Harvey showing how twisted magnetic flux tube may be separated from the main body of sunspot and swept to the network by flows; *left side* of cartoon is Wilson’s (1986) sketch showing a possible formation of MMFs in form of the new flux loops generated by an oscillatory velocity field



**Fig. 11.2** Cartoon visualizing even more mysterious magnetic features—MDFs, moving *toward* parental sunspot against the main stream of Evershed flow directed from sunspot to its periphery. Reprinted from Bernasconi et al. (2003) by permission from Springer copyright 2002, Kluwer Academic Publishers

Bernasconi et al. showing a possible motion of MDF's (Type IV MMFs) moving against the background flow toward the sunspot.

Wilson (1986) suggested that new flux loops may be generated by suitable oscillatory velocity field near the boundaries of existing magnetic structures with subsequent detachment (!) of loops, which may appear as compact bipoles. Wilson, however, objects the Harvey and Harvey's cartoon mainly on the basis of energy disbalance: comparison of magnetic energy density (for a 1,500 G flux tube) and the energy density of granular motions shows that energy density of granular motions is smaller than the former one by two orders of magnitude.

Finally, Wilson justly concludes: "It is hard to see how the motions could deform such a flux tube into the required kink, far less maintain the tube in this form during the passage across the moat". Indeed, if flux tubes and outer motions are considered as a conservative system, origin of MMFs, moving faster than background flows and even upstream, is impossible to explain.

And yet, most of the subsequent attempts to visualize MMFs were somehow or other connected with the Harvey and Harvey's "sea-serpent" picture. For example, it was tempting to represent Type I MMF as a  $\cap$ -shaped kink formed along a thin horizontal filament, which would indeed have the appearance of a bipolar formation with the inner footpoint of the same polarity as the sunspot. Similarly,  $\cup$ -shaped kinks would appear as MDF or MMF with the inner footpoint having opposite to sunspot polarity. The fundamental problem here is that either kind of kink is highly unstable: under the action of magnetic tension and buoyancy forces, a  $\cup$ -shaped kink straightens in 1–2 min, while a  $\cap$ -shaped kink may at best first oscillate, and survive only for several minutes longer (Ryutova et al. 2003).

But the problem goes even deeper. One needs not only to overcome the stability issue but find the forces that push MMFs to travel faster than the background flows with lifetimes from tens of minutes to hours. In case of MDF's (Fig. 11.2) mysterious forces make the kink to travel even upstream, against the background flows.

In other words, the properties of the MMFs are inconsistent with energy and momentum conservation laws and require approach of nonconservative, energetically open systems. We will see below that the mechanism that operates in an energetically open system describes all the observed types of MMFs and their properties.

### 11.2.1 The Mechanism

The mechanism that explains the origin of MMFs and their observed properties is based on a natural coexistence of flux tubes and adjacent shear flows, that form non-conservative system, and must be considered as such. The system with unbalanced sources and sinks of energy cannot maintain (locally) conservation laws and, as open energetically, becomes the subject of vigorous nonlinear dynamics (Kadomtzev et al. 1964; Dikasov et al. 1965; Coppi et al. 1969; Ostrovsky et al. 1986; Ryutova 1988). In our case, an unaccounted energy source comes from mass flows, sinks are played by any dissipative effects.

As shown in Chap. 5, the exchange of energy and momentum between magnetic flux and outer motions results in the development of two kinds of shear flow instabilities. The onset of the instabilities occurs respectively at two thresholds with respect to velocity:

- (1) Kelvin–Helmholtz instability (KHI) which develops at a linear stage and leads to the excitation of natural oscillations propagating along the magnetic flux tube; and
- (2) Instability of negative energy waves (NEW) which leads to nonlinear growth of oscillations excited along the flux tubes.

Recall that the dispersion relation for linear kink oscillation in the presence of flow,  $u$ , has a form; cf. (5.12):

$$\omega_{\pm} = \frac{k}{1 + \eta} \left[ u \pm \sqrt{\eta(1 + \eta), v_A^2 - u^2} \right] \quad (11.1)$$

and that super-Alfvénic velocities,  $u > v_A \sqrt{1 + \eta}$  correspond to the KHI threshold, whereas dissipative instabilities of NEWs develop at sub-Alfvénic shear velocities. Namely, when the shear velocity,  $u$ , drops into the interval

$$v_A \sqrt{\eta} \leq u < v_A \sqrt{1 + \eta} \quad (11.2)$$

Thus, dissipative instabilities require weaker flows to trigger the energy and momentum exchange between the magnetic flux and outer motions. In other words, under the condition (11.2), the kink along flux tube not only becomes stable, but may grow under the action of any dissipative effect, including the action of nondissipative damping mechanisms specific for the flux tubes, i.e., due to anomalous damping in the Alfvén resonance layer, or due to radiative damping. First mechanism is provided by the smooth radial profiles of flux tube, while the second mechanism is provided by the radiation of secondary acoustic or MHD waves. Both mechanisms are inherent for the photospheric flux tubes, thus making formation of a kink and its further behavior unrestricted.

It must be noted that the range of the flow velocities observed in sunspot region are enough to “deform” a flux tube and generate a stable kink, that later may evolve into the shock, traveling soliton or series of solitons.

### 11.3 Nonlinear Kink and Its Evolution in the Presence of Shear Flows

To describe the evolution of a kink mode in the presence of shear flow, we use nonlinear equations obtained in (4.114), complemented by the additional dissipative terms that represent the intrinsic dissipative features of flux tube:

$$\begin{aligned} \frac{\partial \psi}{\partial t} + \alpha \psi \frac{\partial \psi}{\partial x} + \beta_{\text{disp}} \frac{\partial^3 \psi}{\partial x^3} = \nu \frac{\partial^2 \psi}{\partial x^2} - \frac{\gamma_{\text{res}}}{\pi} \mathcal{P} \int_{-\infty}^{\infty} \frac{\partial \psi}{\partial s} \frac{ds}{x-s} \\ + \frac{\mu}{\pi} \mathcal{P} \int_{-\infty}^{\infty} \frac{\partial^3 \psi}{\partial s^3} \frac{ds}{x-s} \end{aligned} \quad (11.3)$$

Here  $\psi = B_y^2 + B_z^2$ ,  $\alpha \simeq 3c_k/4B^2$  is the coefficient of nonlinearity,  $\beta_{\text{disp}}$  is the dispersion coefficient,  $\nu$  is the dissipative coefficient provided by usual dissipative losses (viscous, thermal, and Ohmic),  $\gamma_{\text{res}}$  corresponds to anomalous damping of kink oscillations in the Alfvén resonance layer, and  $\mu$  represents the radiative damping of oscillations.  $\mathcal{P}$  denotes the principal value of the integral. The equation is written in a frame moving with the group velocity of linear kink oscillation  $c_k = v_A \sqrt{\eta/(1+\eta)}$ .

Although (11.3) in the presence of mass flows formally remains the same as without flows, coefficients,  $\alpha$ ,  $\beta_{\text{disp}}$ ,  $\gamma$ , and  $\mu$  are now the functions of the shear velocity  $u$ :

$$\alpha \simeq \frac{3}{4} \frac{c_k^\pm}{B^2} \quad (11.4)$$

$$\beta_{\text{disp}}^\pm = \mp \frac{R^2}{2\eta v_A^2} \frac{(c_k^\pm - u)^4}{\sqrt{\eta[(1+\eta)v_A^2 - u^2]}} \quad (11.5)$$

$$\gamma = \pm \frac{\pi}{4} \frac{\epsilon}{\eta} \frac{(c_k^\pm - u)^2}{\sqrt{\eta[(1+\eta)v_A^2 - u^2]}} \quad (11.6)$$

Here  $c_k^\pm = [(1/(1+\eta))] \left[ u \pm \sqrt{\eta[(1+\eta)v_A^2 - u^2]} \right]$  is the group velocity of linear kink oscillations in the presence of shear flow,  $u$ , and  $\epsilon$  is a measure of the diffused boundary of a magnetic flux. We assume that the initial magnetic field is constant across the effective radius,  $R$ , and then drops to zero linearly in thin boundary layer of thickness  $l$ , thus  $\epsilon = l/R$ . In the analytical approach we assume that  $\epsilon \ll 1$  and consider magnetic field well concentrated in the effective radius  $R$ . In the numerical studies (see Sect. 11.4) this restriction will be removed, and a more realistic situation with smooth radial dependence of flux tube parameters and velocities on radius will be considered.

Equation (11.3), as a typical KdV-Bürger's describes several scenarios of the evolution of the initial kink perturbation depending on the interplay of the nonlinear, dissipative, and dispersive effects. Besides, the sign of dispersion plays a crucial role in the properties of the equation and its solution.

For example, if nonlinear and dispersion effects are in balance the steepening of the amplitude gets compensated by dispersive stretching, and leads to formation of a long-lived soliton, which travels with its own velocity that is higher than the shear flow velocity. In observations, such a formation appears along the line of sight as a compact bipole.

If nonlinearity prevails over dispersion, the soliton becomes asymmetric and acquires shocklike form, i.e., one side of the soliton becomes steeper than the other. Such a formation appears along the line of sight either as a single polarity element, or as a bipole with one sharp and one diffuse footpoint. Its velocity may be even higher than that of a soliton.

It is important that in case of a *positive* dispersion of medium there appears a *bright* soliton, i.e., nonlinear kink is  $\cap$ -shaped. If the dispersion changes sign, the soliton becomes *dark*, negative soliton, acquiring  $\cup$ -shape (Karpman 1975).

First, we shall discuss in detail the case of the soliton formation and its evolution in medium with positive dispersion. In other words, we choose the lower branch of the dispersion relation (11.1), and lower signs of all parameters given by (11.4)–(11.6).

The right-hand side of (11.3) is assumed to be small compared to each term in the left-hand side. In this case one can use a well developed technique (e.g., Whitham 1974; Ostrovsky et al. 1986) to find quasi-stationary solutions of (11.3). This technique consists mainly of two steps. First, we find solution of a stationary KdV Equation, and then assuming that the amplitude and other parameters of the system are slowly varying functions of time, we find the evolutionary equation for the amplitude.

In the absence of dissipative terms, a stationary solution of (11.3) is a solitary wave with amplitude  $A$  (in our case  $A \simeq B_{\perp}^2$ ), width  $\Delta$ , and travel velocity of soliton,  $v_s$ ,

$$\psi = A \operatorname{sech}^2 \frac{x - v_s t}{\Delta} \quad (11.7)$$

$$\Delta = \sqrt{\frac{12\beta_{\text{disp}}}{\alpha A}}, \quad (11.8)$$

$$v_s = c_k + \frac{\alpha A}{3} \quad (11.9)$$

Now, to obtain a solution of (11.3) for the dissipative system (with nonzero, but small right-hand side) one assumes that the amplitude, width, and the speed of a soliton are a slowly varying functions of time.

The time dependence of these parameters is determined by the energy equation that can be obtained by multiplying (11.3) by  $\psi$  and integrating over a distance large compared with the size of a soliton. This procedure leads to the evolutionary equation for the amplitude:



$$\frac{dA}{dt} = \frac{2.92}{\pi} \gamma \left( \frac{\alpha}{12\beta_{\text{disp}}} \right)^{1/2} A^{3/2} - \frac{16}{15} \frac{\alpha}{12\beta_{\text{disp}}} \nu A^2 \quad (11.10)$$

By analyzing this equation we can conceive the nature of its solution. First, in the beginning of soliton evolution, when its amplitude is small enough, the first term in the right-hand side of (11.10) is leading one; the amplitude in this case experiences an explosive growth:

$$A \simeq \frac{A_0}{(1 - t/t_{\text{expl}})^2} \quad (11.11)$$

with the ‘‘explosion’’ time  $t_{\text{expl}} = \pi \sqrt{12\beta_{\text{disp}}/\alpha A_0}/2.92\gamma$ . Under photospheric conditions this time is quite large; i.e., the phase of the explosive growth is short: after several inverse growth rates the amplitude gets stabilized by higher nonlinear effects (Coppi et al. 1969; Ryutova 1988). At about this time the second term in (11.10) becomes more important, and the amplitude of soliton decays as follows:

$$A(t) = \frac{A_0}{1 + t/t_{\text{diss}}}, \quad (11.12)$$

where  $t_{\text{diss}} \simeq 12\beta_{\text{disp}}/\nu\alpha A_0$ . With (11.11) and (11.12) and basic relationships between the parameters of soliton, (11.7)–(11.9), one can easily draw a qualitative picture of the formation of magnetic soliton and its further behavior. Moreover, these relations, containing directly observable parameters, allow one to perform the quantitative analysis and comparison with the observations.

Thus, at flow velocities in the range defined by condition (11.2), one should expect the formation of a stable soliton with the properties described by the simple relationships between the soliton parameters (11.7)–(11.9). The simplicity of these relations makes the conclusion regarding the validity of soliton solution quite rigorous. One can see that all three relations are *interdependent*: the amplitude, the width of the soliton, and its velocity are all functions of each other. So that, for the kinked formation to be a soliton, these parameters must obey all three conditions simultaneously. In other words, if one of these conditions breaks, the kinked formation cannot be considered as a solitary wave.

In the solar photosphere, and in particular in the sunspot area, two of the above-mentioned parameters, the travel velocity,  $v_s$  and width of the soliton,  $\Delta$ , are directly measured quantities. The amplitude,  $A$ , which is proportional to magnetic field strength  $B^2$ , is also well measurable parameter. In this sense, (11.8) and (11.9) are the first to be checked. We will perform the quantitative analysis and comparison with the observations in Sect. 11.5. Before doing this, in the next section we present numerical studies of soliton-like and shocklike formations, which extend the analytical studies, and allow, for example to study temperature distribution inside a kinked formation.

## 11.4 Soliton and Shocklike Formations Along the Flux Tube—Numerical Studies

Numerical studies are based on a three-dimensional simulation code of a normalized set of MHD equations in which the numerical scheme is the modified 2-step Lax–Wendroff method (Fushiki and Sakai 1995; Suzuki and Sakai 1996). The region of calculation or the system sizes in the  $x$ ,  $y$ , and  $z$  directions are, respectively,  $0 < x < 4\pi L_0$ ,  $0 < y, z < 2\pi L_0$ . The density, the magnetic field, and the pressure are normalized by  $\rho_0$ ,  $B_0$ , and  $p_0$ ; the velocity is normalized by the Alfvén velocity,  $v_A$ . The space and time are normalized by  $L_0$  and  $\tau_A = L_0/v_A$ . Thus, the normalized set of MHD equations is as follows:

$$\frac{\partial \rho}{\partial t} + \text{div}(\rho \mathbf{v}) = 0 \quad (11.13)$$

$$\rho \left( \frac{\partial \mathbf{v}}{\partial t} + \mathbf{v} \nabla \mathbf{v} \right) = -\beta \nabla p + \nabla \times \mathbf{B} \times \mathbf{B} + \rho \tilde{g} \mathbf{e}_z \quad (11.14)$$

$$\frac{\partial \mathbf{B}}{\partial t} = \nabla \times \mathbf{v} \times \mathbf{B} + \frac{1}{R_m} \nabla^2 \mathbf{B} + A_D \nabla \times \left( \frac{1}{\rho} \mathbf{B} \times \mathbf{B} \times \nabla \times \mathbf{B} \right) \quad (11.15)$$

$$\frac{\partial \rho}{\partial t} + \mathbf{v} \nabla \rho + \Gamma p \text{div} \mathbf{v} = \frac{\Gamma - 1}{\beta R_m} (\nabla \times \mathbf{B})^2 \quad (11.16)$$

where the plasma beta is  $\beta = c_s^2/v_A^2$ ,  $R_m$  is the magnetic Reynolds number defined by  $R_m = \tau_B/\tau_A$ , where  $\tau_B = 4\pi\sigma L_0^2/c^2$  is the magnetic diffusion time,  $\tilde{g} = g\tau_A/v_A$  is normalized gravitational acceleration, the coefficient of ambipolar diffusion  $A_D$  is defined as  $A_D = B_0^2\tau_A/4\pi\Gamma\rho_0\rho L_0^2$ .

The system sizes are  $0 \leq x \leq 4\pi L$ , and  $0 \leq y = z \leq 2\pi L$  in the  $x$ ,  $y$ , and  $z$  directions, respectively. The mesh points are  $N_x = 80$ ,  $N_y = 50$ , and  $N_z = 50$  in the  $x$ ,  $y$ , and  $z$  directions, respectively. Free boundary conditions (first derivatives of all physical quantities are continuous) are used for the  $y$  and  $z$  directions, while a periodic boundary condition is used in the  $x$  direction.

The flux tube (containing the current) initially is placed along the  $x$  direction, and satisfies an equilibrium. The flux tube magnetic fields are given by

$$B_\theta = \frac{B_m r/R}{1 + (r/R)^2}, \quad (11.17)$$

$$B_z = \frac{B_{z0}}{1 + (r/R)^2} \quad (11.18)$$

For computations the radius of a flux tube is taken as  $R = 0.5$ , and  $B_m = 1.2$ ,  $B_z = 1.0$ .  $r$  means the distance from the center line of a flux tube. The initial density is  $\rho = \rho$  and the initial pressure  $p$  is taken to satisfy an equilibrium as follows:

$$p = \rho = \exp(-\tilde{g}z/\beta) + \frac{B_m^2 - B_{z0}^2}{2\beta(1 + r^2/a^2)^2} \quad (11.19)$$

where the first term shows the balance with gravity, and the second is the pressure needed to balance the Lorentz force. Plasma flow outside the flux tube is assumed to be directed along the flux tube (i.e., along  $x$ -axis), and with  $r$ -dependence of the form:  $u(r) = u_0(1 - 0.8/(1 + (r/R)^2))$ . The velocity perturbations,  $v_z$ , are imposed at  $x = \pi L$  as  $v_z = v_m \exp[-(x - \pi)^2]/(1 + (r/R)^2)$ . The parameters used here are as follows:  $\Gamma = 5/3$ ,  $\beta = 1.0$ ,  $R_m = 10^4$ ,  $A_D = 10^{-3}$ ,  $\tilde{g} = 0.05$ ,  $u_0 = 0.2 - 1.0$ , and  $v_m = 1.2$ .

Numerical simulations were performed in several regimes, changing mainly the external flow velocity,  $u_0$ . It was found that depending on the shear flow velocity there are two different and well distinguishable regimes of the evolution of a kink perturbation, which can be identified as shocklike and soliton-like cases.

The shocklike regime requires lower amplitude shear velocities. It is remarkable, however, that the propagation velocity of shocklike kinks is larger than shear velocity. From the observational point of view, the shocklike regime may correspond to either a unipolar MMF (if the front of a shock is much more pronounced than its tail) or to those MMFs whose legs have different propagation velocities: the outer (leading) leg should be faster than the trailing one.

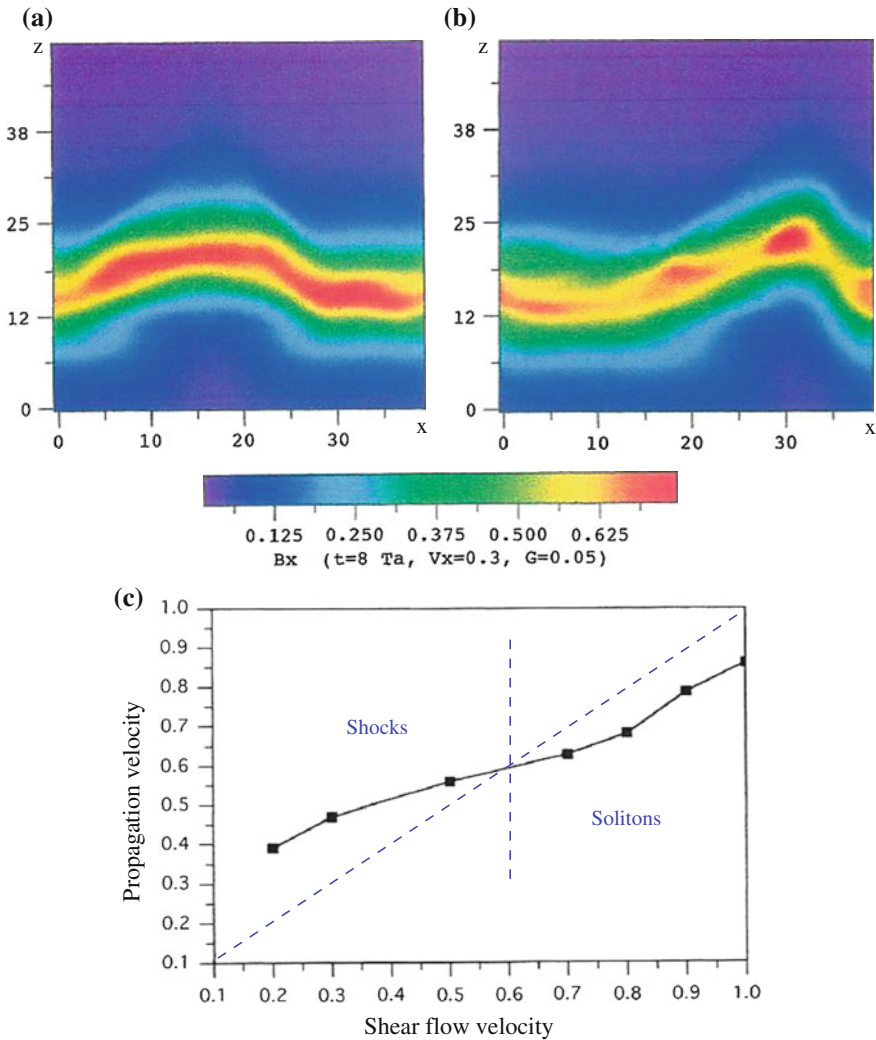
Soliton-like kinks always appear as bipole features. Their propagation velocity may be both, lower or higher than the speed of the shear flow.

In Figs. 11.3a, b the evolution of kinks into the (a) shocklike and (b) soliton-like events at time  $t = 8\tau_A$  are shown. In Fig. 11.3c, the relation between the velocity of shear flow and the propagation velocity of the generated kink is shown. At the velocities less than  $0.6v_A$ , the generated kink shows shocklike behavior. Region of flow velocities  $\simeq 0.6v_A$ , for chosen parameters of magnetic flux tube and its environment corresponds to the bifurcation point. At the shear velocities higher than these velocities, the generated kink acquires the properties of a stable solitary wave.

In Fig. 11.4 the time history of the soliton-like kink is shown for a shear velocity  $v_x = 0.8v_A$ . One can see that with a “decreasing” of the “amplitude” (which corresponds to decreasing the magnetic field strength), the width of the soliton—the separation between the “two legs” increases; cf. (11.8). The last panel in this figure corresponds to time  $t = 3\tau_A$  and shows three-dimensional view of the same event along the tube axis.

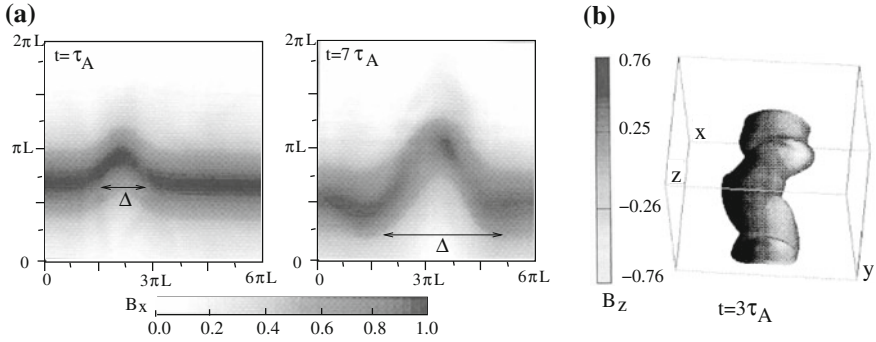
Figure 11.5 shows well developed three-dimensional view of soliton and shocklike formations and their line of sight magnetic field. Figure 11.5a is a stable propagating soliton—a typical bipole, with both, positive and negative footpoints clearly seen. Figure 11.5b is shocklike formation whose line of sight magnetic field differs from the soliton case: its leading footpoint is sharp and compact, while the trailing one is diffuse (cf. Fig. 11.3a, b). From observational point of this means, that shocklike MMF may appear as bipolar feature with uneven emission from its legs, or even as a single polarity MMF.

It is important to discuss the change of the temperature distribution inside the magnetic flux during the formation and propagation of a kink. Note that the analytical theory does not allow us to include the temperature distribution in the nonlinear dynamics of magnetic flux tube, but the numerical calculations proved to be very helpful.

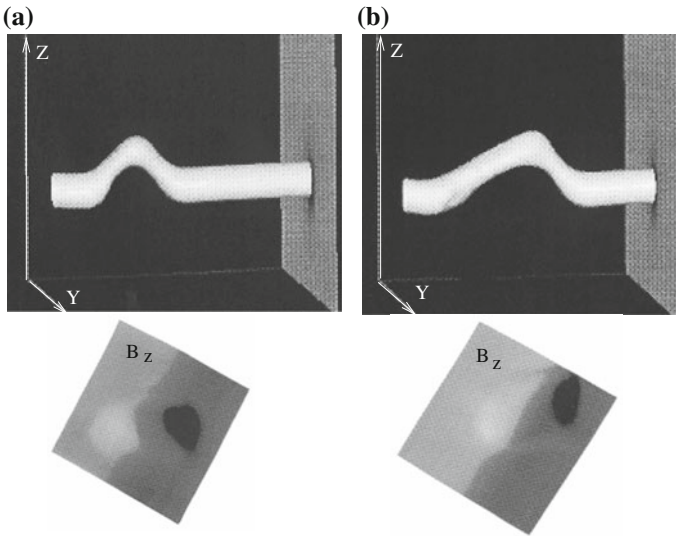


**Fig. 11.3** Two different regimes of the evolution of a magnetic kink. *Top* snapshots of the shocklike event at  $t = 8\tau_A$  (a), and the soliton-like event at  $t = 8\tau_A$  (b); *Bottom* (c) the relation between the velocity of shear flow,  $u(r)$ , which facilitates the generation of a magnetic kink, and the propagation velocity of a new-born kink; *dashed lines* demarcate the approximate regions of the shocklike and soliton-like formations

In both cases, shocklike and soliton-like kink formation, quite uneven redistribution of the temperature takes place. A numerical modeling clearly shows the regions with some energy excess in the new-born magnetic features. For example, in the case of a soliton both legs have higher temperature than the surrounding plasma. The temperature in the following leg is slightly higher than in the leading one (Fig. 11.6a).

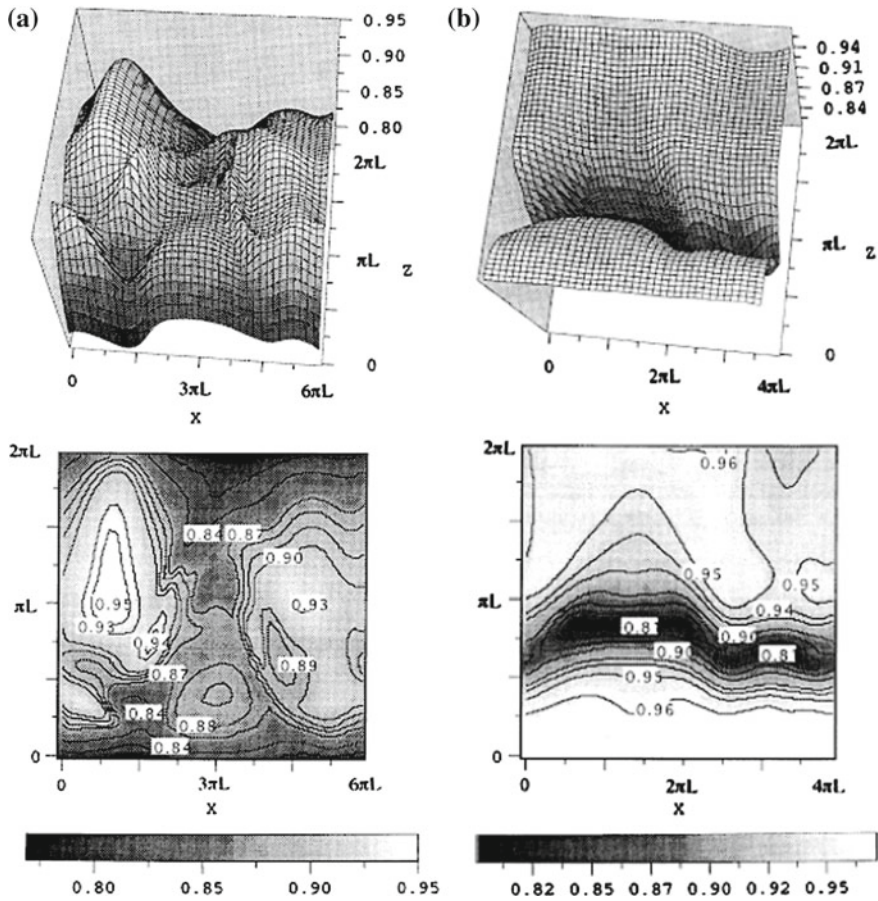


**Fig. 11.4** Soliton-like kink at the shear velocity  $v_x = 0.8v_A$ : **a** The time history of the soliton evolution at two time steps; note how weakening of magnetic field is accompanied by the increase of separation between the two legs, i.e., the width of the soliton, and growth of its kink; a bar shows the magnetic field scale along the flux tube,  $B_x$ . **b** The snapshot of three-dimensional view of the same event at  $t = 3\tau_A$  with the scale bar showing one of the transverse component of magnetic field,  $B_z$



**Fig. 11.5** The three-dimensional view (*upper panels*) and line of sight magnetic field (*lower panels*) for **a** a stable propagating soliton corresponding to type I MMFs, and **b** for the shocklike MMF. Note that in case of soliton both footpoints are equally well pronounced, while in case of the shocklike formation one footpoint along the line of sight is sharp and compact, while its pair is weaker and diffuse

In the case of a shocklike formation the temperature behind the shock front is, as it should be, significantly higher than in the rest of medium (Fig. 11.6b). The described temperature distribution may explain the excess of the emission in the Ca II K-line that almost exactly mimics the path of the MMFs in the photosphere.



**Fig. 11.6** The temperature distribution in the well developed nonlinear kink: **a** The soliton-like kink at  $t = 7\tau_A$ , the shear velocity is  $v_x = 0.8v_A$ . **b** The shocklike kink at  $t = 7\tau_A$ , the shear velocity is  $v_x = 0.2v_A$ . Note the elevated temperature level in the soliton legs, (**a**), and strong behind-shock heating at shocklike formation, (**b**)

The animated process of the magnetic kink propagation shows several remarkable features, such as the shredding of the magnetic field at the late stage of its evolution. These kind of events are usually well seen in the movie sets.

### 11.5 Observations and Comparison with Theory

In this section, when discussing and comparing the theoretical results with the observed properties of moving magnetic features, we use several examples from the set of observations taken on June 14, 1994, at the Swedish Vacuum Solar Telescope (SVST) on La Palma. The observations include simultaneous images in Ca

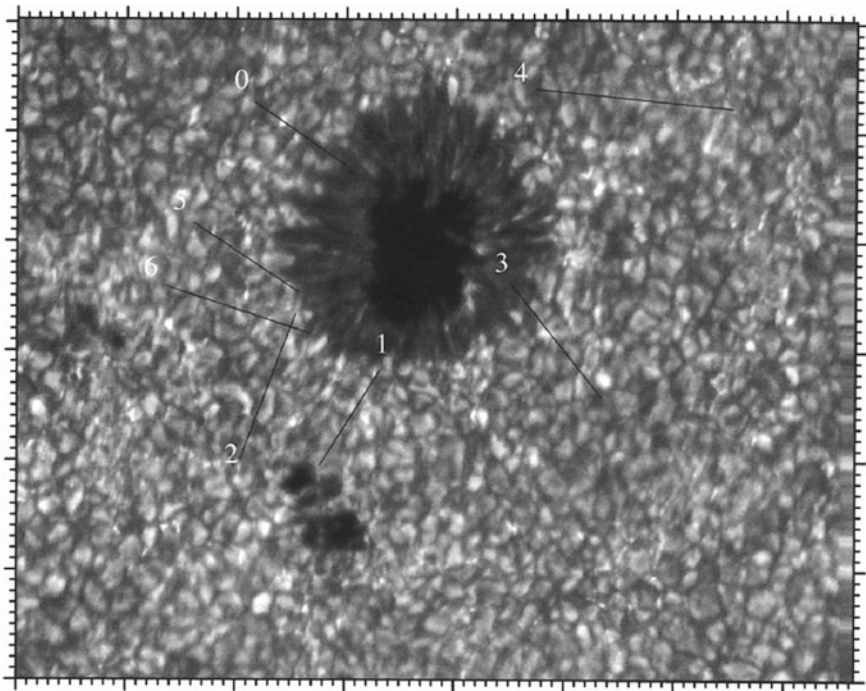
II K-line, G-band, and magnetograms. The 0.3 nm bandpass Ca II K filter has some contribution from the chromosphere but in nonactive areas most of the intensity is from the inner wings of the line profile which originate in the upper photosphere.

Hence the images show dark patches during the early stages of flux emergence and the movies show many examples of emerging flux in the moat area, especially near the outer edge of the penumbra. These appear as dark elongated features which expand and develop bright points at opposite ends which then continue to separate while traveling outward. Each end becomes a MMF. The long axis of the emergence is generally in the radial direction.

The time series for the magnetograms, K-line filtergrams, and G-band filtergrams have been co-aligned. The observing time is 175 min.

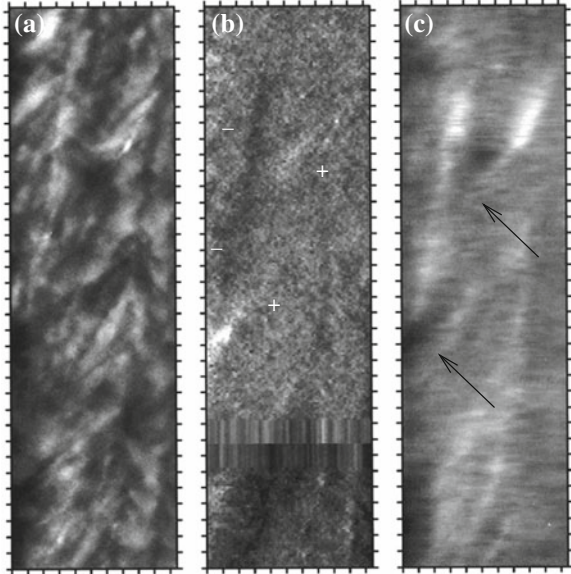
To display their time evolution, the space-time images were constructed for several of these MMFs using the long axis of the emergence as the space dimension. These are shown in Fig. 11.7.

For detailed analysis we choose three examples, namely space-time slices 1, 3 and 4. The space-time images resulted from cuts 1 and 3 are shown in Figs. 11.8 and 11.9, respectively, and those resulted from cut 4 is shown in Fig. 11.10.

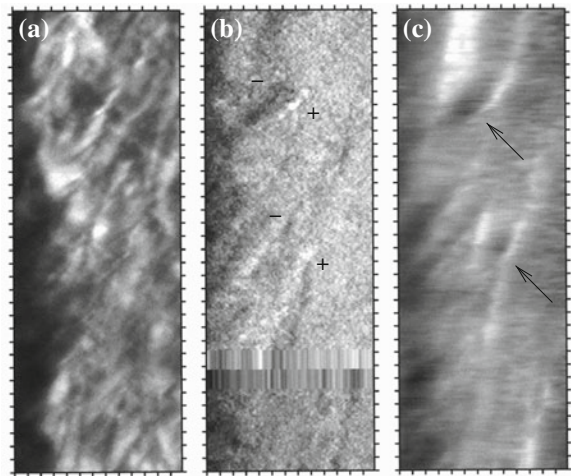


**Fig. 11.7** A G-band image of the sunspot area taken on June 14, 1994 at the SVST on La Palma. The labeled lines represent the spatial component of space-time images made from the movies to follow various emerging flux events and their variation in time

**Fig. 11.8** Space-time slices along the line labeled 1 in Fig. 11.7 for **a** the G-band filtergrams movie, **b** the magnetogram movie, and **c** the K-line filtergram movie. Time is along the vertical axis increasing upward with tick marks every 5 min. Observation period is 175 min. The horizontal axis is distance along the line with tick marks every arc second (about 726 km). One can see two beautiful MMFs especially well recognizable in the magnetogram and Ca II K-line movies (marked by *black arrows*)



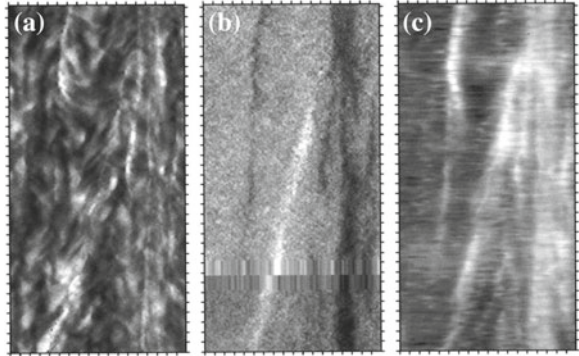
**Fig. 11.9** Same as Fig. 11.8 but for the line labeled 3 in Fig. 11.7



Each of the paths corresponding to 1 and 3 slices shows the appearance of two quite similar MMFs. All four events have high velocities in the initial phase, about  $4 \text{ km s}^{-1}$ . In the region where a well-defined darkening is seen in the Ca II K images, indicating the emergence of magnetic field, the separation between two legs, the *width* of a soliton, gets stabilized and becomes almost constant; after this, the travel velocities of the MMFs drop to  $1.0\text{--}0.7 \text{ km s}^{-1}$ , after which all four events show a slow evolution: their width gradually increases, while the propagation velocity gradually decreases.



**Fig. 11.10** An exemplary magnetic soliton. This body has emerged obviously before the start of the observations. Its behavior, growth of the separation between the legs, slowing down, etc., strictly obey the laws of evolutionary soliton



The most spectacular MMF which can be interpreted as an exemplary solitary wave is revealed by cut 4, and is shown in Fig. 11.10. The evolution of all the observed MMFs fits amazingly well the analytical description given by (11.7)–(11.12). Besides, their appearance and location where they emerge can be also well understood in the frame of theory. For example, we will see below that the 1 and 3 events are most likely shallow events, while the MMF shown on the slice 4 should have been originated at some depth below the visible surface. This can be explained along the following line of reasoning.

If the stable kink (a kink soliton) is formed close to the surface, the buoyancy force may be neglected. From the observational point of view such events should be seen both in their initial phase which corresponds to fast growth and fast propagation (in accordance with 11.13 and 11.14), and in the second stage, which corresponds to their slow evolution after the moment of stabilization. The four MMFs shown in Figs. 11.8 and 11.9 are good candidates to be considered shallow kinks formed on or slightly below the surface. Their proximity to the edge of the penumbra is also consistent with a shallow origin, since at least some of the nearly horizontal field at the outer penumbra boundary may extend just below the visible surface.

If the MMF is formed well below the surface then its initial fast phase develops below the surface and the MMF may appear while in its second phase of slow evolution. This type of event may be more likely to appear further from the penumbra as is the case for event 4 shown in Fig. 11.10.

During the initial stage of soliton formation while the amplitude is small (so that the first term in (11.10) is a leading one), its growth is governed by (11.11). This phase is accompanied by the fast emergence of magnetic flux and may start below the visible surface. The emerging kink appears as closely spaced, opposite polarity couple moving with relatively high velocity (see all four MMFs shown in Figs. 11.8 and 11.9).

When the amplitude of a kink becomes such that both terms in the right-hand side of (11.10) are comparable, the soliton becomes stabilized. Its amplitude remains constant until some other dissipative processes make the second term in (11.10) more important. At this stage the amplitude of the soliton decreases slowly in accordance with (11.12). Its travel velocity (11.9) also decreases, and its width, or the separation

between the opposite polarity legs (11.8), gradually increases. This stage can be easily identified in all four events shown in Figs. 11.8 and 11.9. As the dark structure seen in the Ca II K images expands and fades, the propagation velocity drops to values of 1.0–0.7 km s<sup>-1</sup>, after which their behavior is described by (11.12).

Thus, we may conclude that qualitatively, these MMFs show both phases of the evolution: the fast, explosive phase, and the phase of a gradual decay.

The exemplary event shown in Fig. 11.9 may be an excellent demonstration of an observed solitary kink formed well below the visible surface. It is seen only in the second stage and from the period of about  $t = 20$ –60 min the width of a soliton remains almost constant and then very gradually decreases.

The moment of the transition from one phase to another (i.e., the moment when the amplitude  $A$  reaches its stationary value,  $A_{st}$ ) carries some additional information about the nature of the effect and, also, about the physical parameters of the medium. Roughly, at this moment

$$\frac{2.92}{\pi} \gamma \left( \frac{\alpha}{12\beta_{disp}} \right)^{1/2} A^{3/2} \simeq \frac{16}{15} \frac{\alpha}{12\beta_{disp}} \nu A^2 \quad (11.20)$$

i.e.,

$$A_{st}^{1/2} \simeq 0.87 \sqrt{\frac{12\beta_{disp}}{\alpha} \frac{\gamma}{\nu}} \quad (11.21)$$

or, taking into account (11.8), we can estimate the stationary value of the width,

$$\Delta_{st} \simeq 1.15 \frac{\nu}{\gamma} \quad (11.22)$$

This result is analogous to a well-known fact in the theory of solitary waves: after some time, the “memory” of soliton weakens and soliton “forgets” its initial conditions. As noted earlier,  $\nu$  represents any kind of dissipative losses. If the soliton formation occurs close to visible surface we may suggest that dissipation is provided mostly by the viscous losses. If the formation of soliton occurs in deeper layers, say at  $h = -1,000$  km, then thermal and radiative losses become more important.

## 11.6 Quantitative Analysis

For quantitative estimates we consider two examples:

- (1) The formation of a soliton on or slightly below the surface, and
- (2) The formation of a soliton at a depth  $h = -1,000$  km.

For the first case of a shallow soliton we adopt the following typical values: mass density (outside the magnetic flux tube),  $\rho_e = 3.4 \times 10^{-7}$  g cm<sup>-3</sup>; temperature  $T = 0.94 \times 10^4$  K; sound speed, respectively, is  $c_s = 10.2$  km s<sup>-1</sup> (see e.g., Maltby et al. 1986); the ratio of mass densities  $\eta = \rho_i/\rho_e = 0.9$ ; the flux tube radius

$R = 500 \text{ km}$ ;  $\epsilon = l/R = 0.05$ ; and magnetic field strength (for analytical estimates, the unperturbed value of the field along the tube axis)  $B_x = 500 \text{ G}$ .

With these parameters, we may find the Alfvén velocity, the range of shear velocities corresponding to dissipative instabilities (11.2), and, choosing some critical value for the shear velocity, compute the width, the amplitude, and the speed of the propagation of a soliton.

At the Alfvén velocity is  $v_A = 2.6 \text{ km s}^{-1}$ , the range of shear velocities that would generate a kink is then  $2.45 \text{ km s}^{-1} < u < 3.55 \text{ km s}^{-1}$ . This is higher than the usual outflow velocities seen in the sunspot moat (Shine et al. 1987) by about a factor of 2 but lower than the the maximum Evershed velocities seen at the outer edge of the penumbra. Localized and perhaps transitory shear velocities between the magnetic flux tube and the surrounding medium of this magnitude seem likely in this environment. Taking a value of  $u = 3 \text{ km s}^{-1}$  we then have a phase velocity of  $c_k = 0.63 \text{ km s}^{-1}$  and  $\gamma = 0.12 \text{ km s}^{-1}$ . At this depth dissipative losses may be provided both by the effective viscosity and thermal diffusivity. The estimate for the dissipative coefficient, assuming kinematic viscosity, may be taken as  $\nu \simeq 10^2 - 10^3 \text{ km}^2 \text{ s}^{-1}$ .

In accordance with expression (11.22), we should expect the stabilization of a soliton when its width reaches the value of  $\Delta_{st} = 1.15 \nu/\gamma$ . At this moment, the travel velocity of a soliton, (11.9), should approach its stationary value,  $v_{st} = c_k + \alpha A_{st}/3$ , which corresponds to changing the regime of the evolution of a soliton in time. We can write this estimate through the directly observed parameter, the width of a soliton,  $\Delta$  (separation between the opposite polarity legs):

$$v_{st} = c_k + \frac{4\beta_{disp}}{\Delta_{st}^2} \quad (11.23)$$

After this moment, according to (11.10) the evolution of a soliton is governed by (11.12): Its amplitude gradually decreases, which means that its width increases gradually, resulting in the slowing down of its propagation velocity. Equation (11.12) rewritten for the width of a soliton has a form:

$$\Delta = \Delta_{st} \sqrt{1 + \frac{t}{t_{diss}}} \quad (11.24)$$

where  $t_{diss} \simeq 12\beta_{disp}/\nu\alpha A_{st}$ , or  $t_{diss} \simeq \Delta^2/\nu$ .

If we adopt  $\nu \simeq 100 \text{ km}^2 \text{ s}^{-1}$ , for the chosen example, we get:  $\Delta_{st} \simeq 960 \text{ km} = 1.3''$ , which is less than  $\Delta_{st}$  for given observed MMFs in Figs. 11.7, 11.8, and 11.9. If we take  $\nu \simeq 200 \text{ km}^2 \text{ s}^{-1}$ ,  $\Delta_{st} \simeq 2.6''$ , which is very close to observed values. We can estimate the velocity of a soliton in both, fast (emerging) and slow phases. For this let us estimate the dispersion coefficient:  $\beta_{disp} = 3.6 \times 10^5 \text{ km}^3 \text{ s}^{-1}$ . The theory does not allow us to estimate the initial width of a soliton, but if we make a natural suggestion that is well justified by the observational data, that the initial width of a solitary kink is of the order of a flux tube radius or slightly larger, say,  $\Delta_0 \simeq 1''$ , then for the speed of a soliton in the fast phase we get the soliton propagation speed

$v_{0A} = c_k + 4\beta_{\text{disp}}/\Delta_0^2 \simeq 0.63 + 2.74 = 3.4 \text{ km s}^{-1}$ . This is very close to the observed values of  $4 \text{ km s}^{-1}$ .

After the bifurcation point (at the moment of stabilization), the propagation velocity drops to the values determined by  $\Delta_{\text{st}}$ , so that in a slow phase the speed of a soliton is  $v_s \simeq c_k + 4\beta_{\text{disp}}/\Delta_{\text{st}}^2 \simeq 0.63 + 1.59 = 2.2 \text{ km s}^{-1}$  with  $\nu = 100 \text{ km}^2 \text{ s}^{-1}$ . At  $\nu = 200 \text{ km}^2 \text{ s}^{-1}$ ,  $v_s \simeq 0.63 + 0.4 = 1.0 \text{ km s}^{-1}$ . This result shows that as the “resistance” of the medium (the effective viscosity or thermal diffusivity) becomes higher, the propagation speed of the soliton decreases.

Given the wealth of the observational data, this simple approach may be used for the estimation of the effective viscosity of the medium. The estimate for  $t_{\text{diss}}$  for  $\nu = 100 \text{ km}^2 \text{ s}^{-1}$  is  $t_{\text{diss}} \simeq 156 \text{ min}$ , which means, in accordance with (11.24) that the width of a solitary kink remains almost constant for a long time. This is one of the main observed features of MMFs.

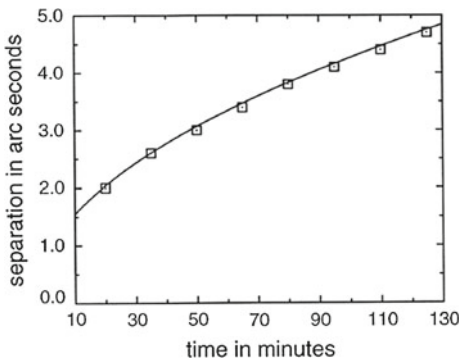
Let us consider now the event shown in Fig. 11.10. This MMF is seen only in its slow phase and its evolution in time should be governed by (11.24). Our goal here is to find out if the observed separation between the bipoles fits the time dependence given by (11.24) and then to compare the most crucial parameter in this expression,  $t_{\text{diss}}$  found from the observations and theory.

Comparison of the measured separations as a function of time with the theoretical curve is shown Fig. 11.11. The squares are the observed values. Times are just from the beginning of the series; the transition time is unclear here, and we adopt an offset below to fit the observations. Independent of the start time, it follows from (11.12) that for different moments of time,  $t_{k,i}$ , the separation between the legs of the MMF,  $\Delta_{k,i}$ , should satisfy the relationship

$$a_{ki} = \frac{\Delta_k^2 - \Delta_i^2}{t_k - t_i} = \frac{\Delta_{\text{st}}^2}{t_{\text{diss}}}, \tag{11.25}$$

which should be constant. The observed separations show an average value for  $a$  of 0.17. We can then make a reasonable fit to the data with  $\Delta_{\text{st}} = 1.0''$  and a start time at 2 min.

**Fig. 11.11** The time dependence of the width of a solitary kink. *Squares* indicate the observed values for the event shown in Fig. 11.10. The *solid line* is a fit using (11.24) showing a perfect match of theory and observations



The resulting curve is displayed as the solid line in Fig. 11.11 and shows that the observed temporal behavior of the separations is indeed totally consistent with (11.24).

Comparison of the observations with theory allows one to develop quite reliable diagnostic tool. For example, from the above example follows the estimate for  $t_{\text{diss}}$  which is  $t_{\text{diss}} = \Delta_{\text{st}}/a = 1.0/0.17 = 5.88$  min. To compare this value with the theoretical one we have to take into account the effect gravity. In this case, the dispersion caused by the force of gravity is much stronger than the cubic dispersion caused by the compressibility of the medium. The linear dispersion relation for the incompressible kink perturbations of the horizontal magnetic slab in a stratified atmosphere has a form:

$$\eta[(\omega - ku)^2 - k^2 v_A^2] + \omega \sqrt{\omega^2 - N^2} \tanh kR - (1 - \eta)gk \tanh kR = 0 \quad (11.26)$$

where  $N$  is a Brünt-Väisälä frequency,

$$N^2 = -g \frac{1}{\rho} \frac{d\rho}{dz} \quad (11.27)$$

In a long-wavelength approximation (thin magnetic flux tube),  $kR \ll 1$ , for the phase velocity we have

$$c_k = u \pm \sqrt{\frac{(1 - \eta)}{\eta} gR + v_A^2}, \quad (11.28)$$

and the lower threshold for the KH instability is:

$$u_{c1} = \sqrt{\frac{(1 - \eta)}{\eta} gR + v_A^2} \quad (11.29)$$

Therefore, the growth rate of the negative energy kink (at  $u > u_{c1}$ ) is:

$$\gamma = -NR \frac{u - u_{c1}}{u_{c1}} \quad (11.30)$$

Note that this case, i.e., the effect of gravity on nonlinear kink oscillations described by (11.26)–(11.28), is quite general and may be applied to the magnetic flux emerging elsewhere at the solar surface and not necessarily in the vicinity of a sunspot.

Returning now to the quantitative analysis of the exemplary soliton shown in Fig. 11.10, we need to use the dispersion relation (11.26). Let us assume that the instability of a negative energy kink occurs at  $h = -1,000$  km below the surface. At this depth we adopt the following parameters: the mass density (outside the magnetic field),  $\rho_e = 0.27 \times 10^{-5}$  g cm<sup>3</sup>, temperature,  $T = 1.5 \times 10^4$  K; sound speed,  $c_s = 14$  km s<sup>-1</sup>, and the ratio of mass densities,  $\eta = \rho_i/\rho_e = 0.8$ . We choose the magnetic

field strength as  $B = 1,000$  Gs, which gives an Alfvén velocity of  $v_A = 1.92 \text{ km s}^{-1}$ . The lower limit of a critical shear velocity for the instability is then  $u_{c1} = 6.16 \text{ km s}^{-1}$ . We have no direct evidence of local shear velocities at this depth, but values of such magnitude is plausible. If we take  $u = 8 \text{ km s}^{-1}$ , then the phase speed is  $c_k = 0.84 \text{ km s}^{-1}$ . Now we can calculate the first dissipative coefficient,  $\gamma$ , responsible for the growth rate of the negative energy kink:

$$\gamma = -NR \frac{c_k}{u_c} = 1.96 \text{ km s}^{-1} \quad (11.31)$$

where the Brünt-Väisälä frequency  $N = 0.013 \text{ s}^{-1}$ . With  $\nu = 10^3 \text{ km s}^{-1}$  we obtain, for the width of a solitary kink in the moment of stabilization, a value  $\Delta_{st} = 587 \text{ km}$ , and for  $t_{diss} = \Delta_{st}^2/\nu$  we have  $t_{diss} = 5.7 \text{ min}$ , which is in good agreement with the fitted values of 725 km and 5.88 min.

## 11.7 Unification of Known Types of Moving Magnetic Features

As we have seen throughout this chapter, the general problems associated with the MMFs are their great variety and their nonconformity with conservation laws. It is just the second point, i.e., their energetically open character that explains all the observed types of MMFs and different scenarios of their evolution. The variety of MMFs is determined by a great variety of flux tube themselves, their adjacent sheared mass flows, and dispersion and dissipative properties of a whole system. The most attractive point here is that the most parameters that enter the theory are directly observable. This fact itself not only serves as tools for understanding the nature of the MMFs, but may serve as a powerful tool to infer physical parameters that are not directly observable.

Thus, (11.7)–(11.12) must carry the information about all “five” types of MMFs, their lifetimes, and behavior. Besides, as there are clear differences in the observed properties of MMFs, that have lead to their classification listed in Sect. 11.1, the theory must provide means to put a particular MMF into its own class.

According to general theory the MMFs may be either soliton-like or shocklike formation. Now we need to find out, for example, why one soliton may behave as Type I MMF, i.e., move outward from parental sunspot with velocity higher than background flows, and the other soliton may behave as the MDF, i.e., move slowly upstream toward parental sunspot.

To describe different properties of all five types of MMFs we need to analyze various combinations of the system parameters.

First, we need to emphasize how important role is played by the dispersion of the medium. If the dispersion is positive, the generated kink is a *bright* soliton propagating as a  $\cap$ -shaped kink (Fig. 11.12a). If the dispersion is negative, the solution is a *dark* soliton forming a  $\cup$ -shaped kink (Fig. 11.12b). Properties of these solitons are

very different. Before we come to the main differences, note, e.g., that the propagation velocity of a bright soliton is higher than that of a dark soliton. This is obvious from (11.9) representing the soliton velocity. Written through the dispersion and the width of a soliton it gives:  $v_{\text{sol}}^{\pm} = c_k \pm 4\beta_{\text{disp}}/\Delta^2$ . Respectively, lifetime of a bright soliton is longer and it travels farther from sunspot than that of the dark soliton. But the main difference, as one can see from Fig. 11.12, is that the bipoles formed by the kinked flux tube are mirror opposite.

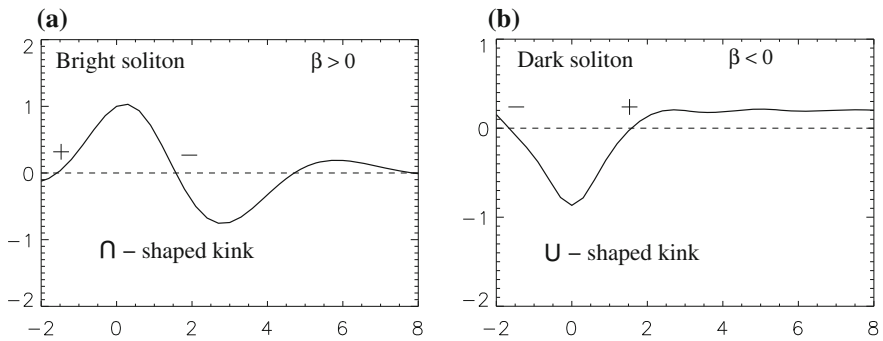
Indeed, in case of positive dispersion, the observer sees along the line of sight a bipole whose leading footpoint has a polarity opposite to that of the parental sunspot, while the trailing footpoint (the one that is closer to sunspot) has the same polarity as the sunspot (Fig. 11.12a). In case of negative dispersion, it is vice versa, and the observer sees a bipole with a leading footpoint having the same polarity as the sunspot, and the trailing footpoint of the opposite polarity (Fig. 11.12b).

Two other major conditions that farther determine the character and properties of generated kink are in the first place, whether the nonlinearity is balanced by the dispersion or not. And then it is a relation between the phase velocity of a kink and its propagation velocity determined by (11.32). Note that the solutions shown in Fig. 11.12 correspond to a solitary wave when the nonlinearity is balanced by the dispersion effects.

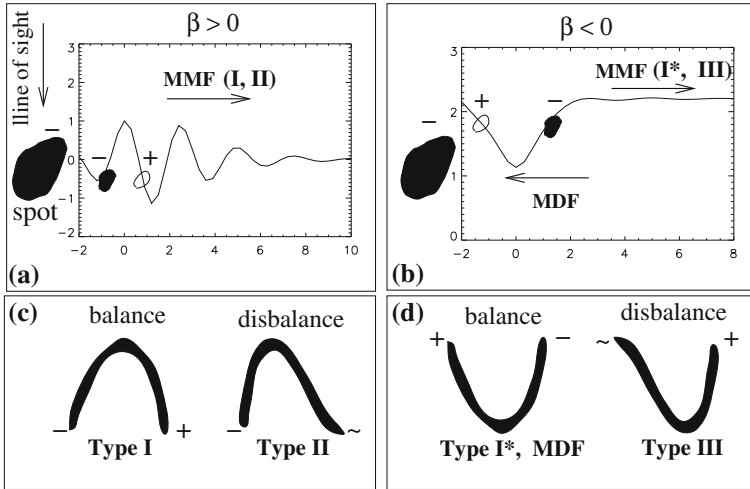
Breaking down the classes of the solution with respect to above three conditions we arrive to all five types of moving magnetic features. These are illustrated in Fig. 11.13 and described below.

*Type I.* At the positive dispersion,  $\beta_{\text{disp}} > 0$ , when the nonlinearity is balanced by the dispersion, the solution correspond Type I MMFs that are observed as a compact bipoles with *the inner footpoint sharing the sunspot's polarity*. Moving outward from the sunspot, they gradually slow down. During their lifetime, which may be *hours*, they still move with velocities higher than background plasma flows (Fig. 11.13a, c—balance).

*Type II.* If under above conditions (i.e., at positive dispersion,  $\beta_{\text{disp}} > 0$ ) nonlinearity prevails over dispersion, the soliton becomes asymmetric and acquires shocklike



**Fig. 11.12** Analytical solutions for nonlinear kink: **a** a *bright soliton* at positive dispersion; **b** a *dark soliton* at negative dispersion. Vertical axes are  $\psi$  normalized by  $B^2$ , horizontal axes are  $x$  normalized by flux tube radius



**Fig. 11.13** Analytical solutions for nonlinear kink (*upper panels*), and cartoons depicting all types of MMFs. Balance means that nonlinearity is balanced by dispersion, and disbalance that nonlinearity prevails over dispersion. If at negative dispersion,  $\beta_{\text{disp}} < 0$ , the phase velocity is such that  $c_k < \alpha A/3$ , and a moving magnetic feature has negative velocity it will travel upstream toward sunspot (MDF)

form, i.e., one side of the soliton becomes steeper than the other. In this case the observer sees either a bipole with one footpoint clearly seen and another being diffuse, or only one footpoint. This solution corresponds to Type II MMFs which appear as a unipolar features emitted from the edge of a sunspot. They share the sunspot’s polarity. Often type II MMFs may have two footpoints: well pronounced inner one having the same polarity as the parental sunspot, and a diffuse outer footpoint having opposite polarity (Fig. 11.13a, c—disbalance).

*Type I\**. At the negative dispersion,  $\beta_{\text{disp}} < 0$ , when the nonlinearity is balanced by the dispersion, the solution correspond to Type I\* MMFs that are outflowing as opposite polarity pairs with the inner footpoint having the polarity opposite to the sunspot (Fig. 11.13b, d—balance).

*Type III*. If at  $\beta_{\text{disp}} < 0$ , nonlinearity prevails over dispersion, just like in the case of positive dispersion, the soliton becomes asymmetric: one side of the soliton becomes steeper than the other, so that the observer sees either a bipole with one footpoint clearly seen and another being diffuse, or only one footpoint. This solution corresponds to Type III MMFs which appear as unipolar features emitted from the edge of a sunspot and having the same polarity as sunspot (Fig. 11.13b, d—disbalance).

*Type IV*. The most mysterious magnetic bipoles dubbed moving dipolar features (MDFs), unlike all other MMFs travel *toward* the sunspot against background mass flows. But even these remarkable features are part of the general scheme: they require a negative dispersion, and flux tube parameters such that the condi-



tion  $c_k < \alpha A/3$  be fulfilled. In this case, according to (11.9), the soliton propagation velocity becomes negative. According to the same equation, their propagation velocity is always less than that of other types of MMFs, and less than the background flows. Indeed, the MDFs were observed as slowly migrating bipoles with velocities ranging  $0.3\text{--}0.8\text{ km s}^{-1}$  (Fig. 11.13b, d—balance).

It must be noted again that observations of MMFs during their long passage across the penumbra and moat may provide a reliable tool for inference of physical parameters of the photosphere that are not directly observable. Simple relations, (11.7), (11.8) and (11.9), between its size (separation between the footpoints), velocity, and line of sight magnetic field (with new satellite the vector magnetic fields are also readily available), allow one to infer such parameters as dispersive properties of a system, dissipative effects, and others. These parameters then may be used for the evaluation of their dissipative properties, which determine coupling with the upper atmosphere.

## 11.8 Impact of MMFs on the Overlying Atmosphere

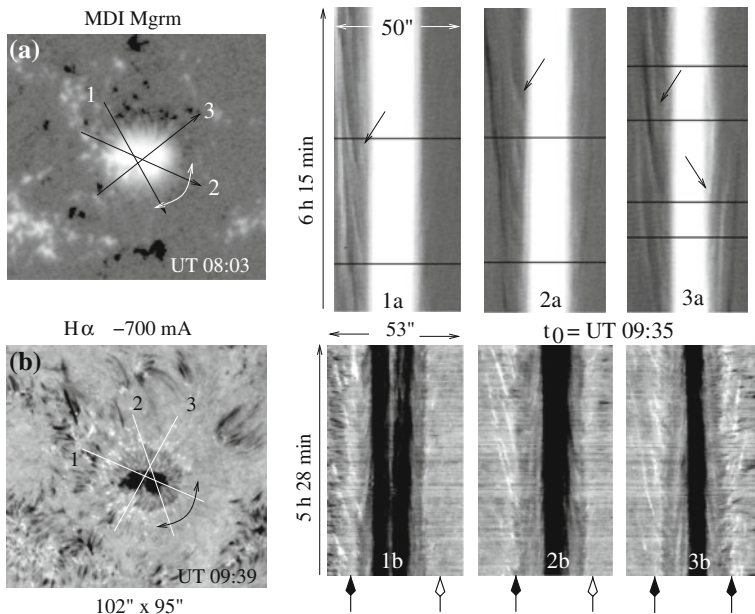
In the above section we saw that all types of MMFs, often having conflicting properties, can be described on a unified basis. Note, that MMFs may appear in any other magnetized regions where magnetic flux tubes interact with shear mass flows and are subject of gravity forces.

In this section we will study the response of the upper atmosphere to individual MMFs, i.e., how dynamics and energetics of MMFs affect the upper layers of atmosphere. We must expect, of course, that these effects depend on the type of MMFs. For example, the soliton type bipolar MMFs, being quite sturdy, should mainly participate in the formation of a moat, unless conditions for explosive instability turn on. The shocklike MMFs, however, being the subject of gravity acceleration may trigger the energetic events in the chromosphere, such as jets and microflares.

We use here several data sets of multiwavelength observations of the photosphere and its overlying chromosphere and corona to demonstrate the response of the upper atmosphere to dynamics of MMFs.

We start with the data taken on June 10, 1999 (N18.5W5.0), which consist of time series of high resolution MDI magnetograms co-aligned with the TRACE chromospheric and coronal time series in  $1,600\text{ \AA}$ , Fe IX/X  $171\text{ \AA}$ , and Fe XII  $195\text{ \AA}$  lines complemented by time series of  $H\alpha$  filtergrams obtained from the Swedish Vacuum Solar Telescope (SVST) on La Palma.

Figure 11.14 shows a sample MDI magnetogram (panel a) of the central sunspot co-aligned with the image of overlying atmosphere in the  $\pm 700\text{ m\AA}$  wings of  $H\alpha$  (panel b). To study temporal variability of small magnetic features we use again the procedure of space-time cuts. Three examples of such cuts in both wavelengths are shown in the upper and lower right panels (1a, b); (2a, b); (3a, b). The population of MMFs and their association with mass flows around the sunspot are well seen in the  $\pm 700\text{ m\AA}$  wings of  $H\alpha$  showing the motions at somewhat elevated photospheric level.



**Fig. 11.14** The sunspot observed on June 10, 1999. **a** MDI magnetogram scaled from  $-1,000$  to  $1,000$  G. **b** Co-aligned image of the same area in the  $-700$  mÅ wing of  $H\alpha$ ; *Upper right panels*: three cuts made over the central sunspot showing propagation of negative (*black*) and positive (*white*) magnetic footpoints lying along these cuts; *small arrows* show some long-living MMFs; *Lower panels* As in the magnetogram movie, left sides of cuts 1 and 2, and the entire cut 3 pass through the region well populated by MMFs (*thick black arrows*); the right ends of cuts 1 and 2 reveal very little activity of small-scale bipoles (*thick white arrows*)

More than three-quarters of the moat area is well populated by MMFs. The paths of corresponding cuts and their directions are shown, respectively, in panels (a) and (b). The left sides of cuts 1 and 2 and the entire cut 3 through the diameter of a moat pass through the region well populated by MMFs. One can see different types of MMFs on the left sides of panels (1a, b) and (2a, b), and at both sides of panel (3a, b), streaming outward from sunspot; whereas the right ends of cuts 1a, b and 2a, b pass through the moat region devoid of MMFs (a curved arrows in the left panels mark the region depleted of MMFs). We will see below that regions with a deficit of MMFs usually serve as a preferred site for coronal loop formation (Ryutova et al. 2007).

Features of individual MMFs as well as expected response of overlying atmosphere are consistent with the predictions of the theory.

The processes of energy transfer and release by soliton (Type I, I\*, MDF) and shocklike kinks (Type II, III), and therefore their impact on the dynamics of the overlying atmosphere, are quite different.

Solitons, once formed, remain “self-contained” and sturdy for a long time. Their amplitude slowly decays as  $1/(1+t/t_{\text{diss}})$ . During the passage of a soliton through the moat it gradually slows down, separation between the footpoints increases, and a kink

straightens out. The slow process of energy loss by a traveling soliton may produce a faint emission in chromospheric lines, which may end up at the moat boundary by the appearance of bright points. Under certain and rare conditions, though, solitons may experience an explosive growth, as  $1/(1 - t/t_{\text{expl}})^2$ . This corresponds to quick and violent energy release which may produce well concentrated jets and microflares even at coronal temperatures.

A shocklike kink is a more unsteady state than a soliton. Its lifetime may be as long as that of a soliton, but to remain in a quasi-stable state, it requires an intense process of energy supply and release.

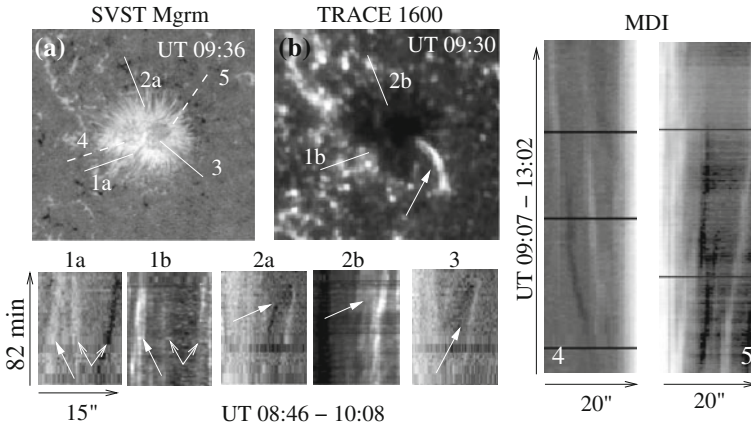
One should bear in mind that the very existence of evolutionary soliton- and shocklike kinks is possible only in energetically open systems, i.e., in systems with continuous energy inflow and outflow (sources and sinks). Therefore, the intensified process of the absorption and release of energy by shocklike formation should be accompanied by the enhanced emission in the upper layers of atmosphere during most of its lifetime. The energy of a shocklike kink is concentrated in a small volume. When this volume decreases, the kink quickly dissipates its energy, and may cause the appearance of jets and microflares.

Examples of different types of MMFs and their counterparts in the overlying atmosphere are shown in Fig. 11.15. Cuts 1a, b contain two MMFs, type I, marked by double arrows, and type II, marked by a single arrow. The size of the footpoints is about  $1''$ – $1.3''$ . This type I feature was born obviously long before the SVST data were taken; its footpoints are already far apart exceeding a separation of  $4''$ . It continues a steady motion with further gradual spreading, typically seen in the numerous long-lived MMFs. At transition region temperatures, as expected, this MMF is barely noticeable. Its neighbor, a type II MMF with shocklike properties, on the contrary, produces strongly enhanced emission at the temperatures  $T \sim 6 \times 10^4 - 2.5 \times 10^5$  K during its passage throughout the moat.

The third example is quite rare. This is a type I MMF born during the SVST observations. Its short path resembling the Greek  $\lambda$  is consistent with the explosive behavior leading to collapse and violent energy release. Indeed, the collapse of this MMF was accompanied by a strong and short-lived ( $\sim 6$  min) micro-flare seen in its maximum phase on the TRACE 1,600 image (panel b).

To obtain more information about the influence of MMFs on an overlying atmosphere, a high cadence ( $\leq 30$ s) movies in G-band  $4,305 \text{ \AA}$  were compiled together with co-spatial Dopplergrams.

In Fig. 11.16 we compare space-time slices made along cuts 1–3 using Dopplergram and G-band movies. Cut 1 lies in the region of a significant deficit of the MMFs. The corresponding Dopplergram image (Fig. 11.16a, upper panel), shows characteristic umbral oscillations and running penumbral waves. The left vertical lines in these panels mark the umbra/penumbra boundary, and the right lines the approximate boundary of the penumbra. The rest is the moat region. One can see how a regular umbra/penumbra plane waves smooth out in the moat and leave a place to a vague pattern of granular motions. Note here a short-lived chromospheric transient appeared at UT 12:50.

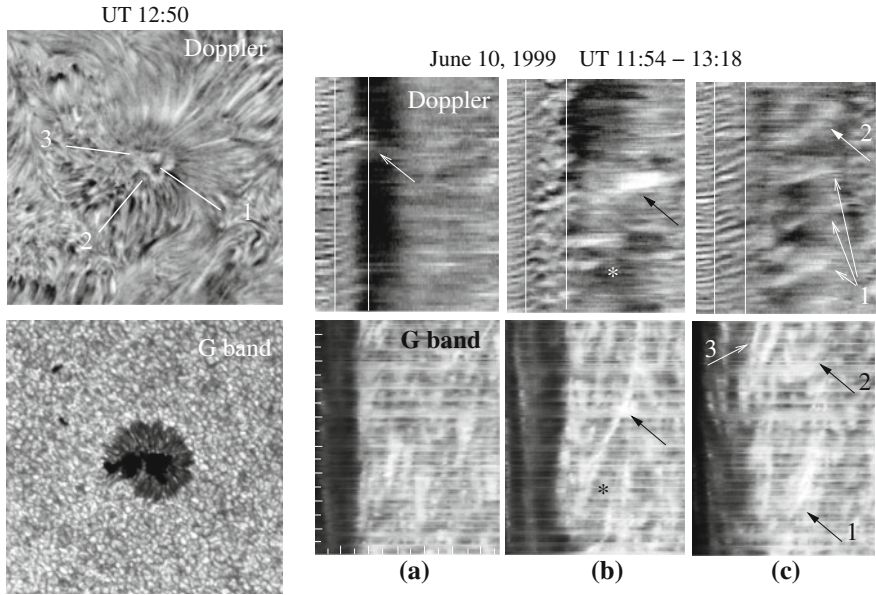


**Fig. 11.15** Examples of different types of MMFs and their counterparts in the transition region. *Upper panels a* SVST magnetogram of the central sunspot form Fig. 11.14 with resolution  $0.2''$ . *b* The same region in TRACE 1600 at  $T \sim 6 \times 10^4 - 2.5 \times 10^5$  K; three *straight lines* show corresponding space-time cuts in the *lower panels*. Cut 1 contains two most typical MMFs, Type I (*double arrow*) and Type II (*single arrows*); stable soliton (Type I) leaves a very faint trace at high temperatures, while Type II which has shocklike properties, produces strongly enhanced emission in the TR. Cut 2 shows type I MMF (with the inner footpoint of polarity opposite the sunspot's), which after about an hour of a steady state starts to shrink and quickly disappears; this process is accompanied by the extended brightening (2b); Cut 3 shows another Type I MMF under the condition when it experiences an “explosive” collapse, which results in the intense, but short-lived micro-flare (snapshot in panel (b) shows its maximum phase). *Panel (4)* shows a long-lived Type I MMF at the MDI resolution with the inner footpoint of the same polarity as parental sunspot (Type I, bright soliton), and *Panel (5)* shows type I MMF with the inner footpoint of the opposite to sunspot polarity (Type I\*, dark soliton)

The bottom-left panel is a G-band image at  $4,305 \text{ \AA}$ . This line has been commonly used to track the small-scale magnetic elements that appear as G-band bright points. The space-time slice in the G-band passing through region devoid of MMFs (lower panel a) shows irregular motions, appearance and disappearance of a small-scale network magnetic elements.

The other two cuts, 2 and 3, corresponding to images in panels (b) and (c), lie in regions dominated by type II MMFs having shocklike properties. Cut 2 reveals a typical example of such an MMF. Its emergence is accompanied by the strongly enhanced up-flows seen in Dopplergram image (marked by stars). Traveling with high velocity,  $\simeq 6 \text{ km s}^{-1}$ , the MMF generates along its path strong disturbances that culminate at about the time when the MMF “settles down” and starts to migrate slowly toward the moat boundary (black arrows in panels b). Note, that a lateral motion of the  $H\alpha$  disturbance at this time is about  $14 \text{ km s}^{-1}$ , which at  $T \simeq 10^4 \text{ K}$  is already (but slightly) supersonic.

Cut 3 reveals three features, two MMFs of type II marked by black arrows in lower panel (c), and one MMF of type I, marked by white arrow. During the passage of the MMF # 1 through the moat, Dopplergram movie shows how a regular pattern of oscillations disintegrates into two distinct velocity fields associated with the ridges



**Fig. 11.16** Computed Dopplergram in  $H\alpha \pm 0.350 \text{ \AA}$  and SVST G-band images of a target area (*left panels*). Corresponding space-time images for three cuts shown in the *right panels* (*upper row* is from a Dopplergram movie, *lower row* is from G-band movie): **a** Cut 1 is made over the region devoid of MMFs. **b** Cut 2 reveals “unipolar” type II MMF and its imprint on overlying chromosphere. **c** Cut 3 shows two MMFs of type II marked by *black arrows*, 1 and 2, and one MMF of type I marked by *white arrow*, 3. See text for details. Tick marks in the *x*-axis correspond to  $2.5''$  and tick marks in the *y*-axis to 5 min

of up-flow material followed by the post-ridge downflows, marked by white arrows in the upper panel, (c). The velocity of the ridges associated with the first MMF is over  $16 \text{ km s}^{-1}$ , and is clearly supersonic, while the lateral motion of a ridge 2 is about  $9 \text{ km s}^{-1}$ , and seem to be subsonic.

As already mentioned, simple relations between the width of a soliton, its velocity, amplitude ( $B_z^2$ ), and lifetime, expressed in directly observable quantities allow detailed analysis of the data and inference of such parameters as dissipative coefficients (which determine the lifetime of MMFs), dispersion, the slope of a soliton, etc. Most importantly these parameters may be used to study observational signatures of dissipation processes which are associated with the energy transfer and release by MMFs.

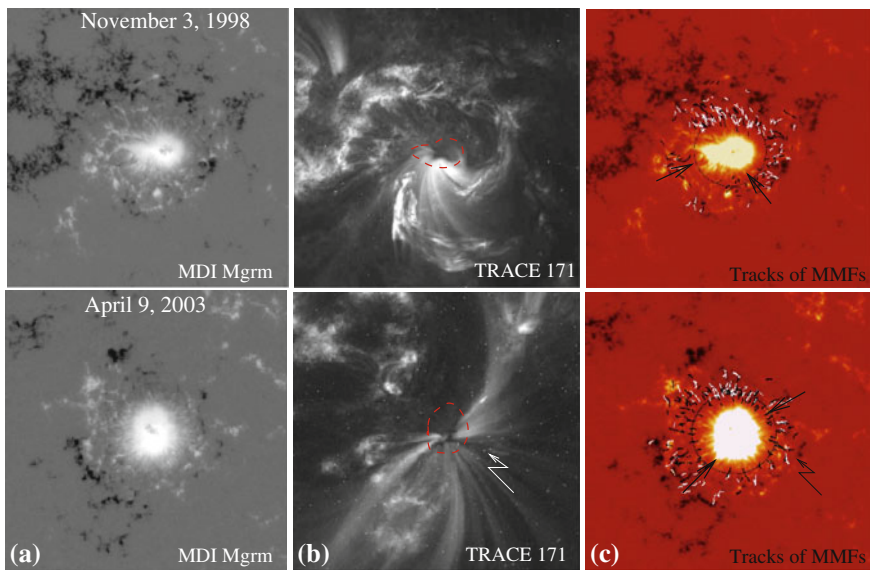
### 11.9 Anticorrelation Between Population of MMF’s and Coronal Loop Formation

So far we were discussing the properties of individual MMFs and their observed signatures. It is interesting that as an ensemble, the families of MMFs have an essential influence on the dynamics of solar atmosphere from its visible surface to corona.

It was found that very intense formation of an ensemble of MMFs as a collective phenomenon is strictly correlated with the absence of large-scale “stable” coronal loops (Ryutova et al. 2007). Such loops are usually rooted at the side of the sunspot with no or few MMFs. We will discuss below possible reasons that may cause the observed anticorrelation. For these studies several sets of multiwavelength observations of different sunspot areas from the photosphere to the corona have been used.

Hagenaar and Shine (2005) studied statistical properties of MMFs using time sequences of high resolution magnetograms of eight sunspots. They have developed an automated algorithm to find and track unipolar magnetic field concentrations, and derived flow maps around the spots to compare plasma flow patterns with the tracks of moving magnetic features. These results were compared with the corresponding images of overlying corona.

The examples of the data taken on November 3, 1998 and April 9, 2003 are shown in Fig. 11.17. Figure 11.17a, b are a co-aligned MDI magnetogram and the overlying corona in the TRACE 171 Å line. Figure 11.17c shows tracks of unipolar magnetic elements obtained from the time sequence covering a 19h period. In all studied cases, the number and distribution of MMFs around sunspots is uneven: one side of a sunspot may show a much higher population of MMFs than the other. The side of



**Fig. 11.17** Connection between the number of MMFs and the preferable site for the formation of coronal loops. *Left and middle panels* co-aligned MDI magnetogram and overlying corona. *Right panels* Paths of outflowing unipolar magnetic features obtained from the MDI movies covering a 19h period. *Black arrows* show the side of the sunspot where the population of MMFs is low and where large-scale coronal loops are originated. The *zigzag arrows* indicate a tiny region with quite sturdy MMFs and respectively a gap in the coronal loops rooting. *Red dashed curves* outline the position of the umbrae, and *black circles* the approximate penumbrae radii

the sunspot with a small population of MMFs is indicated by black arrows, and as in all studied cases, it is just this side where large-scale coronal loops are rooted.

It is important to note, however, that only intense MMF production strictly correlates with the absence of loops. Moderate MMF production may or may not prevent coronal loop formation, and prominent loop bundles do not necessarily mean the absence of MMFs. And yet, in a long-term period a dynamic ensemble of a large number of MMFs seems to create physical conditions unfavorable for the formation of long-lived coronal loops. The correlation between the deficiency of MMFs and the preferable location of coronal footpoints definitely calls for further studies.

For the time being, it is obvious, that whatever is the reason for coronal loops to avoid regions highly populated by MMFs, it should be sought in the nature of MMFs as a collective phenomenon. Below we discuss two possible reasons that may cause the observed anticorrelation:

1. According to the observations, MMFs appear along horizontal magnetic filaments usually located in areas of strong horizontal flows. From the theoretical point of view, as well, a primary condition for the soliton formation is a horizontal magnetic flux tube (with gravity force perpendicular to its axis) in the presence of aligned shear flow (Ryutova et al. 1998). Some parts of the sunspot penumbra, however, may be dominated by elevated magnetic filaments that cannot support formation of MMFs but may well serve as a base for coronal loops. The key element here seems to be the natural coexistence and uneven distribution of horizontal and elevated filaments in the penumbra: an intense MMF formation and the lack of loops correspond to strong predominance of horizontal filaments, while regions with a preference to more elevated filaments produce coronal loops. The coexistence of horizontal and vertical filaments explains the emergence of a few MMFs in the presence of coronal loops.
2. The other effect that may cause a lack of MMFs around sunspots with horizontal penumbral filaments and co-aligned flows (i.e., under satisfactory primary conditions) is a deviation of local physical parameters of a system from values adequate for the formation of MMFs. To discuss this effect, we first briefly address some key properties of MMFs and conditions for their formation based on (11.3)–(11.9).

As we know, the solution of (11.3) has several branches, determined by the phase velocity, (11.1), the sign of dispersion, and the interplay of nonlinear, dispersion, and dissipative effects. If dispersion is balanced by nonlinearity, stationary solution of (11.3) is known to be a stable solitary kink with a simple relation between the width of a soliton,  $\Delta$  (separation between MMF footpoints), its velocity,  $v_{\text{sol}}$ , and amplitude  $A \simeq B_z^2$  ( $B_z$  is the line of sight magnetic field at the MMF footpoint) given by (11.7)–(11.9).

Order-of-magnitude comparison of the two last terms in the left-hand side of (11.3) gives a condition for balance between nonlinear and dispersive terms,  $\alpha\psi \sim \beta_{\text{disp}}/\Delta^2$ ; for positive dispersion we have

**Table 11.1** Measured and estimated parameters of MMFs

Directly observed parameters						Estimated parameters		
MMF	$B_z$ (G)	$R$	$\Phi$ ( $10^{18}$ (Mx))	$\Delta$	$v_{\text{sol}}$ ( $\text{km s}^{-1}$ )	$c_k$ ( $\text{km s}^{-1}$ )	$v_A$ ( $\text{km s}^{-1}$ )	$c_k^{(\text{th})}$ ( $\text{km s}^{-1}$ )
1	480	1.2''	3.6	4''	1.2	0.48	3.8	0.42
2	230	2.2''	5.1	8''	0.8	0.32	1.8	0.32

$$\frac{3}{4} \frac{B_z^2}{B^2} c_k \simeq \frac{R^2}{\Delta^2} \frac{1}{2\eta v_A^2} \frac{(c_k - u)^4}{\sqrt{\eta[(1 + \eta)v_A^2 - u^2]}} \quad (11.32)$$

By slight violation of the equivalence (11.32) toward increasing dispersion, roughly for thicker flux tubes, solitons become flat, their width increases, and their velocity drops. Thus, if the penumbral filament is thick enough, the kink produced by the shear flow instability will not survive. Finally, when the nonlinear term in (11.3) can be neglected, i.e., the problem becomes linear, a kink generated by shear flow after few undulations will disappear as usual wave. This will also happen if the dispersion term exceeds the nonlinearity by one or two orders of magnitude.

To estimate the radius of the flux tube at which in otherwise suitable conditions solitons do not form, we use two examples of a long-lived type I MMFs shown in Fig. 11.15 (panels 4 and 5).

The observed and estimated parameters are shown in Table 11.1. The first five columns are directly observed parameters. The two next columns containing  $v_A$  and  $c_k$  are values of Alfvén and phase velocities deduced from observations. The value  $c_k^{(\text{th})}$  is calculated with (11.1). We must add this table to the values of an angle and radii that at given physical conditions *are not suitable* for the formation of MMFs. These are: for MMF 1,  $\theta = 10^\circ - 15^\circ$ ,  $R_\theta = 7'' - 4.6''$ , and for MMF 2,  $\theta = 16 - 27^\circ$ ,  $R_\theta = 8'' - 4.8''$ .

We adopt the following values: the plasma density outside the flux tube  $\rho_e = 2.8 \times 10^{-7} \text{ g cm}^{-3}$ , the ratio of mass densities,  $\eta = \rho_i/\rho_e = 0.9$ , and the flux tube inclination in the developed soliton,  $\theta = 45^\circ$ , so that  $B_z = B \sin \theta$ .

Using condition (11.32), and the soliton velocity, from (11.7)–(11.9), we may exclude a quantity  $\beta_{\text{disp}}/\Delta^2$  and estimate the phase velocity directly through the observed speed of a soliton. This gives  $c_k \simeq 0.4 v_{\text{sol}}$ . For the lower sign in (11.1) the shear flow velocity should be taken in the range of  $\sqrt{\eta}v_A \leq u \leq \sqrt{1 + \eta}v_A$ . Taking a value of  $u = 4 \text{ km s}^{-1}$  for MMF # 1, and  $u = 2 \text{ km s}^{-1}$  for MMF # 2, we obtain, respectively,  $c_k^{(\text{th})} = 0.42 \text{ km s}^{-1}$ , and  $c_k^{(\text{th})} = 0.38 \text{ km s}^{-1}$ . Both values are close to values estimated from observations.

If the slope of the kink legs levels down, nonlinearity becomes negligible, and conditions for the formation of MMFs are no longer satisfied. For small enough angles ranging over interval  $15 - 10^\circ$ , the right-hand side of (11.32) exceeds the left-hand side by a factor of 15–33. This means that if under the condition of MMF 1, with a radius of 1.2'', a flux tube with a radius of about 4.6''–7'' (and higher) cannot form a stable kink. For a comparable size of flux tubes, under conditions allowing



formation of “thicker” kinks, such as MMF # 2, “unfavorable” angles may be as high as  $16^{\circ}$ – $27^{\circ}$ .

Most probably, it is a combination of both effects, uneven coexistence of elevated and horizontal magnetic filaments in the penumbra and the presence of thick horizontal filaments, that causes the observed correlation between coronal loops and the deficiency of MMFs. The effects of MMFs in the dynamics of the upper atmosphere seems to be quite pronounced and call for further studies. An analysis of flow maps in and around the sunspot together with the vector magnetograms may provide reliable information on the nature of the photosphere-corona coupling.

## References

- P.N. Bernasconi et al., *Sol. Phys.* **209**, 119 (2003)  
 N. Brickhouse, B. LaBonte, *Sol. Phys.* **115**, 43 (1988)  
 B. Coppi, M.N. Rosenbluth, R. Sudan, *Ann. Phys.* **55**, 201 (1969)  
 V.M. Dikasov, L.I. Rudakov, D.D. Ryutov, *Sov. Phys. JETP* **21**, 1965 (1965)  
 I. Fushiki, J.I. Sakai, *Sol. Phys.* **161**, 317 (1995)  
 H. Hagenaar, R. Shine, *Astrophys. J.* **635**, 659 (2005)  
 K. Harvey, J. Harvey, *Sol. Phys.* **28**, 61 (1973)  
 B.B. Kadomtzev et al., *Sov. Phys. JETP* **20**, 1517 (1964)  
 V.I. Karpman, *Nonlinear Waves in Dispersive Media* (Pergamon Press, London, 1975)  
 J.W. Lee, *Sol. Phys.* **139**, 267 (1992)  
 P. Maltby, E. Avrett, M. Carlsson, O. Kjeldseth-Moe, R. Kuruz and R. Loeser, *Astrophys. J.* **306**, 284 (1986)  
 L.A. Ostrovsky, S.A. Rybak, L.Sh. Tsimring, *Sov. Phys. Uspekhi* **29**, 1040 (1986)  
 M.P. Ryutova, *Sov. Phys. JETP* **67**(8), 1594 (1988)  
 M. Ryutova, R. Shine, A. Title, J.I. Sakai, *Astrophys. J.* **492**, 402 (1998)  
 M. Ryutova, T. Tarbell, R. Shine, *Sol. Phys.* **213**, 231 (2003)  
 M. Ryutova, H. Hagenaar, *Sol. Phys.* **246**, 281 (2007)  
 M. Ryutova, H. Hagenaar, A. Title, *Astrophys. J.* **656**, L45 (2007)  
 N.R. Sheeley, *Sol. Phys.* **1**, 171 (1967)  
 R.A. Shine, A.M. Title, T.D. Tarbell, K.P. Topka, *Science* **238**, 1203 (1987)  
 R. Shine, A. Title, in *Encyclopedia of Astronomy and Astrophysics*, ed. by P. Murdin (IOP, Bristol, 2001)  
 M. Suzuki, J.I. Sakai, *Astrophys. J.* **465**, 393 (1996)  
 D. Vrabc, in *Solar Magnetic Fields*. IAU Symposium 43, vol. 329, ed. by R. Howard (Reidel, Dordrecht, 1971)  
 G.B. Whitham, *Linear and Nonlinear Waves* (Wiley, New York, 1974)  
 P.R. Wilson, *Sol. Phys.* **106**, 1 (1986)  
 V.B. Yurchyshyn, H. Wang, P. Goode, *Astrophys. J.* **550**, 470 (2001)  
 J. Zhang, S.K. Solanki, J. Wang, *Astron. Astrophys.* **399**, 755 (2003)  
 F. Zuccarello et al., *Astron. Astrophys.* **500**, 5 (2009)

## Chapter 12

# Reconnection of Flux Tubes—Specifics of High Plasma $\beta$

**Abstract** Two fundamental mechanisms of magnetic reconnection worked out by Sweet-Parker tandem (Parker (1957); Sweet (1958) and Petschek (1964)), were both aimed to explain an enormous amount of energy produced by coronal flares. Since then extensive studies of a topological change of magnetic field resulted in a huge body of refined reconnection theories, beautiful laboratory experiments, and numerical modeling. One thing, however, remained for a long time unchanged: the subject of studies, magnetized plasma, has been a priori considered magnetically dominated, i.e., having very low plasma beta,  $\beta = 8\pi p/B^2 \ll 1$ . It is just this condition that provides release of a huge amount of energy stored in magnetic fields due to their topological change. This simple fact dominated so strongly that during almost six decades there was no attempt to investigate the opposite situation, i.e., when topologically favorable conditions for reconnection appear in gas-dominated plasma with finite or even larger than unity plasma beta,  $\beta = 8\pi p/B^2 \geq 1$ . As the quest was for a large amount of magnetic energy, the case of high beta plasma (with magnetic energy less than gas-kinetic energy) did not seem promising. This, however, proved to be wrong. It turned out that in case of small-scale magnetic flux tubes under real conditions of solar photosphere, high  $\beta$  reconnection is unavoidable process. In the photosphere magnetic flux, tubes buffeted by convective motions collide and reconnect. True that the photospheric reconnection does not give the immediate gain in energy, but it sets the system in strongly unstable state. Now the central problem becomes to understand how the post-reconnection products evolve. In this chapter we shall study the peculiarities of high  $\beta$  reconnection, and what is more important, the post-reconnection processes. We shall see that high beta reconnection triggers various nonlinear processes that are responsible for a wide range of observed phenomena.

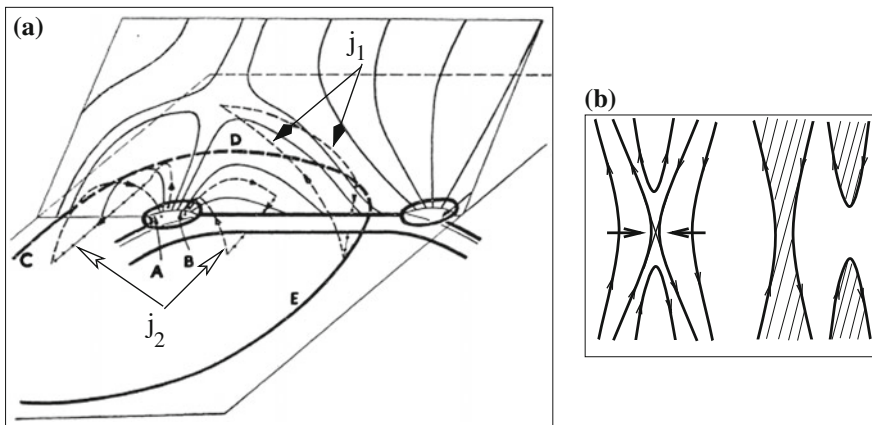
### 12.1 Basics of Magnetic Reconnection

It all started with trying to solve a mystery of chromospheric flares. Back in the 1940s there were accumulated quite a rich observational data in Ca H and K lines and in  $H\alpha$  showing clear association of chromospheric flares with underlying sunspot groups.

Giovanelli (1946), who involved himself in these observations, in a short note on a theory of chromospheric flares pointed out that the changing magnetic flux of ever-evolving sunspot groups leads to formation of an X-type neutral points in the magnetic field lines, and, to formation of at least two types of current systems, whose evolution eventually lead to electrical discharges along neutral lines. Figure 12.1a shows Giovanelli's sketch of currents flowing in a system of a bipolar sunspot group. Magnetic field lines are shown in a "dividing" plane containing the sun's general magnetic field, and intersecting the two sunspots. A current filament, one in the neutral point current sheet ( $j_1$ ), and two others flowing into sunspots ( $j_2$ ), are shown by dashed lines. Arrows show their relative direction. The line AB is the locus of points where the dividing plane meets the surface of the sunspot. The line CDE is the locus of points where lines of force from near the neutral point meet the sun's surface. This line serves as a base of the neutral point current sheet.

The most remarkable fact in Giovanelli's studies is that his model of magnetic field reorganization is essentially *three dimensional*. Although Giovanelli does not talk about "breaking" and "rejoining" lines of forces, the very idea and accompanying drawing form the bases of all types of future reconnection models.

The very first statement that "lines of force can be regarded as being broken and rejoined" belongs to Dungey (1953), who suggested that near-neutral point magnetic field may go unstable and result in the reconfiguration of magnetic field and the fast dissipation of magnetic energy. Figure 12.1b illustrates Dungey's examples which he describes as follows. When "two parts of a loop of force are close together with their fields in opposite directions, the result is that the loop of force breaks into two loops, whose total length is less than that of the original loop." And Dungey concludes that "the field energy from relatively large region is concentrated on particles in the neighborhood of the neutral point, and that part of energy is released."



**Fig. 12.1** Earliest representation of magnetic energy release: **a** Three dimensional (!) cartoon by Giovanelli (1948), showing *currents* near a growing bipolar spot group (see details in text); **b** Dungey (1953) "lines of force" that "can be regarded as being broken and rejoined"

Bumba (1958) was first to observe that the  $H\alpha$  emission in the largest flares begins over a series of small-scale magnetic elements, dubbed at that time as flare knots, that form to strips on either side of the polarity inversion boundary. It was found that the flare knots are associated with strong electric currents (Moreton and Severny 1968).

Simple and appealing, Dungey’s two-dimensional cartoon took a long journey. And reconnection theories became two-dimensional for decades.

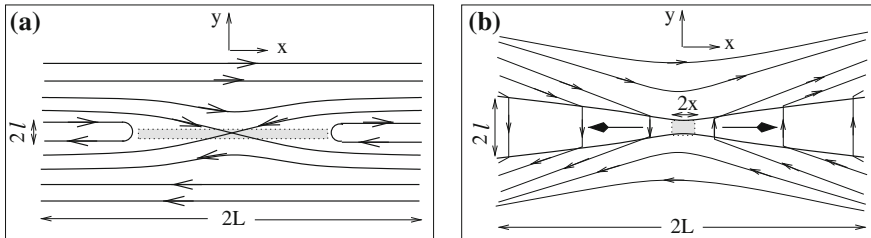
Sweet (1958) presented a talk at the 1956 IAU Symposium in Stockholm on theory of solar (chromospheric) flares based on formation of a neutral collision layer as a result of merging of opposite polarity magnetic field systems, with subsequent change in their topology leading to strong radiation of energy and production of high-energy particles.

Parker (1957), impressed by Sweet’s presentation derived scaling laws of the process and coined the term “reconnection”. When two oppositely directed magnetic fields approach each other (Fig. 12.1b), the field gradient steepens and the electric current density  $(c/4\pi)\nabla \times \mathbf{B}$  becomes large. At the same time, at small characteristic distance, the dissipative effects turn on and strong dissipation occurs.

To be consistent with Sweet’s hydrodynamic analogy of expelling gas occupying a space between two rigid plates forced to move toward each other, Parker derives the rate of steady-state reconnection from the basic conservation laws. The total pressure,  $p + B^2/8\pi$  is uniform across the current sheet, so the gas pressure is highest on the neutral plane where  $B$  goes through zero (Fig. 12.2a). This excess pressure ejects the gas from the mid-plane region along the lines of force in the  $\pm x$  directions with velocity  $v$ . For irrotational and steady motion Bernoulli’s equation is

$$\rho v \frac{\partial v}{\partial x} + \frac{\partial p}{\partial x} = 0 \tag{12.1}$$

Integrating along  $x$ -axis from the origin at the center, where  $v = 0$  to a point outside the fields, one obtains  $\rho v^2 = 2\Delta p$ , where  $\Delta p$  is the pressure excess  $B^2/8\pi$ . Thus the velocity of expulsions is just the Alfvén velocity,  $v_A = B/\sqrt{4\pi\rho}$ .



**Fig. 12.2** Magnetic field and flow configuration in the reconnection process. **a** Diffusion dominant mechanism by Sweet-Parker: the plasma moves toward boundary from both sides and after field lines reconnect at the  $x$ -point due to finite conductivity, is ejected along it. **b** Petschek’s mechanism includes standing waves, shown by vertical arrows off the  $x$ -type neutral point. Flow geometry is the same as in the previous case, but now it is independent on the diffusivity and is controlled by Alfvén waves

If  $l$  is the characteristic length of the gradient of  $\mathbf{B}$  across the neutral plane, then the characteristic rate of the net expulsion of gas out of both ends is  $4lv$ . If the two magnetic fields approach each other with velocity  $w$ , then the mass conservation of gas requires that

$$wL = v_A l. \quad (12.2)$$

As the field changes by  $2B$ , across the thickness  $2l$ , the current density (perpendicular to the  $xy$ -plane) is  $j = cB/4\pi l$ . The Ohmic dissipation across the width  $l$  is  $lj^2/\sigma$  which, in fact, equals the magnetic energy influx  $wB^2/8\pi$ . Hence the velocity with which the opposite fields move toward each other is  $w = (2/l)(c^2/4\pi\sigma)$ , or

$$w = \frac{2\eta}{l} \quad (12.3)$$

where  $\eta = c^2/4\pi\sigma$  is the resistive diffusion coefficient. Thus,  $w$  has a simple meaning of the characteristic diffusion velocity over a scale  $l$ . Solving for  $w$  and  $l$ , (12.2) and (12.3) give

$$w = \frac{2v_A}{\sqrt{R_m}}, \quad l = \frac{2L}{\sqrt{R_m}} \quad (12.4)$$

where  $R_m$  is magnetic Reynolds number  $R_m = 2Lv_A/\eta$ . Thus the rate (12.4) is larger by  $\sqrt{R_m}$  than pure diffusion, but it is still too small compared to the Alfvén speed. In the solar atmosphere, magnetic Reynolds number is of the range  $10^6$ – $10^{12}$ , and reconnection rates are then  $10^{-3}$ – $10^{-6}$  of the Alfvén speed. In other words, the rate at which magnetic energy can be released by Sweet-Parker mechanism is by several orders of magnitudes less than the observed one.

At AAS-NASA Symposium on Physics of Solar Flares Petschek (1964) gave a talk on “Magnetic Field Annihilation” and showed that the rate of magnetic energy release due to the merging of opposite polarity magnetic fields can be made comparable with that observed in solar flares.

Petschek pointed out that on the basis of resistive instability analysis of Furth et al. (1963) the boundary in the Sweet-Parker model would be unstable. However, the linearized instability analysis is not sufficient for estimate of the actual reconnection rate. Petschek showed that the two opposite fields could meet and form much shorter current sheet than that assumed by Sweet and Parker. The Petschek’s drawing is shown in Fig. 12.2b. Once the field lines in this small region ( $2l \times 2x$ ) are reconnected, their tension ejects the plasma vigorously generating the Alfvén waves that accelerate further to form slow magnetosonic shocks. The reconnection rate in this process depends strongly on system parameters and may be arbitrary. Sweet-Parker’s solution is one of the special cases. Petschek, deriving the maximum reconnection rate which can be presented as

$$w = \frac{v_A}{\ln R_m} \quad (12.5)$$

comments: “It is a fortunate circumstance that this answer depends only logarithmically on the magnetic Reynold’s number and is therefore rather insensitive to our ignorance of the effective conductivity of plasma.”

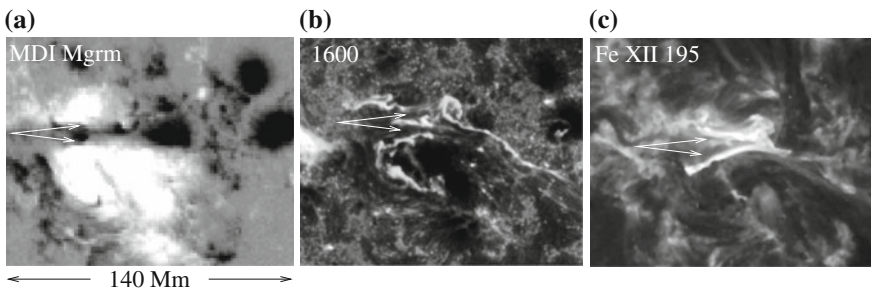
Sweet, during discussion after Petschek’s presentation said: “Dr. Parker and I have been living with this problem for several years and have got the feel of it. Your solution struck me at once as the solution for which we have been seeking.”

Petschek’s work was prophetic in that simple way which gives an extremely wide range of the reconnection outcome depending on the physical parameters of medium. Nature, from laboratory plasma devices, near earth magnetosphere, the sun and outer space consists of plasma which never is at rest. This means that any moving plasma is magnetized, and naturally, is strongly inhomogeneous. Thus magnetic fields are permanently subject to topological changes. This is exactly what the reconnection is, but the outcome, depending on physical parameters of a particular system, has many faces.

Since those early days, all studies of magnetic reconnection were focused exclusively on those areas where the reconnection would lead to a strong *in situ* heating and particle acceleration (Rosenau 1979; Syrovatskii 1981; Axford 1984; Biskamp 1986). And the requirement of plasma beta to be much smaller than unity became an imperative.

Highly improved solar observations made the marsh of reconnection mechanism triumphant: favorable magnetic configuration (such as shown in Fig. 12.3), rearrangement of overlying coronal loops, and subsequent flare became regularly observed. The observed timescales, however, are still too far from those estimated theoretically. And refining of reconnection models, their study in laboratory experiments that allows to change and control the system parameters, continues to this day (Parker 1991; Somov 1992; Priest and Forbes 2000; Yamada et al. 2010; Kulsrud 2011).

This concludes our brief look at the “orthodox”,  $\beta \ll 1$ , magnetic reconnection. In this and in subsequent chapters we shall study the opposite case, the reconnection



**Fig. 12.3** Magnetogram of a huge active region AR 10486 taken on 28 October 2003 by the MDI instrument on SOHO. **a** White arrows shows two parallel regions with possibly two separate current sheets. **b** The same region in the chromospheric 1,600 Å line, and **c** in the coronal Fe XII 1995 Å line. Enhanced emission at chromospheric and coronal temperatures mimic the possible current sheets

and post-reconnection processes in high beta plasma containing magnetic flux tubes, i.e., the case when magnetic energy stored in flux tubes is less than gas-kinetic energy of medium.

Odd enough, but during almost six decades of reconnection studies the case of high beta reconnection was not questioned until the late 1990s. The problem of high-beta reconnection was first considered in a series of papers by Tarbell et al. (1999, 2000), and Ryutova and Tarbell (2000); Ryutova et al. (2001, 2003). These studies originated from the attempts to explain new regularities established in simultaneous multi-wavelength observations of the photosphere and its overlying chromosphere/transition region.

## 12.2 Photospheric Reconnections—No Immediate Gain in Energy

Throughout this book we talked and will come back to the fact that small-scale magnetic flux tubes in the photospheric network are the subject of a complex dynamics that includes continuous emergence of new flux tubes, total or partial cancellation of opposite polarity elements, merging and splitting processes, the appearance of bright points in their vicinity, etc.

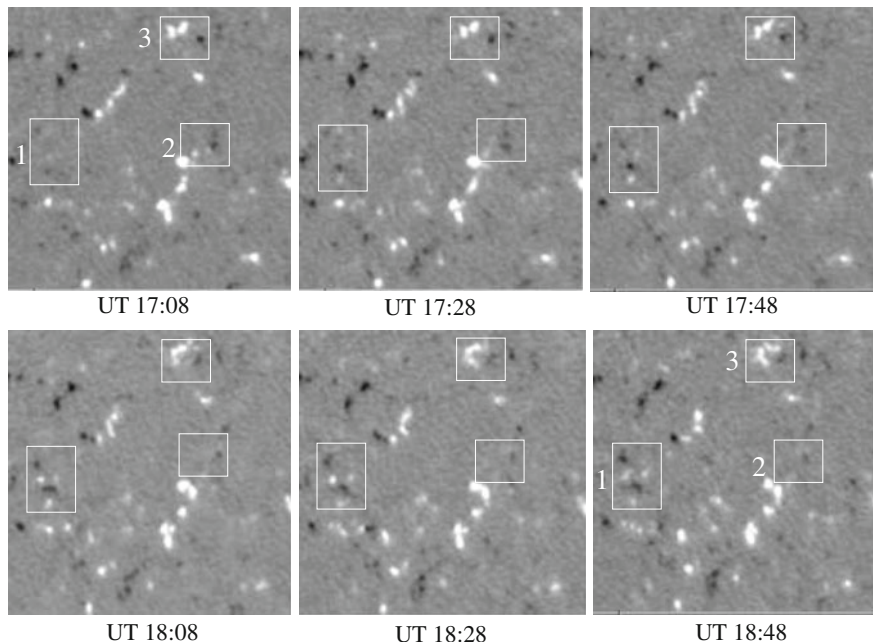
An exemplary set of magnetograms illustrating various processes in a very quiet sun is given in Fig. 12.4. Shown are the magnetograms of  $90'' \times 90''$  area at six instances of time with 20 min intervals taken by the MDI/SOHO instrument on January 22, 1997. Three white boxes identify the most typical events.

Box 1 is a region of newly emerging flux: at UT 17:08 the box is almost empty, in 20 min newly emerged bipole shows up, and in another hour the box is full of mixed polarity “pairs”. This region produces strongly enhanced emission at the transition region temperatures.

Box 2 contains two bipolar objects. Both bipoles during a given time get strongly reduced, which also coincides with strongly enhanced emission in the chromosphere/transition region temperatures.

The region inside Box 3 is dominated by magnetic elements of a single (positive) polarity. It shows a distinct fragmentation which at the given resolution ( $\simeq 1.2''$ ) roughly may be described as two “thick” magnetic concentrations (UT 17:08) breaking eventually into six “thinner” elements (UT 18:28).

Multi-wavelength observations taken simultaneously at different heights of the solar atmosphere reveal a clear connection between dynamic changes in the photospheric magnetic fields and the energetic events in the overlying atmosphere (Harrison et al. 1997; Brekke et al. 1997; Benz and Krucker 1999; Tarbell et al. 1999). These observations provided the bases for studies of reconnection processes between the photospheric magnetic flux tubes (Tarbell et al. 1999, 2000; Ryutova and Tarbell 2000; Ryutova et al. 2001).



**Fig. 12.4** Magnetograms of a quiet sun region taken by the MDI instrument on SOHO at six instances of time with 20 min intervals. Field of view is  $90'' \times 90''$ . Three most typical events are marked by boxes: the emergence of new magnetic flux (*box 1*), cancellation of opposite polarity magnetic elements (*box 2*), and fragmentation process in the system of one polarity fluxes (*box 3*)

### 12.2.1 Specifics of Photospheric Reconnections

Brought together by convective or other motions, flux tubes collide and *must* reconnect. The reconnection of photospheric flux tubes proceeds and results in essentially different effects than that in the coronal plasma. Unlike the low beta corona where the reconnection process liberates a large amount of energy stored in the magnetic field ( $B^2 \gg 8\pi p$ ) and deposits it “on the spot,” in the photosphere with much smaller magnetic energy than the gas-kinetic energy of environment, the reconnection does not give an immediate gain in the energy, but puts the system in strongly nonlinear unsteady state whose further evolution is determined by physical parameters of the the post-reconnection products.

The key elements of photospheric reconnection, which in fact, are absent in low beta corona, are provided by the specific conditions near the solar surface, the most important of which are the following:

- (1) Photospheric magnetic fields are concentrated in well-defined flux tubes embedded in an almost nonmagnetic environment; i.e., the plasma beta in the surrounding medium is very large,



$$\beta = \frac{8\pi p_{\text{ext}}}{B_{\text{ext}}^2} \gg 1 \quad (12.6)$$

(2) At the same time, because of the pressure equilibrium, the ratio of external gas-dynamic pressure and magnetic pressure inside flux tubes are finite:

$$\beta^* = \frac{8\pi p_{\text{ext}}}{B^2} \geq 1 \quad (12.7)$$

(3) Flux tubes are *always* noncollinear, i.e., approaching each other always make some angle.

(4) The low atmosphere is sharply stratified.

The first and second conditions ensure that after reconnection, the post-reconnection products that acquire strongly curved shape are kept in dynamic equilibrium by external gas kinetic pressure. Under such conditions the post-reconnection products behave like elastic bands: straightening and shortening they create a slingshot effect triggering strongly nonlinear processes in the external plasma.

The third condition, i.e., the fact that photospheric flux tubes are noncollinear, is extremely important: reconnection occurs not only between the opposite polarity flux tubes, but between the same polarity flux tubes as well.

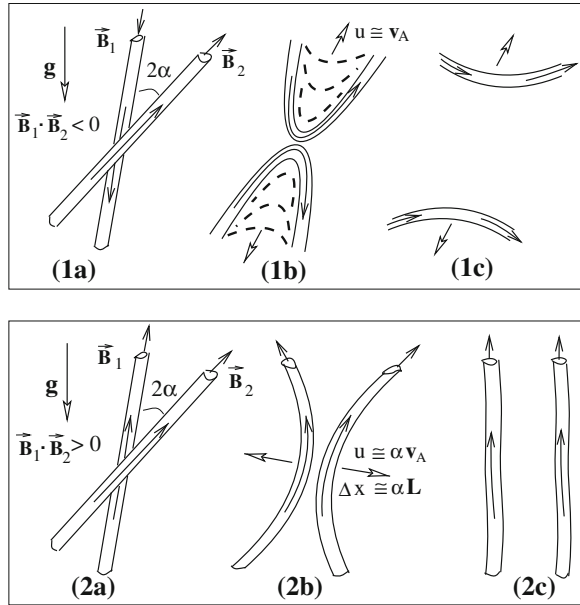
The fourth condition, strong stratification of low atmosphere, plays a decisive role in the development of strongly nonlinear processes. When the kick produced by the slingshot effect generates acoustic or MHD waves, those waves that propagate upward against gravity quickly steepen and become shocks. Farther evolution of shocks leads to a wide class of phenomena that are directly observable higher in the transition region and corona.

Before we consider these phenomena in detail and put them in practical use, let us discuss some general properties of flux tube reconnections. Consider first an interaction of two noncollinear flux tubes containing equal magnetic fluxes as shown in Fig. 12.5. When two slender (noncollinear) flux tubes with magnetic fields  $\mathbf{B}_1$  and  $\mathbf{B}_2$  collide, they overlap only in a short region. Along the line of sight these flux tubes may be seen as opposite polarity elements if they approach each other in such a way that the smaller angle,  $\alpha$  is formed between the opposite polarity ends. If the smaller angle,  $\alpha$  is formed between the same polarity ends, the observer sees the same polarity pairs.

Reconnection occurs in both cases creating a slingshot effect due to the straightening of reconnected flux tubes. Depending on the relative amount of flux and whether the colliding fluxes are the same or opposite polarities, the magnetic reconnection leads to different scenarios of the evolution of post-reconnection products and their observational signatures. In principle, orientation of colliding flux tubes making an angle  $2\alpha$  may be arbitrary. We assume for convenience that the bisector of the angle  $2\alpha$  is oriented along the line of sight.

Thus, in case of the opposite polarity flux tubes (Fig. 12.5 top), immediately after reconnection, the new flux tubes are strongly curved. Magnetic tension in this strongly curved state causes a fast shortening and straightening of post-reconnection

**Fig. 12.5** Reconnection of noncollinear flux tubes. *Top* opposite polarity flux tubes; *Bottom* the same polarity flux tubes. *Inside panels 1a–2a* just before the collision; *1b–2b* post-reconnection slingshot effect; *1c–2c* the reconnection products in the final moment of action of a restoring magnetic force.  $\Delta x$  in *panel 2b* is the displacement of the flux tube tip in the time interval between the reconnection and the straightening



flux tubes. The energy release in this process is approximately  $W_{\text{magn}} \sim (B^2/8\pi)SL$ , where  $B$  is the absolute value of the magnetic field strength,  $S$  is the cross section of interacting area, and  $L$  is the effective length of a flux tube participating in the reconnection process.

In case of the same polarity flux tubes (Fig. 12.5 bottom), the reconnection creates an illusion of scattering of flux tubes. Soon after reconnection the restoring magnetic force acting on the reconnection products straightens and drags them away from each other. The change in flux tube half-length in this process is proportional to  $\delta L \simeq \alpha^2 L$ . The magnetic energy content in this process is  $\delta W_M \simeq \delta L S (B^2/8\pi) \simeq \alpha^2 L S (B^2/8\pi)$ .

The velocity of post-reconnection flux tube motion can be estimated from the released energy:  $LS(\rho v^2/2) \simeq \delta W_M$ , which gives  $v \simeq \alpha v_A$ . The time for the flux tube straightening is:

$$\Delta t = \frac{\Delta x}{v} \simeq \frac{\alpha L}{v} \simeq \frac{L}{v_A} \tag{12.8}$$

For the flux tube to participate in the reconnection process over its whole cross-section, the characteristic reconnection time should be less than a straightening time. This condition sets the limit on the flux tube radius  $R_{\text{max}}$  at which the whole flux tube reconnects and behaves as a single elastic band in a slingshot effect. The maximum rate in the fast reconnection process is estimated as  $w_{\text{max}} \simeq v_A/(\ln Re_m)$ , where  $Re_m = Lv_A/D_m$  is magnetic Reynolds number and  $D_m$  is a magnetic diffusivity

(Petschek 1964). The reconnection time is, therefore

$$\tau_{\text{rec}} \simeq \frac{R}{w_{\text{max}}} = \frac{R \ln Re_m}{v_A} \quad (12.9)$$

From (12.8) and (12.9) one gets the estimate for a maximum radius of the flux tube participating in the elemental act of reconnection:

$$R_{\text{max}} < \frac{L}{2 \ln Re_m} \quad (12.10)$$

At the photospheric conditions the Reynolds number is between  $10^3$  and  $10^6$ , so that the condition for the flux tube to be thin enough to participate in the reconnection process “as a whole” (i.e., over a whole flux tube radius), is  $R_{\text{max}} < L/6 - L/13$ .

The same estimate is valid for reconnection between the opposite polarity elements. In this case the straightening time is  $\simeq L/u$ , where the ascending/descending velocity of flux tube  $u \simeq v_A$  (see below). If we take the half-length of the flux tube as  $L = 500$  km, the estimate for the radius drops into the interval  $R_{\text{max}} \sim 36\text{--}70$  km.

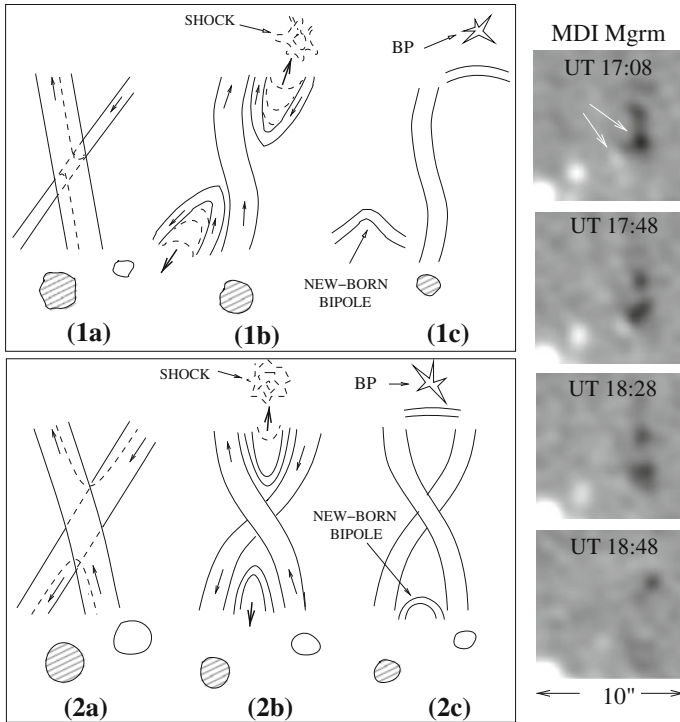
Thus, in either case magnetic flux concentrations having as small a radius as 150–200 km may be the sites of multiple reconnection processes. Moreover, the straightened segments of post-reconnection products may participate further in similar processes, creating a cascade of shocks in case of the opposite polarity pairs, and continuous fragmentation in case of the same polarity pairs.

## 12.2.2 Flux Tubes Carrying Different Amount of Magnetic Flux

The fact that under photospheric conditions magnetic flux concentrations having a radius larger than  $R_{\text{max}} \sim 36\text{--}70$  km may participate in multiple reconnection processes that result in shredding the flux tubes, is totally consistent with the observations (see e.g., Berger and Title 1996). It is important, therefore, to consider the reconnection of flux tubes carrying different amount of magnetic flux and having different radii. We consider the most typical scenarios shown in Figs. 12.6 and 12.7.

Consider first the case shown in Fig. 12.6 depicting the interaction of opposite polarity flux tubes. Top left: “thick” and “thin” flux tubes reconnect resulting total cancellation of thin flux tube. Bottom left: the initial stage of two “thick” flux tube interaction when they only *partially* cancel each other.

The timescale and energetics of the reconnection and post-reconnection processes are governed mainly by the parameters of the thinner flux tube. From the observational point of view, if a bisector of collision angle is directed along the line of sight, this process corresponds to the apparent cancellation of the smaller magnetic flux and shrinking of the thicker flux tubes. It is accompanied by possible acoustic emission

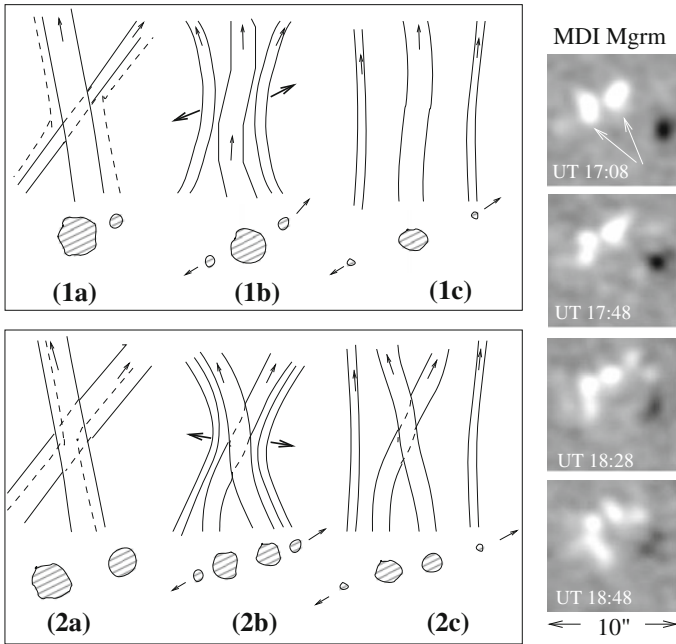


**Fig. 12.6** Reconnection of opposite polarity flux tubes carrying different amount of magnetic flux. *Top left* opposite polarity “thick” and “thin” (elementary) magnetic flux tubes showing total cancellation of thin and partial cancellation of thick flux; *Bottom left* partial cancellation in the collision of thick flux tubes; *Right panels* give an observational example; the MDI magnetograms of  $10'' \times 10''$  area at four instances of time show the interaction of “thick” negative (*black*) polarity flux and total cancellation of “thin” positive (*white*) polarity flux. After Ryutova et al. (2003)

and shock formation caused by the U-shaped part of the reconnection product. The shocks may produce a bright point in the overlying chromosphere/transition region.

The four right panels in Fig. 12.6 are the MDI magnetograms of  $10'' \times 10''$  area marked by box 2 in Fig. 12.4. Sequence of snapshots at four instances of time show the interaction of mixed polarity elements where partial cancellation of “thick” negative polarity flux and total cancellation of “thin” positive polarity flux occurs. One can follow the process of reconnection until almost total disappearance of both fluxes.

Consider now the interaction of the same polarity flux tubes having different parameters. Figure 12.7 is constructed in the same way as Fig. 12.6. The top left panel shows the interaction of “thick” and “thin” flux tubes, which results in splitting of the thicker flux tube, while the reconnection products move away from the remnants of the thicker flux tube. Thus the observer should see three dynamic objects instead of the initial two.



**Fig. 12.7** The same as in Fig. 12.6 but now reconnection occurs between the same polarity flux tubes. See text for details

The bottom left panel shows the interaction of two “thick” flux tubes. In its initial stage this event is a fragmentation process. Next, the new-born fragments, accelerated by the slingshot effect, will inevitably hit other magnetic flux tubes. In any case, the process of apparent cancellation (the opposite polarity fluxes) or fragmentation and scattering (the same polarity fluxes) will repeatedly take place down to the smallest possible scales until the magnetic flux disappears diffusively.

Observational example of the interaction of the same polarity thick flux tubes is shown in the right panels in Fig. 12.7. The  $10'' \times 10''$  area (box 3 in Fig. 12.4) initially containing two large positive flux tubes approached each other. Subsequently, flux tubes experience multiple reconnections ending up with a whole string of smaller flux tubes.

A simple general conclusion here is that the most pronounced effects in the regions of mixed polarity is partial or total cancellation of magnetic fluxes and frequent appearance of photospheric and chromospheric bright points, while in the regions dominated by a single polarity the most typical event is fragmentation of neighboring fluxes into smaller elements and an illusion of a scattering process.

### 12.2.3 Number of Events—Importance of Noncollinearity of Flux Tubes

The frequency of events shown in Figs. 12.5, 12.6 and 12.7 depends on the magnetic filling factor of a given area and the velocity of surface motions,  $u$ . Let us denote the characteristic distance between two neighboring flux tubes at the surface by  $l$ , and the characteristic flux tube radius by  $R$ . Obviously, the number of flux tubes intersecting the unit area,  $\sigma$ , is  $\sigma \sim 1/l^2$ . The filling factor is  $f \sim R^2\sigma \simeq R^2/l^2$ , and for the quiet sun  $f \ll 1$ .

Let us evaluate the number of collisions,  $n$ , per unit time, experienced by a particular flux tube, in both cases, collinear flux tubes and noncollinear flux tubes with the degree of noncollinearity  $\sim 1$ .

In the first case the collision rate  $n_{\parallel}$  can be estimated analogously to the estimate of gas-kinetic theory,

$$n_{\parallel} \simeq R\sigma u \quad (12.11)$$

Note that in case of collinear flux tubes two of them merge together if they come to a distance comparable with flux tube radius over the whole length of the flux tube. For any particular flux tube, the number of such events per unit time is estimated by (12.11). One can see that in the case of collinear fluxes  $n_{\parallel}$  scales as  $\sigma$ .

In the case of noncollinear flux tubes, the collision rate does not explicitly depend on the radius of flux tube,  $R$ , because two noncollinear flux tubes inevitably intersect even at  $R \Rightarrow 0$ . Therefore,  $n_{\Psi} \simeq (u/l) \simeq u\sqrt{\sigma}$ . The ratio of the number of events in the case of noncollinear and collinear flux tubes is thus,  $n_{\Psi}/n_{\parallel} \simeq (1/R\sqrt{\sigma}) \gg 1$ . So, in the case of noncollinear flux concentrations the frequency of collisions is much higher than in the collinear case.

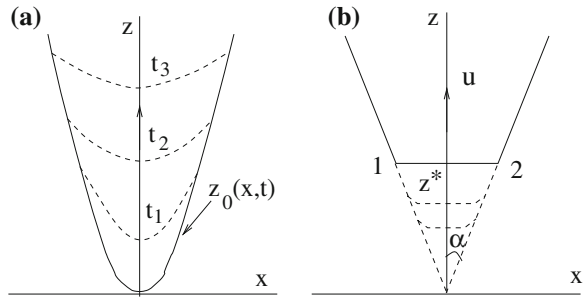
The total number of collisions occurring per unit area is given by

$$N_{\Psi} = n_{\Psi}\sigma \simeq u\sigma^{3/2} \quad (12.12)$$

Since the filling factor is  $f \simeq R^2\sigma$ , the number of events *per unit time* occurring with every particular flux concentration,  $n_t$  equals to  $n_{\Psi}$ , i.e.,  $n_t = u\sqrt{\sigma}$ . To estimate the number of particular events, we need to introduce a probability of the “proper” geometry of the collision,  $\nu$ . Then the number of particular events  $N_{\nu}$  per unit area of the solar surface is  $N_{\nu} = \nu u\sigma^{3/2}$ . In fact, no flux tube seems to be left without colliding with its neighbor.

The outcome of flux tube interaction, depending on the specifics of the process, produces its own impact on the overlying atmosphere. It is therefore not surprising that at any height (and temperatures), the solar atmosphere mimics the pattern of small-scale elements in the photosphere. Before we discuss the details of the response of the atmosphere to reconnection events among the ensembles of small-scale magnetic fields (which will be done in the following chapters), it is useful to investigate the dynamics of post-reconnection product immediately after reconnection occurs.

**Fig. 12.8** The shape of magnetic field lines,  $z(x, t)$ . **a** Solid line,  $z_0(x, t)$ —just after reconnection; the dashed lines—time sequence of the straightening and shortening of the flux tube due to the action of the magnetic field tension. **b** Simplified shape of the reconnection product



### 12.3 Dynamics of Post-reconnection Products

Here we consider the dynamics of a flux tube motion after the reconnection has occurred, starting from the configuration shown in Fig. 12.8. We assume that the flux tube radius  $R$  is small compared to the other dimensions of the problem, in particular, the characteristic length  $L$  of the flux tube involved in the post-reconnection motion. The upper points of the flux tube merging the asymptotes of magnetic field lines at  $B \rightarrow B_\infty$  are supposed to remain at rest.

In further discussions, to reduce the number of parameters entering the problem, we assume that the flux tube is empty, i.e., the pressure of the ambient plasma is counterbalanced by the magnetic pressure inside the tube,  $p_e = B^2/8\pi$ . In other words we assume that the internal plasma beta is very small,  $\beta_i = 8\pi p_i/B^2 \ll 1$ . This approach is quite reasonable for regions close to the surface (Almeida 2001).

We describe the shape of the flux tube by a curve  $z = z_0(x, t)$  (sketched in Fig. 12.8). After reconnection occurs, the magnetic tension inside the flux tube tends to straighten it and the initial configuration begins to evolve along a sequence of states  $1 \rightarrow 2 \rightarrow 3 \dots$

In the case of an empty flux tube the inertia is determined by the added-mass effect, i.e., by the inertia of the external fluid that gets involved in the motion as soon as the flux tube begins to move (Ryutov and Ryutova 1976).

At large Reynolds numbers typical even for solar photosphere, the friction force is relatively small at subsonic motions of the flux tube. Per unit length of the flux tube can be evaluated as Parker (1979)

$$F_{\text{drag}} = C_D \rho u^2 2R \tag{12.13}$$

where  $C_D$  is a dimensionless drag coefficient, which, in the parameter domain  $Re \geq 10^3$ ,  $u < c_s$ , is  $\simeq 0.1-0.2$ . When  $u$  exceeds the sound speed,  $c_s$ , a bow shock is formed in front of the flux tube, and a friction force increases abruptly. For a flow with  $u \simeq 2c_s$ ,  $C_D$  becomes of the order of unity (Landau and Lifshitz 1987). We approximate it by the step function. When evaluating the friction force for transsonic motions of the flux tube, we discuss the constraints imposed by this approximation.

### 12.3.1 Self-similarity of Solution

In this section we consider the dynamics of post-reconnection flux tube in the absence of gravity, assuming that the scale  $L$  satisfies the condition:

$$\rho g L < \frac{B^2}{8\pi} \quad (12.14)$$

This is equivalent to the condition of  $L$  being smaller than the scale height,  $L < \Lambda$ , which is usually satisfied in the upper layers of atmosphere.

The case without the effects of gravity is directly applicable to the flux tube dynamics when the reconnection occurs between the same polarity magnetic elements and reconnection products move across the gravity force (Fig. 12.7). In this case the magnetic tension is almost perpendicular to the gravitational acceleration and gravity does not play a role. Therefore, the  $xz$  plane of Fig. 12.8 should not necessarily be perceived as a vertical plane. Besides, the non-gravity situation is also valid for upper layers of the atmosphere where the atmospheric stratification strongly weakens.

We begin the analysis with an incompressible case. In other words, we assume that the velocity of a flux tube is much less than  $c_s$ , and the drag force may be neglected. The other forces acting on a certain small segment of the flux tube are the magnetic tension acting through the ends of the segment, and the gas pressure acting through the side surface. Simple calculations give the following expression for the net force acting on a curved segment of the flux tube (per unit length):

$$F_{\text{net}} = \frac{B^2}{4\pi} \frac{\pi R^2}{r} \quad (12.15)$$

where  $r$  is the curvature radius. Note that there are two degrees of freedom in the problem: the minor radius of the flux tube,  $R$ , and the major radius of curvature,  $r$ . With respect to  $R$  the flux tube is in equilibrium, while with respect to  $r$  the flux tube is straightening. Let the shape of the flux tube be described by  $z = z_0(x, t)$ .

Consider a shape of the flux tube at the time  $t + \Delta t$ . Let  $\xi$  be a normal displacement of a certain point to its new position. Obviously,  $(\partial z_0 / \partial t) = (1/n_z)(\partial \xi / \partial t)$ , where  $n_z$  is a  $z$ -projection of a unit vector normal to the tube:  $n_z = [1 + (\partial z_0 / \partial x)^2]^{-1/2}$ . Therefore,

$$\frac{\partial \xi}{\partial t} = \frac{\partial z_0}{\partial t} [1 + (\partial z_0 / \partial x)^2]^{-1/2} \quad (12.16)$$

We take the second derivative of  $\xi$  over the time and multiply it by the added mass per unit length, which in the case of a cylinder is  $\pi R^2 \rho$ . Equating this to the normal component of the force acting on a certain segment of the flux tube, we obtain:

$$\pi R^2 \rho \frac{\partial}{\partial t} \left( \frac{\partial z_0}{\partial t} [1 + (\partial z_0 / \partial x)^2]^{-1/2} \right) = F \quad (12.17)$$



According to (12.15),

$$\rho \frac{\partial}{\partial t} \left( \frac{\partial z_0}{\partial t} [1 + (\partial z_0 / \partial x)^2]^{-1/2} \right) = \frac{B^2}{4\pi} \frac{1}{r} \quad (12.18)$$

From the equations of differential geometry for the radius of curvature,  $r$  we have:

$$\frac{1}{r} = \frac{\partial^2 z_0}{\partial x^2} [1 + (\partial z_0 / \partial x)^2]^{-3/2} \quad (12.19)$$

and the equation of motion of the flux tube acquires the form:

$$\frac{\partial}{\partial t} \left( \frac{\partial z_0}{\partial t} [1 + (\partial z_0 / \partial x)^2]^{-1/2} \right) = v_A^2 \frac{\partial^2 z_0}{\partial x^2} [1 + (\partial z_0 / \partial x)^2]^{-3/2} \quad (12.20)$$

One can see that the parameter  $R$  does not enter the problem and (12.20) looks like the equation for an infinitesimally thin “string”. Note that, in the limit of small curvature, (12.20) coincides with the linear equation of motion for magnetic flux tube (Ryutov and Ryutova 1976; Spruit 1981).

We present a solution where after reconnection the flux tubes arms are asymptotically straight lines. Hence, there is no parameter of the dimension of the length in the system and the solution can depend on the variable  $z$  only in the combination  $\beta = x/v_A t$ . This solution is *self-similar*. Moreover, it corresponds to a motion with a constant velocity. We can check this property by presenting  $z_0$  in the form:  $z_0 = v_A t f(\beta)$ . For space and time derivatives we have:

$$\frac{\partial z_0}{\partial t} = -v_A \beta^2 \frac{d}{d\beta} \left( \frac{f}{\beta} \right); \quad \frac{\partial z_0}{\partial x} = \frac{df}{d\beta}, \quad (12.21)$$

and similarly for the higher order derivatives. With these equations, (12.20) acquires the form of an ordinary differential equation for  $f(\beta)$ :

$$\beta \frac{d}{d\beta} \left\{ \beta^2 \frac{d}{d\beta} \left( \frac{f}{\beta} \right) [1 + (df/d\beta)^2]^{-1/2} \right\} = \frac{d^2 f}{d\beta^2} [1 + (df/d\beta)^2]^{-3/2} \quad (12.22)$$

Thus, the self-similar solution does exist. Taking derivatives, we find:

$$f_{\beta\beta} [\beta f_{\beta} f + \beta^2 - 1] = 0 \quad (12.23)$$

The motion described by this equation is an ascent with a constant velocity. Note that a constant velocity motion corresponds to a zero inertial force, and, therefore, to a zero magnetic tension. This means that the part of the flux tube involved in the motion should be a straight line, i.e., the flux tube has the shape shown in Fig. 12.8b.

The presence of the multiplier  $f_{\text{BB}}$  in (12.23) means that the evolving flux tube consists of straight segments for which  $f_{\text{BB}} = 0$ . The initially resting material begins an ascending motion near the points 1 and 2 (Fig. 12.8b), where the magnetic curvature is large. We do not resolve this region in the asymptotic solution, but realistic velocity  $u$  of ascending flux tube can be found using energy analysis.

### 12.3.2 Energy Analysis

We start with the energy conservation law:

$$W_{\text{kin}} = -\Delta W_{\text{pot}} \quad (12.24)$$

where  $\Delta W_{\text{pot}}$  is the change in potential energy. The kinetic energy for the segment 1–2 (Fig. 12.8b) is:

$$W_{\text{kin}} = 2z^* \tan \alpha \frac{\rho u^2}{2} S \quad (12.25)$$

The change in potential energy consists of the change in the magnetic energy plus the  $pdV$  work associated with the change of flux tube volume. If gravity is neglected, the external pressure is constant and, therefore, due to pressure equilibrium, the magnetic field is also constant, leading to:

$$\Delta W_{\text{pot}} = \left( 2z^* \tan \alpha - \frac{2z^*}{\cos \alpha} \right) \frac{B^2}{4\pi} S \quad (12.26)$$

where we have used the fact that the  $pdV$  work, according to the analysis related to (12.15), is equal to the release of the magnetic energy. From (12.24) to (12.26) one finds:

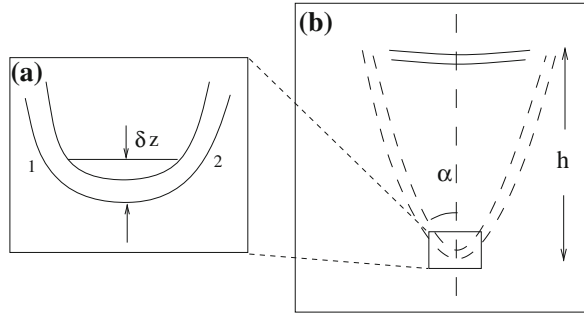
$$u = v_A \sqrt{2(1 - \sin \alpha) / \sin \alpha} \quad (12.27)$$

The model neglecting dissipation is good for subsonic velocities  $u$ . From the pressure balance,  $p_e = B^2/8\pi$ , and the expression for sound speed,  $c_s^2 = \gamma p/\rho$ , the condition for the subsonic motion of flux tubes is:

$$\sin \alpha > 4/(4 + \gamma) \quad (12.28)$$

which for  $\gamma = 5/3$  gives  $\alpha \geq 45^\circ$ . Hence, for a wide range of angles  $\leq 45^\circ$  the motion of flux tube may be trans- and supersonic which we discuss in the following section.

**Fig. 12.9** A straightening flux tube: **a** moving segment of flux tube with finite curvature; **b** sketch for the estimate of a total energy release



### 12.3.3 Transsonic Motion

At smaller intersection angles ( $\leq 45^\circ$ ), segment 1–2 (Fig. 12.8b) reaches the sound speed and the drag caused by the formation of a bow shock enters the problem. We first evaluate the drag force for the case where the velocity  $u$  exceeds the sound speed by the order of unity.

From (12.13) we find that the drag force  $F_{\text{drag}}^*$  acting on segment 1–2 is approximately (for  $\alpha \simeq 1$ )  $F_{\text{drag}}^* \simeq 2R\pi\rho c_s^2 z^*$ . On the other hand, the lifting force produced by the magnetic tension is  $F_{\text{magn}} \simeq 2\pi R^2(B^2/4\pi)$ . Taking the ratio, one finds:  $(F_{\text{magn}}/F_{\text{drag}}^*) \simeq (R/z^*)$ . For  $z^* \gg R$ , the magnetic force is much less than the drag force. This will restrict the upward velocity to values only slightly above the sound speed and the drag coefficient,  $C_D$  in (12.13) becomes much less than unity ( $\simeq R/z^*$ ). Note that a stepwise approximation of the friction force as used above does not allow one to find a complete solution in the domain of velocities of about  $(2/3)c_s \leq u \leq c_s$ , where a transition from small values of  $C_D$  to  $C_D \simeq 1$  occurs.

If friction is present, the flux tube will have a finite curvature at segment 1–2. This deviation from a straight line gives only a second-order (in  $\delta z$ ) correction to the length of a segment 1–2 and, in the evaluation of the energy release  $W_{\text{therm}}$ , we will assume that segment 1–2 is straight (Fig. 12.9). From the balance equation

$$W_{\text{therm}} = -\Delta W_{\text{pot}} - W_{\text{kin}}, \tag{12.29}$$

after substituting  $u = c_s$  into (12.25) and (12.29), we have:

$$W_{\text{therm}} = S \frac{\rho c_s^2}{2} 2z^* \frac{4 - (\gamma + 4)\sin \alpha}{\gamma \cos \alpha} \tag{12.30}$$

Here we must assume that  $\sin \alpha < 4/(4 + \gamma)$  (otherwise, the motion is subsonic). When the flux tube finally straightens out (Fig. 12.5b), the energy released per unit length of the final state is:

$$\tilde{W} = \frac{\Delta W_{\text{pot}}}{2h \tan \alpha} = S \frac{B^2}{4\pi} \frac{1 - \sin \alpha}{\sin \alpha} \quad (12.31)$$

At small  $\alpha$ 's, the energy release diverges, indicating the significance of a slingshot effect for almost anti-parallel flux tubes.

## 12.4 Dynamics of U-shaped Flux Tubes

Consider now the motion of post-reconnection flux tubes in the presence of gravity. For simplicity we adopt an isothermal model,  $\rho = \rho_0 \exp(-z/\Lambda)$ , with a constant scale height,  $\Lambda = p/\rho g$ . The subscript "0" refers to the region where intersection of flux tubes occurred.

The pressure balance condition in the initial state is

$$\frac{B^2}{8\pi} = p_0 \exp(-z/\Lambda) \quad (12.32)$$

From (12.32) and the magnetic flux conservation,  $B_0 S_0 = BS$ , we find the initial magnetic energy of a flux tube,  $W_{\text{mag}}^0$ :

$$W_{\text{mag}}^0 = \frac{2}{\cos \alpha} \int_0^h \frac{B^2}{8\pi} S dz \quad (12.33)$$

or,

$$W_{\text{mag}}^0 = \frac{1}{\cos \alpha} \frac{B_0^2 S_0}{4\pi} 2\Lambda (1 - \exp(-h/2\Lambda)) \quad (12.34)$$

The final magnetic energy is

$$W_{\text{mag}}^f = 2h \tan \alpha \frac{B^2}{8\pi} S = 2h \tan \alpha \frac{B_0^2}{8\pi} S_0 \exp(-h/2\Lambda), \quad (12.35)$$

and the change in the magnetic energy,  $\Delta W_{\text{mag}} \equiv W_{\text{mag}}^f - W_{\text{mag}}^0$ , is:

$$\Delta W_{\text{mag}} = -\frac{B_0^2 S_0 \Lambda}{2\pi \cos \alpha} \exp(-h/2\Lambda) \left[ \exp(h/2\Lambda) - 1 - \frac{h}{2\Lambda} \sin \alpha \right] < 0 \quad (12.36)$$

Now we evaluate the work of the gravity force over the ascending (straight) segment of the flux tube. At some height  $z$  above the reconnection point the length of the segment is  $2z \tan \alpha$ , and its cross section is  $S = S_0 \exp(z/2\Lambda)$ , so that the gravity force acting upward is:

$$F_{\text{gr}} = 2\rho g S_0 z \exp(z/2\Lambda) \tan \alpha \equiv 2\rho_0 g S_0 z \exp(-z/2\Lambda) \tan \alpha \quad (12.37)$$

Accordingly, the change in the gravitational energy between the final and initial states is negative,  $\Delta W_{\text{gr}} = -\int_0^h F_{\text{gr}} dz$ :

$$\Delta W_{\text{gr}} = \frac{\Lambda S_0 B_0^2}{\pi \exp(h/2\Lambda)} \tan \alpha \left[ 1 + \frac{h}{2\Lambda} - \exp(h/2\Lambda) \right] < 0 \quad (12.38)$$

We used here the pressure equilibrium condition. In addition to the variation of the magnetic energy,  $\Delta W_{\text{mg}}$ , the  $pdV$  work makes an equal contribution to the total variation of a potential energy of the system, i.e.,

$$\Delta W_{\text{pot}} = 2\Delta W_{\text{mg}} + \Delta W_{\text{gr}} \quad (12.39)$$

The kinetic energy of the flux tube in the final state can be found from the energy conservation law:

$$W_{\text{kin}} = -\Delta W_{\text{pot}} \quad (12.40)$$

Collecting (12.36)–(12.40), we find:

$$W_{\text{kin}} = \frac{S_0 B_0^2}{4\pi \cos \alpha} \exp(-h/2\Lambda) \left[ 4\Lambda(1 + \sin \alpha)(\exp(h/2\Lambda) - 1) - 4h \sin \alpha \right] \quad (12.41)$$

The kinetic energy of the fluid in the final state is (12.25), and with  $z^* = h$ ,  $\rho = \rho_0 \exp(-h/\Lambda)$  and  $S = S_0 \exp(h/2\Lambda)$  we have

$$W_{\text{kin}}^f = 2h \tan \alpha \frac{\rho_0 u^2}{2} S_0 \exp(-h/2\Lambda) \quad (12.42)$$

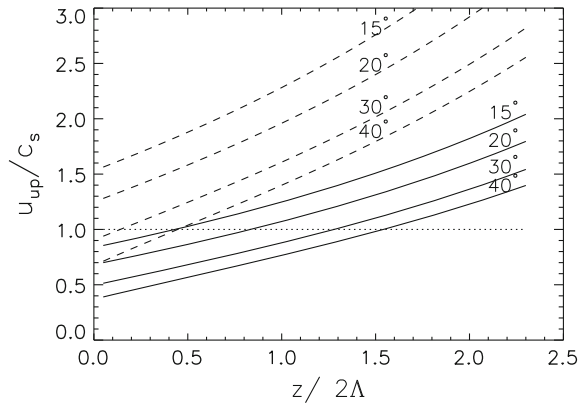
From (12.41) and (12.42) one finds the velocity of a tip at the moment when U-shaped tube gets straightened:

$$u^{(f)} = v_A \sqrt{2 \frac{(\exp(h/2\Lambda) - 1)(1 + \sin \alpha) - 2(h/2\Lambda) \sin \alpha}{(h/2\Lambda) \sin \alpha}} \quad (12.43)$$

In the limit where gravity may be neglected, i.e., at  $\Lambda \rightarrow \infty$ , this expression naturally coincides with (12.27).

When the velocity of flux tube exceeds the sound speed, a bow shock is formed in front of ascending segment of flux tube. At the same time the velocity of the flux tube still increases which leads to an increase in the friction force and thus to dissipation of energy. This keeps the final velocity of the flux tube close to  $c_s$ , and the excess of the potential energy will be spent on plasma heating. The threshold for

**Fig. 12.10** The velocity of the ascending portion of a flux tube as a function of height for several angles of collision; *solid lines* correspond to the ratio  $v_A/c_s = 0.35$ , and *dashed lines* to  $v_A/c_s = 0.64$ . The *dotted line* shows the  $M = 1$  level



sub/transonic motion, unlike the simplified estimate (12.28) for “empty” flux tube, now depends on the height where the reconnection occurs.

Using (12.43) we can roughly estimate the height where transonic motions sets in. In Fig. 12.10 the plots of the ascending velocity (actually the Mach number) versus the normalized height are shown for an “empty” flux tube, i.e., in virtue of pressure equilibrium condition.

Several qualitative conclusions can be drawn here. A smaller collision angle results in faster upward motion of flux tubes, so that its motion becomes transonic at lower altitudes. At very small angles of collision (almost anti-parallel flux tube), the reconnection process leads mainly to the conversion of magnetic energy into thermal energy in the immediate vicinity of the collision region.

With increasing angle of collision, shock formation and dissipation of the energy occurs at higher altitudes. As the initial velocity of a tip is proportional to Alfvén velocity, the stronger the magnetic field the higher the regions of the shock formation (the dashed lines in Fig. 12.10).

## 12.5 Dynamics of ∩-shaped Flux Tube

Here we consider the motion of the lower, ∩-shaped part of flux tube formed after reconnection. If the magnetic field is strong enough, the ∩-shaped part of the reconnection product starts moving in the downward direction against the gravity force. We again use the piecewise model of the flux tube (Fig. 12.11), and perform an energy analysis to find the character of the motion of flux tube and its velocity.

The gravitational energy increase caused by the deformation of flux tube shown in Fig. 12.11, similar to (12.37) and (12.38), is

$$\Delta W_{gr} = -8\Lambda S_0 \frac{B^2}{8\pi} \tan \alpha \left[ \exp\left(\frac{z_0}{2\Lambda}\right) - \frac{z_0}{2\Lambda} \exp\left(\frac{z_0}{2\Lambda}\right) - 1 \right] \quad (12.44)$$

Integration has been carried here downward from the point of reconnection. In the downward motion of a curved flux tube (forced by slingshot effect) the change in potential energy is positive as the final state has higher gravitational energy. The change in the magnetic energy, plus  $pdV$  work, is  $2\Delta W_{\text{mg}}$ :

$$2\Delta W_{\text{mg}} = -\frac{B_0^2 S_0}{\pi \cos \alpha} \left[ \exp\left(\frac{z_0}{2\Lambda}\right) - 1 - \frac{z_0}{2\Lambda} \exp\left(\frac{z_0}{2\Lambda}\right) \sin \alpha \right] \quad (12.45)$$

It is remarkable that the function

$$\Delta W_{\text{pot}} = \Delta W_{\text{gr}} + 2\Delta W_{\text{mg}} \quad (12.46)$$

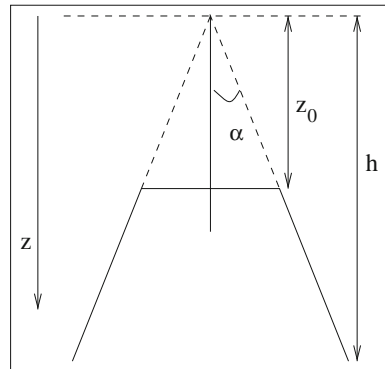
may have a minimum at some height  $z^*$  less than  $h$ . The flux tube will then evolve to reach an equilibrium state in which the buoyancy force is balanced by the magnetic tension.

Note that immediately after reconnection the top of the  $\cap$ -shaped flux tube will always move downward; because of a high curvature the magnetic tension acting on the tip is universally dominant over the buoyancy force. Besides, the gravitational energy variation scales as  $z^2$ , whereas the magnetic energy variation scales as  $z$ , which can be easily verified by expansion of (12.44) and (12.45) with respect to  $z_0/2\Lambda$ . Therefore, magnetic energy is always dominant at the beginning.

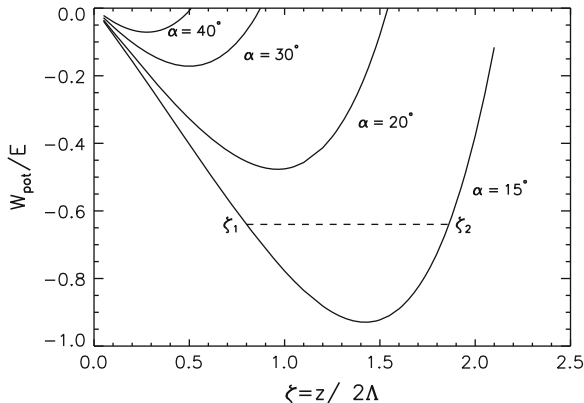
There are a variety of possibilities for how the flux tube reaches equilibrium state depending on physical parameters of a system and, in particular, on the angle  $\alpha$ .

For example, the flux tube may reach an equilibrium state with subsonic motion. Then, because of inertia, it overshoots the equilibrium state and oscillates around it, gradually dissipating the energy. The repercussions of these oscillations may be visible as periodic bright transients on the solar surface. Figure 12.12 shows plots of the potential energy versus height for different angles of collision. The energy is normalized by the factor  $8\Lambda S_0(B^2/8\pi)$  and the height by  $2\Lambda$ .

**Fig. 12.11** Sketch for the motion of the  $\cap$ -shaped part of the reconnection product



**Fig. 12.12** A plot of the potential energy normalized by the factor  $8\Lambda S_0(B^2/8\pi)$  versus height for different angles of collision. The dashed line shows the energy level where oscillation periods are estimated (see text for details)



At smaller half-angles,  $\alpha = 15^\circ, 20^\circ$ , the potential well is deep enough for the flux tube to oscillate about some equilibrium height, gradually dissipating its energy. The period of the oscillations can be found through the velocity of downward motion,  $u(z)$ :

$$T = \oint \frac{dz}{u(z)} \tag{12.47}$$

The velocity of downward motion, on the other hand, can be derived from the energy conservation law  $W_{\text{kin}}^{\text{seg}} = -\Delta W_{\text{pot}}$ , where now the kinetic energy of a segment is

$$W_{\text{kin}}^{\text{seg}} = 2z \tan \alpha \frac{\rho_0 u^2}{2} S_0 \exp\left(\frac{z}{2\Lambda}\right) \tag{12.48}$$

and,

$$\Delta W_{\text{pot}} = \frac{B^2}{\pi} \frac{\Lambda S_0}{\cos \alpha} \left[ (1 + \sin \alpha) \left( 1 - \exp\left(\frac{z}{2\Lambda}\right) \right) - \frac{z}{\Lambda} \sin \alpha \exp\left(\frac{z}{2\Lambda}\right) \right] \tag{12.49}$$

Finally, for the velocity of the downward motion we obtain:

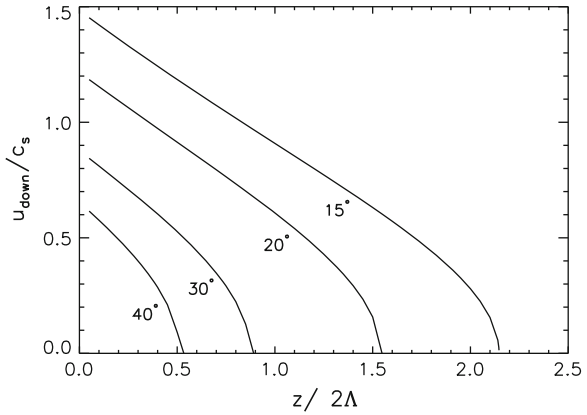
$$u = v_A \sqrt{2 \frac{(1 + \sin \alpha)(1 - e^{-\zeta}) - 2\zeta \sin \alpha}{\zeta \sin \alpha}} \tag{12.50}$$

In the limit of  $\zeta = (z/2\Lambda) \rightarrow 0$ , i.e.,  $\Lambda \rightarrow \infty$ , this expression, just like (12.43) for the upward motion, coincides with expression (12.27) for unstratified media.

From the observational point of view this analysis is useful because it allows direct measurements of some parameters and, in particular, the velocities. Figure 12.13 shows plots of the velocity of downward motion of the flux tube normalized by the atmospheric sound speed. One must bear in mind that these velocities are subsonic.



**Fig. 12.13** The velocity of downward motion of the apex of a  $\cap$ -shaped part of a flux tube as a function of depth (measured from the reconnection point)



If immediately after reconnection the downward motion is supersonic (see velocity plots for  $\alpha = 15^\circ, 20^\circ$ , in Fig. 12.13), the energy of the flux tube is converted quickly into thermal energy. At some height, when its motion slows down to subsonic velocity, the flux tube approaches equilibrium in the oscillatory regime. Thus, at sufficiently small angles of collision, a slingshot effect produced by the  $\cap$ -shaped part of flux tubes results in a multistep process of energy release. Initially, the straightening flux tube pushes surrounding plasma to move with the transsonic velocity leading to local heating. Then the flux tube oscillates gradually releasing its energy.

At larger collision angles and/or weaker magnetic field, the oscillatory regime is reached without preliminary heating of the surrounding plasma.

Finally, with increasing angle of collision (e.g., at half-angle  $\alpha = 40^\circ$ ) the potential well becomes so shallow that buoyancy quickly overcomes the magnetic force and the flux tube stops its downward motion and reaches equilibrium. Note that in all the cases described above, the equilibrium is a priori marginal: any fluctuations in the medium will trigger the *upward* motion of flux under the action the buoyancy, and possible appearance of a next generation bipole.

Consider a quantitative example of flux tubes colliding, say at half-angle  $\alpha = 15^\circ$ . Immediately after collision, a flux tube moves with transsonic velocity. This motion is accompanied by an energy release estimated from the difference between the potential energy (12.49) and the kinetic energy of the flux tube at height  $z^*$  where the velocity of the flux tube becomes equal to sound speed:

$$W_{\text{therm}} = -\Delta W_{\text{pot}}(z^*) - 2z^* \tan \alpha \frac{\rho c_s^2}{2} S_0 \exp\left(\frac{z^*}{2\Lambda}\right) \quad (12.51)$$

For  $\alpha = 15^\circ$ ,  $z^* \simeq 1.6 \Lambda$ . This corresponds to an energy level  $W_{\text{pot}}/E = -0.64$  (Fig. 12.12, dashed line). At this level the flux tube will oscillate in the interval  $z_1 - z_2 = 1.6 \Lambda - 3.72 \Lambda$ .

The oscillation period is easily estimated. Using (12.47) and (12.50), we have:

$$T = \frac{2\Lambda}{v_A} \int_{\zeta_1}^{\zeta_2} \frac{\zeta \sin \alpha \, d\zeta}{(1 + \sin \alpha)(1 - e^{-\zeta}) - 2\zeta \sin \alpha} \equiv \frac{4\Lambda}{v_A} I \quad (12.52)$$

where  $I$  is the integral:

$$I = \frac{1}{2} \int_{\zeta_1}^{\zeta_2} \frac{\zeta \sin \alpha \, d\zeta}{(1 + \sin \alpha)(1 - e^{-\zeta}) - 2\zeta \sin \alpha} \quad (12.53)$$

For this example with end points  $\zeta_1 = 0.8$  and  $\zeta_2 = 1.86$ , numerical integration gives  $I = 0.98$ . Assuming a collision close to the surface, we take  $\rho = 2.7 \times 10^{-7} \text{ g cm}^{-3}$  and scale height  $\Lambda = 150 \text{ km}$  (Maltby 1986). The Alfvén velocities for magnetic field values  $B = 300, 500, \text{ and } 1,000 \text{ G}$ , are  $v_A = 1.6, 2.7, \text{ and } 5.4 \text{ km s}^{-1}$ , respectively. Periods of oscillation are, respectively,  $T \simeq 5.2; 3.1; 1.6 \text{ min}$ .

Note again that if the velocity of flux tube reaches the acoustic velocity, the dissipation rate becomes large, and the flux tube will approach the equilibrium state in an essentially aperiodic fashion. Acoustic waves will be generated running in front of the flux tube, but they will not be enhanced to strong shocks because the density grows in the direction of their propagation. Eventually, all the potential energy is converted into thermal energy of plasma. The loss of energy in the case of transsonic motion will make the oscillatory regime possible again.

With high resolution and high cadence data all the processes described in Sects. 12.3–12.5 are, in principle, directly observable. Simple analytical relations can be used for developing the diagnostic tools .

## References

- W.I. Axford, Geophysical Monograph Series, in *Magnetic Reconnection Space and Laboratory Plasmas*, ed. by E.W. Hones Jr (AGU, Washington, 1984), pp. 1–8
- D. Biskamp, *Phys. Fluids* **29**, 1520 (1986)
- A.O. Benz, S. Krucker, *Astron. Astroph.* **341**, 286 (1999)
- T. Berger, A. Title, *Astrophys. J.* **463**, 365 (1996)
- P. Brekke, D.M. Hassler, K. Wilhelm, *Sol. Phys.* **175**, 349 (1997)
- V. Bumba, *Publ. Crim. Ap. Obs.* **19**, 105 (1958)
- J.W. Dungey, *Philos. Mag.* **44**, 725 (1953)
- H.P. Furth, J. Killeen, M.N. Rosenbluth, *Phys. Fluids* **6**, 459 (1963)
- R. Giovanelli, *Nature (London)* **158**, 81 (1946)
- R. Giovanelli, *Mon. Not. R. Astron. Soc. (MNRAS)* **108**, 163 (1948)
- R.A. Harrison et al., *Sol. Phys.* **170**, 123 (1997)
- R. Kulsrud, *Phys. Plasmas* **18**, 111201 (2011)
- L.D. Landau, E.M. Lifshitz, *Fluid Mechanics* (Pergamon Press, Oxford, 1987)
- P. Maltby et al., *Astrophys. J.* **306**, 284 (1986)
- G.E. Moreton, A.B. Severny, *Sol. Phys.* **3**, 282 (1968)
- E.N. Parker, *J. Geophys. Res.* **62**, 509 (1957)

- E.N. Parker, *Cosmical Magnetic Fields* (Clarendon Press, Oxford, 1979)
- E.N. Parker, *Astrophys. J.* **376**, 355 (1991)
- E. Petschek, in *The Physics of Solar Flares*, ed. by W.N. Hess. Proceedings of the AAS-NASA Symposium on AAS-NASA Symposium on the Physics ( NASA, 1964), pp. 425–439
- E. Priest, T. Forbes, *Magnetic Reconnection-MHD Theory and Applications* (Cambridge University Press, Cambridge, 2000)
- P. Rosenau, Three dimensional flow with neutral points. *Phys. Fluids* **22**, 5 (1979)
- D.D. Ryutov, M.P. Ryutova, *Sov. Phys. JETP* **43**, 491 (1976)
- M.P. Ryutova, T.D. Tarbell, *Astrophys. J.* **541**, L29 (2000)
- M. Ryutova, S. Habbal, R. Woo, T. Tarbell, *Sol. Phys.* **200**, 213 (2001)
- M. Ryutova, T. Tarbell, R. Shine, *Sol. Phys.* **213**, 231 (2003)
- J. Sánchez Almeida, *Astrophys. J.* **556**, 928 (2001)
- B.V. Somov, *Physical Processes in Solar Flares* (Kluwer Academic Publishers, Boston, 1992)
- H.C. Spruit, *Astron. Astrophys.* **98**, 155 (1981)
- P.A. Sweet, in *IAU Symposium on Electromagnetic Phenomena in Cosmic Plasmas*, vol. 1956 (Stockholm, 1958), p. 123
- S.I. Syrovatskii, *Annu. Rev. Astron. Astrophys.* **19**, 163 (1981)
- T. Tarbell, M. Ryutova, J. Covington, A. Fludra, *ApJ* **514**, L47 (1999)
- T. Tarbell, M. Ryutova, R. Shine, *Sol. Phys.* **193**, 195 (2000)
- M. Yamada, R. Kulsrud, H. Ji, *Rev. Mod. Phys.* **82**, 603–664 (2010)

## Chapter 13

# Post-reconnection Processes—Shocks, Jets, and Microflares

**Abstract** In the previous chapter, we began to study the reconnection of magnetic flux tubes under the photospheric conditions where magnetic energy is less than the gas-kinetic energy of surrounding plasma ( $\beta \geq 1$ ). We saw that unlike a low  $\beta$  reconnection that liberates large amount of magnetic energy leading to a in situ heating, high  $\beta$  reconnection does not give an immediate gain in energy, but it sets the system in a highly dynamic state triggering strongly nonlinear processes. These processes, determined by the evolution of post-reconnection products, occur higher in the atmosphere at a considerable distance from the reconnection area. In this chapter, we shall study how the post-reconnection products evolve and what determines the form and energetics of their impact on the overlying atmosphere. We will see that there are three major forms of the post-reconnection outcome:

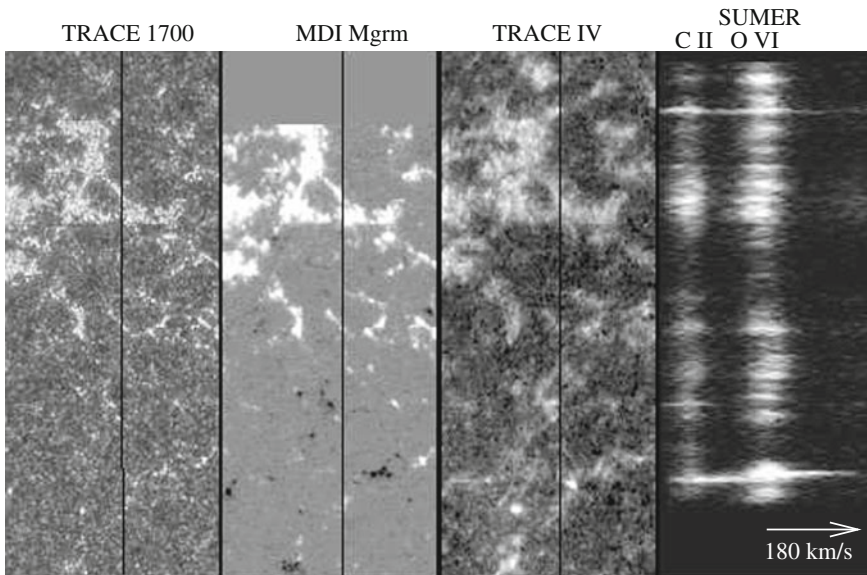
- (1) generation of supersonic plasma jets,
- (2) formation of microflares, and
- (3) various combinations of jets and microflares. These were found to be in a perfect agreement with observations. Moreover, multiwavelength observations show details and interrelation of a ubiquitous sequence of events that start from cancellation of photospheric magnetic fields, pass through shock formation, and result in appearance of supersonic jets, microflares, and their combinations in the overlying atmosphere.

### 13.1 Key Regularities Observed in the Photosphere/Transition Region

The uninterrupted time series shows distinctive properties in the response of the chromosphere and transition region to dynamic changes in the photospheric network. It was found that appearance of sporadic bright transients and mass flows in the upper atmosphere strongly correlates with the cancellation (total or partial) of opposite polarity network magnetic fields in the photosphere. The observed plasma flows are found to have a steady, nonsteady, or explosive character, with amplitudes varying from a few  $\text{km s}^{-1}$  up to hundreds of  $\text{km s}^{-1}$ . Hot localized regions (emitting soft X-rays) often correlate with lower velocity regions of  $40 \text{ km s}^{-1}$  rather than with

the high-velocity explosive events (Dere 1994; Harrison et al. 1997; Brekke 1999; Tarbell et al. 1999, 2000; Ryutova and Tarbell 2000; Ryutova et al. 2001, 2003). New generation of space-based instruments allow to study the jets and explosive events in higher cadence time series that add more details to their behavior (Mendoza-Torres et al. 2005; Fludra and Warren 2010; Curdt and Tian 2011; Innes and Teriaca 2013).

Example of the key elements in the observed regularities in the quiet sun atmosphere is shown in Fig. 13.1, which contains snapshots from an uninterrupted time series taken by several instruments on SOHO and TRACE on May 16, 1999. High-resolution magnetograms taken by MDI compiled in the 2.2-h movie show changes in small-scale magnetic flux concentrations. TRACE images in the C IV lines and UV continuum are taken simultaneously with 15 s cadence and co-aligned with the MDI magnetograms and SUMER data. The field of view is  $128 \times 320$  arcsec near disk center. The time series of C IV images shows the appearance and evolution of bright transient phenomena. The SUMER spectra allow one to study mass flows along the slit position. The far right panel in Fig. 13.1 shows C II and OVI lines which correspond to chromospheric ( $\sim 2.5 \times 10^4$  K) and transition region ( $\sim 3 \times 10^5$  K) temperatures. The imprint of the magnetic field pattern in the photosphere is clearly seen in the 1,700 Å continuum and C IV images showing the unambiguous connection between the photospheric magnetic fields and significant emission in the chromosphere and transition region.



**Fig. 13.1** Snapshots of the  $90 \times 230$  Mm region: *first* and *third* panels are the TRACE images in UV continuum ( $\sim 5 \times 10^3$  K) and C IV line ( $\sim 10^5$  K); the *second* panel is the MDI magnetogram; the *fourth* panel shows SUMER spectra in *two* lines: C II 1037.0 Å corresponding to  $\sim 2.5 \times 10^4$  K (*left*) and OVI 1037.6 Å corresponding to  $\sim 3 \times 10^5$  K (*right*). The SUMER slit position is indicated on three images by *vertical* line

The most persistent regularities in the photosphere/transition region coupling can be described as follows:

1. At any moment of time the enhanced emission in the continuum (1,700 Å) and C IV line mimics the magnetic pattern.
2. The appearance of bright transients usually correlates with reduction of magnetic flux in the photosphere, observed in canceling mixed polarity elements.
3. Microflares and other bright transients are often accompanied by two-directional plasma jets. A supersonic jet associated with bright transients and observed over the canceling magnetic features, may appear several thousands of kilometers away from the center of a C IV transient.
4. If the radiative transient is accompanied by plasma flows the energy is distributed between the two: usually the stronger localized emissions correspond to lower velocity jets, and vice versa.
5. Plasma flows are always seen whenever the slit crosses the site of magnetic flux tubes or a region of converging supergranules, a vertex.
6. If the magnetic flux concentrations in the vicinity of a “vertex” are weak or even below the MDI resolution, multiple flows are seen in cooler (C II) lines without much activity in the transition region.
7. Multiple flows and explosive events occurring repeatedly are seen in the O VI line above the converging supergranules if they harbor significant number of magnetic flux concentrations.
8. Explosive events may appear in both SUMER lines or in only one. Events seen in both lines, i.e., both in chromosphere and transition region, are also accompanied by C IV microflares, as would be expected from the temperatures of formation. In the events seen only in one of SUMER lines, C IV microflares are usually very weak or even absent.

There are a lot of works devoted to explanation and modeling of the transition region jets and microflares. As a rule, the explanations are based on the low  $\beta$  magnetic reconnection, as indeed, in upper chromosphere and transition region  $\beta \ll 1$ . But unresolvable problem here is that the reconnection theories do not have the specific conditions that would correspond to one or the other form of released energy. In other words, even the most sophisticated reconnection theories cannot explain why the observed energetic events take the form of either only a supersonic jet, or that of pure microflare (heating), or their various combinations.

Contrary to this, the photospheric reconnection serving as a triggering mechanism, and being only an initial phase of a long chain of upcoming events, may explain not only the fact that the pattern of energetic events in the upper atmosphere mimics exactly the magnetic pattern in the photosphere, but allows to follow the process of energy transfer and its release that may develop in very different ways depending on the behavior of post-reconnection products.

Thus, at the photosphere, flux tubes collide and reconnect at any given moment of time and at any place. Post-reconnection products begin their “own life” and the system soon “forgets” about the reconnection. The farther evolution of a system is the

subject of simple lows determined by the specific conditions that allow to distinguish the final form of the energy release. These conditions not only predict formation of jets, microflares, and their diverse combinations, but allow the quantitative analysis as well. This will be discussed below.

## 13.2 Post-reconnection Shocks and Hydromagnetic Cumulation of Energy

The nature of photospheric reconnection and, most importantly, the nature of post-reconnection processes, are determined by specific conditions in the photosphere. As discussed in previous chapter, the most important of which are:

- (1) The property of network magnetic fields to be concentrated in isolated flux tubes and being in pressure equilibrium with almost nonmagnetic high plasma beta environment ( $\beta = 8\pi p_{\text{ext}}/B_{\text{ext}}^2 \gg 1$ ).
- (2) The property of flux tubes to be essentially noncollinear.
- (3) Sharp stratification of the low atmosphere.

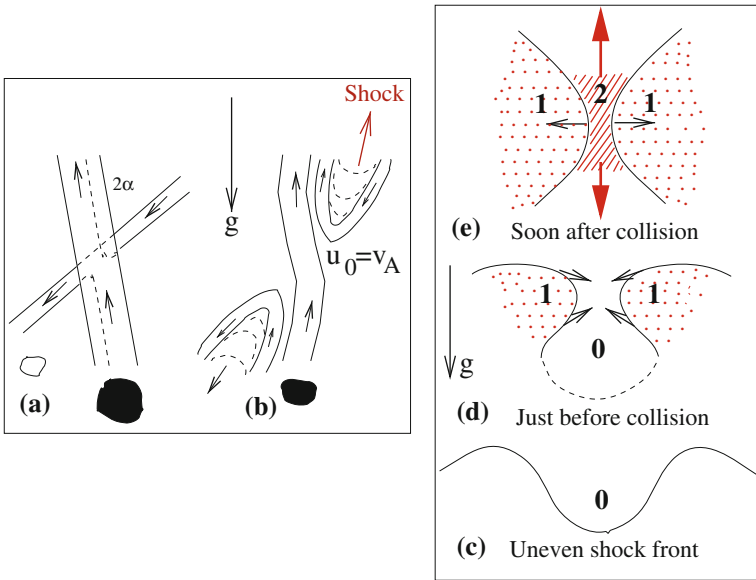
The first condition implies that after reconnection strongly curved magnetic field lines, due to pressure equilibrium,  $p_{\text{ext}} = p_{\text{in}} + B_{\text{tube}}^2/8\pi$ , still remain confined in thin flux tubes. The magnetic tension results in fast straightening and shortening of the reconnection products creating a slingshot effect (Fig. 13.2a, b).

The initial velocity of tips,  $u_0$  is proportional to Alfvén speed,  $u_0 \simeq v_A$ , but is less than the sound speed  $u_0 < c_s$ . The tip of the U-shaped part of flux tube that is moving upward accelerates quickly under the magnetic tension and the buoyancy force that are acting in the same direction. Depending on the angle of collision  $\alpha$  between the flux tubes, the velocity of a tip itself reaches the velocity of ambient sound speed in 1 or 2 scale heights (see Fig. 12.10, Chap. 12).

At transonic velocities, the slingshot effect generates acoustic shocks. Most importantly, the shock front itself, because of the inhomogeneity of the medium, has an uneven curved surface. So that some elements of the shock front may move faster than others. Propagating upward in a stratified atmosphere, the front of a shock will become more uneven: faster elements of the shock front lead, and slower elements lag (Fig. 13.2c, d).

The stability analysis shows that the perturbation of the shock front displacement,  $\xi$ , evolves in time as  $\partial\xi/\partial t = \xi(\partial u/\partial z)|_{z=H}$ , where  $u(z)$  is the velocity and  $H$  is a position of the unperturbed shock front (Gurevich and Rumyantsev 1969; Luo and Chevalier 1994). Note that perturbations grow with the increment proportional to  $\partial u/\partial z > 0$ .

In those regions where a shock front has a concave form, self-focusing and the collision of the advanced shock fronts occur (Fig. 13.2d, e). This leads to hydrodynamic cumulation, i.e., the concentration of the kinetic energy in a small volume (Stanyukovich 1960; Landau and Lifshitz 1987; Zababakhin and Zababakhin 1988).



**Fig. 13.2** Reconnection of photospheric flux tubes and post-reconnection outcome. *Left* **a** non-collinear flux tubes approaching each other at a half-angle  $\alpha$ ; **b** the post-reconnection slingshot causing straightening of reconnection products and generating shock; *Right* **c** uneven shock front in gravitational field becomes more uneven: faster elements accelerate faster and slower elements lag; **d** converging shock fronts just before the self-focusing; **e** reflection of shocks immediately after collision

The form and amount of released energy depends on the angle at which shock fronts collide. We will see below that the head-on shock front convergence leads to deposit of entire energy of a system in the kinetic energy of plasma. Whereas, the shock convergence at some angle leads to deposit of the energy either into supersonic jets or to the distribution of energy between the plasma jets and microflares.

### 13.2.1 Head-On Convergence of Shock Fronts

Thus shocks generated by post-reconnection slingshot effect and propagating in strongly inhomogeneous atmosphere must have an uneven form and may experience self-focusing in upper layers of atmosphere (Fig. 13.2). Besides, the shocks resulted from neighboring reconnections are also the subject of collision as well. These effects are as ubiquitous as the reconnection of flux tubes in the photosphere. Obviously, a great variety of shock–shock collision, implies that shock fronts may approach each other at an arbitrary angle, including head-on collision when shock fronts are almost parallel to each other.

Figure 13.3 shows shock front configurations corresponding to head-on collision. In a small vicinity of the collision region, shock fronts may be considered as planar.



**Fig. 13.3** Wave front configuration in case of head-on collision: **a** shock fronts approaching each other with the velocity  $u$  with respect to laboratory system,  $u \simeq v_A(\rho_0/\rho)$ ; **b** reflection of shock fronts after a head-on collision ( $\theta = 0$ )

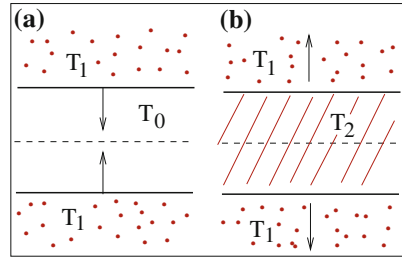


Figure 13.3a shows two parallel segments of shock front approaching each other in the unperturbed region with temperature  $T_0$  (zone 0). Behind the shocks (zone 1) the temperature increases to the value  $T_1$  (e.g., Landau and Lifshitz (1987)):

$$T_1 = \frac{2\gamma(\gamma - 1)}{\gamma + 1} M^2 T_0 \tag{13.1}$$

After collision, behind reflected shocks (Fig. 13.3b) the temperature increases farther and becomes:

$$T_2 = \frac{3\gamma - 1}{\gamma} T_1 \tag{13.2}$$

If shocks are of about equal Mach numbers, the matter in zone 2 with temperature  $T_2$  (behind reflected shocks) immediately after collision is at rest. Therefore, all the initial kinetic energy is converted entirely into the thermal energy of plasma. It must be emphasized that this is *additional*, 2.4 times more heating of a region which was already heated behind the shocks prior their collision.

Some quantitative estimates are shown in Table 13.1. We consider two examples, one when the reconnection of flux tubes occurs at the photospheric level, and the other, when flux tubes reconnect slightly above the surface, near the temperature minimum region. At the surface  $\rho_0 \simeq 2.8 \times 10^{-7} \text{ g cm}^{-3}$ , and for magnetic field strength of  $B = 1,000 \text{ G}$ ,  $v_A = 5.35 \text{ km s}^{-1}$ . Thus, the initial velocity of plasma pushed by slingshot is  $u_0 \simeq 5.35 \text{ km s}^{-1}$ . The wave propagating against gravity accelerates according to a power law as (e.g., Whitham (1958)):

$$u(z) = u_0 \left( \frac{\rho_0}{\rho(z)} \right)^\sigma \tag{13.3}$$

**Table 13.1** Examples of the heating of the chromosphere at height  $h = 1,100 \text{ km}$  by the head-on collision of shocks resulted from reconnection of flux tubes at two different heights: (1) at the surface,  $h_0 = 0$ , and at the temperature minimum,  $h_0 = 200$

$h_0$ (km)	$T_0$ (K)	$\rho_0$ ( $\text{g cm}^{-3}$ )	B (G)	$u_0 = v_A$ ( $\text{km s}^{-1}$ )	$u$ ( $\text{km s}^{-1}$ )	$M$	$T_1$ (K)	$T_2$ (K)
0	6,520	$2.8 \times 10^{-7}$	1,000	5.35	41.4	5	$5.1 \times 10^4$	$1.2 \times 10^5$
200	4,990	$8.2 \times 10^{-8}$	500	4.9	28.4	3.5	$2.4 \times 10^4$	$6.0 \times 10^4$

$M = u/c_s$  being Mach number

where  $u_0$  and  $\rho_0$  are the velocity and density of a preshock plasma at the reference point, and

$$\sigma = \left[ 2 + \sqrt{\frac{2\gamma}{\gamma - 1}} \right]^{-1} \tag{13.4}$$

With  $\gamma = 5/3$ ,  $u = u_0(\rho_0/\rho)^{0.236}$ .

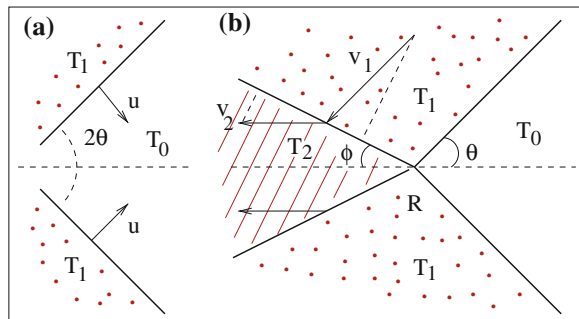
At the height  $h = 1,100$  km,  $\rho = 4.8 \times 10^{-11}$  g cm $^{-3}$ , and the shock is accelerated up to the velocity  $u = 41.4$  km s $^{-1}$ . At this height  $T_0 = 6,100$  K,  $c_s = 8.2$  km s $^{-1}$ , and Mach number  $M = 5$ . Therefore, the temperature *behind* the shock *prior* the collision becomes  $T_1 = 5.1 \times 10^4$  K. Additional heating *after* the collision gives  $T_2 \simeq 2.4 T_1 = 1.2 \times 10^5$  K.

In the region of temperature minimum at about  $h = 200$  km, where  $\rho_0 = 8.20 \times 10^{-8}$  g cm $^{-3}$ , and the temperature is lower than at the surface,  $T = 4,990$  K. The magnetic field in flux tube drops and we may take for  $B = 500$  G. The initial velocity is then  $u_0 \simeq v_A = 4.9$  km s $^{-1}$ . Note, that the parameter  $\beta^* = 2.66$ . At the same height as above ( $h = 1,100$  km),  $M \simeq 3.6$ , and the temperature *behind* the shock will be  $T_1 = 2.4 \times 10^4$  K, and the *after*-collision additional heating gives  $T_2 \simeq 6.0 \times 10^4$  K. For atmospheric parameters a reference model by Maltby et al. (1986) is used.

### 13.2.2 Energy Distribution Between Heat, Jet, and Their Combinations

If the shock fronts intersect at some angle  $\theta \neq 0$  (Fig. 13.4a), the temperature increase occurs in a larger volume and will be less than in the case of head-on collision. At the same time, a finite angle between the reflected shock fronts,  $2\phi$ , gives the plasma space to escape (Fig. 13.4b). Therefore, only a part of the kinetic energy of a system is converted into heat. The other part is converted into directed flows of plasma or cumulative jets.

**Fig. 13.4** Wave front configuration for converging shocks: **a** Shock fronts moving with the velocity  $u$  with respect to laboratory system at the angle  $2\theta$ ; **b** collision and reflection of shock fronts in the coordinate system moving with the velocity  $u/\sin \theta$



With increasing collision angle, the velocity of the jet increases at the expense of local heating. At some critical angle, there is no reflected wave, and most of the energy is concentrated in the hot and dense plasma jets. The main characteristics of this process may be obtained from general theory of shock reflection (Stanyukovich 1960; Landau and Lifshitz 1987).

Let us take a closer look on the process shown in Fig. 13.4b. When shock fronts collide, a preshock plasma is at rest, i.e., the velocity in zone 1 is zero, and in the laboratory system, the intersection line,  $R$ , moves to the left with the velocity  $v_R = u/\sin \theta$ . We will carry out analysis in the coordinate system moving with the  $v_R$ , where the process is stationary.

The relations across the reflected shocks, i.e., conservation of mass, normal momentum, tangential velocity, and energy, respectively, are

$$\rho_2 v_2 \sin \phi = \rho_1 v_1 \sin (\theta + \phi) \quad (13.5)$$

$$p_2 + \rho_2 v_2^2 \sin^2 \phi = p_1 + \rho_2 v_1^2 \sin^2 (\theta + \phi) \quad (13.6)$$

$$v_2 \cos \phi = v_1 \cos (\theta + \phi) \quad (13.7)$$

$$h_2 + \frac{1}{2} v_2^2 \sin^2 \phi = h_1 + \frac{1}{2} v_1^2 \sin^2 (\theta + \phi) \quad (13.8)$$

where  $h_i = \gamma/(\gamma - 1)(p_i/\rho_i)$  is the enthalpy. Excluding  $v_2$ ,  $p_2$  and  $\rho_2$ , this system reduces to a single equation of the form

$$\begin{aligned} & 2[(1 - \tau_1 \tau_2)^2 + (\tau_1 + \tau_2)^2] \\ & = \tilde{M}^2 (\tau_1 + \tau_2) [(\gamma + 1)\tau_2(1 - \tau_1 \tau_2) - (\gamma - 1)(\tau_1 + \tau_2)] \end{aligned} \quad (13.9)$$

where we used notations:  $\tilde{M} = v_1/c_s$ ,  $\tau_1 = \tan \theta$  and  $\tau_2 = \tan \phi$ . Equation (13.9) is a quadratic equation for  $\tau_1$ , and may be written as

$$A\tau_1^2 + B\tau_1 + C = 0 \quad (13.10)$$

For each value of incident angle,  $\tau_1$ , there is a maximum value of  $\tau_2$  at a given Mach number beyond which this equation has imaginary roots; i.e., there is no reflected wave in the process. This regime corresponds to *pure jet formation*.

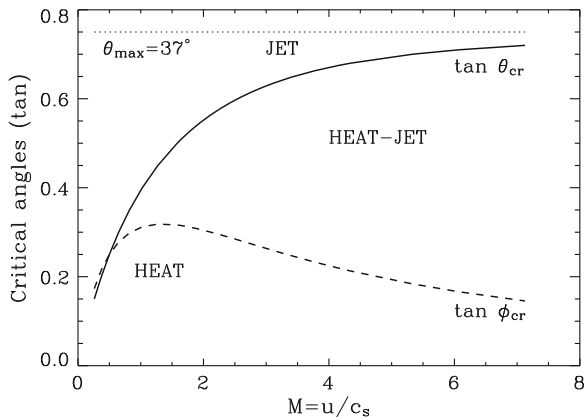
Thus, the condition of the vanishing of the discriminant,

$$\Delta = B^2 - 4AC = 0 \quad (13.11)$$

determines the regions of varying energy release: dominant heating, jet formation, and distribution of energy between the two.

Solving (13.9) with  $\Delta = 0$ , one obtains critical angles versus Mach number. Results are shown in Fig. 13.5. We took into account that  $\tilde{M} = M/\tan \theta$ . In the region below dashed curve (the plot of the critical reflection angle), the energy of a system is converted entirely into heat. The region between the two curves corresponds

**Fig. 13.5** Critical angles of shock front convergence,  $\theta_{cr}$ , and reflection,  $\phi_{cr}$ , versus the Mach number defining regions of predominant heating (HEAT), jet formation (JET), and the distribution of energy between the two (HEAT-JET). The dotted line shows a limiting angle corresponding to maximum jet velocity



to the distribution of energy between the thermal energy and cumulative jets. Above the solid curve, the parameters of colliding shock fronts correspond to jet formation. The critical incident angle,  $\theta_{cr}$ , approaches a limit and, at large Mach numbers, becomes independent of  $M$ .

The maximum value of  $\theta_{cr}$  can be found directly from (13.9) setting  $M \gg 1$ . This gives a simple equation:

$$(\gamma + 1)\tau_1\tau_2^2 - \tau_2 + (\gamma - 1)\tau_1 = 0. \tag{13.12}$$

The discriminant of this equation,  $\Delta = 1 - (\gamma^2 - 1)\tau_1^2$ , gives  $\tau_1^{\max} = 1/\sqrt{\gamma^2 - 1}$  for limiting value of incident angle, or  $\theta_{\max} = \tan^{-1}(1/\sqrt{\gamma^2 - 1})$ , which coincides with the classical result of  $\theta_{\max} = \sin^{-1}(1/\gamma)$  (Stanyukovich 1960; Landau and Lifshitz 1987). In our case, for  $\gamma = 5/3$ ,  $\theta_{\max} = 36.87^\circ$ .

The jet velocity ( $v_{jet} = v_2$ ) can be found from (13.5)–(13.8). In the laboratory system, one obtains:

$$v_{jet} = u \left( \frac{1}{\tan \theta} - \frac{2 \tan^2 \theta}{M^2} \right) \left( 1 + \frac{2 \tan^2 \theta}{M^2} \right)^{-1/2} \tag{13.13}$$

At large Mach numbers this reduces to  $v_{jet} \simeq u \cot(\theta/2)$ , which is also in agreement with classical theory (Stanyukovich 1960). Here  $\theta$  should be understood as its limiting value  $\theta_{\max} = \tan^{-1}(1/\sqrt{\gamma^2 - 1})$ , so that  $v_{jet}^{\max} = u(\gamma + \sqrt{\gamma^2 - 1})$ . For  $\gamma = 5/3$ ,  $v_{jet}^{\max} = 3u$ . Thus, even at moderate Mach numbers,  $M \simeq 2$ , at the collision angles close to  $37^\circ$ , most of the kinetic energy of a system is concentrated into the hot and dense plasma jets. The density of jet is estimated as  $\rho_{jet} \simeq \rho_1 \gamma / (\gamma - 1)$ .

Using above quantitative examples (Table 13.1), and suggesting that shock fronts collide at the angle close  $37^\circ$ , we find that the usual after-shock heating ( $T_1$ ) is accompanied by strong cumulative jets with high velocities; in the first example,  $v_{jet} \simeq 124 \text{ km s}^{-1}$  ( $T_1 = 5.1 \times 10^4 \text{ K}$ ), and in the second example,  $v_{jet} \simeq 103 \text{ km s}^{-1}$  ( $T_1 = 3.4 \times 10^4 \text{ K}$ ).

In three-dimensional geometry, there may occur the rare but violent event of cylindrical focusing. This happens when the initial shock front is close to the figure of revolution. In this case, a cylindrical cumulation similar to Guderley's effect will occur, and strong two-directional hot jets of material will be formed in the intersection point (Guderley 1942; Landau and Lifshitz 1987). This will be addressed in subsequent sections.

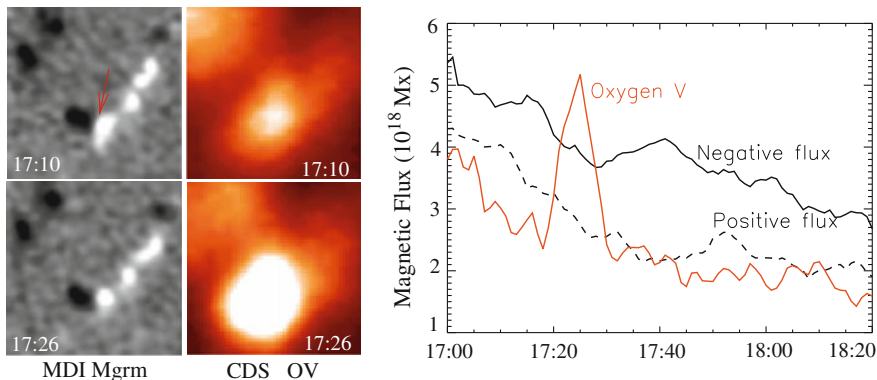
Note again that the above consideration applies to the case where the magnetic pressure is small everywhere, except *inside* the flux tubes. So that the slingshot generates almost purely acoustic waves, and the magnetic effects are not involved in further dynamics. On the other hand, even if the magnetic pressure in the ambient plasma is non-negligible, all the essential features of the phenomena will remain in place. In the same manner as above, the MHD waves will be driven by the slingshot effect, and the waves will steepen when propagating upward, leading to the formation of MHD shocks and to the cumulation in the areas of the appropriate curvature of shock fronts (Whitham 1958; Pai Shih-I 1962; Sokolov 1991).

A great variety of the quiet sun magnetic network that covers 90% of the solar surface ensures all possible combinations of the process that starts from magnetic flux reduction in the photosphere, passes through shock formation, and ends up in the various forms of energy release. Accordingly, the recycling time of the magnetic network is very short (Schrijver et al. 1997): in about 40 h magnetic field in the entire network replaces itself providing continuous energy supply to the upper atmosphere. The energy flux estimated on the basis of this time scale is enough to explain the observed UV/EUV radiation of the order of  $5-10 \times 10^5 \text{ erg cm}^{-2} \text{ s}^{-1}$ . The height of the most intensive shock formation and subsequent appearance of the impulsive phenomena corresponds to the empirical height of the sharp temperature jump. The high rate of emergence of new fluxes and diversity of their parameters result in the cascade of shock waves, thus creating a magnetic energy avalanche and "steady" energy input into higher layers of atmosphere. This is an on-going process which works all the time and is independent of the phase of magnetic activity of the sun.

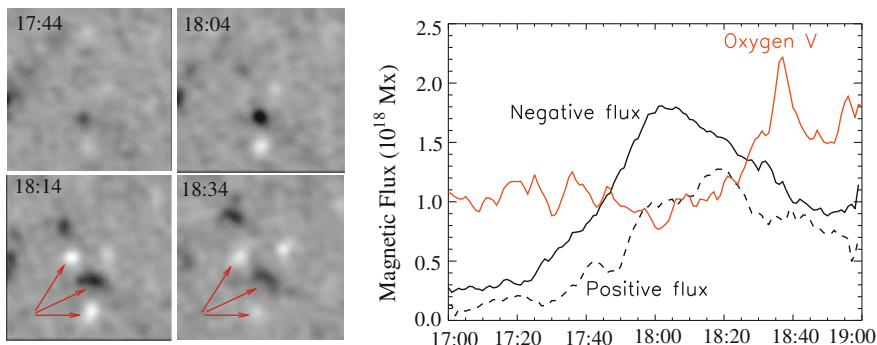
### 13.3 Observation of Photospheric Reconnections and Their Impact on Overlying Atmosphere

To demonstrate relation between the reconnecting flux tubes and subsequent energy transfer and release in overlying atmosphere we shall compare high-resolution magnetograms with the observational data taken simultaneously for the chromosphere and transition region.

We start with data taken on January 22, 1997. High-resolution MDI magnetograms of a very quiet region were co-aligned with the simultaneous CDS/SOHO images taken in the O V line (629 Å), which shows plasma at  $2.5 \times 10^5 \text{ K}$ . The data were compiled in the 2.5 h movie that shows motions and changes in the photospheric magnetic fields and the response of the transition region to these changes. At any moment of time, the enhanced intensity in the O V line mimics the magnetic pattern of the photosphere. The appearance of bright transients is correlated with the flux



**Fig. 13.6** Magnetic flux cancellation and subsequent appearances of bright transient in the transition region at  $2.5 \times 10^5$  K. *Left four panels* are magnetograms of a small,  $30 \times 30$  arcsec region of quiet sun at two instances of time together with the same area in the Oxygen V 629 Å. The *right panel* shows a quantitative picture of this process in time. Magnetic flux is in  $10^{18}$  Mx, UT time is minutes, and the O V intensity is in arbitrary units



**Fig. 13.7** Time variation of negative (*solid line*) and positive (*dashed line*) fluxes in region of newly emerging bipole, and corresponding intensity curves. The reconnection starts at about UT 18:10 and proceeds with several steps. The microflare peaks up at UT 18:40

reduction in the colliding opposite polarity magnetic elements. Two examples of such events are shown in Figs. 13.6 and 13.7.

Figure 13.6, left four panels, show magnetograms of a small region with reconnecting flux tubes (marked by red arrow) and the same area at the transition region temperature ( $2.5 \times 10^5$  K) at two instances of time.

Right panel shows time history of this process before and after the reconnection occurred. A black solid curve is the time variation of measured negative flux (black spots in left panels) and dashed curve is that of positive flux (white spot in left panels). The corresponding intensity variation is shown by the red curve. The reconnection started at UT 17:15, and in about 5 min when magnetic flux reduced by 30–40% a strong microflare appeared in the transition region.

Another example of the reconnection process and its impact to overlying transition region is shown in Fig. 13.7. Left four panels are magnetograms showing a newly emerging bipoles and their interaction. The right panel contains measured magnetic flux and the Oxygen V intensity. The reconnection process begins at about UT 18:10 and continues with several steps until UT 18:30. Soon after that the microflare appears and reaches its maximum at UT 18:40.

The events shown in Figs. 13.6 and 13.7 represent the most typical pattern for the majority of the observed mixed polarity neighbors. Several flux tubes show such pattern repeatedly during the time of observation. In particular, the above examples come from quite a short (2.2 h) data set, and the  $128'' \times 320''$  area of a quiet sun region. There were observed over 200 different events of bright radiative transients in the transition region, and appearance of each event was preceded by reduction of the photospheric magnetic field.

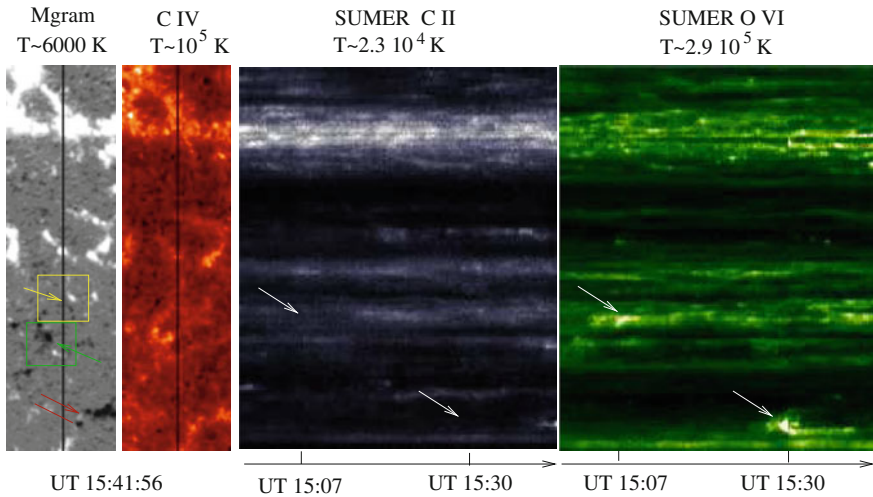
### 13.3.1 Microflares, Jets, and Their Combinations

The picture becomes more complete when complimented by the observation of mass flows. Now one can observe not only time history of microflares resulted from the photospheric reconnections, but whether these microflares are accompanied by generation of mass flows or not. To demonstrate these processes we will use the data sets shown in Fig. 13.1.

Figure 13.8 is an example from these observations. The MDI magnetogram of the target region is shown in left panel, the second panel is the TRACE image of the same region in C IV transition region line. Two right panels show time variation of C II (chromospheric) and O VI line (transition region) intensities at each position of the slit during about 45 min (out of 2.2 h) time sequence.

A well-distinguished normal set of supergranules in the magnetogram is outlined by small-scale network magnetic elements. The hot plasma in the transition region (C IV line) mimics exactly the photospheric magnetic pattern. The SUMER slit that captures flows, extends over about 10 supergranules crossing several vertices and a short,  $\sim 15$  arcsec, section of a plage highly populated by positive (white) magnetic concentrations. The enhanced intensities in the C II and O VI lines clearly reflect the topology of the photosphere as well. For example, the SUMER spectra above the plage region with dense conglomerate of magnetic fluxes (in the upper part of images), show continuing enhanced emission, while above the cell interiors with little magnetic field there are only rare sporadic events.

The enhanced emission in the cooler C II line traces the magnetic field sites more closely than the O VI line and has a more diffuse character. While the enhanced emission in the O VI line is more discrete. This difference is quite remarkable, and reflects the evolution of post-reconnection shocks: at low chromosphere there are much more shocks that provide a regular behind-shock heating, while higher in the atmosphere, where the cumulative effects, and cylindrical focusing turn on (not all the shocks are subject of cylindrical focusing!), and lead to more concentrated sporadic events. Note that the explosive events accompanied by strong jets such as



**Fig. 13.8** *Left Panel* The MDI magnetogram of the  $66'' \times 220''$  region shows small-scale network magnetic elements of positive (*white*) and negative (*black*) polarities that outline the regular set of supergranules; *Middle panel* The same region at transition region temperatures showing the enhanced emission in C IV line that mimics the network magnetic pattern. *Solid lines* on these images show the SUMER slit position (slit width is  $1''$ ); *Right panels* The time variation of C II chromospheric and O VI transition region line intensities at each position of the slit during a 45 min (out of 2.2 h) time sequence. Each *bright dot* on this image correspond to the enhanced plasma flows. Their occurrence also traces closely the sites of magnetic elements

those marked by white arrows on the O VI image (the velocity of these jets exceed  $100 \text{ km s}^{-1}$ ) do not usually appear in C II images. This again, means that cumulative effects associated with shock front convergence occur higher in the atmosphere.

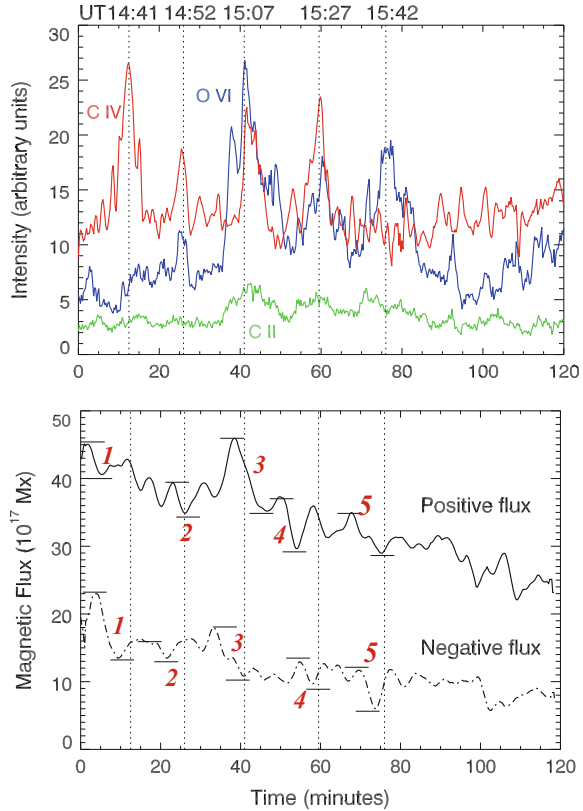
Thus, the usual behind-shock heating is continuously sustained above the magnetic flux concentrations and should appear as diffuse “clouds” with the temperatures higher than that of unshocked material. This particular stage of the energy production is what the enhanced emission in the C II line shows. Higher in the atmosphere, shocks experience either self-focusing or collision with other shocks leading to hydrodynamic cumulation, i.e., concentration of energy into a small volume. These events are strongly localized and appear as small-scale isolated features with significantly enhanced emission. Note again that the enhanced emission in a hot O VI line is much more discrete than corresponding emission in underlying chromosphere (C II line).

Each bright grain (i.e., enhanced emission) in a hot C IV and O VI lines has its own character and may represent one of three forms of energy release:

- (1) microflare alone corresponding to pure C IV emission;
- (2) a strong jet corresponding mainly to O VI emission; and
- (3) combination of two. To see these regularities in detail and distinguish three type of events from each other, we plot measured positive and negative magnetic fluxes in time and compare them with time evolution of CDS and SUMER intensities. Example of such procedure is shown in Fig. 13.9.



**Fig. 13.9** Time variation of positive and negative magnetic fluxes in the compact bipole inside the *yellow box* in Fig. 13.8, and corresponding changes in the C IV (the red line in the upper panel), C II (green line) and O VI (blue line) intensities over this area. The flux reduction marked by “1” in lower panel caused appearance of microflare alone without significant flows (a pure “HEAT” regime); the next three events correspond to the “HEAT-JET” regime when microflares are accompanied by the O VI plasma jets, and the event marked by “5” is the example of a pure “JET” regime



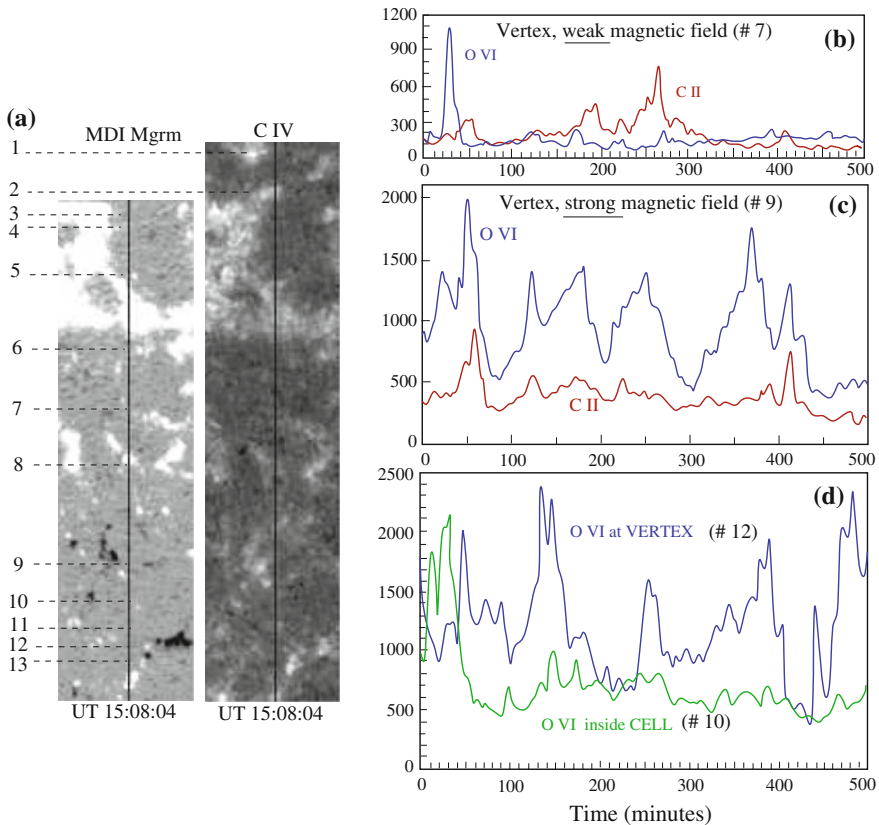
Lower panel here shows time variation of positive and negative magnetic fluxes of a bipole inside the yellow box in Fig. 13.8. The upper panel shows the response of the chromosphere and transition region to magnetic field variations. Green and red lines are C II and C IV microflare intensities and blue line shows strength of generated flows. The numbers 1–5 on the magnetic curves mark changes of magnetic fields in the most prominent events produced by on-going reconnection in this bipole during 2 h period.

The flux reduction marked by “1” resulted in appearance of microflare alone without significant flows (a pure “HEAT” regime). The next three events, 2–4, correspond to the “HEAT-JET” regime: microflares are accompanied by supersonic jets, the most spectacular of which is #3 event. In this particular case a multistep reduction of magnetic fluxes, i.e., multiple reconnection processes, lasted almost 10 min, generating enough energy to trigger appearance of a strong microflare and supersonic jet with velocity of about  $120 \text{ km s}^{-1}$  (see also below). Note that a significant energy was deposited even in low chromosphere (C II green line in upper panel). Finally, case 5 corresponds to pure “JET” regime.

### 13.3.2 Effects of Converging Supergranular Flows

The supergranular topology and convective flows in general play very important role in electromechanical coupling between the photosphere and chromosphere/transition region. Converging flows attract all possible magnetic elements, which then float along the supergranular lanes, collide, and reconnect. Vertices where three supergranules meet are the most populated areas, and thus the most active energy production sites.

Figure 13.10 shows examples of energy release in the chromosphere and transition region along the SUMER slit passing through differently magnetized and



**Fig. 13.10** Illustration of the influence of supergranular motions on the energy production. Panel **a** The magnetogram of the  $66'' \times 190''$  region together with overlying chromosphere/transition region in C IV line. Numbers 1–13 correspond to differently magnetized and topologically distinct regions; *Panels b* and *c* show O VI and C II intensities (in arbitrary units) above vertices #7 and #9: vertex #7 contains weak magnetic concentrations while #9 vertex is site of a strong magnetic field concentration; Panel **d** compares intense energetic events occurring above strongly magnetized vertex #12 with the cell interior #10 depleted of magnetic elements

topologically distinct regions. The left panel is a magnetogram, with uneven circles marking the supergranular pattern. Numbers with arrows indicate several areas along the SUMER slit to be discussed. We will also discuss event overlying a strong magnetic concentration marked as #13, which lies in the intergranular lane of the SUMER slit, but supersonic jets generated by post-reconnection shocks were so strong that they reached the slit and were well detectable.

We choose four examples, vertices marked as #7, #9, and #12, where supergranules converge, and #10 which represents the cell interior. The right panels in Fig. 13.10 are computed intensity curves in SUMER O VI and C II lines for chosen examples.

The process of energy production, transfer, and release is very sensitive to local conditions. There are also clear differences in the outcome depending on whether magnetic flux tubes near the vertex are weak (like region #7) or strong (like regions #9 and #12).

At vertices, converging flows will attract magnetic elements, including the smallest. High-resolution observations show that cancellation, merging, and splitting processes among the tiny flux tubes persist to the limit of resolution.

The process of heating and jet formation caused by reconnection of the smallest possible elements should have two general features:

- (1) The shock convergence and formation of jets may occur at lower altitude (because of small magnetic fluxes), i.e., in cooler emission lines; and
- (2) The reoccurrence of generated flows will happen frequently in the same place, because the long lifetime of supergranules make a long-lived attracting centers. On the other hand, if there is a strong magnetic flux concentration near the attracting center, the multiple flows may be observed at higher altitudes and in hotter emission lines.

Example of a vertex with very weak magnetic field is region #7 shown in Fig. 13.10b. Generated flows, as expected, are seen predominantly in the C II line. The strong explosive event seen in O VI at  $t = 30$ , may have an origin associated with the strong downflows observed a few moments earlier in C II line (not shown). This type of event is quite common: appearance of sporadic explosive events and complex dynamical structures with multiple velocities in regions of maximum downflows, is ubiquitous.

If in the region of converging supergranules strong magnetic flux concentrations are present, the series of reconnections releases energy at higher altitudes which manifests itself in hot and dense multiple flows observable in the hotter O VI line. Example of such event is shown in Fig. 13.10c. One can see the appearance of series of hot plasma flows and some explosive events during the entire time span, just as expected due to the supergranular converging flows that provide continuous supply of small-scale magnetic elements which interact with longer-lived strong magnetic field.

To illustrate one more time the effect of a vertex, we superimpose the O VI intensities for the vertex region #12 and cell interior region #10, which is quite distant from the supergranular lane (Fig. 13.10d). One can see that during more than 2h nothing spectacular happens in region #10. While the repetitive explosive events seen, e.g., at  $t = 140$ ,  $t = 390$ , and  $t = 480$  above the vertex (#12) are quite natural.

In each case one can estimate the energy content in the radiative events and compare it with magnetic energy, reduced during reconnection. One should bear in mind, however, that this energy is not a direct deposit, but triggers multistep process of shock formation and shock–shock interaction.

Now the question is do the observations show formation shocks and their possible association with the reconnection of flux tubes. The answer is yes, and we address this question in the next section.

### 13.4 Key Elements of Energy Production and Observation of Shocks

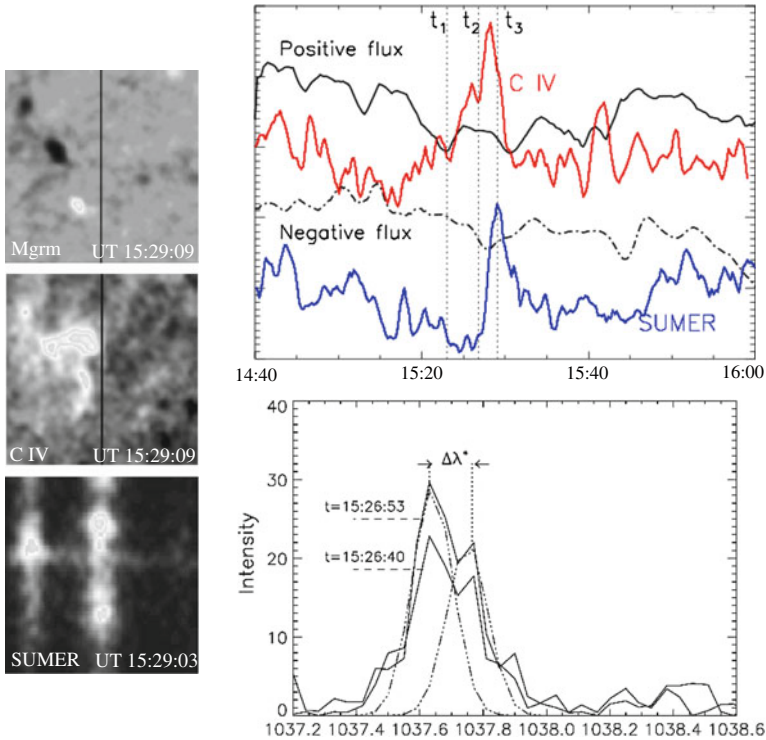
Let us first overview key elements of energy production and its release in the chromosphere/transition region. As discussed throughout this chapter, the process starts with reconnection of *opposite polarity* photospheric flux tubes, passes through shock formation, and ends up with one of the forms of energy release determined by the system parameters and evolution of shocks. The main steps of this process are shown again in Fig. 13.11. Left panels are the MDI magnetogram of  $30'' \times 30''$  region marked by green box in Fig. 13.8 together with radiative events in the chromosphere/transition region (Trace C IV and SUMER O VI lines). Time history of negative and positive magnetic fluxes and corresponding changes in C IV and O VI intensities are shown in upper right panel. The lower panel shows line profiles of SUMER spectra as function of wavelength extracted at two instances of time,  $t = 15:26:53$  and  $t = 15:26:40$  (solid lines). The approximate moment of the maximum flux reduction is marked by  $t_1 = 15:23$ . High-velocity jets appear about 6 min later ( $t_3 = 15:29:03$ ). The peak intensity in C IV slightly precedes the appearance of the jet. Before the maximum of intensities about 2 min earlier at  $t_2 = 15:26:53$  (also at  $t = 15:26:40$ ) SUMER spectra showed clear shock signatures (lower right panel): the left intensity peak is significantly stronger than the right one. The difference between the two peaks,  $\Delta\lambda^*$ , is a measure of the shock velocity. Indeed,  $\Delta\lambda^*$  is a difference between the Doppler shifted lines resulted from mass motions,  $v_2$  (left peak) and  $v_1$  (right peak). The velocity difference  $v^* = v_2 - v_1$  is

$$v^* \cos \theta = \frac{\Delta\lambda^*}{\lambda_0} c \quad (13.14)$$

where  $\theta$  is the angle between the direction of flow and line of sight,  $\lambda_0$  is the wavelength of unshifted line (e.g.,  $\lambda_0 = 1037.656 \text{ \AA}$ ). The velocity in front of the shock  $v_1$  and behind the shock velocity  $v_2$  are related by (e.g., Landau and Lifshitz (1987)):

$$v_2 - v_1 = c_s \frac{2(M^2 - 1)}{(\gamma + 1)M} = v^* \quad (13.15)$$

This expression can be used to estimate the Mach number  $M = v_{\text{sh}}/c_s$ . For strong shocks ( $M \gg 1$ ) (13.15) gives  $v_{\text{sh}} = (\gamma + 1)v^*/2$ .

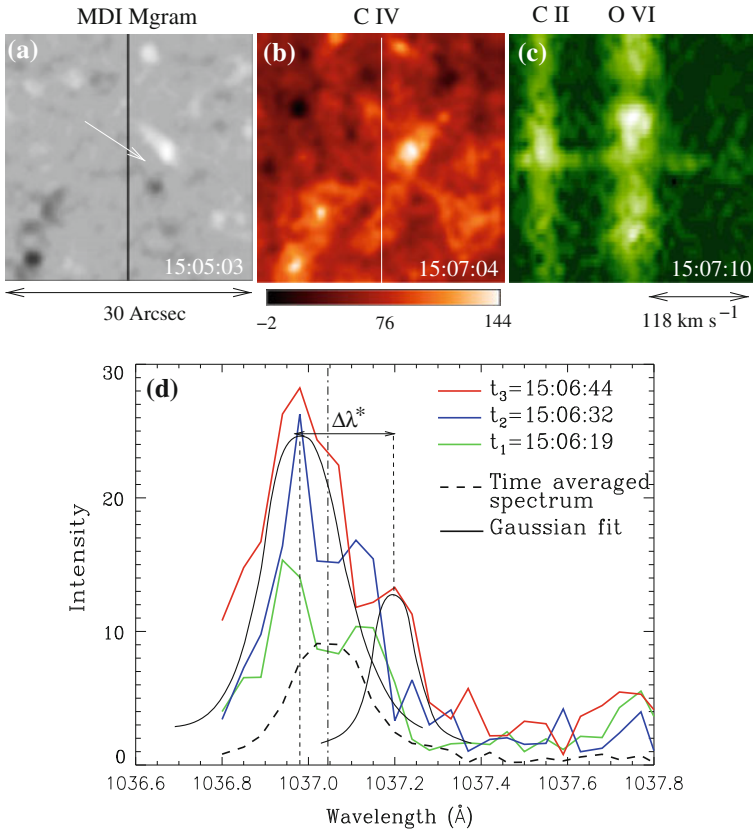


**Fig. 13.11** Key elements of energy production and its release associated with the photospheric reconnection. The *left three panels* are snapshots of the  $30'' \times 30''$  region, marked by *green box* in Fig. 13.8, at the moment of the intensity maximum in the O VI line. The *upper right panel* shows time history of positive and negative magnetic fluxes and corresponding changes in the intensities of C IV (*red*) and O VI (*blue*) lines. The *lower right panel* contains line profiles versus wavelength ( $\text{\AA}$ ) extracted from exposures at  $t = 15:26:40$  and  $t = 15:26:53$  (*solid lines*). *Dash-dotted line* is Gaussian fit

The estimate for a shock velocity in the example shown in Fig. 13.11 with  $\Delta\lambda^* = 0.135\text{\AA}$  is  $v_{\text{sh}} = 60 \text{ km s}^{-1}$  (we took  $\theta = 30^\circ$ ).

Note that usually the first generation shocks appear predominantly in the C II, and occasionally in the O VI line (including the above example). This fact is quite natural: shock formation is the earlier stage of the energy production that occurs shortly after the flux tubes reconnect. Therefore, the average enhancement in the C II and even C IV lines can be explained by the direct behind-shock heating and behind-shock flows, while strong radiative events (blinkers, microflares) and explosively growing flows are consequences of further evolution of shocks.

It is remarkable that high cadence data compiled in movies show not only shock signatures, but allow to see and measure step-by-step evolution of shocks. Figure 13.12 shows a typical example of the evolution of shock triggered by reconnection of opposite polarity flux tubes (marked by the white arrow in panel a).



**Fig. 13.12** Example of a step-by-step evolution of shock and its accompanying phenomena. *Panel a* Magnetogram of  $30'' \times 30''$  area (yellow box in Fig. 13.8) with compact bipole near the SUMER slit just before the reconnection occurred; *Panels b* and *c* appearance C IV microflare and a strong O VI jet with velocity  $v_{jet} = 118 \text{ km s}^{-1}$ . *Panel d* Line profiles of C II SUMER spectra extracted from exposures with 13 s time step; from  $t_1 = 15:06:19$  (green line) a double-humped profile typical of shocks rapidly evolves into a strong shock (blue line,  $t_2 = 15:06:32$ ), and at  $t_3 = 15:06:44$  (red lines) reaches its maximum resulting strong radiative transient in less than 20 s

As mentioned above, the C II ( $T \simeq 10^4 \text{ K}$ ) shocks appear soon after the reconnection but before the enhanced emission in hotter C IV and O VI lines appear (panels b and c respectively).

Line profiles of C II SUMER spectra at 13 s time steps are shown in Fig. 13.12d. From  $t_1 = 15:06:19$  (green line) a double-humped profile typical of shocks rapidly evolves into a strong shock (blue and red lines). At  $t_3 = 15:06:44$ , when peaks reach maximum, the difference between the two peaks is  $\Delta\lambda^* = 0.18 \text{ \AA}$ . This gives for the shock velocity  $v_{sh} = 0.5(\gamma + 1)(v_2 - v_1) = 69 \text{ km s}^{-1}$ . At C II temperature ( $2.3 \times 10^4 \text{ K}$ , sound speed  $c_s = 24 \text{ km s}^{-1}$ ) this corresponds to Mach number  $M = v_{sh}/c_s \simeq 3$ . At transition region heights such a shock may generate jets

in the HEAT-JET regime, with velocities ranging from 105 to 170 km s<sup>-1</sup>. Indeed, fast evolution of the shock (shown in panel d in three instances of time) is followed by the appearance of a bright transient in C IV line and a hot O VI plasma jet. The measured velocity of the jet at  $t = 15:07:10$  is 118 km s<sup>-1</sup>. This is a typical explosive event—one of the main features observed in the transition region. In the next section we address this issue in more detail.

### 13.5 Explosive Events

There are basically two major classes of explosive events in the chromosphere/transition region (coronal mass ejection, CMEs, and polar plumes belong to totally different classes of high-velocity events and are not discussed here):

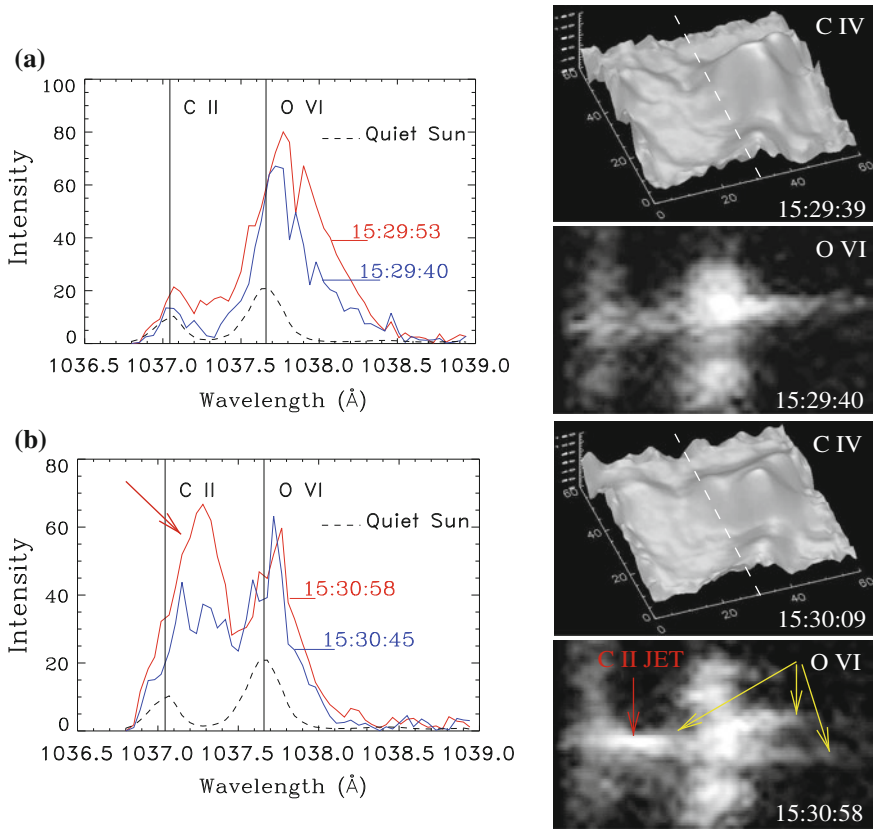
- (1) those that may be generated by post-reconnection shocks, and
- (2) those that are associated with the nonlinear explosive instability of Negative Energy Waves (NEWs). Naturally, the explosive events produced by these two different mechanisms *must have* different signatures.

Consider first the mechanism associated with post-reconnection shocks. As we have discussed earlier, shocks produced by the post-reconnection slingshot effect, propagating upward and having uneven surface, may experience self-focusing (Guderley's effect). In which the entire energy of a system, squeezed in a small volume, gets violently released in form of a hot bidirectional jets. Similar effects may occur when two different shocks produced by two independent reconnections, collide. This effect is universal and well observable.

Figure 13.13 shows an example demonstrating shock–shock interaction and subsequent generation of strong explosive event. Reconnections occurring in close bipoles marked by double red arrows in Fig. 13.8 (#13 in Fig. 13.10) cause a series of upward propagating shocks (Fig. 13.13a): left peaks are higher than right peaks corresponding to higher intensity behind the shock than in front of it. These shocks result in two close microflares and strong bidirectional jets in O VI (right panels in Fig. 13.13a).

The jet generates the downward shock in O VI line: now the double-humped spectrum has its right peak higher than the left one, which interacts with the upward propagating C II shock at  $t = 15:30:45$  UT (blue line in Fig. 13.13b). This results in the immediate appearance of the O VI explosive event (marked by yellow arrows in lower right panel of Fig. 13.13b) and a strong C II jet.

Prior to the collision temperature increases only due to regular, behind-shock heating,  $T_1 = 2\gamma(\gamma - 1)(\gamma + 1)^{-2}M^2T_0$  (subscripts “0” and “1” denote the unperturbed and behind-shock plasma, respectively). In this example, the shock velocity (before the collision) is  $v_{sh} \simeq 88$  km s<sup>-1</sup>, and  $T_1 = 8.5 \times 10^4$  K. After the collision behind the reflected shocks the temperature increases further and becomes:  $T_2/T_1 = (3\gamma - 1)\gamma^{-1}$ ,  $T_2 = 2.46 \times 10^5$  K. This is accompanied by strong plasma jets. The jet velocities are in the range of 115–220 km s<sup>-1</sup>. These are typically observed parameters in the transition region explosive events.



**Fig. 13.13** Example of the observed shock–shock interaction and the resulting sporadic events. **a** A series of strong shocks continuing to occur during and after the double microflare at C IV temperature accompanied by the downward propagating O VI jet (peaks are significantly red-shifted) with velocity exceeding  $180\text{ km s}^{-1}$ ; **b** downward propagating shocks (O VI line profiles show the right peaks exceeding the left peaks) interact with a series of upward propagating C II shocks at  $t = 15:30:45$ ; The right panels show 3D plots of C IV emission together with the jet images taken by SUMER; the approaching shocks cause a triple humps seen at  $t = 15:30:09$  in the C IV line; immediately after the shock collision, at  $t = 15:30:58$  a strong C II jet and the explosive event in O VI line (marked by yellow arrows) appear. The field of view in panels and scales of the SUMER spectra are the same as in Fig. 13.12

The probability of the explosive events produced by collision of neighboring shocks is quite high and can be observed everywhere from the quiet sun regions to plages where shocks produced by *noncollinear* flux tubes may reach each other when accelerating and expanding in overlying chromosphere. Typically, these explosive events are accompanied by a strong microflares as well (cf. Fig. 13.13).

In case of self-focusing of a single shock front when the entire cumulative energy goes into the strong bidirectional jets, there is usually little energy left for microflare. Strong support for such events is the absence or weakness of transient microflares



(the cylindrical focusing corresponds to a pure “jet” regime). The probability of such events, in principle, is also quite high. But in those regions where shock production is high, cylindrical convergence can be easily destroyed by the cascade of shocks produced by neighboring reconnection processes. Therefore, cylindrical focusing and resulted pure “JET” regime must be expected at least above the regions that are magnetically underpopulated, such as cell interior and magnetically poor vertices. Besides, as these events have the character of impulsive phenomena, their lifetimes must be short.

Thus, we have two subclasses in class of explosive events associated with post-reconnection shocks. From observational point of view the observed signatures of these two subclasses of explosive events are well distinguishable.

Another, totally different class of explosive events is associated with the instability of negative energy waves. These explosive events, having totally different origin, may look quite similar to those associated with the shock convergence, and yet have their own signatures.

In the first place, the instability of NEWs requires the presence of downflows in a system of structured magnetic field and can develop in a wide interval of velocities (Ryutova 1988):

$$40 \text{ km s}^{-1} \leq u \leq 220 \text{ km s}^{-1} \quad (13.16)$$

These conditions are easily met in the chromosphere, and we should expect this class of events to be quite common. Among the observed signatures of this kind of explosive events, we should expect

- (1) downflows with velocities of about  $40 \text{ km s}^{-1}$  and higher;
- (2) microflares, since such downflows correspond to the heat-jet regime in shock–shock collision; and
- (3) a high birthrate.

Note that the lifetimes of the explosive events caused by the instability may vary from a few seconds to minutes depending on the physical conditions of the instability, which may be realized in a wide range of parameters.

Most of the chromosphere/transition region explosive events fall into one of the two classes and have the properties listed above. These properties are summarized in Table 13.2.

Numbers in the first column correspond to chosen examples along the slit shown in Fig. 13.10. The second column shows the photospheric features at a given position along the slit; e.g., “Vertex, B” denotes a supergranular vertex with a strong magnetic field. The third column shows recurrence of the explosive events during the entire observed interval (2.2 h). Column 4th shows the reduction of magnetic flux before the appearance of the explosive event. Column 5th shows the intensity of the C IV transient. The velocities and lifetimes in columns 6–8 are approximate. Column 9 reflects the mechanism causing an explosive event: “instability” stands for the explosive instability of NEWs, and “Gudereley” for a cylindrical focusing of shock waves or shock–shock collision.

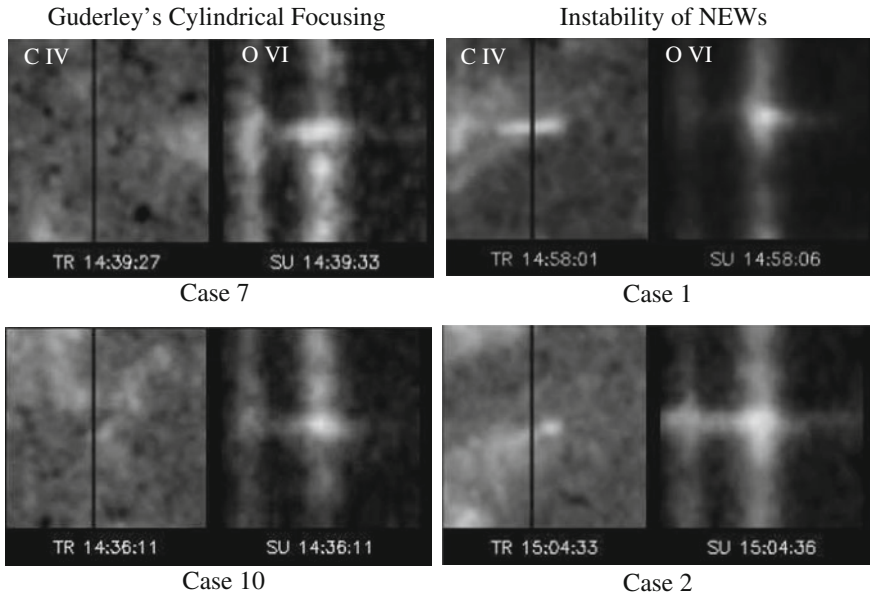
**Table 13.2** Examples of explosive events and their properties

Case	Location	Recurrence	$\Delta\Phi$ Mx	C IV intensity	C II ( $\text{km s}^{-1}$ )	O VI ( $\text{km s}^{-1}$ )	Lifetime	Class
1	Cell	Rare	n/a	Strg	40	80	$\sim 120$ s	Instb
2	Vertex(B)	Multi	n/a	Strg	30	120	$\geq 180$ s	Instb
2	Vertex(B)	Multi	n/a	Strg	40	180	$\sim 90$ s	Instb
3	Cell	Rare	$> 10^{18}$	Weak	20	80	$\sim 100$ s	Gudrl
4	Edge B	Multi	$10^{18}$	Weak	20	60	$\sim 3$ min	Instb
5	Edge B	Multi	$2 \times 10^{18}$	Med	20	60	$\sim 6$ min	Instb
6	Cell	Rare	$3 \times 10^{17}$	Weak	20	80	$\sim 4$ min	Instb
7	Vertex	Rare	$4 \times 10^{17}$	None	20	110	$\sim 90$ s	Gudrl
8	Vertex, B	Multi	$10^{18}$	Med	20	80	$\sim 3$ min	Instb
9	Vertex, B	Multi	$2 \times 10^{18}$	Strg	40	180	$\leq 120$ s	Instb
10	Cell	Rare	$< 10^{17}$	Weak	10	120	$\geq 70$ s	Gudrl
11	Vertex	Rare	$2 \times 10^{17}$	Weak	40	80	$\geq 120$ s	Instb
12	n/a	Few	$6 \times 10^{18}$	Strg	50	200	$\geq 5$ min	Instb
13	n/a	Few	$2 \times 10^{18}$	Med	10	80	$\sim 90$ s	Instb

Among more than 40 analyzed events, only a few cases (10%) could be explained by cylindrical focusing. Some examples shown in Table 13.2 are: case 7 which is above the vertex with no magnetic field (below the MDI resolution), and cases 3 and 10 that are both above the cell interiors. In all cases, the peak velocities are more than  $100 \text{ km s}^{-1}$ , the C IV event is absent, and lifetimes are quite short (90 s). Examples of the explosive events in cases 7 and 10 are shown in left four panels in Fig. 13.14. One can see that C IV emission that would represent microflare is absent, while SUMER O VI jet is quite prominent.

The properties of strong jets generated by the explosive instability of NEWs are more diverse. This is quite natural because the interval of the critical velocities, (13.16), is quite wide. For example, downflows close to the lower critical limit lead to long-lasting explosive events and are often accompanied by a medium or weak microflares. Stronger downflows lead to explosive events of shorter duration and are usually accompanied by a strong microflares. Examples of this type of jets are shown in right panels, Fig. 13.14. In both cases 1 and 2, strong microflares occur first and are accompanied by downflows. Then very quickly the explosive events appear. The time interval corresponding to the development of the explosive instability is roughly estimated as  $t_{\text{expl}} \sim 30\text{--}100$  s. This means that as soon as cumulative effects create the microflare and downflows, in a few tens of seconds the explosive instability develops, leading to extremely fast acceleration of jets.

The examples in Fig. 13.14 show that explosive events can be detected by SUMER even when the main emission is located in several arcseconds from the slit. The overall birthrate for explosive events can be roughly estimated as  $f = N/(ST)$ , where the number of events  $N = 40$ , the “effective” area  $S = 5'' \times 360'' = 9.5 \times 10^{18} \text{ cm}^2$ ,



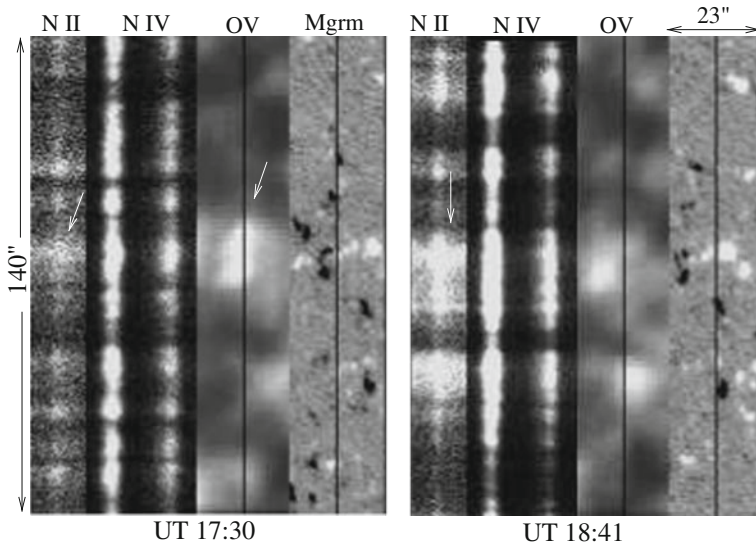
**Fig. 13.14** Four examples of explosive events shown in TRACE C IV and SUMER O VI lines. *Left panels* are events driven by the cylindrical focusing of shock fronts; the remarkable feature of this class of explosive events is the absence of emission in the C IV line. *Right panels* are the explosive events driven by the explosive instability of NEWs; the necessary attribute here is the appearance of a prominent microflare accompanying the strong jets

and the time of observation  $T = 7,800$  s. This gives  $f = 5.4 \times 10^{-20} \text{ cm}^{-2} \text{ s}^{-1}$ , which is consistent with the earlier estimates,  $f = 4 \times 10^{-21} \text{ cm}^{-2} \text{ s}^{-1}$  for coronal holes and  $10^{-20}$  for the quiet sun (e.g., Dere (1994)).

### 13.6 Response of the Upper Atmosphere to Reconnection of Unipolar Flux Tubes

We saw that the reconnection processes occur both in the system of the opposite polarity flux tubes and the same polarity flux tubes. The post-reconnection processes, however are quite different, and response of the overlying atmosphere is quite different as well.

Figure 13.15 shows an example of the response of the upper layers of atmosphere to dynamic changes in the photospheric magnetic field. Three left images in both panels are the SUMER spectra in N II (corresponding to chromosphere at temperature  $\simeq 2.7 \times 10^4$  K), N IV (transition region at  $T \simeq 1.4 \times 10^5$  K), and O V (transition region at  $T \simeq 2.3 \times 10^5$  K). Two right images in both panels are the O V emission taken by the CDS, and high-resolution magnetogram taken by the MDI.



**Fig. 13.15** Response of the chromosphere (N II and N IV SUMER spectra) and transition region (SUMER O V and CDS O V images) to reconnections of the photospheric flux tubes. *Left panels* example of opposite polarity magnetic flux tubes; *Right panels* the reconnection between the same polarity flux tubes. *Solid line* is a SUMER slit

One can see that when slit crosses the center of the mixed polarity group (Fig. 13.15, left panels), strongly enhanced transient emission in CDS O V line is detected. This is a typical example of the hydrodynamic cumulation of upward propagating shock produced by the post-reconnection slingshot.

When the slit crosses the region dominated by one polarity element (Fig. 13.15, right panels), the slingshot effect must be tilted, or be perpendicular to gravity, so that in this case the lateral motions dominate over the upward propagating shocks. As a result, the motions are detected in lower chromosphere (N II line is significantly broadened), while upward propagating shocks are suppressed. The enhanced emission on the CDS image is still seen over the mixed polarity group, now left from the slit.

Concluding this chapter, we must say that the energy supply for highly energetic events at all temperature levels from chromosphere to corona overlying the small-scale magnetic network, lies in the continuous hydromagnetic activity of small-scale magnetic flux tubes.

The fact that the atmosphere above the quiet sun is far from quiet is, therefore, only natural. It is just here, within a narrow transition region, the sharp temperature jump from 6,000 K to the million degree corona occurs. We saw that the chromosphere and transition region are the first to amass the energy coming from below and transport it into the corona. And it is also only natural that the chromosphere/transition regions are the sites of continuous radiative transients, microflares, plasma jets, and explosive

events. Indeed, localization of all these events in the transition region is co-spatial with the photospheric magnetic pattern, and their appearance correlates with canceling mixed polarity magnetic elements. Moreover, each observed event, be it just a microflare, supersonic jet, or combination of two can only be explained by various conditions for the generation of post-reconnection shocks and their interaction. Theoretical solution for the parameter range gives a simple set of physical parameters that corresponds to all three regimes. Of which the largest range of parameters is the release of energy in the form of combined microflares and jets. Naturally, just like it is observed, stronger microflare assumes the weaker jet and vice versa. A simple theory allows to easily perform quantitative analysis.

## References

- P. Brekke, *Sol. Phys.* **190**, 379 (1999)
- W. Curdt, H. Tian, *Astron. Astrophys.* **532**, L9 (2011)
- K.P. Dere, Explosive events, magnetic reconnection, and coronal heating. *Adv. Space Res.* **14**, 13–22 (1994)
- A. Fludra, H. Warren, *Astron. Astrophys.* **523**, 47 (2010)
- G. Guderley, *Luftfahrtforschung* **19**, 302–312 (1942)
- L.E. Gurevich, A.A. Romyantsev, *AJ* **13**, 908 (1969)
- R.A. Harrison et al., *Sol. Phys.* **170**, 123 (1997)
- D.E. Innes, L. Teriaca, *Sol. Phys.* **282**, 453 (2013)
- L.D. Landau, E.M. Lifshitz, *Fluid Mechanics* (Pergamon Press, Oxford, 1987)
- D. Luo, R.A. Chevalier, *Astrophys. J.* **435**, 815 (1994)
- P. Maltby et al., *Astrophys. J.* **306**, 284 (1986)
- J.E. Mendoza-Torres, J.P. Torres-Papaqui, K. Wilhelm, *Astron. Astrophys.* **431**, 339 (2005)
- S.-I. Pai, *Magnetogasdynamics and Plasma Dynamics* (Springer, Berlin, 1962)
- M.P. Ryutova, *Sov. Phys. JETP* **67**(8), 1594 (1988)
- M.P. Ryutova, T.D. Tarbell, *Astrophys. J.* **541**, L29 (2000)
- M. Ryutova, S. Habbal, R. Woo, T. Tarbell, *Sol. Phys.* **200**, 213 (2001)
- M. Ryutova, T. Tarbell, R. Shine, *Sol. Phys.* **213**, 231 (2003)
- K.P. Stanyukovich, *Unsteady Motion of Continuous Media* (Pergamon Press, Oxford, 1960)
- I.V. Sokolov, *Sov. Phys. Uspekhi* **33**, 960 (1991)
- C.J. Schrijver et al., *Astrophys. J.* **487**, 424 (1997)
- T. Tarbell, M. Ryutova, J. Covington, A. Fludra, *Astrophys. J.* **514**, L47 (1999)
- T. Tarbell, M. Ryutova, R. Shine, *Sol. Phys.* **193**, 195 (2000)
- G.B. Whitham, *J. Fluid Mech.* **3**, 337 (1958)
- E.I. Zababakhin, I.E. Zababakhin, *Unbounded Cumulative Phenomena* (Nauka, Moscow, 1988)

## Chapter 14

# Photospheric Network as Energy Source for Quiet Sun Corona

**Abstract** In previous chapters, we studied post-reconnection processes resulted from interaction of photospheric flux tubes, embedded predominantly in nonmagnetic environment. Higher in the atmosphere, magnetic field preserves its filamentary structures, but is surrounded by low beta-magnetized plasma. In this chapter, we will study post-reconnection processes occurring in the arbitrarily magnetized plasma. We will see that in this case a reconnection triggers various branches of MHD shocks, and cumulation of energy occurs higher in the atmosphere reaching coronal heights and beyond. We are still dealing here with the atmosphere above the rarefied ensembles of flux tubes. Thus imprint of quiet sun at coronal heights is the most expected outcome of post-reconnection processes occurring at all levels. Moreover, these processes seem to be the reliable energy source to fuel the fast solar wind which is rooted in coronal holes outside sunspots and active regions.

### 14.1 Post-reconnection Processes in Arbitrarily Magnetized Environment

In previous chapters, we studied post-reconnection processes resulted from constantly interacting photospheric flux tubes, and in particular, the evolutionary shocks that experience strong gradient acceleration in the sharply stratified photosphere/chromosphere region. We saw that a great variety of transition region radiative transients, microflares, jets, and their combinations, can be explained by post-reconnection processes that evolve along many different ways depending on local physical parameters. Although all these processes occur far from the reconnection region, and in time when the system has long “forgot” the flux tube reconnection itself, the fact that the reconnection occurred at the photospheric level, i.e., in predominantly magnetic free environment, determines the range of parameters for radiative transients observed in the chromosphere/transition region.

In this chapter, we will see that similar processes occur when reconnection occurs above the surface in arbitrarily magnetized environment. In this case the post-reconnection shocks and their further evolution follow the same path as those triggered by the photospheric reconnection, but final energy release occurs higher in the atmosphere, and the process itself fits different range of parameters.

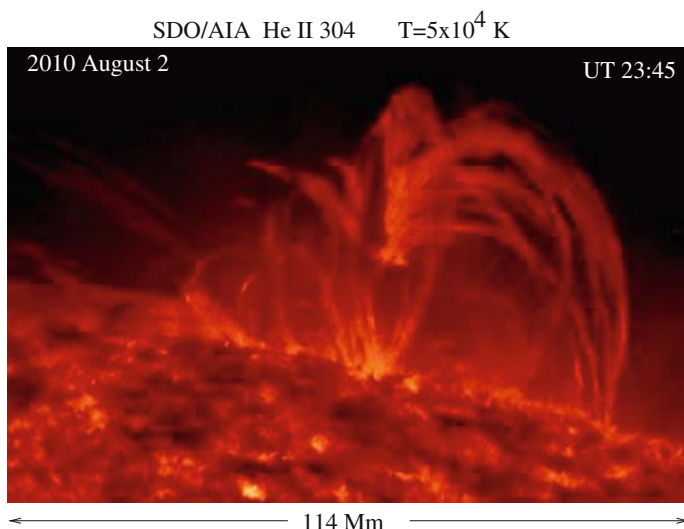
### 14.1.1 Magnetic Loop Arcades in the Chromosphere

One of the key elements of the entire mechanism of energy production by reconnection of individual flux tubes is the *very existence* of intermittent magnetic structures, which implies that parameter  $\beta^*$ , is finite:

$$\beta^* = \frac{P_{\text{ext}}}{B^2/8\pi} \geq 1 \quad (14.1)$$

This condition, which is always true for the photospheric flux tubes, also holds in highly inhomogeneous chromosphere and even corona. Let us estimate heights at which the condition (14.1) can still be applied. We use the reference model of the solar atmosphere given by Maltby et al. (1986). For example, the gas pressure at heights  $h = 200, 500,$  and  $800$  km, respectively is:  $p_e \simeq 2.65 \times 10^4 \text{ dyn cm}^{-2}$ ,  $\simeq 1.77 \times 10^3 \text{ dyn cm}^{-2}$ ,  $\simeq 18.9 \text{ dyn cm}^{-2}$ . At  $h = 200$  km  $\beta^* \geq 1$  for magnetic field strength  $B \leq 800$  G, at  $h = 500$  km,  $\beta^* \geq 1$  for  $B \leq 160$  G, and at  $h = 800$  km for the magnetic field  $\leq 60$  G  $\beta^* \geq 1$  and there still will be an interface between the magnetic flux and the external plasma.

Figure 14.1 shows example of the chromosphere/transition region magnetic loop arcades taken by AIA instrument on the SDO on August 2, 2010. The well defined thin magnetic loops forming such arcades is the most typical form of magnetic field at all heights of solar atmosphere. In other words, the filamentary structure of magnetic field is an intrinsic property of the solar atmosphere. This means that as far



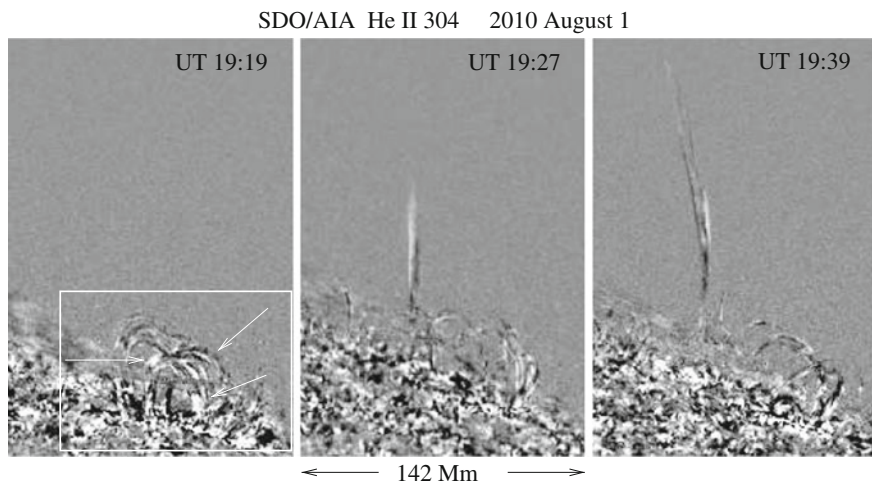
**Fig. 14.1** Image of the magnetic loop systems at chromosphere/transition region temperatures taken by the SDO/AIA instrument in the He II 304 Å line. The very existence and dynamic stability of chromospheric loops implies the pressure equilibrium across the loops and favorable conditions for post-reconnection slingshot that generates microflares and jets

as the magnetic loops preserve their identity and have their well-defined boundaries with the environment, the post-reconnection processes will have qualitatively similar character as those under the photospheric conditions.

As the very first step, just like in the photosphere, magnetic field forming thin loops and being in equilibrium with environment, after reconnection will still be confined in loops but now in strongly curved form. This as we know immediately leads to slingshot effect. As mentioned above, the parameter range for the initial stage of the process, and for subsequent steps, is of course different than those for photospheric reconnections.

The system of loops is usually long-living. It lives as long as photospheric magnetic flux concentrations serving as footpoints, last. The individual loops however are in constant motion, changing their shape and orientation. At any moment of time the neighboring loops may come close to each other at some point and reconnect. This is obviously a continuous process providing a continuous generation of post-reconnection shocks and subsequent energy release in various forms. In other words, ever evolving magnetic loop arcades are sites of cascades of shocks and appearance of microflares, supersonic jets, and their combinations.

Figure 14.2 shows snapshots of the “same” arcade of loops as in Fig. 14.1 (i.e., loops rooted in the same magnetic region at the photosphere). These are difference images made by subtracting the subsequent movie frames with 60 s interval to increase a contrast. Three instances of time show the system in different phases. At UT 19:19 a nice-shaped arcade looks quiet peaceful, but harbors several strong



**Fig. 14.2** Example of microflares and strong supersonic jet originated in the magnetic loop arcades at the chromosphere/transition region temperatures. To increase a contrast, the images were obtained by subtracting the subsequent movie frames with 60 s interval. The *left panel* shows one of “quiet” moments of the arcade exhibiting a few microflares (marked by *arrows*); *white frame* is the area occupied by loop system shown in Fig. 14.1. At UT 19:27 (*middle panel*) a well-developed jet reaches a projection height of about 100 Mm. The *right panel* shows the maximum phase of the jet



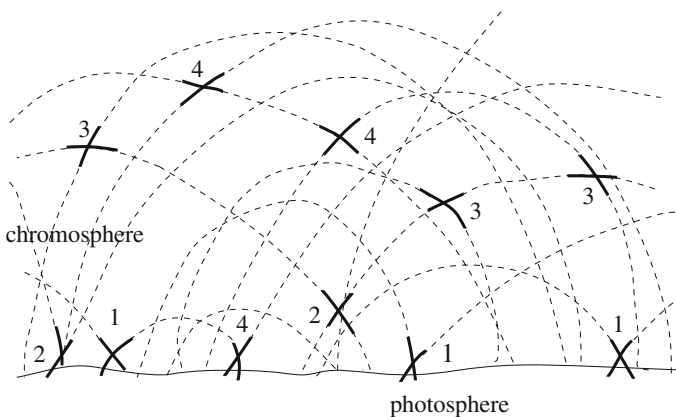
microflares (marked by arrows). White frame in this panel is the area occupied by loop system shown in Fig. 14.1. At UT 19:27 (middle panel) a well-developed supersonic jet continues it raise. The right panel shows the maximum phase of the jet. The loop system has been significantly reorganized.

Thus, rooted in the photospheric small-scale network magnetic elements, magnetic loops form arcades of different sizes in the chromosphere/transition region. In these ever evolving arcades magnetic loops may reconnect at any time at any given height. And, of course, the reconnection occurs in various environments. The most typical cases are shown in Fig. 14.3. Dark crosses mark the reconnection regions. Numbers correspond to different magnetic status of environmental plasma in the vicinity of reconnection region. Reconnections marked by #1 occur in magnetic free environment. #2 corresponds to reconnections occurring in vicinity of vertical magnetic field. In cases marked by #3 the neighboring magnetic field makes some angle with gravity force, and #4 is when external magnetic field is almost horizontal.

The post-reconnection waves generated in these different cases will have different properties depending on the magnetic status of the environmental plasma. The evolution of shocks and final energy release will be also different. Detailed analysis of each case will be considered below. Before doing this we need to emphasize the direction of energy transport.

It is important that in any case, whether the environment is nonmagnetic, or there is a magnetic field having parallel, oblique, or perpendicular direction with respect to the gravity force, the most efficient energy transfer provided by the post-reconnection shocks occurs in the direction of decreasing density, i.e., *always radially outward* from solar surface.

The fact that the energy released due to the post-reconnection processes in the environment of arbitrary magnetic topology is carried out radially outward is extremely



**Fig. 14.3** Sketch of magnetic structures above the photosphere and examples of reconnection regions in different magnetic environments. Numbers correspond to different magnetic status of plasma in the vicinity of reconnection region: #1 is magnetic free case; #2 corresponds to vertical magnetic field near reconnection region (i.e., parallel to gravity force); #3 is when magnetic field makes some angle with gravity force, and #4 is when external magnetic field is almost horizontal

important for understanding one of the puzzles associated with the fast solar wind. It was found (Woo 1996; Woo and Habbal 1999) that the fast solar wind is organized in a form of small-scale filamentary ray-like structures.

Observations of density and velocity distribution in the outer corona obtained from radio occultation measurements (Woo 1996; Woo and Habbal 1999) showed for example, that the density profile closest to the Sun at  $1.15 R_{\odot}$ , representing the imprint of the Sun, is carried radially into interplanetary space by small-scale ray-like structures that pervade the entire solar corona. Moreover, a significant fraction of mass fluxes which extend into interplanetary space originate from the quiet sun and the coronal hole areas (Cranmer 2009; Nistico et al. 2011; Zhao et al. 2014).

Hassler et al. (1999) have also reported on the connection between the fast solar wind outflow and the chromospheric magnetic network. This means that the mechanism responsible for the formation of fast solar wind must not only connect the roots of the wind with the chromospheric network, but also explain how generated flows are guided through strongly inhomogeneous atmosphere radially outward. From this perspective the post-reconnection processes occurring in very different magnetic regions, but always carrying energy radially outward, seem to be the most reliable mechanism.

### 14.1.2 Post-reconnection Shocks in Upper Atmosphere—Types and Characters

To illustrate the basic properties of post-reconnection processes in arbitrarily magnetized environment, characteristic to upper atmosphere, we consider a two-dimensional problem with  $\mathbf{B}_0 = (B_{0x}, B_{0z})$ , and assume that all the equilibrium parameters depend only on the coordinate  $z$ , directed along the gravity force,  $\mathbf{f}_g = -gz$ .

2D nonlinear MHD equations, in Riemannian coordinates (method of characteristics, see, e.g., Landau and Lifshits 1987; Whitham 1974) reduce to a single equation for  $z$ -component of the velocity  $u(z)$  which, for homogeneous medium, has a form of the simple wave:

$$\frac{\partial u}{\partial t} + [v + \alpha u] \frac{\partial u}{\partial z} = 0, \quad (14.2)$$

whose parameters are constant at fixed characteristics

$$\frac{dz}{dt} = v + c_s, \quad (14.3)$$

where  $c_s = (\partial p / \partial \rho)$  is a sound speed, and  $v$  is characteristic velocity (Jeffrey and Taniuti 1964):

$$v_{\pm}^2 = \frac{1}{2} \left\{ c_s^2 + \frac{B^2}{4\pi\rho} \pm \sqrt{\left( c_s^2 + \frac{B^2}{4\pi\rho} \right)^2 - \frac{c_s^2 B_z^2}{\pi\rho}} \right\} \quad (14.4)$$

$B^2 = B_x^2 + B_z^2$ , and  $\alpha$  is a coefficient of nonlinearity:

$$\alpha = \frac{1}{v} \left[ \frac{\partial(v\rho)}{\partial\rho} + \frac{4\pi\rho(v^2 - c_s^2)}{B_x} \frac{\partial v}{\partial B_x} \right] \quad (14.5)$$

Note that other quantities, e.g., transverse velocity  $u_x(z)$  and the magnetic field  $B_x(z)$  evolve according to linear equations: in these quantities nonlinearity appears in higher order (Sagdeev 1966; Sokolov 1991; Ryutova and Sakai 1993).

In the stratified medium, nonlinear distortions of the wave profile can still be described by a Riemann equation if the spatial scale of nonlinear perturbations is assumed to be small compared to the scale height. In this case all the wave parameters vary slowly on characteristics, and (14.2) acquires a form of a quasi-simple wave with nonzero body force,  $F(\rho, B, v)$  in its right-hand side (Asano and Taniuti 1969; Ostrovskii and Rubakha 1974):

$$F(z) = v^2(z) \frac{1}{W(z)} \frac{dW(z)}{dz} \quad (14.6)$$

where

$$W(z) \simeq \left[ \frac{\rho(z)v(z)}{\rho_0 v_0} \right]^{-1/2} \quad (14.7)$$

with  $\rho(z)$  and  $v(z)$  being the values of density and characteristic velocity in the undisturbed gas ahead of the shock front; subscript “0” marks their initial values. The solution of (14.2) with the body force (14.6) is a quasi-simple wave (Landau and Lifshits 1987; Ostrovskii and Rubakha 1974):

$$t - \int_0^z \frac{dz'}{v_{\pm}(z')} + \frac{u}{W(z)} \int_0^z \frac{\alpha W}{v_{\pm}^2(z')} dz' = \Phi \left( \frac{u}{W} \right), \quad (14.8)$$



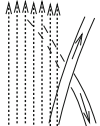
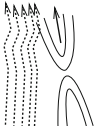
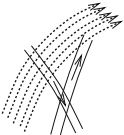
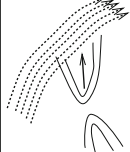

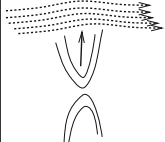
where  $\Phi$  is a function determined by the boundary conditions.

The height of shock formation and its amplitude are determined by simultaneous conditions on the derivatives of (14.8) (Landau and Lifshits 1987):

$$\frac{\partial t}{\partial u} = 0, \quad \frac{\partial^2 t}{\partial u^2} = 0 \quad (14.9)$$

For a given magnetic field geometry two branches of the velocity  $v_{\pm}(z)$  (14.4) determine two independent characteristics along which nonlinear MHD waves evolve.

We know that thin magnetic loops forming canopy-shaped arcades of different sizes is an intrinsic property of the solar atmosphere from the chromosphere to corona. In these arcades magnetic flux tubes may collide and reconnect. Notably, the reconnections may occur in the differently magnetized environment. As shown in Fig. 14.3 there are basically four most typical cases marked by numbers 1–4.

Case No.	External Magnetic field	Characteristic Velocities	Flux Tubes Prior Reconnection	Sling-shot Effect	Aftereffect
1	$\vec{B} = 0$ (Non-magnetic environment)	$v_{\pm}^2 = c_s^2$			Acoustic Shocks Jets Microflares
2	$B_x \ll B_z$ (Vertical field)	$v_+^2 = c_s^2$ $v_-^2 = \frac{B_z^2}{4\pi\rho}$			Acoustic Shocks & HF Alfvén Waves Jets Microflares
3	$B_x = B \sin \theta$ $B_z = B \cos \theta$	$v_+^2 = \frac{B^2}{4\pi\rho}$ $v_-^2 = c_s^2 \cos^2 \theta$			Acoustic & MHD Shocks; HF Alfvén Waves Jets Flares
4	$B_x \gg B_z$ (Horizontal field)	$v_{\pm}^2 = c_s^2 + v_A^2$			Fast MHD Shocks Jets Flares

**Fig. 14.4** Reconnection of magnetic flux concentrations in nonmagnetic (*case no. 1*) and magnetic (*cases no. 3–4*) environments. The second column shows external magnetic field, the next column shows the characteristic velocities; the fourth and fifth columns depict the flux tubes prior and after the reconnection, and the last column contains a slingshot outcome

Below we describe these four cases in more details, and illustrate them in Fig. 14.4. Case numbers 1–4 correspond to cases marked by the same numbers in Fig. 14.3.

No. 1 corresponds to the case when intense magnetic flux tubes collide at the photosphere level in totally magnetic free environment (the external plasma  $\beta \gg 1$ ). Therefore, a slingshot effect generates pure acoustic waves,

$$v_{\pm} = c_s \tag{14.10}$$

Propagating upward these waves steepen and become shocks with complex wavy surfaces, whose further evolution leads to strong hydrodynamic cumulation and production of high-energetic events as we have seen in previous chapter.

No. 2 is the process when flux tubes collide and reconnect in the vicinity of some vertical magnetic field,  $B_x \ll B_z$ . This case is typical for areas at or slightly above the surface where magnetic field tends to be vertical. It may be realized as well in higher layers of the atmosphere underlying coronal hole regions where the “background” magnetic field is predominantly vertical. In this case the slingshot effect generates MHD waves, and characteristic velocity, (14.4), has two branches: the upper branch

is a pure acoustic wave, while the lower branch corresponds to the Alfvén wave, propagating along the vertical magnetic field:

$$v_+ = c_s, \quad v_- = \frac{B_z}{\sqrt{4\pi\rho}} \quad (14.11)$$

No. 3 corresponds to the case when the slingshot effect operates in an arbitrarily oriented magnetic field which is typical of magnetic canopies, i.e., throughout entire solar atmosphere. Two branches of (14.4) correspond to the fast and slow MHD waves with phase velocities (respectively,  $v_+$  and  $v_-$ ):

$$v_+ = \frac{B}{\sqrt{4\pi\rho}}, \quad v_- = c_s \cos \theta \quad (14.12)$$

where  $\theta$  is the angle between the  $z$ -axis and the magnetic field ( $B_x = B \sin \theta$ ,  $B_z = B \cos \theta$ ). Only for this case we assume that plasma beta is small (actually,  $\beta \leq 0.1$  is already a good approximation).

No. 4 is the case when the shock is formed in the presence of a predominantly horizontal magnetic field. In this case ( $B_z = 0$ ), the characteristic velocity, (14.4) then has only one root corresponding to fast magnetosonic waves:

$$v_+ = \sqrt{c_{s0}^2 + v_{A0}^2} \quad (14.13)$$

This situation is readily realized in upper chromosphere where magnetic fields form an hierarchy of canopies. It is also often met in lower atmosphere, especially in regions occupied by compact bipoles. In high-plasma beta the process is similar to that of the acoustic shocks, while in low-plasma beta the process is dominated by the properties of nonlinear Alfvén waves.

In all cases considered above it is the acoustic component that provides the action of strong hydrodynamic cumulation, i.e., transport of energy by post-reconnection acoustic shocks, and subsequent formation of radiative transients and collimated jets. As we will see below, formation of shocks associated with the Alfvén component occurs in a restricted range of parameters, but frequency of these waves may be quite high.

## 14.2 Heights of Shock Formation

To find the height of shock formation and the shock amplitude, we use (14.8) and (14.9) and specify boundary conditions by assuming that the kick produced by slingshot effect has a form of sinusoidal pulse with the initial velocity  $v_A$ :

$$u(0, t) = \begin{cases} v_A \sin \omega t & 0 \leq t \leq \pi/\omega \\ 0 & t > \pi/\omega \end{cases} \quad (14.14)$$

where  $\omega \simeq v_A/R$  ( $R$  being a characteristic radius of reconnecting flux tubes). Then the function  $\Phi$  in (14.8) acquires a form:

$$\Phi(u, W) = \frac{1}{\omega} \sin^{-1} \left( \frac{u}{v_A W} \right) \tag{14.15}$$

With this function the first of two conditions (14.9) gives:

$$- \int_0^z \frac{\alpha(z') W(z')}{v_{\pm}^2(z')} dz' + \frac{1}{\omega \sqrt{v_A^2 - (u/W)^2}} = 0 \tag{14.16}$$

The second condition,  $\partial^2 t / \partial \alpha^2 = 0$ , gives

$$\frac{1}{\omega} \frac{u/W}{[v_A^2 - (u/W)^2]^{3/2}} = 0 \tag{14.17}$$

Thus, the shock formation occurs at the height  $z_{sh}$ , determined by the integral (14.16), with  $u = 0$ :

$$\int_0^{z_{sh}} \frac{\alpha W(z')}{v_{\pm}^2(z')} dz' = \frac{R}{v_A^2} \tag{14.18}$$

The shock amplitude,  $u(z)$  as a function of height, can be found from (14.16).

A crucial role in the height of shock formation and the amplitude of the shock is played by parameters  $\alpha(z)$  and  $W(z)$ , which in fact, reflect thermodynamic properties of medium and its magnetic status.

To solve (14.16) and (14.18) one needs to use a specific model of the atmosphere, and, in principle, take into account a back reaction of the temperature on the propagation of shock waves. Here we restrict ourselves by description of basic properties of the energy transfer process associated with the post-reconnection shocks produced at different heights and in differently magnetized regions of a low atmosphere. For this we assume that the equilibrium atmosphere is an ideal gas ( $p = (k/m)\rho T$ ) and the temperature gradient is adiabatic,  $(dT/dz) = [(\gamma - 1)/\gamma](gm/k)$ . For  $\gamma$  we will use below  $\gamma = 5/3$  and a harmonic mean value  $\gamma = 1.29$ .

As shown in Fig. 14.4, pure acoustic branch is a necessary component in almost all cases (even the case No. 4 for a weak external field drops into this category). This means that in any magnetic field geometry one of the channels of the energy transport and its release is governed by properties of the acoustic shocks.

To illustrate the general properties of the shock formation, first we consider the acoustic branch and then discuss the fast MHD wave associated with  $v_+ = B/\sqrt{4\pi\rho}$  ( $B = \sqrt{B_x^2 + B_z^2}$ ).

For the acoustic waves the parameters  $\alpha(z)$  and  $W(z)$  are as follows:

$$\alpha_+ = \frac{\gamma + 1}{2}, \quad W = \exp \left( \frac{\gamma + 1}{4} \frac{z}{\Lambda} \right) \tag{14.19}$$

Equation (14.18), determining the height of the shock formation becomes as follows:

$$\frac{\gamma + 1}{2c_{s0}^2(0)} \int_0^{z_{\text{sh}}} \exp\left(\frac{5\gamma - 3}{4} \frac{z'}{\Lambda}\right) dz' = \frac{R}{v_A^2}, \quad (14.20)$$

Integrating this equation yields:

$$\frac{1}{z_{\text{sh}}^{(0)}} \frac{4\Lambda}{(5\gamma - 3)} \left[ \exp\left(\frac{5\gamma - 3}{4} \frac{z}{\Lambda}\right) - 1 \right] = 1 \quad (14.21)$$

where  $z_{\text{sh}}^{(0)}$  is the height of shock formation in an unstratified atmosphere ( $\Lambda \rightarrow \infty$ ):

$$z_{\text{sh}}^{(0)} = \frac{2}{\gamma + 1} \frac{c_{s0}^2}{v_{A0}^2} R \quad (14.22)$$

Equation (14.21) immediately gives the expression for the height of the shock formation in the stratified atmosphere:

$$z_{\text{sh}} = \frac{4}{5\gamma - 3} \Lambda \ln\left(1 + \frac{5\gamma - 3}{4} \frac{z_{\text{sh}}^{(0)}}{\Lambda}\right) \quad (14.23)$$

For the Alfvén branch out of (14.12) the height of shock formation is as follows (Asano and Taniuti 1969; Ostrovskii and Rubakha 1974):

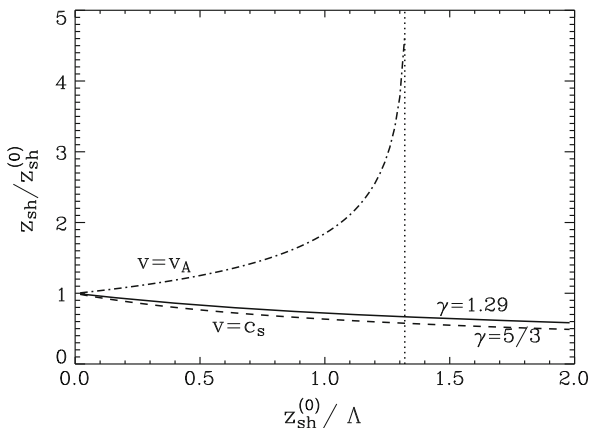
$$z_{\text{sh}} = \frac{4}{3} \Lambda \ln\left[1 - \frac{3}{4} \frac{z_{\text{sh}}^{(0)}}{\Lambda}\right]^{-1} \quad (14.24)$$

with  $z_{\text{sh}}^{(0)} \simeq (2/3)R$ .

Figure 14.5 shows the height of the shock formation in stratified atmosphere  $z_{\text{sh}}$ , normalized to its value in the unstratified medium,  $z_{\text{sh}}^{(0)}$ : solid and dashed lines correspond to the acoustic branch, while dash-dotted line to Alfvén waves. Naturally, the acoustic shock formation in the stratified atmosphere for upward propagating waves occurs at lower heights than in the homogeneous medium, as always  $z_{\text{sh}} < z_{\text{sh}}^{(0)}$ . At the same time, for essentially different specific heat ratios there is a little difference between the corresponding values of  $z_{\text{sh}}$ . In both cases it decreases monotonically with decreasing scale height and remains almost the same for  $\gamma = 1.29$  and  $\gamma = 5/3$ . We will see below that the shock amplitude, on the contrary, is very sensitive to thermodynamic properties of medium.

Unlike the acoustic waves, the shocks associated with the Alfvén waves are formed in the stratified atmosphere at much higher altitudes than in the homogeneous medium. The height of their formation quickly increases with decreasing scale height, and if the parameters of medium and magnetic field are such that  $z_{\text{sh}}^{(0)} > (4/3)\Lambda$ , the shocks associated with Alfvén waves do not develop at all; see

**Fig. 14.5** Height of the shock formation in stratified atmosphere,  $z_{sh}$ , versus its value in the unstratified medium,  $z_{sh}^{(0)}$ : *solid* and *dashed* lines correspond to the acoustic branch, while *dash-dotted* line to Alfvén waves. The *dotted* line is a boundary beyond which (to the *right*) the shocks associated with Alfvén waves do not develop



(14.17). This threshold is marked by dotted line in Fig. 14.5. Physically this means that in photosphere/chromosphere region where scale height is small, the formation of Alfvén shocks is not favorable even in the presence of strong magnetic fields, i.e., in low atmosphere (or in any other height where  $z_{sh}^{(0)} > (4/3)\Lambda$ ) the generated Alfvén waves will rather participate in other nonlinear processes. For example, they may release the energy through the strong phase mixing, or evolve into solitary waves.

It is important to note that the frequency of these waves may be quite high—the fact consistent with observations. The theoretical value of characteristic frequency can be estimated as  $\omega \simeq 2\pi w/R$ , where  $w$  is the reconnection rate,

$$w = v_A / \ln Re_m, \tag{14.25}$$

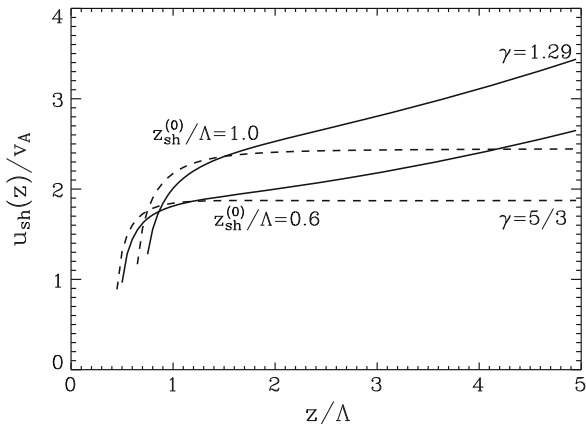
$Re_m$  being a magnetic Reynolds number (Petschek 1964).  $R$  is a characteristic size of reconnection area. Remember that we deal with the post-reconnection processes, and that the waves are generated by post-reconnection slingshot. For the photosphere and low chromosphere, the characteristic radius of magnetic flux participating in one act of reconnection is  $R \sim 35\text{--}70\text{ km}$  (Tarbell et al. 1999, 2000; Ryutova and Tarbell 2000). Quantitative estimates are as follows. Magnetic Reynolds number in these regions is  $Re_m \sim 10^3\text{--}10^6$ . If we take  $R \sim 40\text{ km}$ , then in the photosphere region for  $v_A \simeq 10\text{ km s}^{-1}$ ,  $\omega \sim 0.11\text{--}0.23\text{ s}^{-1}$ , in low chromosphere, for  $v_A \simeq 50\text{ km s}^{-1}$ ,  $\omega \sim 0.6\text{--}1.14\text{ s}^{-1}$ ; at  $v_A \simeq 100\text{ km s}^{-1}$ ,  $\omega \sim 1.14\text{--}2.27\text{ s}^{-1}$ .

The shock amplitude immediately after the shock formation,  $u_{sh}(z)$  as a function of altitude and scale height can be found by evaluating the integral in (14.16) for given parameters  $\alpha$ ,  $W(z)$ , and  $z_{sh}^{(0)}$ , and resolving the equation with respect to  $u(z)$ . The results of these calculations for the acoustic and Alfvén waves are shown in Figs. 14.6 and 14.7, respectively. Two values of  $z_{sh}^{(0)}/\Lambda = 0.6, 1.0$ , have been used.

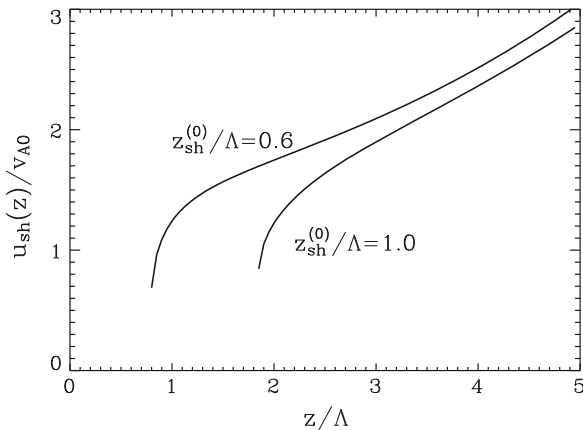
One can see that immediately after the shock is formed, its amplitude sharply increases in all cases whether it is acoustic or Alfvén wave. At large heights the amplitude of the acoustic shock is proportional to  $\exp[(5 - 3\gamma)/8]$ , and for monatomic gas it reaches some constant value (at about Mach numbers  $M \simeq 2$ ). For medium



**Fig. 14.6** The shock amplitudes at the moment of the shock formation as a function of height for the acoustic branch. *Solid lines* correspond to  $\gamma = 1.29$ , and *dashed lines* to  $\gamma = 5/3$



**Fig. 14.7** The same as in Fig. 14.6 but for the Alfvén waves. Unlike the acoustic waves the amplitude of the Alfvén waves grows exponentially at high altitudes



with  $\gamma = 1.29$ , the shock amplitude grows exponentially as  $\sim \exp(0.14z/\Lambda)$ . The amplitude of the Alfvén shocks at large distances is proportional to  $\exp(z/4\Lambda)$ , providing their fast exponential growth with height (Fig. 14.7). Such a behavior of the shock amplitude, however, is valid only up to the altitudes of 2.5–3 $\Lambda$  from the height of shock formation or up to the heights where Mach number reaches quite moderate values of 1.5–2 (which is earlier). As one can see from Figs. 14.6 and 14.7, in all cases this happens approximately at about the same time. After which the shock amplitude becomes independent of the Mach number and being subject to gradient acceleration, increases in accordance with the power law (Whitham 1974; Landau and Lifshits 1987):

$$u_{sh} = u_0(\rho_0/\rho)^\kappa \tag{14.26}$$

where  $u_0$  and  $\rho_0$  are shock velocity and pre-shock plasma density at the reference point, and  $\kappa = [2 + \sqrt{2\gamma/(\gamma - 1)}]^{-1}$ . For  $\gamma = 5/3$ ,  $\kappa = 0.236$  and for  $\gamma = 1.29$ ,  $\kappa = 0.201$ . Below we will use the results of this section for some quantitative estimates.

## 14.3 Energy Release in the Chromosphere-Transition Region

The universal character of the mechanism which works in wide range of physical parameters and in any place where magnetic flux tubes or loops collide and reconnect, makes the after-shock jets and radiative transients ubiquitous throughout the entire atmosphere overlying the quiet sun. To look into the mechanism deeper and use it in practice let us make some quantitative estimates based on the observational data.

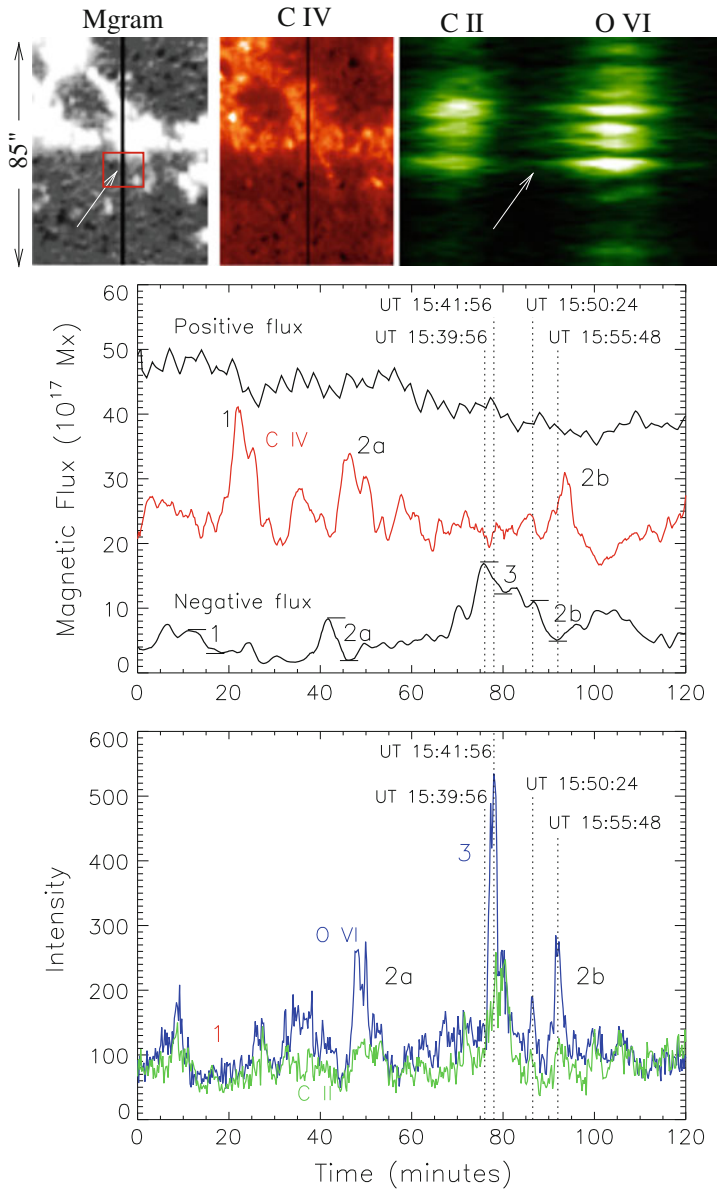
### 14.3.1 Quantitative Analysis

Consider again example demonstrating direct connection between the changes of the photospheric fields and their association with the transition region plasma flows and bright radiative transients (Fig. 14.8). The upper panels are the MDI magnetogram of the  $66'' \times 85''$  area at some instance of time and C IV image of the same region together with the SUMER spectra showing how the enhanced emission in the chromosphere/transition region mimics the photospheric magnetic pattern. The middle panel shows the time variation of positive and negative magnetic fluxes in the area marked by red square in the MDI magnetogram, and corresponding changes in the C IV intensity over this area (red line). The lower panel is the co-aligned time variation of SUMER spectra in C II (green) and O VI (blue) lines. The most prominent radiative transients produced above chosen area are marked by numbers 1, 2a, 2b, and 3.

The radiative transients highlighted in (Fig. 14.8) have very characteristic features and precursors that are most typical of the majority of the observed bright and high velocity events. The event marked by '1' corresponds to energy release in a form of a microflare alone without significant flows. Two similar events marked by '2a' and '2b' are typical to the 'HEAT-JET' regime when highly concentrated cumulative energy is distributed between the radiative transient (having the enhanced intensity in the C IV line) and plasma jets (cf. Fig. 13.5). The event marked by '3' corresponds to pure jet regime. It is remarkable that before this event quite significant portion of negative magnetic flux has been moved into the marked area. Simultaneous reduction of this newly emerged negative and pre-existed positive fluxes resulted in the series of events, the strongest of which are marked by '3' and '2b'.

As discussed through the book, these regularities are universal features of the energy buildup process that starts from the reconnection of opposite polarity elements passes through shock formation, then through shock–shock interaction that results in the release of energy in upper layers of atmosphere in one of the three forms:

- (1) microflare;
- (2) microflare accompanied by plasma jets; and
- (3) only plasma jets. The largest range of physical parameters corresponds to energy distribution between the radiative transients and plasma flows. Usually weaker microflare is accompanied by a stronger jets and v.v.



**Fig. 14.8** Microflares and jets produced by reconnecting flux tubes. *Upper panels* are the magnetogram, chromosphere in C IV line and corresponding SUMER spectra with mass flows in lower chromosphere (C II line) and transition region (O VI line); a small region marked by a *red square* in the MDI magnetogram is where the studied reconnection occurred. *Middle panel* shows the time variation of positive and negative magnetic fluxes in the marked area, and corresponding changes in the C IV intensity over this area (the *red line*); *lower panel* is time variation of SUMER spectra in C II (*green*) and O VI (*blue*) lines; Numbers *1*, *2a*, *2b*, and *3* label the events used for quantitative estimates

The time history of the photospheric magnetic fluxes (Fig. 14.8, middle panel) shows, as always, a clear connection between the magnetic flux reduction and subsequent appearance of energetic events in the chromosphere-transition region. Before we discuss these particular events in detail, let us recall that in each reconnection process only a limited portion of the magnetic flux is involved. For typical magnetic flux tubes in the photosphere a characteristic radius of magnetic flux tube participating in one elemental act of reconnection is  $\sim 40$  km (Tarbell et al. 2000). Usually, colliding flux tubes are of different sizes, but each reconnection reduces the magnetic flux of either polarity by equal amounts. In our example the positive magnetic flux belongs to a large magnetic flux concentration while the negative flux is small and isolated. Although the positive flux decreases with time, its sawtooth character caused by the measurements taken at the edge of magnetic conglomerate, is not as informative as time variation of the negative flux.

For quantitative estimates we will use the measurements of the negative magnetic flux (lower curve in Fig. 14.8, middle panel). For the background photospheric parameters we adopt a reference model by Maltby et al. (1986) where at “zero” level, ( $z = 0$ ) the plasma density  $\rho \simeq 2.8 \times 10^{-7}$  g cm $^{-3}$  and the temperature  $T = 6,500$  K; the sound speed  $c_s = 8.5$  km s $^{-1}$ , and the scale height  $\Lambda \simeq 160$  km.

First, we need to estimate the height of the shock formation,  $z_{\text{sh}}$ , (14.23), and the shock amplitude at this height which can be obtained from (14.16):

$$u_{\text{sh}}(z) = v_{A0} + v_{A0} \exp\left(\frac{\gamma + 1}{4} \frac{z}{\Lambda}\right) \frac{\sqrt{[\mathcal{I}(z) - 1]}}{\mathcal{I}(z)} \quad (14.27)$$

where  $\mathcal{I}(z)$  is the left-hand side expression of (14.21) with the running coordinate  $z$  instead of the fixed one  $z_{\text{sh}}$ :

$$\mathcal{I}(z) = \frac{4\Lambda}{(5\gamma - 3)z_{\text{sh}}^{(0)}} \left[ \exp\left(\frac{5\gamma - 3}{4} \frac{z}{\Lambda}\right) - 1 \right] \quad (14.28)$$

Note that at  $z = z_{\text{sh}}$ ,  $\mathcal{I}(z_{\text{sh}}) = 1$ , by definition.  $v_{A0}$  is the pre-shock velocity of the wave generated initially by the post-reconnection slingshot effect. This velocity is determined by the magnetic flux participating in the reconnection process,  $\Delta\Phi = \pi R^2 B$ , and the reconnection rate, (14.16), or time,  $\tau = R \ln Re_m / v_A$ . For the quantitative estimates we will use for  $\Delta\Phi$  the measured drops of the magnetic flux and for  $\tau$  the corresponding observed times in which these drops occur.

Excluding from  $\Delta\Phi$  and  $\tau$  the radius of the magnetic flux, we obtain an estimate for the Alfvén velocity:

$$v_A^3 = \frac{\Delta\Phi}{\pi\sqrt{4\pi\rho}} \left[ \frac{\ln Re_m}{\tau} \right]^2 \quad (14.29)$$

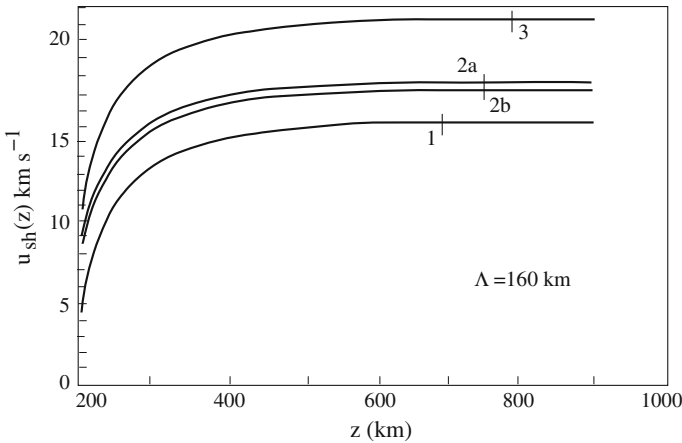
With the magnetic Reynolds number  $Re_m \simeq 10^3$  typical to the photosphere (cf. Parker 1979), measured times and corresponding magnetic flux changes give for the events 1, 2a, 2b, and 3 respectively,  $v_A = 3.61; 4.18; 4.12$  and  $4.5$  km s $^{-1}$ . These are typical values for the Alfvén velocities in the photospheric flux tubes with magnetic field strength ranging from 500 to 1,000 G:  $v_A = 2.7\text{--}5.3$  km s $^{-1}$ .

**Table 14.1** Parameters and results of quantitative estimates

Events	1	2a	2b	3
$\Delta\Phi$ ( $10^{17}$ Mx)	3.7	6.6	6.3	5.0
$\tau$ (s)	252	270	270	120
$v_{A0}$ ( $\text{km s}^{-1}$ )	3.61	4.18	4.12	4.5
$\bar{R}$ (km)	132	163	161	137
$z_{\text{sh}}^{(0)}$ (km)	549	505	514	370
$z_{\text{sh}}$ (km)	206	198	199	169
$z_{\text{sh}}^{\text{sat}}$ (km)	750	780	780	800
$u_{\text{sh}}^{\text{sat}}$ ( $\text{km s}^{-1}$ )	14.5	16.0	16.2	19.3
$M_0$	1.7	1.9	1.9	2.3

The radius of the magnetic flux participating in the reconnection process is estimated as  $R = \tau v_A / \ln Re_m$ , which gives for these four events the values: 132, 163, 161, and 137 km. Now we can find the height of shock formation corresponding to given parameters in the homogeneous atmosphere,  $z_{\text{sh}}^{(0)}$ , using (14.22), and respectively, the height of the shock formation in the stratified atmosphere,  $z_{\text{sh}}$ , using (14.27). We then find the shock amplitude,  $u_{\text{sh}}(z)$ . Results of these calculations are shown in Table 14.1 and Fig. 14.9.

One can see that height of the shock formation,  $u_{\text{sh}}$  is very close to the solar surface: from these heights shock wave quickly accelerates, and in a few scale heights gets saturated. Figure 14.9 shows the velocity of a shock as a function of the atmospheric height ( $z = 0$  corresponds to  $\rho \simeq 2.8 \times 10^{-7} \text{ g cm}^{-3}$  and  $T = 6,500 \text{ K}$ ). The vertical bars indicate the height at which the shock amplitude saturates: from there the velocity of shock, which becomes independent of the Mach number and scale height, increases



**Fig. 14.9** The shock velocity for chosen events as a function of height. The vertical bars indicate the approximate height at which the shock amplitude saturates

in accordance with the power law, (14.26), i.e., as

$$u_{\text{sh}}(z) = u_{\text{sh}}^{\text{sat}} \left[ \frac{\rho(z)}{\rho_{\text{sat}}} \right]^{0.236} \quad (14.30)$$

As expected, the shock amplitude saturates at Mach numbers  $M_0 \sim 1.5\text{--}2$  (see last line in Table 14.1). The corresponding heights are between 750 and 800 km. The mass density here is  $\rho_{\text{sat}} \simeq 4 \times 10^{-10} \text{ g cm}^{-3}$ . At height  $z = 2,000 \text{ km}$  ( $\rho \simeq 3 \times 10^{-13} \text{ g cm}^{-3}$ ), (14.30) gives following estimates for the shock velocities produced, respectively, in the events 1, 2a, 2b, and 3: 79, 87, 88, and  $105 \text{ km s}^{-1}$ .

To estimate a behind shock temperature,  $T_2 = M^2 T_1 (3\gamma - 1)\gamma^{-1}$ , at this height we adopt for the sound speed the value  $13 \text{ km s}^{-1}$  and background temperature  $T_1 = 7,300 \text{ K}$ . Then Mach numbers for each event are:  $M^{(1)} = 6.1$ ;  $M^{(2a)} = 6.7$ ;  $M^{(2b)} = 6.8$ ;  $M^{(3)} = 8$ . Respectively, the behind shock temperatures are  $T_2^{(1)} = 8.5 \times 10^4$ ;  $T_2^{(2a)} = 10.2 \times 10^4$ ;  $T_2^{(2b)} = 10.5 \times 10^4$ ;  $T_2^{(3)} = 1.46 \times 10^5$ .

The obtained estimates are the most typical for the measured and inferred physical parameters of the chromosphere and transition region.

### 14.3.2 Total Energy Flux in Quiet Sun Atmosphere

The total energy flux released by the entire quiet sun “magnetic carpet” is consistent with the observed UV/EUV radiation. It can be estimated on the basis of observed time scale ( $\sim 40 \text{ h}$ ) in which the total magnetic field in the quiet sun network is replaced (Title and Schrijver 1997). The energy release in each event of the reconnection is on the order of

$$W_{\text{mag}} \simeq \frac{B^2}{8\pi} SL \quad (14.31)$$

where  $S$  is the cross section of the interacting area,  $S = \pi R^2$ , and  $L$  is a characteristic length of the flux tube. In the quiet sun the magnetic filling factor,  $f \simeq (S/d^2) \ll 1$  ( $d$  being a characteristic distance between the flux tubes). Let the velocity of relative motion of colliding flux tubes be  $v_T$ , then a “collision” rate in the system of non-collinear flux tubes,  $n_{\parallel}$ , may be estimated as  $n_{\parallel} \simeq v_T/d$ . The number of events per unit area of solar surface per unit time, is  $N = n_{\parallel}/d^2$ . The energy released per unit area of solar surface per unit time, is:

$$E = \frac{B^2}{8\pi} SL \frac{1}{d^2} \frac{v_T}{d} \simeq \frac{B^2}{8\pi} f v_T \quad (14.32)$$

or in terms of a mean flux density  $\bar{B} = B(S/d^2) = Bf$ ,

$$E = \frac{\bar{B}^2}{8\pi} \frac{v_T}{f} \quad (14.33)$$

The velocity  $v_T$  can be estimated as  $v_T = d/\tau$ , where  $\tau$  is the time of the total replacement of the quiet sun magnetic flux,  $\tau \simeq 40$  h (Title and Schrijver 1997). This gives:

$$E = \frac{\bar{B}^2 v_T}{8\pi f} = \frac{\bar{B}^2 d}{8\pi f\tau} = \frac{\bar{B}^2 \sqrt{S}}{8\pi f^{3/2}\tau} \quad (14.34)$$

Examples: for  $\bar{B} \simeq 2$  G,  $f \simeq 5 \times 10^{-3}$ ,  $\bar{R} \simeq 200$  km, the energy flux  $\simeq 10^5$  erg/(cm<sup>2</sup> s). For  $\bar{B} \simeq 5$  G,  $f 10^{-2}$ , the energy flux  $\simeq 2.5 \times 10^5$  erg/(cm<sup>2</sup> s).

This energy supply is maintained continuously by constant addition and replacement of newly emerging small-scale network magnetic fluxes, keeping thus the chromosphere/corona above the quiet sun warm and topologically imitating the pattern of small-scale magnetic elements.

## 14.4 Magnetic Energy Avalanche and the Fast Solar Wind

What we see within a few solar radii of the solar surface as a slow and fast wind seems to be a natural consequence of the two different types of magnetic field clusters observed on the solar surface:

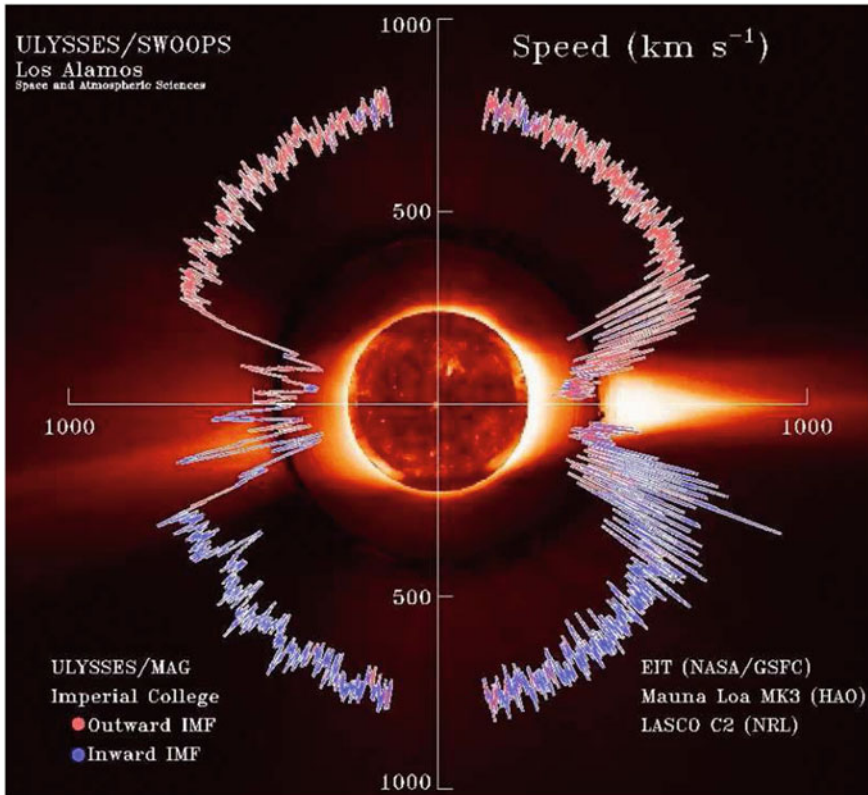
- (1) the dense conglomerates of active regions, and
- (2) the rarefied ensembles of small-scale magnetic flux tubes covering the rest, 90 % of the solar surface.

The slow wind, flowing from the sun's equatorial belt with typical velocities below 500 km s<sup>-1</sup> and having highly variable physical properties, seems to be associated with the active regions which form the near-equatorial belt of active latitudes and exhibit a strong variability over the solar cycle.

The fast wind flowing on average at 750 km s<sup>-1</sup> fills the remaining vast regions of interplanetary space and consists of highly intermittent thin streamers (Fig. 14.10). Although the small-scale structures are highly dynamic, the overall properties and background physical parameters of the fast wind appear to be almost constant (see, e.g., proceedings of the Solar Wind Eight conference, Gosling et al. 1996).

Intuitively, it is obvious that the slow wind is associated with the active regions and the fast wind with the quiet sun magnetic network. But how these two components of the solar wind are connected to their too far removed source regions, and where are they actually rooted in the Sun, were long standing questions.

Earlier studies of the solar wind has been based mainly on remote in situ measurements conducted beyond 0.3 AU. Restricted by extrapolations, high speed streamers were related to coronal holes, and, respectively, the heating and acceleration mechanisms in the fast component of the wind were based on large-scale open magnetic structures typical to coronal hole regions (Hundhausen 1977; Zirker 1977; Gosling 1995). And it was *the corona*, that has been unquestionably considered as the base of the solar wind.



**Fig. 14.10** Polar plots of the solar wind speed over Ulysses' orbit showing slow wind over the equator and a fast wind over the poles. The solar wind speed is color coded by the interplanetary magnetic field (IMF) orientation: *red* indicates outward pointing IMF, while *blue* indicates inward pointing. Both traces are overlotted on three concentric images of the Sun: the EIT Imager (*center*), the HAO Mauna Loa coronagraph (*inner ring*), and the LASCO C2 coronagraph (*outer ring*). Reprinted from McComas et al. (2000) by permission from John Wiley and Sons through Copyright 2000 the American Geophysical Union

Detailed observations of density and velocity structure in the outer corona obtained from radio occultation measurements (Woo 1996; Habbal et al. 1997; Woo and Habbal 1999) provided a link for understanding the connection between the Sun and interplanetary space by probing the solar wind before it evolves with heliocentric distance. These data combined with later ultraviolet and white light measurements of solar atmosphere, showed for example, that the density profile closest to the Sun at  $1.15 R_{\odot}$ , representing the imprint of the Sun, is carried essentially *radially* into interplanetary space by small-scale ray-like structures that pervade the entire solar corona, and that a significant fraction of mass fluxes which extend into interplanetary space originate from the quiet Sun regions, and are indistinguishable in properties from those emanating from polar coronal holes. In other words, the primary energy



source of the fast wind seems to be associated with small-scale magnetic flux tubes both, in large quiet sun regions and regions underlying coronal holes. It was also found that there is a direct connection between the fast solar wind outflow and the chromospheric magnetic network (Hassler et al. 1999).

One of the most important details of the above observations is the fact the energy flow occurs *radially* outward from the sun. This means, that no matter how complicated are the magnetic structures through the solar atmosphere from its surface, the energy that fuels the fast solar wind always finds its way vertically upward, which obviously requires action of some universal mechanism. Such a mechanism may well be associated with the post-reconnection shocks produced all over the quiet sun surface in arbitrarily magnetized environment as shown in Figs. 14.3, and 14.4. We saw that in any case, no matter what the environmental magnetic field is, even if it is horizontal (case #4), the energy released due to the post-reconnection processes always flows radially outward along the gravity. The energy content in these processes (Sect. 14.3) is comparable with the energy estimated at the base of the solar wind.

We may conclude, therefore, that the fast solar wind can originate from the entire quiet sun surface supported by the following facts:

- (1) Intense hydromagnetic activity resulting from interacting small-scale network magnetic elements in the quiet sun and regions underlying coronal holes creates the magnetic energy avalanche maintained by the continuous supply of emerging magnetic elements and their all-time reconnections;
- (2) Cumulative jet formation as an intrinsic feature of the post-reconnection dynamics of flux tubes in the arbitrary magnetic environment is always in place;
- (3) In the presence of vertical or near-vertical magnetic fields the jet formation is accompanied by the generation of high frequency Alfvén waves (Axford and McKenzie 1992);
- (4) The resulting energy flux estimated on the basis of observed time scale ( $\sim 40$  h) in which the total magnetic field in the quiet sun is replaced, is enough to explain the observed UV/EUV radiation of the order of  $5\text{--}10 \times 10^5 \text{ erg cm}^{-2} \text{ s}^{-1}$ ;
- (5) The high rate of the emergence of new fluxes and diversity of their parameters result in the cascade of shock waves, creating thus magnetic energy avalanche and relatively steady energy input into higher layers of atmosphere: short recycling time of total magnetic field in the quiet sun network ensures that produced energy flux will be uniformly felt in the corona. This in turn provides the observed steady character of the fast wind;
- (6) The most efficient energy transport provided by the gradient acceleration in strongly stratified photosphere/chromosphere region and occurring radially outward from solar surface, strongly supports the observations showing that the fast solar wind may be organized in a form of small-scale filamentary ray-like structures diverging radially outward from the solar surface.

It is important to note that the purpose of this section is to address the problem of primary energy source that may originate the fast wind. A priori it is clear that there is no other energy than that stored in the convective zone and highly dynamic

magnetic network that could produce the quiet sun corona and start the fast wind. This mechanism seems to provide a natural way of the energy transfer from a huge photosphere/convective zone energy reservoir to upper layers of atmosphere and is consistent with the observed properties of heating and high-velocity events in the bottom of the fast wind. Obviously, these processes occur at much earlier stages (and at much lower altitudes) than the body of the wind is formed and get accelerated. The link between these two stages is subject of future studies.

## References

- N.I. Asano, T. Taniuti, *J. Phys. Soc. Jpn.* **29**, 209 (1969)  
 W.I. Axford, J.F. McKenzie, *Solar Wind Seven* (Pergamon Press, Oxford, 1992)  
 S.R. Cranmer, *LRSP* **6**, 3 (2009)  
 J.T. Gosling, *Geophys. Res. Lett.* **22**, 3329 (1995)  
 J.T. Gosling, S.R. Habbal, W.S. Kurth, M. Neugebauer (eds.), *Solar Wind Eight* (AIP, New York, 1996)  
 S.R. Habbal, R. Woo, S. Fineschi, R. O'Neal, J. Kohl, G. Noci, C. Korendyke, *Astrophys. J. Lett.* **489**, 103 (1997)  
 D.M. Hassler et al., *Science* **283**, 810 (1999)  
 A.J. Hundhausen, in *Coronal Holes and High Speed Wind Streams*, ed. by J.B. Zirker (Colorado Association University Press, Boulder, 1977), p. 225  
 A. Jeffrey, T. Taniuti, *Non-linear Wave Propagation* (Academic Press, New York, 1964)  
 L.D. Landau, E.M. Lifshits, *Fluid Mechanics* (Pergamon Press, Oxford, 1987)  
 D.J. McComas et al., *JGR* **105**, 10419 (2000)  
 P. Maltby et al., *Astrophys. J.* **06**, 284 (1986)  
 G. Nistico et al., *Adv. Space Res.* **48**, 1490 (2011)  
 L.A. Ostrovskii, N.R. Rubakha, *Radiophys. Quantum Electron.* **15**, 986 (1974)  
 E.N. Parker, *Cosmical Magnetic Fields* (Clarendon Press, Oxford, 1979)  
 H.E. Petschek, *NASA Spec. Publ.* **SP-50**, 425 (1964)  
 M. Ryutova, J. Sakai, *JETP Lett.* **58**, 507 (1993)  
 M.P. Ryutova, T.D. Tarbell, *Astrophys. J.* **541**, L29 (2000)  
 R.Z. Sagdeev, in *Review of Plasma Physics*, ed. by M.A. Leontovich (Consultants Bureau, New York, 1966)  
 I.V. Sokolov, *Sov. Phys. Uspekhi* **33**, 960 (1991)  
 T. Tarbell, M. Ryutova, J. Covington, A. Fludra, *Astrophys. J.* **514**, L47 (1999)  
 T. Tarbell, M. Ryutova, R. Shine, in *Solar Physics* (2000), in press  
 A.M. Title, C.J. Schrijver, in *Cool Stars, Steller Systems, and the Sun*, ed. by R. Donahue, J.A. Bookbinder, (Astronomical Society of the Pacific Conference Series 1997)  
 G.B. Whitham, *Linear and Nonlinear Waves* (Wiley, New York, 1974)  
 R. Woo, *Nature* **379**, 321 (1996)  
 R. Woo, S.R. Habbal, *Astrophys. J.* **510**, L69 (1999)  
 J.S. Zhao, D.J. Wu, J.Y. Lu, *Astrophys. J.* **735**, 114 (2014)  
 J.B. Zirker (ed.), *Coronal Holes and High Speed Wind Streams* (Colorado Association University Press, Boulder, 1977)

## Chapter 15

# Response of the Corona to Magnetic Activity in Underlying Plage Regions

**Abstract** The fact that corona is strongly inhomogeneous in space and evolves in time in very different ways means that the processes of energy production, flow, and release have several branches. The processes of the extraction of energy stored in the photosphere, strongly depend on the magnetic filling factor, i.e., whether we deal with the quiet sun network, plages, or active regions. So far we were studying rarefied ensembles of flux tubes typical to quiet sun. In this chapter, we move to denser ensembles of flux tubes typical to plages and consider the response of the upper atmosphere to magnetic activity in underlying plage regions. We will see that the character of the EUV emission above plage regions that are dominated by single polarity magnetic elements, i.e., unipolar plages, always has an amorphous shape that topologically mimics the shape of the underlying plage. Contrary to this, the EUV emission above mixed polarity plages is highly discrete and consists of sporadic localized radiative transients. Such a different response of the chromosphere/corona to unipolar and mixed polarity plages obviously implies the action of different mechanisms for energy production, flow, and release. In all cases, however, the primary energy source lies in continuous hydromagnetic activity among the photospheric magnetic fields. It is just the character of this activity, different in differently magnetized regions, that determines the processes of the extraction of energy and its transport throughout the solar atmosphere.

### 15.1 Magnetic Imprint of Plage Regions in the Corona

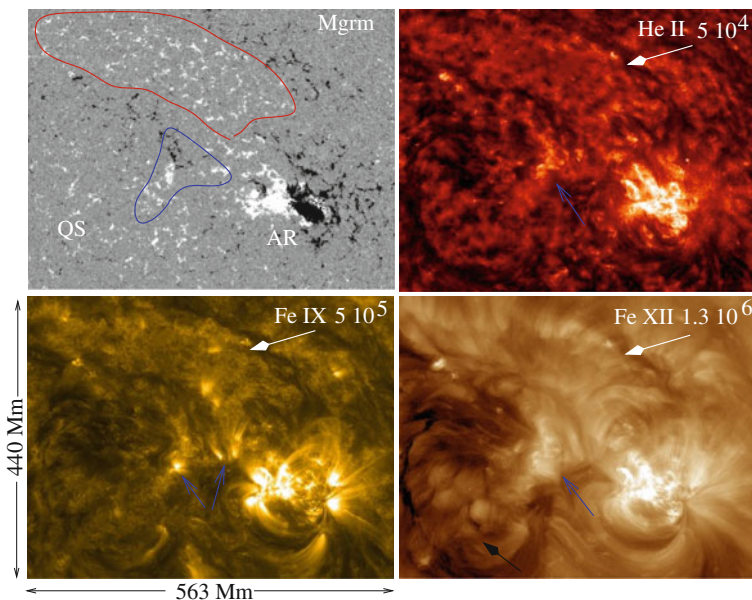
A great variety of the coronal structures, from large-scale steady loops associated with active regions, amorphous structures seen above unipolar plages, all kinds of flares and microflares, evolve in time in different ways and have underneath (at the photosphere) very different patterns of magnetic fields and plasma flows. It is, however, obvious that despite of all the diversities of the observed phenomena, the primary energy source is associated with the photospheric magnetic fields.

The specifics of the photospheric magnetic fields, and their interaction with highly dynamic environment determine in large the action of particular physical mechanism of energy production and its flow into upper layers of atmosphere. These mechanisms lead, in the first place, to formation of one or the other type of chromospheric and

coronal structures, reflecting the composition of the underlying photosphere, and then to the release of incoming energy. It is important that along the filling factor, a decisive role in the energy production is played by the dominant polarity of the region. This is especially prominent in plages and quiet sun regions which may either consist of mixed polarity elements or be dominated by one polarity features. This is also true for sunspots and active regions where inclusions of opposite polarity elements are permanently observed.

Response of the chromosphere and corona to hydromagnetic activity in these largely different magnetic clusters is quite different. We have already seen that regions with mixed polarity flux tubes in quiet sun produce localized microflares and jets in the overlying chromosphere and corona. In this chapter, we will see that the EUV emission above unipolar plages has the amorphous structure and very peculiar braidlike behavior in time. As in case of mixed polarity regions, the chromosphere and corona above the unipolar regions also mimic magnetic topology of underlying photosphere.

Figure 15.1 represents a typical view of the sun's region containing various clusters of magnetic elements and its overlying chromosphere and corona. The images are taken on January 10, 2012 by the AIA and HMI instruments on the SDO. The top



**Fig. 15.1** Snapshots of an ordinary region of the sun containing various kinds of magnetic structures: the active region (AR), unipolar plage (demarcated by the *red* contour in the magnetogram), mixed polarity plage (demarcated by the *blue* contour), and quiet sun (QS). A huge body of a fuzzy emission in the chromosphere and corona overlying the unipolar plage region reflects the shape and location of the plage. The same is true for sporadic events occurring above the mixed polarity plage (the *blue* arrows). The images are taken by the SDO instruments in four wavelengths on January 10, 2012. Field of view is 440Mm  $\times$  563Mm

left panel is a magnetogram containing the active region (AR), unipolar plage (the red contour), mixed polarity plage (the blue contour), and quiet sun (QS). The top right panel is the overlying chromosphere at  $5 \times 10^4$  K in the He II line. Two bottom panels are the corona at  $6.5 \times 10^5$  and  $1.3 \times 10^6$  K temperatures in Fe IX 171 and Fe XII 193 lines, respectively. The white arrows in the chromosphere and coronal images show a huge body of the amorphous emission that overlies and mimics the magnetic pattern of a unipolar plage. The blue arrows show sporadic events in the chromosphere and corona localized above mixed polarity plage. The hot coronal loops and sporadic events overly the active region. Note that the chromospheric emission above the quiet sun has a discrete character, obviously associated with the isolated network elements. Higher in the corona the emission above the quiet sun becomes diffusive. It is interesting that this emission often looks “perforated”, which is well seen in the Fe XII 193 line (bottom right). The dark lanes making the bushy pattern coincide with supergranular lanes. These are the sites of spicules whose cool material protrudes the hot coronal plasma.

## 15.2 Coronal Dynamics Above Unipolar and Mixed Polarity Plages

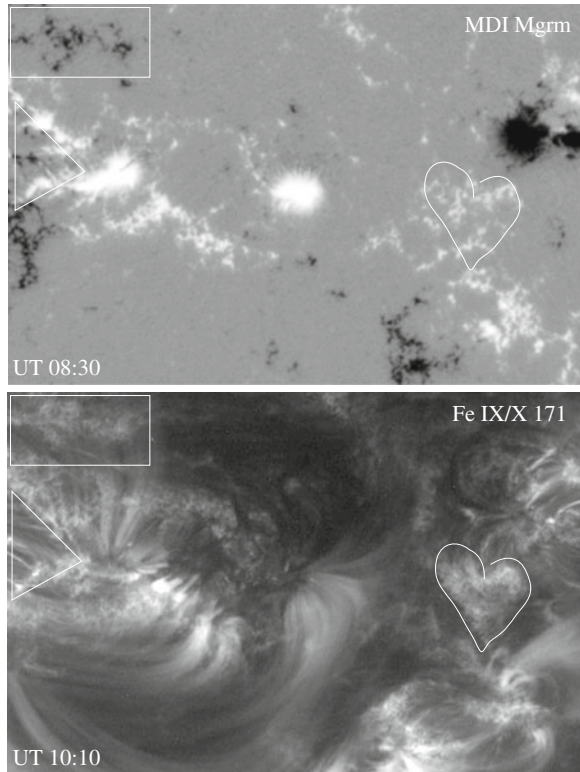
To illustrate the details of the photosphere/corona coupling and see associated regularities between the coronal emission and the underlying chromosphere and photosphere, we use multiwavelength observations from the TRACE instruments and the MDI on SOHO.

The analyzed data sets, obtained on June 10, 1999, consist of time series of high resolution MDI magnetograms co-aligned with the TRACE 1,600 Å, Fe IX/X 171 Å and Fe XII 195 Å lines. The data cover a  $166'' \times 270''$  area near disk center. There are several sunspot groups and both types of plages, unipolar and mixed polarity. The period of observation is over 10h. Figure 15.2 shows a sample MDI magnetogram (top) and overlying corona in Fe IX/X 171 Å line (bottom). One can see three sunspots in the region and several plages. The region marked by a triangle is a typical mixed polarity plage, rectangular- and heart-shaped regions are examples of unipolar plages.

The corona above the sunspots and plages shows all kinds of formations: steady large-scale loops, patchy amorphous structures, X-ray bright points, and various radiative transients. To study temporal variability of these formations, the data were compiled in co-aligned movies with a 15 s cadence to use again the procedure of spacetime cuts, and follow the motions of various bright patches lying along the cut (Ryutova and Shine 2004). Simultaneous movies taken in the TRACE 171, 195, and 1,600 Å lines allow to study a character of temporal behavior of the enhanced emission at different heights and temperatures. Figure 15.3 shows snapshots of corona at two temperatures with five spacetime cuts shown by straight lines and marked by numbers 1–5.

The near horizontal slices are made from left to right; the vertical slices are made from top to bottom. Note that the difference between the start times of these two sets is about 6h, and yet the properties of the hotter  $\lambda$  195 emission are remarkably similar to those of  $\lambda$  171.

**Fig. 15.2** Aligned MDI and TRACE images taken on June 10, 1999. MDI magnetogram is scaled from  $-1,000$  to  $1,000$  G. Field of view  $120\text{ Mm} \times 196\text{ Mm}$ . The region demarcated by a *triangle* is an example of plage with mixed polarity magnetic elements; *rectangular*- and *heart-shaped* regions are examples of unipolar plages



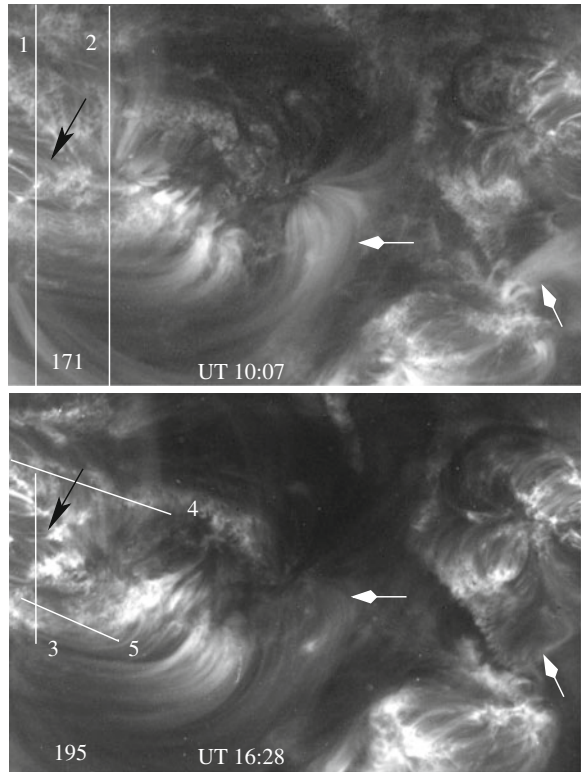
Spacetime slices reveal clear differences in the properties of the emission at the coronal and chromospheric temperatures associated with the sunspot and plage regions.

Intersections through large-scale coronal loops (marked by curved arrows in Fig. 15.4) show a slow process of brightening up and dimming down. These are long-living quasi-steady loops showing transverse oscillations accompanied by merging and splitting processes.

The enhanced emission above the unipolar plages is *always* of amorphous texture. When observed in high cadence time series this fuzzy emission shows extremely sturdy well organized coherent structures having braidlike appearance. These are indicated by thin white arrows in Fig. 15.4.

Braidlike coherent structures remain regular as long as the plage preserves its properties. They are not affected by overlying or neighboring coronal loops. Their destruction is associated only with the emergence of opposite polarity magnetic elements in the unipolar plage. Such an event is marked, for example, by the thick white arrow in the top left panel of Fig. 15.4. Just before the appearance of a compact flare, additional magnetic flux of the opposite polarity has emerged in the underlying plage, and destroyed the braided coherent structure. This interesting phenomena were discovered by Shine (1999). We will see below that the braidlike structures

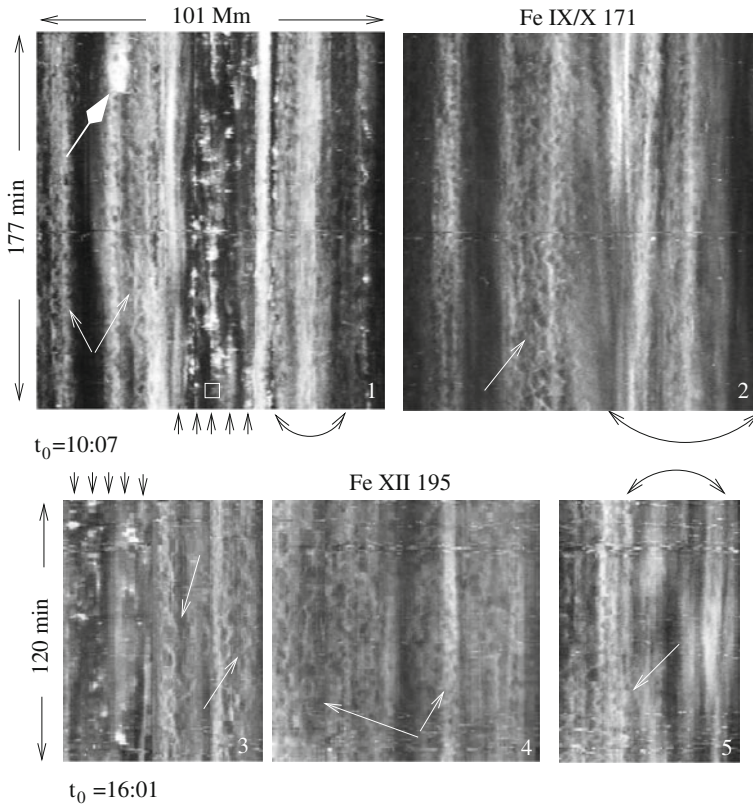
**Fig. 15.3** Snapshots of the entire field of view at  $T \simeq 10^6$  K (171 Å) and  $T \sim 2 \times 10^6$  K (Fe XII 195 Å). The *straight lines* marked by numbers 1–5 are the spacetime cuts unfolded in Figure 15.4. It is remarkable that large-scale loops, prominent in 171 Å (*white arrow*) faded significantly in the Fe XII 195 Å line, while all spongy structures seen in the 171 Å emission remain in place at the higher temperatures. Note that time difference between 171 and 195 Å snapshots is 6 h 20 min, and yet the amorphous emission in both coronal *lines* mimics closely the magnetic pattern of unipolar plagues. *Black arrows* mark a mixed polarity plate



are ubiquitous for the corona overlying the unipolar plagues and have very natural explanation (Ryutova and Shine 2004).

Contrary to long-living braidlike structures, coronal emission above mixed polarity plagues is highly discrete and consists of frequent localized transients, resembling a continuous irregular firework.

The system of mixed polarity magnetic elements intrinsically prevents the formation of coherent structures. This is clearly seen in the spacetime cut # 1 (Fig. 15.4). This cut (made from top to bottom) first crosses a negative polarity unipolar plague (see Fig. 15.3, upper panel), then enters the region of mixed polarity plague (black arrows in Fig. 15.3), and finally crosses the site of quasi-steady loops. Accordingly, the spacetime image (Fig. 15.4 upper left panel) shows first a braided coherent structures, then frequent sporadic microflares (marked by the set of short arrows), and finally the “lazy” motions of quasi-steady loops. Another cut through this area is made in the hotter 195 Å line (cut # 3 in Fig. 15.3, lower panel). One can see that sporadic radiative transients produced by the mixed polarity plague are as frequent at  $2 \times 10^6$  K temperatures as in lower corona. It is important that coherent structures are also formed at  $2 \times 10^6$  K temperatures (cuts 3–5), and have the same properties and longevity as their counterparts in lower corona.

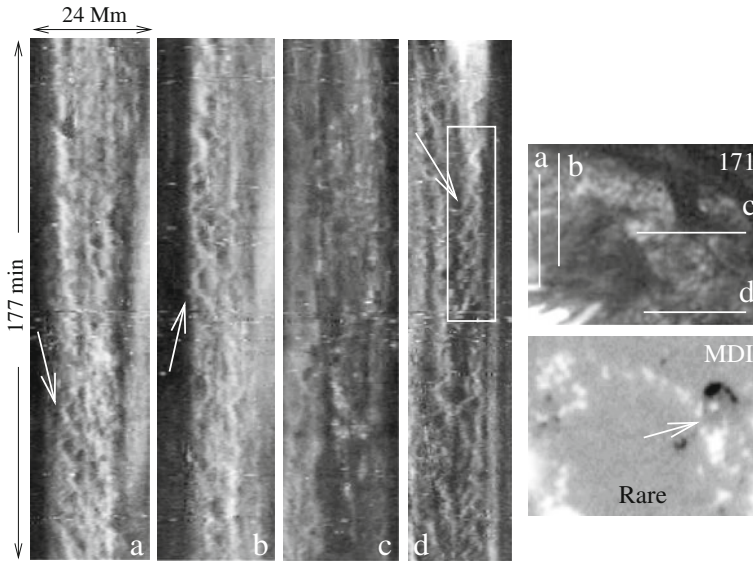


**Fig. 15.4** Examples of the spacetime tracks along *lines* 1–2 in Fe IX/X 171 images (*upper panels*) and along *lines* 3–5 in Fe XII 195 images (*lower panels*). All over the chosen area coherent braidlike structures are well seen above each unipolar plage (some are marked by *thin white arrows*); the mixed polarity plage produces a frequent radiative transients—jets and microflares, hot enough to be seen at  $10^6$  K (series of *small arrows* along slices 1 and 3). Thus, the response of corona to hydrodynamic activity in a unipolar and mixed polarity flux tubes is radically different. *Curved arrows* demarcate intersections through long-living quasi-steady coronal loops with their subtle motions and slow intensity variations

### 15.3 Properties of Braidlike Coronal Structures

The braidlike structures, being quite similar, still have quite distinguishable properties from one region to another. One of the main causes affecting them is magnetic filling factor of underlying plage. To see what can we learn from comparing the various regions, we choose the most typical cases that may be characterized as *Rare*, *Medium*, and *Dense* plages. These are illustrated in Figs. 15.5a–d and 15.6e–h. Each figure contains the snapshots of the magnetogram and its overlying corona in Fe IX/X 171. Spacetime slices made over the coronal emission are represented as always by white



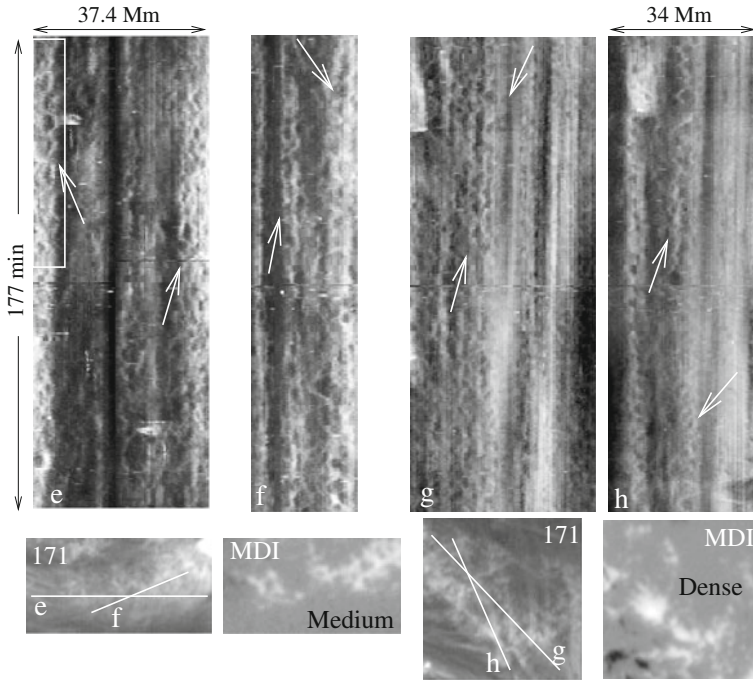


**Fig. 15.5** Some properties of the coherent structures: (1) They have an isotropic nature (cuts **a–b**); (2) The braid period depends on the plage magnetic filling factor; (3) Emergence of opposite polarity fluxes destroys the well organized structures (spacetime image **c**); (4) The braidlike structure along cut (**d**) remains quite regular until the appearance of a “mini-flare” caused by emergence of an opposite polarity flux tube in the photosphere. *White box* are used for quantitative analysis

lines. The time interval is 177 min. Analyzing these figures we may summarize some general properties of the coherent structures as follows.

First of all, the braidlike structures have an isotropic nature. One can see that two parallel cuts, *a* and *b* in Fig. 15.5 over a rarefied plage show similar spacetime behavior. The same is true in case of *medium* plage, demonstrated by cuts *e* and *f* which are made under different angles, and in case of densely populated plage shown by cuts *g* and *h* (Fig. 15.6).

The next important feature of the coherent structures, as we have already mentioned, is their sturdy character. Once formed, they remain regular as long as their underlying plage remains unipolar, which may usually last for hours. Their destruction, sometimes only temporary, occurs if there is emergence of opposite polarity magnetic flux. This is shown in panel *c*, Fig. 15.5 and panels *g* and *h*, Fig. 15.6. In the first case, along the cut *c* a group of negative polarity elements emerged (around the region marked by white arrow in the magnetogram). Interaction of opposite polarity flux tubes totally destroyed the braidlike structures replacing them by frequent sporadic microflares. Note that neighboring coherent structures are not affected by the whole series of radiative transients (cut *d*). In two other cases, along the cuts *g* and *h* (Figs. 15.6) a single opposite polarity element emerged around UT 12:27 and caused appearance of a mini-flare that temporarily destroyed coherent structure. This is also seen in spacetime images *g* and *h*. A flare that appeared at UT 12:27



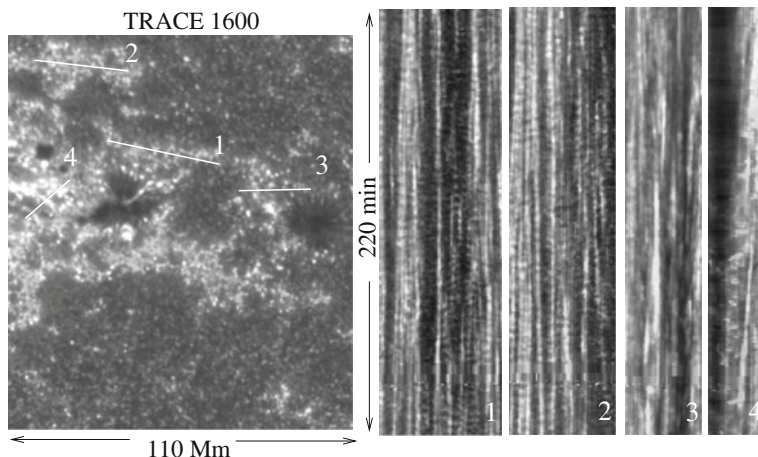
**Fig. 15.6** Properties of the coherent structures (cont.) over medium and densely populated plages showing a ubiquitous nature of a spectacular braidlike structure

(cf. Figure 15.4, panel 1, thick white arrow) destroys only its “own” structures while neighboring structures (to the right) remain unaffected.

The braid period depends mainly on the magnetic filling factor of the underlying plage. The braid period is in fact, a time interval between two neighboring peaks of intensity, and thus is directly measurable. As a result, one finds that the denser the plage, the shorter is the braid period. Using the above observation one gets following. The rarefied plage with a magnetic filling factor,  $f \simeq 0.2$ , produces a coronal emission with a braid period  $T \simeq 20$  min. For a denser, *medium* plage with  $f \simeq 0.3$ ,  $T \sim 10$  min. Above the dense plage *Dense* with  $f > 0.4$ , the braid period is  $T \sim 6$  min. The filling factors were computed from the MDI magnetograms as a fraction of plage area covered by the magnetic field.

To better understand the properties and nature of the coronal emissions above the unipolar and mixed polarity plages, it is important to examine the properties of the underlying chromosphere/transition region, which is the first to respond to magnetic activity in the photosphere. As expected, there is a clear difference between the response of the chromosphere to dynamic changes in the unipolar and mixed polarity plages.

Figure 15.7 is an example of the analyzed data sets. Shown is the eastern part of the studied region in TRACE 1,600 Å, corresponding to a range of temperatures



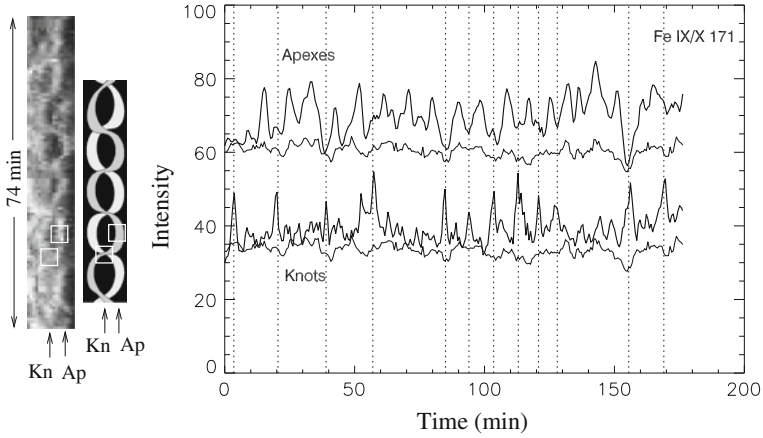
**Fig. 15.7** Spacetime images in the chromosphere. *Cuts 1 and 2* are made over the unipolar plages, while *cuts 3 and 4* are made over the mixed polarity plages. *Panels 1 and 2* show a regular oscillations of intensity corresponding to waves with 3–6 min period; *Panels 3 and 4* show both, long lasting and brief sporadic brightenings typical to chromosphere overlying mixed polarity plage

in the interval  $T \sim 6 \times 10^4 - 2.5 \times 10^5$  K. Spacetime cuts 1 and 2, made over the unipolar plages, show the typical pancakes—regular chromospheric oscillations with periods 3–6 min. Cuts 3 and 4 made over the mixed polarity plages show all kinds of sporadic brightening from quite strong and long lasting ones (marked by white arrow on the image (3)), to whole series of short-living UV flashes (see image (4)). These brightenings turned out to be precursors of coronal radiative transients.

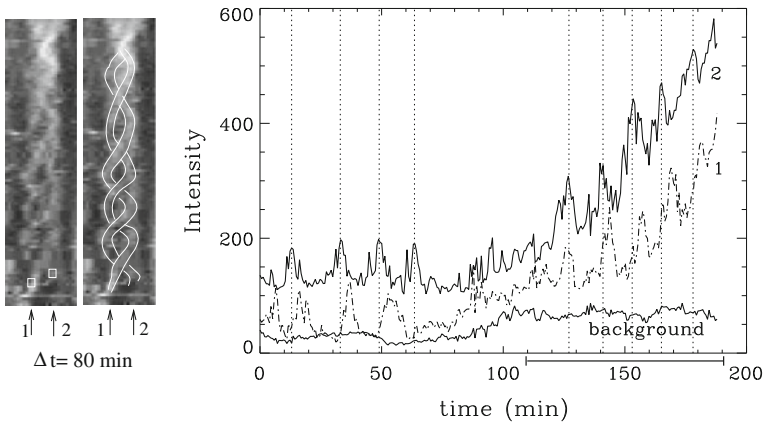
## 15.4 Comparison of Coronal Emission Above Mixed Polarity and Unipolar Plages

Long lifetime and sturdy character of the coronal emission above plage regions allow to perform quantitative analysis of the observations. For example, the spacetime images, which themselves carry valuable information for diagnostics, may be complemented by the intensity variation over a particular area. To demonstrate such an approach, let us allocate several small regions with the area size of some  $S \simeq 2.2 \text{ Mm} \times 2.2 \text{ Mm}$ , and, using the movies, compute the time variation of intensities in these areas. Three examples of such a procedure are shown in Figs. 15.8, 15.9, and 15.10.

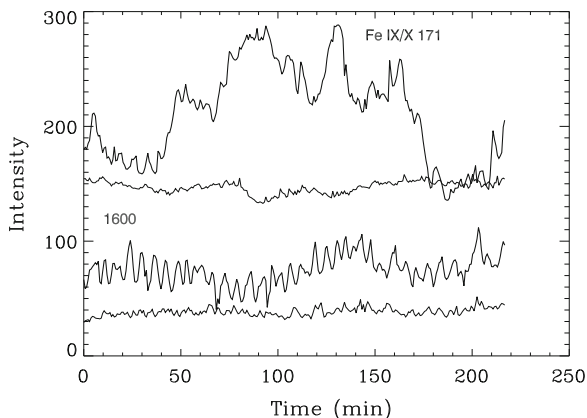
Figure 15.8 represents the coherent emission above the unipolar plage, marked by white rectangle in Fig. 15.6e. A blown up view of this region and a corresponding sketch are shown in Fig. 15.8, left. Small white squares in these images demarcate locations corresponding to the apex of the emission and knots over which the intensity curves are computed. These are shown in right panel of Fig. 15.8. As expected, maximums of intensity in the knot region coincide with minimums of intensity in the



**Fig. 15.8** Intensity curves of the Fe IX/X 171 emission radiated from two  $2.2\text{ Mm} \times 2.2\text{ Mm}$  regions located in the apex and in the knot of the braidlike emission. *Left* Spacetime slice of the exemplary region (elongated box in Fig. 15.6e) and its sketch; white squares indicate the apex (Ap) and knot (Kn) regions where the intensities are measured. *Right* Thick lines show the intensity variation in the knot and apex regions during the 177 min period, and thin curves represent an average background intensity. Maximums in the knot region correlate with minimums in the apex region, and appear with about 10 min periodicity



**Fig. 15.9** Temporal behavior of the Fe IX/X 171 emission radiated above the rarefied plage region along the slice d (Fig. 15.5d, white box). Two left panels show a braided behavior of the emission. The right panel contains the intensity curves measured for  $2.2\text{ Mm} \times 2.2\text{ Mm}$  regions confined in small white boxes: (1) the “left” apex and (2) the “right” apex. Maximums in the “left” and “right” apices are slightly shifted with respect to each other enhancing the visual impression of braidlike appearance. Period is about 15 min. Thin lower curve represents an integrated background intensity in the right panel. A strongly enhanced emission during last 70 min is caused by the emergence of the opposite polarity flux and its interaction with the existing magnetic elements



**Fig. 15.10** Intensity curves measured for  $3 \times 3$  arcsec regions (Fig. 15.4, cut 1): upper curve in Fe IX/X 171 emission line is computed above the mixed polarity plage (short arrows in Fig. 15.4), and shows series of significant flares and microflares of various durations; lower curve in the chromospheric 1,600 emission line is computed above unipolar plage (Fig. 15.7, cut 2), and shows regular oscillations with period less than 5 min. Thin curves represent corresponding background intensities

apex region, and vice versa. The braid period here is about 10 min. The intensities are in arbitrary units. To emphasize the significance of signal of the enhanced emission, we plot the integrated background intensity curves, which are shown for comparison by thin solid lines.

Figure 15.9 also represents the temporal variation of spongy emission above the unipolar plage. The left panel is the spacetime sample marked by white box in Figure 15.5d. One can see an unmistakable braidlike structure of the emission. To enhance the visual effect we made a sketch of a segment marked by box in left panel, trying to follow the intensity borders as they look. One can notice that in this case, “left” and “right” apices’ are slightly shifted with respect to each other. The measured intensity variations over these areas are shown in the right panel of Fig. 15.9. Both peaks appear with about 15 min periodicity. A longer period of these braided structures (compared to previous example) is consistent with the fact that underlying plage region in this case is more rarefied.

Note also that in this case toward the end of observations coronal emission gets strongly enhanced, but still preserves its oscillatory pattern. The enhancement is caused by emergence of a small-scale opposite polarity flux tubes, which by interacting with the existing magnetic flux tubes supply enough energy to enhance the emission, but not destroy the structure itself.

Totally different is the behavior of coronal emission above the mixed polarity plage. Examples of the intensity curves for the Fe IX/X 171 emission line above mixed polarity plage ( $2.2 \text{ Mm} \times 2.2 \text{ Mm}$  white square above the short arrows in upper left panel of Fig. 15.4) are shown in Fig. 15.10 together with the intensity curve measured for TRACE 1,600 above the unipolar plage (Fig. 15.7, cut 2). The

upper, Fe IX/X 171 emission curve is measured above  $2.2 \text{ Mm} \times 2.2 \text{ Mm}$  area marked by white square above the short arrows in upper left panel of Fig. 15.4. The lower, 1,600 emission curve is measured over the region with cut 2 in Fig. 15.7. Thin curves represent corresponding background intensities.

A series of million degree radiative transients of various durations are clearly seen in the upper curve of Fig. 15.10. Contrary to this, UV emission above the unipolar plage (“pancakes”) shows regular oscillations with about 270 s period. Generally, period of these oscillations ranges between 3 and 6 min. Note that in most cases 1,600 oscillations are modulated. One can see that in this particular case the modulation period is about 120 min.

Obviously, the physical processes behind the observed regularities in the chromosphere/coronal emission are directly associated with the mechanisms of the energy extraction from the photospheric magnetic fields, and must be different for differently magnetized regions. Phenomenology of these processes is a subject of the next section. Before we turn to this, it is useful to briefly summarize the results of this section.

Plage dominated by unipolar magnetic flux tubes:

1. The enhanced emission in TRACE 1,600 ( $T \sim 6 \times 10^4 - 2.5 \times 10^5 \text{ K}$ ), Fe IX/X 171 Å, and Fe XII 195 Å ( $T \sim 10^6$  and  $T \sim 2 \times 10^6$ ) lines mimic the plage magnetic pattern.
2. The emissions in Fe IX/X 171 Å and Fe XII 195 Å lines exhibit coherent braidlike structures in spacetime images, and have an isotropic character. The structures remain regular as long as an underlying plage preserves its general properties. The braid period depends on the magnetic filling factor of plage: the denser the plage, the shorter the braid period.
3. There is no direct connection between the *coronal* emission and individual magnetic elements. Moreover, the actual distribution of individual magnetic elements inside the plage does not play a role. Whatever irregular pattern they form inside the plage, the coherent structures are regular and occupy an area somewhat larger than the plage but with boundaries which follow closely the demarcation line of the unipolar plage region.
4. The only factor observed to disrupt these structures was the emergence of the opposite polarity magnetic field in the plage dominated by one polarity magnetic elements.
5. The emission in TRACE 1,600 Å, corresponding to chromosphere and transition region temperatures not only mimics the general shape of underlying plage, but traces the individual magnetic flux tubes to the limit of their resolution.
6. The spacetime images in TRACE 1,600 Å show typical regular oscillations with 3–6 min period seen in spacetime images as pancake structures.

Mixed polarity plage:

1. The enhanced emission in TRACE 1,600 ( $T \sim 6 \times 10^4 - 2.5 \times 10^5 \text{ K}$ ), Fe IX/X 171 Å, and Fe XII 195 Å ( $T \sim 10^6$  and  $T \sim 2 \times 10^6$ ) always exists above the mixed polarity plages, but has a discrete nature.

2. The emission in Fe IX/X 171 Å and 195 Å lines shows a random set of sporadic radiative transients in the region confined by boundaries which coincide with the general boundaries of the underlying plage.
3. There is a correlation between the numbers of radiative transients and the density of mixed polarity flux tubes.
4. Mixed polarity plages intrinsically prevent formation of any kind of stable structures and fill the coronal space by randomly distributed frequent flares and microflares.
5. The emission in TRACE 1,600 Å is quite irregular and dynamic, but traces closely the magnetic pattern of underlying plage.
6. The spacetime images in TRACE 1,600 Å show random “flashes”—localized, sporadic brightening which may be attributed as precursors for the coronal radiative transients.

## 15.5 Energy Extraction Mechanisms from the Ensembles of Photospheric Flux Tubes

In this section, we discuss a phenomenology of physical processes that may extract the energy stored in the plages and provide the transport of this energy into upper layers of atmosphere. These processes include the formation of a million degree plasma exhibiting regular structures observed above the unipolar plages, and sporadic radiative transients above the mixed polarity regions. It is important, that in the first case, the mechanism should explain not only the fact that the regular coronal structures are observed only above the unipolar plages, but also two different characteristic time scales: the short period of braiding and the longevity of their duration. As to the second case, i.e., energy production and transfer in mixed polarity plages, the physical processes here must be similar to those in the quiet sun region where mixed polarity flux tubes form a rarefied ensembles and sustain ubiquitous reconnection events. The main difference, however, is that the reconnection and post-reconnection processes that occur in the quiet sun regions, are strongly intensified in plages due to higher magnetic filling factor. This will be discussed below before we turn to the problem of unipolar plages.

### 15.5.1 Mixed Polarity Plage

In previous chapters, we saw that the photospheric reconnections between the opposite polarity flux tubes lead to multistep process of energy buildup that involves formation of post-reconnection shocks and their further evolution. As a result, the final energy release falls into three main classes of radiative transients:

- (1) strong localized emissions, just microflares, not exhibiting significant flows of material;

- (2) microflares with lesser intensities, but accompanied by one or two directional plasma jets: as a rule, stronger microflare corresponds to lower velocity jets, and *vice versa*;
- (3) strong supersonic jets and explosive events not associated with

microflares. The appearance of any kind of radiative transients usually correlates with canceling mixed polarity magnetic elements. Moreover, the observations clearly show that the sequence of events that start with cancellation of the photospheric magnetic fields, pass through shock formation, and result in the transition region radiative transients—microflares, jets, and their combinations—have a universal character and are ubiquitous.

It is important to emphasize again that the photospheric reconnection is only a triggering mechanism for multistep processes of post-reconnection shocks and their subsequent interaction. These processes, as we saw, occur higher in the atmosphere at a large distance from the reconnection area where post-reconnection shocks are already well developed and lead to hydrodynamic cumulation of energy.

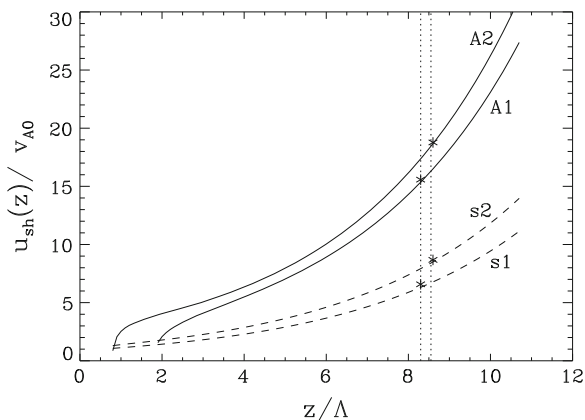
The similar processes occur obviously, in mixed polarity plage regions. Here, however, magnetic filling factor is much higher than in the quiet sun regions, and shock production is strongly enhanced. Respectively, the rate of appearance of jets and microflares, significantly increases. Besides, unlike a quiet sun where flux tubes reconnect in almost nonmagnetic environment, in plage regions with higher magnetic filling factor flux tubes may collide and reconnect in the environment of arbitrarily oriented magnetic fields (see Figs. 14.3 and 14.4, Chap. 14). In this case, along the acoustic branch, there are MHD and Alfvén waves which propagate much higher into the atmosphere and result in the generation of a million degree coronal jets and microflares.

In the case of the acoustic branch, as we have seen, the shock amplitudes saturate at heights where the Mach number reaches quite moderate values of 1.5–2 (this corresponds to 2–4 scale heights). After that the shock amplitude becomes independent of the Mach number and being subjected to gradient acceleration, increases in accordance with the power law (Whitham 1958; Stanyukovich 1960; Landau and Lifshitz 1987).

In the case of the MHD and Alfvén branches, their steepening starts at much higher altitudes, and their shock amplitudes do not saturate, but rather increase exponentially from heights where their Mach numbers reach values of 1.5–2 (Jeffrey and Taniuti 1964; Ryutova et al. 2001).

Figure 15.11 shows the shock amplitude for the acoustic and Alfvén waves as a function of height for two sets of initial parameters of flux tubes. Plots for acoustic shocks are produced with the parameters taken from the observations of a very quiet sun region presented in Ryutova et al. (2001). In particular, line 1 in Fig. 15.11 corresponds to a magnetic flux reduction of  $\Delta\Phi = 3.7 \times 10^{17}$  and reconnection time  $\tau = 252$  s; line 2 corresponds to  $\Delta\Phi = 5.0 \times 10^{17}$  and  $\tau = 120$  s (cf. Fig. 6 and Table 1 in Ryutova et al. 2001). The calculated temperatures produced in these cases are respectively,  $T^{(s1)} = 8.5 \times 10^4$ ,  $T^{(s2)} = 1.46 \times 10^5$ , and are consistent with the transition region temperatures. Plots for the Alfvén shocks are obtained assuming that the similar flux tubes collide and reconnect in the vicinity of the external magnetic





**Fig. 15.11** Comparison of the shock amplitudes as a function of height: *dotted lines* correspond to the acoustic shocks generated by reconnection of magnetic flux tubes in nonmagnetic environment; *solid lines* are the amplitudes (actually Mach numbers) of the Alfvénic shocks generated by the reconnection of flux tubes in the neighborhood of other magnetic structures. Lines s1–A1 correspond to shock resulted from the magnetic flux reduction of  $\Delta\Phi = 3.7 \times 10^{17}$ , and lines s2–A2 are obtained for flux reduction of  $\Phi = 5.0 \times 10^{17}$ . Alfvén shocks accelerate faster and dissipate their energy with much more efficiency than the acoustic shocks, producing temperatures close to 1 MK

field. If the Alfvén shocks dissipate at the same height as their acoustic counterparts (as shown by stars in Fig. 15.11), the plasma temperature would increase up to the values  $T^{(A1)} = 5.1 \times 10^5$ , and  $T^{(A2)} = 7.5 \times 10^5$ , respectively. These are already close to coronal temperatures. In two more scale heights these temperatures would be  $T^{(A1)} = 8.2 \times 10^5$ , and  $T^{(A2)} = 1.3 \times 10^6$ .

It is important to emphasize that this is an ongoing process and requires only the existence of the opposite polarity magnetic flux tubes. It has a random character giving the appearance of sporadic radiative transients in a wide range of temperatures from chromospheric flashes to million degree mini-flares. The wide range of temperatures in these radiative transients is ensured by various heights of the shock formation and their energy release.

### 15.5.2 Unipolar Plage

In contrast to mixed polarity plagues, the unipolar plagues heat the corona more uniformly, and, what is most important, the *heated* corona not only mimics the general shape of an underlying plage, but exhibits an extremely stable braidlike oscillatory pattern. These million degree structures, as we saw, remain regular as long as the unipolar plage preserves its general properties. It must be noted that although reconnections between the same polarity magnetic flux tubes is as ubiquitous as between the opposite polarity flux tubes, the post-reconnection dynamics is completely different. As discussed in Chap. 12, the post-reconnection sling shot

in this case works mainly across the tube axis and leads to fragmentation of the magnetic flux tubes. This may be accompanied by possible excitation of waves propagating along the flux tubes but can hardly contribute to million degree corona. (Tarbell et al. 2000; Ryutova and Tarbell 2003; Ryutova et al. 2003). Therefore, the mechanism for heating corona by small-scale flux tube ensembles that works so well in the mixed polarity plages is not that efficient in the unipolar regions.

What is then the dominant process in the ensemble of unipolar magnetic flux tubes? How does this process extract the energy stored in the dynamic plage, and how does this energy flow into corona? One thing is clear, whatever are the mechanisms causing these processes, they must be associated with collective phenomena in the entire ensemble of flux tubes. In other words, the problem requires consideration of a plage as a whole, i.e., as an ensemble of magnetic flux tubes randomly distributed in space and over their physical parameters.

In Chap. 6 we have studied the interaction of acoustic waves and unsteady wave packets with an ensemble of random magnetic flux tubes. It was shown, for example, that the physical processes of energy transfer to the medium, as well as the maximum available energy input, crucially depend on the distribution of the random flux tubes in space and over their parameters (see also Ryutova and Priest 1993a, b).

The remarkable feature of these processes is that they are accompanied by specific morphological effects occurring in overlying atmosphere. The most important role in these processes is played by resonant interaction. Recall that due to Landau damping the energy of an acoustic wave (of wave vector  $\mathbf{k}$  and sound speed  $c_{se}$ ) damps out at a rate

$$\nu_L \sim fkc_{se} \quad (15.1)$$

and remains for a long time in the form of flux tube oscillations.  $f = R^2/d^2$  being a magnetic filling factor of the medium. The corresponding resonance condition is:

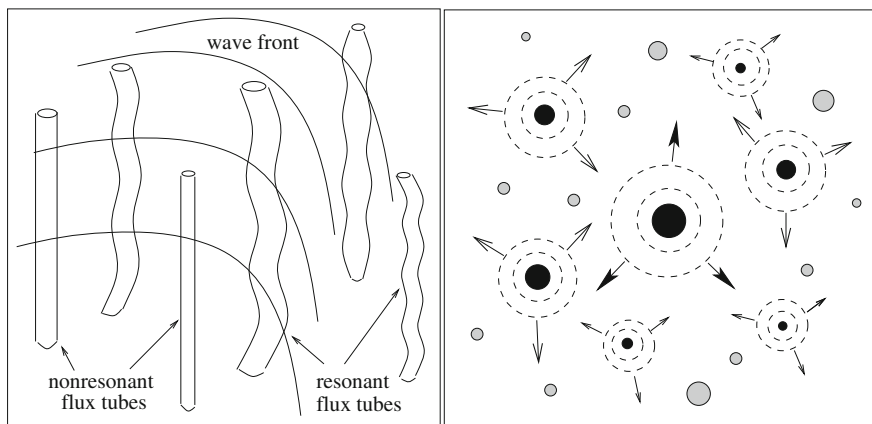
$$\omega = (\vec{k}\vec{n})v_{ph}^m, \quad (15.2)$$

where  $\vec{n}$  is a unit vector along the flux tube axis.  $v_{ph}^m$  is the phase velocity of the flux tube oscillation:

$$\begin{aligned} v_{ph}^{m=\pm 1} &= c_k = \frac{\sqrt{\eta}v_A}{\sqrt{1+\eta}} \\ v_{ph}^{m=0} &= c_T = \frac{c_{si}v_A}{\sqrt{c_{si}^2 + v_A^2}} \end{aligned} \quad (15.3)$$

with  $\eta = \rho_i/\rho_e$  being the ratio of plasma densities inside and outside the flux tube.

Thus, under the condition (15.1) the resonant flux tubes absorb the energy of the sound wave in a time  $\tau_L = \nu_L^{-1}$ , and carry it into upper layers of atmosphere in form of a kink or sausage oscillations propagating along the flux tubes. This is sketched in Fig. 15.12, left (see also Figs. 6.4, 6.5, 6.6, and 6.7 of Chap. 6). Then, in a time  $\tau_{rad} = \nu_{rad}^{-1}$  the resonant flux tubes radiate the accumulated energy as secondary acoustic or MHD waves. The radiative damping rate is:



**Fig. 15.12** Interaction of a wave packet with the random ensemble of flux tubes. *Left* Energy of wave packet is transferred to flux tubes, some of which are nonresonant, while others are resonant with respect to excitation either of kink or sausage oscillations. *Right* Radiation of secondary acoustic or MHD waves by oscillating flux tubes. After Ryutova and Priest (1993b)

$$\nu_{\text{rad}} \sim \omega k^2 R^2 \tag{15.4}$$

Since  $\tau_{\text{rad}}$  depends on the tube radius  $R$ , different tubes radiate secondary waves in different times and at different heights (Fig. 15.12, right panel), e.g., thicker flux tubes give off their energy earlier than thinner ones. This leads to the energy release in a form of patchy EUV emission that fills the region of a finite thickness spread over the entire space occupied by a given ensemble of flux tubes.

### 15.5.3 *N*-Solitons

Most importantly, as flux tube oscillations propagate upward into a more rarefied atmosphere, many of them reach the nonlinear regime. These waves are subject to modulation instabilities which may lead to formation of regular coherent structures (Zakharov and Shabat 1972; Mjølhus 1976).

Consider example of nonlinear kink oscillations. The analysis presented below may also be performed for the sausage modes. Nonlinear kink oscillations of flux tubes are described by the MKdV-Burgers equation for  $\vec{B}_\perp = (B_x, B_y)$  and can be written as an energy equation for  $\psi = B_x^2 + B_y^2$  (see Chap. 11, 11.3, of three dissipative terms we retain below only the term associated with radiative damping):

$$\frac{\partial \psi}{\partial t} + \alpha \psi \frac{\partial \psi}{\partial z} + \beta \frac{\partial^3 \psi}{\partial z^3} = \frac{\mu}{\pi} v.p. \int_{-\infty}^{\infty} \frac{\partial^3 \psi}{\partial s^3} \frac{ds}{z-s} \tag{15.5}$$

The coefficients,  $\alpha$ ,  $\beta$ , and  $\mu$  are, respectively, those of nonlinearity, dispersion, and radiative damping:

$$\alpha \simeq \frac{3}{4} \frac{c_k}{B_0^2}, \quad \beta = \frac{c_k R^2}{8(1 + \eta)^2}, \quad \mu = \frac{\pi c_k R^2}{4} \frac{c_k^2 - c_s^2}{(1 + \eta)c_s^2} \quad (15.6)$$

$c_k$  is the phase velocity of the kink mode (15.3).

In the absence of dissipation a stationary solution of (15.5) is a solitary wave with the amplitude  $A \simeq B_{\perp}^2$ , width  $\Delta$ , and travel velocity of the soliton,  $v_{\text{sol}}$ :

$$\psi = A \operatorname{sech}^2 \left( \frac{z - v_{\text{sol}} t}{\Delta} \right)$$

$$\Delta = \sqrt{\frac{12\beta}{\alpha A}}, \quad v_{\text{sol}} = c_k + \frac{\alpha A}{3} \quad (15.7)$$

To obtain a nonstationary solution one has to derive the evolutionary equation for the amplitude, suggesting that all the parameters of soliton, its amplitude,  $A$ , width,  $\Delta$ , and velocity,  $v_{\text{sol}}$ , are slowly varying functions of time. Using a standard procedure of fast and slow variables (Mjølhus 1976), we obtain the evolutionary equation for slowly varying amplitude for the modulated MKdV soliton,  $\tilde{A}(\zeta, \tau)$ , which is known to be a Schrödinger equation with cubic nonlinearity (Dodd et al. 1982):

$$i \frac{\partial \tilde{A}}{\partial \tau} + 3k \frac{\partial^2 \tilde{A}}{\partial \zeta^2} + \left( \frac{3}{4} - \frac{c_k^2}{4c_s^2(1 + \eta)} \right) |\tilde{A}|^2 \tilde{A} = 0 \quad (15.8)$$

Here  $\tilde{A} = A(\zeta, \tau)/A_0$  ( $A_0$  being a soliton amplitude in the initial moment of time), and  $\tau$  and  $\zeta$  are slow time and space (dimensionless) variables:

$$\tau = (c_k/\beta)^{3/2} t, \quad \zeta = \tilde{z} - (1 - 3k^2)\tau \quad (15.9)$$

$\tilde{z} = (c_k/\beta)^{1/2} z$ , and  $k$  is the wavenumber of a carrier wave, normalized by the inverse radius.

Equation (15.9) has two different solutions depending on the sign of the cubic term. If this term is negative, then (15.5) together with the Schrödinger (evolutionary) equation describes a soliton with slowly decaying amplitude.

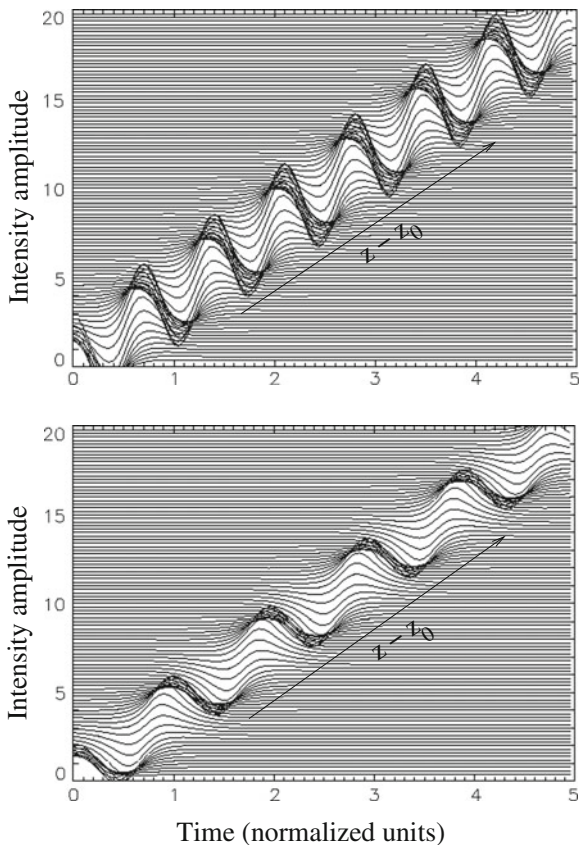
The situation changes dramatically if this term is positive. At

$$\epsilon = \frac{3}{4} - \frac{c_k^2}{4c_s^2(1 + \eta)} > 0 \quad (15.10)$$

Equations (15.5) and (15.8) describe the interaction in the soliton gas which results in self-focusing (and self-modulation) of solitons. This is a well known N-soliton solution in the exact theory of two-dimensional self-focusing of waves in nonlinear media pioneered by Zakharov and Shabat (1972).

It was shown that only pair interactions of solitons can occur. Therefore, since in the self-focusing problem the soliton has the meaning of a homogeneous waveguide, the N-soliton solution describes the intersection of N “homogeneous” channels with a bound state having a form of a “complicated” oscillating channel (Zakharov and

**Fig. 15.13** Visualization of N-soliton solution with radiation for two slightly different regimes. *Top* Magnetic filling factor of plage is  $f = 0.35$ ; *Bottom*  $f = 0.28$



Shabat 1972; Kuznetsov et al. 1995). Examples of the corresponding solution as applied to our problem are shown in Fig. 15.13. For background atmospheric parameters we adopt the reference model of the solar atmosphere (Maltby et al. 1986).

Solutions shown in Fig. 15.13 are obtained for height  $h = 2,200$  km. The background temperature at this height is  $T = 2.1 \times 10^4$  K. The temperature in the self-focused structures, i.e., in the oscillating “energy” channel, is about  $10^6$  K. We adopted a flux tube radius at the surface of  $R = 500$  km. The top panel shows the solution for a plage filling factor  $f = 0.35$ , and average magnetic field in flux tubes,  $\langle B \rangle = 30$  G. The bottom panel corresponds to a solution for  $f = 0.28$  and  $\langle B \rangle = 20$  G. As expected from the observations, the braiding period increases with decreasing filling factor of the flux tubes ensemble.

It is important to emphasize that there are two necessary conditions for the formation of these structures. First, the Schrödinger equation must have an N-soliton solution; i.e., condition (15.10) must be satisfied, i.e.,

$$c_k < \sqrt{3(1 + \eta)}c_s \tag{15.11}$$

Second, for solitons to interact through radiation, their velocity must be higher than the environmental (background) sound speed:

$$v_{\text{sol}} = c_k + \frac{\alpha A}{3} > c_s \quad (15.12)$$

These two conditions determine a finite thickness of self-organized structures and the optimal height of their formation. Quantitative estimates for the above examples give heights of formation  $h \simeq 2\text{--}4$  Mm.

The mechanism described above may serve as a natural basis for models of coronal heating above the unipolar plages. Moreover, as the braided structures is easy to observe, they may serve as a valuable tool for the inference of physical parameters that are not directly observable.

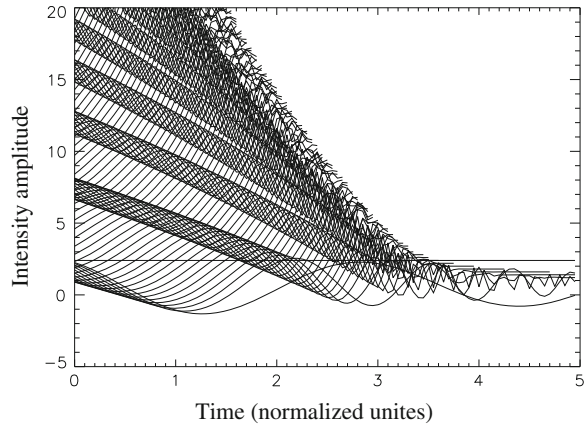
It must be noted that the theoretical problem is treatable in a frame of energetically open turbulence and structure formation. Here again, a starting process is the one shown in Fig. 15.12: random flux tubes absorb the energy of the waves and convective motions; because of the randomness of flux tubes, the accumulated energy is transferred and released by the individual flux tubes at different times and different heights; the reradiated waves have random phases. Such a process most naturally generates plasma turbulence. Given a permanent energy supply and radiative losses, this is an energetically open turbulence that has a tendency for self-organization and structure formation.

As a next step, one can study coupling processes between the coherent braided emission and the overlying hotter corona. If the observed structures above the unipolar plages have similar properties as “moss” (Berger et al. 1999), then above these structures  $3 - 5 \times 10^6$  K coronal loops should be observed (Berger et al. 1999). In the frame of the present theoretical model this seems quite natural and may be attributed to well-studied phenomena of collapse in soliton gases and in energetically open turbulence (Grimshaw et al. 2001). Collapse in the system of solitons (as well as in turbulence) leads to concentration of energy in a small volume and thus to a dramatic increase of temperature in this volume. As a result of self-focusing in the coherent coronal emission, the system will bifurcate into the state of much hotter loops. Qualitative picture of the N-soliton collapse is shown in Fig. 15.12.

Concluding this chapter, we must emphasize that strong inhomogeneity of the EUV emission at  $1\text{--}2 \times 10^6$  K temperatures, and the fact that it evolves in time in very different ways is largely determined by the “magnetic status” of underlying photosphere.

In particular, the EUV emission above plage regions dominated by single polarity magnetic elements always has an amorphous structure spread over the region that topologically mimics the shape of the underlying plage. Spacetime slices of the amorphous EUV emission show coherent braidlike structures with almost constant period for a given area. The braid period depends mainly on the magnetic filling factor of the underlying plage. The denser the plage, the shorter is the braid period. The structures remain regular as long as the plage preserves its general properties.

**Fig. 15.14** Visualization of a collapse in soliton gas that leads to concentration of energy in a small volume and thus to the dramatic increase of the temperature in a squeezed volume. Due to self-focusing the system of solitons bifurcates into the state of hot loops that should overlie the spongy structures



The only factor observed to disrupt these structures was the emergence of opposite polarity magnetic field in the otherwise unipolar plage (Fig. 15.14, see also Fig. 15.4).

Contrary to the case of unipolar plages, coronal emission above the mixed polarity plages is highly discrete and consists of sporadic localized radiative transients—jets, microflares, and their combinations.

Although physical mechanisms that may explain the observed properties of the coronal emission are different for the mixed polarity plages and plages dominated by a single polarity magnetic elements, the primary energy source in either case is associated with hydromagnetic activity among the photospheric magnetic flux tubes. Thus, sporadic radiative transients observed in the corona above the mixed polarity plages are produced by the cumulative effects triggered by post-reconnection processes among the opposite polarity photospheric flux tubes.

On the other hand, the corona above plages dominated by single polarity elements is heated by the energy flux resulting from collective phenomena in the interaction of a random ensemble of flux tubes with the acoustic or MHD waves and unsteady wave packets. This energy flux is released in the corona over the finite region that mimics the underlying plage and has the properties of energetically open turbulence with a tendency to self-organization. These properties manifest themselves as periodically spaced regions of enhanced brightening forming braidlike structures in time similar to those obtained from observations. The observed coherent structures are extremely sturdy which is characteristic of any self-organized state.

## References

- T.E. Berger et al., *Astrophys. J.* **519**, L97 (1999)  
 R.K. Dodd et al., *Solitons and Nonlinear Wave Equations* (Academic Press, London, 1982)  
 R.H.J. Grimshaw, E.A. Kuznetsov, E.G. Shapiro, *Physica D* **152**, 325 (2001)  
 A. Jeffrey, T. Taniuti, *Non-linear Wave Propagation* (Academic Press, New York, 1964)

- E.A. Kuznetsov, A.V. Mikhailov, I.A. Shimokhin, *Physica D* **87**, 201 (1995)
- L.D. Landau, E.M. Lifshitz, *Fluid Mechanics* (Pergamon Press, Oxford, 1987)
- P. Maltby et al., *Astrophys. J.* **306**, 284 (1986)
- E. Mjølhus, *J. Plasma Phys.* **16**, 321 (1976)
- M.P. Ryutova, E. Priest, *Astrophys. J.* **419**, 349 (1993a)
- M.P. Ryutova, E. Priest, *Astrophys. J.* **419**, 371 (1993b)
- M. Ryutova, S. Habbal, R. Woo, T. Tarbell, *Sol. Phys.* **200**, 213 (2001)
- M. Ryutova, T. Tarbell, R. Shine, Interaction and dynamics of the photospheric network magnetic elements. *Sol. Phys.* **213**(2), 231 (2003)
- M.P. Ryutova, T.D. Tarbell, MHD shocks and the origin of the solar transition region. *Phys. Rev. Lett.* **90**, 191101 (2003)
- M.P. Ryutova, R. Shine, *Astrophys. J.* **606**, 571 (2004)
- R. Shine et al., 1999 Fall AGU Meeting, SH41A-06 (1999)
- K.P. Stanyukovich, *Unsteady Motion of Continuous Media* (Pergamon Press, Oxford, 1960)
- T. Tarbell, M. Ryutova, R. Shine, Electro-mechanical coupling between the photosphere and transition region. *Sol. Phys.* **193**, 195 (2000)
- G.B. Whitham, *J. Fluid Mech.* **3**, 337 (1958)
- V.E. Zakharov, A.B. Shabat, *Sov. Phys.-JETP* **34**, 62 (1972)



## Chapter 16

# Electrodynamic Coupling of Active Region Corona with the Photosphere

**Abstract** In the previous chapters we studied response of the chromosphere and corona to magnetic activity in the underlying quiet sun regions and both types of plages, unipolar and mixed-polarity ones. In this chapter we turn to the question how the chromosphere and corona respond to magnetic activity in the active regions where filling factor is close to unity. Our consideration will be based on a specific case favorably caught in multiwavelength observations showing the entire process from the birth and evolution of a compact active region to formation and dynamics of coronal structures above it. We then discuss a general theory based on energetically open systems of currents that may be driven into various dynamic forms via nonlinear processes with continuous flow of matter and energy. Depending on the system parameters these may be long-living steady loops showing subtle oscillations, loops in the relaxation regime, and the periodically flaring and exploding loop systems. The theory also predicts that the EUV loops must have a filamentary structure and allows one to estimate the limiting currents and critical radii of elemental filaments associated with the stability criteria.

### 16.1 The Problem of Multifaceted Corona

The problem of energy production, transfer, and release throughout the solar atmosphere not only involves ambiguous mechanisms of the magnetic energy dissipation but also includes a wide range of phenomena that shape the upper layers of atmosphere and link their structure and dynamics to photospheric motions and magnetic fields. Especially rich in its diversity is the active region chromosphere and corona. Note that studies of active region corona were strongly dominated by attempts to explain coronal flares. However, observations show a great variety of coronal structures that do not produce the major flares. Most long-living coronal loop may slowly decay, oscillate, periodically result in flare-like events, produce a series of microflares, and even show spatiotemporal periodicity of microflares resembling the echo effects. In other words, the question why the solar flare *occurs* is, of course, important but no less important is the question why, under seemingly equal conditions, the flare *does not occur*. The answer to this question is closely related to the very basic question: how the coronal structures are formed and what makes them to take one or the other form.

To look into this problem we shall consider some characteristic features of electromagnetic coupling throughout the solar atmosphere, and in particular, we shall study links between the photospheric driver and structure formation in the overlying chromosphere/corona. Special attention will be paid to the fact that the magnetic structures rooted in an unsteady photosphere/convective zone are necessarily the current carrying systems. This fact plays a crucial role in the formation, evolution, and disruption of any magnetic structure throughout the solar atmosphere. As a first step one needs to investigate how the observed hydromagnetic effects may generate electric currents.

Generation of electric currents and their role in the astrophysical plasma is a longstanding problem and has been studied by many authors (Alfvén and Fälthammar 1963; Alfvén and Carlqvist 1967; see also Alfvén (1981), and references therein). In applications to the solar atmosphere it was, for example, shown that plasma pressure at the base of magnetic flux tubes can drive large currents along the entire length of flux tube (Boozer 1988). In the nonlinear regime (when the interaction of flux tubes with convective motions are included) this effect leads to the generation of both longitudinal and azimuthal currents in flux tubes (Ryutova et al. 1996). Elfmov et al. (1996) showed that Alfvén waves can drive significant currents in solar coronal loops that may support loops in a quasi-stationary state.

Alfvén and Carlqvist (1967) suggested that the coronal loops and storage of flare energy can be represented by force-free currents analogous to the circuit currents and even performed laboratory experiment on current limitation and disruption. Because an inductive circuit has a general tendency to “explode,” it was supposed that it also may explain the coronal flares.

The advantage of the circuit approach is quite clear, as it naturally consolidates many different aspects of electrodynamic into a simple scheme. The concept of the electric circuit has been further exploited by several authors in application to a wide range of phenomena from the solar flares to ionospheric substorms (see monograph by Alfvén (1981) and literature therein). Ionson (1982), addressing the problem of stellar coronal heating, emphasized that all the proposed mechanisms that were thought as unique in their own right “are based upon a unifying foundation of electrodynamic whose principal ingredients are capacitance  $C$  (the ability of a magnetoplasma to store electric and kinetic energy), inductance  $L$  (the ability to store magnetic energy), resistance  $R$  (the ability to convert the above electrodynamic energy into thermodynamic end products such as heat). Extending the LRC circuit analogue to a continuously driven system with a  $\beta \leq 1$  velocity field as a secondary voltage generator, Ionson established coupling between the surface driver and coronal dissipation region. The model gives scaling laws that are in a good agreement with the observations. These are, however, valid only for large scale, long-living (stable) coronal loops.

In fact, due to flexibility of the equivalent circuit parameters that reflect the physical properties of a system both at macroscales and microscales, the LRC circuit approach has a great potential in studying an overall behavior of coronal structures. The main point here is that the formation of a current system, storage and dissipation of electromagnetic energy, is ongoing and energetically unbalanced process. In other words this is a typical dissipative, energetically open system, driven into various

dynamic forms via internal processes and sustained by a continuous flow of matter and energy.

The main properties of a system are determined by several key factors, such as

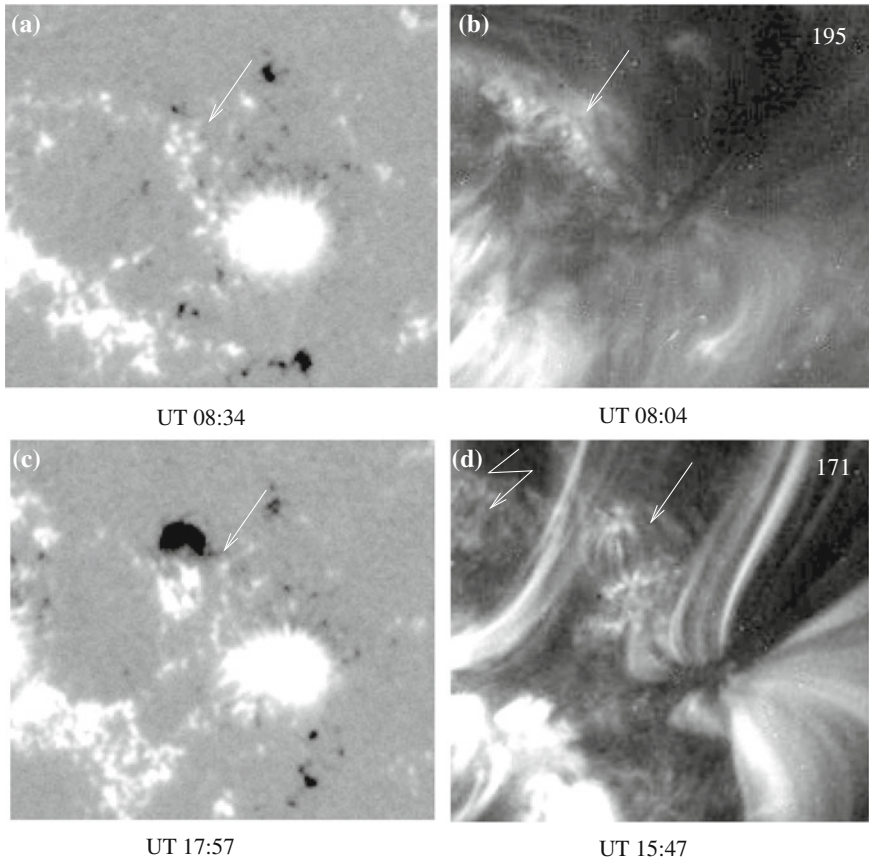
- (1) character of the photospheric driver;
- (2) magnetic field that interconnects the  $\beta \geq 1$  energy source region with the  $\beta \ll 1$  dissipation region;
- (3) local height of the chromosphere/transition region where the most efficient generation of currents occurs (Ryutova and Shine 2006; Ryutova 2006);
- (4) feedback between the current generation and dissipation regions; and
- (5) characteristic spatial scales and timescales of a system. A theory is quite transparent, and containing directly measurable parameters, allows quantitative analysis and comparison with the observations.

To clarify theoretical analysis by comparing them with observations we use here specific events associated with the birth, formation, and evolution of compact coronal structures caused by strong localized motions generated by emerging magnetic flux in the photosphere. Multiwavelength observations show that long before the magnetic pore is formed, the chromosphere and transition region show a high activity above the future site of pore formation: rising but not yet visible magnetic flux exerts a strong pressure on the overlying plasma generating highly collimated plasma flows seen in the  $H\alpha$  images. About the time when the magnetic pores are formed and the  $H\alpha$  surges bifurcate into the established arc-like flows, a system of compact coronal loops is formed, showing direct connection between the motions associated with the evolving magnetic fields and the coronal structure formation.

## 16.2 Emerging Magnetic Flux and Structure Formation in Overlying Atmosphere

The primary data sets that we will use in this section are observations from the Swedish Vacuum Solar Telescope (SVST) on La Palma, complemented by the TRACE data sets, used in the previous chapter to describe the response of corona to magnetic activity in underlying plage regions. A target region now is a central sunspot and its nearby environment.

Figure 16.1 shows snapshots of the sunspot area and its overlying corona made at two instances of time several hours apart. The white arrow in Fig. 16.1a shows a part of a unipolar plage, and in particular, a group of the positive polarity flux tubes that form in the beginning of the observation, a pattern resembling a *kitten paw*. The corona above this region (panel b) shows an amorphous emission typical of regions overlying unipolar magnetic plagues. Figure 16.1c, d taken hours later show a fully developed pores of opposite polarities, and a completely different shape of the coronal emission. Part of the spongy emission seen before the pore formation is replaced by the system of compact loops overlying and “connecting” two opposite polarity pores.



**Fig. 16.1** Snapshots of the studied region. Aligned MDI and TRACE 171 and 195 images of the  $56'' \times 51''$  area. MDI magnetogram is scaled from  $-500$  to  $500$  G. *Thin arrows* show a future site of flux emergence and pore formation. **a** Positive polarity magnetic flux tubes form a “kitten paw” in the beginning of the observation. **b**  $2.0 \times 10^6$  K emission in Fe XII  $195 \text{ \AA}$  has amorphous structure typical of unipolar plages. **c** Hours later, MDI magnetogram shows fully developed bipolar pores; **d**  $10^6$  K emission in Fe IX/X  $171 \text{ \AA}$  line shows well-established system of compact loops overlying the pore and large-scale “open” loops rooted in the central sunspot; *broken arrow* shows a sturdy character of the amorphous structure above the unipolar plage

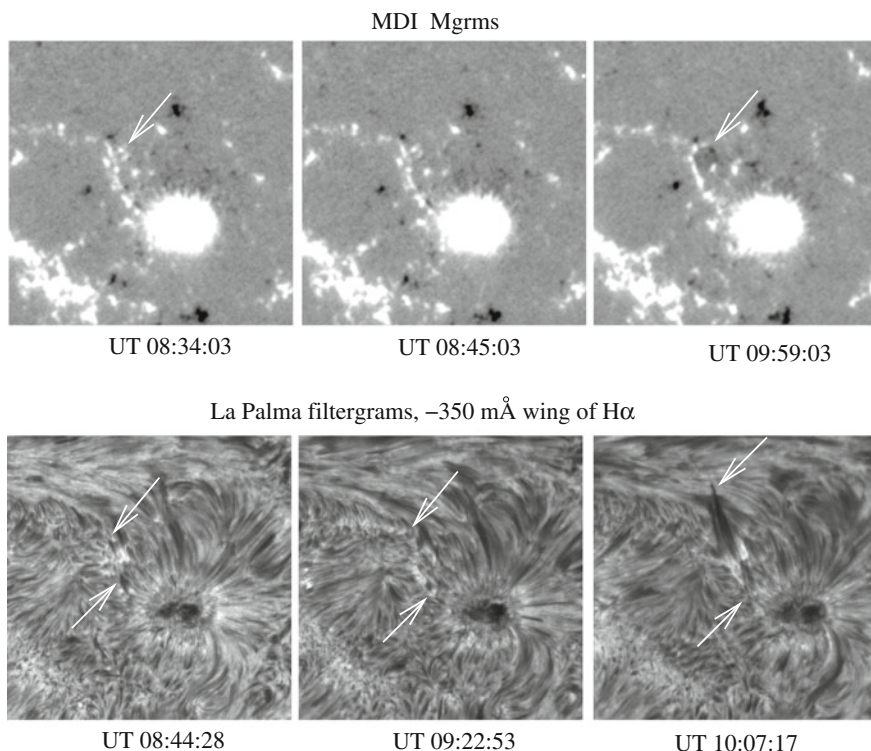
It is remarkable that part of the amorphous emission outside newborn pores has preserved its unipolar properties and remains amorphous (panel c, broken arrow). As discussed in the previous chapter, space-time slices of the amorphous EUV emission show coherent braid-like structures that remain regular as long as the plage preserves its general properties. The only factor observed to disrupt these structures is the emergence of opposite polarity magnetic field in the unipolar plage.

In what follows we describe the evolution of coronal structures from the amorphous stage shown in Fig. 16.1b to much more complicated picture shown in

Fig. 16.1d that includes compact loop structures overlying newly formed pores and prominent open structures rooted in the north side of the central sunspot.

Initially, there are few changes in the magnetic field configuration in and around the central sunspot. But, gradually, during the first two hours, a group of positive polarity magnetic flux tubes that form the kitten paw move out and form a circle (Fig. 16.2, upper row). We know from the observations that this is a future site of a large-scale magnetic pores in form of a double compact sunspot. It is therefore natural to suggest that upward moving but not yet surfaced large magnetic flux generates plasma motions that sweep out the small-scale flux tubes. This suggestion indeed is readily supported by the chromospheric data: overlying chromosphere and even corona respond to these motions at very early stage.

Snapshots taken in a blue wing of  $H\alpha$  (lower row in Fig. 16.2) show piercing plasma flow directed upward from *kitten paw* area and their evolution in time. As early as about UT 08:45 when positive polarity magnetic flux tubes are still arranged in a kitten paw pattern, coronal plasma above this region is already significantly



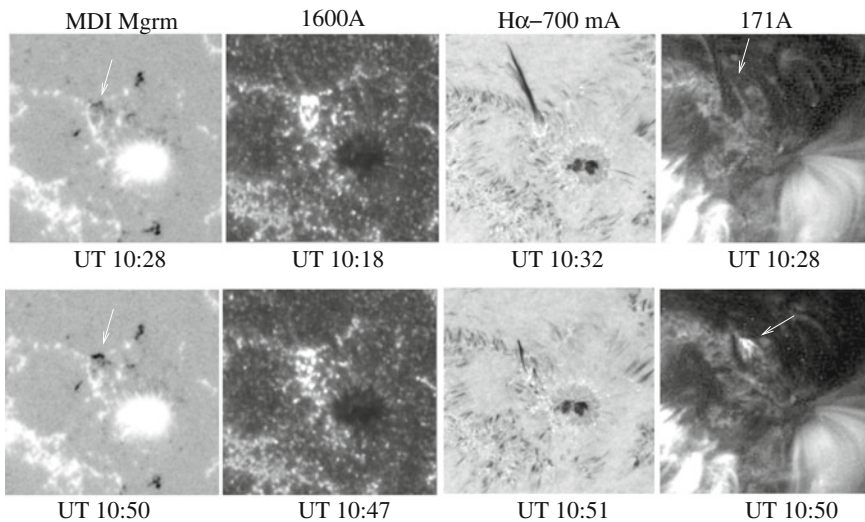
**Fig. 16.2** Time sequence of snapshots showing changes in the configuration of the photospheric magnetic field and response of the chromosphere to these changes. During about 1 h 25 min positive polarity flux tubes forming the kitten paw, gradually move out and arrange into a circle with inclusions of a few negative magnetic flux tubes; *lower panels* show the origination and evolution of an accelerating mass flow in the chromosphere

disturbed, and acquires a form of a dagger shaped upward flow. A primary coronal emission having an amorphous structure still remains amorphous but now is pierced by these flows. The appearance of a few negative polarity magnetic flux tubes before the large-scale magnetic flux surfaces, cause at the transition region temperatures appearance of sporadic brightening. In the kitten paw region, the number of sporadic events increases with appearance of more and more negative polarity inclusions.

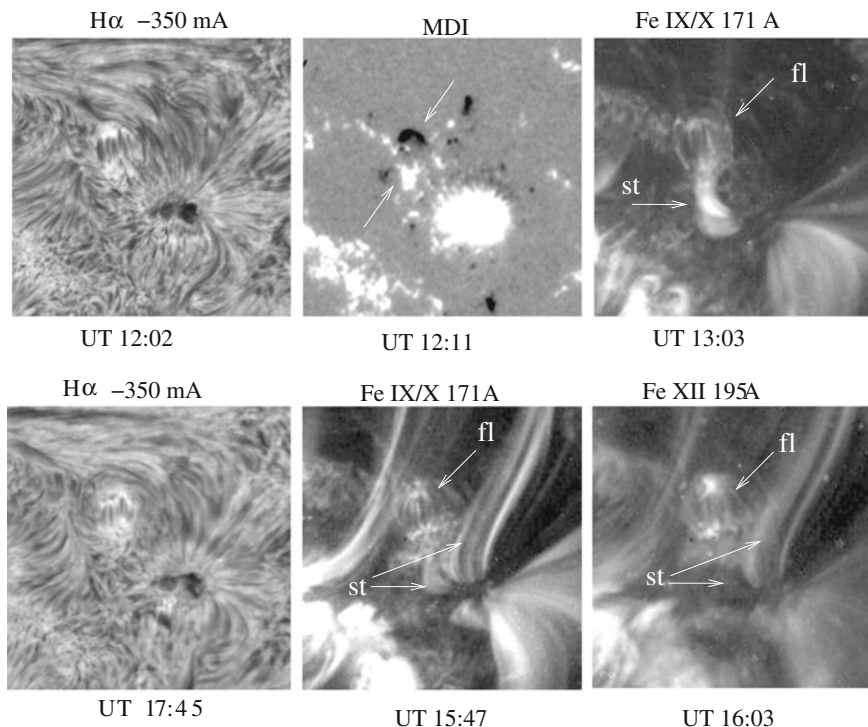
It is important to note that the newly generated plasma flows themselves do not heat the surrounding coronal plasma. But they play an essential role in the final rearrangement of a hot coronal plasma and its additional heating, as we will see below. During the maximum activity of  $H_{\alpha}$  surges, the “damaged” corona still remains amorphous. Only when the  $H_{\alpha}$  surges abruptly decay does the coronal emission get enhanced, suggesting that the energy of these flows somehow is converted into heat.

The maximum activities of the  $H_{\alpha}$  surges and their decay phase are shown in Fig. 16.3, upper row. Lower row shows corresponding images during the decay phase. The former amorphous emission at the maximum phase in the 171 Å line (black dagger in upper image) is replaced by the appearance of the “first light,” a new enhanced emission (right panel in lower row).

At about the time when both positive and negative polarity pores are formed, two different types of formations develop in the overlying corona. One may be characterized as a system of “stable” loops rooted at the north edge of the sunspot and overlying unipolar region (marked by arrow “st” in Fig. 16.4). The other formation, also resembling a loop system, consists of frequent X-ray microflares, appearing at different places along the virtual lines that eventually become loops (marked by



**Fig. 16.3** Target region around the time of maximum activity of  $H_{\alpha}$  surges (*upper row*) and around the decay phase (*lower row*). The pores are not yet formed, but unipolar kitten paw pattern is replaced by mixed-polarity magnetic fields resulting in significant energy input and release in the transition region (e.g., 1,600 Å images)

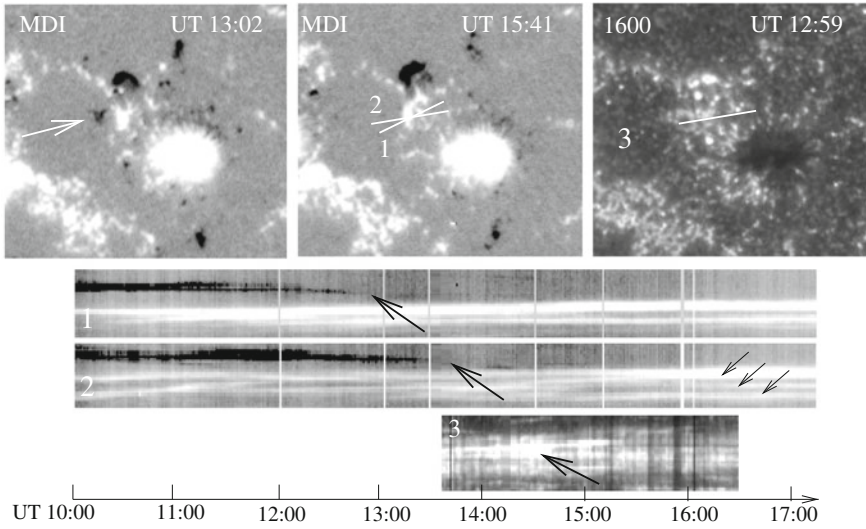


**Fig. 16.4** Formation of compact coronal structures and their evolution. *White arrow* marked by “st” shows the compact loops that remain stable for over two h (*upper row*). In *lower row* these compact “stable” loops are shown disrupted and replaced by large scale open spurs. The unstable structures consisting of sporadic microflares (marked by arrow “fl”), on the contrary, become stabilized.  $H\alpha$  images corresponding to these structures show a well-established flow pattern; a clear arc system formed by flows mimics the tiny arc system of loops seen in both coronal lines, 171 and 195 Å

arrow “fl” in Fig. 16.4). Shortly after this stage, taken around UT 12:00, a seemingly unstable structure overlying the bipolar pore region forms a very regular loop system; from now on (e.g., after UT 13:03), this system keeps its identity for many hours (to the end of available data sets). Its persistent character is supported by a well-established flow system seen in  $H\alpha$  images.

The loop system marked by arrow “st” from the moment of its formation up to some time around UT 13:03 (period that lasted over two h) remained “quiet” and showed neither changes nor any microflare activity. At around UT 13:03 these loops seem to be gained some energy, and in a couple of hours (at about UT 15:22), the compact loop system was gone, and in place of it large-scale open structures were formed. These structures are quite prominent in hotter 195 Å line as well (lower row in Fig. 16.4).

Obviously, their stable period was provided by the monotonic polarity of underlying region. In other words, the lack of opposite polarity magnetic elements ensured



**Fig. 16.5** Photospheric reconnections and chromospheric microflares preceding the structure formation in overlying corona. *Left panel* is the magnetogram showing a newborn negative and positive polarity pores at UT 13:02, with a negative satellite flux next to the positive pore (*white arrow*). It is in this area where a continuous reconnection occurs. At the *central panel* showing magnetogram at UT 15:41, the satellite negative flux is already gone. The *horizontal panels 1 and 2* are the space-time images made along the paths (1, 2) in the magnetogram, and 3 in the 1,600 Å image. Space-time images 1–2 show the tracks of the motions of the magnetic elements, and 3 shows a temporal variability of the enhanced emission in the transition region. *Large black arrows* show photospheric reconnections; *small black arrows* show the splitting of the positive polarity flux into several flux tubes

the lack of sporadic injection of energy into system. The appearance of additional energy and its source can be traced in space-time cuts shown in Fig. 16.5. Cuts made along lines 1 and 2 on the MDI image show motions of magnetic fluxes (horizontal panels 1 and 2) and cut 3 on the 1,600 Å image. Two cuts made on the magnetogram show the motion of magnetic elements with slightly different orientations, and cut 3 shows a temporal variability of the enhanced emission in the transition region.

One can see that during the period between UT 14:40 and UT 15:10 the negative polarity flux disappeared completely (shown by white arrow in the MDI snapshot at UT 13:02), and positive flux has been reduced and fragmented. There is a slight time lag between the final magnetic flux reduction and appearance of a strong chromospheric microflare of about 6 min. This is just the time needed to transfer and release the energy at the  $T \simeq 10^5$  K in the transition region produced by the reconnection of the photospheric magnetic flux tubes (Tarbell et al. 1999; Rytova and Tarbell 2003). Series of reconnection processes (black arrows in panels 1, 2 of Fig. 16.5) that provided the strong energy supply to previously stable loop system naturally lead to its destruction. This series of reconnection events could also trigger



the processes along the entire North edge of the sunspot resulting in the formation of large-scale open coronal loops (see 171 and 195 Å coronal images in Fig. 16.4).

Obviously, the mechanisms that may explain the observed regularities must, in the first place, link the formation of coronal structures with their *forerunner*, strong plasma motions generated by emerging but not yet visible magnetic flux. We will see below that such mechanisms are uniquely associated with the current drive, arising due to a strong disturbances propagating in the magnetized plasma. In the next section we will address these mechanisms and estimate possible values of generated currents.

### 16.3 Current Drive Mechanisms Associated with the Emerging Magnetic Flux

Strong disturbances confined in a limited surface area and propagating upward in the magnetized and sharply stratified atmosphere may provide several sources for efficient current drive. The kick produced by the large emerging flux generates acoustic and Alfvén waves. The exchange of energy and momentum between the induced waves and the electrons leads to an efficient generation of electric currents. Strong collimated flows (analogue of a beam-plasma system) cause generation of currents as well. Finally, helical motions clearly seen in the generated  $H_\alpha$  surges (see, e.g., Fig. 16.3) may also contribute to the current drive.

Noninductive current drive is a fundamental process used for decades to generate and continuously sustain the toroidal currents in tokamak fusion devices (see, e.g., Fish 1987 and the literature therein). It can be studied as a natural process occurring in various space plasmas as well (Otani and Strauss 1988; Ryutov and Ryutova 1989; Block et al. 1998). Although there are a number of very different noninductive methods of current generation, they all rely upon two basic principles: (i) beam-particle interactions (Ohkawa 1970), and (ii) wave-particle interactions (Wort 1971). In any case it is the energy and momentum exchange between the electrons and wave/particles that determines the efficiency of the current drive,  $\eta = j/\mathcal{P}$ .  $j$  is a current density, and  $\mathcal{P} = dW/dt$  is work done by the “source,” i.e., the induced power per unit volume of plasma:

$$\mathcal{P} = \frac{1}{2} m_p \frac{d(nu^2)}{dt} \quad (16.1)$$

In other words, the plasma electrons interacting with particles and/or waves gain a momentum  $m_e n u$ , where  $n$  is a plasma density and  $u$  is a longitudinal component of the injected beam (or wave) velocity; this momentum (and the electric current associated with it) is subject to losses due to electron–ion collisions. Thus, the momentum balance is determined by (Fish 1987):

$$\frac{dj}{dt} \simeq \frac{e}{m_e} m_p u \frac{dn}{dt} - \nu_{ei} j \quad (16.2)$$

where  $\nu_{ei}$  is electron–ion collision frequency,  $u$  is the velocity of the injected beam or the phase velocity of a source wave. Equation (16.2) gives a standard estimate for the efficiency of current drive in the stationary regime:

$$\eta = \frac{j}{\mathcal{P}} \simeq \frac{e}{m_e \nu_{ei} u} \quad (16.3)$$

The induced power depends on the specific mechanism of the current drive. We will consider three major cases.

### 16.3.1 Proper Motion

First we will estimate the currents that may be driven by strong collimated flows similar to those observed in our data set (cf. Fig. 16.3). As the hydrogen plasma is injected into the atmosphere, the streaming particles with velocity,  $u$ , interact with the background electrons. Induced power per unit volume of plasma may be estimated using the standard transport equations (Trubnikov 1965), which give:

$$\mathcal{P} \simeq m_p n \tilde{\nu}_{ie} u^2 \alpha \frac{u^2}{v_{Te}^2} \quad (16.4)$$

Here  $\tilde{\nu}_{ie} = (m_e/m_p)\nu_{ie}$  is the inverse slowing down time of particles via electron–ion collisions; the factor  $\alpha(u/v_{Te})^2$  is the cross section of electron–ion collisions, where  $\alpha$  is a coefficient of the order of unity (Stanyukovich 1960), and  $v_{Te}$  is the electron thermal velocity. With this estimate and (16.3), the current density is estimated as  $j \simeq neu(u/v_{Te})^2$ .

The quantitative estimates for our observations are as follows. The average velocity of  $H_\alpha$  surges is  $u \simeq 2.0 \times 10^6 \text{ cm s}^{-1}$ . Low in the atmosphere, say at  $T = 2.0 \times 10^5 \text{ K}$  and density  $n = 4.0 \times 10^{10} \text{ cm}^{-3}$  ( $v_{Te} = 5.5 \times 10^8 \text{ cm s}^{-1}$ ), generated current density may be quite high,  $j \simeq 0.17 \text{ Am}^{-2}$ . Higher in the atmosphere, the efficiency drops. Thus, at  $T = 10^5 \text{ K}$ ,  $n = 4.0 \times 10^{10} \text{ cm}^{-3}$ , and  $T = 8.0 \times 10^5 \text{ K}$ ,  $n = 2.0 \times 10^9 \text{ cm}^{-3}$ , current densities become, respectively,  $j \simeq 8.5 \times 10^{-3} \text{ Am}^{-2}$  and  $j \simeq 2.1 \times 10^{-4} \text{ Am}^{-2}$ . These estimates are close to current densities in the EUV loops estimated from the analysis of vector magnetograms of active regions (Georgoulis et al. 2004).

### 16.3.2 Acoustic Waves

It was shown (Ryutov and Ryutova 1989) that strong disturbances generated in the solar atmosphere from a limited area and propagating upward against gravity may excite electric currents (and magnetic fields) in the transition region between the chromosphere and corona.

Two simple properties of the solar atmosphere provide the basis of the mechanism:

- (1) upward propagating waves quickly steepen due to sharp stratification and at the chromospheric height break into sequence of shocks, and
- (2) at these heights the plasma is strongly collisional. It was shown that in strongly collisional plasma

for the perturbations emitted from a limited surface area, half of the wave momentum is transferred to electrons and half to ions. This means that the velocity of the electrons becomes  $m_i/m_e$  times higher than that of the ions providing the generation of currents. The mean force acting on the electron gas,  $F_e$ , has been evaluated in two cases, for purely sinusoidal wave (low atmosphere), and for a nonlinear wave that reaches the sawtooth (weak shock) regime. In the linear case  $F_e$  has a form:

$$F_e = \frac{4\pi^2}{15} \frac{m_p c_s \kappa_e}{\lambda^2 n} \xi \quad (16.5)$$

where  $\kappa_e = nkT\tau_e/m_e$  is the electron thermal conductivity,  $\lambda$  is the wavelength, and  $\xi = W/\rho c_s^2$  is actually a squared Mach number,  $W$  being an acoustic wave energy. In the second case the energy dissipation occurs at the front of a shock and no longer depends on  $\kappa_e$  (Landau and Lifshitz 1988).  $F_e$  then has the form:

$$F_e = \frac{8\sqrt{3}m_p c_s^2}{\lambda} \xi^{3/2} \quad (16.6)$$

In a stationary regime which is established in about time associated with skin effect, the generated currents reach the value:

$$j = \frac{\sigma}{e} F_e \quad (16.7)$$

First, we estimate the generated currents by the sinusoidal waves (linear regime). This regime may be valid only up to heights of a few hundred km above the surface. For example, let us take the temperature  $T = 6.2 \times 10^3$  K, electron density  $n_e = 10^{11} \text{ cm}^{-3}$ , and the wavelength  $\lambda = 3 \times 10^7$  cm. Sound speed is then  $c_s \simeq 9.2 \text{ km s}^{-1}$ , the wave amplitude is about  $8 \text{ km s}^{-1}$  (assuming that the initial wave amplitude is  $0.5 \text{ km s}^{-1}$ , and the average scale height is 200 km), and  $\xi \simeq 0.76$ . With these parameters (16.5) and (16.7) give an estimate of the generated current density  $j = 1.3 \times 10^{-8} \text{ A/m}^2$ .

In weakly nonlinear, sawtooth regime ( $\xi \geq 1$ ), the efficiency of current drive increases dramatically, in fact, by about 6 orders of magnitude. From (16.6) and (16.7) we have

$$j = 0.275 \frac{e}{m_e} \frac{T^{3/2}}{\ln \Lambda} \frac{8\sqrt{3}m_p c_s^2}{\lambda} \xi^{3/2} \quad (16.8)$$

Now, for example, at  $T = 8 \times 10^3$  K ( $h \simeq 2,000$  km),  $c_s \simeq 10.4 \text{ km s}^{-1}$ ,  $\ln \Lambda = 16$ ,  $\lambda = 3 \times 10^7$  cm, and  $\xi = 1.1$ , we have  $j = 2.1 \times 10^{-2} \text{ A/m}^2$ . This is a typical current density for the EUV loops.

### 16.3.3 Alfvén Waves

To estimate the efficiency of current drive by Alfvén waves we need to find the power dissipated by the Alfvén waves in the presence of plasma flows. Current drive by Alfvén waves in coronal loops in the absence of mass flows was studied, e.g., by Elfimov et al. (1996). The effects of mass flows on the dissipation of Alfvén waves in the solar atmosphere has, however, very characteristic features (Ryutova and Habbal 1995). It was found that in the approximation of geometrical optics the energy dissipation rate,  $\mathcal{P}$ , has a form:

$$\mathcal{P} \simeq \nu_* (\nabla_{\perp} S)^2 \frac{\rho_0 (v_{0A} + u_0)^2}{2} \exp \left( - \int^l \nu_* \frac{(\nabla_{\perp} S)^2}{v_A + u} dl \right) \quad (16.9)$$

Here  $\nu_* = (\eta_0/\rho) + \eta_D$  is combined dissipative coefficient;  $\eta_0 = 0.96nkT\tau_1$  is the ion viscosity and  $\eta_D = c^2/4\pi\sigma$  is the magnetic diffusivity, and  $\tau_1$  is the ion collision time (Braginskii 1965).  $u$  is the flow velocity.  $\nabla_{\perp} S$  is the gradient of eikonal across the magnetic field structure. The integration is performed along the ray trajectory. With the simplified magnetic field geometry  $\vec{B} = \vec{B}(0, B_{\phi}(r), B_z)$ , and plasma flow directed along the vertical  $B_z$  component, the dissipation rate at height  $z$  can be estimated as follows:

$$\mathcal{P} \simeq \nu_* \frac{\rho \omega^2 (v_A + u)^2}{2 (v_A + u)^2} z^2 \exp \left[ - \frac{2}{3} \nu_* \frac{\omega^2 (v_A + u)^2}{(v_A + u)^5} z^3 \right], \quad (16.10)$$

The height dependence of  $\mathcal{P}$  has a form  $f(\zeta) = \zeta^2 e^{-\frac{2}{3}\zeta^3}$ . This function has a maximum at  $\zeta = 1$ , which for given physical parameters, determines maximum amount of the power absorption,  $\mathcal{P}_m$ , and its height,  $z_m$ . With the approximation  $(v_A + u)/(d(v_A + u)/dr) \sim R$ , where  $R$  is a radius of a separate filament in a magnetic structure, the estimates for these quantities are as follows:

$$z_m \simeq (v_A + u)\tau_{\omega}, \quad \mathcal{P}_m \simeq \frac{\rho(v_A + u)^2}{2\tau_{\omega}} e^{-2/3} \quad (16.11)$$

where we introduced notation

$$\tau_{\omega} = \left[ \frac{R^2}{\nu_* \omega^2} \right]^{1/3} \quad (16.12)$$

$\tau_{\omega}$  has a meaning of the inverse damping rate of the Alfvén waves due to the phase mixing (Ryutova and Habbal 1995). Using (16.2) we can now estimate the maximum current density,  $j_m = [e/m_p \tilde{\nu}_{ei} (v_A + u)] \mathcal{P}_m$  (the z-dependence of generated currents is the same as in (16.10)):

$$j_m \simeq 0.257ne(v_A + u) \frac{1}{\tilde{\nu}_{ei}\tau_\omega} \quad (16.13)$$

For quantitative estimates we choose some exemplary values for temperature, density, and the Alfvén speed typical for the chromosphere and lower transition region. These are shown in Table 16.1 together with kinetic coefficients calculated via standard expressions:

$$\nu_* = 1.32 \times 10^9 \frac{T^{5/2}}{n \ln \Lambda} + 5.25 \times 10^{11} \frac{\ln \Lambda}{T^{3/2}}, \quad (16.14)$$

and  $\tilde{\nu}_{ei} = 1.97 \times 10^{-3} n \ln \Lambda / T^{3/2}$ . For the plasma flow we take again  $u = 2.0 \times 10^6 \text{ cm s}^{-1}$ , and for radius of a magnetic filament  $R = 2.0 \times 10^6 - 10^7 \text{ cm}$ .

The last six rows in Table 16.1 contain the height of the maximum absorption and corresponding maximum density of the generated currents estimated for Alfvén wave frequencies, 0.1 and 0.3  $\text{s}^{-1}$ . The efficiency of the current drive is quite sensitive to the frequency of the Alfvén waves—higher frequency waves can generate stronger currents and at lower altitudes. Nonetheless, the variation of the basic physical parameters (corresponding to chromosphere/transition region) gives the range of current densities close to those shown in Table 16.1 and are consistent with observations.

The estimate of corresponding heights shows that generated currents mainly reach their maximum values at the transition region level. It is important to also mention that the injection of a magnetic helicity, which is a necessary part of the emergence of complex magnetic fields, can also play an important role in the current drive.

Each effect or their combinations may contribute to generation of currents. The dominance of one or the other effect depends on the specific situation and the local physical parameters of the system.

**Table 16.1** Estimate of the generated current densities and corresponding heights

Parameter	Set 1	Set 2	Set 3
$T$ (K)	$2.0 \times 10^4$	$10^5$	$3.0 \times 10^5$
$n$ ( $\text{cm}^{-3}$ )	$4.0 \times 10^{10}$	$2.0 \times 10^{10}$	$10^{10}$
$\tilde{\nu}_{ei}$ ( $\text{s}^{-1}$ )	$4.4 \times 10^2$	25.0	2.4
$\nu_*$ ( $\text{cm}^2 \text{ s}^{-1}$ )	$1.2 \times 10^8$	$10^{10}$	$3.27 \times 10^{11}$
$v_A$ ( $\text{cm s}^{-1}$ )	$6.5 \times 10^6$	$9.2 \times 10^6$	$1.3 \times 10^7$
$R$ (cm)	$2.0 \times 10^6$	$4.0 \times 10^6$	$10^7$
$\omega = 0.1 \text{ s}^{-1}$	–	–	–
$z_m$ (cm)	$1.3 \times 10^9$	$6.13 \times 10^8$	$4.73 \times 10^8$
$j_m$ ( $\text{Am}^{-2}$ )	$2.1 \times 10^{-3}$	$7.0 \times 10^{-2}$	0.82
$\omega = 0.3 \text{ s}^{-1}$	–	–	–
$z_m$ (cm)	$6.13 \times 10^8$	$2.93 \times 10^8$	$2.33 \times 10^8$
$j_m$ ( $\text{Am}^{-2}$ )	$4.4 \times 10^{-2}$	0.14	1.7

## 16.4 Energy Flow Throughout Solar Atmosphere

In previous sections we studied formation and properties of the EUV structure formation associated with the emergence of a large-scale magnetic flux which eventually formed two opposite polarity pores. We saw that long before the magnetic pore is formed, chromosphere and corona show a high activity above the future site of pore formation: rising but not yet visible magnetic flux exerts a strong pressure on the overlying plasma generating highly collimated plasma flows seen in the  $H\alpha$  images. About the time when the magnetic pores are formed and  $H\alpha$  surges bifurcate into the established arc-like flows, a system of compact coronal loops is formed, showing direct connection between the plasma motions, the evolving magnetic fields, and the coronal structure formation. It was suggested that the triggering mechanism for structure formation may be associated with generation of currents caused by strong disturbances propagating upward from a limited surface area.

The kick produced by highly concentrated emerging flux is not only accompanied by the observed  $H\alpha$  flows but may also generate acoustic and Alfvén waves. Therefore, the efficiency of current drive has been analyzed for three main sources:

- (1) the proper motion of hydrogen plasma,
- (2) the acoustic waves, and
- (3) the Alfvén waves.

Quantitative estimates of current densities for each of these mechanisms are in the range of  $j_m = 2.1 \times 10^{-3} - 2 \text{ Am}^{-2}$ , which agrees with the reported range of measured current densities (Leka et al. 1996; Georgoulis et al. 2004; Georgoulis and LaBonte 2004). We saw that generated currents reach their maximum values mainly at the transition region heights. It should be emphasized again that the current drive is considered as the initial stage of the EUV structures *formation*.

Now we turn to the question how the structures evolve in time. We shall use the electric circuit analogue to address this problem focusing on major questions: what makes the coronal structures take one or the other observed form, and what are the conditions for their realization.

Once a current system is formed, its further evolution depends on the capacity of a system to store electromechanical and magnetic energies, on its dissipative properties and thus the ability to release the accumulated energy. These properties are determined by several key factors, such as:

- (1) character of the photospheric driver;
- (2) magnetic field that interconnects the  $\beta \geq 1$  energy source region and  $\beta \ll 1$  dissipation region;
- (3) local height of the chromosphere/transition region where the most efficient generation of currents occurs;
- (4) feedback between the current generation and dissipation regions; and
- (5) characteristic spatial and timescales of a system.

The key element of the present approach is the recognition of the fact that the transition region plays an essential role in the process of energy transfer throughout the

atmosphere (see, e.g., Title 2000; Tarbell et al. 2000; Ryutova and Tarbell 2003; Ryutova and Shine 2004). On one hand, this is a region where the most efficient generation of currents occurs, and on the other hand, it is where presumably the energy transfer from large to small scales culminates, thus providing interconnection between corona and its underlying atmosphere through the resistive stresses.

### 16.4.1 An Equivalent Circuit—Earlier Attempts

The evolution of newly formed current system may proceed in different ways depending on hydromagnetic activity of underlying photosphere and on physical and kinetic properties of a system, in other words on the nature of photospheric driver and the overlying region.

The equivalent LRC approach turned out to be very helpful to study not only coupling between the energy source and remote dissipation regions, but also to analyze the various scenarios and find conditions for their realization on a unified basis.

The circuit equation follows directly from the global electrodynamics, and has been derived by many authors in application to laboratory plasma (see, e.g., Lehnert 1963) and to various space objects (Alfvén and Falthammar 1963; Alfvén and Carlqvist 1967; Ionson 1982; Spicer 1982; Melrose 1995). Generally, the equation has a standard LRC form, but its coefficients obtained from the MHD equations written for a particular system reflect the specific parameters of this system.

For convenience, we will demonstrate here the equivalence of an LRC circuit and electrodynamic equations:

$$\frac{4\pi}{c^2} \frac{\partial \vec{j}}{\partial t} = \nabla \times (\nabla \times \vec{E}) \quad (16.15)$$

$$\nabla \cdot \vec{j} = 0 \quad (16.16)$$

$$\vec{j} = \sigma \left( \vec{E} + \frac{\vec{v} \times \vec{B}}{c} \right) \quad (16.17)$$

$$\rho \frac{d\vec{v}}{dt} = -\nabla P_e + \frac{\vec{j} \times \vec{B}}{c} \quad (16.18)$$

One can start from the equation of motion for the electron gas and arrive to the equation for the generation of the electric field (Spicer 1982; Melrose 1995). This approach leads to a simple circuit equation of a “transmission line.” In this case, however, the physical mechanism of coupling which occurs at small resistive scales is obscured.

As it was pointed out by Ionson (1982), the electrodynamic coupling between the two regions occurs through the turbulent stressing of the common magnetic field in the photosphere that results in generation of a Poynting flux of energy that propagates upward and subsequently dissipates. This process is directly related to the dissipation

of the surface Alfvén waves (and associated heating) where energy is transferred from large to small scales by phase mixing.

Indeed, because of high conductivity of coronal plasma, dissipative effects turn on at small transverse scales,  $\Delta x_r$ , where the resonance absorption of the Alfvén waves occurs. In other words,  $\Delta x_r$  is a characteristic distance at which the dissipative terms link the perturbations at the magnetic field lines (Heyvaerts and Priest 1983; Ryutova and Habbal 1995):

$$\Delta x_r = \frac{a}{Re_m^{1/3}}, \quad (16.19)$$

$Re_m = v_A a / \eta_D$  is magnetic Reynolds number with  $\eta_D = c^2 / 4\pi\sigma$  being magnetic diffusivity, and  $\sigma = 1.96ne^2 / (m_e \nu_{ei})$  plasma conductivity. Parameter  $a$  is the width of magnetic structure.

### 16.4.2 LRC Circuit with Mutual Inductance (Transition Region)

Thus physics of coupling is associated with the dissipative stresses that operate at small scales characterized by generalized skin depth,  $\Delta x_r$ , which is in fact the local cross-field shear length of the induced current.

Here we adopt the approach used by Ionson (1982, 1984). Figure 16.6a illustrates the prototype of physical system from subsurface layers to the corona and its equivalent electrodynamic circuit. The system comprises a  $\beta < 1$  magnetic loop and an underlying region of  $\beta \geq 1$  velocity fields which are electrodynamically coupled via the interconnecting magnetic field. It is important to note, however, that Ionson's model (as well as all other previous models) ignores the influence of the transition region. The points marked by the question marks and the straight line passing them in Fig. 16.6a is only a formal boundary between the two regions, and is not reflected in the circuit equation. On the other hand, Fig. 16.6b that illustrates the energetically open circuit includes the presence of the transition region and its influence. This will be discussed in the next section. Before doing this, we will continue Ionson's (1982) line of reasoning.

Despite the above-mentioned disadvantage, the Ionson's model is important to discuss. Let us choose a coordinate system with  $l$  directed along the magnetic field, and  $x_\perp = (x_r, x_\theta)$ , where  $x_r$  represents the radial direction, with characteristic scale  $\Delta x_r$ , and  $x_\theta$ —the azimuthal direction, with characteristic scale of the width of elemental loop,  $a$ . It is assumed that physical parameters vary only in the  $l$  and  $x_r$  directions. Using  $(\nabla \times \vec{E})_l \simeq 0$ , which follows from the condition that Poynting flux be directed along the loop, one has from (16.15):

$$\frac{4\pi}{c^2} \frac{\partial \vec{j}_\perp}{\partial t} + \nabla_\perp \left( \frac{\partial E_l}{\partial l} \right) - \frac{\partial^2 \vec{E}_\perp}{\partial l^2} = 0 \quad (16.20)$$



$$\frac{4\pi}{c^2} \frac{\partial j_l}{\partial t} + \frac{\partial}{\partial l} (\nabla_{\perp} \cdot \vec{E}_{\perp}) - \nabla_{\perp}^2 E_l = 0 \quad (16.21)$$

Obviously,  $\partial/\partial x_r \gg \partial/\partial x \gg \partial/\partial l$ . This implies that  $E_{\theta} \ll E_r$ , and since  $\vec{j}_{\perp} \sim \partial \vec{E}_{\perp} / \partial t$ ,  $j_{\theta} \ll j_r$ . Taking into account that  $\nabla \vec{j} = 0$ , one can see that (16.20) and (16.21) are redundant.

Thus, formally it is sufficient to consider one of the above equations. But as will be discussed later choice of the equation is not only matter of convenience but may cause essential limitations. To demonstrate this we briefly describe below Ionson's derivation who has focused upon (16.21). Using Ohm's law and taking time derivative of (16.21) one obtains:

$$\frac{4\pi}{c^2} \frac{\partial^2 j_l}{\partial t^2} + \frac{\partial^2}{\partial x_r \partial l} \left( \frac{1}{\sigma} \frac{\partial j_r}{\partial t} \right) - \nabla_{\perp}^2 \left( \frac{\partial j_l}{\partial t} \right) - \frac{1}{c} \frac{\partial^3 (v_{\theta} B)}{\partial x_r \partial l \partial t} = 0 \quad (16.22)$$

With the use of the Heaviside step function of plasma beta,  $H(1 - \beta)$ , this equation can be rewritten in the form that reflects the contribution of various terms of this equation in the  $\beta \geq 1$  and  $\beta < 1$  regions. Note, that the second term in this equation can be neglected since it is small compared to the other terms. The last term has a meaning of the driving emf in the  $\beta \geq 1$  region, which cannot be evaluated explicitly. In the  $\beta < 1$  region this term represents the reactance of the overlying plasma to driving emf, and can be easily determined from the force balance, (16.18):

$$\rho \frac{\partial v_{\theta}}{\partial t} \simeq - \frac{j_r B}{c}, \quad (16.23)$$

Now (16.22) can be written as follows:

$$\frac{4\pi}{c^2} \frac{\partial^2 j_l}{\partial t^2} - H(1 - \beta) \frac{1}{\sigma} \frac{\partial^3 j_l}{\partial x_r^2 \partial t} - H(1 - \beta) \frac{4\pi v_A^2}{c^2} \frac{\partial^2 j_l}{\partial l^2} = H(\beta - 1) \frac{1}{c} \frac{\partial^3 (v B_0)}{\partial x_r \partial l \partial t} \quad (16.24)$$

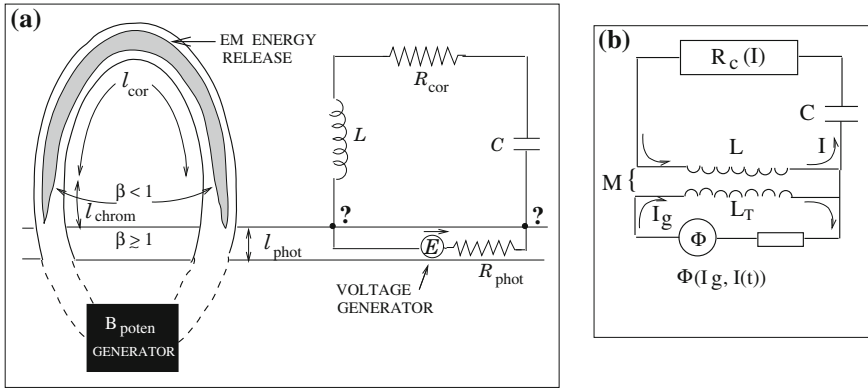
This equation has already a form of a simple LRC equation: the first term is an inductive reactance, the second term is associated with the resistance, the third term is a capacitive reactance and the term on the right-hand side is the external source of emf.

Using the equivalence  $\partial/\partial x_r \rightarrow i\pi/\Delta x_r$ ,  $\partial/\partial l \rightarrow i\pi/l$ , (16.24) can be integrated over the total volume of the magnetic loop. Note that this integration is equivalent to averaging procedure in which (16.24) is multiplied by volume of the elemental loop of the length  $l$ , i.e., by  $la\Delta x_r$ . One should bear in mind that  $j_l$  currents are localized within a cross-sectional area,  $a\Delta x_r$ .

Assuming that *most of the resistive load is associated with the  $\beta < 1$  region*, the result of this integration is as follows:

$$L \frac{d^2 I}{dt^2} + R \frac{dI}{dt} + \frac{I}{C} = \frac{d\Phi(t)}{dt}, \quad (16.25)$$

where the equivalent inductance  $L$ , capacitance  $C$ , and resistance  $R$  are given by



**Fig. 16.6** Model of the equivalent LRC circuit for the coronal loops: **a** Prototype magnetic loops system proposed by Ionson (1982); question marks highlight the cloudy points on line dividing a  $\beta \geq 1$  and  $\beta < 1$  regions; **b** energetically open LRC circuit (Ryutova 2006); Chromosphere/transition region is reflected by the necessarily present mutual inductance,  $M$

$$L = \frac{4l}{\pi c^2}, \quad C = \frac{lc^2}{4\pi v_A^2}, \quad R = \frac{1}{\sigma} \frac{l}{(\Delta x)^2}, \quad (16.26)$$

with the current and emf as

$$I = j_l a \Delta x_r = j_r a l \quad (16.27)$$

$$\Phi(t) = \frac{a v_\theta B}{c} \quad (16.28)$$

Equations (16.25)–(16.28) obtained by Ionson (1982, 1984) allowed him to perform detailed analysis and obtain several important results. In particular, the coupling between the photospheric driver and coronal loop features was established, and implicit equations for the maximum temperature and base pressure were found in a good agreement with observations. It was shown that coronal loops have a classic feature of high-quality resonators, which allows, for example, to study the resonant properties of a system and make reasonable predictions.

This model, however, can be applied only to a “stable” (long living) coronal loops, and does not describe their *evolution*. The important restricting factor here is the assumption (highlighted above in italic) that the resistive load of a system is associated only with the  $\beta \ll 1$  coronal region. But, as discussed earlier, the energy production and transfer necessarily involves the transition region where the resistive stresses already operate at the corresponding small scales. The coupling mechanism, therefore must reflect connection between the resistive properties of both corona and the transition regions (Fig. 16.6b).

## 16.5 Energetically Open Circuit

To represent transition between the chromosphere and corona, we take into account that the resistive load is associated not only with the corona, but with the chromosphere/transition region as well. This leads to appearance of an equivalent mutual resistance in the circuit equation, which in fact is equivalent to appearance of mutual inductance. This element is crucial for stability of newly formed EUV structures and realization of different scenarios of the structure evolution. Besides, as the system has all the properties of energetically open, locally nonconservative system with source and sink of energy, we extend the analysis to nonlinear processes. Fully nonlinear treatment of the problem is hardly possible, but the advantage of circuit approach is that it allows quite a simple treatment of weakly nonlinear unsteady processes.

One of the basic principles of the circuits is that, if Ohm's law,  $\Phi = RI$ , does not hold, the circuit must be considered *nonlinear*. There are many factors that brake Ohm's law in practice. First of all, if there is some functional relation between  $I$  and  $\Phi$ , the circuit becomes intrinsically nonlinear. Among numerous so called, contingently nonlinear elements, one of the most important is thermally sensitive resistance. Even a weak dependence of the resistance on temperature, leads to nonlinear function of  $I = I(\Phi)$  (see, e.g., Harnwell 1949). Present study will be restricted only by the intrinsic nonlinearity of a system.

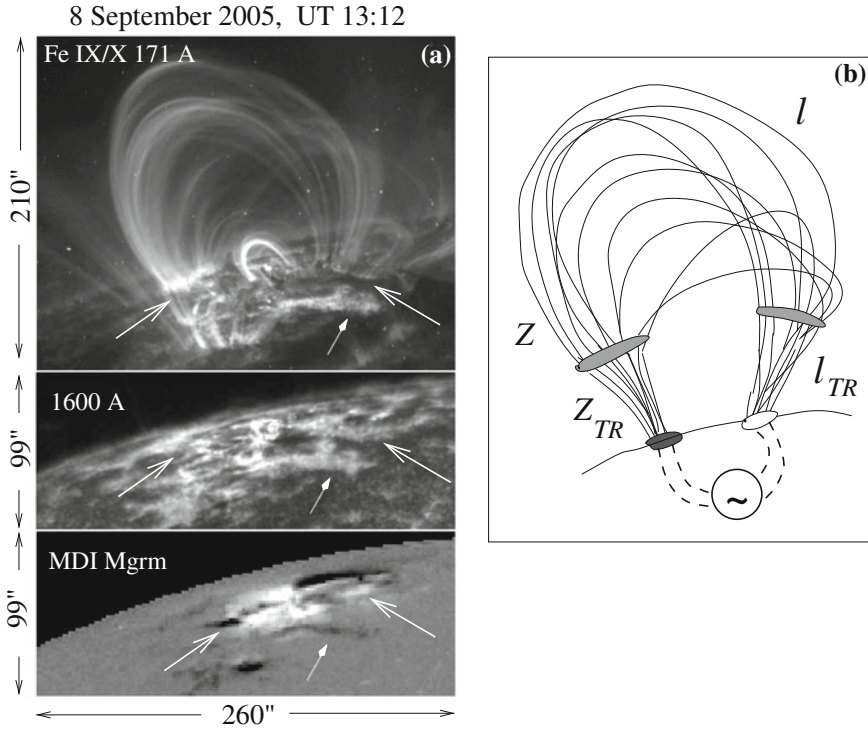
As shown in Sect. 16.2, the triggering mechanism for the EUV structure formation is associated with electric currents generated by strong disturbances produced by the emerging flux. We have discussed the efficiency of current drive for three types of disturbances: proper motion of hydrogen plasma (the observed  $H\alpha$ ), acoustic waves, and Alfvén waves.

It is hard to tell which of these mechanisms is dominant during the formation process. However, after the current system is formed, one can accept that its sustaining source of energy has a periodic or quasiperiodic character. It is therefore only natural to assume that during the entire process, the currents are "voltage-dependent,"  $I = I(\Phi)$ , and the sustaining photospheric driver is quasiperiodic. This, of course, does not exclude some sporadic injection of energy caused, for example, by the reconnection processes.

We will distinguish three interconnected regions:

- (1) the photosphere with the quasiperiodic driving force,
- (2) chromosphere/transition region where the most efficient generation of currents occurs, and
- (3) corona.

Figure 16.7 illustrates a typical example of well-established system of coronal loops near the eastern limb of the Sun (the image is rotated by  $90^\circ$  so that north is to the right, upper panel) together with co-aligned MDI magnetogram of underlying region and its image at the transition region temperatures (lower panels). The average length of the coronal part of loops is about  $l \simeq 280$  arcsec ( $\simeq 2 \times 10^{10}$  cm), and width of elemental filament is in a range of  $a \simeq 1 - 3$  arcsec ( $\simeq 0.73 - 2.2 \times 10^8$  cm).



**Fig. 16.7** Model of coronal loops for the equivalent circuit. **a** Example of well-established system of coronal loops close to limb, together with co-aligned MDI magnetogram of underlying region and its image at the transition region temperatures (TRACE 1,600 Å). Note that the family of loops is rooted in the photosphere at compact sunspots with well-defined boundaries, while corresponding enhanced emission in 1,600 and 171 Å lines is spread over much larger area (marked by large arrows). **b** Schematic of the model for the equivalent circuit with the photospheric driver, corona, and the transition region that links these regions through mutual resistance,  $Z_M = \sqrt{ZZ_{TR}}$

The aspect ratio is of the order of  $(a/l) \simeq 0.01$ . This estimate will be used below for quantitative analysis.

Note that as longitudinal currents are localized within a cross-sectional area,  $a \Delta x_r$ , where  $\Delta x_r$  is determined by (16.19), each elemental loop resolved in TRACE 171 Å line consists of thousands of current carrying filaments.

The family of loops is rooted at relatively compact sunspots with well-defined boundaries (marked by large arrows). The enhanced emission at the transition region temperatures corresponding to these sunspots is spread over much larger area that mimics the bright conglomerate of coronal loop footpoints. Note that transition region shows high activity above the entire active region, while response of the corona is quite selective: coronal loops appear at some preferable (and limited) sites, while rest of the corona is either covered by mossy emission (marked by small arrows) or

seems intact (except a spectacular short-living compact loops lying over the polarity inversion line).

A sketch in Fig. 16.7b illustrates the model studied here with the photospheric driver and overlying transition and coronal regions coupled through mutual resistance,  $Z_M = \sqrt{ZZ_{TR}}$ . This in fact is equivalent to mutual inductance because  $Z_i = \omega L_i$ , and  $M = \sqrt{LL_{TR}}$  (see below for details). Thus we take into account that the resistive load is associated not only with the corona, but with the chromosphere/transition region as well. To reflect this in the equivalent circuit equation, it is convenient to use (16.20) which with Ohm's law has a form (as discussed above,  $j_\theta \ll j_r$ , and  $j_\perp$  is carried mostly by  $j_r$ ):

$$\frac{4\pi}{c^2} \frac{\partial j_r}{\partial t} - \frac{\partial^2}{\partial r^2} \frac{1}{\sigma} j_r + \frac{1}{c} \frac{\partial^2 v_\phi B}{\partial l^2} = 0 \quad (16.29)$$

We use the Heaviside step function of plasma beta in the form:  $H(\beta_{TR} - \beta)$ , where  $\beta_{TR}$  denotes the plasma beta at about the transition region heights. We apply the same averaging procedure that established equivalence between (16.22) and (16.25).

It is convenient to represent the coronal part of (16.29) in terms of induced emf,  $\Phi = (v_\theta B a)/c$ . Using (16.23) one obtains:

$$j_r = -\frac{c^2}{4\pi v_A^2} \frac{1}{a} \frac{\partial \Phi}{\partial t} \quad (16.30)$$

Now (16.22) can be written as follows:

$$H(\beta_{TR} - \beta) \left[ \frac{1}{a} \frac{c^2}{4\pi v_A^2} \left( \frac{4\pi}{c^2} \frac{\partial^2 \Phi}{\partial t^2} - \frac{1}{\sigma} \frac{\partial^3 \Phi}{\partial x_r^2 \partial t} \right) - \frac{1}{a} \frac{\partial^2 \Phi}{\partial l^2} \right] = H(\beta - \beta_{TR}) \frac{4\pi}{c^2} \frac{\partial j_r(\Phi)}{\partial t} \quad (16.31)$$

The term on the right-hand side (kept in general form) includes dependence on the driving emf in the  $\beta \geq 1$  region, and reactance of the transition region plasma. Integrating over the volume of the system gives:

$$LC \frac{d^2 \Phi}{dt^2} + RC \frac{d\Phi}{dt} + \Phi = \frac{4l}{\pi c^2} \frac{dI_g(\Phi)}{dt} \frac{\Delta x_{TR}}{\Delta x} \quad (16.32)$$

where we used (16.27), i.e. that  $I_g = j_r a_{TR} l_{TR}$ , and divided (16.32) by  $\Delta x/l$ . Using expression (16.26) for resistance, and assuming that  $R/R_{TR}$  is proportional to  $(1/\sigma)/(1/\sigma_{TR})$ , one obtains that  $(\Delta x_{TR}/\Delta x) \simeq \sqrt{l_{TR}/l}$ . With this, (16.32) takes the following form:

$$LC \frac{d^2 \Phi}{dt^2} + RC \frac{d\Phi}{dt} + \Phi = 4 \frac{\sqrt{l l_{TR}}}{\pi c^2} \frac{dI_g(\Phi)}{dt}, \quad (16.33)$$

or

$$LC \frac{d^2\Phi}{dt^2} + RC \frac{d\Phi}{dt} + \Phi = M \frac{dI_g}{d\Phi} \frac{d\Phi}{dt}, \quad (16.34)$$

where  $M$  has a meaning of the equivalent mutual inductance determined by the resistive coupling between the corona and its underlying region:

$$M = \frac{4}{\pi c^2} \sqrt{ll_{\text{TR}}}, \quad (16.35)$$

Note that the spatial extent of the resistive coupling covers the cross-sectional area of the family of loops at the transition region heights (shaded area in Fig. 16.7b, marked by long arrows in Fe  $IX/X$  171 and 1,600 Å images in Fig. 16.7a).

The functional  $I_g(\Phi)$  cannot be determined explicitly, but as a first step we may assume that the current is a weakly nonlinear function of the quasiperiodic emf. This can be treated with the perturbation theory, using the standard asymptotic methods of oscillation theory (Bogolubov and Mitropolsky 1961; Hagedorn 1988):

$$I_g = I_g(0) + \left. \frac{dI_g}{d\Phi} \right|_0 \Phi + \frac{1}{2} \left. \frac{d^2I_g}{d\Phi^2} \right|_0 \Phi^2 + \frac{1}{6} \left. \frac{d^3I_g}{d\Phi^3} \right|_0 \Phi^3 + \dots \quad (16.36)$$

In the first approximation  $dI_g/d\Phi \simeq I_0/\Phi$  (where  $I_0$  is the induced current in a stationary state), and the first expansion coefficient in (16.36) can be estimated as

$$\left. \frac{dI_g}{d\Phi} \right|_0 \simeq \frac{I_0}{\Phi} = C \frac{I_0}{\int Idt} = \Gamma_0 \quad (16.37)$$

The second expansion coefficient,  $d^2I_g/d\Phi^2$  corresponds to the inflection point, and can be put zero. This assumption is not essential, as it does not change the final result. The third expansion coefficient can be estimated using the assumption that at weak nonlinearity, (16.36) remains valid for maximum currents corresponding to saturation limit,  $\Phi = \Phi_{\text{sat}}$ , where  $\Phi_{\text{sat}} \simeq v_\theta Ba/2c$  is coronal loop's capacitive emf (cf. (16.28)). Taking derivative of (16.36) at this limit and using maximum power balance,  $I_g\Phi|_{\text{sat}} = RI_g^2|_{\text{sat}}$ , we have

$$\frac{1}{2} \left. \frac{d^3I_g}{d\Phi^3} \right|_0 \simeq -\frac{1}{R} \frac{1}{\Phi_{\text{sat}}^2} = -\Gamma_2, \quad (16.38)$$

and (16.36) becomes

$$I_g = I_g(0) + \Gamma_0\Phi - \frac{1}{3}\Gamma_2\Phi^3 \quad (16.39)$$

Note that this is analogous to sinusoidal volt-ampere characteristic at weak nonlinearity,  $\sin x = x - (1/3!)x^3$ . Respectively,

$$\frac{dI_g}{d\Phi} = \Gamma_0 - \Gamma_2\Phi^2, \quad (16.40)$$

and (16.34) takes a form

$$L \frac{d^2 \Phi}{dt^2} + (R - M\Gamma_0 + M\Gamma_2 \Phi^2) \frac{d\Phi}{dt} + \frac{1}{C} \Phi = 0 \quad (16.41)$$

Taking into account that

$$I = C \frac{d\Phi}{dt}, \quad (16.42)$$

and using the balance of capacitive and inductive reactance,  $(1/2)C\Phi^2 \simeq (1/2)MI^2$ , for the third term in brackets, (16.41) reduces to the following electrodynamic equation having a form of the equivalent circuit equation with a weak nonlinearity:

$$LC \frac{d^2 I}{dt^2} + (RC - MS_0 + MS_2 I^2) \frac{dI}{dt} + I = 0 \quad (16.43)$$

where

$$S_0 = C\Gamma_0 = C \frac{I_0}{\int I(t)dt}, \quad (16.44)$$

and

$$S_2 = \frac{M}{RC} \frac{1}{\Phi_{\text{sat}}^2}. \quad (16.45)$$

Coefficients of nonlinear expansion,  $S_0$  and  $S_2$  have natural physical meanings (Bogolubov and Mitropolsky 1961; Gaponov-Grekhov and Rabinovich 1992).  $MS_0$  represents the excess of energy supply over the generation threshold.  $MS_2$  reflects the nonlinear effect associated with the back-reaction of a circuit to the induced currents and is a measure of the amplitude of self-excited oscillations.  $\Gamma_0$  is a measure of a current drive rate and can be estimated from the momentum balance (16.2):

$$\Gamma_0 = \frac{I_0}{\int I(t)dt} \simeq \tilde{\nu}_{\text{ei}}. \quad (16.46)$$

where  $\tilde{\nu}_{\text{ei}} = (m_e/m_p)\nu_{\text{ie}}$  is the inverse slowing down time of particles via electron-ion collisions.

The presence of the new terms,  $-MS_0 + MS_2 I^2$ , in (16.43) significantly changes the situation. First of all, as is well known, if the coefficients in the circuit equation are not of the *same sign*, the system is subject to instabilities. The evolution of the system strongly depends on the interplay between the coefficients, and most importantly, on the sign of parameter,

$$\mu = MS_0 - RC, \quad (16.47)$$

which determines the solution of the circuit equation (16.43), and thus the actual behavior of the current system. This parameter reflects the basic physical properties of the current loops both at microscales (skin depth, kinetic coefficients, density) and at large scales (spatial dimensions, magnetic field).

Physically,  $MS_0 - RC < 0$  corresponds to the situation when the energy supply is less than the current generation threshold; in other words, the characteristic current build up time,  $\sim M/R$ , is less than the inverse current generation rate,  $1/\tilde{\nu}_{ei}$ .

At  $MS_0 - RC > 0$  the additional energy supply exceeds the generation threshold, i.e., is analogous to high-quality resonator.

Finally, proximity to  $MS_0 - RC \simeq 0$  corresponds to a parameter range where the bifurcation of the system from one regime to another occurs.

Instabilities can develop in all three cases including linear regime. But the character of the instability and conditions for its stabilization are different, providing thus realization of a wide range of coronal loop regimes from lengthy oscillatory states to flare-type disruption. In the next section, we will present the solutions of (16.43), and discuss conditions for several basic regimes.

## 16.6 Evolution of Current Systems

### 16.6.1 Linear Regime

We start with the brief analysis of linear regime, i.e., when the term,  $MS_2 I^2$  in (16.43) is negligibly small. There are two classes of the coronal loop evolution, determined, again by the sign of  $\mu$ .

If  $\mu < 0$ , (16.43) is a standard circuit equation that describes three well-known types of behavior depending on the determinant  $\Delta = \tilde{R}^2 - 4L/C$  (with  $\tilde{R} = R - M_0 S_0/C$ ):

1.  $\Delta < 0$  gives a regime of underdamped oscillations of currents, with frequency  $\omega = \omega_0 \sqrt{1 - \tilde{R}^2 C/4L}$  and damping rate  $\gamma_{\tilde{R}} = \tilde{R}/2L$ ; this corresponds to long-living “stable” loops showing the intensity oscillations with the above parameters.
2.  $\Delta > 0$  corresponds to overdamped oscillations of currents with damping rate  $\gamma_{\pm} = (\tilde{R} \pm \Delta^{1/2})/2L$ .
3.  $\Delta = 0$  corresponds to marginal state, critically damped oscillations, which can bifurcate into the weakly damped state or v.v. due to the external disturbances.

If  $\mu = MS_0 - RC > 0$ , i.e., when the energy supply exceeds the generation threshold, the system becomes unstable, and the damping rate  $\gamma_{\tilde{R}}$  becomes a growth rate. As the instability is linear it may result in a not too violent and yet the flare-like energy release without disruption of the global loop system. This process may occur repeatedly as long as a particular loop system exists. At any time when the accumulated energy exceeds the threshold and gets released the system starts to gain energy back until it again reaches the critical conditions for the release of the excess of energy. This regime corresponds to quasi-stable periodically flaring coronal loops.



### 16.6.2 Nonlinear Regime

To discuss the nonlinear regime, first we rewrite (16.43) in dimensionless form:

$$\frac{d^2 i}{d\tau^2} - \epsilon(1 - i^2) \frac{di}{d\tau} + i = 0 \quad (16.48)$$

Time is dimensionalized by  $\omega_0^{-1} = \sqrt{LC}$ , and current by the coefficient of nonlinearity:

$$\tau = t/\sqrt{LC}, \quad i = \sqrt{\frac{MS_2}{|\mu|}} I, \quad \epsilon = \mu/\sqrt{LC}. \quad (16.49)$$

Equation (16.48) is a typical Van der Pol equation for an energetically open oscillator with the dissipation and the driving force. The solution to this equation is known to be a modulated oscillations of the form:

$$i(\tau) = A(\tau)\cos(\tilde{\omega}\tau + \phi) - \frac{\epsilon}{32}A^3(\tau)\sin 3(\tilde{\omega}\tau + \phi) \quad (16.50)$$

with  $\tilde{\omega} = 1 - \epsilon^2/16$ , and slowly varying amplitude  $A(\tau)$  satisfying the evolutionary equation (see Appendix):

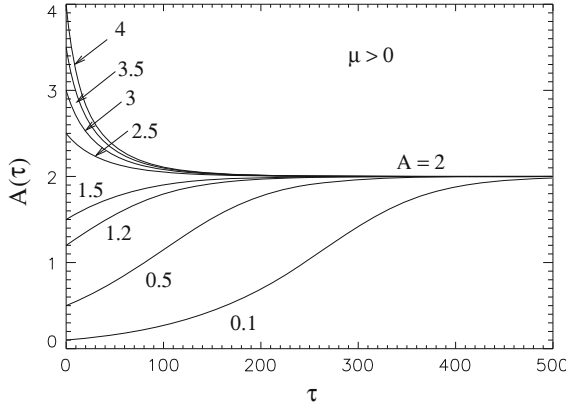
$$\frac{dA(\tau)}{d\tau} = \frac{\epsilon}{2} \left\{ A(\tau) - \frac{A^3(\tau)}{4} \right\} \quad (16.51)$$

The solution to this equation is:

$$A(\tau) = \frac{2A_0}{\sqrt{A_0^2 + (4 - A_0^2)\exp(-\epsilon\tau)}} \quad (16.52)$$

As discussed above, the time dependence of the current amplitude is determined by the sign of  $\mu$  (i.e. on the sign of  $\epsilon$ ).

If  $\mu > 0$ , currents evolve in accordance with a typical Poincare limit cycle; i.e., whatever the initial amplitude of the generated currents is “large” ( $A_0 > 2$ ) or “small” ( $A_0 < 2$ ), asymptotically the currents tend to a stationary value of  $A = 2$ . In other words, currents with initial amplitude  $A_0 > 2$  evolve in a decreasing regime, while currents with the initial amplitude  $A_0 < 2$  increase until they reach the limiting value. The larger the initial amplitude the faster it drops (i.e., the shorter is its limiting cycle) and the faster is the release of excess energy. The opposite regime corresponds to longer living systems gradually accumulating energy until the system reaches a stationary regime. Note that any stationary regime may be destroyed by some additional source of energy like reconnection process or interaction of the system with neighboring loops.



**Fig. 16.8** Poincare limit cycle ( $\mu > 0$  regime of the coronal loop evolution): Coronal loops with the initial current amplitude higher than  $A = 2$  quickly approach the quasi-stable state releasing the excess of energy until currents drop to a limiting value. Loops with the initial current amplitude less than  $A = 2$  gradually gain energy until currents reach a limiting value. The plots of the amplitudes are calculated for  $\epsilon = 0.1$

Figure 16.8 shows the time dependence of the current amplitude for different values of the initial amplitude starting from  $A_0 = 0.1$  to  $A_0 = 4$ . In all examples we used  $\epsilon = 0.1$ , i.e., we assumed that the energy supply exceeds the generation threshold by 10%. This solution describes a quasi-stationary oscillatory regime of coronal loops.

If  $\mu < 0$  (i.e.,  $\epsilon < 0$ ), (16.51) describes two qualitatively different evolution of currents. For high enough initial amplitudes, i.e., for  $A_0 > 2$ , the system becomes subject to explosive instability. In a finite time the currents reach infinitely large values. To illustrate this we may drop the linear term in (16.51), and rewrite the equation in the form

$$\frac{d\tau}{dA} \simeq \frac{8}{|\epsilon|} \frac{1}{A^3} \tag{16.53}$$

Integration of  $\tau$  gives straightforward a standard expression for explosively growing amplitude

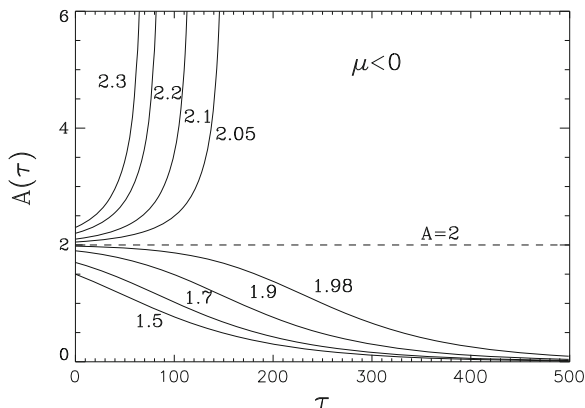
$$A(\tau) = \frac{A_0}{\sqrt{1 - (\tau/\tau_{\text{expl}})}} \tag{16.54}$$

with the explosive time (in this approximation)  $\tau_{\text{expl}} = 4/(|\epsilon|A_0^2)$ . The actual explosive time is somewhat longer and follows from the general solution of (16.51) with  $\epsilon = -|\epsilon|$ .

Written in the form:

$$A(\tau) = \frac{2}{\sqrt{1 - \exp\{|\epsilon|(\tau - \tau_{\text{expl}})\}}}, \tag{16.55}$$

**Fig. 16.9** The  $\mu < 0$  regime of the coronal loop behavior. Numbers next to plots are the initial (nondimensional) amplitude  $A$ ;  $\epsilon = 0.02$  for all cases. Loops with the initial current amplitude higher than  $A = 2$  show the explosive growth of currents; higher are the initial currents, shorter is the explosive time. Loops with the initial current less than  $A = 2$  are in a gradually decaying state



this solution clearly shows the explosive behavior with the characteristic time

$$\tau_{\text{expl}} = \frac{1}{|\epsilon|} \ln \frac{A_0^2}{A_0^2 - 4} \tag{16.56}$$

After the onset of the explosive instability, the system may develop in several different ways. This is determined by effects that may suppress, or sustain the instability. Formally, in time  $\tau_{\text{expl}}$  the currents indeed reach infinitely large values. This means that the system becomes strongly nonlinear, and other nonlinear effects turn on that may stabilize the instability (Weiland and Wilhelmsson 1977; Rytova 1988).

There are two major regimes:

- (1) the disruption of the circuit occurs before the instability gets stabilized, and
- (2) higher nonlinear effects stabilize the explosive instability which leads to partial energy release.

The first case corresponds to strong flare event which may destroy the current system.

If at  $\mu < 0$  the initial amplitude of the injected current is less than  $A = 2$ , the currents are in the decaying regime and loops gradually (and quite slowly) lose their energy.

The plots of the amplitude, (16.55) for both regimes are shown in Fig. 16.9. Numbers next to plots are nondimensionalized values of initial amplitude. In these examples we used  $\epsilon = 0.02$ , i.e., the supplied energy is close to the generation threshold, but below it by 2%.

## 16.7 Quantitative Analysis

To perform quantitative analysis we need to represent solutions in the dimensional units:

$$I = i\sqrt{\frac{|\mu|}{MS_2}}, \quad t = \tau\sqrt{LC}, \quad \epsilon = \frac{|\mu|}{\sqrt{LC}}, \quad (16.57)$$

It is also useful to introduce a dimensional amplitude of current  $\mathcal{I}(t)$ :

$$\mathcal{I}(t) = \sqrt{\frac{|\mu|}{MS_2}} A(\tau) \quad (16.58)$$

Now we need to express the above quantities through the basic physical parameters including the specific parameters of coronal loops. For  $\mu = MS_0 - RC$  using (16.26) and (16.35)–(16.46) we obtain:

$$\mu = CL \frac{m_e}{m_p} \nu_{ei} \left[ \sqrt{\frac{l_{TR}}{l}} - \frac{\pi^2 m_p}{m_e} \frac{\delta^2}{(\Delta x_r)^2} \right] \quad (16.59)$$

where  $\delta = c/\omega_{pe}$  is a plasma skin depth,  $\delta = 5.3 \times 10^5/\sqrt{n}$ , and  $\Delta x_r$  is given by (16.19). Note, that parameter  $\mu$  is determined by the loop properties at microscales as well as at large scales. With (16.19)–(16.26)  $\mu$  takes a form:

$$\mu = \frac{\tilde{\nu}_{ei}}{\omega_0^2} \alpha \quad (16.60)$$

where we introduced parameter  $\alpha$ , which determines the sign of  $\mu$ :

$$\alpha = \sqrt{\frac{l_{TR}}{l}} - 1.06 \times 10^7 \frac{T}{n} \left( \frac{v_A}{a^2} \right)^{2/3} \quad (16.61)$$

Using (16.26) and (16.45) with  $\Phi \simeq vBa/2c$  we have for  $S_2^{-1}$ :

$$S_2^{-1} = \frac{R}{4M} m_p v^2 n l a^2 = \frac{Re_m^{2/3}}{\sigma} \frac{m_p v^2 n l^2}{4M} \quad (16.62)$$

Now the normalization factor for dimensional current reduces to:

$$\sqrt{\frac{|\mu|}{MS_2}} = nev l \frac{\sqrt{|\alpha|}}{2M\omega_0} \frac{Re_m^{1/3}}{\sigma}, \quad (16.63)$$

and for the amplitude of current we have:

$$\mathcal{I}(t) = nev \sqrt{|\alpha| \frac{l}{l_{\text{TR}}} \frac{\pi}{2Re_m^{2/3}} a} |A| \quad (16.64)$$

It is also convenient to make quantitative estimates in terms of the current density. As  $|I| = ja \Delta x_r$ , the current density is given by:

$$j = nev \sqrt{|\alpha| \frac{l}{l_{\text{TR}}} \frac{\pi}{2Re_m^{1/3}} \frac{l}{a}} |A| \quad (16.65)$$

The velocity of the induced coronal flow,  $v$ , can be estimated by balancing the capacitive and inductive resistances (Ionson 1982):

$$v \simeq 5 \times 10^{-3} v_A Re_m^{1/6} \quad (16.66)$$

The above equations, containing the physical parameters simply associated with the observed quantities allow perform the quantitative analysis and use results both for diagnostic goals and prediction of the behavior of loop systems.

### 16.7.1 Examples

For quantitative estimates we will choose three temperature regimes:  $T = 2 \times 10^6$ ,  $T = 10^6$ , and  $T = 3 \times 10^5$  K. We will also assume that some million degree loops may be quite compact and reach only transition region heights. Therefore for each temperature regime we consider examples of the loop lengths of  $l = 10^{10}$ ,  $l = 2 \times 10^9$  and  $l = 5 \times 10^8$  cm. We choose for the aspect ratio  $a/l = 0.01$ .

First we need to find values of  $\alpha$  that define the regions with  $\mu > 0$  and  $\mu < 0$ , and thus two basic groups of different regimes of the loop evolution. Using the dependence of the Alfvén speed on the temperature and plasma beta as

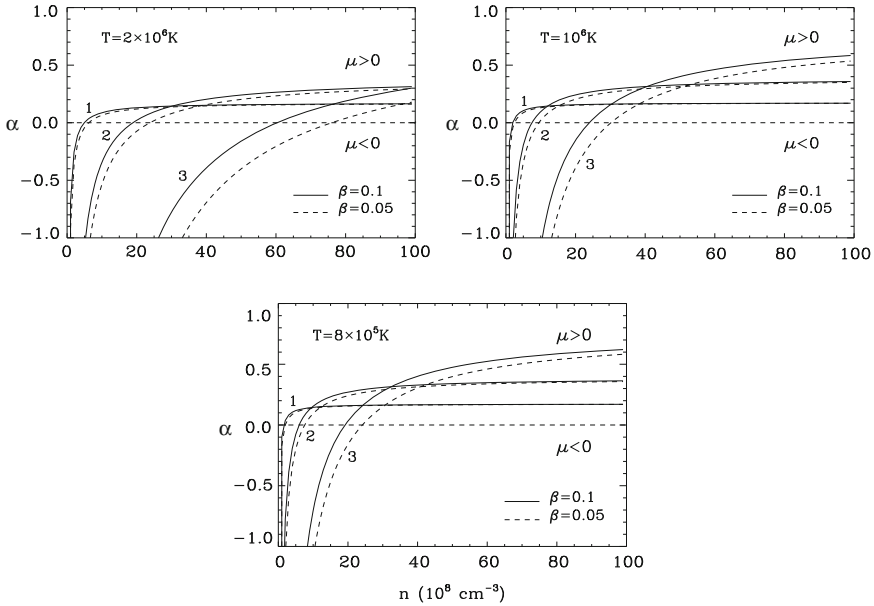
$$v_A = 1.82 \times 10^4 \sqrt{T/\beta}, \quad (16.67)$$

we have:

$$\alpha = \sqrt{\frac{l_{\text{TR}}}{l}} - 7.3 \times 10^9 \frac{1}{n\beta^{1/3}} \left(\frac{T}{a}\right)^{4/3} \quad (16.68)$$

Parameter  $\alpha$  as a function of density is shown in Fig. 16.10. Three panels correspond to three temperature regimes. Each temperature regime contains plots for three different lengths of loops, reflecting the examples of the chromosphere and corona. Solid lines correspond to  $\beta = 0.1$ , and dashed lines to  $\beta = 0.05$ .

Some qualitative conclusions follow immediately from these plots. The regime with  $\mu > 0$ , which corresponds to dynamics of coronal loops evolving in accordance



**Fig. 16.10** Parameter  $\alpha$  as a function of plasma density at three different temperatures. Numbers ‘1’, ‘2’ and ‘3’ correspond to loop lengths of  $l_1 = 10^{10}$ ,  $l_2 = 2 \times 10^9$  and  $l_3 = 5 \times 10^8$  cm, respectively. In all examples *solid lines* correspond to plasma beta  $\beta = 0.1$  and *dashed lines* to  $\beta = 0.05$ . The range of parameters with  $\alpha < 0$  ( $\mu < 0$ ) corresponds to explosively unstable loops, whereas  $\alpha > 0$  ( $\mu > 0$ ) to loops evolving according to Poincare limit cycle

with the Poincare limit cycle requires quite high densities for loops to be in a stable state. For example, for 2 MK loops with  $l = 10^{10}$  cm to be in a stable regime, densities should be higher than  $2 \times 10^9 \text{ cm}^{-3}$ . At lower temperatures, the density threshold slightly decreases. This result is consistent with recent observations showing that densities in large and hot loops are by the order of magnitude higher than those believed earlier (Aschwanden et al. 2000). It was also shown that not only the loops with moderate length  $l \leq 10^9$  cm, but even long loops with  $l > 10^{10}$  cm, have densities higher than  $10^9 \text{ cm}^{-3}$ .

If the density drops below some critical value, and  $\mu$  becomes negative (cf. (16.68)), the loop becomes either subject to explosive instability if the initial current density exceeds the critical values ( $A_0 > 2$  in dimensionless units), or slowly decays if  $A_0 < 2$ .

Parameters close to  $\mu \simeq 0$  ( $\alpha \simeq 0$ ) correspond to the bifurcation region.

The range of parameters corresponding to negative values of  $\mu$  also describes different regimes of loop behavior, which, again, depends on the initial energy supply. Thus, in the  $\mu < 0$  regime the explosive instability may develop only if  $A_0 > 2$ ; if  $A_0 < 2$  loops just gradually loose their energy, as shown in Fig. 16.9.

As the normalized factor for currents contains the specific parameters of coronal loops, the limiting value is different for different loops. Some quantitative examples

**Table 16.2** Estimates of critical currents and current densities for loops of three different length at coronal temperatures

$T$ (K)		$2 \times 10^6$			$10^6$		$8 \times 10^5$
$\eta_D$ ( $\text{cm}^2 \text{s}^{-1}$ )		$3.7 \times 10^3$			$1.05 \times 10^4$		$1.47 \times 10^4$
$v_A$ ( $\text{cm s}^{-1}$ )		$8 \times 10^7$			$5.7 \times 10^7$		$5 \times 10^7$
$l$ ( $10^8 \text{ cm}$ )	100	20	5	100	20	5	5
$Re_m$ ( $10^{10}$ )	200	43	10	54	10	2.7	1.7
$\omega_0$ ( $\text{s}^{-1}$ )	0.025	0.13	0.5	0.02	0.1	0.36	0.31
$\alpha$ ( $\mu < 0$ )	-0.1	-0.15	-0.2	-0.1	-0.2	-0.3	-0.5
$n$ ( $10^8 \text{ cm}^{-3}$ )	3.2	14	48	1.2	5	17	11
$\tilde{\nu}_{ei}$ ( $10^{-2} \text{ s}^{-1}$ )	0.45	2	6.7	0.48	2	6.7	6.1
$\mathcal{I}_{cr}$ ( $10^6 \text{ A}$ )	76	17	3	42	10	2.6	2.4
$I_{cr}^{(a)}$ ( $10^{10} \text{ A}$ )	96	12.8	1.33	34	4.4	0.77	0.63
$j_{cr}$ ( $\text{Am}^{-2}$ )	0.96	3.2	5.4	0.34	1.1	3.1	2.5
$\alpha$ ( $\mu > 0$ )	0.1	0.15	0.2	0.1	0.2	0.3	0.5
$n$ ( $10^8 \text{ cm}^{-3}$ )	12	31	82	5	16	40	57
$\tilde{\nu}_{ei}$ ( $10^{-2} \text{ s}^{-1}$ )	0.17	4.3	0.12	2	6.3	0.16	0.32
$\mathcal{I}_{lim}$ ( $10^6 \text{ A}$ )	290	38	5	180	30	6.1	12
$I_{lim}^{(a)}$ ( $10^{10} \text{ A}$ )	360	28.6	2.3	140	14	1.82	3.17
$j_{lim}$ ( $\text{Am}^{-2}$ )	3.6	7.1	9.2	1.4	3.5	7.3	12.7

are shown in Table 16.2. The upper section has some basic parameters for chosen lengths of coronal loops at three temperatures. The middle part of the table contains the quantitative estimates of critical currents and current densities for loops in the  $\mu < 0$  regime. The lower part of the table contains the estimates for limiting currents for loops in the  $\mu > 0$  regime. We defined the  $A = 2$  value in dimensional units for the  $\mu < 0$  regime as  $\mathcal{I}_{cr}$  and for  $\mu > 0$  as  $\mathcal{I}_{lim}$  to distinguish them from the initial current amplitude  $\mathcal{I}_0$ .

The values of  $\mathcal{I}_{cr}$  and  $\mathcal{I}_{lim}$  are given by (16.64) with  $A = 2$ . To estimate these values we choose  $\alpha = \pm 0.1, \pm 0.15$  and  $\pm 0.2$  for loops at  $T = 2 \times 10^6 \text{ K}$ ;  $\alpha = \pm 0.1, \pm 0.2$  and  $\pm 0.3$  for loops at  $T = 10^6 \text{ K}$ , and  $\alpha = \pm 0.5$  at  $T = 8 \times 10^5 \text{ K}$  for loop of  $5 \times 10^8 \text{ cm}$  length. The choice of  $\alpha$  determines the densities of loops (see Fig. 16.10).

It is important to note that  $\mathcal{I}_{cr}$  and  $\mathcal{I}_{lim}$  are calculated for elemental current filaments with cross section  $a\Delta x_r$  using (16.27). The total average current flowing through the visible loop with cross section  $\simeq a^2$ , will be obviously  $I^{(a)} = j_l a^2$ , or  $I^{(a)} = \mathcal{I} Re l/3$ . As measured currents in the literature are related to visible loops (see e.g. Leka et al. (1996)), it is useful to calculate the critical values of these averaged currents as well. These values are given in Table 16.2 as  $I_{cr}^{(a)}$  and  $I_{lim}^{(a)}$ . Thus, e.g. for loop with  $l = 10^{10}$  and  $a \times 10^8 \text{ cm}$  at  $T = 2 \times 10^6 \text{ K}$ , the critical current is  $I_{cr}^{(a)} = 9.6 \times 10^{11} \text{ A}$ ; for loop with  $l = 2 \times 10^9 \text{ cm}$  at  $T = 10^6 \text{ K}$ ,  $I_{cr}^{(a)} = 4.4 \times 10^{10} \text{ A}$ .

Take, for example, a loop with  $l = 10^{10}$  cm at  $T = 2 \times 10^6$  K with  $\alpha = -0.1$ . The critical current for such a loop is  $\mathcal{I}_{\text{cr}} = 7.6 \times 10^7$  A ( $\mathcal{I}_{\text{cr}}^{(a)} = 9.6 \times 10^{11}$  A). If the initial amplitude of injected current is, say  $\mathcal{I}_0 \simeq 2 \times 10^7$  A, then the loop is subject to explosive instability. In dimensional units the explosive time is  $t_{\text{expl}} = \tau_{\text{expl}} \sqrt{LC}$ , where  $\tau_{\text{expl}}$  is determined by (16.56). Using (16.57) and (16.60) we have

$$t_{\text{expl}} = \frac{1}{\tilde{\nu}_{\text{ei}}|\alpha|} \ln \frac{\mathcal{I}_{\text{cr}}^2}{\mathcal{I}_{\text{cr}}^2 - \mathcal{I}_0^2} \quad (16.69)$$

In the above example, currents with initial amplitude of  $2 \times 10^8$  A will reach the “infinitely” large values in about 6 min. If the initial amplitude of the injected current is somewhat smaller (but still higher than the critical value), say  $10^8$  A, it will take about 32 min to bring the system to the regime of explosive instability. Obviously, the larger the injected currents the shorter the explosive time. These processes are directly associated with the coronal flare events.

At  $\mu > 0$  the initial current,  $\mathcal{I}_0 = 2 \times 10^8$  A, for the same loop is less than  $\mathcal{I}_{\text{lim}} = 2.9 \times 10^9$  A, and the loop will continue to accumulate energy until currents reach this limiting value. The ratio  $\mathcal{I}_0/\mathcal{I}_{\text{lim}}$  in this case 0.069, so time for currents to reach the limiting value is longer than  $\tau = 500$  (cf. curve “0.1” in Fig. 16.8).

In dimensional units for loop with  $l = 10^{10}$  cm and  $v_A = 8 \times 10^7$  cm s $^{-1}$ , this time translates into  $t = \tau \sqrt{LC} = 5.5$  h. Consider for example the loop with  $l = 2 \times 10^9$  cm at  $T = 2 \times 10^6$  K. The critical current with  $\alpha = -0.15$  is  $\mathcal{I}_{\text{cr}} = 1.7 \times 10^7$  A. If the initial amplitude of the injected current is only  $\mathcal{I}_0 = 4 \times 10^7$  A ( $A_0 = 2.3$ ), the explosive instability will develop in about 8 min. The same loop with the initial current  $\mathcal{I}_0 = 2.5 \times 10^7$  A ( $A_0 = 1.5$ ) will cool down in about 1.2 h.

It is important to emphasize again that the parameter  $\mu = MS_0 - RC$  that defines two major groups for coronal loop conditions, reflects the physical properties of a system both at large scales (e.g.,  $l$ ,  $a$ ,  $B$ ), and at microscales (e.g.,  $\sigma$ ,  $\tilde{\nu}_{\text{ie}}$ , etc.).

Wide range of these parameters and their combinations provide various regimes for the coronal loop evolution. Within each of the major group, loops may behave in a very different ways. As seen in Fig. 16.8 ( $\mu > 0$ ), loops with high initial currents cool down and quickly approach a quasi-stable state—this may well represent the post-flare cooling regime; loops with sublimited currents gradually gain the energy until they reach a quasi-stable state. Figure 16.9 shows, e.g., that within the range of parameters defined by  $\mu < 0$ , loops with high initial currents are subject to the explosive instability that correspond to fast and violent energy release, while loops with subcritical currents remain for a long time in slowly decaying phase.

## 16.8 Limiting Currents and Filamentary Structures

When plotting parameter  $\alpha$  as a function of plasma density (Fig. 16.10), we fixed the aspect ratio  $a/l = 0.01$ . Clearly, one can fix any other parameter, say density or temperature, and plot  $\alpha$  as a function of thickness,  $a$ , or aspect ratio. Character



**Table 16.3** Estimates of limiting currents,  $\mathcal{I}_{\text{lim}}$ , and critical radii of filamentary structures,  $a_{\text{cr}}$ , for the “stable” loops observed with TRACE and SXT

No	Observations				Estimates	
	$l$ ( $10^8$ cm)	$w$ (MK)	$T$ ( $10^8$ cm $^{-3}$ )	$n$ ( $10^{10}$ A)	$\mathcal{I}_{\text{lim}}$ ( $10^8$ cm)	$a_{\text{cr}}$
1	4.0	1.9	1.2	12.2	2.11	0.91
2	10.0	2.3	1.2	14.7	6.99	1.1
3	17.0	1.5	1.2	9.1	5.94	1.9
4	18.0	2.2	1.2	15.2	12.7	1.4
5	26.2	9.9	6.7	40.6	44.4	4.2
6	28.1	10.3	6.0	25.5	32.2	5.4
7	28.7	21.1	5.8	18.5	34.8	6.7
8	29.5	19.5	5.1	17.3	34.3	6.3

of these plots will be similar to those shown in Fig. 16.10, and will show the critical values of the structure dimensions at given density or temperature.

According to recent observations coronal loops should indeed have a filamentary structure (see, e.g., Aschwanden et al. 2000; Winebarger et al. 2003). It is remarkable that in the circuit model *small scales of current carrying filaments arise automatically*. Radius of the filamentary structure is restricted from above roughly speaking by the Reynolds number (Ryutova and Habbal 1995). More precise estimate involve many factors which are the subject of future studies. Whereas minimum, critical value of radius,  $a_{\text{cr}}$  follows directly from the parameter  $\mu$  which determines regime of the loop dynamics (see (16.60) and (16.68)).

If density, temperature and loop length are known from observations, (16.68) allows one to estimate the limiting current for a particular loop, and find critical radius of elemental filament,  $a_{\text{cr}}$ , below which the filament becomes unstable. Examples of such estimates are given in Table 16.3, where we used results of Winebarger et al. (2003) for 8 loops.  $w$  here is the observed loop width. One can see that it exceeds the calculated critical radius of filamentary structure in all cases except one (# 3 loops in Table 16.3). Indeed, the “stable” loops should have higher radii than  $a_{\text{cr}}$ . If the radius of some filament drops below this value, the filament becomes unstable.

In conclusion, it is useful to briefly overview the results of this chapter and make some additional remarks.

We started this chapter with consideration of the particular events associated with magnetic flux emergence that eventually forms two opposite polarity pores, and triggers formation of magnetic loop structures in the overlying chromosphere/corona. This is an ordinary event occurring in the solar atmosphere in any moment of time at various scales. Particular event considered in this chapter stands out only in virtue of the acquisition of a rich multiwavelength data that show step by step development of events that starts from detection of the subsurface motions and ends up with the formation of the EUV structures that outline well-established flows above the newly formed pores. Changes in the photospheric magnetic fields occur “hand in hand”

with dynamic changes in EUV structures, and serve as evidence for unambiguous coupling of the photosphere, chromosphere, and corona.

High cadence multiwavelength observations show how the emergence of a large-scale magnetic flux is accompanied by strong collimated plasma flows which appear at coronal heights at the very early stage of the flux emergence. The corona and chromosphere quickly respond to these motions, and show a high activity above the future site of pore formation long before the pore is formed. Coronal structures acquire their “final” forms only after the strong  $H_{\alpha}$  flows are significantly reduced and acquire a more or less stable shape of a compact arcades “connecting” two opposite pores. The EUV structures as well consist of an arcades of many thin loops of the same shape as the flow pattern.

These observations clearly indicate that the impulsive phenomena associated with strong magnetic flux emergence (whose visible manifestation is, e.g., a highly collimated plasma flows) are directly responsible for the EUV structure formation. Combination of magnetic fields and impulsive phenomena suggest the involvement of electric currents.

We have analyzed the efficiency of current drive associated with the photospheric drivers. In particular, we have concentrated on those mechanisms of current drive which are directly connected with strong disturbances produced by emerging magnetic flux. These are

- (1) the currents generated by the proper motion of hydrogen plasma,
- (2) the wave-induced currents, and
- (3) currents driven by the Alfvén waves in the presence of mass flows. Each of these mechanisms gives a reasonable range of parameters for generated currents.

The proper motion of plasma is quite efficient at all heights, and may generate currents from  $j \simeq 2.0 \times 10^{-4} \text{ Am}^{-2}$  at high altitudes up to  $j \simeq 0.17 \text{ Am}^{-2}$  at low altitudes. The acoustic waves in linear regime can be ignored, whereas in a weakly nonlinear regime they may drive currents on the order of  $j \simeq 10^{-2} \text{ Am}^{-2}$ . In case of the Alfvén waves, the efficiency of current drive is quite sensitive to wave frequency. For example, higher frequency waves can generate stronger currents and at lower altitudes. Quantitative estimates of current densities at different temperatures (and frequencies) give an interval ranging from  $j \simeq 1.7 \text{ Am}^{-2}$  to  $j \simeq 2.0 \times 10^{-3} \text{ Am}^{-2}$ . The advantage of this mechanism is that it naturally combines the mechanical (flows) and magnetic effects in the process of current drive. Besides, the method itself allows to estimate both, the current densities and corresponding heights.

The effect of the current drive as a natural consequence of a photospheric driver allows to study further evolution of currents and coronal structures associated with the dynamic changes in the photosphere. These processes may be described in terms of the equivalent electric circuit that consolidates mechanical, magnetic, and electrical effects into one scheme, and establishes coupling between the surface driver and dissipation region in the overlying atmosphere.

Further evolution of currents and coronal structures associated with the dynamic changes in the photosphere is studied using the analogue of an energetically open

circuit. This approach is quite general and may be applied to any current systems throughout the solar atmosphere. The system consists of the energy source (in our case a photospheric driver), dissipation region, and region where transition and feedback between the  $\beta \geq 1$  and  $\beta \ll 1$  regions occur (transition region between the chromosphere and corona). Such a system has obviously all the properties of energetically open, dissipative system which has a tendency to self-organization and formation of various forms of dynamic structures. We treated the system as such and extended analysis to nonlinear regime, which allows to study the various regimes of the EUV structures and conditions for their realization.

The major element of the approach is the inclusion of the transition region and its influence on coupling between the corona and photosphere/chromosphere region. Physics of coupling has the resistive character, and consists of the mechanical stressing of the common magnetic field in the photosphere that results in generation of electric currents and corresponding Poynting flux of energy that propagates upward and subsequently dissipates. Because of high conductivity of coronal plasma, dissipative effects turn on only at a small transverse scales of the order of generalized skin depth determined by kinetic coefficients of plasma. The generated currents reach their maximum values mainly at the transition region heights establishing conditions for coronal loop formation.

To reflect influence of transition region on the coupling process we take into account that the resistive load is associated not only with the corona, but with the chromosphere/transition region as well. This leads to appearance of an equivalent mutual resistance in the circuit equation derived from the global electrodynamics. This in fact is equivalent to appearance of mutual inductance (as  $Z_i = \omega L_i$ , cf. Figs. 16.6b and 16.7b).

The nonlinear circuit equation with mutual inductance acquires the form of the Van der Pol oscillator. Depending on the coefficients, determined by the loop parameters, this equation describes various regimes which include long-living steady loops, periodically flaring and exploding loop systems. A crucial element of the problem is a measure of an energy supply and the capacitance of a loop, reflected by parameter  $\mu = MS_0 - RC$ . The sign of this coefficient determines the solution of the circuit equation, and thus the actual behavior of the loop. Physically,  $\mu < 0$  corresponds to the situation when the energy supply is less than the current generation threshold. For  $\mu > 0$  the additional energy supply exceeds the generation threshold; the range of parameters near  $\mu \simeq 0$  corresponds to the state when the system bifurcates from one regime to another.

Table 16.4 briefly summarizes typical regimes of coronal loop evolution.  $A_0$  is in dimensional units, and for individual loop system is given by (16.64) with  $|A| = 2$ .

Thus the physical parameters for realization of different scenarios of loop evolution form a simple system and most of them are directly observable. It is important to note that the circuit model also predicts that the EUV loops must have a small-scale filamentary structures. A critical radius of elemental filament for each individual structure is also a simple function of the observed parameters and can be used for diagnostic goals.

**Table 16.4** Linear and nonlinear regimes of the coronal loop dynamics

	$\mu = MS_0 - RC < 0$	$\mu = MS_0 - RC > 0$
Linear regime	Long-living loops showing a weakly damped, overdamped, or critically damped oscillations of intensity	Long-living loops gradually gain and then loose energy periodically resulting a flare-like events
Nonlinear regime, $A_0 < 2$	The oscillating loops gradually lose the energy (Fig. 16.8, solid curves)	Poincare limit cycle: currents grow until they reach a limiting value to establish a quasi-stable long living system
Nonlinear regime, $A_0 > 2$	Explosive instability leading to (1) a violent energy release and disruption of a system, or (2) repetitive flare-like events	Poincare limit cycle: currents drop to a limiting value releasing the excess of energy and approaching a quasi-stable state

One can say that the equivalent circuit model is a very efficient tool to study the physical processes that couple the subsurface and photospheric energy reservoir with the energy dissipation region in the upper layers of atmosphere. The advantage and broadness of this approach is that it includes several important issues in the coronal dynamics and structure formation:

- (1) connection between the remote parts of energy production region and regions of energy flow and release,
- (2) combination of both, magnetic and electric current viewpoints,
- (3) the natural explanation of the diversity of a coronal loop’s behavior from oscillatory to periodically flaring and exploding states,
- (4) simple relations between the physical parameters of a system, most of which are observable.

The model of energetically open circuit is quite general and can be applied to other astrophysical objects consisting of a dynamic magnetized plasma with continuous flow energy and its dissipation.

### Appendix: Method of Slow Variables for van der Pol Equation

In a real time (16.48) has a form

$$\frac{d^2i}{dt^2} - \mu(1 - i^2)\frac{di}{dt} + \omega_0^2i = 0 \tag{16.70}$$

and belongs to the class of nonlinear equations of the type

$$\frac{d^2i}{dt^2} + \omega_0^2i = f\left(i, \frac{di}{dt}\right) \tag{16.71}$$

with

$$f\left(i, \frac{di}{dt}\right) = -\mu(i^2 - 1)\frac{di}{dt} \quad (16.72)$$

The method of slowly varying phase and amplitude is based on the usage of transformation (see e.g. Hagedorn 1988):

$$\begin{aligned} i &= A(t)\sin(\omega_0 t + \psi), \\ \frac{di}{dt} &= A(t)\omega_0\cos(\omega_0 t + \psi) \end{aligned} \quad (16.73)$$

which replaces (16.71) by the system of a simple integro-differential equations:

$$\begin{aligned} \frac{dA}{dt} &= \frac{1}{2\pi\omega_0} \int_0^{2\pi} f(A, \psi) \cos(\phi + \psi) d\phi, \\ \frac{d\psi}{dt} &= -\frac{1}{2\pi\omega_0 A} \int_0^{2\pi} f(A, \psi) \sin(\phi + \psi) d\phi \end{aligned} \quad (16.74)$$

With (16.72) we have

$$\begin{aligned} \frac{dA}{dt} &= \frac{\mu A}{2\pi} \int_0^{2\pi} (1 - A^2 \sin^2 \phi) \cos^2 \phi d\phi, \\ \frac{d\psi}{dt} &= -\frac{\mu}{2\pi} \int_0^{2\pi} (1 - A^2 \sin^2 \phi) \cos \phi \sin \phi d\phi \end{aligned} \quad (16.75)$$

or, equivalently,

$$\begin{aligned} \frac{dA}{dt} &= \mu \frac{A}{2} \left(1 - \frac{A^2}{4}\right), \\ \frac{d\psi}{dt} &= 0 \end{aligned} \quad (16.76)$$

With the nondimensional time  $\tau = t/\sqrt{LC}$  and  $\epsilon = \mu/\sqrt{LC}$ , (16.76) becomes (16.51).

## References

- H. Alfvén, C.-G. Fälthammar, *Cosmical Electrodynamics, Fundamental Principles* (Clarendon Press, Oxford, 1963)
- H. Alfvén, J. Carlqvist, *Sol. Phys.* **1**, 220 (1967)
- H. Alfvén, *Cosmic Plasma* (Springer Verlag, 1981)
- M.J. Aschwanden, R.W. Nightingale, D. Alexander, *Astrophys. J.* **541**, 1059 (2000)
- L. Block, C.-G. Fälthammar, P.L. Rothwell, M.B. Silevitch, *JGR* **103**(A4), 6913 (1998)
- N.N. Bogolubov, Y.A. Mitropolsky, *Asymptotic Methods in the Theory of Non-Linear Oscillations* (Gordon and Breach, New York, 1961)
- A.H. Boozer, *Astrophys. J.* **325**, 891 (1988)
- S.I. Braginskii, 1965, in *Reviews of Plasma Physics*, vol. 1 (Consultants Bureau, New York, 1965) p. 205
- A.G. Elfmov, C.A. de Azevedo, A.S. de Assis, *Sol. Phys.* **167**, 203 (1996)
- N.J. Fish, Theory of current drive in plasmas. *Rev. Mod. Phys.* **59**, 175 (1987)
- A.V. Gaponov-Grekhov, M.I. Rabinovich, *Nonlinearities in Action* (Springer, New York, 1992)
- M.K. Georgoulis, B.J. LaBonte, T.R. Metclaf, *Astrophys. J.* **602**, 446 (2004)
- M.K. Georgoulis, B.J. LaBonte, *Astrophys. J.* **615**, 1029 (2004)
- P. Hagedorn, *Non-Linear Oscillations* (Clarendon Press, Oxford, 1988)
- G.P. Harnwell, *Principles of Electricity and Electromagnetism* (McGraw-Hill Book Co., New York, 1949)
- J. Heyvaerts, E.R. Priest, *Astron. Astrophys.* **117**, 220 (1983)
- J.A. Ionson, *Astrophys. J.* **254**, 318 (1982)
- J.A. Ionson, *Astrophys. J.* **276**, 357 (1984)
- L.D. Landau, E.M. Lifshitz, *Hydrodynamics* (Pergamon Press, Oxford, 1988)
- B. Lehnert, in *Plasma Physics and Thermonuclear Research*, ed. by J.L. Tuck (Macmillan Co., New York, 1963), p. 201
- K.D. Leka, R.C. Canfield, A.N. McClymont, L. van Driel-Gesztelyi, *Astrophys. J.* **462**, 547 (1996)
- D.B. Melrose, *Astrophys. J.* **486**, 521 (1995)
- T. Ohkawa, *Nucl. Fusion* **10**, 185 (1970)
- N.F. Otani, H.R. Strauss, *Astrophys. J.* **325**, 468 (1988)
- M.P. Ryutova, *Sov. Phys. JETP* **67**(8), 1594 (1988)
- D. Ryutov, M. Ryutova, *Sov. Phys. JETP* **69**, 965 (1989)
- M.P. Ryutova, S.R. Habbal, *Astrophys. J.* **451**, 381 (1995)
- M.P. Ryutova, M. Kaisig, T. Tajima, *Astrophys. J.* **459**, 744 (1996)
- M.P. Ryutova, T.D. Tarbell, *Phys. Rev. Lett.* **90**, 191101 (2003)
- M.P. Ryutova, R. Shine, *Astrophys. J.* **606**, 571 (2004)
- M.P. Ryutova, *JGR* **111**, A09102 (2006)
- M.P. Ryutova, R. Shine, *JGR* **111**, A03101 (2006)
- D.S. Spicer, *Space Sci. Rev.* **31**, 351 (1982)
- K.P. Stanyukovich, *Unsteady Motion of Continuous Media* (Pergamon Press, Oxford, 1960)
- T. Tarbell, M. Ryutova, J. Covington, A. Fludra, *Astrophys. J.* **514**, L47 (1999)
- T. Tarbell, M. Ryutova, R. Shine, *Sol. Phys.* **193**, 195 (2000)
- A. Title, *Philos. Trans. R. Soc. Lond.* **358**, 657 (2000)
- B.A. Trubnikov, *Particle Interactions in a Fully Ionized Plasma*, in *Reviews of Plasma Physics*, vol. 1 (Consultants Bureau, New York, 1965)
- J. Weiland, H. Wilhelmsson, *Coherent Nonlinear Interaction of Waves in Plasmas* (Pergamon Press, New York, 1977)
- A.R. Winebarger, H.P. Warren, J.T. Mariska, *Astrophys. J.* **587**, 439 (2003)
- D.J.M. Wort, *Plasma Phys.* **13**, 258 (1971)

## Chapter 17

# Fine Structure of Penumbrae: Formation and Dynamics

**Abstract** In this chapter we shall study amazing properties of sunspot penumbra—a beautiful “crown” surrounding mature sunspots and being one of the long-standing mysteries of solar magnetism. High-resolution observations with the Swedish 1-m Solar Telescope (SST) on La Palma revealed earlier unavailable features of penumbral filaments showing their fine substructure and new properties in their dynamics (Scharmer et al. in *Nature* 420:151, 2002). We shall see that these properties are associated with the nature of umbra which itself is a dense conglomerate of twisted flux tubes. Being more or less vertical in the center of sunspots, twisted and interlaced flux tubes branch out at the periphery from the “trunk” due to an ongoing reconnection processes, and arc downward to the photosphere forming the penumbral “umbrella.” The twist of individual filaments, and resulted distribution of magnetic fields and temperature inside them are consistent with the onset of screw pinch instability, which in large explains the properties and behavior of penumbral filaments.

### 17.1 Peculiarities of Sunspot Penumbrae—Observations

Penumbrae consist of an “uncombed” system of thin magnetic filaments arcing radially outward from the umbra and terminating in the photosphere. The inclination of the magnetic field is found to vary across the penumbra from  $45^\circ$  to  $90^\circ$  to the sunspot normal (Title et al. 1993). There are also strong intensity inhomogeneities across the penumbra, resulting in a visual effect of interlaced dark and bright filaments.

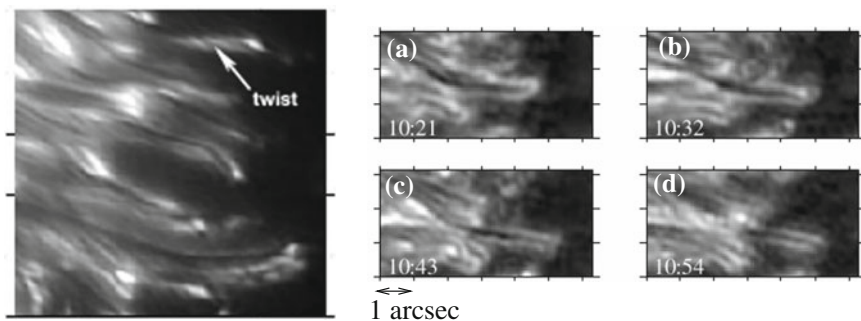
The Evershed flow (unsteady plasma outflow at the photospheric level) is also found to be structured on the scale of the penumbral filaments. The flow is more horizontal than the mean magnetic field at all radii in the penumbra and has a spatial correlation with dark penumbral filaments (Shine et al. 1994). The bright filaments are usually less horizontal making thus some angle with the direction of Evershed flows.

Livingston (1991), comparing images of sunspot with different exposures, came to the conclusion that the sunspot umbra also has a filamentary structure, and may exhibit presence of vertical, diverging, and horizontal filaments.

Observations with the 1-m Swedish Solar Telescope (Scharmer et al. 2002) in the different wavelength bands (e.g., 4,305 Å G-band and 4,368 Å continuum) have revealed unprecedented details in the penumbral structure and dynamics. It was found that many of individual filaments show dark cores surrounded by bright walls. The footpoints of the dark cores are mostly adjacent to the bright dots or grains. Filament often look twisted. High-cadence movies show continuous branching of the filaments into several filaments which also have dark cores. Figure 17.1 shows an example of a typical appearance of penumbral filaments at highest possible resolution of about 70 km. Left panel is one of the first reported image showing dark-cored filaments of different shapes that include twisted configuration as well (Scharmer et al. 2002). Four right panels show temporal evolution of a system of an exemplary dark-cored filaments showing their growth, merging, and splitting processes (Sütterlin et al. 2004). After the first results all the persistent features were confirmed and complemented in subsequent observations with the SST (Berger et al. 2004; Rouppe van der Voort et al. 2005; Bellot Rubio et al. 2005; Langhans et al. 2005; Rimmele and Marino 2006), and the Dutch Open Telescope (DOT, see e.g. Rutten et al. 2007). These may be summarized as follows:

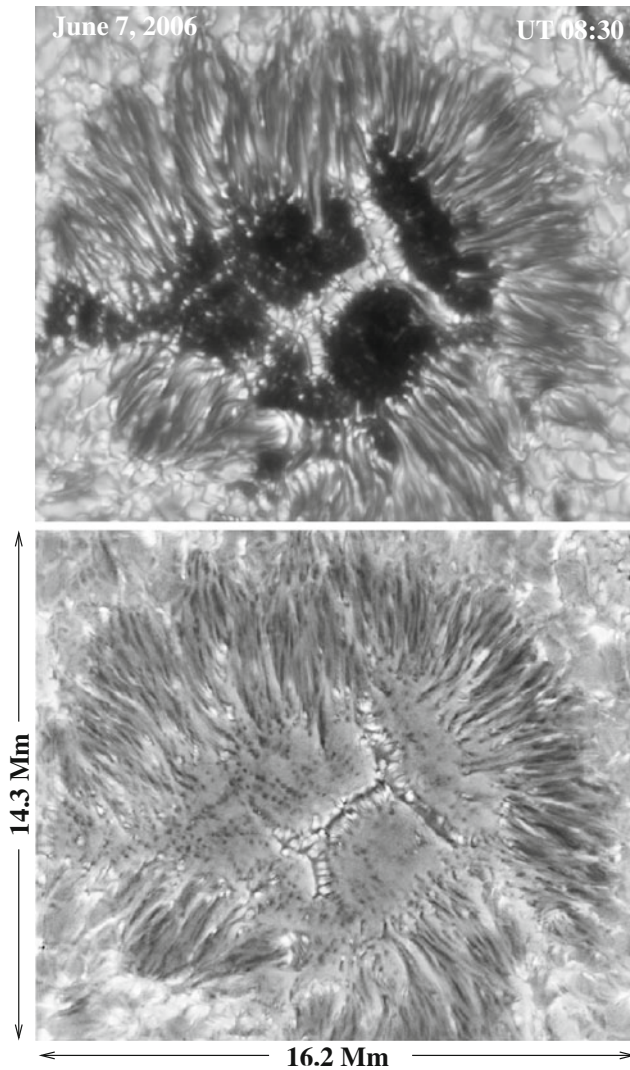
1. The widths of filaments close to their point of origin are 150–180 km.
2. The width of dark cores may be below the resolution ( $\leq 70$  km).
3. Filament lengths range from 300 to 3,000 km.
4. The average lifetime of individual filaments is 1–2 h.
5. The inclination of the dark-cored filaments with respect to the normal varies from  $35^\circ$  in the inner penumbra to about  $60^\circ$  toward the outer penumbra.
6. The magnetic signal is lower in the dark (cooler) cores than in the lateral (warmer) brightenings.

The SST observations of a sunspot obtained on 2006 June 6, in 4,305 Å G-band and 4,364 Å continuum lines confirmed the basic properties of penumbral filaments



**Fig. 17.1** *Left* Dark-cored filaments first reported by Scharmer et al. (2002), Reprinted from Scharmer et al. (2002), by permission from Nature Publishing Group. *Right* Temporal evolution of a dark-cored filaments, that includes splitting of filaments. Credit: Sütterlin et al. (2004), reproduced with permission copyright ESO





**Fig. 17.2** Images of the 2006 June 6 sunspot. *Top* G-band filtergram in the beginning of the observation. *Bottom* Simultaneous G-band/4,396 Å continuum difference image. Along the filamentary penumbra one can see well-defined small scale structures in the middle of the umbra, which are especially prominent in the difference image. These tiny black dots are the individual flux tubes forming the sunspot umbra

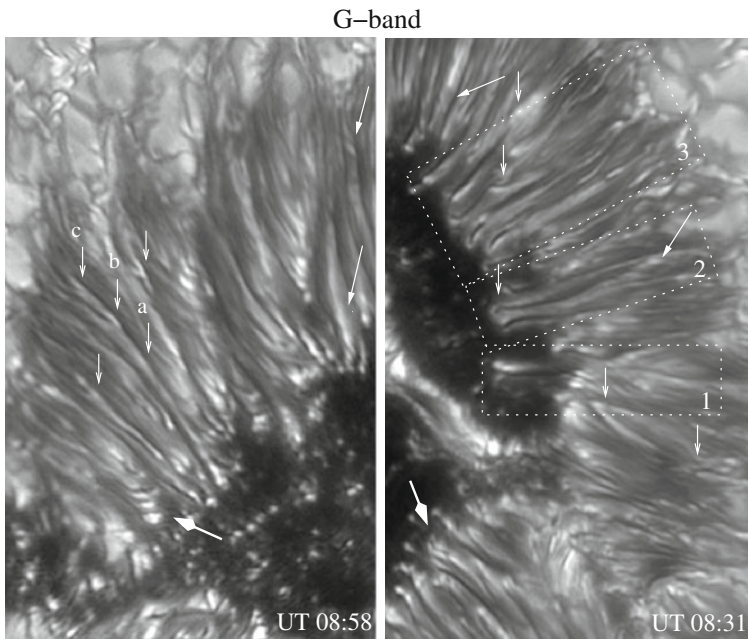
listed above and extended the analysis to their temporal evolution (Ryutova et al. 2008a). Figure 17.2 shows two simultaneous images of the studied sunspot.

The observations covered a  $23.8 \times 16.8 \text{ Mm}^2$  area of active region (AR 10892) near the disk center with the period of observation of 1 h 25 min. The data were taken

simultaneously every 5–7 s in the 4,305 Å G-band and a nearby “pseudo-continuum” bandpass centered at 4,364 Å. The G-band, commonly used to trace small scale photospheric magnetic elements, is excellent bandpass to reveal high contrast (and brightness) in penumbral filaments. Continuum images also show bright contrast in the observation of penumbral filaments continuum.

The fact that continuum images show a contrast by a factor of 10 less than in the G-band turns out to be quite useful. Given the precise alignment of the G-band and continuum images and a contrast difference, a subtraction of the two images intensifies the structures having the magnetic origin. The top panel in Fig. 17.2 shows the sunspot in the 4,305 Å G-band. The bottom panel shows the result of subtraction of the 4,364 Å continuum image from the G-band. Note that the umbral dots show up in the difference image with reversed contrast. The typical size of the umbral dots is  $\sim 70$  km and may be below the resolution limit.

A closer look from these observations is shown in Fig. 17.3.



**Fig. 17.3** Eastward and westward parts of the sunspot showing various topological structures in penumbral filaments. *Small downward arrows* show the apparent splitting of filaments. Note that all the branching points show enhanced brightening. *Three arrows* marked by *a*, *b* and *c* show multiple branching of one filament. Although the snapshot caught them together, the branchings occurred in different times. The *thick arrow* in the *left panel* shows regular series of intense bright points that may represent a strongly twisted individual filament or branching points of several filament below the surface; In the *right panel* the *thick arrow* shows multiwire view of filaments. The westward part of the penumbra (*right*) is center side and therefore shows more dark-cored filaments than the eastward part of the penumbra. See text for discussion of *dotted boxes* marking several ubiquitous events

In addition to already established properties (listed above) these observations revealed new properties of penumbral filaments. Most important of them are illustrated in Fig. 17.3 and listed below:

1. All filaments, whether or not they show obvious dark cores, are associated with a bright point which may be found *anywhere* along their length, and often inside umbra.
2. The umbral end of the filaments often splits into a series of bright dots, each having their own tails (left panel, thick arrow).
3. Filaments with or without dark core may branch into several filaments anywhere in the penumbra. The branching region is always brighter than the filament itself (small vertical arrows).
4. Several filaments may twist around each other into a bunch resembling multiwire cable. When unwinding, the individual filaments often keep their identity, but the process itself is accompanied by localized sporadic brightenings (right panel, thick arrow).
5. Many filaments exhibit twist along their lengths, resembling cylindrical helices having various pitch (thin long arrows). Strongly twisted filaments are usually short lived.
6. The ratio of filament radius and pitch is about the same for the majority of the long-lived filaments.

The temporal variability of penumbral filaments studied by space-time procedure shows the motions of various bright and dark patches revealing the true nature of an apparent twisting of filaments. It was found that the twisting motion is an intrinsic property of penumbral filaments. Screw-type motion is well observed in the majority of filaments, including those which do not show a clear twist in single snapshots. This property of penumbral filaments determines in large the observed peculiarities of penumbral filaments.

## 17.2 Dynamics of Penumbral Filaments and Ongoing Reconnections

Before we discuss the details of the observed regularities in the temporal behavior of penumbral filaments, let us recall a well-known fact from basic plasma physics: long, cylindrical magnetic structures are subject to helical instabilities, and a long magnetic flux tube with both azimuthal and axial components twists into a kinked helical shape, forming the screw pinch configuration (Shafranov 1956; Kruskal and Kulsrud 1958; Kadomtsev 1966; Parker 1979).

In other words, long penumbral filaments, as any other long magnetic flux tubes, are intrinsically unstable unless they wind into a helical shape with nonzero field-aligned current components that provide their dynamic stability in twisted shape. The magnetic field lines are therefore helices of some radius  $r$ . The pitch angle  $\theta(R)$ , i.e., the angle between a line of force and the direction of flux tube axis ( $z$ -direction)

is:  $\tan \theta(R) = B_\phi/B_z$ , where  $B_z$  and  $B_\phi$  are axial and azimuthal components of magnetic field. The pitch of the helical configuration, i.e., the distance in which the field line makes one revolution around the flux tube is:

$$h(R) \equiv \frac{2\pi R}{\tan \theta} = \frac{2\pi R B_z}{B_\phi} \quad (17.1)$$

The twisted state is characterized by the safety factor defined as follows:

$$q = \frac{2\pi R B_z}{L B_\phi} \equiv \frac{h}{L} \quad (17.2)$$

where  $R$  is the radius of the flux tube,  $L$  is its length. The screw pinch instability turns on when the safety factor becomes less than one:

$$q \equiv \frac{h}{L} < 1 \quad (17.3)$$

The most readily excited configuration is usually the kink mode ( $m = 1$ ), when the flux tube winds along the screw direction together with the axis. It is interesting that in the case of penumbral filaments the safety factor is observed directly, and it is such that (17.3) is applicable virtually to all the penumbral filaments.

Examples of space-time slices made in the G-band and G-band/4,364 Å continuum difference movies are shown in Fig. 17.4. The top panels are snapshots of penumbra segments, where the space-time cuts are made. The paths of these cuts are marked by numbers 1–4. The corresponding space-time images are shown in the lower panels. One can see that the twists seen in the snapshots indicate “cork screw” motions, which may be either right-handed or left-handed. In any case, twisting motion remains regular for a long time probably during the entire lifetimes of filaments. Duration of these observations is 85 min.

Not all the filaments show a helical shape in single snapshots, while movies reveal the twisting motions much more readily. In any case the pitch of the helical structure is directly measurable.

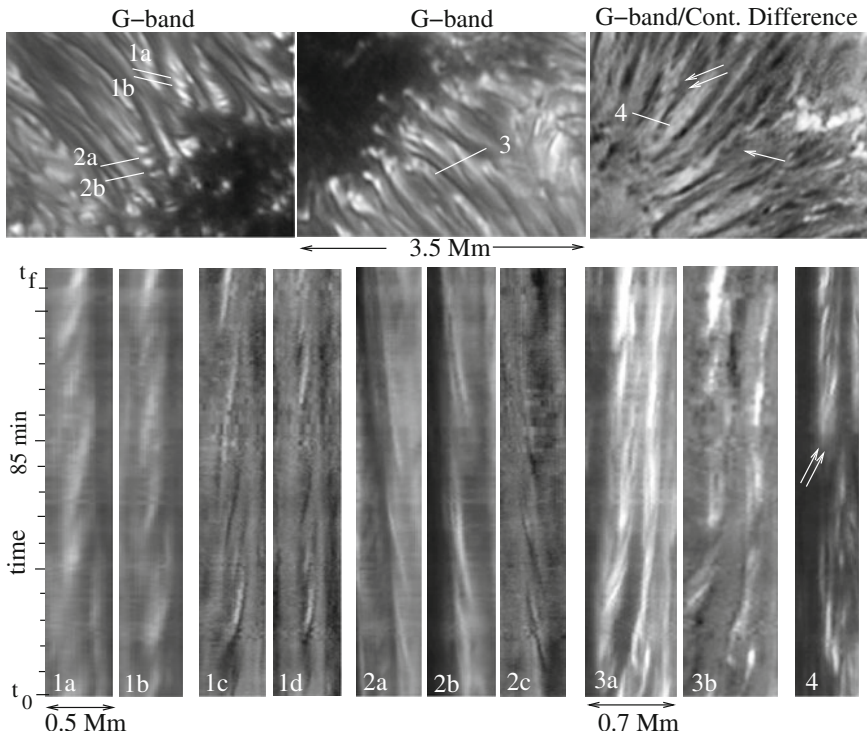
To measure the pitch using the movies, one needs to make at least two nearby cuts over a filament at some distance from each other,  $\Delta x$ . A pitch,  $h$ , will be then  $h = \Delta x(T/\Delta t)$ , where  $T$  is a period, e.g., time between maxima of intensity in the space-time image, and  $\Delta t$  is the time shift between the maxima in the neighboring cuts.

Examples of such a procedure are shown in Fig. 17.4. Cuts 1*a* and 1*b* are made in the G-band movie, and cuts 1*c* and 1*d* in the G-band/Continuum difference movie (the corresponding snapshot is not shown). One can see immediately that the maximum intensities in cuts 1*a* and 1*b* are phase shifted, while in cuts 1*c* and 1*d* they are in phase. The distance between cuts 1*a* and 1*b* is  $\Delta x \simeq 300$  km, measured times are  $T \simeq 22$  and  $\Delta t \simeq 12$  min. For the pitch, we have then  $h \simeq 550$  km. To confirm this result, we made cuts 1*c* and 1*d* about 550 km apart. Indeed, the corresponding

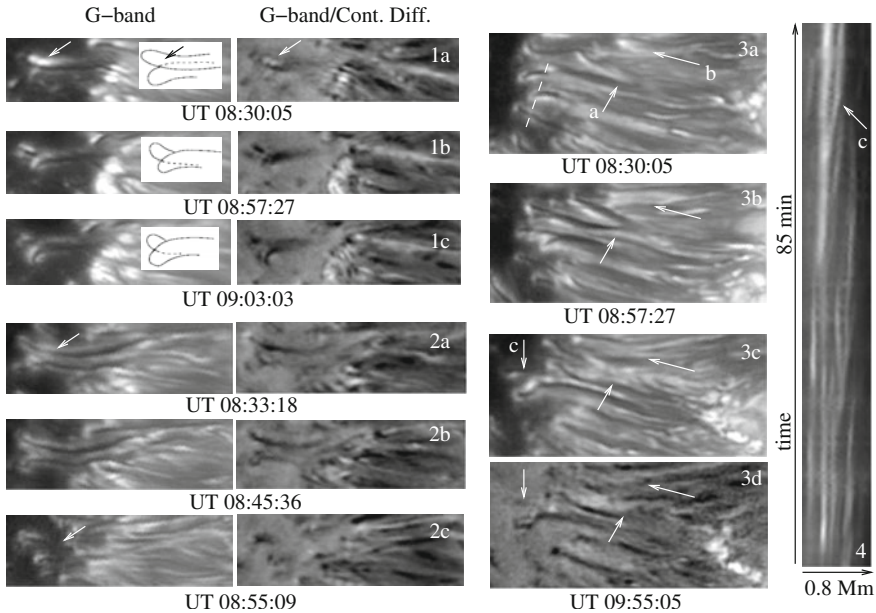
space-time images are perfectly synchronous. The same is true for cuts *2a* and *2b* (cut *2c* made in the G-band/Continuum difference movie is located in the same place as *2a*). All three twists are in phase. In this case,  $T = 20$  min, and  $\Delta x \simeq 700$  km. Thus the pitch  $h \simeq 700$  km.

Cuts *3a* and *3b* made in the G-band and G-band/Continuum difference movies in the same place over the “multiwired” filaments show the coexistence of closely located filaments. This cluster of filaments remains quite sturdy during the observation period. One can see, however, signs of interaction between the individual filaments accompanied by the enhanced brightening.

Signs of interaction are also seen in panel 4 of Fig. 17.4. Cut 4, made in the G-band/Continuum difference movie shows the birth of a strong twist occurring at about 09:20 UT (double arrows). The newly generated twist is quite strong and oriented in such a way that is well recognized even in the snapshot (marked by double arrows in upper third panel). One should bear in mind that different orientations of a cut show different patterns in motions of bright and dark patches lying along this cut. Cut 4 is made to reveal a birth of twist but does not clearly show interaction of filaments which could result in it. Although one can see several interlaced filaments



**Fig. 17.4** Space-time images revealing helical structure and corkscrew motions of the penumbral filaments (see text for details). The tick marks on the time axis have 5 min spacing,  $t_0 = \text{UT } 08:30:05$ ,  $t_f = \text{UT } 09:55:05$



**Fig. 17.5** Examples of interacting filaments in three instances of time. *Panels 1 a–c* show simultaneous G-band and G-band/Continuum difference images of two neighboring filaments; initially, the longer filament overlays the shorter one. In subsequent instances it seems that filaments have exchanged their *left* ends. This process is sketched in the *white boxes*. *Panels 2 a–c* show another example of filaments in the later stage of their interaction. In both cases the interaction is accompanied by enhanced brightening (marked by *arrows*). *Panels 3 a–d* show the evolution of the system of filaments. *Arrows a* and *b* show the regions where filaments possibly reconnect, and acquire the twisting shape. The *dotted line* in panel *3 a* is the cut passing through several filaments. Corresponding space time image (*panel 4*) shows several splitting events

in the first half of observing period before the appearance of a twist, changing their locations and intensities.

The most pervasive kind of interaction seen in high-cadence movies is apparent splitting of filaments. Most importantly, this process is always accompanied by the enhanced brightening of splitting region. Some examples are highlighted by small arrows in Fig. 17.3.

To see more details we selected three regions marked by dotted boxes in the right panel, Fig. 17.3. Boxes 1 and 2 contain filaments that are protruding deep into umbra and are therefore well seen on its background. The third box represents bunch of dark cored filaments. All three groups of filaments are shown in Fig. 17.5 in three instances of time.

Panels 1a–c in Fig. 17.5 are simultaneous G-band and G-band/Continuum difference images of the “first couple” of filaments. One can clearly see that at UT 08:30:05 longer (“upper”) filament overlays the shorter one. This is especially well noticeable in the G-band/Continuum difference image. At this instant of time (beginning of

the observations) an enhanced brightening is quite prominent in the small region marked by arrows. This region becomes the place where left parts of two filaments “exchange” their places, now the longer filament is overlaid by the shorter one. This process is sketched in white boxes embedded in the G-band images, 1a-c. By its nature such a process can obviously be understood as reconnection of filaments.

Panels 2a–c show another example of filament interaction. The beginning of this process has occurred before the observations started. The enhanced brightening of the region of intersection (marked by arrow in panel 2a and 2c) is still visible. As in the previous case, this region becomes the place where filaments separate from each other. Note that in about 20 min filaments seem to disappear (panel 2c). There might be several reasons for this: one is that orientation of filaments has changes, or that they indeed started to decay.

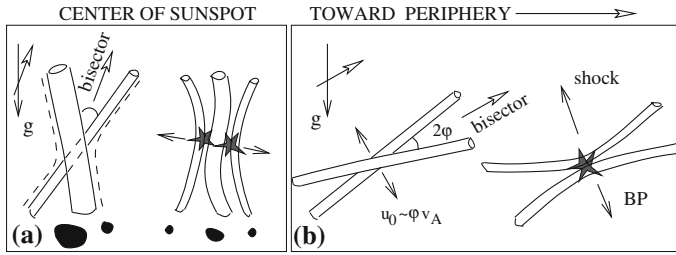
Panels 3a–d show the complex behavior of the filaments as a dense conglomerate. Here we highlight two splitting processes, marked by arrows a and b. In both cases, after splitting, the filaments acquire a twisted shape. In case a splitting is seen in both G-band and difference images, while the arrow b splitting is noticeable only in the difference image. The dashed line in panel 3a is the cut passing through several dark-cored filaments. The corresponding space time image (panel 4) shows several splitting events during the time of observation, as well as the major “survival”: the filament strongly protruding into the umbra, marked by arrow c in panels 3c and 4.

Obviously, the apparent splitting of penumbral filaments, helical shape, and enhanced brightening of the region of splitting are caused by ongoing reconnections. In the next section we discuss specifics of the reconnection and post-reconnection processes in the penumbra and their relevance to the observed regularities.

### 17.3 Formation of Filamentary Penumbrae

Fine structures seen at the visible surface suggest that physical processes in deeper layers also occur at small spatial scales: the nature of the surface umbra–penumbra is determined by the subphotospheric structures. One of the ways to visualize a sunspot (in a vertical cut) is a tree-trunk analogue with branches of tree running along the length of a trunk and gradually deviating outward, forming an umbrella-like ensemble of thin magnetic filaments.

It is important to emphasize that not only penumbra, but the umbra itself is highly inhomogeneous (Fig. 17.2). Observations of filamentary structure of umbrae go back to 50s, leading to studies of an umbral fine structures long before the recent high-resolution observations became available. For example, Papanthanasoglou (1971) showed that widths of umbral filaments are  $<1''$ , and dark spacing between them are about  $0.6''$ . As mentioned in the Introduction ((Livingston 1991), see also review by Solanki (2003), and literature therein), a filamentary structure of umbrae is quite complex, and may exhibit presence of vertical, diverging, and horizontal filaments. Such random alternation of magnetic fluxes and almost nonmagnetic spacing between them is indicative that the umbrae consist of a dense conglomerate of noncollinear



**Fig. 17.6** Visualization of photospheric and subphotospheric reconnections between the same polarity flux tubes: **a** Reconnection between the umbral (almost vertical) flux tubes colliding at the angle with the bisector close to the line of sight; in this case the post-reconnection slingshot drags away the fragmented parts. **b** Reconnection between the peripheral filaments when the bisector of the collision angle strongly deviates from the vertical; in this case the *upper* slingshot generates shocks and plasma jets; the appearance of the *bright point* in the reconnection region is always in place

flux tubes that are in constant motion relative to one another. Among fundamental processes in such a conglomerate are reconnection and post-reconnection processes.

### 17.3.1 Phenomenology of Basic Mechanism

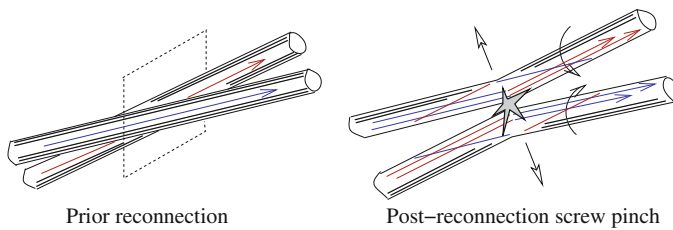
The penumbral filaments are obviously of the same polarity as the parental sunspot. However, they are strongly noncollinear, and being in such vicinity to each other, they are subject of frequent reconnections.

The reconnection and post-reconnection processes in penumbra, as well as their observed signatures strongly depend on the orientation of filaments and the *bisector* of the collision angle between the interacting flux tubes.

If the bisector is close to vertical, situation most typical to the sunspot center (Fig. 17.6a), the magnetic force acting in the plane perpendicular to the bisector, straightens the reconnection products and drags them away from each other (see Chap. 12). Line-of-sight picture will show a fragmentation process. Toward periphery, penumbral filaments deviate from vertical, so does the bisector of their collision angle. In this case along the magnetic tension the reconnection products experience action of the buoyancy force. For upper part of reconnection product (Fig. 17.6b) the magnetic tension and buoyancy force are acting in the same, upward direction, which leads to the generation of shocks, and eventually the appearance of lateral jets (Tarbell et al. 1999; Ryutova et al. 2003; Ryutova and Tarbell 2003; Katsukawa et al. 2007; Ryutova et al. 2008b). Besides, region of reconnection always has some excess of energy, which manifests itself in enhanced brightening, usually observed as bright points (BP).

Most importantly, the reconnection generates an inevitable twist (Fig. 17.7). This fact plays a crucial role in the topological features of penumbral filaments, and in





**Fig. 17.7** The post-reconnection screw pinch resulted from an inevitable twist inherited by the reconnection products

particular, in the appearance of dark cores along their axes, first observed by Scharmer et al. (2002).

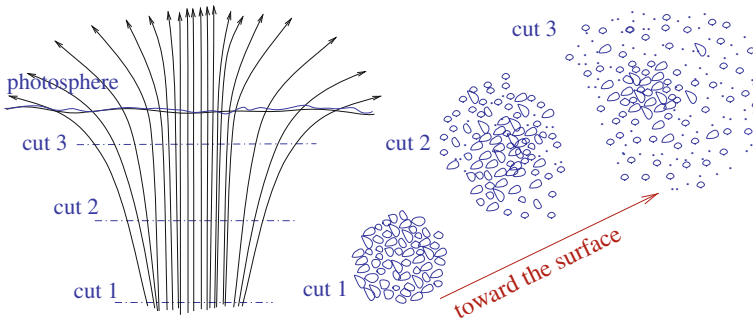
It is important to remind that only a limited portion of flux participates in each elemental reconnection. Recall (Chaps. 12 and 13) that the effective radius is determined mainly by the magnetic Reynolds number,  $R_{\max} < L/2\ln Re_m$ . With  $Re_m \simeq 10^3 - 10^6$ , and a typical length of  $L \simeq 10^3$  km, we have  $R_{\max} \sim 36-70$  km. As discussed earlier, this means that magnetic flux tubes having a radius as small as 150–200 km may be the sites of multiple reconnection processes. Good illustration of such a process is an example of multiple branching of penumbral filament shown, e.g., by vertical arrows in Fig. 17.3. As mentioned in the figure caption, although the snapshot caught all these branching together, they did not appear simultaneously, i.e., interaction of a given filament occurred with different neighbors in different times. This process is ubiquitous and is well observed both in G-band and G-band/continuum difference movies, suggesting that it just these continuous reconnections, fragmentation and branching are responsible for the formation of filamentary structure of penumbra and the sunspot as a whole.

### 17.3.2 Filamentary Structure of Sunspot

A schematic of the formation of the fine structures of the sunspot and the branching out of the peripheral flux tubes that form the penumbra is shown in Fig. 17.8.

Thus the process of fragmentation in the sunspot, and branching out of the newborn flux tubes will occur repeatedly until the reconnection products reach their critical radii. As flux tubes have different parameters, branching occurs at different heights. In the central region of sunspot fragmented flux tubes remain mostly vertical, but may also diverge (Livingston 1991).

Toward the edge of the umbra flux tubes deviate more and more from the vertical. So does the bisector of the collision angle between the interacting flux tubes. In this case, the upward slingshot generates oblique shocks and leads to the appearance of lateral jets. Note that the reconnection region is always marked by enhanced brightening corresponding to the bright points seen throughout the penumbra.



**Fig. 17.8** Schematic of the sunspot illustrating the formation of a filamentary umbra/penumbra

The larger the deviation, the stronger the shocks leading to stronger jets. In addition, the reconnection of noncollinear flux tubes leads naturally to a twist in the reconnected filaments. This twist as already mentioned, plays a crucial role in stability, dynamics, and properties of penumbral filaments. This will be discussed in the next section.

### 17.3.3 Properties of Individual Filaments

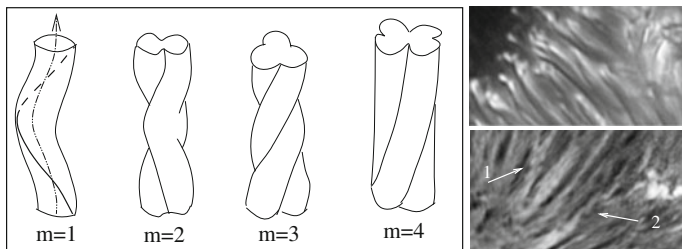
Thus, the ongoing reconnection and fragmentation processes that determine the morphology and properties of a sunspot, shape as well the penumbral filaments. All the observed properties of the penumbral filaments listed in Sect. 17.2 are natural consequences of these processes: the very formation of the filamentary penumbra, the multiple splitting of individual filaments and their footpoints, the enhanced brightening of the footpoints (region of reconnection), a twist of filaments, and as we will see below, the presence of dark cores in most of the filaments.

A simple phenomenological approach allows one to make a reasonable quantitative analysis.

We start with the most readily excited, a kink mode configuration ( $m = 1$ ). The condition (17.3) for safety factor, defined by (17.2), puts a constraint on the azimuthal electric current known as the Kruskal–Shafranov limit:

$$I_\phi > I_{KS} = \frac{2\pi Rc}{L} B_z, \quad (17.4)$$

where  $I_{KS}$  is the Kruskal–Shafranov current below which the magnetic field is supposed to be stable with respect to screw pinch instability. Laboratory experiments, however, show that the screw pinch configuration is surprisingly stable far below the Kruskal–Shafranov limit. Theoretical studies show that there are indeed many factors (such as finite plasma  $\beta$ , nonzero resistivity, the finite length of the plasma column, the presence of plasma flows, field reversal, and others) that provide



**Fig. 17.9** Screw pinch configurations. *Left panel* Various modes of helical perturbations. *Right panel* Possible observational evidence for various modes shown in the fragments of penumbra—G-band (*top*), and G-band/4396 Å continuum difference image (*bottom*). The arrows show strongly twisted filaments; pitch/radius ratio for the first helical structure is slightly larger than unity, and for the second structure it is between 1.5 and 2

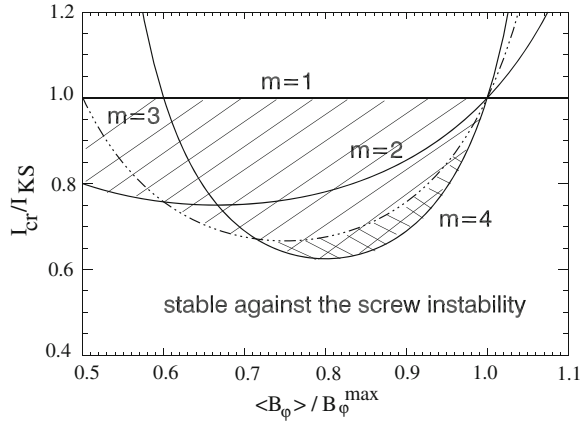
realization and stability of a screw pinch configuration far below the expected limit (Schuurman et al. 1968; Goedbloed and Zwart 1975; Miyamoto 1988; Lehnert and Scheffel 1992; Martynov and Medvedev 2003; Ryutov et al. 2006; Bergerson et al. 2006).

In case of the penumbral filaments, the safety factor,  $q = h/L$ , is observed directly and allows infer  $B_\phi$  from the direct measurements of the pitch and  $B_z$ . As we know, along the most common  $m = 1$  kink mode, the current-carrying magnetic flux tubes are subject to higher modes of MHD instabilities,  $\sim \exp(im\phi)$ . The mode  $m$  determines the “entry” of helical perturbations (Fig. 17.9, left; cf. Fig. 3.3). For qualitative comparison, we illustrate possible high azimuthal modes of twisted filaments in Fig. 17.9, right panels. The next step in observations is obtaining vector field maps with high spatial resolution that became available with spectropolarimetric measurements with the SOT aboard the Hinode satellite and the SDO instruments. Detection of higher modes in the observations, which will allow a direct measurement of the basic parameters in the screw pinch provide an additional means to infer the electric currents and other physical parameters.

Theoretically, it is shown that there is a considerable range of parameters for higher modes of the screw pinch configuration (Ryutov et al. 2004). We use here their calculations to plot the stability boundary for various magnetic field profiles (Fig. 17.10). The ratio  $I_{cr} \geq I_{KS}$  demarcates the stability boundary as a function of the azimuthal component of the magnetic field. The kink mode,  $m = \pm 1$ , e.g., develops for  $I_{cr} \geq I_{KS}$ , i.e., above the straight line  $m = 1$  in Fig. 17.10; see (17.4). Below this line, there is a significant range of parameters where screw pinch configuration with one of the higher modes may be formed.

The excitation of other modes, as well as the manifestation of the individual properties of a given filament, depends on the actual distribution of the magnetic fields and currents inside it. It is important that the helical shape of the magnetic field has a significant effect on the temperature distribution inside a magnetic flux tube that naturally accounts for the appearance of dark-cored filaments.

**Fig. 17.10** Stability boundary determined by the critical current and azimuthal magnetic field. There is a significant range of parameters below the line  $m = 1$  where the screw pinch configuration with one of the higher modes may be formed (after Ryutov et al. (2004))



## 17.4 Screw Pinch Instability and Dark Cores

To see how the screw pinched flux tube acquires the dark cores, let us find profiles of the temperature, magnetic fields, and currents in a twisted flux tube. We start with a stationary form of the energy balance equation, which can be written as:

$$\kappa_{\parallel} \frac{\partial^2 T}{\partial z^2} = -\frac{j^2}{\sigma} + Q_{\text{rad}} - H_{\text{visc}} \quad (17.5)$$

where  $\kappa_{\parallel}$  is the parallel thermal conductivity,  $j$  is a current density,  $\sigma$  is the electric conductivity, and  $Q_{\text{rad}}$  and  $H_{\text{visc}}$  are the radiative loss function and viscous heating, respectively.

In order to isolate the effect of the helical structure on the temperature and electric current distributions, we assume that the filament is kept in radiative equilibrium by viscous heating. Roughly, this can be justified by estimating the two last terms in (17.5).

The radiative cooling time,  $\tau_{\text{rad}}$  (Spiegel 1957), calculated for a photospheric magnetic flux tube of radius  $R = 50 \text{ km}$ , plasma density  $\rho = 2 \times 10^{-7} \text{ g cm}^{-3}$  and temperature change from 12,000 to 4,800 K is about  $\tau_{\text{rad}} = 200 \text{ s}$  (Schlichenmaier et al. 1999). The estimate for radiative heat flux at  $T = 4,800 \text{ K}$  is  $Q_{\text{rad}} \simeq (3/2)nkT/\tau_{\text{rad}} = 413 \text{ erg cm}^{-3}\text{s}^{-1}$ . Viscous heating is provided mostly by turbulent motions, and may be estimated as  $H_{\text{visc}} \simeq \eta_{\text{turb}} e_{ij}^2$ , where  $e_{ij} = [(\partial v_i / \partial r_j) + (\partial v_j / \partial r_i)]$ , and  $\eta_{\text{turb}} \simeq \rho v R$ . For the above parameters with a turbulent velocity  $v \simeq 2 \text{ km s}^{-1}$ , we have  $H_{\text{visc}} \simeq 320 \text{ erg cm}^{-3}\text{s}^{-1}$ .

Profiles of equilibrium magnetic fields and currents in twisted magnetic flux tubes are calculated by balancing the Lorentz force and the pressure gradient:

$$\frac{1}{c} \mathbf{j} \times \mathbf{B} = \nabla p \quad (17.6)$$

where  $p$ ,  $\mathbf{j}$ , and  $\mathbf{B}$  are the pressure, current density, and magnetic field. For a simple axisymmetric state, magnetic field profiles can be expressed through a generating function  $f(r)$  defined as the total pressure,  $f(r) = p + (B_\phi^2 + B_z^2)/8\pi$  (see e.g. Parker (1979)):

$$p(r) + \frac{B_z^2}{8\pi} = f(r) + \frac{1}{2} \frac{df}{dr}, \quad \frac{B_\phi^2}{8\pi} = -\frac{1}{2} r \frac{df}{dr} \tag{17.7}$$

The generating function is arbitrary except that in order that  $B_\phi$  and  $B_z$  are real,  $f(r)$  should decline monotonically with  $r$ , but not faster than  $1/r^2$ , i.e.,  $0 \geq df/dr \geq -2f(r)/r$ . For illustrative purpose we consider a force-free field,  $\mathbf{j} \times \mathbf{B} = \mathbf{0}$  ( $p = \text{constant}$ ), with a simple generating function:

$$f(r) = P_0 \frac{1 + R^2 \mu^2}{1 + r^2 \mu^2}, \tag{17.8}$$

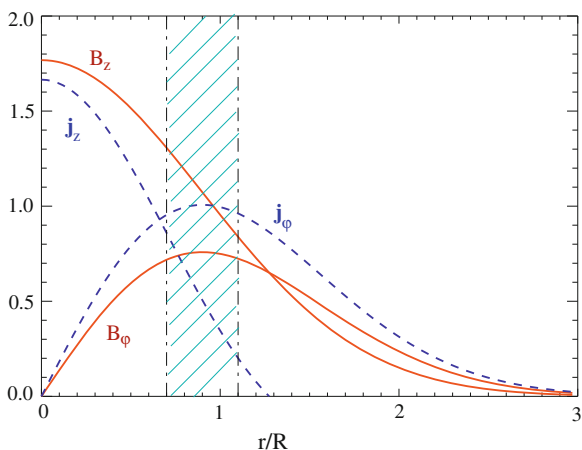
where  $\mu$  is the inverse pitch of a helical flux tube,

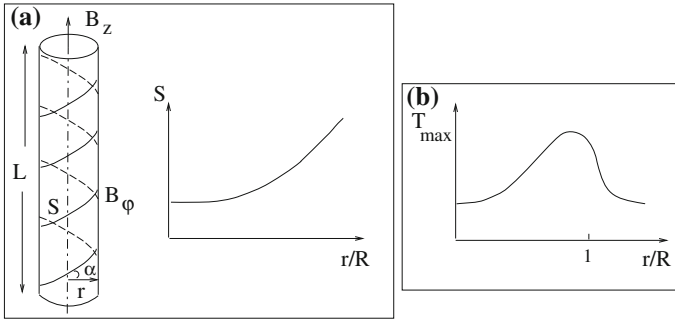
$$\mu \equiv \frac{2\pi}{h} \tag{17.9}$$

Corresponding solutions for magnetic fields and currents are shown in Fig. 17.11. We use here typical observed parameters of penumbral filaments, e.g.,  $R = 4 \times 10^1$  km,  $h = 5 \times 10^2$  km,  $B_z = 1,500$  G.

The individual magnetic lines of force are helices of radius  $r$ . The entire length of the helix,  $S$  (the connection length between the ends of flux tube), depends on the pitch angle,  $\theta(r)$ , defined as  $\tan \theta(r) = B_z/B_\phi$  at a given flux surface. Simple

**Fig. 17.11** Magnetic field and current profiles. The shaded area is where the enhanced heating occurs providing a cooler interior of the flux tube compared to its hotter walls





**Fig. 17.12** A helical flux tube: **a** Flux tube and a plot of length of helix,  $S(r)$ . **b** Sketch of the temperature profile across the flux tube

geometrical considerations show that the length of the helix,  $S$  considerably exceeds the physical length of a tube,  $L$ :

$$S = L\sqrt{1 + B_\phi^2/B_z^2} \tag{17.10}$$

For the magnetic field distribution shown in Fig. 17.11,  $S$  is minimum at the axis (where  $B_\phi = 0$ ), and rapidly grows toward periphery (Fig. 17.12a).

If according to the above estimates the filament is kept in radiative equilibrium by the viscous heating, the effect of helical structure on the temperature distribution can be evaluated by the approximate equation for the temperature in the middle of the flux tube (along the axis) determined by the balance of the Joule heating and parallel thermal conductivity. Then along the field line we have:

$$\kappa_{\parallel} \frac{\partial^2 T}{\partial z^2} = -\frac{J^2}{\sigma} \tag{17.11}$$

This gives an estimate

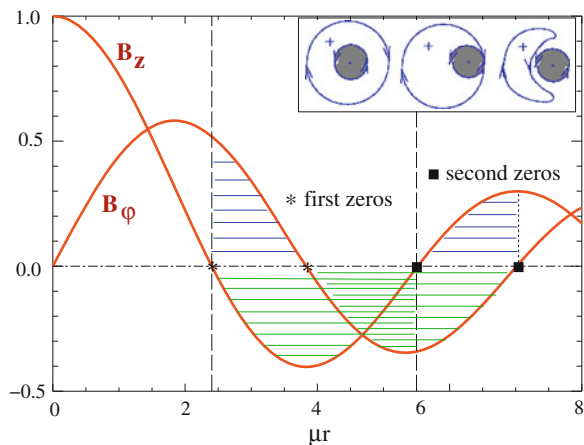
$$T \simeq T_{\max}(1 - 4z^2/S^2), \tag{17.12}$$

with  $T_{\max}$  as

$$T_{\max}(r) \simeq \frac{j^2(r)S^2(r)}{8\sigma\kappa_{\parallel}}, \tag{17.13}$$

The presence of the factor  $S^2(r)$  makes the hollow temperature profiles a natural occurrence (Fig. 17.12b). The fact that these are rotating, axially flowing plasma fluid structures (i.e., plasma vortex tubes) means that the density profile increases from its minimum along the tube axis to a maximum at the walls. This fact again, supports the occurrence of the dark cores and their consistency with the optically thin radiative transfer.

**Fig. 17.13** Oscillatory character of the Bessel functions. Shown are several regimes determined by the critical current and azimuthal magnetic field. The inset shows the cross section of the reversed pinch in the interval  $3.85 < 2\pi R/h < 5.5$  with formation of a reversed core and its dynamics (after Miyamoto (1988))



### 17.4.1 More on Substructures of Filaments

Now we turn to a more general solution of (17.6). The simplest solution in cylindrical geometry is known to be a Lundquist field (Lundquist 1951), having form of Bessel functions (Fig. 17.13):

$$\begin{aligned} B_z(r) &= B_0 J_0(\mu r), & B_\phi(r) &= B_0 J_1(\mu r) \\ j_z(r) &= \frac{B_0 c}{2\pi} \mu J_0(\mu r), & j_\phi(r) &= \frac{B_0 c}{2\pi} \mu J_1(\mu r) \end{aligned} \quad (17.14)$$

where  $\mu$  is the inverse pitch of a helix, defined by (17.9). Note, that the solution shown in Fig. 17.11 is qualitatively the same if  $\mu r$  is less than the first zero of  $J_0(\mu r)$ . The above field configuration, often met in laboratory plasmas, has been extensively studied both theoretically and in advanced experiments. Similar studies of solar and space magnetic fields with helical configurations have been carried out (Van Hoven et al. 1977; Parker 1979; Lothian and Hood 1989; Rust and Kumar 1994; Linton et al. 1996; Li 2000; Wissink et al. 2000).

A characteristic feature of the Lundquist solution is the reversal of the magnetic field and electric currents (Fig. 17.13), first emphasized by Taylor (1974) and later observed in numerous laboratory experiments (see, e.g., Okada et al. 2007 and references therein). The oscillatory character of the Bessel functions provides several regimes of magnetic field distribution inside flux tubes. Depending on the magnetic field geometry inside flux tubes represented by parameter  $\mu R$ , and the degree of twist, there are several regimes of magnetic field configuration:

1. The parameter  $\mu R$  is below the first zero of  $J_0(\mu R)$ , i.e.,  $2\pi R/h < 2.4$ , which translates into a condition for a pitch/radius ratio,  $(h/R) > 2.62$ . In this case the magnetic field components preserve their initial direction and chirality.

2. The parameter  $\mu R$  exceeds the first zero of  $J_0(\mu R)$  but is below the first zero of  $J_1(\mu R)$ , i.e.,  $2.4 < 2\pi R/h < 3.85$ , or  $1.63 < (h/R) < 2.62$ . In this case the axial magnetic field reverses, but the chirality of the filament remains the same.
3. In the interval  $3.85 < 2\pi R/h < 5.5$  ( $1.14 < (h/R) < 1.63$ ) the axial magnetic field reversal is accompanied by reversed chirality. The interval with higher zeros is unlikely, as it leads to strong twist and a likely disruption of the filament.

Field reversal configurations, well studied in laboratory plasmas, have clear morphological effects that can be observed. For example, the internal reconnections lead to a typical magnetic field rearrangement, shown in the inset of Fig. 17.13. This corresponds to a pitch/radius ratio in the interval  $3.85 < 2\pi R/h < 5.5$ . With high-resolution observations, such multicomponent configurations of the magnetic field can be observed as local reversals in the direction of the field in the penumbra. If the filament twist is very strong (see filaments marked by white arrows in Fig. 17.9, bottom right), the core per se may not be visible, but the effect of the small scale local field reversals may be observationally detectable.

In many cases, the force-free approximation gives a reasonable qualitative picture. However, for most of the problems associated with the solar atmosphere, especially in the lower layers with high plasma  $\beta$  and nonzero resistivity, the equilibrium magnetic field must depart from the force-free configuration. And yet, under reasonable conditions, a modified nonforce-free magnetic field is still described by the Bessel functions of the Lundquist solution (Chiuderi et al. 1977; Rust and Kumar 1994).

### 17.4.2 Effects of Axial Flows

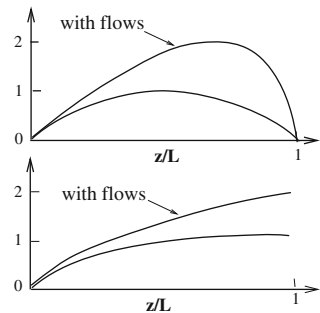
Here we briefly discuss the effects of axial flows on the twisted flux tubes. This problem is extremely important for solar flux tubes, and, in particular, for umbra/penumbral filaments where mass flows are the necessary accomplice of their dynamics. However, this problem did not receive much attention, and yet there are some specific effects that can directly observed. These will be described below.

Laboratory studies (Ryutov et al. 2006; Furno et al. 2006) show that the presence of an axial flow causes rotation of the kink in the flux tube, and the perturbation amplitude increases in the flow direction. An axial flow causes the advection of perturbations and a *skewing* of the eigenfunction toward the outer edges of the filaments (Fig. 17.14). If both ends of the filament are line-tied (Fig. 17.14, top), skewing occurs in such a way that the line-of-sight magnetic field will be observed to be opposite to the parental sunspot polarity. This may explain why the majority of penumbral filaments dive into the moat region at the outer edge of the penumbra, naturally showing an opposite polarity.

We may conclude that all the observed properties of the penumbral filaments, and the formation of the penumbra itself, are natural consequences of the ongoing reconnection processes in a conglomerate of random, interlaced flux tubes forming the sunspot.



**Fig. 17.14** Revolution over which the axis of filament is wound. *Top* Both ends of a filament are line-tied. *Bottom* Only the inner foot is line-tied. Reprinted from (Rytov et al. 2006) by permission from AIP publishing LLC



In the central umbra, the flux tubes are close to vertical, and thus the bisector of their collision angle is also close to vertical. Therefore in the central region of sunspot fragmenting flux tubes remain mostly vertical. Toward the periphery, flux tubes deviate more and more from the vertical, and branch out from the parental sunspot. As flux tubes have different parameters, branching occurs at different heights thus forming the observed “uncombed” penumbra. Most importantly, the bisector of the collision angle between the interacting flux tubes deviates from the vertical as well providing conditions for shock formation and their subsequent evolution.

The process of fragmentation in the sunspot, and branching out of the newborn flux tubes occurs repeatedly until the reconnection products reach their critical radii ( $\sim 20\text{--}40\text{ km}$ ), determined by the local Reynolds number.

The reconnection processes that take place continually in sunspot penumbra lead to twisting of the post-reconnection flux tubes. The inherent twist of individual filament facilitates the onset of a screw pinch instability, which determines the distribution of electric currents and temperature inside the filaments. These in turn lead to the appearance of dark cores surrounded by bright walls. Moreover, all the observed properties are not only qualitatively understood but may be used for quantitative estimates. These again, are:

1. The sunspot umbra is a dense conglomerate of random flux tubes where the reconnection of same polarity neighbors leads to their farther fragmentation accompanied by bright points.
2. The formation of filamentary penumbra by means of peripheral flux tubes continuously reconnecting and branching out from the “trunk.”
3. Occurrence of multiple splitting of individual filaments and their footpoints.
4. Enhanced brightening of footpoints (region of reconnection).
5. Generation of post-reconnection twist of filaments.
6. Occurrence of dark cores associated with the redistribution of magnetic field and temperatures inside filaments due to the onset of screw pinch configuration.
7. The fact that filaments with or without dark core may branch into several filaments anywhere in penumbra, with branching region being always brighter than the filament itself.

8. The visual effect that not all filaments show the dark-cored structure is pure geometrical one.
9. The fact that several filaments may spin around each other into a bunch resembling multiwire cable (high azimuthal modes). When unwinding the individual filaments often keep their identity, but the process itself is accompanied by the localized sporadic brightenings.

It is important to note that the simplicity of screw pinch physics, based on directly measurable parameters, such as pitch, radius, and magnetic field, allows quantitative analysis of the penumbral properties.

The next obvious question is: what is the impact of the penumbral dynamics on the overlying atmosphere. We shall address this problem in the next chapter, and see that the reconnection between the penumbral filaments leads to expected post-reconnection jets and sporadic brightenings in the overlying chromosphere.

## References

- L. Bellot Rubio, K. Langhans, R. Schlichenmaier, *Astron. Astrophys.* **443**, L7 (2005)  
 T. Berger et al., *Astron. Astrophys.* **428**, 613 (2004)  
 W.F. Bergerson et al., *Phys. Rev. Lett.* **96**, 015004 (2006)  
 C. Chiuderi, R. Giachetti, G. Van Hoven, *Sol. Phys.* **54**, 107 (1977)  
 I. Furno et al., *Phys. Rev. Lett.* **97**, 015002 (2006)  
 J.P. Goedbloed, J.W.A. Zwart, *Plasma Phys.* **17**, 45 (1975)  
 B.B. Kadomtsev, in *Reviews of Plasma Physics*, vol. 2, ed. by M.A. Leontovich (Consultants Bureau, New York, 1966) p. 153  
 Y. Katsukawa, T. Berger, K. Ichimoto et al., *Science* **318**, 1594 (2007)  
 M.D. Kruskal, R.M. Kulsrud, *Phys. Fluids* **1**, 265 (1958)  
 K. Langhans et al., *Astron. Astrophys.* **436**, 1087 (2005)  
 B. Lehnert, J. Scheffel, *Plasma Phys. Control. Fusion* **34**, 1113 (1992)  
 M.G. Linton, D.W. Longcope, G.H. Fisher, *Astrophys. J.* **469**, 954 (1996)  
 L.-X. Li, *Astrophys. J.* **531**, L111 (2000)  
 W. Livingston, *Nature* **350**, 45 (1991)  
 R.M. Lothian, A.W. Hood, *Sol. Phys.* **122**, 227 (1989)  
 S. Lundquist, *Phys. Rev.* **83**, 307 (1951)  
 A.A. Martynov, S.Yu. Medvedev, *Phys. Rev. Lett.* **91**, 085004 (2003)  
 K. Miyamoto, *Plasma Phys. Control. Fusion* **30**, 1493 (1988)  
 S. Okada et al., *Fusion Sci. Tech.* **51**, 193 (2007)  
 D. Papathanasoglou, *Sol. Phys.* **21**, 113 (1971)  
 E.N. Parker, *Cosmical Magnetic Fields* (Clarendon Press, Oxford, 1979)  
 T. Rimmele, J. Marino, *Astrophys. J.* **646**, 593 (2006)  
 L. Rouppe van der Voort, et al., *Astron. Astrophys.*, **435**, 327 (2005)  
 D.M. Rust, A. Kumar, *Sol. Phys.* **155**, 69 (1994)  
 R.J. Rutten et al., in ASP Conf. Ser. vol. 236: *Advanced Solar Polarimetry-Theory, Observation, and Instrumentation*, ed. by M. Sigwarth (ASP, San Francisco, 2001), p. 25  
 M. Ryutova, T. Tarbell, R. Shine, *Sol. Phys.* **213**, 231 (2003)  
 M. Ryutova, T. Tarbell, *Phys. Rev. Lett.* **90**, 191101 (2003)  
 D.D. Ryutov, R.H. Cohen, L.D. Pearlstein, *Phys. Plasmas* **11**, 4740 (2004)  
 D.D. Ryutov et al., *Phys. Plasmas* **13**, 032105 (2006)

- M. Ryutova, T. Berger, A. Title, *Astrophys. J.* **676**, 1356 (2008a)  
M. Ryutova, T. Berger, Z. Frank, A. Title, *Astrophys. J.* **686**, 1404 (2008b)  
V.D. Shafranov, *At. Energy* **30**, 38 (1956)  
R.A. Shine, A.M. Title, T.D. Tarbell, K. Smith, Z.A. Frank, *Astrophys. J.* **430**, 413 (1994)  
G. Scharmer et al., *Nature* **420**, 151 (2002)  
R. Schlichenmaier, J.H.M.J. Bruls, M. Schüssler, *Astron. Astrophys.* **349**, 961 (1999)  
W. Schuurman, C. Bobeldjik, R.F. de Vries, *Plasma Phys.* **11**, 495 (1968)  
S. Solanki, *Astron. Astrophys. Rev.* **11**, 153 (2003)  
E.A. Spiegel, *Astrophys. J.* **126**, 202 (1957)  
P. Sütterlin et al., *Astron. Astrophys.* **424**, 1049 (2004)  
T. Tarbell, M. Ryutova, J. Covington, A. Fludra, *Astrophys. J.* **514**, L47 (1999)  
J.B. Taylor, *Phys. Rev. Lett.* **33**, 1139 (1974)  
A. Title et al., *Astrophys. J.* **403**, 780 (1993)  
G. Van Hoven, C. Chiuderi, R. Giachetti, *Astrophys. J.* **213**, 869 (1977)  
J.G. Wissink, P.M. Matthews, D.W. Hughes, M.R.E. Proctor, *Astrophys. J.* **536**, 982 (2000)

# Chapter 18

## Bow Shocks and Plasma Jetting over Penumbrae

**Abstract** Penumbral filaments being in constant motion, reconnecting, splitting, and twisting, strongly affect the overlying atmosphere. In this chapter we shall study the response of the chromosphere to penumbral dynamics, which shows spectacular cascades of bow shocks and plasma jetting. These spectacular events are produced by the ongoing reconnection processes between neighboring penumbral filaments, basically at the periphery of sunspot where penumbral filaments become more and more horizontal. There post-reconnection products moving upward quickly accelerate. At transonic velocities a bow shock (detached) is formed in front of the accelerated flux tube, as it usually occurs in cases of blunt bodies moving with supersonic velocities. In the chromosphere bow shocks are seen in the form of elongated transients moving as a whole in a direction almost perpendicular to their long axes. On some much more rare occasions compared to “drifting” bow shock type transients, there appear compact “true” microjets moving in the radial direction, and having much higher velocities compared to bow shocks.

### 18.1 Response of the Overlying Atmosphere to Penumbral Dynamics

High cadence observations with the Solar Optical Telescope (SOT) on Hinode have led to the discovery of frequent transient brightenings in the penumbral chromosphere with lifetimes of  $\sim 1$  min (Katsukawa et al. 2007), referred to as penumbral microjets. They are seen in Ca II H line observations in the form of bright strokes abundantly covering the entire chromosphere above penumbra. Their typical length is found to be between 1,000 and 4,000 km, some may reach 10,000 km. Their width is  $\sim 400$  km. It was found also that microjets are almost parallel to the penumbral filaments in the radial direction (which makes them difficult to identify when the sunspot is close to disk center), but are more vertical to the surface than penumbral filaments. The estimated elevation angles range from  $20^\circ$  to  $60^\circ$ . Katsukawa et al. (2007) suggested that the observed microjets could be associated with magnetic reconnection in the

penumbra. As the physical nature of these phenomena at the time of their discovery was not clear, the authors left room for two possible, but different explanations:

1. One is that “the jetlike brightenings are a signature of plasma transiently heated to much higher temperatures.”
2. The other is that transients represent true mass motion with supersonic velocities, i.e., microjets.

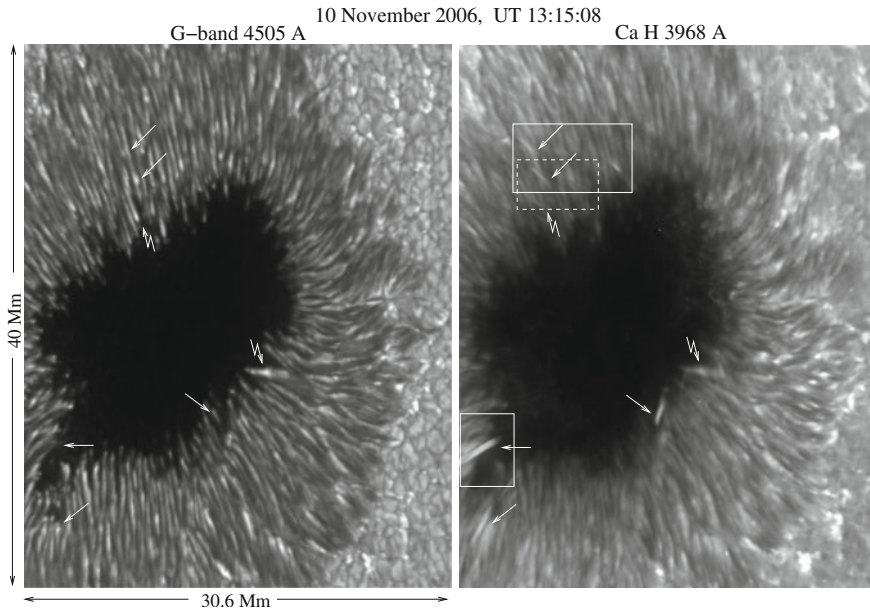
We will see below that both explanations are true, but are related to two different classes of events. One class includes bright elongated transients drifting as a whole in a direction almost perpendicular to their long axes. Their properties are well represented by bow shocks and we classify them as bow shock type transients. The other class includes compact, short-lived, and much faster bright transients exhibiting true plasma motion “along” their axes. We classify these events as microjets. The triggering mechanism for either kind of transient is the reconnection between the neighboring penumbral filaments but it is the post-reconnection processes and local physical conditions that determine their specific nature.

### ***18.1.1 Penumbral Transients—Double Structures and Jets***

To demonstrate the observed properties of radiative transients above sunspot penumbrae, we present the observations obtained during the disk passage of active region (AR 10923) on November 10–20, 2006. The data were taken with the SOT instrument on Hinode in 4,305 Å G-band and 3,968 Å Ca II H line (Ryutova et al. 2008b). Movies taken at 8 s cadence, show detailed dynamics of jetlike phenomena under different angles as sunspot takes various positions when it passes the solar disk from limb to limb. Such a favorable circumstance allowed to perform detailed analysis of observation and reveal the nature of the impact of penumbral dynamics to the overlying atmosphere.

Figure 18.1 shows the target region on November 10 when sunspot was located at a heliospheric angle of 55° toward the east of the disk center. At any moment of time, the penumbra is covered with bright elongated transients that last from 30 s to several minutes. Their appearance always correlates with the appearance of bright points in the corresponding G-band image. Some examples are marked with white arrows in Fig. 18.1. White boxes demarcate two regions whose time sequences are shown in Figs. 18.2 and 18.3. Transients marked by broken arrows are in the decay phase, while their parental bright points in G-band are still prominent.

Figure 18.2 shows evolution of three well-shaped transients during a 4 min 30 s period. The first frame at UT 13:13:36 shows when transient 1 has just appeared. Transient 2 appeared 30 s earlier. Transient 3 is seen here during its entire lifetime (UT 13:15:06–13:16:37). Note that all three transients are quite similar. They have the same position angle in the plane of the sky. Their intensity increases in time, and then either gradually decreases (as in cases 1 and 2), or vanishes abruptly, as in case 3. Lifetimes are  $\geq 6$  min (transient 1), 2 min (transient 2), and 90 s (transient 3). All three transients seem to be almost *motionless*. In fact, they are slowly drifting



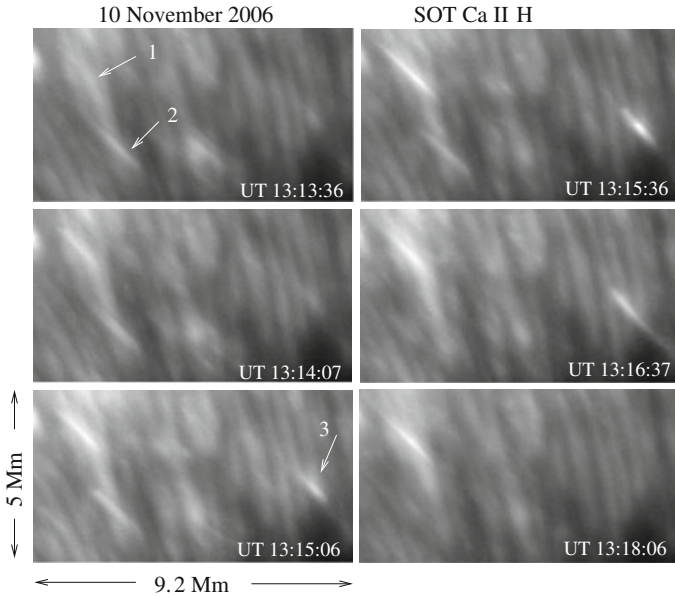
**Fig. 18.1** Snapshots of the sunspot on November 10, 2006. *Left* G-band filtergram. *Right* 3968 Å Ca II H line. Usually, transients (seen in the Ca II H line) are closely related to bright points seen in the G-band image (some are marked by *arrows*). Transients marked by *broken arrows* are decaying, while their “parental” bright points in G-band are still prominent. *White boxes* demarcate regions shown in Figs. 18.2, 18.3 and 18.4 at several instances in time. Note that the event shown in Fig. 18.3 occurred about 45 min earlier (its area is marked by a *dashed box*)

in the direction perpendicular to their long axes, with velocities  $v_1 = 0.6 \text{ km s}^{-1}$ ,  $v_2 = -1.3 \text{ km s}^{-1}$  (a minus sign formally means that, unlike the other two transients, transient 2 is drifting “downward”), and  $v_3 = 3.3 \text{ km s}^{-1}$ , indices correspond to prescribed numbers. This is however, a visual effect associated with the angle between the line of sight and the direction of motion of the transients. So that the true velocities of transients must be considerably higher.

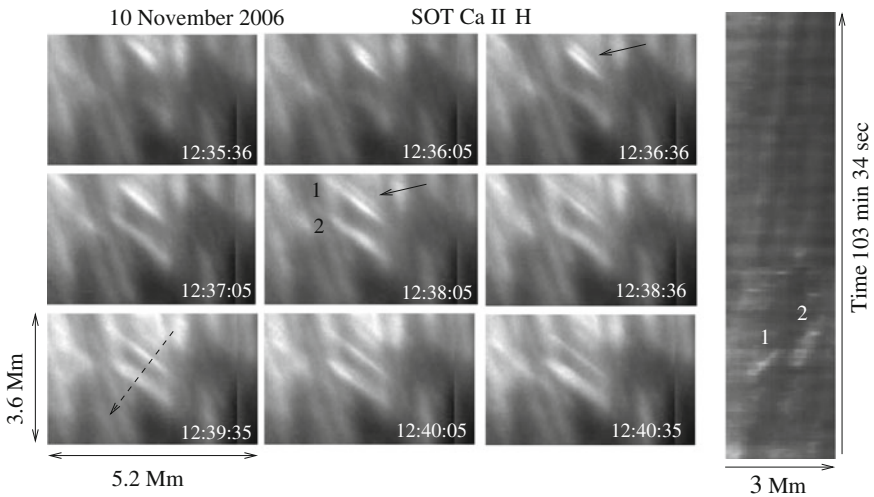
These three examples represent the vast majority of the transient brightenings that *always move as a whole in the direction perpendicular to their long axes*. Their visual velocities range from  $\leq 1$  to  $20 \text{ km s}^{-1}$ . We shall see below that this type of transient has all the properties of bow shocks.

Another set of slowly drifting transients is shown in Fig. 18.3. We focus on two of them marked as 1 and 2 in a middle frame (UT 12:38:05). The lifetime of both transients is about 5 min. The black dashed arrow in lower left panel shows the spacetime cut. The corresponding spacetime image is shown in the vertical panel. The cut is made from top to bottom, which, together with the vertical panel indicates that transients are moving downward. Measured velocities are  $v_1 = 3.9 \text{ km s}^{-1}$  and  $v_2 = 3.1 \text{ km s}^{-1}$ .

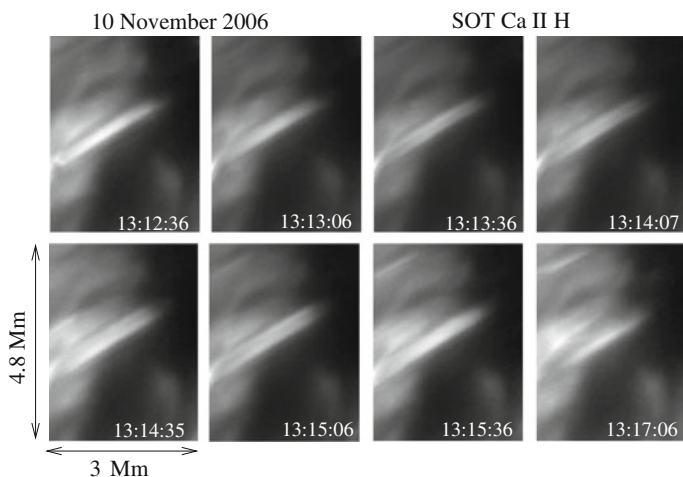
A remarkable new feature revealed in these observations is that some transients, in particular, the transient 1 in Fig. 18.3, has a double structure. This structure starts



**Fig. 18.2** Examples of three transients, from the *upper white box* in Fig. 18.1, slowly drifting in a direction perpendicular to their long axes



**Fig. 18.3** Slowly drifting transients with specific feature showing a double structure. The *black dashed arrow* in the *lower left panel* shows the path along which a spacetime cut is made. The *vertical panel* is the corresponding spacetime image. The velocities in the direction of the cut are  $v_1 = 3.9 \text{ km s}^{-1}$ ,  $v_2 = 3.1 \text{ km s}^{-1}$ . *Black solid arrows* show a new feature found in these observations: the double structure of chromospheric transients



**Fig. 18.4** Double structure of the elongated transient drifting with velocity  $\sim 1.5 \text{ km s}^{-1}$ . Its true motion, if measured in its trajectory plane, may well be supersonic

to develop soon after the transient has appeared (i.e. just 30 s after its “first light”) and, in this particular example, is easily visible during its maximum phase. This important feature turned out to be quite pervasive: many elongated transients show a double structure and patterns similar to those seen in Fig. 18.3.

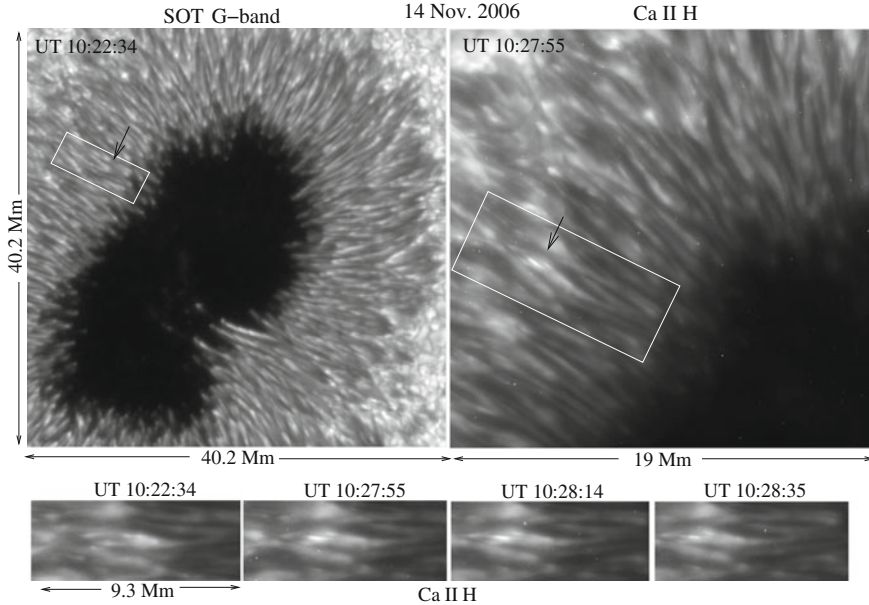
Another example of transients exhibiting double structure and the same pattern as above, is shown in Fig. 18.4. One can see that this transient seen at UT 13:13:36 as a single bright stroke, soon develops a clearly visible double structure and remains oriented in such a way that its double structure is seen during most of its lifetime ( $\geq 5 \text{ min}$ ). The transient is drifting from top-left to bottom-right with velocity  $\sim 1.5 \text{ km s}^{-1}$ . Note again that this velocity, restricted by two-dimensional viewing, strongly depends on the orientation of the plane of motion. In three dimensions the transient may move either toward or away from a viewer.

In any case, a double structure turns out to be a basic property of drifting transients and, in fact, has a natural explanation in the frame of the theory based on post-reconnection processes. Before we discuss the details of the theory, it is useful to study other observed properties of chromospheric transients that show up under different viewing angles, namely when sunspot is located at the disk center, and then when it moves toward the west limb.

### 18.1.2 Viewing Under Different Angles

The main feature of transients described in the previous section is that their direction of motion is perpendicular to their long axis. This fact makes them easily observable. There are other types of transients whose behavior is similar to jets, i.e. when a collimated plasma moves *along* its axis. Such transients oriented in radial directions



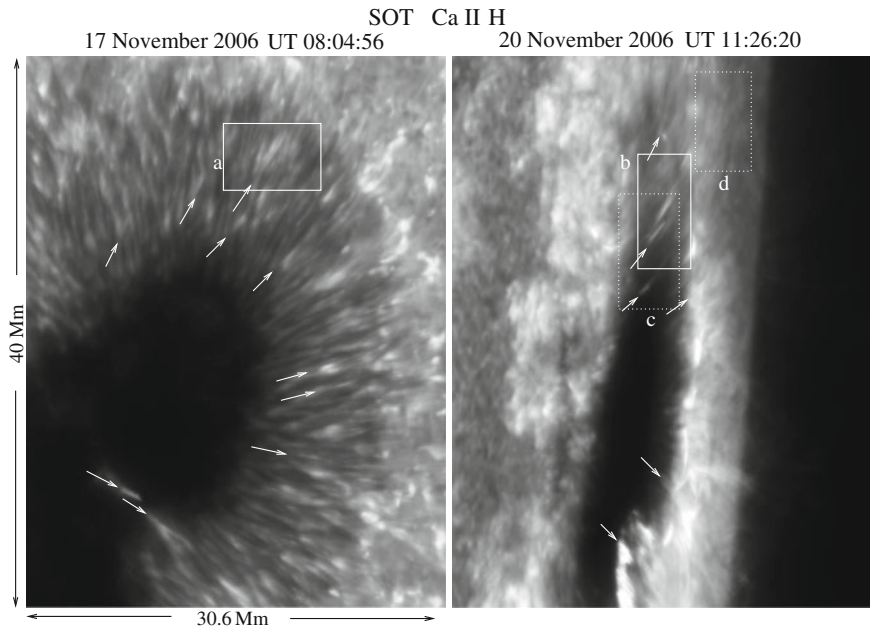


**Fig. 18.5** Same sunspot, AR 10923, near the disk center. Shown are a G-band image of the sunspot and the enlarged Ca II H image of its upper east quarter. The birth and evolution of a supersonic microjet is shown in Ca II H images at four instances of time. The microjet originated at the base of a fork made by penumbral filaments (marked by *black arrows*). Its average velocity during the first 5 min is  $\simeq 9 \text{ km s}^{-1}$  reaching  $\simeq 30 \text{ km s}^{-1}$  during the last minute

usually coincide with the underlying penumbral filaments and are barely detectable. On some occasions though, if the transient exhibits proper motion, it can be observed. An example of such event is shown in Fig. 18.5.

The same sunspot, AR 10923, is now shown on November 14, 2006 when it moved closer to the disk center. Shown are a G-band and Ca II H line images of the chromosphere above the sunspot. A tiny microjet with proper motion is shown in a Ca II H line image. It originates at the base of the fork (marked by black arrows in the upper images) and first appears as an enhanced brightening in the Ca II H line at about UT 10:22:34 (bottom left panel). It slowly accelerates and moves during the first 5 min with an average velocity  $\simeq 9 \text{ km s}^{-1}$ . Starting from UT 10:27:55, it quickly accelerates reaching a velocity of  $\simeq 30 \text{ km s}^{-1}$ , and then suddenly disappears. This is one of the examples of collimated plasma streaming which can be classified as a true microjet. Generation of collimated plasma flows requires special conditions (Tarbell et al. 1999; Ryutova et al. 2003; Ryutova and Tarbell 2003). The key elements, as we have discussed throughout the book, are associated with the geometry of a shock profile and environmental magnetic fields, which may provide conditions for self-focusing of the shock, and generation of microjets.

As the sunspot moves toward the limb, the transients become clearly visible and appear elevated with respect to penumbral filaments with angles ranging from  $30^\circ$

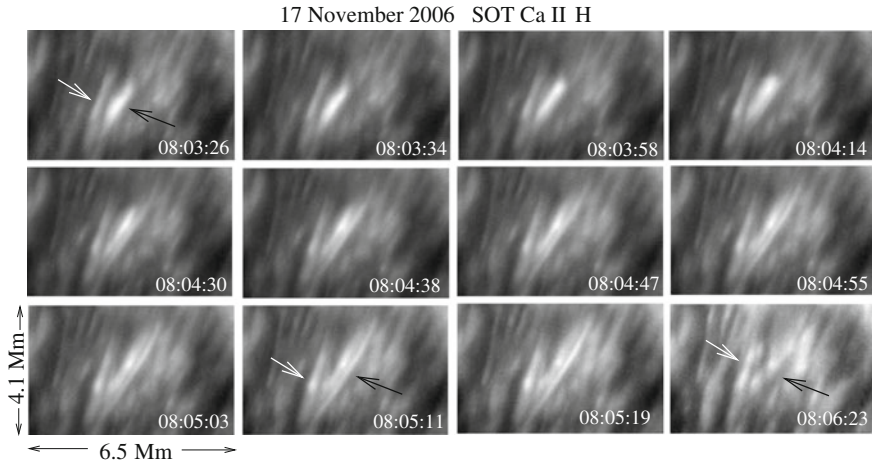


**Fig. 18.6** Sunspot at two Western hemisphere locations:  $42^{\circ}\text{W } 6^{\circ}\text{S}$  on 17 November 2006 (*left*) and  $85^{\circ}\text{W } 6^{\circ}\text{S}$  on 20 November 2006 (*right*). *White arrows* imitate a position angle of some transients showing their fan-like distribution in the plane of the sky. *White boxes*, *a*, *b*, *c*, and *d* demarcate regions shown in subsequent figures

to  $50^{\circ}$ . Figure 18.6 shows the same sunspot (approaching the West limb) at two heliographic locations:  $42^{\circ}\text{W}, 6^{\circ}\text{S}$  on 17 November 2006 (*left*) and  $85^{\circ}\text{W}, 6^{\circ}\text{S}$  on 20 November 2006 (*right*). *White arrows* imitate the azimuthal direction of some transients showing their fan-like distribution with quite regular position angles. All of the marked examples belong to bow shock-type transients drifting as a whole in a direction perpendicular to their long axes. As already mentioned, the overwhelming majority of bright transients seen at any given instance of time belong to this class of events. On some occasions there appear true “microjets”—collimated plasma streaming. *White boxes* in Fig. 18.6 are drawn in solid and dotted lines to emphasize that the events shown in these boxes occur at different times.

Figure 18.7 shows the evolution of two transients during about a 3 min period. The area with these events is demarcated by a solid box “a” in the snapshot of 17 November 2006 (Fig. 18.6 left panel). The transient marked “a” by a black arrow is oriented in quite a favorable way to show the formation of a double structure. This is a very typical process that starts with an enhanced brightening already having an elongated form. Soon after formation, the double structure gets quickly stretched until the dissipation process turns on.

This example is a good illustration of the process associated with the post-reconnection flux tube moving upward with supersonic velocity. Note that the



**Fig. 18.7** Formation and evolution of a bow shock

flux tube, still being cold inside, is not visible in Ca II H, but the shock, generated by a slingshot effect resulting from its straightening, heats the plasma. This is a regular occurrence of behind shock heating which appears as a “first light”, and should manifest itself in a way similar to that shown in the upper left frame, including its elongated form (at UT 08:03:26).

It is important to note that the flux tube is still a “body” which continues to travel with supersonic velocity. As such, it creates a *bow shock* in front of it, as any solid object that moves with supersonic velocity. Indeed, soon after the appearance of the first behind-shock brightening, the double structure starts to form and becomes visible at UT 08:04:14. In this particular case, the bow shock appears in about 48 s after the behind-shock brightening.

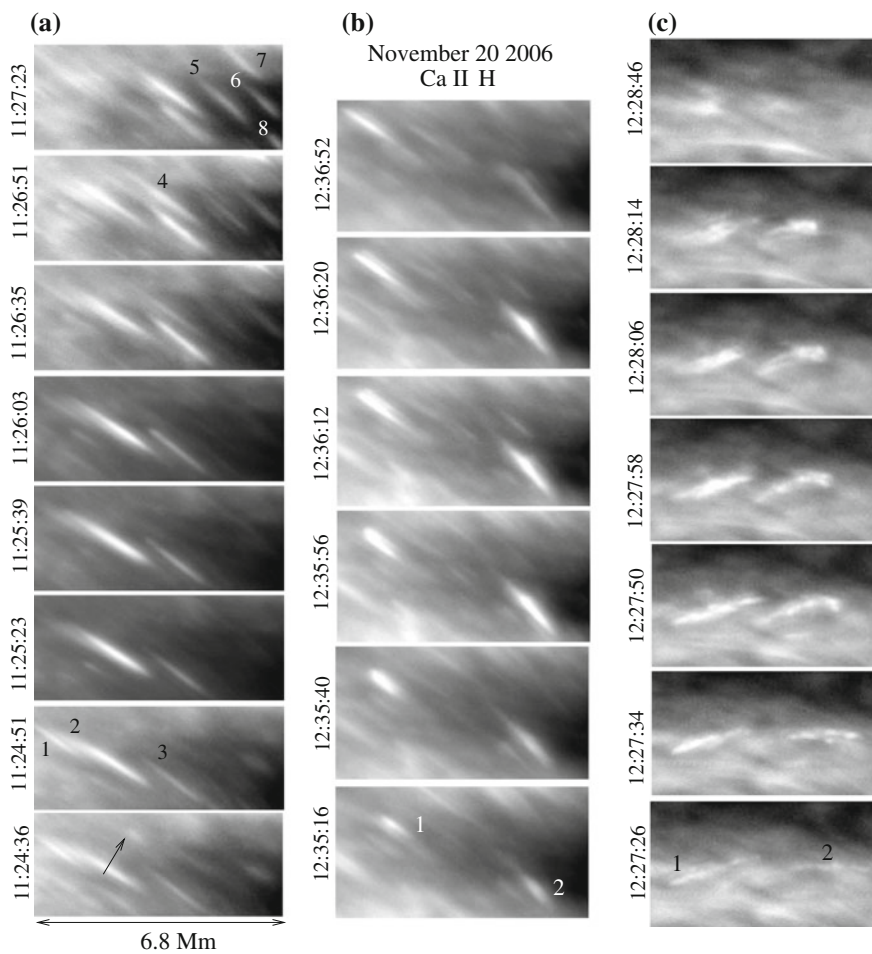
As the original shock propagates faster than the flux tube, the bow shock always appears *after* the regular behind shock heating. This pattern, with various time delays, is confirmed in all the observed cases of double structures. We will return to this process in the next section and present quantitative analysis.

It must be noted that a standoff distance, i.e. the space between the bow shock and the object created it, which is necessary attribute of bow shocks, is clearly visible during entire evolution of the bow shock until the whole structure starts to dissipate. The velocity of the structure in the plane at a given orientation is  $5.6 \text{ km s}^{-1}$  (directed from top-left to bottom-right). A true velocity of the transient, however, should be transonic. If the measured velocity of a transient is  $v_{\text{obs}}$ , then its true velocity can be estimated as  $v \simeq v_{\text{obs}}/\sin \theta$ , where  $\theta$  is an angle between the line of sight and the trajectory plane of the transient. For example, if angle  $\theta = 20\text{--}40^\circ$ ,  $v \simeq 16.4\text{--}10.1 \text{ km s}^{-1}$ .

Another transient in Fig. 18.7, marked with a white arrow, shows only its “thermal” evolution, and slowly drift with velocity  $1.5 \text{ km s}^{-1}$ . The velocity component of the apparent motion of the transient in the plane of the sky is only  $2.24 \text{ km s}^{-1}$ . To be

supersonic, the angle between the plane of motion and line of sight should be  $\leq 16^\circ$ . Nothing contradicts such an orientation; the plane may be parallel to the line of sight, in which case the transient will appear motionless and will only exhibit its thermal evolution. Given their abundance, quite a large number of transients, however, have a favorable orientation to show their double structure.

Some other examples of transients differently orientated and having thus different velocities are shown in Fig. 18.8. These were taken on November 20, 2006 when the sunspot moved quite close to the western limb. The first column (the area marked by a solid white box b in Fig. 18.6 right panel) shows the most typical occurrence of several transients (marked 1–8); they are appearing, evolving and disappearing in time intervals less than 3 min. In this orientation the transients barely show a double



**Fig. 18.8** Examples of three bright transients under different viewing angles. See text for details. The images are rotated by  $90^\circ$

structure and the highest drift velocity measured (transient 2) is  $4.2 \text{ km s}^{-1}$ . This time series shows transient 2 during its entire life ( $\simeq 2 \text{ min}$ ,  $15 \text{ s}$ ). At UT 11:24:51, the transient 1 is in its final stage. Transient 3, which seems practically motionless, shows its thermal evolution, reaching maximum brightness at UT 11:26:51. From this moment on, it quickly dissipates energy and disappears. Its lifetime is about 3 min. At the end of this time sequence (UT 11:26:51) a strong transient appears (transient 4), which quickly gains energy and disappears in 2 min. About this time (UT 11:27:23), in the small area of a given frame, four new transients appear almost simultaneously, showing a typical abundance of “one type” of transients.

The central column (the area marked by dotted white box c in Fig. 18.6) shows evolution of two fast “conveniently” oriented transients. In other words, their orientation is such that their measured velocities are, indeed, supersonic,  $v_1 = 16.8 \text{ km s}^{-1}$  (transient 1), and  $v_2 = 8.8 \text{ km s}^{-1}$  (transient 2), and a double structure of transient 1 is well observable.

The right column (the area marked by dotted white box d in Fig. 18.6) is located on the farther side of the penumbra) shows the evolution of two other supersonic transients. Their measured velocities exceed  $v_1 = 14 \text{ km s}^{-1}$ . Both transients show vague but recognizable double structures. Their lifetimes are less than 1 min. Again, all the events shown in Fig. 18.8, as well as an overwhelming majority of transients at any moment of time, belong to the bow shock class. Contrary to this, events that may be classified as true microjets—collimated plasma streaming (cf. Fig. 18.5) are much more rare. For comparison of their observed signatures, we show one more example seen in the November 20 data set.

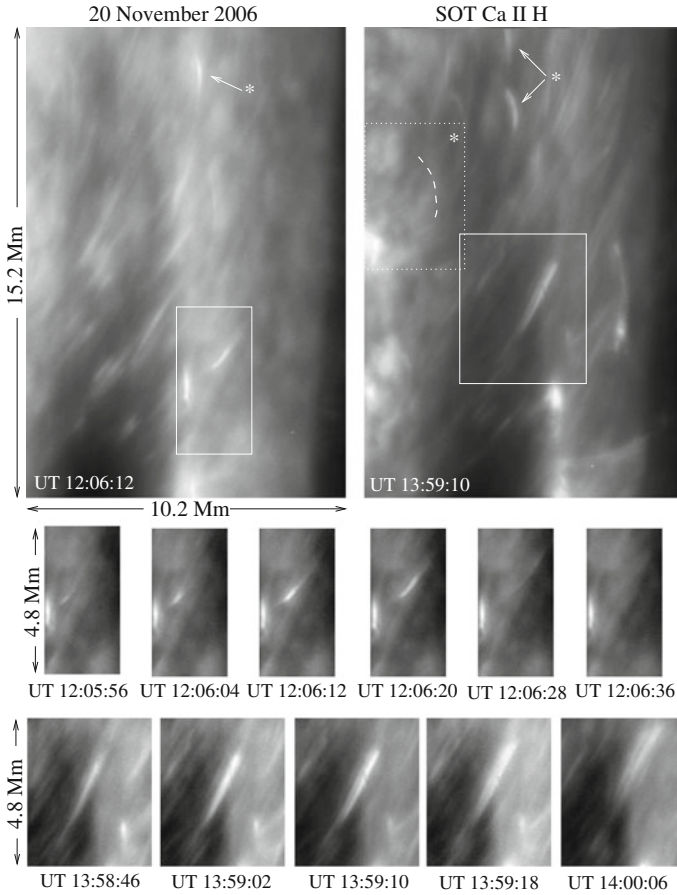
Figure 18.9 shows snapshots of the upper penumbra at two instances of times, with a  $10.2 \times 16.2 \text{ Mm}^2$  field of view. The white box at UT 12:06:12 demarcates the region with a fast transient that clearly exhibits proper, jetlike motion. A time series of the microjet is shown in a middle row. Its lifetime is a little over 30 s and velocity exceeds  $50 \text{ km s}^{-1}$ . Its motion is directed *along* its axis unlike the “transverse” motion of bow-shock type transients. For comparison, the lower row shows an example of a “favorably” oriented bow-shock type transient. Its measured velocity is  $\simeq 20 \text{ km s}^{-1}$ , lifetime about 2 min, and its double structure is clearly visible.

The white dotted box in Fig. 18.9 (upper right panel) and three arrows marked by asterisks are related to Fig. 18.10 which is used to illustrate the process of bow shock formation (see next section). The position of the bow shock is marked by a white dashed arc. It appears around UT 13:29:26 (half an hour earlier than the snapshot shown in Fig. 18.9). Similar events under less favorable angles showing only bright arcs, are marked by arrows with a star.

### 18.1.3 Brief Summary of Properties

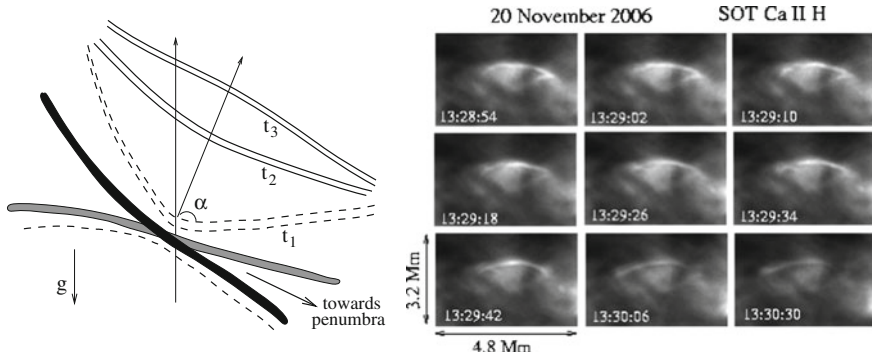
Briefly, the above observational results can be summarized as follows.

1. The chromosphere above penumbrae is highly dynamic and shows an abundance of bright, elongated transients at any given moment of time.



**Fig. 18.9** Comparison of true microjet and bow shock. *Top* snapshots of the upper part of the penumbra at two instances of time. *Middle row* a true microjet with a lifetime of about 30 s, traveling in the radial direction with velocity  $\geq 50 \text{ km s}^{-1}$ . *Bottom* more favorably oriented transient of a bow shock nature—its measured velocity is  $\simeq 20 \text{ km s}^{-1}$ , lifetime about 2 min, and its double structure is quite visible. The meaning of the dotted box and white arrows marked by stars in the upper right panel is explained in the text

2. Transients are always associated with bright points seen in G-band images.
3. Bright points are usually located at the Y-shaped fork made by neighboring penumbral filaments but may be found anywhere in the penumbra.
4. There are two different types of chromospheric transients. One type shows strongly elongated brightenings that move almost perpendicular to their long axes. Their measured velocities range from  $\leq 1.5$  to  $\simeq 20 \text{ km s}^{-1}$ . They have clear properties of bow shocks. The other type is collimated plasma motion directed along their long axis. These are true mass motions representing supersonic microjets. Their measured velocities are well above  $20 \text{ km s}^{-1}$ .



**Fig. 18.10** Bow-shock formation. *Left* Sketch of the straightening U-shaped reconnection product with an opening angle  $2\alpha$ . *Right* A possible observational analogy. The image, rotated by  $90^\circ$ , is located on the side of penumbra closest to disc center and marked by the dotted box in Fig. 18.9 (top right). Similar events are marked in the same snapshot by white arrows and asterisks

5. The bow shock type transient makes the vast majority of chromospheric brightenings above the penumbra. Many of them exhibit a double structure.
6. The lifetime of bow shocks ranges from  $\leq 40$  s to  $\geq 6$  min. Their apparent length is between 2,000 and 10,000 km and their width is 300–600 km. The lifetime of microjets is usually  $\leq 1$  min, and their length is  $\leq 1,000$  km.
7. The appearance of bow shocks (from the observers point of view), whether or not their double structure is seen, their spatial scale, and apparent (measurable) velocities strongly depend on their location, the position of the sunspot, and the orientation of their trajectory planes with respect to the line of sight.

In the next section we address the phenomenology of post-reconnection processes in penumbral filaments and associated mechanism of formation of the bow shocks and microjets.

## 18.2 Phenomenology and Quantitative Analysis

As discussed in Chaps. 12 and 13, the specific character of post-reconnection dynamics at the photospheric level is determined basically by finite plasma beta and sharp stratification of the low atmosphere. Pressure equilibrium in a high plasma  $\beta$  environment implies that, after reconnection, magnetic field lines remain confined in thin flux tubes. Straightening, the reconnection products create a slingshot effect. At the periphery of a sunspot, flux tubes strongly deviate from the vertical as does the bisector of their collision angle (see Fig. 17.6). In this case, the reconnection products acquire U- and  $\cap$ -shaped forms with respect to gravity.

We focus here on further dynamics of the U-shaped reconnection product. In this case, two major forces, the magnetic tension and buoyancy force, both act in the upward direction leading to shock formation. Also, under specific conditions, this

leads to the appearance of lateral jets (Tarbell et al. 1999; Ryutova et al. 2003). The process is always accompanied by an enhanced brightening of a small reconnection region.

One more important effect associated with finite plasma  $\beta$  and sharp stratification occurs when a U-shaped post-reconnection product straightens and accelerates upward *itself*, exceeding the sound speed, i.e., moving with transonic velocity. In this case, a bow shock is formed in front of the flux tube, as it behaves as a usual blunt body moving with supersonic velocity. It is just this macroscopic effect which is observed in the form of bright, elongated transients all over penumbrae.

The formation of bow shocks is as ubiquitous as the ongoing reconnection processes between penumbral filaments. More importantly, unlike special conditions required for the generation of true plasma jetting, the formation of bow shocks require only that flux tube, still having well-defined boundaries, reaches transonic velocities. This simple condition makes bow shocks appear easily and densely occupy the chromosphere above penumbrae.

Below we detail some basic calculations of the formation of bow shocks and perform quantitative analysis.

### 18.2.1 Dynamics of U-shaped Filaments

We follow the energy analysis carried out by Ryutova et al. (2003) and evaluate major forces acting on the U-shaped reconnection product (see Chap. 12). As mentioned above, magnetic and buoyancy forces act in the same, upward direction accelerating the straightening segment of a flux tube. On the other hand, the flux tube, as well-defined body moving with velocity  $u$  in the ambient plasma, experiences the action of a frictional force,  $F_{\text{drag}} = (1/2)C_D\rho u^2 S_{\text{srf}}$ , where  $C_D$  is drag coefficient, and  $S_{\text{srf}}$  is the flux tube area transverse to the direction of motion.

It is important that the drag force is negligibly small at large Reynolds numbers (small  $C_D$ ) and small velocities, e.g., in the parameter domain  $Re \geq 10^3$ ,  $u < c_s$ , is  $C_D \simeq 0.1\text{--}0.2$  (see e.g. Parker 1979). However, when  $u$  exceeds the sound speed, the frictional force increases abruptly. At the velocity  $u \simeq 1.5\text{--}2c_s$ ,  $C_D$  becomes of the order of unity (Landau and Lifshitz 1987) and the drag force becomes strong enough to restrict the upward motion of the flux tube to values not exceeding  $M = u/c_s \simeq 1.5\text{--}2.5$ . At the same time, conditions for bow shock formation are met.

In the following, we adopt an isothermal model of the atmosphere,  $\rho = \rho_0 \exp(-z/\Lambda)$ , with a constant scale height,  $\Lambda = p/\rho g$ . The subscript “0” refers to the point where reconnection occurred. Consider first, a U-shaped flux tube with vertical axis of symmetry as shown in the left panel of Fig. 18.10. The right panel of the figure contains snapshots of Ca II H brightenings whose configuration may illustrate the process shown in the left sketch. It should be noted that such a configuration is seen repeatedly in the observations. Some examples are marked by asterisks in Fig. 18.9. Dashed box in this figure is the area shown in Fig. 18.10, right panel. The location of the bow shock itself is marked by the dashed arc: at UT 13:59:10 it was already gone.



At some height,  $z$ , above the reconnection level, the length of the straightened segment is  $2z \tan \alpha$  (Fig. 18.10 left). Its cross-section is  $S = S_0 \exp(z/2\Lambda)$ . Recall that the upward motion of U-shaped reconnection product is governed by action of magnetic tension and gravity forces. Using results of energy consideration, from (12.36)–(12.39), we have the following expression for the total variation of the potential energy of the system,  $\Delta W_{\text{pot}} = 2\Delta W_{\text{mag}} + \Delta W_{\text{gr}}$ ,

$$\begin{aligned} \Delta W_{\text{pot}} = & -\rho_0 v_{A0}^2 \frac{4\Lambda S_0}{\cos \alpha} \exp(-h/2\Lambda) \\ & \times \{(1 + \sin \alpha)[\exp(h/\Lambda) - 1] - (h/\Lambda) \sin \alpha\} \end{aligned} \quad (18.1)$$

Respectively, a total force acting upward on the ascending segment at height  $h$  is:

$$\begin{aligned} F_{\text{up}} = & \rho_0 v_{A0}^2 \frac{4\Lambda S_0}{h \cos \alpha} \exp(-h/2\Lambda) \\ & \times \{(1 + \sin \alpha)[\exp(h/\Lambda) - 1] - (h/\Lambda) \sin \alpha\} \end{aligned} \quad (18.2)$$

It is important to note that, when the velocity of the ascending flux tube,  $u$ , exceeds the sound speed, the friction coefficient,  $C_D$  becomes of the order of unity, and the drag force increases abruptly restricting the upward motion of the flux tube. The tip of the straightening segment reaches transonic velocities quite quickly, only in a few scale heights. From then on, the motion of the flux tube is determined by the balance of upward acting forces, (18.2) and the drag force:

$$F_{\text{drag}} = \frac{1}{2} C_D \rho_0 u^2 S_{\text{srf}} \quad (18.3)$$

where  $S_{\text{srf}} = \pi R_0 h \tan \alpha = S(2h/R_0) \tan \alpha$  is flux tube area transverse to the direction of motion,  $S = \pi R_0^2$ . With this, the drag force at height  $h$  becomes

$$F_{\text{drag}} = \frac{1}{2} C_D \rho_0 u^2 S_0 \exp\left(-\frac{3h}{4\Lambda}\right) \frac{2h \tan \alpha}{R_0} \quad (18.4)$$

From (18.2) and (18.4), we find the velocity at the tip where these forces are balanced (which implies  $C_D \simeq 1$ ) to be:

$$u_f = v_{A0} \left\{ \frac{4\Lambda R_0 \exp(h/4\Lambda)}{h^2 \sin \alpha} [(1 + \sin \alpha)[\exp(h/\Lambda) - 1] - (h/\Lambda) \sin \alpha \right\}^{1/2} \quad (18.5)$$

The height where the bow shock is expected to form corresponds to a final velocity of the flux tube on the order of  $u_f \simeq 1.5 - 2 c_s$ .

For quantitative estimates, assuming the reconnection occurs close to the surface, we take  $\rho_0 = 2.25 \times 10^{-7} \text{ g cm}^{-3}$ , scale height  $\Lambda = 150 \text{ km}$ , and sound speed  $c_s = 8 \text{ km s}^{-1}$ . We assume a filament radius of  $R_0 = 40 \text{ km}$ . The Alfvén velocity in

**Table 18.1** Final velocity of a shock at different heights and angles

$\alpha$	$h = 800$ (km)			$h = 1,000$ (km)			$h = 1,100$ (km)		
	$60^\circ$	$50^\circ$	$40^\circ$	$60^\circ$	$50^\circ$	$40^\circ$	$60^\circ$	$50^\circ$	$40^\circ$
$M$	1.35	1.42	1.5	1.9	2	2.1	2.3	2.4	2.5
$u_f$ (km s $^{-1}$ )	10.8	11.36	12	16.2	16	16.8	18.4	19.2	20

a magnetic field of  $B = 1,000$  G is  $v_A = 6$  km s $^{-1}$ . For these parameters, Table 18.1 shows estimated heights where the Mach number,  $M = u_f/c_s$  reaches values of 1.5–2 for different angles of collision, and corresponding opening angles,  $2\alpha$ .

### 18.2.2 Nature of Double Structures

Let us now return to the phenomenology of the observed double structure and, in particular, look at the connection between the regular behind shock heating and the bow shock. As mentioned earlier, a regular shock produced by a slingshot effect propagates faster than the flux tube, and must therefore appear before the straightened flux tube reaches transonic velocities, and becomes able to generate a bow shock.

In Chap. 14 we have studied photospheric reconnections and shock formation in various magnetic environments, and calculated corresponding heights of shock formation and shock velocities. In case of the chromospheric transients, shocks evolve in the magnetic environment, i.e., correspond to the case 3 shown in Figs. 14.3 and 14.4. Now we need to compare the shock velocity from expression (14.16), with velocity of ascending flux tube, (18.5). The expression for the shock velocity (solution of (14.16)) has the form:

$$u_{\text{sh}}(z) = v_{A0} \frac{\sqrt{(3z_0/\Lambda)\exp(z/2\Lambda)[1 - \exp(-3z/4\Lambda) - 3z_0/4\Lambda]}}{1 - \exp(-3z/4\Lambda)} \quad (18.6)$$

where  $z_0$  is the height of shock formation in a homogeneous atmosphere:

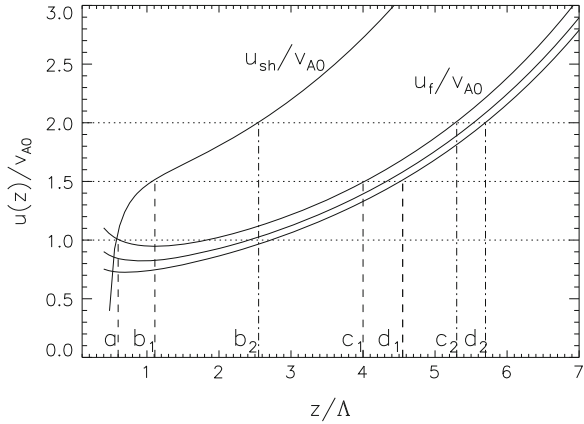
$$z_0 = \frac{2}{\gamma + 1} \frac{c_{s0}^2}{v_{A0}^2} R \quad (18.7)$$

Plots of  $u_{\text{sh}}$  and  $u_f$ , (18.5), for three opening angles, are shown in Fig. 18.11. We use the same parameters as those used above for construction of Table 18.1.

One can see that the regular shock reaches the transonic region earlier than the bow shock is formed. Note that for chosen parameters,  $c_s = 8$  km s $^{-1}$ ,  $v_{A0} = 6$  km s $^{-1}$ , Mach one,  $M = u/c_s = 1$ , corresponds to  $u/v_{A0} = 1.5$  (Fig. 18.11).

To estimate times needed for regular shocks and bow shocks to reach approximately the same height, we need to integrate (18.5) and (18.6), i.e., evaluate the integral  $t = \int_a^b dz/u(z)$ . Vertical dashed lines in Fig. 18.11 intersecting the plots, mark end points for numerical integration. We choose for lower limit of integrals  $a_1 = 0.5$ ,

**Fig. 18.11** Shock amplitudes as a function of height: the upper curve, marked as  $u_{sh}/v_{A0}$ , corresponds to the shock resulting from post-reconnection sling shot. Three lower curves, marked as  $u_f/v_{A0}$ , correspond to the velocity of the ascending flux tube for three opening angles,  $40^\circ$ ,  $50^\circ$ ,  $60^\circ$ —from top to bottom. For the meaning of dashed lines and letter marks see the text



i.e.  $z \simeq 75$  km (half of the scale length,  $\Lambda$ ) above the reconnection point.  $b_1 = 1.1$  corresponds to the height of a regular shock formation,  $M = 1$  ( $u/v_{A0} = 1.5$ ). Corresponding heights for bow shock are  $c_1 = 4$  at  $\alpha = 40^\circ$ , and  $d_1 = 4.55$  at  $\alpha = 60^\circ$ . Numerical integration of  $u_{sh}$  (18.6), between  $a_1$  and  $b_1$ , gives a time of  $t_{b1} = 16.5$  s.

Numerical integration of  $u_f$ , (18.5), with end points  $a_1 = 0.5$  and  $c_1 = 4$ ,  $a_1 = 0.5$  and  $d_1 = 4.55$  gives the estimates of time when the velocity of the ascending portion of flux tubes reaches  $M = 1$ :  $t_{c1} = 65.5$  s ( $\alpha = 40^\circ$ ),  $t_{d1} = 74$  s ( $\alpha = 60^\circ$ ). These estimates show that there is a finite time interval,  $\Delta t$  between the appearance of a regular shock and following bow shock. Thus, for  $M = 1$ , the delay times are, respectively,  $\Delta t = 49$  s ( $\alpha = 40^\circ$ ), and  $\Delta t = 57.5$  s ( $\alpha = 60^\circ$ ).

For higher Mach numbers, the delay times slightly drop. A similar procedure for  $M = 1.5$  ( $u/v_{A0} = 2$ ), gives the following estimates. The regular shock reaches this level in  $t_{b2} = 39$  s. The flux tube reaches this velocity in  $t_{b2} = 83.5$  s, for  $\alpha = 40^\circ$ , and in  $t_{b2} = 88.7$  s, for  $\alpha = 60^\circ$ . Respectively, “delay times” are,  $\Delta t = 44.5$  s, and  $\Delta t = 49.7$  s.

The observed delay times for the appearance of a bow shock range from tens of seconds to minutes. For the examples given above, we have the following numbers. The bow shock shown in Fig. 18.3 appears in 29 s after a regular behind shock heating. The time delay, in the case of the bow shock shown in Fig. 18.4 is about 1 min. In the case shown in Fig. 18.7, the time delay is 48 s. In the example shown in Fig. 18.8a, the bow shock appears in about 40 s, and, in the last example (Fig. 18.9 bottom), time delay is only 24 s. Thus, the observed and estimated time delays are in good agreement.

### 18.3 Bow Shocks

Thus, formation of bow (*detached*) shocks in front of accelerating flux tubes is a natural occurrence. Parameters of bow shock are determined by Mach number and relation between pressure,  $p$ , density,  $\rho$ , and temperature,  $T$  relations across the

shock (Landau and Lifshitz 1987):

$$\frac{p_2}{p_1} = \frac{2\gamma M^2 - (\gamma - 1)}{\gamma + 1}, \quad \frac{\rho_2}{\rho_1} = \frac{(\gamma + 1)M^2}{2 + (\gamma - 1)M^2} \quad (18.8)$$

$$v_2 = v_1 \frac{2 + (\gamma - 1)M^2}{(\gamma + 1)M^2} \quad (18.9)$$

$$T_2 = T_1 \frac{[2\gamma M^2 - (\gamma - 1)][2 + (\gamma - 1)M^2]}{(\gamma + 1)^2 M^2} \quad (18.10)$$

Subscript “2” refers to the region behind the bow shock and subscript “1” denotes the parameters of the incident stream associated with the flux tube;  $\gamma$  is a specific heat ratio. These are determined by the standard expressions for the variation of quantities along the streamline (Landau and Lifshitz 1987, Par. 83), e.g.  $T_1 = T_0[1 + (1/2)(\gamma - 1)M^2]$ .

A standoff distance of the bow shock,  $\Delta$  (distance between the bow shock and the body creating it) is known to be proportional to the inverse density ratio across the shock,  $\Delta \sim h(\rho_1/\rho_2)$ :

$$\frac{\Delta}{h} = \zeta \frac{2 + (\gamma - 1)M^2}{(\gamma + 1)M^2} \quad (18.11)$$

Coefficient of proportionality,  $\zeta$ , is usually of the order of unity. For cylindrical objects it can be approximated as (see e.g. Hayes and Probstein 1966):

$$\zeta = \ln \frac{4}{3\epsilon}, \quad \epsilon = \frac{2 + (\gamma - 1)M^2}{(\gamma + 1)M^2} \quad (18.12)$$

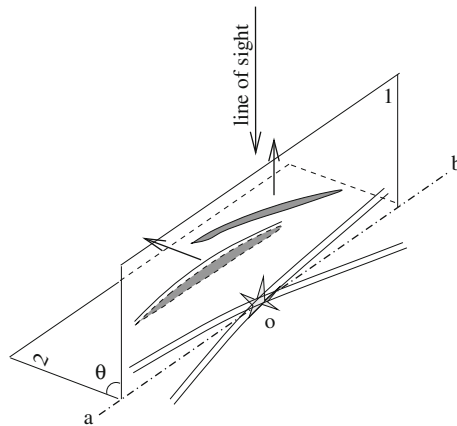
With (18.8)–(18.12) one can estimate the position of the bow shock,  $h_{\text{bow}} = h + \Delta$ , temperature, and velocity. In addition, given that the lateral extension of the bow shock is of the same order of magnitude as the straightened segment of the flux tube, the “length” of the bow shock,  $L_{\text{bow}}$ , can be estimated as  $2h \tan \alpha$ , and its thickness should be on the order of the standoff distance,  $d_{\text{bow}} \simeq \Delta$ .

In Table 18.2 we estimate bow shock parameters at different Mach numbers for three different angles. In principle, most of the transient parameters are observable. The observed length of transients (ranging from 2,000 to 10,000 km), their width (300–600 km), and lifetime are in good order of magnitude agreement with the calculated quantities given in Table 18.2. There are of course uncertainties in measuring velocities and linear scales of transients which are largely due to the uncertainty of their true orientation with respect to the line of sight. This is illustrated in Fig. 18.12.

Thus, when penumbral filaments reconnect, the reconnection region may have arbitrary orientation with respect to observer, depending on the heliographic location of sunspot and the azimuthal location of the reconnecting filaments in the penumbra. The orientation and location of the penumbral bisector is also essential. If the final orientation of the plane in which the bow shock moves is similar to plane “1” in

**Table 18.2** Calculated bow shock parameters

	$h = 800$ (km)			$h = 1,000$ (km)			$h = 1,100$ (km)		
	$60^\circ$	$50^\circ$	$40^\circ$	$60^\circ$	$50^\circ$	$40^\circ$	$60^\circ$	$50^\circ$	$40^\circ$
$\alpha$	$60^\circ$	$50^\circ$	$40^\circ$	$60^\circ$	$50^\circ$	$40^\circ$	$60^\circ$	$50^\circ$	$40^\circ$
$M$	1.35	1.42	1.5	1.9	2	2.1	2.3	2.4	2.5
$\epsilon$	0.662	0.622	0.583	0.458	0.437	0.420	0.392	0.380	0.370
$\Delta$ (km)	370	379	386	489	487	485	528	525	522
$h_{\text{bow}}$ (km)	1,170	1,179	1,186	1,489	1,487	1,485	1,628	1,625	1,621
$L_{\text{bow}}$ (km)	2,770	1,910	1,343	3,464	2,384	1,678	3,810	2,622	1,846
$T_1$ ( $10^4$ K)	0.96	1.01	1.05	1.32	1.4	1.5	1.66	1.75	1.85
$T_2$ ( $10^4$ K)	1.29	1.41	1.57	2.58	2.90	3.30	4.13	4.62	5.16
$u_{\text{bow}}$ ( $\text{km s}^{-1}$ )	10.8	11.36	12	16.2	16	16.8	18.4	19.2	20

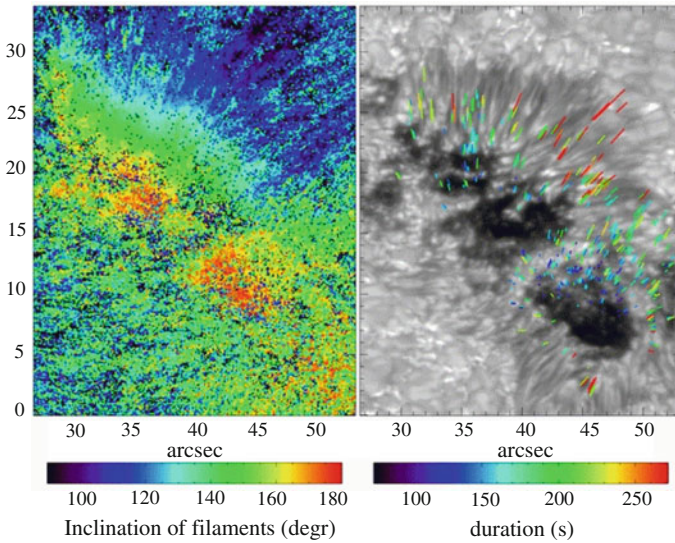


**Fig. 18.12** Orientation of the plane in which the bow shock travels depends on the orientation of the upper post-reconnection flux tube producing a slingshot effect and may be arbitrary. This in turn determines the appearance, velocity, and dimensions of the bow shock from the observer's point of view. Point "o" is a reconnection region, "ab" is bisector of a collision angle between interacting penumbral filaments. If the plane is in position 1, the transient appears as a single elongated brightening; but, with increasing angle  $\theta$ , the double structure of the transient becomes visible

Fig. 18.12, i.e., if the line of sight lies almost in the same plane, the transient will appear almost motionless, as is often seen in observations.

With arbitrary angle  $\theta$ , the velocity of the transient from the observer's point view may range from almost zero to its maximum value. In these data sets (showing the sunspot traveling from limb to limb) the maximum measured velocities, perpendicular to the transient long axis, are found to be  $19\text{--}20 \text{ km s}^{-1}$ . Calculated velocities show a strong dependence on height of the transient formation and range from  $11$  to  $20 \text{ km s}^{-1}$ .

The image of the transient, in addition to the direction of motion, is also affected by its orientation. When the line of sight is parallel to the plane of transient motion, ( $\theta = 90^\circ$ ), the transient appears as a single elongated brightening. With a finite



**Fig. 18.13** Relation between magnetic field inclination and filament lifetime and length. The *left panel* shows a map of the magnetic field inclination from LTE inversion of the Ca II 8542 Stokes data.  $180^\circ$  is a vertical, negative polarity field;  $90^\circ$  is a horizontal field. The *right panel* shows a continuum Ca II 8542 image with the paths drawn on the top of 460 filaments. The color of the paths indicates the duration of the filaments. Reprinted from Rouppe van der Voort and de la Cruz Rodriguez (2013) by permission from IOP, copyright AAS

angle  $\theta$ , the double structure of the transient becomes visible and may appear to be moving either away from or toward the observer (Fig. 18.12). Obviously, the longer and more horizontal are penumbral filaments, the more chance they have to produce multiple shocks and multiple bright transients in the chromosphere. Luckily, the penumbra is organized in such a way that shocks are abundantly observed. Figure 18.13 shows example of the relation between the magnetic field inclination in filaments and filament parameters (Rouppe van der Voort and de la Cruz Rodriguez 2013).

For theoretical estimates of the lifetimes, we shall consider shock-related dissipation as the dominant process at this spatial scales. First, we find the released thermal energy, and then the corresponding dissipation rate. This is done in the next section.

## 18.4 Energy Release and Lifetime of Bright Transients

In this section we perform the energy analysis and estimate the lifetime of transients. In fact, one of the most accurate parameters for comparison with observations is just the lifetime of transients.

For theoretical estimates of the lifetimes, we shall consider shock-related dissipation as the dominant process. First, we find the released thermal energy, and then the corresponding dissipation rate.

Energy release during the final stage of the straightening flux tube, when its velocity reaches  $u_f$ , can be estimated from the difference between the potential energy, (18.1), and the kinetic energy of the flux tube at the corresponding height  $h$ :

$$\Delta W_{\text{therm}} = -\Delta W_{\text{pot}} - \frac{\rho_0 u_f^2}{2} 2h \tan \alpha S_0 \exp\left(-\frac{h}{2\Lambda}\right). \quad (18.13)$$

Using (18.1) and (18.5) one obtains

$$\begin{aligned} \Delta W_{\text{therm}} &= \delta \rho_0 v_{A0}^2 \frac{4\Lambda S_0}{\cos \alpha} \exp\left(-\frac{h}{2\Lambda}\right) \\ &\times \left[ (1 + \sin \alpha) \left( \exp\left(\frac{h}{2\Lambda}\right) - 1 \right) - \frac{h}{\Lambda} \sin \alpha \right] \delta \end{aligned} \quad (18.14)$$

here

$$\delta = \left[ 1 - \frac{R_0}{h} \exp\left(\frac{h}{4\Lambda}\right) \right] \quad (18.15)$$

Using the same parameters as above ( $\rho_0 = 2.25 \times 10^{-7} \text{ g cm}^{-3}$ ,  $\Lambda = 150 \text{ km}$ ,  $R_0 = 40 \text{ km}$ ,  $v_A = 6 \text{ km s}^{-1}$ ), for the chosen heights (or equivalently, Mach numbers), and angles, (18.14) gives the estimates for thermal energy shown in Table 18.3. One can see that the released energy is in the range of  $3 \times 10^{26} - 6 \times 10^{26} \text{ erg}$ . This is comparable to the energy of blinkers, microflares, and other short-lived transients observed in the chromosphere/transition region.

To calculate the lifetimes of bow shocks, we recall the fact that the strength of a weak shock, and its energy,  $E(t)$ , are known to diminish as  $1/t^2$  (Landau and Lifshitz 1987), namely

$$E(t) = \frac{E_0}{(1 + \alpha_n ut/h)^2} \quad (18.16)$$

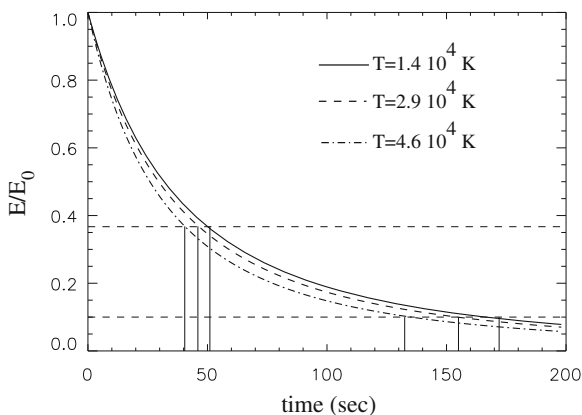
where  $\alpha_n = (1/2)(\gamma + 1)$  is a coefficient of nonlinearity for a polytropic gas,  $\alpha_n = 4/3$ . Plots of  $E(t)$  normalized by the initial energy carried by a shock are shown in Fig. 18.14.

For illustrative purposes, we use an example with  $\alpha = 50^\circ$ . The solid line corresponds to a bow shock at  $h \simeq 1,200 \text{ km}$ , velocity  $u_{\text{bow}} = 11.36 \text{ km s}^{-1}$ , and temperature  $T = 1.4 \times 10^4 \text{ K}$ . The dashed line corresponds to  $h \simeq 1,500 \text{ km}$ ,  $u_{\text{bow}} = 16 \text{ km s}^{-1}$ , and  $T = 2.9 \times 10^4 \text{ K}$ . The dash-dotted line to  $h = 1,625 \text{ km}$ , velocity  $u_{\text{bow}} = 19.2 \text{ km s}^{-1}$ , and  $T = 4.6 \times 10^4 \text{ K}$ . The characteristic time in which

**Table 18.3** Thermal energy at different heights and angles

$\alpha$	$60^\circ$	$50^\circ$	$40^\circ$	$60^\circ$	$50^\circ$	$40^\circ$	$60^\circ$	$50^\circ$	$40^\circ$
$M = u_{\text{bow}}/c_s$	1.35	1.42	1.5	1.9	2	2.1	2.3	2.4	2.5
$W_{\text{therm}} (10^{26} \text{ erg})$	5.5	6.0	6.13	4.12	4.48	4.56	3.26	3.53	3.57

**Fig. 18.14** Decay of the bow shock energy. Characteristic lifetimes range from 40 s to 3 min



the energy of the bow shock drops by factor of  $e = 2.7$  is in range of 40–50 s. For the chosen example, the average thermal energy is  $W_{\text{therm}} = 4 \times 10^{26}$  erg, which drops to  $\simeq 1.5 \times 10^{26}$  erg in about 1 min. A more significant order of magnitude decay occurs in 130–180 s. Thus, roughly, the lifetime of the bow shock may be from 40 s to 3 min. This is the time interval corresponding to the observed lifetimes of transient brightenings.

Concluding this chapter it is useful to summarize the observational results and their interpretation. These results represent the clear picture of a particular phenomena in the solar atmosphere that are well observed and quite well understood. Moreover, as other events that are quantitatively interpretable, they can be used for diagnostic goals.

Thus, high resolution and high cadence observations of sunspot penumbrae reveal an abundant population of highly dynamic transient phenomena in the overlying chromosphere and show clear regularities in their properties. Useful details in chromospheric dynamics were obtained thanks to observations of the sunspot at different locations during its passage from the east to west limb, showing the penumbra at various angles.

There are basically two different classes of bright elongated transients above penumbrae. The first discriminator that stands out is a difference in the *direction* of their motion with respect to their long axes.

One class includes the transients that move as a whole in a direction almost perpendicular to their long axes. These are classified as bow shocks. It is just this type of transients that make up the vast majority of all observed transients over the penumbrae.

Their measured velocities range from  $\leq 1.5$  to  $\simeq 20$  km s $^{-1}$ . As the orientation of the plane of the transient motion may be arbitrary, measured velocities may range from almost zero (when the plane of transient motion is parallel to the line of sight) to their maximum values (when the plane of transient motion is normal to line of sight). This explains a wide range of velocities measured when the sunspot was in various locations on the disk.

A remarkable property of the bow shock type transients is their double structure, which usually develops soon after the appearance of the “first light” at a characteristic



standoff distance from it. The double system then travels as a whole until it starts to dissipate. This feature strongly supports the bow shock nature of transients. The fact that not all the transients show a double structure is, like apparent velocities, affected by the orientation of the plane of the transient motion with respect to the line of sight.

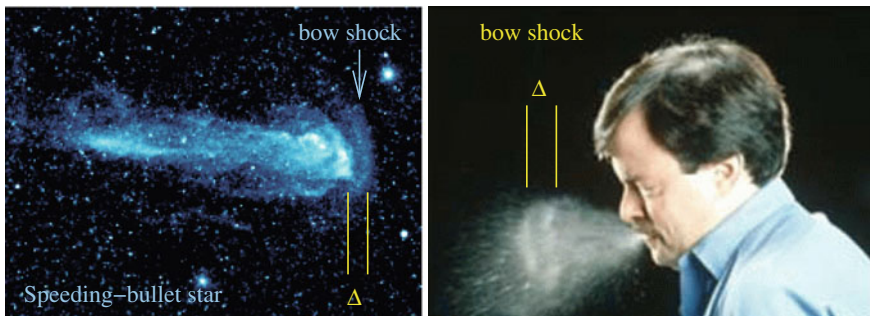
Lifetimes of bow shock type transients range from  $\leq 40$  s to  $\geq 6$  min. Their apparent length is between 2,000 and 10,000 km and their width is 300–600 km. In double structures, the standoff distance is of the order of, or less than, the width of the “secondary” transient (the bow shock itself).

The other type, representing the minority of chromospheric transients, fall into class of microjets. They have properties of collimated plasma streaming directed *along* their axes.

Their measured velocities range from 20 to 50 km s<sup>-1</sup>. Lifetimes of microjets are  $\leq 1$  min. Their apparent length hardly exceeds 1,000 km. As already mentioned, the number of microjets is significantly less than the ubiquitous bow shock type transients covering the entire penumbra at any instance of time.

The observed properties of chromospheric transients can be well understood in the framework of penumbral model based on the filamentary structure of sunspots where the most natural processes are the ongoing reconnections among interlaced filaments (Ryutova et al. 2008a). The specific character of photospheric reconnection and post-reconnection processes (provided by high plasma  $\beta$  and strong stratification of the low atmosphere) lead to macroscopic effects that are consistent with all observed properties of individual filaments, and explain the very formation of penumbrae.

The most striking and well observed effects produced by reconnecting filaments are shocks resulting from a slingshot effect associated with the straightening U-shaped reconnection product. Besides, under the action of magnetic tension and a buoyancy force acting in the same upward direction, a U-shaped flux tube itself quickly accelerates. At transonic velocities in front of it a bow (*detached*) shock is formed as it usually occurs in cases of blunt bodies moving with supersonic velocities (Fig. 18.15).



**Fig. 18.15** Bow shocks in *front* of blunt objects moving with supersonic velocities. *Left* Reprinted from <http://www.galex.caltech.edu>. Credit NASA/JPL-Caltech/C. Martin/M. Seibert(OCIW); *Right* Reprinted from <http://www.gettyimages.com>. Credit: R. Grapes-Michaud

In case of the flux tubes moving with supersonic velocities, i.e., reaching Mach numbers  $\simeq 1.5\text{--}2$ , the bow shock, once formed, tends to remain at the initial standoff distance until the whole system starts to dissipate. The lifetimes, spatial scales, velocities, and even temperatures of bow shocks are directly observable quantities. This fact allows to verify the validity of theory of entire process, and use the observed quantities for parameter studies.

For the time being, bright radiative transients and jets in the sunspot chromospheres were studied from various points of view (Louis et al. 2009a; Katsukawa and Jurcak 2010; Nishizuka et al. 2011; Reardon et al. 2013; Rouppe van der Voort and de la Cruz Rodriguez 2013; Anan et al. 2014).

It was found, for example, that transients propagating upward above penumbrae, are associated with supersonic downflows close to umbra–penumbra boundary, detected in high-resolution spectropolarimetric observations (Louis et al. 2009b). The orientation of the penumbral filaments at the site of the downflows were found to be consistent with those resulted from the post-reconnection process in penumbral filaments (Ryutova et al. 2008b). It is interesting that some observations show that outer penumbra filaments are associated with running waves. Moreover, the redshift ridges seen in the time-distance plots of velocity often merge, forming a fork-like pattern (Chae et al. 2014). Extremely rich picture of penumbral dynamics, shocks, jets, and evolutionary waves that became well observable, open rich possibilities to study farther the sunspot dynamics and energy production sources.

## References

- T. Anan, R. Casini, K. Ichimoto, *Astrophys. J.* **786**, 94 (2014)  
 J. Chae et al., *Astrophys. J.* **789**, 108 (2014)  
 W.D. Hayes, F.R. Probstein, *Hypersonic Flow Theory* (Academic Press, New York, 1966)  
 Y. Katsukawa, T. Berger, K. Ichimoto et al., *Science* **318**, 1594 (2007)  
 Y. Katsukawa, J. Jurcak, *Astrophys. Astron.* **524**, 20 (2010)  
 L.D. Landau, E.M. Lifshitz, *Fluid Mechanics* (Pergamon Press, Oxford, 1987), p. 390  
 R.E. Louis et al., *Astrophys. J.* **704**, L29 (2009a)  
 R.E. Louis et al., *Astrophys. J.* **727**, 49 (2009b)  
 N. Nishizuka et al., *Astrophys. J.* **731**, 43 (2011)  
 E.N. Parker, *Cosmical Magnetic Fields* (Clarendon Press, Oxford, 1979)  
 K. Reardon, A. Tritschler, Y. Katsukawa, *Astrophys. J.* **779**, 143 (2013)  
 L.R. van der Voort, J. de la Cruz Rodriguez, *Astrophys. J.* **776**, 56 (2013)  
 M. Ryutova, T. Tarbell, R. Shine, *Sol. Phys.* **213**, 231 (2003)  
 M. Ryutova, T. Tarbell, *Phys. Rev. Lett.* **90**, 191101 (2003)  
 M. Ryutova, T. Berger, A. Title, *Astrophys. J.* **676**, 1356 (2008a)  
 M. Ryutova, T. Berger, Z. Frank, A. Title, *Astrophys. J.* **686**, 1404 (2008b)  
 T. Tarbell, M. Ryutova, J. Covington, A. Fludra, *Astrophys. J.* **514**, L47 (1999)

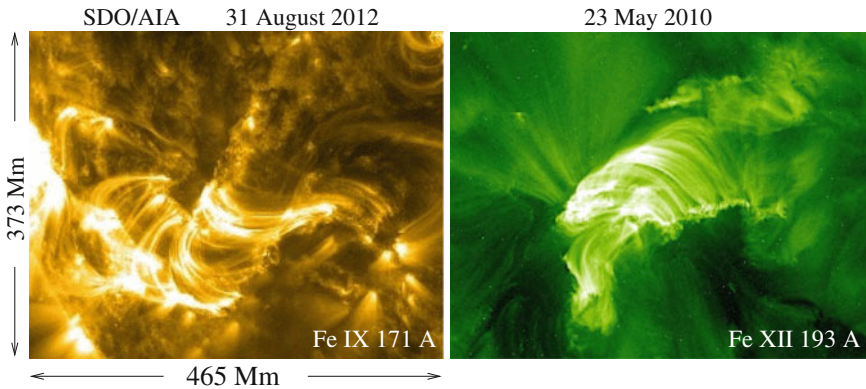
# Chapter 19

## Self-organization in the Corona and Flare Precursors

**Abstract** Exploding loop systems producing X-ray flares often, but not always, bifurcate into a long-living, well-organized system of multithreaded loop arcades resembling solenoidal slinkies. The subject of this chapter is to look into the physical conditions that cause or prevent this process. We shall see that the X-class flares that bifurcate into long-living slinky arcades have different signatures than those which do not produce such structures. The most striking difference is that, in all cases of slinky formation, a high-energy proton (HEP) flux becomes significantly enhanced 10–40 h before the flare occurs. No such effect was found prior to the “non-slinky” flares. This fact is found to be associated with the difference between energy production by a given active region and the amount of energy required to bring the entire system into the form of self-organized loop arcades. One of the important features is that post-flare coronal slinky formation is preceded by scale invariant structure formation in the underlying chromosphere/transition region. The observed regularities may serve as long-term precursors of strong flares and may help to study predictability of system behavior, and in particular, flare occurrence. We shall also discuss some aspects of recurrency of coronal microflares and flares which have signatures consistent with a spatial and temporal plasma echoes.

### 19.1 Well-Organized Multithreaded Coronal Arcades–Slinkies

We have discussed throughout this book that coronal structures above the Sun’s active regions appear in various forms, have lifetimes ranging from days to minutes, and show different behaviors from subtle oscillations of large-scale quasi-steady loops to exploding loop systems producing strong EUV flares. In this chapter, we shall study some systematic peculiarities in major X-ray flares that often bifurcate into a long-living, well-organized system of multithreaded loop arcades resembling the winding in a curved solenoid or a funnel. Due to this resemblance, these solenoidal structures were dubbed slinkies. Examples of two different slinkies one at  $6.4 \times 10^5$  K and other at  $0.2 - 1.6 \times 10^6$  K are shown in Fig. 19.1. Slinkies are usually associated with X-class flares, but they may well be produced by the M-class and even by the C-class flares.



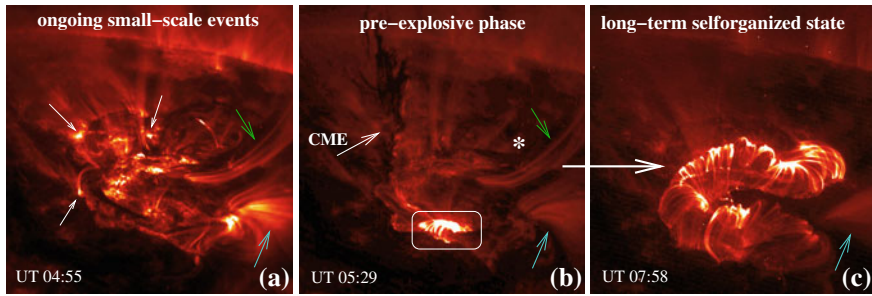
**Fig. 19.1** Snapshots of the most typical post-flare slinkies at two different temperatures. *Left* The SDO/AIA image of corona in Fe IX line at  $6.4 \times 10^5$  K taken on August 31, 2012; *Right* the image of a slinky at a temperature range of  $0.2\text{--}1.6 \times 10^6$  K taken by TRACE. A regular filamentary structure of slinkies formation turns out to be a backbone of their long-term dynamic stability

High resolution and high cadence observations show coronal structures and dynamics in great details (Gibson et al. 2002; Ryutova and Shine 2006; Kosugi et al. 2007; Aschwanden and Aschwanden 2008; Cirtain et al. 2013; Brooks et al. 2013; Winebarger et al. 2014). One of the most important facts revealed in recent observations is that *all coronal formations*, regardless of their size, shape, and lifetime, have filamentary structure. Individual filaments and their clusters are in constant motion reflecting various stages of coronal activity.

Figure 19.2 shows an example of three stages in the evolution of corona overlying a large active region (AR 10792 on July 30, 2005). Figure 19.2a is a typical picture of a strongly inhomogeneous conglomerate of coronal loops in its “regular” state, characterized by the quasi-steady behavior of long-living loops (marked by green and blue arrows), periodic brightening and dimming of individual filaments, and the appearance of frequent microflares (marked by small white arrows). No matter how complicated an inhomogeneous conglomerate is, it may remain for hours and days in such a “chaotic” state until some sudden increase in activity causes an explosive release of energy, leading to a major flare.

Figure 19.2b shows a pre-flare phase of the coronal system around the time of its growing activity accompanied by the appearance of a strong coronal mass ejection, CME (marked by the thick white arrow), and several moderate flares, such as the one that occurred at UT 05:29 (highlighted by the white box). The major X1.3 flare occurs at UT 06:35, in the location marked by the white star (not shown, note the time difference). When this happens, within a few minutes of the explosive phase/flare, the “messy” corona bifurcates into dynamically stable, well-organized arcades of thin flux tubes (Fig. 19.2c). This regime usually lasts for many hours or/and days, signifying the self-organized character of the state.

This pattern, i.e., when a long-lasting chaotic state that turns into a well-organized system of self-similar loop arcades due to the increased activity and flare, being quite



**Fig. 19.2** Image of the corona in the TRACE Fe IX/X ( $0.2 - 1.6 \times 10^6$  K), overlying a large active region. Field of view is  $230 \times 230 \text{ Mm}^2$ . **a** Large and small-scale loops of different forms show well-defined filamentary structure. Snapshots represent a long-term dynamic state of coronal structures being in constant motion and harboring numerous microflares that appear continuously in different places. **b** At some point, the corona shows a sudden increase in pre-flare activity including several moderate flares (one of them occurring around UT 05:29 is highlighted by the *white box*) and strong CME (marked by the *white arrow*). The major X1.3 flare occurs at UT 06:35, in the location marked by the *white star*. **c** Within a few minutes after the major flare, a huge “chaotic” conglomerate of coronal structures bifurcates into a well-organized dynamic state having the form of a multithread solenoid and remains in this state for many hours

typical, is not, however, universal. Not all of the major X-class flares end up with the formation of long-living, well-organized structures. In many cases, post-flare loops quickly cool down and disappear from the EUV images. The physical conditions that determine or prevent formation of long-living, well-organized structures are to be addressed in this chapter.

Our goal here is twofold. One objective is to investigate the nature of well-organized systems of self-similar loops and their formation. The other is to look into the question of why, among seemingly similar flares, some may bifurcate into a long-living, well-organized slinky stage and others not. These problems also include an important fact: the regularities observed in the corona must have their precursors in the underlying chromosphere/transition region whose topological and functional relations need to be also identified.

To address these problems we follow studies of the most prominent (major X-class and some C-class) flares occurred in about a decade period (Ryutova et al. 2011). It was found that the flares that bifurcate into long-living slinky arcades differ significantly from those that do not produce such structures. As mentioned above, the most striking difference is that, in all cases of slinky formation, the GOES high-energy proton (HEP) flux becomes significantly enhanced many hours before the flare occurs. There is also a correlation between the occurrence of slinky formation and an active region size.

To illustrate the process of post-flare slinky formation, first, we use Hinode observations of a large active region (NOAA AR 10930) during the time period of 5–13 December 2006. Events associated with this active region show extremely well a time sequence of pre-flare and flare activity, and the formation of a dynamically stable, well-organized structures. These observations have also provided a unique

opportunity to compare data taken simultaneously at different heights of the solar atmosphere. As a result, it was revealed that post-flare coronal slinky formation is preceded by scale-invariant structure formation in the underlying chromosphere/transition region. Such a pattern is characteristic to process of self-organization that takes place simultaneously at several spatial and time scales (Prigogine 1961; Gaponov-Grekhov and Rabinovich 1992). This will be discussed in more detail in subsequent sections.

It must be emphasized that any system that is potentially subject of self-organization need to be treated as an energetically open, dissipative system. In case of slinky formation, the system must include coupling between photospheric energy reservoir and the overlying chromosphere/corona, assuming also the back-reaction of coronal activity on the underlying atmosphere. In previous chapters, we have already encountered the necessity of applying the method of energetically open systems (see, e.g., Chap. 16). In electrodynamics such a system, as we saw, may be driven into various dynamic forms that include the Poincare limit cycle, and a spontaneous process of self-organization, characterized by scale invariant structure formation. It must be noted that small-scale, current-carrying filaments arise automatically in the model (Ryutova and Shine 2006; Ryutova 2006).

## 19.2 Essential Difference Between “Regular” and Slinky-Producing Flares

One of the established classifications of solar flares is their arrangement into B, C, M, and X classes, which is based on their X-ray output measured by the GOES spacecraft. Although flares in general exhibit common physical phenomena such as particle acceleration, radiation of electromagnetic waves, association with shocks and others, individual flares are quite unique and may exhibit their own set of specific events.

Many individual flares have been studied in great detail, especially with the opportunity given during the last decades by excellent satellite data sets. These were complemented by several survey works that have brought together some general properties of flares (Bai and Sturrock 1989; Battaglia et al. 2005; LaBonte et al. 2007). The existence of common properties naturally indicates common sources and origins of flares, thus facilitating the search for possible predictability criteria.

In this chapter, our primary goal is to study the nature and formation of post-flare well-organized loop arcades by analyzing general signatures observed in the major flares that occurred during a decade period (1998–2007). These analysis revealed quite puzzling fact indicating that among quite congruent flares, some bifurcate into self-organized state, while others do not.

A search for the observational properties distinguishing flares producing long-living slinkies from “non-slinky” flares led to several well defined differences. For example, the non-slinky flares are usually characterized by short post-flare relaxation period, while post-flare slinky configuration has long lifetime. The enhancement of

high-energy proton flux, typical to pre-flare period of slinky-producing flares, is absent in case of non-slinky flares.

Several examples of slinky and non-slinky flares together with their specific properties are shown in Table 19.1. The first column contains dates of the chosen examples; second and third columns are the start and peak times of the flare. The fourth column shows the scale of the event in GOES X-ray classification; fifth column contains the enhancement factor of particle fluxes long before the flare occurs. The approximate duration of these precursors is given in the next, sixth column. The enhancement of particle fluxes only occurs for those flares that bifurcate into self-organized slinkies. This is reflected in the seventh column, where “Yes” designates a slinky structure formation. Once the post-flare self-similar loop arcades are formed, they remain in this dynamically stable state for hours. The approximate lifetime of the self-organized loop arcade is shown in the eighth column. The last column represents parental active region and its size. By size we mean a gross estimate of a visual area occupied by the active region, roughly defined as small (S,  $\sim 100\text{--}500\text{ Mm}^2$ ), medium (M,  $\sim 600 \times 10^3\text{ Mm}^2$ ), large (L,  $\sim 2 \times 10^3\text{--}10^4\text{ Mm}^2$ ), and extra large (XL,  $\sim 2 \times 10^4\text{--}10^5\text{ Mm}^2$ ).

Four examples in Table 19.1 have “No” in the seventh column meaning that, soon after the flare, coronal loops quickly cool down without forming a long-living, self-similar loop arcades. In other words, after a short relaxation regime, the system returns almost to its pre-flare chaotic state. One can immediately see two major differences between this type of flares and slinky-producing ones:

- (1) they are not preceded by the early enhancement of high-energy proton fluxes and
- (2) they are usually associated with large, or super-large active regions.

To visualize more details of these differences and reveal others, we show three examples of the evolution of flares in Figs. 19.3, 19.4, and 19.5. It is interesting to note that although the 2004/03/30 UT 22:53 event was preceded by the enhancement of  $>1\text{ Mev}$  protons, the energy liberated by the flare was not enough to bring the system into the self-organized state. One can hardly determine why, but there are several factors that could be involved here:

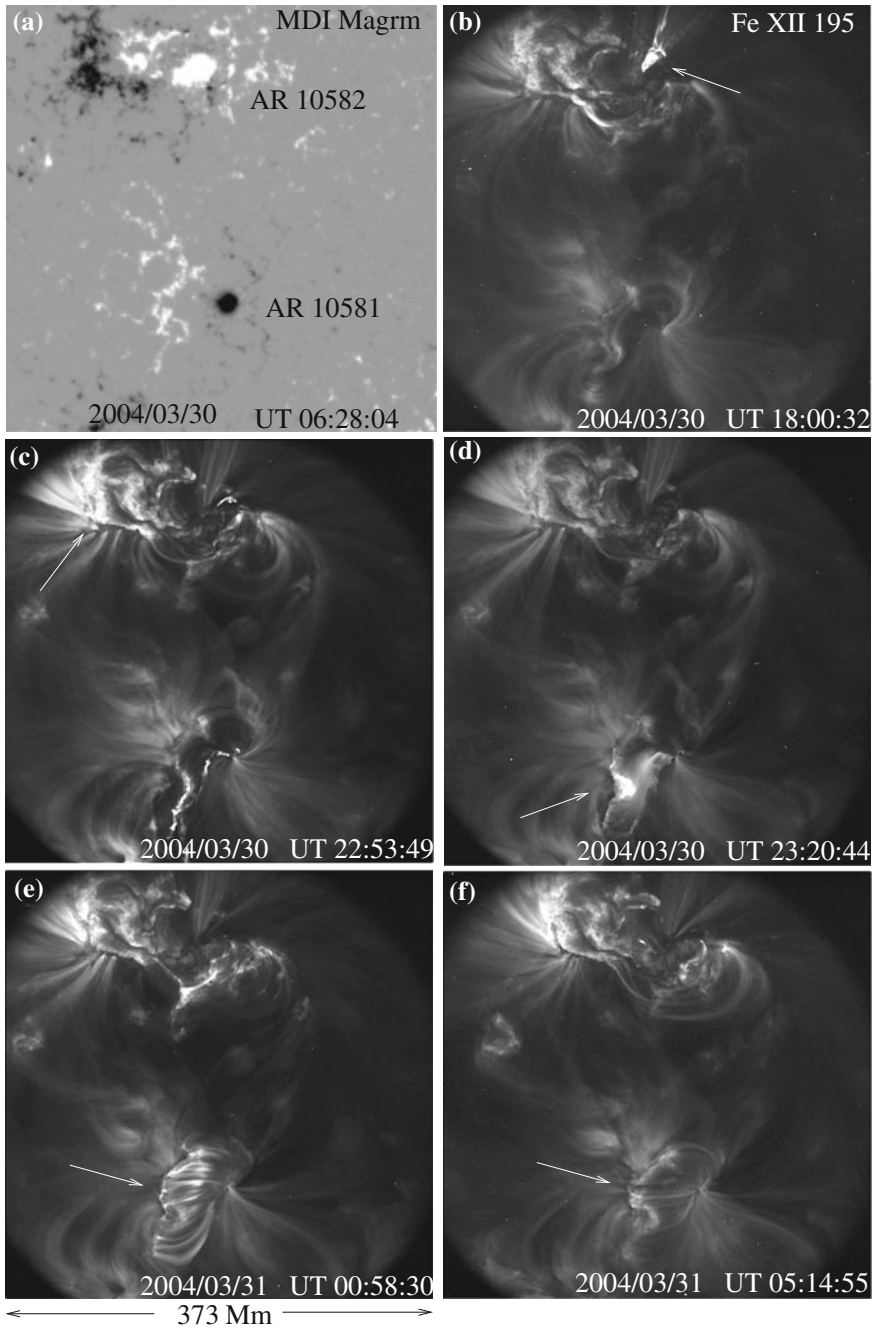
- (1) the higher energy proton fluxes remain normal,
- (2) the active region is too large, and
- (3) the fact that  $>1\text{ Mev}$  proton flux may not be relevant here because usually the cutoff energy at geostationary orbit is typically of the order of several Mev, and therefore the response of  $>1\text{ Mev}$  protons may be primarily due to trapped protons of the outer zone of the magnetosphere (<http://www.swpc.noaa.gov/>).

We now turn to the description of figures listed above. Figure 19.3 shows two neighboring active regions, AR 10581 and AR 10582, and their overlying corona in the TRACE 195 Å line. Of these active regions the much larger and much more complicated AR 10582 has produced seventeen C-class flares in the 24h interval (from UT 05:30, 2004/03/30 to UT 05:30, 2004/03/31). One of these flares is marked by white arrows in Fig. 19.3b–c. Each of these flares has been followed by a short

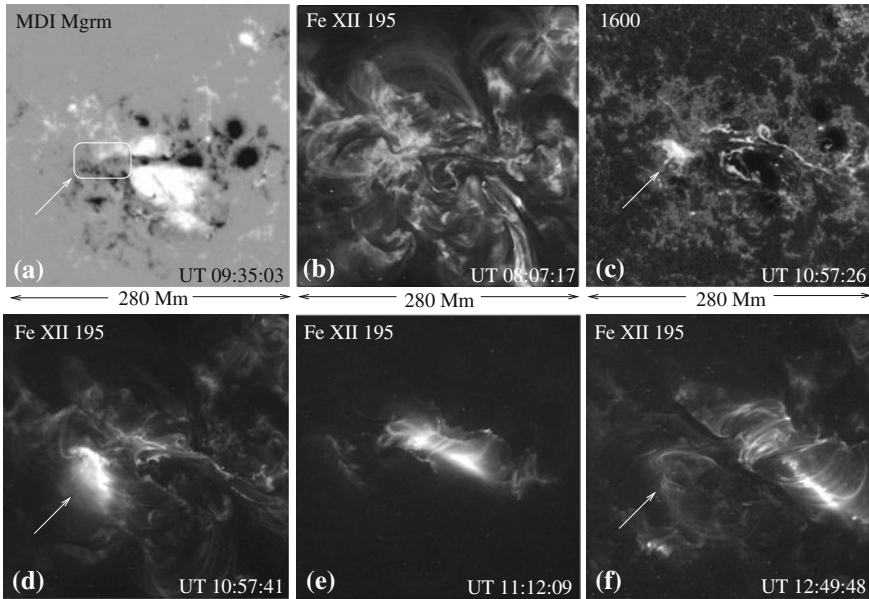
**Table 19.1** Examples of the flares and their signatures

(1) Event year/day	(2) Start time (UT)	(3) Peak time (UT)	(4) GOES class	(5) Enhancement factor			(6) Precursors (pre-flare duration)	(7) Self-organization state	(8) Post-flare lifetime	(9) AR (size)
				1 Mev	5 Mev	10 Mev				
2000/07/14	10:03	10:24	X5.7	$> 10^3$	$10^2$	50	$> 10^2$	Yes	18 h	09077 (L)
2001/04/10	05:06	05:26	X2.3	$> 10^3$	$> 10^2$	$> 80$	$> 10^3$	Yes	8 h	09415 (S)
2003/05/28	00:17	00:27	X3.6	$10^2$	40	60	$10^4$	Yes	4 h	10365 (S)
2003/06/11	20:01	20:14	X1.6	20	Normal	Normal	$\sim 10^4$	No	N/A	10375 (XL)
2003/10/28	09:51	11:10	X17	$10^4$	$10^4$	$10^4$	$8 \times 10^2$	Yes	4 h	10486 (XL)
2003/11/04	19:29	19:44	X18+	$10^4$	$10^5$	$10^4$	No data	Yes	$> 5$ h	10486 (XL)
2004/03/30	22:53	23:01	C8.3	$10^3$	Normal	Normal	$10^4$	No	N/A	10582 (L)
2004/03/30	23:20	23:28	C3.2	$10^3$	Normal	Normal	$10^4$	Yes	10 h	10581 (S)
2004/07/15	01:30	01:40	X1.8	Normal	Normal	Normal	$10^2$	No	N/A	10649 (XL)
2004/07/16	13:49	13:55	X1.7	Normal	Normal	Normal	$< 10^2$	No	N/A	10649 (XL)
2005/07/30	06:17	06:35	X1.3	$4 \times 10^2$	80	3	No data	Yes	10 h	10792 (M)
2005/09/07	17:17	17:40	X17	$< 10^2$	Normal	Normal	$> 10^4$	Yes	$\sim 30$ h	10808 (M)
2005/09/09	19:13	20:04	X6.2	$> 10^4$	$10^3$	$10^2$	No data	Yes	8 h	10808 (M)
2005/09/13	23:15	23:22	X1.7	$\sim 10^3$	50	$\sim 6$	$> 10^4$	Yes	11 h	10808 (M)
2006/12/13	02:14	02:40	X3.4	$> 10^4$	$6 \times 10^2$	60	$> 10^4$	Yes	$\sim 11$ h	10930 (S)





**Fig. 19.3** Two neighboring active regions, AR 10581 and AR 10582, give an excellent examples of absolutely different patterns in their coronal dynamics. Explanation of images shown in *panels a-f* is given in text

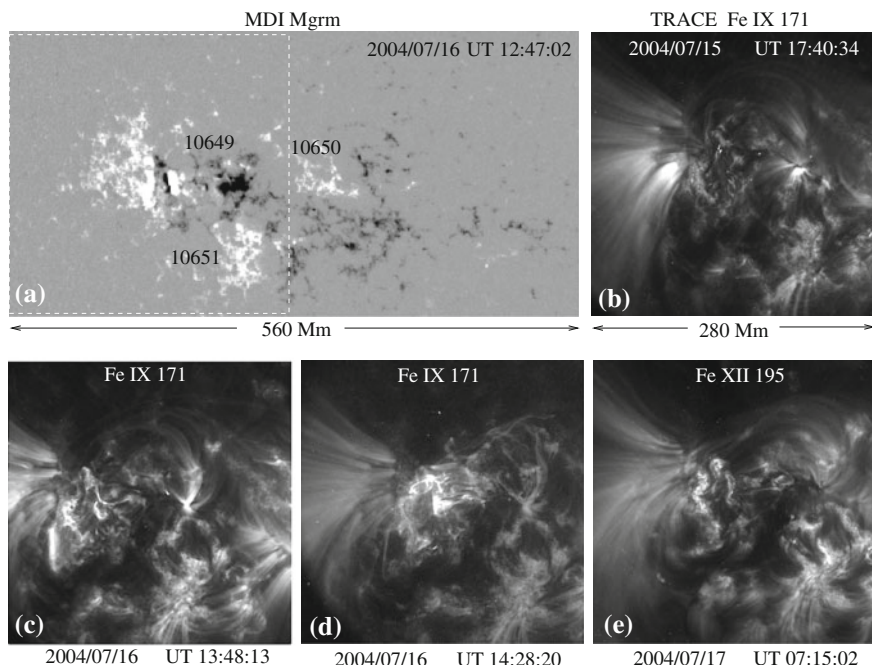


**Fig. 19.4** A major, October 28, 2003, X17-class flare originating at the periphery of a large active region, AR 10486, synchronizes the entire active region, and causes bifurcation of a large chaotic conglomerate of coronal loops into a huge regular solenoid with a lifetime exceeding 4 h. Note that the flare kernel first appears in the chromosphere (*panel c*). The events shown in *panels a–f* are described in text

relaxation regime, after which the system of coronal loops returned approximately to the same, pre-flare chaotic configuration.

A totally different situation eventuates in the southern AR 10581 which, by its topology and size, is far more simple and smaller than AR 10582. Besides these visual properties, AR 10581 had been inactive for many hours. It is remarkable, however, that a single flare of a C3.2 class, occurring during the same 24 h time interval (Fig. 19.3d, white arrow), resulted in an abrupt bifurcation of the entire system of coronal loops into a self-organized loop arcade (Fig. 19.3e, white arrow). The lifetime of this arcade exceeded 10 h. Figure 19.3f shows the corona in the TRACE Fe XII line at 2004/03/31 UT 05:14:55. At this time, the corona above AR 10582 which produced seventeen C-class flares, remains as complex as it was before all of these flares occurred. Contrary to this, the post-flare loop arcades above AR 10581, formed after a single C3.2 class flare, once acquired, keep their well-organized form.

These observed regularities clearly agree with the difference between energy production by a given active region and the amount of energy required to bring the entire system into a self-organized form (cf. Table 19.1). Obviously, none of the seventeen C-class flares have produced enough energy to unify the huge conglomerate of coronal loops above the large active region 10582, and bring it to a self-organized stage; whereas, the energy accumulated before and released after the C3.2 class flare was enough to reorganize the loop system above the compact active region 10581.



**Fig. 19.5** Coronal activity above a huge conglomerate of three active regions. *White dashed box in panel a* shows the TRACE field of view. Numerous flares occurring during the disk passage of this active region conglomerate were not able to synchronize the system, leaving the coronal loops in their chaotic state. *Panels a–e* containing the image of magnetogram (a) and time sequence of associated corona (b–e) are described in text

Similar regularities were observed in all studied cases (see Table 19.1). Figures 19.4 and 19.5 show two other examples of totally different outcome. Figure 19.4a–b show a large and complex active region, AR 10486, with a very irregular and complicated system of coronal loops overlying it. During about a 24 h period before UT 11:00 on Oct 28, 2003, several top C-class, M-class, and low X-class flares were continuously shaking the system. None of these flares, however, was able to change the intricate shape of the huge coronal system (Fig. 19.4b) until before UT 11:00 when the system was struck by a super-major X17 class flare (the famous Halloween flare). The Halloween event started with energy release first recorded in the TRACE 1600 chromospheric line (Fig. 19.4c) and escalated quickly to produce a rare X17-class flare (Fig. 19.4d). A few minutes after the X-ray intensity peak, the huge disarranged system of loops bifurcated into a well-organized, self-similar loop system having the form of a beautiful solenoid (panels e and f in Fig. 19.4). It is remarkable that the energy release, in the form of a major flare and its photospheric counterpart, is associated with a magnetically rarefied peripheral region marked by a white box in Fig. 19.4a and by arrows in panels a, c, d, and e. The shortest distance between the region of flare energy release and the solenoid axis exceeds 80Mm; yet, the blow produced by the X17 flare, and the amount of associated energy, were

enough to synchronize the entire active region, and cause bifurcation of a large chaotic conglomerate of coronal loops into a huge regular solenoid with a lifetime exceeding four hours.

Figure 19.5 shows an example of a post-flare outcome opposite to that of the 2003 Oct 28 flare. This case, dated 2004/07/16, also involves an extra large active region stretched over  $360 \times 162 \text{ Mm}^2$  area, consisting of three “subdivisions”, AR 10649, AR 10650, and AR 10651. The complexity of the overlying corona is, therefore, not surprising. The TRACE field of view of the corona is restricted by the  $280 \times 280 \text{ Mm}^2$  area (marked by the white dashed square in panel a). This huge ensemble of active regions produced during its disk passage numerous flares of all calibers.

For example, during three days, from 2004 July 15 UT 01:00 to July 17 UT 21:00, there were 12 low and mid X-class flares recorded, plus many more C-class and M-class events. Neither individual nor sequences of flares were able to synchronize the huge conglomerate of coronal loops to bring them into a self-organized state. After each and every one of the flares, the corona quickly relaxed back to its chaotic state. Panels b, c, d, and e in Fig. 19.5 show the corona soon after some of the X-class flares. The general character of the corona did not appear to change much from July 15 to July 17. This pattern was held throughout the disk passage of the active region.

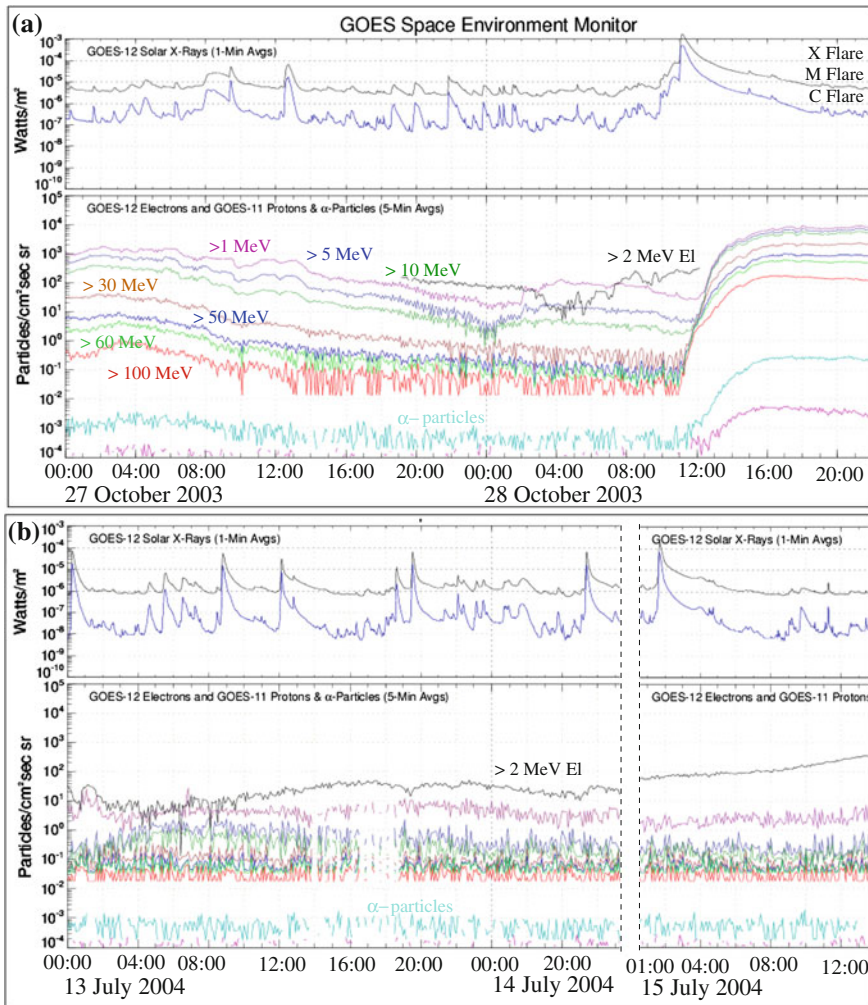
### 19.3 Precursors and Predictability

The fact that high-energy proton (HEP) flux gets enhanced before the slinky-producing flares and v.v., is obviously associated with the ratio between energy production by a given active region and the amount of energy required to bring the entire system into the self-organized form.

Figure 19.6 shows example of the GOES high-energy proton fluxes around the 2003 October 28 X17-class flare (panel a) and series of flares during 2004 July 13–15 associated with AR 10649 (panel b). For the GOES plots we use a collection at the web site <http://goes.ngdc.noaa.gov/data/plots/> and also the SolarSoft GOES Data available at <http://www.lmsal.com/SXT/> (developed by S. Freeland).

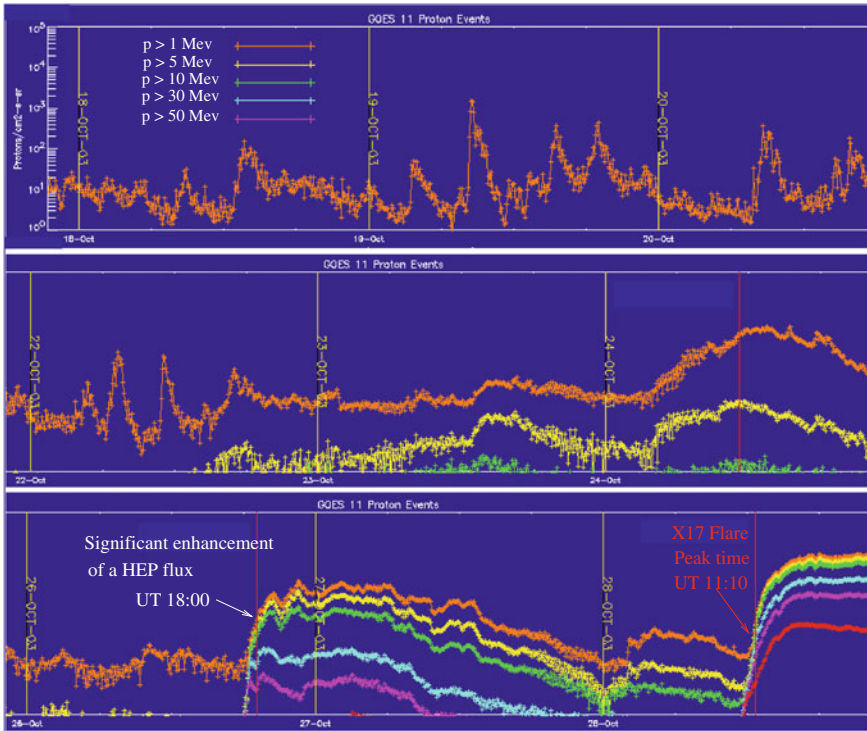
One can see a striking difference between the two cases shown in Fig. 19.6: in the case of the 2003 Oct 28 flare, high-energy proton fluxes are strongly enhanced. More than 40h prior to the flare, the fluxes of protons with energy higher than 1, 5, and 10 Mev are close to the post-flare level; moreover, even protons with energy higher than 50–100 Mev are significantly enhanced.

A totally different picture is seen in the case of the long series of 2004 July 13–15 flares: throughout this time period, the level of high-energy proton fluxes remained normal. Obviously, there was no preliminary accumulation of energy associated with AR 10649 and its neighbors. Therefore, even a long series of X and M-class flares could not reorganize their associated corona. Contrary to this, the energy content and its earlier accumulation in AR 10486 was so high that, despite its huge size, a single X17-class flare was enough to reorganize the entire system and bring it to a self-organized state (Fig. 19.4f).



**Fig. 19.6** Comparison of GOES high-energy proton fluxes for two cases. *Panel a* 2003 Oct 28 X17 flare occurrence that peaked at UT 11:10. High-energy proton fluxes are strongly enhanced more than 40 h prior to the flare. Protons with energy higher than 1, 5, and 10 MeV are close to the post-flare level and even protons with energy higher than 50–100 MeV are significantly enhanced. *Panel b* Series of X-class and M-class flares during a limited time interval. The level of high-energy particles remained normal throughout the chosen time interval

It should be emphasized again that the enhancement of particle fluxes only occurs for those flares that bifurcate into self-organized slinkies. The beginning of the enhancement process, or in other words, the first signs of the precursors develop from several hours to several days prior to the flare, as is shown, for the given examples listed in the sixth column of Table 19.1.



**Fig. 19.7** Plots of high-energy proton (HEP) fluxes 10 days prior to the flare that started at UT 09:51 on October 28, 2003. High-energy particle fluxes ( $>5$  MeV and higher) stay at low level. Precursor shows up at about UT 18:00 on October 26, i.e., about 40 h prior the flare, and appears as a sudden elevation of all channels including even the  $>50$  MeV protons (*purple line*). The  $>1$  MeV proton flux is shown to emphasize the absence of higher energy proton fluxes during several days prior to the precursor and flare (see the text for more details)

For illustrative purposes, we show in Fig. 19.7 the transition from a normal level of particle fluxes to their enhanced state for the 2003 October 28 flare (the fifth example in Table 19.1). The precursor appears at about UT 18:00 on October 26, i.e., over 40h before the start of the flare at UT 09:51 on October 28. These instances of time are shown by arrows on the lower panel in Fig. 19.7. During many days prior to the appearance of the precursor, the level of high-energy particle fluxes remained normal. It should be noted, however, that the elevated level of the  $>1$  MeV protons (light brown curve) can hardly be considered as a precursor, because this channel is mainly due to trapped protons of the outer zone of the magnetosphere. This channel is shown in Fig. 19.7 to emphasize the absence of higher energy proton fluxes prior to the precursor.

The two major components of regularities were observed in all cases of major flares during the last decade, i.e.,

- (1) The occurrence of an early enhancement of high-energy particle flux was inevitably followed by the bifurcation of pre-flare chaotic loop systems into post-flare self-organized loop arcades;
- (2) When early enhancement of high-energy particle flux was absent, the pre-flare and post-flare corona remained in its chaotic state divided only by a short post-flare relaxation period.

These regularities indicate that any system must be characterized by some critical parameters and, in particular, by some critical energy level above which the system must undergo a phase transition from one energetic and morphological state to another. In our case, spontaneous transition of a dynamic system of coronal loops from a chaotic state to a state characterized by coherent structure formation, is a typical process of self-organization observed in all dynamic systems in nature (Mandelbrot 1967; Gaponov-Grekhov and Rabinovich 1992), including the solar atmosphere (Mogilevsky and Shilova 2006; Golovko et al. 2009; Nishizuka et al. 2009).

Additional strong support for identifying the spontaneous formation of slinkies as a process of self-organization, is the observation of a scale invariance associated with it. This became possible with simultaneous multiwave observations taken by the Hinode spacecraft. Hinode shows the formation of self-organized structures not only at two levels of temperature in the corona (Fe IX 171 and Fe XI 195), but also at chromospheric and transition region temperatures. In the next section, we give an example of a corresponding case study and show that post-flare coronal structure formation is preceded by scale invariant structure formation in the underlying chromosphere/transition region.

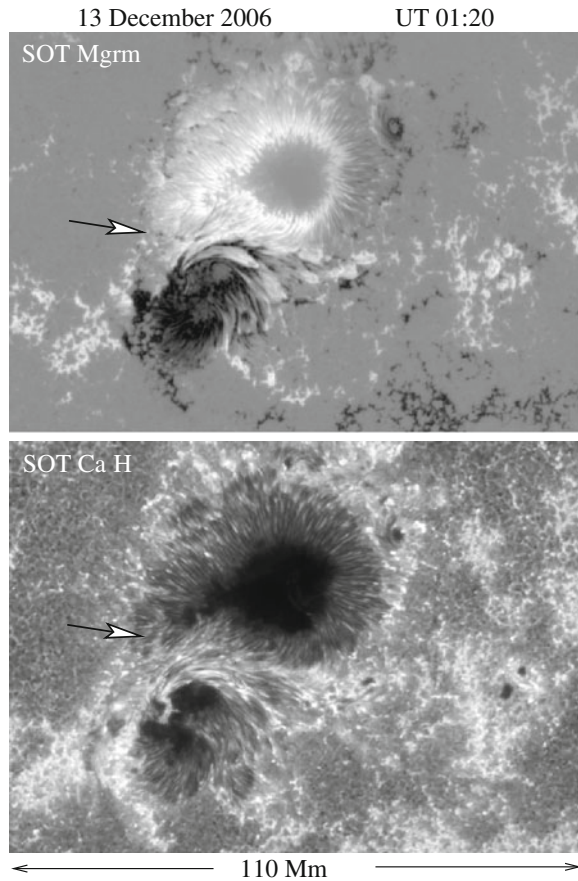
## 19.4 Exemplary Case of X-Class Flare and Formation of Slinkies

In this section we will show step-by-step process that starts from energy production in the photosphere, passes through pre-flare stage, resulting a strong flare, and ends up with formation of long-living well-organized multithread arcades of coronal loops. We will address here the following questions:

- (1) How the multithread arcades are formed;
- (2) Why they live so long;
- (3) What determines Energy *inflow* and *outflow*;
- (4) What role is played by photospheric activity; and
- (5) How the energy release by coronal flare affects the lower layers of atmosphere.

For this purpose we use the uninterrupted sets of the SOT magnetograms and chromospheric images in Ca II  $\lambda$  3968 H line ( $\simeq 10^4$  K) combined with simultaneous images of the corona taken with the TRACE spacecraft in Fe XII  $\lambda$  195 line ( $1.2\text{--}2.6 \times 10^6$  K), showing the step-by-step evolution of the entire system.

**Fig. 19.8** SOT magnetogram of an exemplary active region (*top*) and its overlying chromosphere in Ca H line at  $\sim 10^4$  K (*bottom*). The arrow points to the polarity inversion line surrounded by the most active clusters of opposite polarity elements

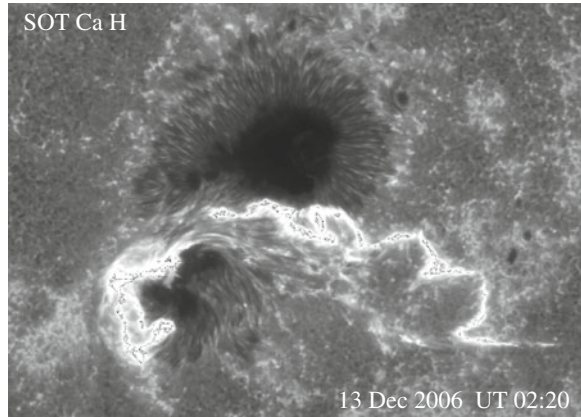


The target is a complex active region consisting of closely located opposite polarity sunspots surrounded by a mixed polarity plage. Figure 19.8 shows the SOT magnetogram of the region and chromosphere above it in Ca H line. While the sunspots do not show drastic changes with time, the clusters of small-scale magnetic concentrations around the polarity inversion line (marked by arrows in Fig. 19.8) are extremely dynamic.

A continuous energy supply coming from permanent interactions among small-scale mixed polarity elements in the polarity inversion region is uniquely felt by the overlying chromosphere. As we saw throughout this book, every small region of mixed polarity elements is reflected in Ca H line in form of enhanced brightenings. The magnetogram movies showing the ubiquitous disappearance of small-scale opposite polarity neighbors obviously represent the ongoing reconnection processes.



**Fig. 19.9** Snapshot of Ca H developing flare at UT 02:20. The maximum phase will peak at UT 02:32. Field of view is  $79 \times 110$  Mm



The co-aligned Ca II and TRACE Fe XII 195 movies show, as expected, that the disappearance of opposite polarity couples uniquely precedes the appearance of chromospheric bright transients, frequently followed by coronal microflares. Note that, during this long-term stage, the general topology of the active region does not vary noticeably.

The situation changes when significantly larger elongated magnetic structures of opposite polarities emerge in the polarity inversion region. This newly emerged magnetix fluxes provide a significant supply of additional energy. This energy soon shows up as a strong chromospheric flare (Fig. 19.9). A hot overlying corona remains for a while in a “modest” shape compared to raging chromosphere/transition region. In other words, a strong chromospheric flare develops earlier than and independently of upcoming coronal flare.

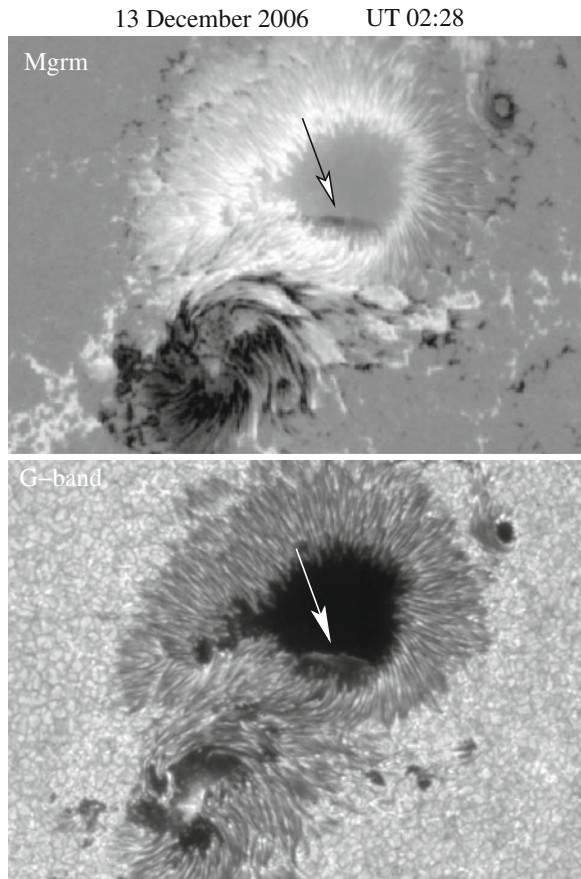
Energy released in the chromosphere affects significantly both, the underlying low atmosphere and the overlying corona. In low atmosphere, the chromospheric flare generates a huge blast wave which first appears in the Ca H line, then at lower temperatures in the G-band, and finally it reaches the photosphere.

In chosen case, the process starts at about UT 02:20 and reaches its maximum at UT 02:30. Figure 19.10 shows the impact of the chromospheric flare on the underlying layers of atmosphere at UT 02:28, with well-developed shock front of finite thickness seen in the south segment of umbra (marked by arrows in Fig. 19.10). In the corona the blast wave triggers explosive release of energy lasting from UT 02:16 to UT 02:28.

Here we come across very important event: the explosive growth of energy is directly associated with the blast wave adding more power to *energy production region* located at the photospheric level. Thus due to this “last drop”, the explosive growth of energy quickly evolves into a major coronal flare that reaches its maximum at UT 02:40. Figure 19.11 shows GOES X-ray intensity curves for the 1.8 keV (upper curve) and for 3.1 keV (lower curve) particles.

Thus the main steps of the process of energy production, transfer, and release can be briefly described as follows. The energy supply coming from reconnection

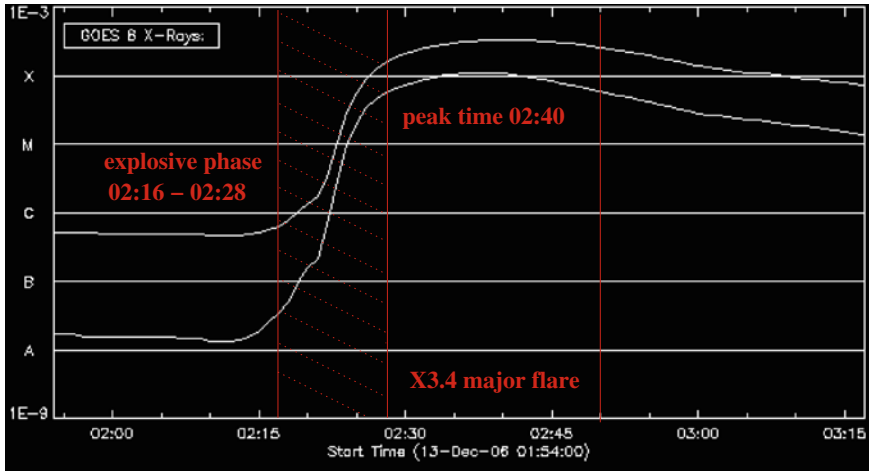
**Fig. 19.10** The impact of the chromospheric flare to underlying photosphere and lower chromosphere regions. The *arrows point* to the shock front, part of which is clearly seen at the south segment of umbra



between small-scale mixed polarity elements continues to accumulate and grow. At some point cumulative effects lead to the explosive release of energy. We see it to happen first in the chromosphere. Starting at about UT 01:40, the Ca H flare becomes so strong that, at UT 02:26, it generates a blast wave and triggers the explosive phase at coronal temperatures (Fig. 19.10). This additional supply of energy leads to further enhancement of explosive release of energy characterized as a major flare of X3.4 class.

After a short phase of flare maximum, the system bifurcates into a well-organized arcade of thin flux tubes at all chromospheric and coronal temperatures (Fig. 19.12). The self-organized regime lasts in the corona over 5 h, until a new flare destroys the structure at about UT 08:02. The chromospheric structures, however, remain in this state only about an hour. In other words, the higher the energy content, the longer the lifetime of the self-organized structures.

It must be emphasized that the peak of energy release in the corona *lags* the peak in the chromosphere by about 8 min, as does the bifurcation of the system into the



**Fig. 19.11** GOES X-ray intensity curves for the 1.8 keV (*upper curve*) and for 3.1 keV (*lower curve*) particles. Peak time of a major (X3.4) flare is UT 02:40. The *red dashed* time interval corresponds to pre-flare explosive energy release

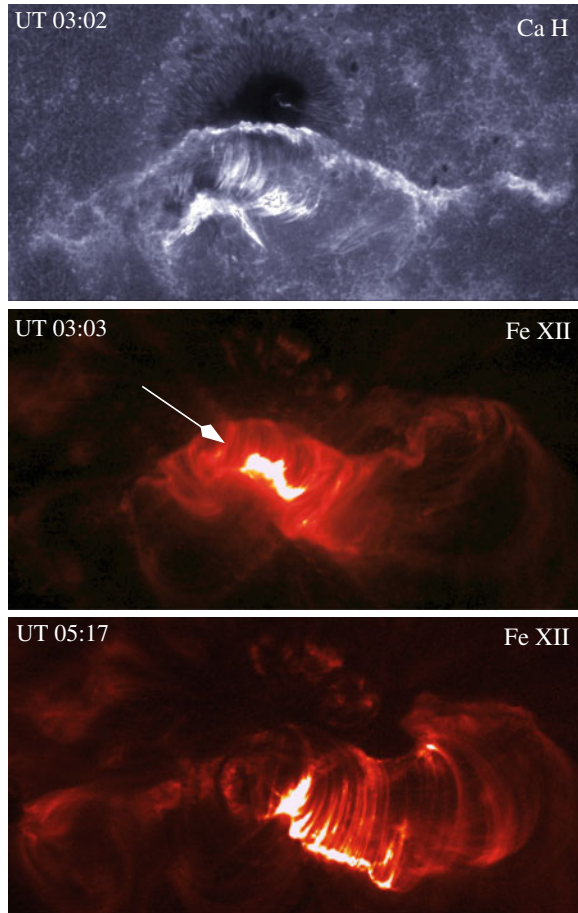
self-organized state (Fig. 19.13). This uniquely indicates that the energy supply and its flow occurs from the photosphere through the chromosphere/transition region.

It is also important to note that the magnetic shear of the whole active region and accompanying helicity injection rate started to increase long before the flare occurred; moreover, the energy and helicity injection rates reached a saturation level almost 24 h prior to the flare (Kubo et al. 2007; Harra et al. 2009). As these processes are directly connected with the energy injection into the system, the observed facts are consistent with the expected enhancement of high-energy proton flux long before the flare occurs.

## 19.5 Phenomenology of Energy Build Up and Quantitative Analysis

The mechanisms governing such a diverse observed regularities as ongoing small-scale sporadic events, the explosively growing pre-flare activity ending with a major flare, and bifurcation of systems into a self-organized state, must have a common origin, and need to be explained on unified basis. The theory that may unify description of various forms of coronal activity must also explain a ubiquitous filamentary structure of the coronal formations. Such a theory and its quantitative application is the subject of this section.

**Fig. 19.12** *Upper panel* well-developed multithread system in the chromosphere at  $10^4$  K; *Lower panels* Self-organized arcade in the corona in the initial stage of its formation (UT 03:03) and in the “mature” stage at UT 05:15. The coronal self-organized arcades outlive its chromospheric counterpart by more than 5 h. The *white arrow* in a *middle panel* indicates still flaring heart of the system

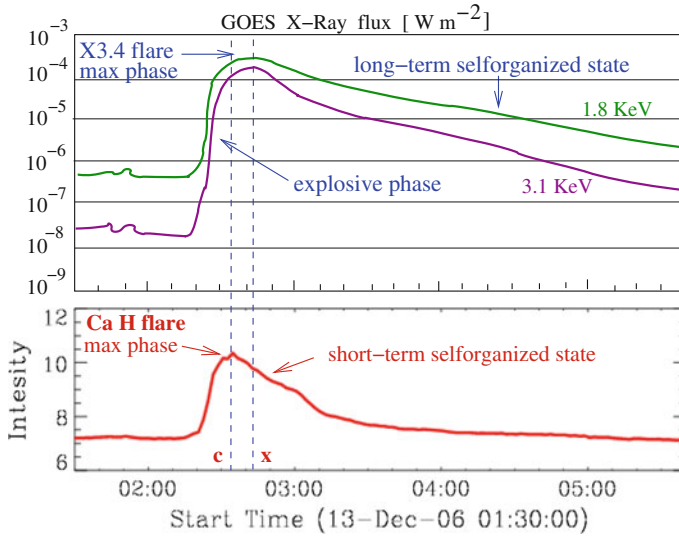


At all the diversity of coronal structures, they have several properties in common, e.g.,

- (1) the energy source lies in an intense hydromagnetic activity of photospheric magnetic fields,
- (2) any coronal formation has a small-scale filamentary structure, and
- (3) elemental filaments must carry electric currents.

Together, these properties indicate *modus operandi* is a typical energetically open, dissipative system. Therefore, various processes in formation and evolution of coronal structures can be consolidated and understood by employing methods of dissipative systems based on global electrodynamics with source and sink of energy as discussed in Chap. 16.

Thus, the system consists of current-carrying magnetic loops that interconnect the photosphere—a high  $\beta$  energy production region—with an overlying low  $\beta$  dissipation region. Source is photospheric driver associated with the turbulent and



**Fig. 19.13** GOES X-ray curves co-aligned with the SOT Ca H intensity curve. *Top* The explosive phase and long-term, self-organized state of coronal plasma; *Bottom* Ca H intensity curve which shows that the peak of energy release in the chromosphere (*line c*) precedes the peak in the corona (*line x*) by about 8 min. Post-flare regime is significantly shorter in the chromosphere than in the corona

electromagnetic stresses which generate a pointing flux of energy and magnetic helicity that propagate upward, *get accumulated* and subsequently dissipate.

The high conductivity of the chromosphere/coronal plasma causes dissipative effects to turn on at small transverse scales,  $\Delta x_r = a/Re_m^{1/3}$ , where  $a$  is the width of an elemental loop,  $Re_m = v_\Delta a/\eta_D$  is the magnetic Reynolds number ( $\eta_D = c^2/4\pi\sigma$  is magnetic diffusivity, with  $\sigma = 1.96ne^2/(m_e\nu_{ei})$  being the plasma conductivity (Ionson 1982; Ryutova and Habbal 1995)).

The dissipative stresses that operate at very small scales of generalized skin depth,  $\Delta x_r$ , determine the width of a local cross-field shear and cause a filamentation process in magnetic structures.

The system of electrodynamic equations, i.e., Maxwell’s equations together with the generalized Ohm’s law fully represent the ability of a magnetoplasma to produce the energy, represented by driving electromotive force (e.m.f.), the ability to store electric and kinetic energy (system capacitance), the ability to store magnetic energy (system inductance), and the ability to release the accumulated energy (resistive loads). Below we follow analysis of an energetically open circuit presented in Chap. 16, and reproduce here a logic and some equations for convenience.

As shown in Chap. 16, with the use of the Heaviside step function of plasma beta,  $H(1 - \beta)$ , the set of electrodynamic equations describing the system of current-carrying magnetic loops that interconnect a high  $\beta$  energy production region, with an overlying low  $\beta$  corona, is reducible to a single 3D equation for longitudinal

electric current,  $j_l$ ; (cf. (16.24)):

$$\frac{4\pi}{c^2} \frac{\partial^2 j_l}{\partial t^2} - H(1 - \beta) \frac{1}{\sigma} \frac{\partial^3 j_l}{\partial x_r^2 \partial t} - H(1 - \beta) \frac{4\pi v_A^2}{c^2} \frac{\partial^2 j_l}{\partial l^2} = H(\beta - 1) \frac{1}{c} \frac{\partial^3 (vB)}{\partial x_r \partial l \partial t} \quad (19.1)$$

The first term in this equation is, indeed, an inductive reactance of a system, the second term is associated with the resistance, the third term is a capacitive reactance of the overlying plasma, and the term on the right-hand side is the source of driving electromotive force (e.m.f.), with  $v$  being a turbulent velocity. The competition, balance, and imbalance of these parts in an active region and its coronal counterparts, determine the system behavior.

For an adequate description of the energy flow, it is necessary to take into account the resistive losses that are associated not only with the corona, but with the chromosphere/transition region which is the first to amass the energy coming from below and “transport” it into the corona (Kjeldseth-Moe et al. 1988; Dere et al. 1989; Golub et al. 1999; Ryutova and Tarbell 2000, 2003).

The feedback between the corona and the underlying atmosphere is also transmitted through the transition region. This leads to the appearance of nonlinear terms in the equation for the electric current. With this in mind, integrating (19.1) over the volume of elemental loop,  $la\Delta x_r$ , one obtains the equation for a total longitudinal current flowing along the elemental loop,  $I = ja\Delta x_r$ , which after some algebra (Ryutova 2006), acquires the form of the forced Van der Pol equation (Van der Pol 1927):

$$\frac{1}{\omega_0^2} \frac{d^2 I}{dt^2} - (\mu - Z_M Q I^2) \frac{dI}{dt} + I = 0 \quad (19.2)$$

Here  $\omega_0 = \pi v_A / l$  is the natural frequency of the elemental loop,  $l$  being the length of the loop, and  $Z_M = (4v_A / c^2) \sqrt{l_{TR} / l}$  is mutual resistance, with  $l_{TR}$  being the height of the transition region. The parameter  $Z_M Q$  reflects the nonlinear effects associated with the back-reaction of a system to the induced currents,  $Q \sim \tau_j \Phi^{-2}$ , where  $\tau_j$  is the characteristic current buildup time, and  $\Phi = (vBa) / c$  is the driving e.m.f.

The evolution of the system is determined by the interplay between the coefficients in (19.2), i.e., by the amount of energy supply and its accumulation (associated with the driving e.m.f. and capacitive reactance), and ability of the system to build up the electric currents (cf. Chap. 16).

The important role in the realization of various scenarios of the current loop evolution, is played by the sign of parameter  $\mu$  (16.59),

$$\mu = \frac{v_{ei}}{\omega_0^2} \frac{m_e}{m_p} \left[ \sqrt{\frac{l_{TR}}{l}} - 1.06 \times 10^7 \frac{T}{n} \left( \frac{v_A}{a^2} \right)^{2/3} \right] \quad (19.3)$$

which is a measure of the excess of energy supply or its deficiency with respect to the current generation threshold. It is important to note that (19.2), along the

“individual” loops, contains parameters that interconnect the entire system in the photosphere (e.g., via e.m.f.), and realize the interpenetration of elemental loops and their environment through the cross-field share ( $\Delta x_r$ ). As  $\Delta x_r$  is very small, the signal quickly propagates throughout the entire system of loops united by a common active region.

The solution to (19.2) for time varying current amplitude  $I(\tau)$  is:

$$I(\tau) = \frac{2I_0}{\sqrt{I_0^2 + (4I_{cr} - I_0^2)\exp(-\epsilon\tau)}}, \quad (19.4)$$

where  $\tau = t\omega_0$  is dimensionless time,  $\epsilon = \mu\omega_0$ , and  $I_{cr}$  a critical current threshold, at which the system may bifurcate to one or another regime depending on the initial current amplitude, i.e., whether  $I_0 > 2I_{cr}$ , or  $I_0 < 2I_{cr}$ .

$$I_{cr} = 5 \times 10^{-3} \frac{nev_A}{Re_m^{1/6}} \sqrt{\frac{|\mu|\omega_0^2}{\tilde{\nu}_{ei}} \frac{l}{l_{TR}} \pi a l} \quad (19.5)$$

It is important that the (19.4) acquires different forms depending on the parameter  $\epsilon$  and the sign and value of coefficient in front of the exponent in the denominator. In fact, the way how the system approaches a quasi-stationary state, is especially sensitive to  $\epsilon$ , or in other words, to the sign and value of  $\mu$ . Depending on the system parameters,  $\mu$  may be positive, negative, or close to zero. In each case, the solution of the Van der Pol equation, (19.4), describes different regimes of system behavior, including the Poincare limit cycle and a spontaneous process of self-organization.

In Chap. 16 we have studied in detail the behavior of currents in different regimes determined by the sign of  $\mu$ . It is useful to recall some basic properties of system evolution here.

If  $\mu > 0$ , the current loops evolve in accordance with a typical Poincare limit cycle, approaching a quasi-stationary regime characterized by a critical current,  $I_{cr}$ . There are two major subregimes across the “Border line” defined by  $I_{cr}/I_0 = 2$  (see Figs. 16.8 and 16.9). In the case of  $I_0 > 2I_{cr}$ , the system periodically releases the energy excess in the form of microflares (e.g., numerous bright “dots” in Fig. 19.2a) or moderate flares (boxed area in Figs. 19.2b and 19.5) approaching a quasi-stationary regime. The opposite regime,  $I_0 < 2I_{cr}$ , corresponds to long-living systems that gradually accumulate energy approaching a stationary regime. In this case, coronal loops can even survive the neighboring flares (such as blue and green arrows in Fig. 19.2 and white arrows in Fig. 19.4).

In other words, at  $\mu > 0$ , regardless of the initial current amplitude, the currents asymptotically tend to a stationary value of  $I_{cr}$ : currents with initial amplitude  $I_0/I_{cr} < 2$  increase until they reach the limiting value, while currents with initial amplitude  $I_0/I_{cr} > 2$  evolve in a decreasing regime. The larger the initial amplitude, the faster it drops, i.e., the shorter its limiting cycle, and the excess energy gets released faster. Several solutions for both subregimes at  $\mu > 0$  are shown in Fig. 16.8. Numbers correspond to the ratio  $I_0/I_{cr}$ .

If  $\mu < 0$ , (19.2) describes several qualitatively different regimes of current evolution depending, again, on the amount of the initial energy supply. If the initial energy supply provides the value of injected currents below their critical values,  $I_0 < 2I_{cr}$ , the currents are in the decaying regime and loops gradually (and very slowly) lose their energy. This regime corresponds to last stage of diffusively disappearing loop systems. The plots of corresponding currents are shown in Fig. 16.9, for several factors (1.5–1.98  $I_0/I_{cr}$ ).

On the other hand, in the case when the energy supply exceeds the generation threshold and  $I_0 > 2I_{cr}$ , the system becomes subject to explosive instability. In finite time, the currents reach infinitely large values, growing explosively in time,  $I(t) = I_0/\sqrt{1 - (t/t_{expl})}$ , with

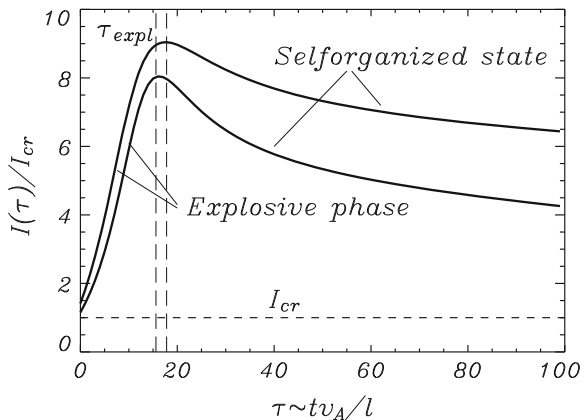
$$t_{expl} = \frac{1}{|\mu|\omega_0^2} \ln \frac{I_{cr}^2}{I_0^2 - I_{cr}^2}. \tag{19.6}$$

In the vicinity of  $t = t_{expl}$ , the system quickly releases energy producing a major flare. The corresponding plots for factors, 2.05–2.3, are shown in Fig. 16.9.

At this strongly nonlinear stage, higher nonlinear effects turn on and stabilize the further growth of the currents leading to the bifurcation of a system into a self-organized state. This process is illustrated by the theoretical curve shown in Fig. 19.14, which is well representing the observed HEP curve shown in Fig. 19.13. A parameter range where the system bifurcates from one regime to another corresponds to proximity of  $\mu \simeq 0$ , or to proximity of the critical current to value, determined by condition,  $\mu - Z_M Q I_{cr}^2 \simeq 0$  (coefficient of the first derivative in (19.2)).

It is important, that parameter  $\mu$ , which reflects the physical properties of a system both at macro- and microscales, and determines the actual behavior of a system, is expressed through the physical quantities most of which are observable, e.g., temperature, density, magnetic field, and spatial scales of coronal loops. This allows quantitative analysis and usage of observational  $I$  data for modeling and studies the predictability of different regimes.

**Fig. 19.14** Evolution of coronal loop currents for the explosive and post-explosive regime at  $\mu \approx 0$  ( $\mu$  approaching to zero from negative values). The upper curve corresponds to  $I_0 = 2.2I_{cr}$  and lower curve is for  $I_0 = 2.4I_{cr}$ ; the higher the initial current, the shorter is the “explosive” time (cf. Fig. 19.13)





**Table 19.2** Estimates of critical currents

$T$ ( $10^4$ K)	$n$ ( $10^9$ cm $^{-3}$ )	$v_A$ (cm s $^{-1}$ )	$l$ ( $10^8$ cm)	$a_{cr}$ ( $10^6$ cm)	$\omega_0$ (s $^{-1}$ )	$ \mu $	$I_{cr}$ (Am $^{-2}$ )
200	1.4	$8 \times 10^7$	20	21	0.13	0.12	3.2
2	23	$9.1 \times 10^6$	2	1.9	0.143	0.15	1.1

Table 19.2 contains the quantitative estimates of critical current densities for loops at coronal and chromospheric temperatures. Alfvén velocity here is calculated through the temperature and plasma  $\beta$ ,  $v_A = 1.82 \times 10^4 \sqrt{T/\beta}$ . We adopt  $\beta = 0.1$  and  $l_{TR} = 2.2 \times 10^8$  cm. The aspect ratio (for the critical value of a loop radius,  $a_{cr}$ ) is of the order of  $(a_{cr}/l) \simeq 0.01$  at both temperatures, consistent with the scale invariance typical of self-organization. Now we can estimate the explosive times for the two regimes shown in Fig. 19.11.

In the first case, when  $j_0 = 1.1 j_{cr}$ ,  $t_{expl}^{cor} \simeq 19$  min, for coronal loops, and  $t_{expl}^{chr} = 12$  min 23 s for the chromospheric ones. In the second case, when  $j_0 = 1.2 j_{cr}$ , we have respectively,  $t_{expl}^{cor} \simeq 13$  min and  $t_{expl}^{chr} = 8$  min 30 s. Thus, in agreement with observations, the onset of the explosive phase and bifurcation of a system into a self-organized state occurs in the corona later than in the chromosphere (Figs. 19.12 and 19.13). The measured explosive times and durations of the explosive phase also agree well with the observations.

Due to flexibility of the system parameters and wide range of their combinations' various scales, this approach has a great potential in studying the overall behavior of coronal structures.

## 19.6 Recurrent Flares and Echoes

Highly intermittent corona consisting of a regular ensembles of a thin magnetic loops and harboring frequent impulsive bursts, is the most natural place for the occurrence of plasma echoes. Before we discuss this spectacular echo-like phenomena seen in the high resolution observations of corona, let us recall the features of echo effect.

Along the familiar sound echo, sonic navigation and a Greek legend about a nymph Echo, there are many echo-like phenomena in macro- and microworlds. Some were discovered and put in practical use long, some only in modern times.

In microworlds, first was a spin echo observed by Hahn (1950) in nuclear magnetic resonance experiment. Two short radiofrequency pulses satisfying the resonance condition and separated by a time interval  $\tau$ , were applied to an ensemble of spins in a liquid placed in a static magnetic field. After removal of the pulses ( $\tau$  being much larger than the duration of a pulse), in the same time interval  $\tau$  after the second pulse, when the ensemble of spins relaxed to thermal equilibrium, a spontaneous nuclear induction signal has been observed. The effect was dubbed spin echo. Soon after first results, Hahn performed experiments with multiple echoes and using the Bloch theory explained the effect. Hahn concluded that the echo technique appears to be

highly suitable as a fast and stable method in searching for unknown resonances, and suggested that it is of technical interest to consider the possibility of applying echo pattern as a type of memory device. This modest prediction turned out to be shortly a key element in biomedical nuclear resonance diagnostics and a computer technology.

Most importantly, any physical system with the “memory” and hidden resonances, may produce the echo effect, and thus be a subject of reliable diagnostics.

Along the diagnostics, the echo may be used in many different ways. For example, the echo effect provides a unique opportunity for electromagnetic field to overpass the skin depth and penetrate through a metal (Kemoklidze and Pitaevskii 1970a). Consider this example for illustrative purpose. Let the thickness of the metal plate,  $d$  be much larger than the skin depth,  $\delta$ ,  $d \gg \delta$ . By the definition an electromagnetic field cannot penetrate a metal deeper than  $\delta$ . If, however, the electron mean free path,  $l$  in the metal is  $l \gg d$  then by applying two electromagnetic fields at both sides of a plate, the echo effect arises and generates the third signal inside the metal. Namely, let an electromagnetic field  $E_1$  of frequency  $\omega_1$  is applied to the left side of metal. If now a field  $E_2$  of frequency  $\omega_2$  is applied at both sides of the plate, the much stronger echo field will appear with the amplitude  $E_e \sim E_1 E_2^2$ , at  $\omega_2 = 3\omega_1$  inside the metal. The key role here, as in all cases of echo effect, is played by the memory of electrons flying through the metal. Note, that the amplitude of echo field  $E_e$  does not decrease with increasing plate thickness, but increases. The example of the penetration of the electromagnetic field into the metal is a *Spatial* echo, while the Hahn’s echo effect is a *Temporal* echo.

Very rich echo-like phenomena were found in plasmas. There were identified and experimentally verified conditions for a temporal, spatial, and spatiotemporal echoes. The main condition for realization of a plasma echo is the ability of a system to maintain the *reversible* processes for which the medium having filamentary structure is extremely favorable. First plasma echoes were described and tested in Collisionless plasmas, where the Landau damping operates and provides the necessary attributes of “memory” (O’Neal 1965; Gould 1965; Gould et al. 1967; Malmberg et al. 1968a, b; Kemoklidze and Pitaevskii 1970b).

### ***19.6.1 Landau Damping, Memory, and Spatiotemporal Echoes***

By its nature, the Landau damping occurs in collisionless plasma due to the phase memory of particles resonantly interacting with the wave (Landau 1946). As Landau damping is not connected directly with dissipative effects, it may be considered as a *reversible* process. In other words, although the macroscopic quantities such as an amplitude of the wave pulse (e.g., electric field) and mass density are damped exponentially, the distribution function becomes only distorted, and may oscillate indefinitely, i.e., a damped wave in a collisionless plasma retains the “memory” of the preceding oscillatory motion. This means that the direction of the phase evolution of the perturbed distribution function can be reversed by the application of a second

wave pulse. As a result, a macroscopic field subsequently reappears after both the previously applied fields have Landau damped away.

The basic mechanism of the plasma echo can be easily understood (O'Neal and Gould 1968; Malmberg et al. 1968a,b; Kadomtsev 1968).

When an electric field of *spatial* dependence  $\exp(-ik_1x)$  is excited in a plasma and then Landau damps away, it modulates the distribution function leaving a perturbation of the form  $f_1(v)\exp(-ik_1x + ik_1vt)$ . For large time,  $t$ , there is no electric field associated with this perturbation, since an integral over velocity will phase-mix to zero. If after a time  $\tau$  a wave  $\sim\exp(-ik_2x)$  is excited and then damps away, it will modulate the unperturbed part of the distribution function leaving a first-order term of the form  $f_2(v)\exp[-ik_2x + ik_2v(t - \tau)]$ , but it also modulates the perturbation leaving a second-order term of the form  $f_1(v)f_2(v)\exp[-i(k_2 - k_1)x + ik_2v\tau - i(k_2 - k_1vt)]$ . The coefficient of  $v$  in the exponent will vanish when

$$t = \tau \frac{k_2}{k_2 - k_1}. \quad (19.7)$$

At this time an integral over velocity will not phase-mix to zero, and an electric field reappears in the plasma. This is a *temporal* second-order echo. In addition to this, higher order echoes can also be observed. For example, a third-order echo is produced when the velocity space perturbation from the first pulse is modulated by the second spatial harmonic of the electric field. The echo then occurs at  $t = \tau[2k_2/(2k_2 - k_1)]$ .

The mechanism of the spatial echo is quite similar to the temporal echo. In this case if an electric field of frequency  $\omega_1$  is continuously excited at one point in a plasma and an electric field of frequency  $\omega_2 > \omega_1$  is continuously excited at a distance  $l$  from this point, then a second-order spatial echo of frequency  $\omega_2 - \omega_1$  will be produced at a distance  $l\omega_2/(\omega_2 - \omega_1)$ . Higher order spatial echoes are also easily produced and observed. For example, the spatial echo of frequency (O'Neal and Gould 1968)

$$\omega_3 = m\omega_2 - n\omega_1. \quad (19.8)$$

will appear at a distance

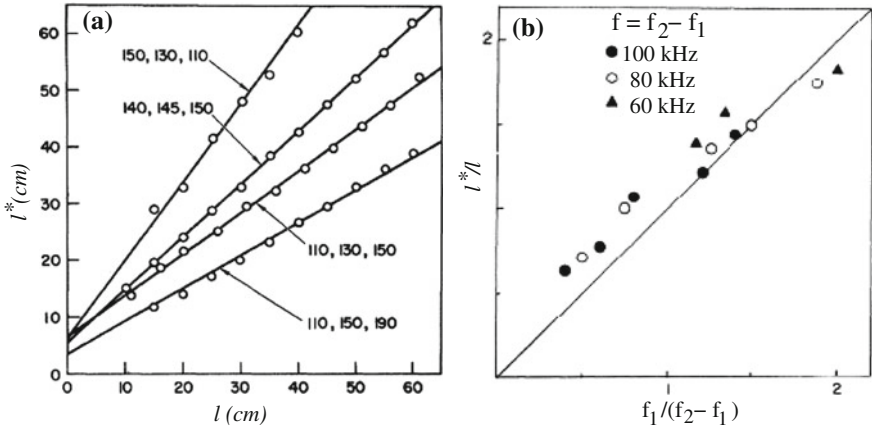
$$l^* = l \frac{n\omega_1}{\omega_3} \quad (19.9)$$

provided that

$$m\omega_2 > n\omega_1 \quad (19.10)$$

Here integers  $m$  and  $n$  ( $m > n$ ) correspond to the order of an echo in the perturbation theory, namely,  $m + n = 2, 3, 4, 5$  correspond to second, third, fourth, and fifth order echoes. For small-amplitude initial waves, the amplitude of the echo,  $A_{\text{echo}}$  is estimated as

$$A_{\text{echo}} \sim A_1^n A_2^m. \quad (19.11)$$



**Fig. 19.15** Experimental results on a plasma wave echo. **a** Echo position versus transmitter separation; the slope of the curves is theory (19.9), the circles are experimental measurements; the numbers on the curves are frequencies  $f_1$ ,  $f_2$ , and  $f_3$  in MHz; reprinted with permission from Malmberg et al. (1968a), copyright APS; **b** Relation between the position of the echo and the frequencies  $f_1$  and  $f_2$  (the solid line is theoretical slope  $x = l f_1 / (f_2 - f_1)$ ); the echo frequencies  $f = f_2 - f_1$  are given for three sets of experiment; reprinted with permission from Ikezi and Takahashi (1968); copyright APS

The existence of various echos, associated with second-, third- and higher order perturbation theory, has been demonstrated experimentally (Malmberg et al. 1968a, b; Ikezi and Takahashi 1968; Yugami et al. 1994). The echoes always appear at the predicted positions. The frequency and wavelength of the echo wave and the dependence of its amplitude on the amplitude of the initial waves are totally consistent with theory.

Figure 19.15 shows examples of earliest experiments on plasma echoes. Figure 19.15a is a plot of the position of a third-order ( $m = 2$ ,  $n = 1$ ) echo as function of the separation of the two transmitters obtained for several values of frequency ratio  $f_1/f_3$  (Malmberg et al. 1968a). The slopes of the straight lines are computed with (19.9). For small signals, as expected from (19.11), the echo amplitude is  $A_{\text{echo}} \sim A_1^n A_2^m$ . At large signal levels the echo amplitude saturates. Figure 19.15b shows results obtained by Ikezi and Takahashi (1968) also for the third-order plasma echo. Shown are the experimental values of the echo position  $l^*$  for several sets of frequencies  $f_2 > f_1$ .

Since the pioneering works on the plasma echoes, the subject obtained a great attention for various diagnostics. For example, the diffusion of plasma electrons in velocity space has been measured using the plasma wave echo as an experimental tool (Jensen et al. 1969). The study of spatial-temporal echoes generated in a magnetized plasma by low frequency external perturbations led to temperature diagnostics of the electrons and ions, and allowed to diagnose their distribution over longitudinal velocities in thermonuclear devices (Gromov and Revenchuk 1990). Plasma echo as diagnostic tool is used in wide range near-earth and space instruments as well (Fung et al. 2003; Benson and Osherovich 2004; Mahmoudian et al. 2011).

The plasma echoes in the solar atmosphere, where they are the most anticipated phenomena, did not get much attention (Frank and Ryutova 2007). Although there were some attempts made before the sun's "space era" when only the ground-based observations were available. For example, Erokhin et al. (1975) explained a series of a small-scale "Mottles"—sporadic brightenings, observed to appear during a chromospheric flare almost simultaneously in different places, as an effect of plasma echo. They also suggested that plasma echo may operate in an often observed phenomena when a coronal flare above one active region triggers a new flare above another active region. Today, having excellent solar missions, the similar studies may open great diagnostic facilities.

### 19.6.2 Echo Effects in Slinkies

The solar atmosphere in general, with its ubiquitous filamentary magnetic fields, and well-organized coronal arcades of thin magnetic filaments, in particular, are indeed, the most natural places where the realization of Landau damping and subsequent appearance of plasma echoes must be expected.

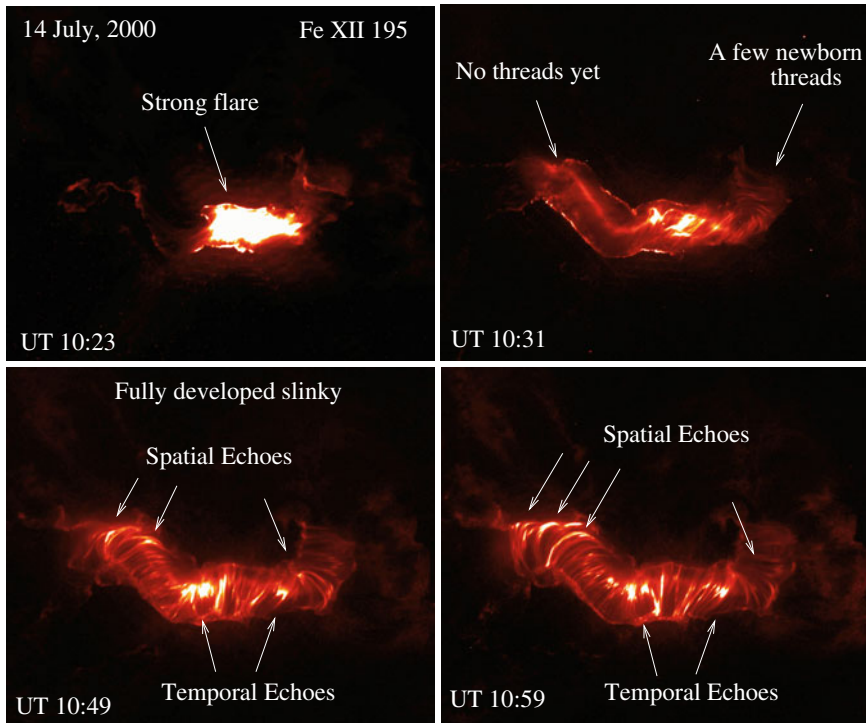
Elemental filaments in arcades being in highly dynamic state, show not only a subtle oscillations, but are harboring frequent microflares. These microflares, having various intensities, often appear simultaneously in different places, i.e., several elemental filaments far removed from each other show synchronous lighting up.

Figure 19.16 shows snapshots of the corona at four instances of time taken by the TRACE in the Fe XII 195 line at  $2 \times 10^6$  K. The upper left panel is the July 14, 2000 flare at its maximum phase (UT 10:23). In several minutes (around UT 10:31) the system of loops relaxes to well-shaped state. Note that in this stage no threads at given resolution are yet seen. By UT 10:49 the system bifurcates into fully developed self-organized slinky consisting of slim self-similar filaments. A frequent sporadic brightenings appearing soon after formation of arcades (marked by arrows) have a clear properties of both, spatial and temporal echoes. The echoes occur continuously in various places in the system until the arcades preserve their filamentary structures.

Time intervals between the first two brightenings and their successors follow a pattern typical to either temporal or spatiotemporal echos. Besides, many individual filaments produce homologous microflares, i.e., strong localized brightenings may occur repetitively along the same elemental flux tube. It is also important that the larger the system the longer it lives, and respectively harbors larger number of echoes.

Another example of self-organized slinky that may be used to observe the echo effects is shown in Fig. 19.17. We have already encountered this slinky as an exemplary evidence of post-flare self-organization (see Fig. 19.2).

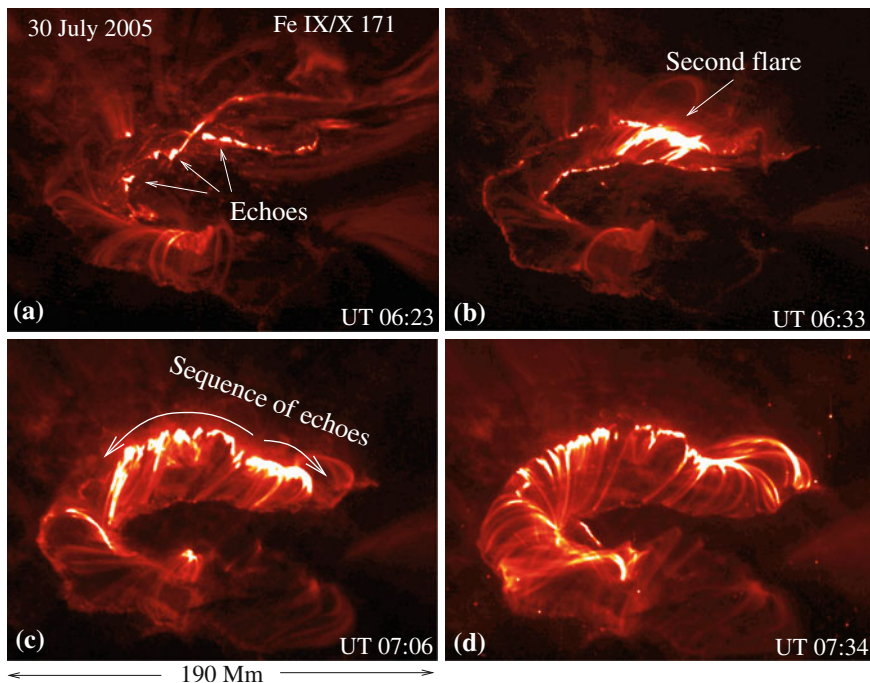
Before the first major flare the system of coronal loops represents a huge chaotic conglomerate. The flare occurred at UT 05:29 generated a powerful CME, brought the system into a "quasi"-organized state (Fig. 19.17a). Already at this stage, the system consists of enough filamentary structure to support series of echoes. Recall that the energy released in the first major flare did not lead to formation of a solenoid, but has been clearly distributed between the loop system and a powerful CME



**Fig. 19.16** Snapshots of the active region corona of July 14, 2000 at four instances of time. The major flare that occurred at UT 10:23, relaxes to well shaped confined state (e.g., UT 10:31) and by UT 10:49 bifurcates into fully developed self-organized system of thin filaments harboring numerous microflares with the spatial and temporal echo pattern

(cf. Fig. 19.2b). In other words, part of energy coming from the first flare, was not enough for the system to bifurcate into self-organized state. This job was done by the second major flare (Fig. 19.17b). Soon after this flare the system acquired a form of fully developed solenoid of self-organized loops and remained in this state for many hours. During the entire period of existence, the observations showed a multiple echoes traveling back and forth along the solenoid. It must be noted again, that time scales of these events are fraction of minutes while lifetime of the entire dynamic system may be hours and days.

The observation of the systematic echoes in slinkies is quite a straightforward matter. One only needs to observe and measure times of their occurrence and distances between different events. This makes the echo observations very promising for the development of diagnostic tools and an important addition to verify basic physics of plasma echoes in action.

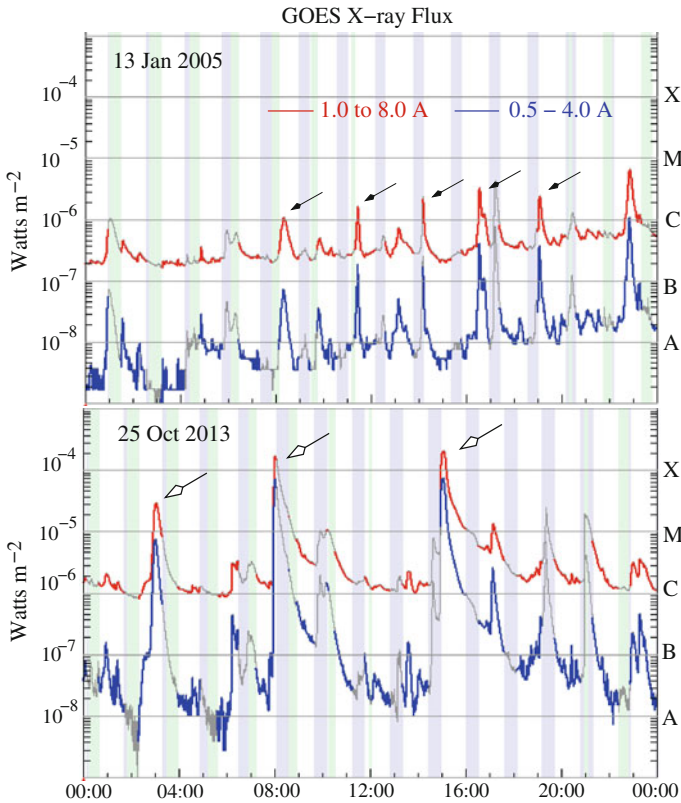


**Fig. 19.17** Snapshots of an active region corona taken on July 30, 2005 in Fe IX/X 171 line. *Panel a* shows the system of coronal loops after the first major flare which occurred at UT 05:29 (see Fig. 19.2); at this stage the system already harbors multiple but sporadic echoes; at UT 06:33 a second flare (*panel b*) brings the system in a long-living well-organized system with sequences of echoes traveling back and forth along the solenoid; the series of echoes generated soon after the UT 06:33 flare propagate in both direction from the flare kernel (*panel c*); during the mature state of slinky echoes are seen all over the slinky (*panel d*)

### 19.6.3 Spatial and Temporal Recurrences in Flares

The echo effects may occur, of course, at much larger spatial and temporal scales. These are usually characteristic of coronal flares that include all the classes, from the weakest C-class flares to largest X-class flares. As a rule, the larger are the flares the larger are the times between the successive flares and larger are the distances between them.

Figure 19.18 contains additional evidence of echo occurrence in large flares. Shown are GOES X-ray plots of 24 h duration measured during the occurrence of two sets of recurrent flares. One was produced by the active region AR 10718 on Jan 13, 2005 (top panel) and the other by the AR 11882 on Oct 25, 2013. In both cases we deal with the temporal echoes. The case of Jan 13, 2005 shows multiple echoes producing C-class flares. The characteristic time interval between the repetitive bursts is about 3 h. In case of Oct 25, 2013, the M2.9-class flare occurring at UT 02:48 and the X1.7 occurring at UT 08:03 with third X2.1-class flare appearing



**Fig. 19.18** Occurrence of temporal echoes in coronal flares illustrated by the GOES X-ray flux. *Top* Multiple echoes in a C-class flares occurring in a characteristic time interval of about 3 h (*small arrows*); the recurrent flares were produced by the same active region AR 10718 on Jan 13, 2005; *Bottom* The temporal echo (*large arrows*) in large M2.9 (UT 02:48), X1.7 (UT 08:03) and X2.1 (UT 14:51) flares produced by the active region 11882 on Oct 25, 2013

in about 7 h (UT 14:51) show a typical pattern of the temporal echo. Note that, as expected, the time interval between the successive flares are significantly larger in case of a stronger X-class flares than in weaker C-class flares.

The fact that the flares show recurrency has been realized decades ago. Richardson (1958), classifying solar flares and their characteristics, describes the pattern in flare occurrence which is consistent with a spatial and temporal echo phenomena. He writes: “A region has been called ‘recurrent’ if 5 or more distinct flares are observed at one station in one transit time” (temporal recurrence). The analogue of a spatial echo is presented as follows: “The question has been investigated of whether two or more flares occur nearly simultaneously over widely separated spot groups more often than would be expected by chance. The number of Multiple flares observed was found to be higher than the number calculated, if they occurred at random, from Poisson’s law”. Since then number of authors studied recurrent flares, where



the recurrent flares were called “sympathetic”, “simultaneous”, and “homologous” (Fritzova-Svestkova et al. 1976; Cheng and Pallavicini 1987; Zhang and Wang 2002; Wheatland and Craig 2006; Chandra et al. 2011).

The subject of solar echoes requires farther studies and development of unified basis for their description and utilization. Using the simple relations in spatiotemporal echoes based on directly measurable quantities open broad opportunities in understanding not only flare characteristics but their precursors and outcome. And, again, due to the “arithmetically” simple relations between the spatial and time scales of simultaneous and homologous flares, it must not be a distant future when solid diagnostic tools will be developed.

Concluding this chapter it is useful to overview some key elements of its subject. A survey of major X-ray flares shows that a complex pre-flare system of coronal loops often, but not always, bifurcate into a long-living, well-organized system of multi-threaded loop arcades having a fundamental scale. Analyzing physical conditions that cause or prevent this process, it was found that those flares which bifurcate into long-living slinky arcades, and those that do not produce such structures, have very different signatures. The most striking difference is that, in all cases of slinky formation, the GOES high-energy proton flux becomes significantly enhanced 10–40h before the flare occurs. No such effect was found prior to the “non-slinky” flares. One of the important features revealed, is that post-flare coronal slinky formation is preceded by scale invariant structure formation in the underlying chromosphere/transition region.

The formation of well-organized loop structures, having a fundamental scale, and occurring subsequently at different temperatures, is consistent with a spontaneous process of self-organization that naturally follows from general electrodynamics of nonlinear energetically open systems. Thus, a method of an energetically open, dissipative system, which describes coupling of the photospheric energy reservoir with the overlying chromosphere and corona, and includes the back-reaction of coronal activity to the underlying atmosphere, proved to be very reliable tool for understanding a wide range of observed regularities. The set of electrodynamic equations reduces to a single equation having the form of a Van der Pol oscillator, which, depending on the system parameters, describes various dynamic forms of the system evolution. This includes, in particular, two major regimes studied in this chapter:

- (1) the Poincare limit cycle, when systems experience the explosive release of energy, returning to a physically similar state in a short relaxation time; this regime corresponds to “regular” flares that do not produce slinkies, and
- (2) a spontaneous process of self-organization, characterized by scale invariant structure formation, usually having form of solenoidal slinkies.

The observations show a clear pattern of continuously appearing microflares traveling back and forth through the body of the solenoidal system of filaments. The timing and spatial distribution of microflares are consistent with multiple spatial and temporal plasma echoes. The echo pattern is also a regular appearance in recurrent (simultaneous and homologous) flares. These observations may be used for reliable “micro” diagnostic of physical parameters, such as electron and ion temperatures and their anisotropies, local electric currents and velocities, and microturbulence associated with them.

Simple relationships between the physical parameters of a system, most of which are observable, may provide reliable diagnostic tools. The observed regularities may serve as a long-term precursor of strong flares. Future observations of precursory events may allow the study of the predictability of system behavior.

## References

- M.J. Aschwanden, P.D. Aschwanden, *Astrophys. J.* **674**, 530 (2008)  
 T. Bai, P.A. Sturrock, *Annu. Rev. Astron. Astrophys.* **27**, 421 (1989)  
 M. Battaglia, P.C. Grigis, A.O. Benz, *Astron. Astrophys.* **439**, 737 (2005)  
 R. Benson, V.A. Osherovich, *Radio Sci.* **39**, RS1S28 (2004)  
 D.H. Brooks et al., *Astrophys. J.* **772L**, 19 (2013)  
 R. Chandra et al., *Sol. Phys.* **269**, 83 (2011)  
 C. Cheng, R. Pallavicini, *Astrophys. J.* **318**, 459 (1987)  
 J.W. Cirtain et al., *Nature* **493**, 501 (2013)  
 K.P. Dere, J.-D.F. Bartoe, G.E. Brueckner, *Sol. Phys.* **123**, 41 (1989)  
 N.S. Erokhin, S.A. Kaplan, S.S. Moiseev, *Sov. Astron.* **18**, 524 (1975)  
 Z. Frank, M. Ryutova, *AGU* **0**, FMSH22A0842F (2007)  
 L. Fritzoza-Svestkova, R.C. Chase, Z. Svestka, *Sol. Phys.* **48**, 275 (1976)  
 S.F. Fung et al., *Geophys. Res. Lett.* **30**, 110000–1100001 (2003)  
 A.V. Gaponov-Grekhov, M.I. Rabinovich, *Nonlinearities in Action* (Springer, New York, 1992)  
 S.E. Gibson et al., *Astrophys. J.* **574**, 1021 (2002)  
 A.A. Golovko, I.I. Salakhutdinova, A.I. Khlystova, *Ge & Ae* **49**, 907 (2009)  
 L. Golub et al., *Phys. Plasmas* **6**, 2205 (1999)  
 R.W. Gould, *Phys. Lett.* **19**, 477 (1965)  
 R.W. Gould, T.M. O'Neal, J.H. Malmberg, *Phys. Rev. Lett.* **19**, 219 (1967)  
 S.N. Gromov, S.M. Revenchuk, *Plasma Phys. Control. Fusion* **32**, 1257 (1990)  
 E.L. Hahn, *Phys. Rev.* **80**, 580 (1950)  
 L.K. Harra et al., *Astrophys. J.* **691**, L99 (2009)  
 H. Ikezi, N. Takahashi, *Phys. Rev. Lett.* **20**, 140 (1968)  
 J.A. Ionson, *Astrophys. J.* **254**, 318 (1982)  
 T.H. Jensen, J.H. Malmberg, T.M. O'Neil, *Phys. Fluids* **12**, 1728 (1969)  
 B.B. Kadomtsev, *Sov. Phys. Usphekhi* **11**, 328 (1968)  
 M.P. Kemoklidze, L.P. Pitaevskii, *JETP Lett.* **11**, 548 (1970a)  
 M.P. Kemoklidze, L.P. Pitaevskii, *JETP* **31**, 994 (1970b)  
 O. Kjeldseth-Moe et al., *Astrophys. J.* **334**, 1066 (1988)  
 T. Kosugi et al., *Sol. Phys.* **243**, 3 (2007)  
 M. Kubo et al., *Publ. Astron. Soc. Jpn.* **59**, S779 (2007)  
 L. Landau, *Sov. Phys. - JETP* **16**, 574 (1946)  
 B.J. LaBonte, M.K. Georgoulis, D.M. Rust, *Astrophys. J.* **671**, 955 (2007)  
 A. Mahmoudian et al., *Ann. Geophys.* **29**, 2169 (2011)  
 J.H. Malmberg, C.B. Wharton, R.W. Gould, T.M. O'Neil, *Phys. Rev. Lett.* **20**, 95 (1968a)  
 J.H. Malmberg, C.B. Wharton, R.W. Gould, T.M. O'Neil, *Phys. Fluids* **11**, 1147 (1968b)  
 A.B. Mandelbrot, *Science* **135**, 63 (1967)  
 E.I. Mogilevsky, N.S. Shilova, *Ge & Ae* **46**, 303 (2006)  
 N. Nishizuka, A. Asai, H. Takasaki, H. Kurokawa, K. Shibata, *Astrophys. J.* **694**, L74 (2009)  
 T.M. O'Neal, *Phys. Fluids* **8**, 2255 (1965)  
 T.M. O'Neal, R.W. Gould, *Phys. Fluids* **11**, 134 (1968)

- I. Prigogine, *Introduction to Thermodynamics of Irreversible Processes* (Interscience, New York, 1961)
- R.S. Richardson, *Astrophys. J.* **114**, 356 (1951)
- M.P. Ryutova, S.R. Habbal, *Astrophys. J.* **451**, 381 (1995)
- M. Ryutova, T. Tarbell, *Astrophys. J.* **541**, L29 (2000)
- M. Ryutova, T. Tarbell, *Phys. Rev. Lett.* **90**, 191101 (2003)
- M. Ryutova, R. Shine, *JGR* **111**, A03101 (2006)
- M. Ryutova, *JGR* **111**, A09102 (2006)
- M.P. Ryutova, Z. Frank, H. Hagenaar, T. Berger, *Astrophys. J.* **733**, 125 (2011)
- B. van der Pol, *Philos. Mag.* **3**, 65 (1927)
- M.S. Wheatland, I.J.D. Craig, *Sol. Phys.* **238**, 73 (2006)
- A.R. Winebarger et al., *Astrophys. J.* **787L**, 10 (2014)
- N. Yugami, S. Kusaka, Y. Nishida, *Phys. Rev. E* **49**, 2276 (1994)
- J. Zhang, J. Wang, *Astrophys. J.* **566**, L117 (2002)

## Chapter 20

# Quiescent Prominences

**Abstract** In this chapter we shall consider dynamics of quiescent prominences. These amazing phenomena offer excellent opportunity to study fundamental properties of various plasma instabilities, and also address to some of the most enigmatic features of solar atmosphere. We shall combine the observational evidence and theory to identify such instabilities as:

- (1) prominence cavity formation and its evolution, associated with a large scale screw pinch instability;
- (2) development of regular series of plumes and spikes typical to the Rayleigh–Taylor (RT) instability; and
- (3) the appearance of growing ripples at the prominence/corona interface, often followed by a sudden collimated mass up- and downflows, attributed to the Kelvin–Helmholtz (KH) instability.

We shall specify the conditions for transition from a linear (rippling mode) to non-linear stage of the KH instability, known to have an explosive character. We show examples of a practical use of direct measurements of the instability parameters and also briefly discuss the natural occurrence of greenhouse-like effect under prominence body.

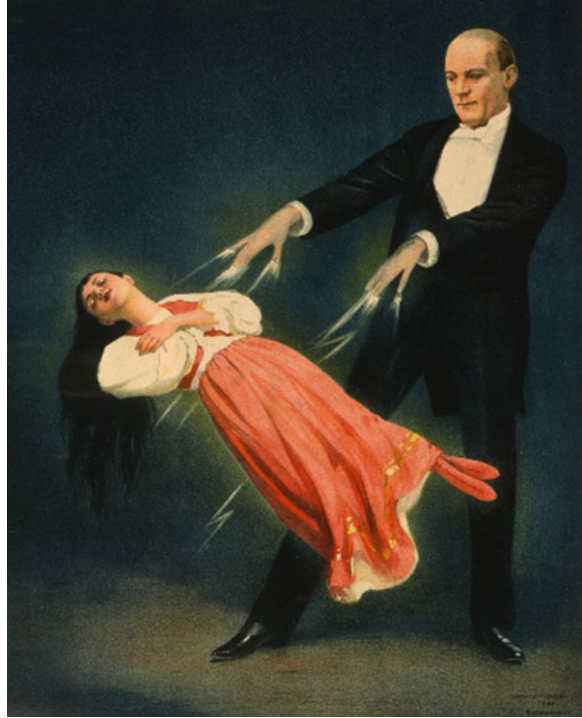
### 20.1 Background—Problem of Stability

A great astronomer and photographer Ferdinand Ellerman said: “He who has never seen a solar prominence has missed one of the most fascinating objects in the Heavens”.

Quiescent prominences are clouds of *cool dense* plasma, suspended over a hot rarefied plasma of corona, akin to heavy dumbbells floating in a thin air or Kellar’s Princess Karnac beautifully levitating (Fig. 20.1).

The prominence enigma includes not only their stability, i.e., the questions what keeps such a heavy material on top of much lighter substance of coronal plasma and why their lifetime, reaching sometimes several solar rotations, is so long, but the very formation of prominences and their highly dynamic behavior. During their lifetimes, prominences show all kinds of irregular motions, changes, and structure formations on a wide range of spatial and timescales, from small scale downflows and oscillatory

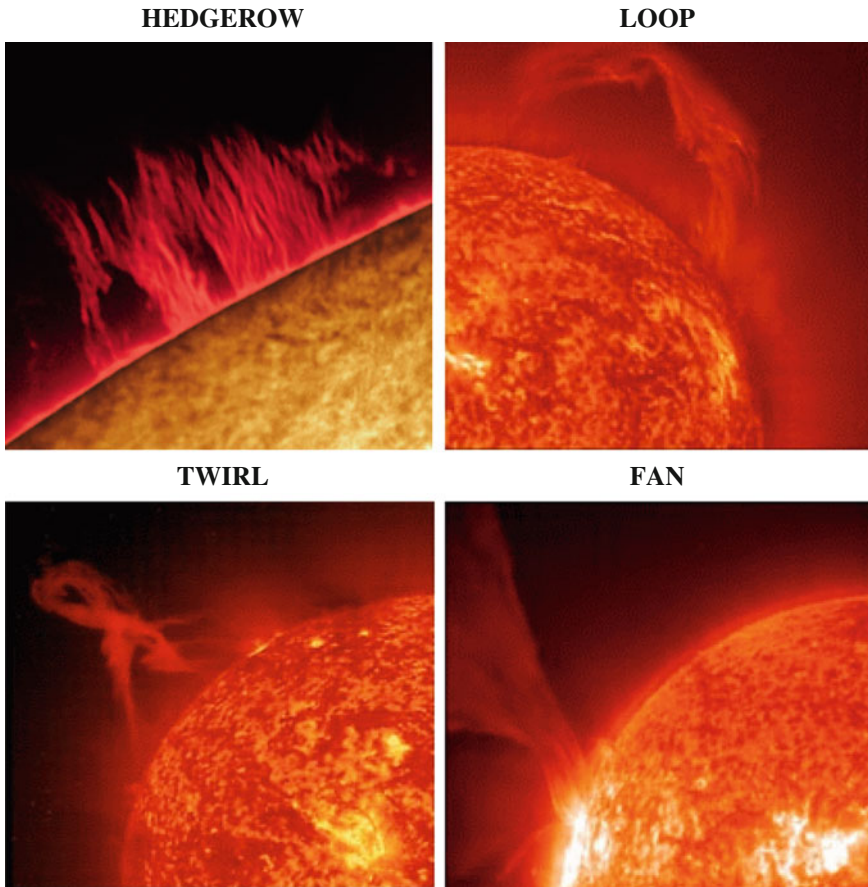
**Fig. 20.1** Miracle of power.  
 Reprinted from <http://www.loc.gov/> Credit Library of Congress



motions to the formation of large-scale prominence cavities, characterized by sudden disruptions of large portions of the prominence body leading to explosive coronal mass ejections (CMEs).

Projected on the sky, the prominences appear in so many faces that people began to call them names, like Hedgerow, Loop-kind, Twirl, Fan, etc. (Fig. 20.2). Simplest of them were chosen to guess at least the magnetic field geometry that could support heavy prominence material.

Extensive studies of prominences have been roughly centered on two classes of closely related problems, their stability and disruption. Work done on the first problem leads to general understanding of the magnetic field topology able, in principle, to support the heavy plasma against gravity (Kippenhahn and Schlueter 1957; Kuperus and Raadu 1974; Vrsnak et al. 1988; Priest 1988; van Ballegoijen and Martens 1990; Low 1993; Kuperus 1996), providing a basis and requirements for improving or reconsidering prominence models. A key issue of the magnetic field topology and a major stumbling block is the fact that the magnetic field embodied by quiescent prominences overlies the neutral (polarity inversion) line. Experiencing the action of photospheric shear motions, it must have a helical structure and carry electric currents. Signs of helical structures, direct or indirect, have been observed decades ago (Severny and Khokhlova 1953; Rothschild et al. 1955; Sakurai 1976; Tandberg-Hanssen 1995).



**Fig. 20.2** A few examples of many faces of quiescent prominences as seen at chromospheric temperatures ( $\sim 5 \times 10^4$  K)

Severny and Khokhlova (1953) reported that one of the most prominent features of quiescent prominences is persistent irregular motions. With frozen magnetic field, this was obviously indicative of a complex magnetic field and current topology.

Rothschild et al. (1955) directly measured motions of 47 knots on a limb prominence. They found knots moving “downward” with an acceleration that was much smaller than gravitational acceleration and a tendency for the acceleration to reverse at a certain point in the trajectory. The authors cautiously concluded that this could be explained by helical motions. They also refer to earlier findings indicating that “accelerations are smaller than gravitational, with little or no relationship even to the direction of gravity”.

Rotational motions have been observed in prominences by Ohman (1972) who also reported the possibility of “ring shaped” objects with helical motions ejected from prominences.

Rust and Kumar (1994) re-examining the Kippenhahn–Schlueter and the Kuperus–Raadu models conclude: “All models known to us, even those with helical fields, rely on some initial distortion of the bordering fields.... They predict either normal or inverted cross-filament components, but the axial component is always incorrect. We conclude that such models are defective.” They propose a model based on observations which clearly indicated that magnetic fields have helical nature, the mass in the filament is supplied during the emergence of helical flux ropes, and that the prominence is lifted bodily out of the chromosphere. To further describe the dynamics and stability of prominences, Rust and Kumar also invoked the screw pinch instability. This provided criteria for a stable helical configuration, determined the distribution of magnetic fields and currents, and resulted in quite a good agreement with observations.

The problem of disruption of prominences, directly related to their stability conditions, includes a wide range of plasma instabilities that must arise in such an environment. To consolidate the problems of prominence equilibrium and stability with respect to various MHD modes, Fong et al. (2001) studied prominence equilibria with respect to pressure- and gravity-driven instabilities using ballooning formalism and found conditions and growth rates for these instabilities. Under prominence conditions, this formalism includes the Rayleigh–Taylor instability, Parker instability, and any unstable modes characterized by long parallel and short cross-field dependencies. For the time being many aspects of plasma instabilities associated with prominence dynamics have been revealed and clarified in analytical and numerical studies (Dolginov and Ostryakov 1980; Matsumoto et al. 1993; De Bruyne and Hood 1993; Strauss and Longcope 1994; Magara 2001; Low and Petrie 2005; Mackay and Ballegoijen 2009).

New data obtained from space observations (Berger et al. 2010; Ryutova et al. 2010; Xing et al. 2012; Dudík et al. 2012; Feng et al. 2013; Druckmüller et al. 2014; Carlyle et al. 2014) offer a unique opportunity to study fundamental plasma instabilities in more details. Here we address this problem and investigate the occurrence and evolution of various instabilities to reveal their role in the dynamics of quiescent prominences. Our approach is twofold. First, we use the observational data to identify a particular kind of instability and its observed signatures. These data allow direct measurements of spatial and temporal parameters of various events. We then compare the measured spatiotemporal characteristics of particular event with corresponding results given by basic plasma theory. We will see that the fundamental plasma instabilities, expected and predicted earlier, continuously develop during the prominence lifetime. Quantitative analysis not only allows reliable identification of plasma instabilities, but may also be used for inference of physical parameters that are not directly measurable.

## 20.2 Large-Scale Observed Regularities

The necessary conditions for prominence formation is accumulation of opposite polarity small scale magnetic elements each forming unipolar ensembles with clear boundary between the areas of their population. Such a process naturally occurs

when dispersed magnetic elements drift toward high latitudes in course of the solar cycle evolution, and encounter the opposite polarity remnants from the previous cycle. This is a regular process and serves as a basis for the majority of the quiescent prominences to encircle near-polar latitudes and endure for several solar rotations.

The focal point of the observations of quiescent prominences has always been the time when part of prominence body passes through the limb, displaying its structure and dynamics at the best viewing angle (Fig. 20.2). Obviously, the portion of prominence positioned at the limb and projected on the sky is only a two-dimensional picture of small part of a huge solenoidal body of prominence.

Wrapped by 3D magnetic field and currents, the body of prominence is usually stretched over the entire polarity inversion line. Figure 20.3 shows example of quiescent prominence taken by the SDO at three temperatures. Lower panel is the magnetogram showing northern high latitude part of solar surface covered by ensembles of opposite polarity small scale flux tubes. One can see a clear polarity inversion line made between near pole region dominated by negative polarity magnetic elements and southern adjusted region dominated by positive polarity elements. Middle panel is the same area in He II 304 at  $5 \times 10^4$  K. Chromosphere shows here a huge quiescent prominence overlying entire polarity inversion line with its beautiful limb portion on the East. Top panel is overlying corona in Fe IX at  $6.3 \times 10^5$  K.

A hot corona seems to be intact by the presence of prominence. In fact, one can see darkened 171 Å emission on the disk caused by the presence of prominence *shadowing* EUV emission. Usually, the prominence shadow is seen throughout entire corona up to temperatures exceeding  $10^7$  K. This is shown in Fig. 20.4. One can see how the prominence following exactly the polarity inversion line blocks the hot EUV emission up to the outermost corona.

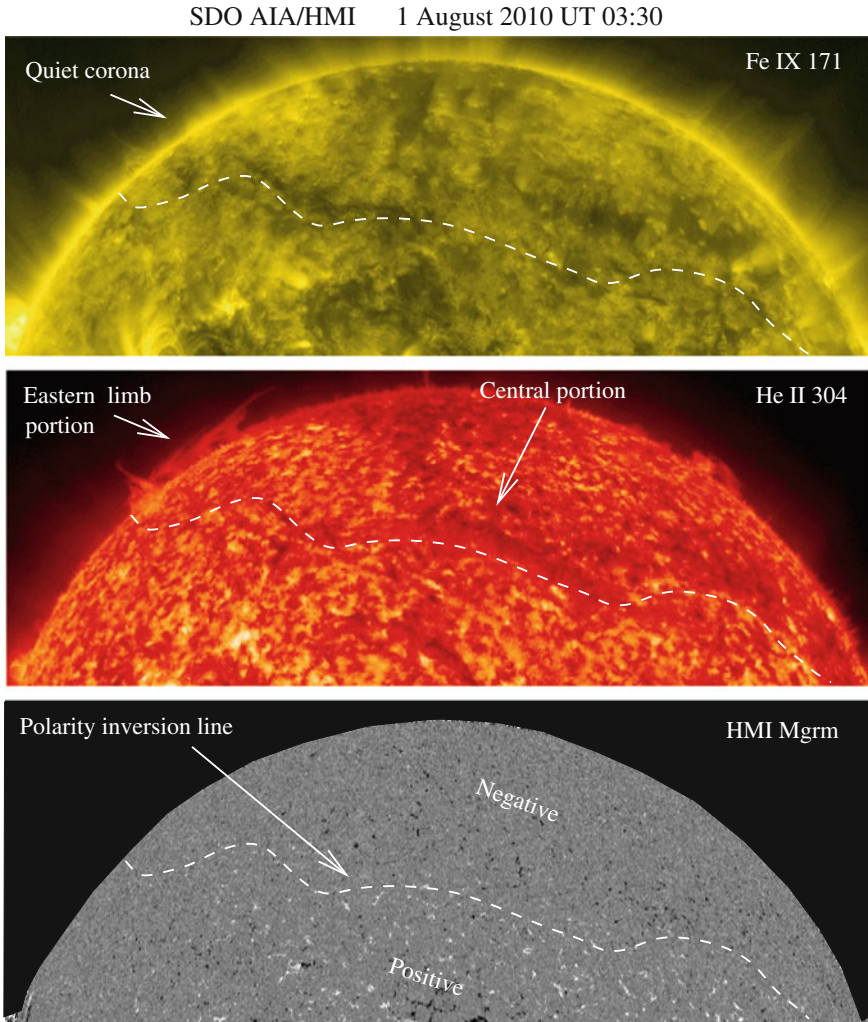
Global three-dimensional magnetic field and currents ( $\mathbf{j} \times \mathbf{B} \neq 0$ ), overlying the highly inhomogeneous photosphere with crooked polarity inversion line, acquire the shape of quite uneven solenoid. With solar rotation a prominence projection on the sky varies quite significantly. The shape and character of its *limb portion* depends on the orientation of a solenoidal body of prominence approaching the limb.

Figure 20.5 shows a carton illustrating several different possibilities. If the prominence approaches the limb with such an orientation as shown by dashed arrows that portion of prominence will appear as hedgerow shaped. In case of the prominence orientation as shown by a solid arrow, the limb portion will appear as a system of loops, which may simply arched, or form the dips and rings.

Accordingly, the details of prominence behavior observed on the limb may vary to a great degree depending on the orientation of a limb portion of prominence. The same is true for manifestation of fundamental plasma instabilities. These limitations, however, do not hinder the regularity of certain events which makes them an intrinsic attribute of prominence dynamics.

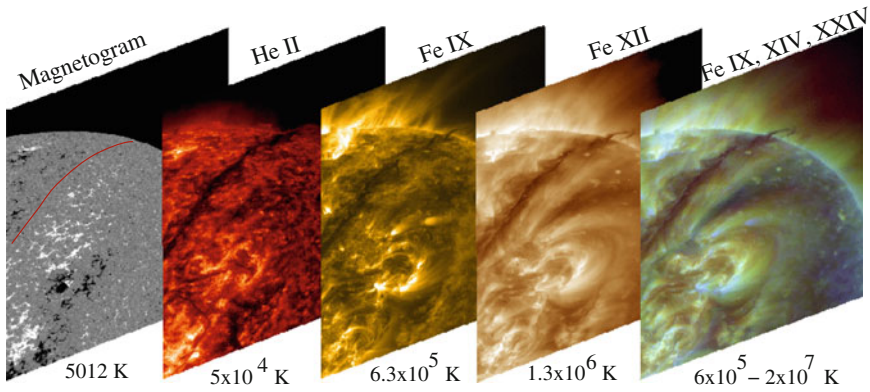
Thus, as the prominences survive several solar rotations, experiencing permanent changes, gaining and losing the energy, their projection on sky may acquire infinitely diverse, never duplicating forms. Often the prominence projection on the sky combines several named shapes simultaneously (cf. Fig. 20.2). Example of such prominence is shown in Fig. 20.6. This is a huge prominence observed on November 30, 2006 by the Hinode. One can see a hedgerow-type body in the middle, a



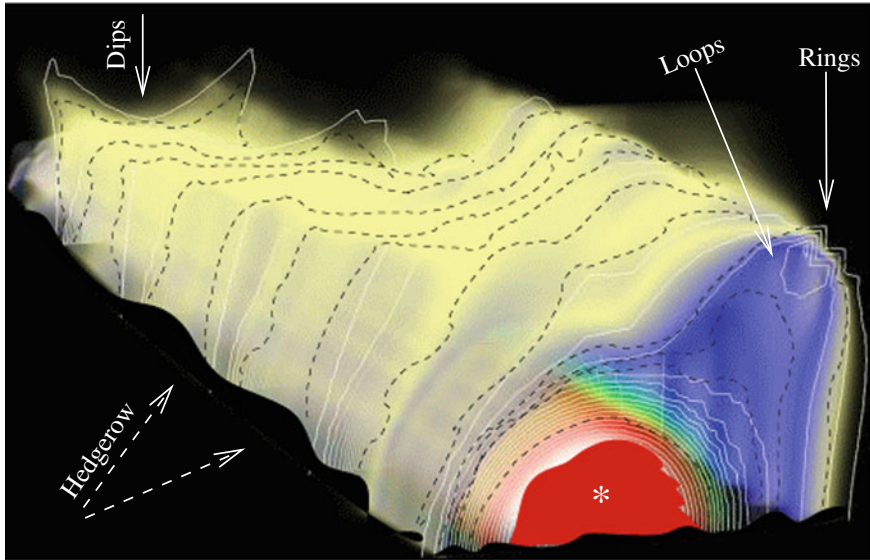


**Fig. 20.3** Example of quiescent prominence taken by AIA instrument in He II 304 line (*middle panel*), simultaneously with underlying photosphere (*lower panel*) and overlying corona in Fe IX line (*upper panel*). *Dashed line* highlights the polarity inversion line which serves as a path to a gigantic solenoid with twisted axis and skewed body. Eastern portion of prominence projected on the sky appears in He II 304 line as a typical loop-type prominence

loop-like system on the northern part, and twisted structures in the southern part that overlies a hot corona represented by black “cavities” under the prominence body. These are marked by white stars. To distinguish these “cavities”, i.e., *hollow space* under prominence body filled by a hot coronal plasma from coronal cavities which are usually understood as a coronal voids *above* the prominences, we shall call them *prominence cavities* or just *cavities*. It is important to bare in mind that plasma in



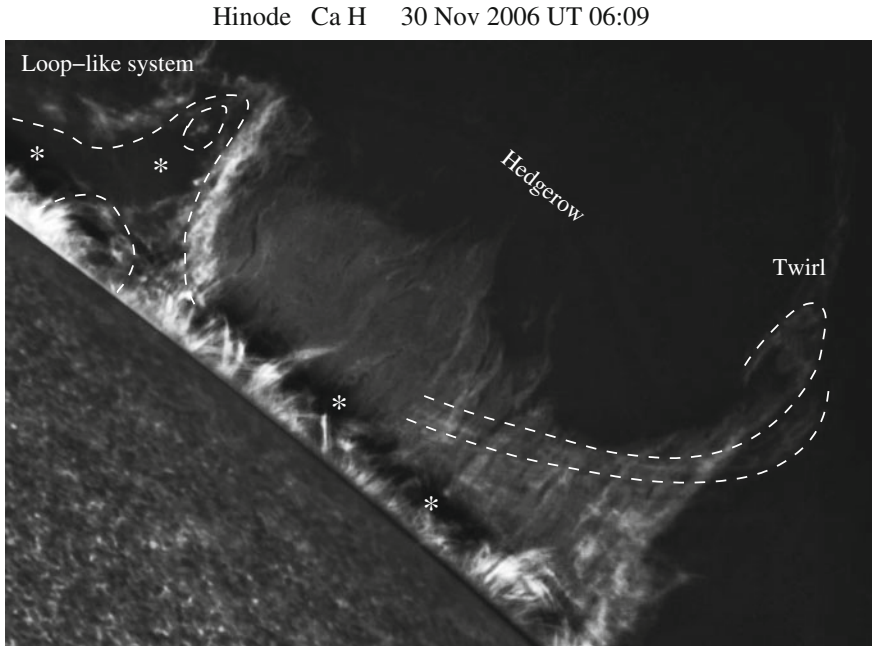
**Fig. 20.4** Note how diligently the prominence demarcates the magnetic shear between two opposite polarity quiet regions. *Red curve* in the magnetogram demarcates the polarity inversion line. The fact that the prominence shadow is seen throughout entire corona up to its highest temperatures shows its enormous body and height



**Fig. 20.5** Cartoon illustrating different forms of the visible portion of prominence situated near the limb. Depending on the orientation of the prominence body at the moment of time when it passes through the limb, the observer may see either the hedgerow shape (*dashed arrows*), or loop-shaped prominence (*solid arrow*), or their combination. *White star* indicates the prominence cavity filled by a hot coronal plasma

these cavities is at coronal temperatures and have much lower densities than those in the prominence body.

To demonstrate some basic properties of quiescent prominences, we use the data sets for six prominences taken with the SOT instrument on Hinode. The images are



**Fig. 20.6** Limb portion of prominence at N 50° latitude, observed on November 30, 2006 showing a complex twisted form which has a loop-like system on the northern part, a hedgerow-type body in the middle, and twisted structures in the southern part. *White stars* indicate location of a hot prominence cavities filled by coronal plasma

taken with 10–30 s cadence with the spatial resolution corresponding to a pixel size of  $0''.16$  in  $H\alpha$ , and  $0''.108$  in Ca II H line. The advanced procedures were used to highly improve the row data (Berger et al. 2008, 2010; Ryutova et al. 2010).

Data were compiled in movies to study temporal variation of chosen events. Duration of the observation usually exceeded 4 hours that allowed to study both, slow processes and short-living events including their possible long-term recurrences. There were found several persistent features that occur at different stages of the prominence evolution and that are common for all the chosen cases. Here we discuss three classes of events.

- I. Formation of large-scale arch-shaped prominence cavities expanding up to 30–50 Mm, and lifting the body of prominence to these heights and beyond. Interior of growing cavity consists of coronal material, and may be characterized as growing hot bulbs *under* the prominence body. Observed regularities in growth and collapse of such cavities can be well understood as a result of screw pinch instability in their early phase of formation (Sakurai 1976; Rust and Kumar 1994), and as a cavity dynamics under the influence of gravity and magnetic field during their further evolution.

- II. Development of a regular series of plumes and spikes seen at any moment of time at any possible orientation of a limb portion of prominence. This ubiquitous phenomena have all the attributes of Rayleigh–Taylor (RT) instability (Rayleigh 1883; Taylor 1950; Chandrasekhar 1981). Using the above-mentioned data sets allowed for the first time to identify several branches of RT instability, and measure their spatiotemporal characteristics. These are: (a) Single mode regime which in its nonlinear stage may produce jets or be stabilized by formation of a mushroom cap analogous to explosive instability; (b) Multimode regime characterized by formation of regular series of plumes and spikes; (c) Two plume competition. Hinode data allowed also to verify the influence of magnetic field on the RT instability.
- III. Development of growing ripples at the lower prominence/corona interface often followed by a sudden appearance of a collimated mass upflows, which can be attribute to the Kelvin–Helmholtz (KH) instability; high cadence data have provided the means to determine conditions for transition of a linear phase (rippling mode) to nonlinear stage of KH instability which is known to have an explosive character.

### 20.3 Formation of Prominence Cavity and Helical Structures

Formation of cavities under prominence body filled by the coronal plasma is an integral part of the 3D helical structure of the prominence and its evolution. It is only natural to expect that quiescent prominences stretched below the polar cap are indeed supported by solenoidal magnetic field composed of a thin arcades formed over the opposite polarity small scale magnetic fragments dispersed at high latitudes.

Uneven distribution of magnetic elements provides quite uneven shape of magnetic solenoid. This, on the other hand, causes various shapes of the limb portion of prominence. In most cases, i.e., almost at any orientation of a limb portion of prominence, cavity formation is a regular phenomenon. Their dynamics and lifetime, however, may be very different. This is determined by the set of local physical parameters. The very fact of a cavity formation, however, is a natural consequence of a solenoidal shape of a twisted prominence body, which, as mentioned above, approaching the limb may appear in various shapes.

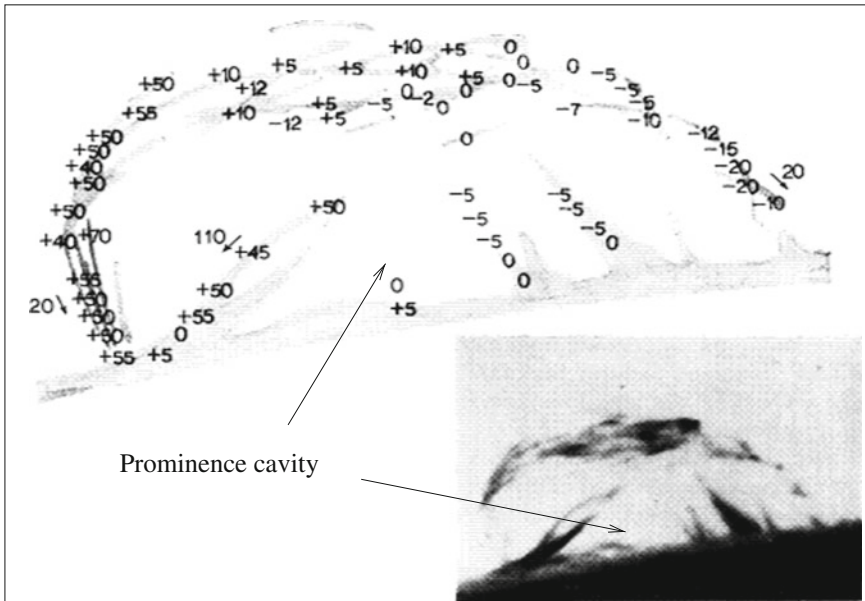
In Chap. 17 we have already used the basic property of magnetized plasma associated with Kruskal–Shafranov law (Shafranov 1956; Kruskal and Kulsrud 1958; Kadomtsev 1966). According to this law long magnetic field configurations having low aspect ratio, i.e., with radius of a magnetic tube being much smaller than its length, are intrinsically unstable unless they wind into a helical shape with nonzero field-aligned current. According, screw pinch configuration acquired by long magnetic filament is dynamically stable if a pitch angle of a kinked helical structure,  $\theta = B_\phi/B_z$ , is such that the safety factor; see (17.1)–(17.3),

$$q \equiv h/L < 1 \quad (20.1)$$

Here  $L$  is the length of the structure, and  $h$  is the pitch, i.e., a distance in which the field line at running radius  $R$  makes one revolution around the axis of filament:

$$h(R) \equiv \frac{2\pi R}{\tan \theta} = \frac{2\pi R B_z}{B_\phi} \quad (20.2)$$

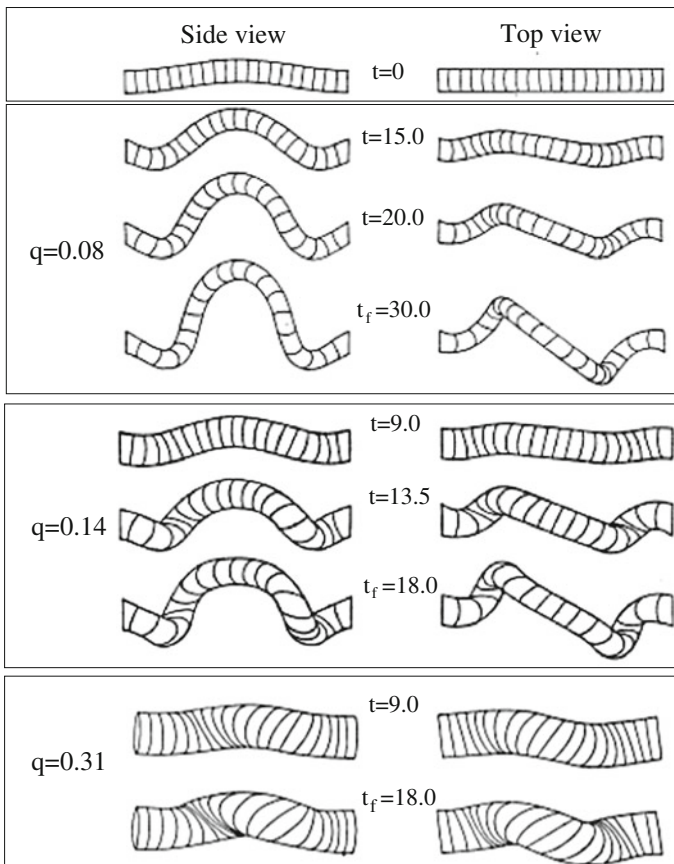
It is important to note that Kruskal–Shafranov condition and equations (20.1) and (20.2) hold on wide range of scales from the Tokamak devices and penumbral filaments to a huge body of prominences. For high latitude quiescent prominences safety factor is always less than unity, i.e., condition for long magnetic configuration to acquire the skewed shape and remain in it, is always satisfied. This explains longevity of quiescent prominences. If, however, structure becomes short, i.e., the aspect ratio  $R/L$  increases, or  $B_\phi$  weakens, safety factor approaches unity,  $q \simeq 1$ , and the prominence loses its global stability. This may occur if the prominence body brakes, which may be caused by disappearance of underlying photospheric magnetic elements, served as roots of given portion of prominence. Or, by some reason, the radius of structure (or large part of prominence) increases and reaches a critical point. Global shape of quiescent prominences as a skewed helical solenoid has been captured as early as in 1950s (Severny and Khokhlova 1953; Rothschild et al. 1955).



**Fig. 20.7** Velocity distribution in the prominence of August 30, 1971 in its remnant loop-system phase. Unit is  $\text{km s}^{-1}$  and *arrows* indicate the direction of transverse velocities. This distribution of velocities suggests a three-dimensional helical structure of the prominence. Reprinted from Sakurai 1976 by permission of Oxford University Press/on behalf of the PASJ

Sakurai (1976) has measured transverse and line of sight velocity distribution in the prominence observed on August 30, 1971 (Fig. 20.7). These measurements clearly showed a three-dimensional helical structure of prominence body.

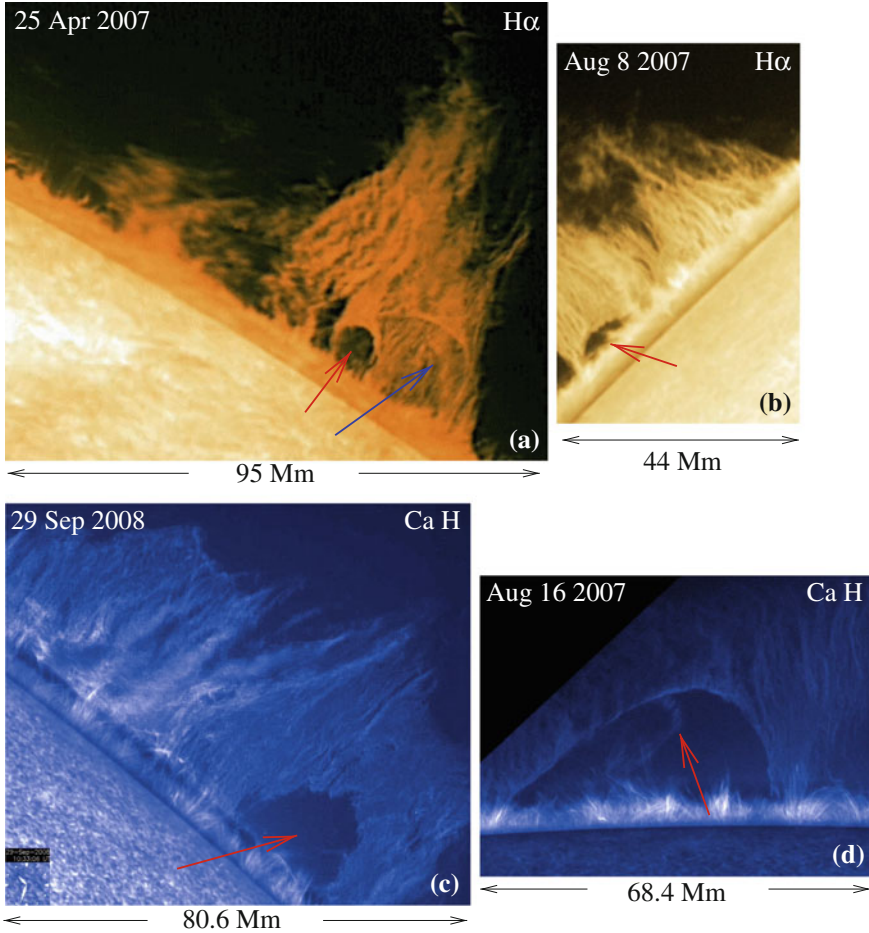
Especially prominent signs were seen near the top of the prominence where the upper part exhibited red shifts, while the lower part exhibited violet shifts. He also observed large-scale ascending motions of prominences and, making a direct connection between the ascending motion and rotational motions, interpreted them unilaterally as a result of a screw pinch instability. In particular, to explain the observed ascending motion of the semi-spherical cavity and its growth, he performed numerical analysis and found a good qualitative agreement with observations. Quantitatively, the range of physical parameters was found to be reasonable.



**Fig. 20.8** Computed motion of magnetic flux tube with a uniform pinch and no gravity force. The top panel shows a portion of flux tube in the initial time,  $t_0$ . The growth of a kinked helical structure depends on the safety factor,  $q$ . A smaller safety factor corresponds to a higher tip of the kinked flux tube (i.e., to a larger cavity).  $t_f$  is the time when the cavity stops growing. The unit of time  $R/v_A$ . Reprinted from Sakurai 1976 by permission of Oxford University Press/on behalf of the PASJ

For illustrative purposes we show some results of Sakurai's numerical calculations in Fig. 20.8, which contains examples of three values of a safety factor,  $q = 0.08; 0.14; 0.31$ . The unit of time is  $R/v_A$ . As expected, the growth of cavity formed by the skewed kink, depends on the safety factor,  $q$ : a smaller safety factor corresponds to a longer lifetime of the cavity, and respectively the kink may reach higher altitudes.

To address the problem of prominence dynamics and structure formation using high-resolution observations, we choose here several exemplary prominences. Some



**Fig. 20.9** Snapshots of exemplary prominences with various bubble/cavity formations. **a** Limb portion of the April 25, 2007 prominence located at the West limb, S 36°; to the south of the well-defined cavity (*red arrow*) there is another cavity hindered by the frontal hedgerow part of the prominence body (*blue arrow*). **b** Small cavity on the East limb, N 49° having a much shorter lifetime due to the sudden development of an explosive instability. **c** Highly dynamic cavity having an almost circular shape observed on September 29, 2008 at the West limb, N 56°. **d** Long-lived, “classical” recurring cavity, observed on August 16, 2008 at the West limb, N 54°

of them are shown in Fig. 20.9. During the observations (of about 5–6 h), each prominence showed various types of cavities, from long-living cavities that reach significant heights (Fig. 20.9 panels a, c, d), to very low lying shallow cavities (panel b). Recall also a huge prominence shown in Fig. 20.6 with series of cavities under its stretched body (marked by white stars).

Despite quite different spatial and temporal characteristics, the dynamics of each cavity's growth and collapse obey simple laws imposed by screw pinch dynamics, providing solid ground for solenoidal helical structures. Note how prominent is a filamentary structure of prominence in all shown cases.

### 20.3.1 The Case of the 16 August 2007 Prominence

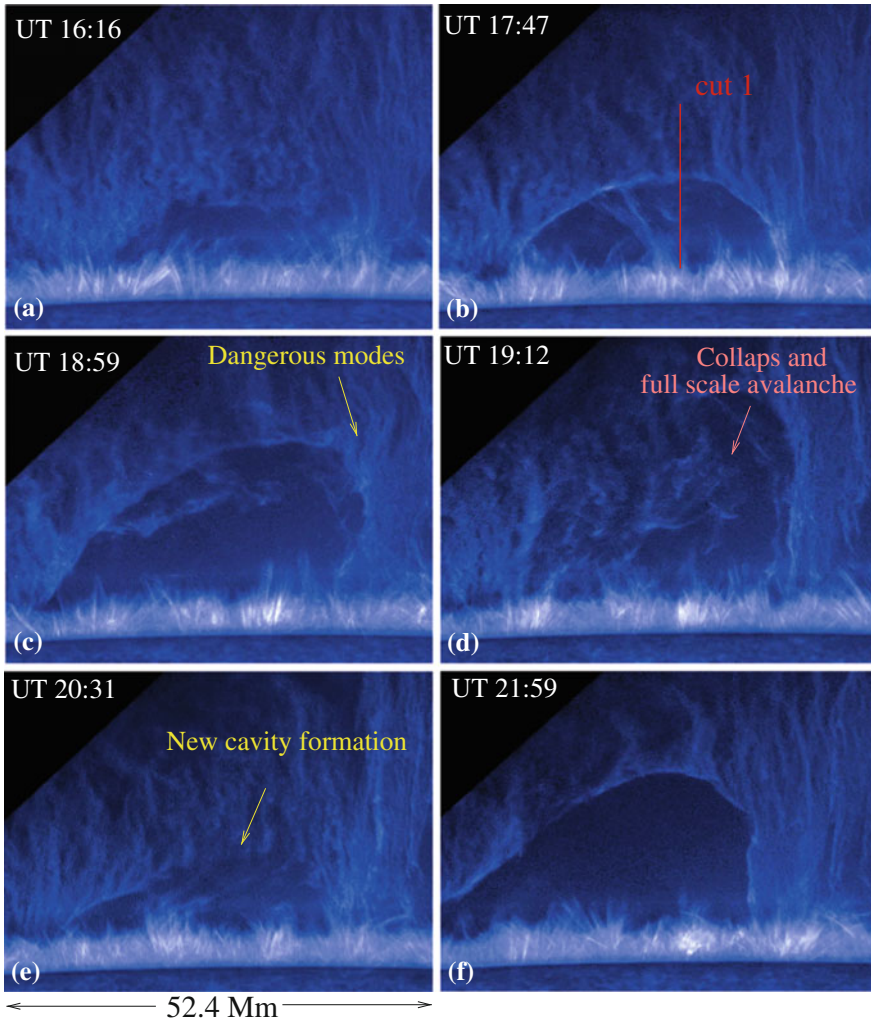
In order to follow typical regularities seen in all studied cases, we consider the detailed dynamics of the cavity formation and evolution observed on August 16, 2007 prominence. The duration of the observation was about 6 h, cadence 25 s.

Figure 20.10 shows the location of the cavity formation at six time intervals. The first panel at UT 16:16 shows the growth phase of the prominence, already noticeable at the beginning of the observation at UT 16:04. The cavity retained its semi-spherical shape as it grew (panel b), until about UT 18:50 when small scale ripples started to appear at the western edge of the prominence/cavity boundary (arrow on panel c shows already well-developed ripples). These quite regular ripples turned out to be an unstable mode that evolved into growing disturbances, resulting in an explosive collapse of the cavity. A full-scale avalanche and collapse of the cavity is shown in panel d. Within about 80 min, a new cavity started to form in about the same area (panel e). Panel f shows the new cavity in its mature phase. The dynamics of new cavity was amazingly similar to its predecessor's behavior.

To study the temporal variability of the cavity, as a first step, we measure the velocity of a tip of the cavity using the space-time procedure. Figure 20.11 shows August 16, 2007 cavity in its well-developed stage. The red line in panel a is the path and direction of a cut. The lower panel b is resulted space-time image of the motion of the cavity apex. The cavity grew almost linearly during the first two hours and then started to accelerate. The dotted line corresponds to UT 17:47, the moment when quasilinear growth of the cavity moves into a nonlinear regime.

At about UT 18:48 the height of the cavity apex reaches a maximum and the cavity collapses. In other words, when a semi-spherical cavity with growing radius,  $R$ , reaches its maximum,  $R_{\max}$ , and its velocity reaches the so-called terminal velocity,  $\dot{R}_{\text{term}}$ , the cavity quickly collapses. The velocity of the ascending motion in the linear regime is  $v_1 \simeq 2.1 \text{ km s}^{-1}$ , average velocity during the acceleration phase is  $v_2 \simeq 15 \text{ km s}^{-1}$ , and collapsing velocity is  $v_3 \simeq -25.6 \text{ km s}^{-1}$ . As mentioned above, about 90 min after the total collapse a new cavity started to form at the same place (see Fig. 20.10e, f). Recurrence of cavities is quite common and, as we will see below, have a natural explanation.



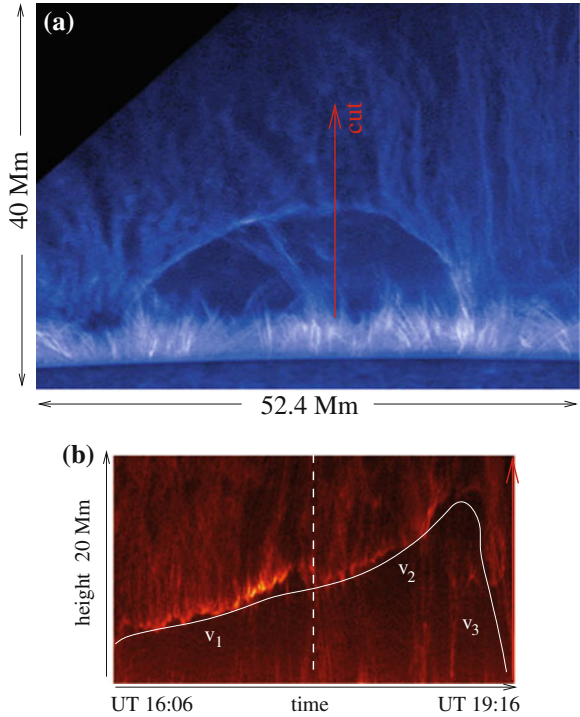


**Fig. 20.10** Classical example of cavity formation, dynamics and recurrences, observed on August 16, 2007. The duration of the observation was about 6 h, cadence 25 s. Meaning of images shown in *panels* from *a* through *f* are explained in text

### 20.3.2 Phenomenology of Cavity Formation

To describe the later stages of an already established semi-spherical cavity and its unsteady motions, we need to consider gravitational forces, nonlinearity, and dissipative effects. Since the semi-spherical shape of the cavity is persistent, even during unsteady motion, it may be described in terms of the Rayleigh–Plesset equation (Rayleigh 1917; Plesset 1949).

**Fig. 20.11** Dynamics of August 16, 2007 long-lived cavity: **a** Snapshot of a well-developed stage just before a linear growth of cavity turned into the accelerated phase. **b** Space-time image of the motion of the cavity apex. *Dotted line* corresponds to UT 17:47, the start of acceleration. Velocity of ascending motion is  $v_1 \simeq 2.1 \text{ km s}^{-1}$ , average velocity during the acceleration phase is  $v_2 \simeq 15 \text{ km s}^{-1}$ , and collapsing velocity is  $v_3 \simeq -25.6 \text{ km s}^{-1}$



The Rayleigh–Plesset equation is the most common nonlinear equation describing the cavitation and bubble dynamics in diverse media including hydrodynamics, laboratory and space plasmas, nuclear reactions and biology. It follows from the compressible Navier–Stokes equations and, being universal, is applicable to various types of cavities, from spherical and semi-spherical bubbles to cavities of very different forms, requiring only minor adjustments mainly related to system parameters (Brennen 1995; Franc and Michel 2004).

Modified for magnetized plasma the Rayleigh–Plesset equation reads as follows:

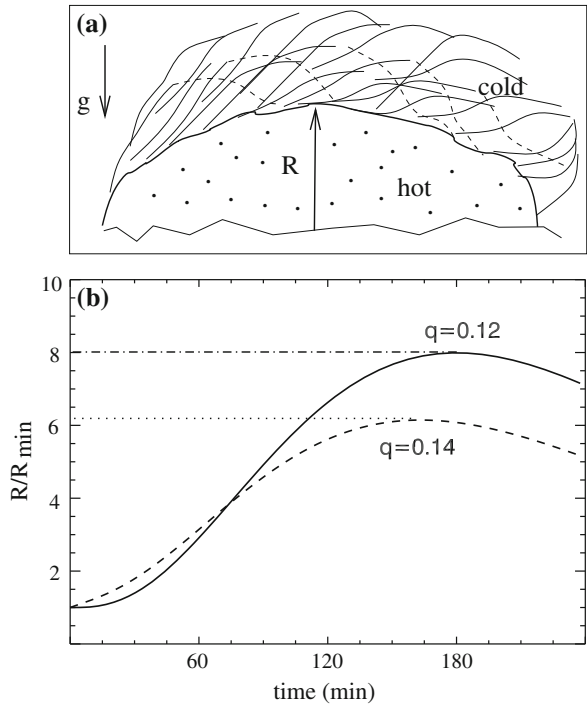
$$R\ddot{R} + \frac{3}{2}\dot{R}^2 = gR - \frac{2\sigma}{\rho R} - \frac{4\nu}{R}\dot{R}, \quad (20.3)$$

here  $R$  is variable radius of cavity (Fig. 20.12a),  $\rho$  is the density of the prominence plasma,  $\sigma$  is the surface tension dominated by the magnetic field,  $\sigma \simeq (B^2/8\pi^2)hq$ , and  $\nu = \eta/\rho$  is the viscosity. As earlier,  $h$  is the pitch and  $q$  is the safety factor. Together they represent a combination of poloidal and toroidal components of magnetic field and the aspect ratio of a solenoidal structure, (20.1) and (20.2).

To see the meaning of the terms in (20.3) as they stand in the Navier–Stokes equation, one can multiply it by a factor  $\rho/R$ :

$$\rho\ddot{R} + \frac{3}{2}\rho\frac{\dot{R}^2}{R} = \rho g - \frac{2\sigma}{R^2} - \frac{4\rho\nu}{R^2}\dot{R}, \quad (20.4)$$

**Fig. 20.12** *Top* Sketch of the kinked shape of a solenoidal prominence; *Bottom* Solution of the Rayleigh–Plesset equation for the prominence Parameters.  $R$  is the radius of a semi-spherical cavity,  $q$  is the safety factor



it is now evident that the two terms on the left-hand side represent acceleration and inertia, and the three terms on the right-hand side are the gravity force, surface tension and viscous forces, respectively.

Neglecting the viscosity and using the identity,

$$R\ddot{R} + \frac{3}{2}\dot{R}^2 \equiv \frac{1}{2} \frac{1}{R^2 \dot{R}} \frac{d}{dt} (R^3 \dot{R}^2), \tag{20.5}$$

(20.3) reduces to a directly integrable form:

$$\frac{d}{dt} (R^3 \dot{R}^2) = \frac{1}{2}g \frac{dR^4}{dt} - \frac{2\sigma}{\rho} \frac{dR^2}{dt}, \tag{20.6}$$

or

$$R^3 \dot{R}^2 = \frac{1}{2}gR^4 - \frac{2\sigma}{\rho}R^2 + \text{const.} \tag{20.7}$$

The integration constant is determined by the initial conditions of the cavity provided by the initial screw pinch configuration and corresponding safety factor.

Equation (20.7) can be further integrated to obtain  $R(t)$ . Plots of  $R(t)$  for two values of safety factor,  $q = 0.12$  and  $q = 0.14$  are shown in Fig. 20.12b.

It is important to emphasize that one can estimate the minimum radius of a cavity,  $R_{\min}$ , necessary for the cavity to grow. The point is that the appearance of kinks is an integral part of the dynamics of the prominence body but, in order to survive and grow the initial radius must be above some critical value,  $R_{\min} \simeq \sqrt{\sigma/\rho g}$ . Taking, e.g.  $B = 6\text{ G}$ ,  $h = 20\text{ Mm}$ ,  $q = 0.12$ ,  $\rho = 8.5 \times 10^{-14}\text{ g cm}^{-3}$ , we get  $v_A = 58\text{ km s}^{-1}$ , and  $R_{\min} \simeq 2.17\text{ Mm}$ . Using the plot corresponding to  $q = 0.12$  we see that a cavity with an initial radius of 2.17 Mm would reach terminal velocity and a maximum radius of 17.36 Mm in about 3 h, which agrees well with the measured parameters of August 16, 2007 cavity dynamics.

Note that presence of  $d^2R(t)/dt^2$  in (20.3) is responsible for the recurrent nature of cavity formation.

### 20.4 Regular Series of Plumes—Multimode Regime of Rayleigh–Taylor Instability

The Rayleigh–Taylor (RT) instability develops when two fluids of different densities accelerating toward each other come into contact (Rayleigh 1883; Taylor 1950). The exemplary case is when a heavy substance with mass density  $\rho_H$  lies in a gravity field over a lighter substance with  $\rho_L < \rho_H$ . The interface between the two media becomes unstable with respect to perturbation with a wave vector  $k = 2\pi/\lambda$ , such that the growth rate of the instability is

$$\nu = \sqrt{gk \left[ A - \frac{k\sigma}{g(\rho_H + \rho_L)} \right]} \tag{20.8}$$

Here  $\sigma$  is the surface tension, and  $A$  is the Atwood number:

$$A = \frac{\rho_H - \rho_L}{\rho_H + \rho_L} \tag{20.9}$$

The RT instability is ubiquitous in a wide range of media from the Earth’s atmosphere and soil to laboratory and space plasmas. It is especially evident in quiescent prominences.

The specifics of the RT instability in prominences as in magnetized plasmas are influenced by supporting three-dimensional magnetic fields. Magnetic field effects can be briefly described as follows (Chandrasekhar 1981):

- I. The magnetic field parallel to gravity ( $\vec{B}||g$ ) has different effects on long and short wavelengths. Long wavelengths are unaffected. The growth rate is

$$\nu = \sqrt{Agk} \tag{20.10}$$

Short wavelengths are restricted by the following growth rate:

$$\nu = (g/V_A) \left[ \sqrt{\rho_H/(\rho_H + \rho_L)} - \sqrt{\rho_L/(\rho_H + \rho_L)} \right] \quad (20.11)$$

II. The magnetic field transverse to gravity ( $\vec{B} \perp g$ ) has a strong effect on the RT instability and may well stabilize it. The growth rate is as follows:

$$\nu^2 = gk \left[ \frac{\rho_H - \rho_L}{\rho_H + \rho_L} - \frac{B^2 k_x^2}{2\pi(\rho_H + \rho_L)gk} \right], \quad k^2 = k_x^2 + k_y^2 \quad (20.12)$$

In this case, the magnetic field creates a “surface tension” and limits the instability ( $\nu^2 > 0$ ) at a critical wavelength,  $\lambda_c$ :

$$\lambda_c^2 = \frac{B^2}{g(\rho_H - \rho_L)} \cos \theta \quad (20.13)$$

where  $\theta$  is the inclination of the wave vector  $\vec{k}(k_x, k_y)$  to the direction of  $\vec{B}$ ,  $k_x = k \cos \theta$ ,  $k_y = k \sin \theta$ . Note that the orientation of the  $x, y$  plane was chosen, so that the uniform magnetic field be along the  $x$ -axis (Chandrasekhar 1981).

Thus, perturbations with wavelengths  $\lambda < \lambda_c$  are stable with respect to the RT instability. Instability on a scale  $L$  parallel to the field, thus requires that magnetic field be below some critical value:

$$B < B_c \equiv \sqrt{Lg(\rho_H - \rho_L)/\cos \theta} \quad (20.14)$$

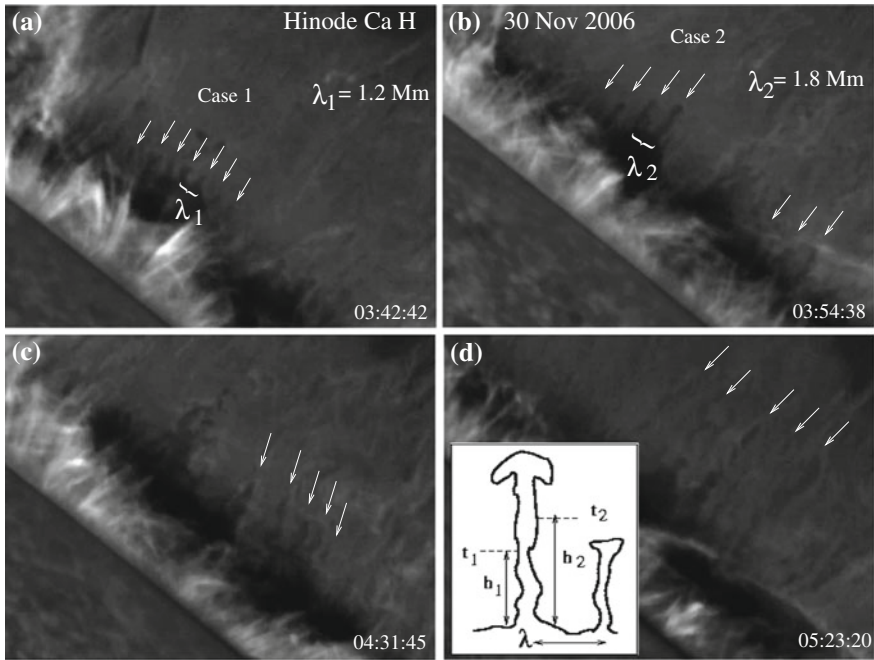
A magnetic field component stronger than  $B_c$  that is transverse to gravity suppresses the RT instability. This fact is very useful to estimate the magnetic field in cases when the RT instability is fully developed.

Depending on system parameters, the instability may evolve in several branches, most typically in a multimode regime where the interface between the heavy and light components breaks into a series of plumes and spikes separated by the characteristic wavelength. Examples of a multimode regime are shown in Fig. 20.13 (see also Fig. 20.14). One can see that all of the necessary features of a classical RT instability are in place:

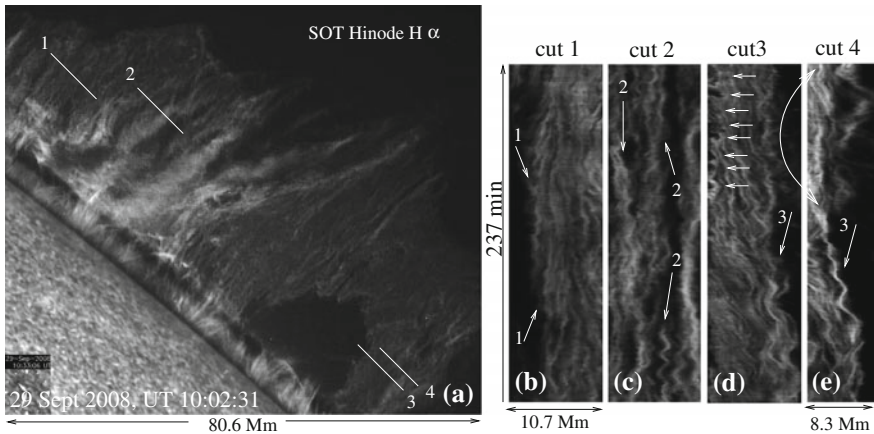
- (1) A multimode front (seen in all 4 panels, a–d in Fig. 20.13 and marked by arrays of small arrows);
- (2) Self-similarity of plumes in one family;
- (3) Similarity of wavelength/height ratio in different families (i.e., larger wavelength, higher plumes);
- (4) Suppression of the regular oscillations of filaments comprising the prominence (see Fig. 20.14).

### 20.4.1 Practical Use

The universality of the RT instability in prominences allows direct comparison of observations and theory. The most reliable parameter is the growth rate. The height



**Fig. 20.13** Examples of Rayleigh–Taylor instability with necessary attributes: self-similarity of plumes in family, similarity of the wavelength/height ratio in different families. Inset in *last panel* shows a way to directly measure the growth rate from observations. Meaning and notations presented in *panels a through d* are explained in text



**Fig. 20.14** Effect of Rayleigh–Taylor instability on regular oscillatory motions of filaments comprising prominences. **a** Sept. 2008 prominence with space-time cuts. **b, c** *Cuts 1* and *2* show a regular oscillatory pattern seen in all observed prominences. **d, e** *Cuts 3* and *4* show the region where the RT instability broke into plumes (*array of small arrows*) and destroyed the regular oscillatory pattern (*curved arrow*)

of the plume during its linear and quasilinear growth changes with time as

$$h(t) = h_0 \exp[-\nu_{\text{obs}}(t - t_0)] \quad (20.15)$$

Measuring the heights of the plume,  $h_i$ , at an arbitrary times,  $t_i$ , one finds the growth rate:

$$\nu_{\text{obs}} = \frac{1}{t_2 - t_1} \ln(h_2/h_1) \quad (20.16)$$

The inset in Fig. 20.13 illustrates this simple procedure. High cadence data easily allow to measure dozens of  $(h_i, t_i)$  pairs in each family of plumes and accurately calculate growth rates.

The beauty of this procedure is that one can do these measurements many times during the lifetime of a regular array of finger-like plumes, and compare the calculated growth rates. As a result, one may easily find when the linear or quasilinear regime ends and the system goes to a weak nonlinear regime. This happens when the growth rate, being quite constant during the linear regime, starts to change. If a strong nonlinear regime develops, this will correspond to turbulence in the medium and the disappearance of the vertical, finger-like structures from the plasma.

In order to compare the measured value of  $\nu_{\text{obs}}$  with the theoretical growth rate, one can use (20.12) written in the form

$$\nu_{\text{th}} = \sqrt{\frac{2\pi g}{\lambda} A \left[ 1 - \frac{B^2 \cos^2 \theta}{(\rho_H - \rho_L) g \lambda} \right]} \quad (20.17)$$

where the magnetic field is perpendicular to the gravitational. It is important to note that  $\nu_{\text{th}}$  itself contains directly measurable parameters, primarily the wavelength,  $\lambda$ . Also, the Atwood number  $A$  can be quite accurately estimated as it only varies between 0.8 and 0.96.

Consider two examples shown in Fig. 20.13a, b. Empirical measurements for case 1 give  $\nu_1 = 8.06 \times 10^{-3} \text{ s}^{-1}$  and for case 2  $\nu_2 = 6.07 \times 10^{-3} \text{ s}^{-1}$ . For theoretical estimates, we take  $\rho_H = 8.5 \times 10^{-14} \text{ g cm}^{-3}$ ,  $\rho_L = 1.7 \times 10^{-15} \text{ g cm}^{-3}$ ,  $|B| = 6 \text{ G}$ , and  $\theta = 85^\circ$ ; then, for  $\lambda_1 = 1.2 \text{ Mm}$ ,  $\nu_{\text{th}} \simeq 9.2 \times 10^{-3} \text{ s}^{-1}$ , and for  $\lambda_2 = 1.8 \text{ Mm}$ ,  $\nu_{\text{th}} \simeq 7.5 \times 10^{-3} \text{ s}^{-1}$ , which are in good agreement with the measured values.

Note that, as measurements of the growth rate are simple and reliable, comparison of  $\nu_{\text{obs}}$  and  $\nu_{\text{th}}$  may be used to infer magnetic field and its direction.

The relationship between the RT plumes and the regular oscillatory pattern observed in the body of a prominence can also be used for quantitative analysis. This approach has a wide and very rich applications for prominence studies. Here we only demonstrate the relationship between the RT plumes and the regular oscillatory pattern. Figure 20.14 shows a typical example, represented by a prominence observed on September 29, 2008 (panel a). Panels b and c and the lower parts of panels d and e show typical oscillations of thin filaments comprising the prominence body.

Prominences with a large projection on the sky show filament oscillations in a wide range of frequencies. In this particular example periods are as follows:  $T_1 \simeq 380 \text{ s}$

(panel b),  $T_2 \simeq 680$  s (panel c), and  $T_3 \simeq 1,040$  s (panels d and e). Note that in all cases, the period of oscillations in one “neighborhood” is nearly constant reflecting more or less uniform physical conditions in a given area (arrows 1, 2, 3). The last two panels show the effect of the RT instability on the long-lasting oscillations of the filamentary medium: the appearance of RT plumes quickly destroys the regular oscillatory pattern (curved arrow in panel e).

## 20.5 Fast-Growing Plumes—Nonlinear Regime

The Kelvin–Helmholtz (KH) instability develops in the presence of shear flows at the interface of two media with different densities and has several branches depending on the dispersion, dissipation, and other physical parameters of the medium (see Chap. 5). Obviously, the highly dynamic cavity/prominence interface as border line between two very different media must be a subject of shear flows and thus various instabilities. The cavity/prominence interface therefore is a natural place to expect, in particular, a manifestation of the KH instability. The most readily excitable mode that may lead to a KH instability, is a kink mode,  $m = \pm 1$ . The corresponding dispersion relation in the presence of shear flows with velocity  $u$ , has a form:

$$D(\omega, k) \equiv \omega_{\pm} - \frac{k}{1 + \eta} \left[ u \pm \sqrt{\eta[(1 + \eta)v_A^2 - u^2]} \right] = 0 \quad (20.18)$$

Here  $\eta = \rho_L/\rho_H$ , with indices  $L$  and  $H$  indicating “light” and “heavy” plasmas. Note that in the corona, the scale height is  $\Lambda \geq 50$  Mm and the linear amplitude of oscillations is  $\simeq 0.5$ – $1$  Mm. This means that the effect of gravity is negligible.

A gross, linear KH instability, when the square root term in the dispersion relation (20.18) becomes imaginary, requires super-Alfvénic shear flows:

$$u > u_c^{(2)} = v_A \sqrt{1 + \eta} \quad (20.19)$$

A much more dangerous branch of the KH instability produces negative energy waves (see Chap. 5). NEWs occur when the system is stable with respect to a linear KH instability, i.e., at sub-Alfvénic velocities when  $u < v_A \sqrt{1 + \eta}$ , but  $\partial D/\partial \omega < 0$ . In this case, the energy of kinked perturbations becomes negative and the damping rate turns into a growth rate.

Indeed, the energy density of kink perturbations in the presence of flows has a form:

$$W = \frac{1}{2} \rho_H \zeta^2 k^2 \left[ (1 + \eta) \frac{\omega^2}{k^2} + \eta v_A^2 - u^2 \right] \frac{v^2 \pm uv}{1 + \eta} \quad (20.20)$$

where  $\zeta$  is the amplitude of perturbations. For convenience, we have defined  $v = \sqrt{\eta[(1 + \eta)v_A^2 - u^2]}$ . Substituting the expression  $\omega^2/k^2$  from the dispersion relation into this equation and taking the lower sign, i.e., considering the case when the system



is stable with respect to the linear KH instability, we have:

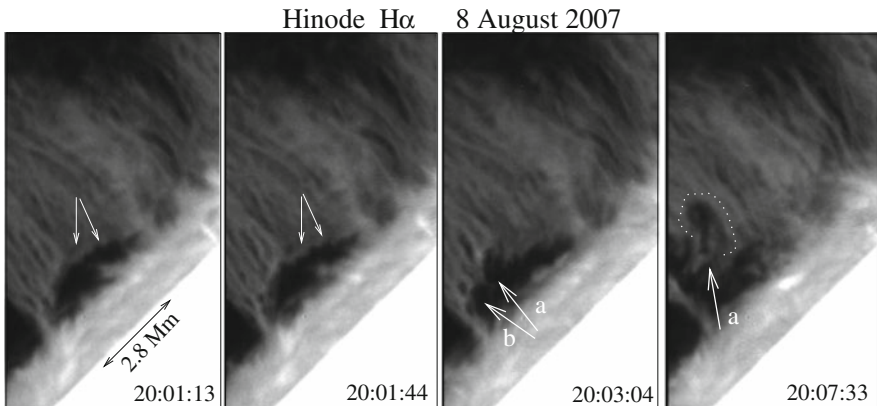
$$W = \rho_H \zeta^2 k^2 (\eta v_A^2 - u^2) \frac{v}{v + u} \tag{20.21}$$

Obviously, the energy of the wave becomes negative as soon as  $u > v_A \sqrt{\eta}$ ; thus, the interval of shear flow velocities,  $v_A \sqrt{\eta} < u < v_A \sqrt{1 + \eta}$ , corresponds to a branch of NEWs that are subject to explosive growth (Ryutova 1988).

Recall that the most remarkable property of NEWs is that the action of any dissipative mechanism which provides an energy loss leads to growth of their amplitudes (Coppi et al. 1969; Ryutova 1988; Ryutova and Tarbell 2000). In this regime, any dissipative effects turn linear perturbations into explosively growing disturbances. In a few inverse growth rates of explosive instability, higher nonlinear effects are initiated and provide stability. This competition often leads to the formation of a classical mushroom cap.

### 20.5.1 Mushroom Formation

An example of this regime is shown in Hinode  $H\alpha$  data of August 8, 2007 prominence (Fig. 20.15). The perturbed cavity/prominence boundary shows a regular rippling mode that lasts over 3 min. In general, the duration of the linear regime is arbitrary and may last much longer. In this particular case at about UT 20:02:33, a strong distortion of the interface appears. The distortion starts to grow while still remaining close to the quasilinear regime. At UT 20:03:04, enhanced disturbances become dominant, suppressing the rippling mode (shown by arrows a and b in Fig. 20.15). Just before UT 20:06:04, slowly growing disturbances show explosive growth and, in about 90 s, acquires a mushroom form, typical to the explosive phase of the KH instability (UT 20:07:33).



**Fig. 20.15** Growth of ripples into explosively growing disturbances and their stabilization phase taking a typical mushroom form

The growth rate of the explosive instability is Ryutova (1988, 2006):

$$\nu_{\text{expl}} \simeq \alpha \frac{\tilde{\nu}_{\text{ei}}}{\ln(|W|/|W_0|)} \quad (20.22)$$

where  $\alpha$  is a parameter of the order of unity,  $\alpha(T, l, n) \simeq 1$ , and  $\tilde{\nu}_{\text{ei}} = (m_e/m_p)\nu_{\text{ie}}$  is the inverse slowing down time of particles via electron-ion collisions. For  $T = 10^6$  K, and  $n = 5 \times 10^{10} \text{ cm}^{-3}$ ,  $\tilde{\nu}_{\text{ei}} = 2.7 \times 10^{-2} \text{ s}^{-1}$ . The logarithmic energy increase may be estimated by measuring the initial (linear) and final (explosive) amplitudes of the perturbation:  $\ln(|W|/|W_0|) \simeq \ln(\zeta^2/\zeta_0^2)$ ; cf. (20.21). For our chosen example,  $\zeta_0 \simeq 0.5 \text{ Mm}$  (Fig. 20.15, UT 20:01:44),  $\zeta \simeq 2.2 \text{ Mm}$  (UT 20:07:33). This gives:

$$\nu_{\text{expl}} \simeq 9.07 \times 10^{-3} \text{ s}^{-1}, \quad (20.23)$$

and the characteristic time of the explosive growth of a single plume acquiring  $e$ -times amplitude is 110 s, very close to the observed times in general and to the measured time of August 8, 2007 explosive event, in particular.

We can also estimate ranges of shear velocities leading to the development of the explosive phase:

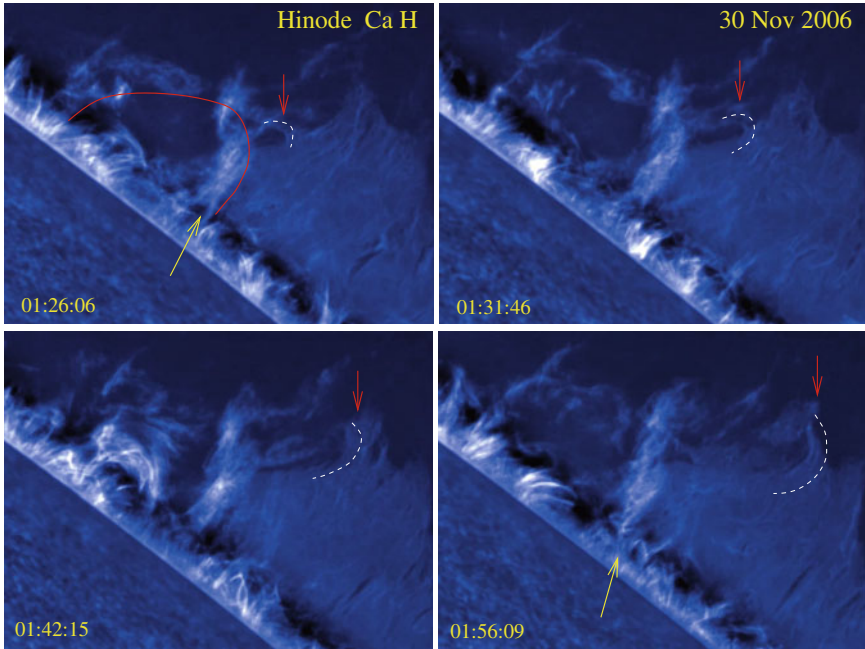
$$v_A \sqrt{\eta} < u < v_A \sqrt{1 + \eta} \quad (20.24)$$

With  $n_L = 5 \times 10^{10} \text{ cm}^{-3}$ ,  $n_H = 10^9 \text{ cm}^{-3}$ ,  $\eta = n_L/n_H = 0.02$ , and for magnetic field values such that  $B = 4; 6; 10 \text{ G}$ ,  $v_A = 39; 58.6; 97.7 \text{ km s}^{-1}$ , we find at any  $u_c^{(1)} = v_A \sqrt{\eta} = 5.5, 8.3, 13.8 \text{ km s}^{-1}$ , rippling modes are subject to the explosive branch of the KH instability.

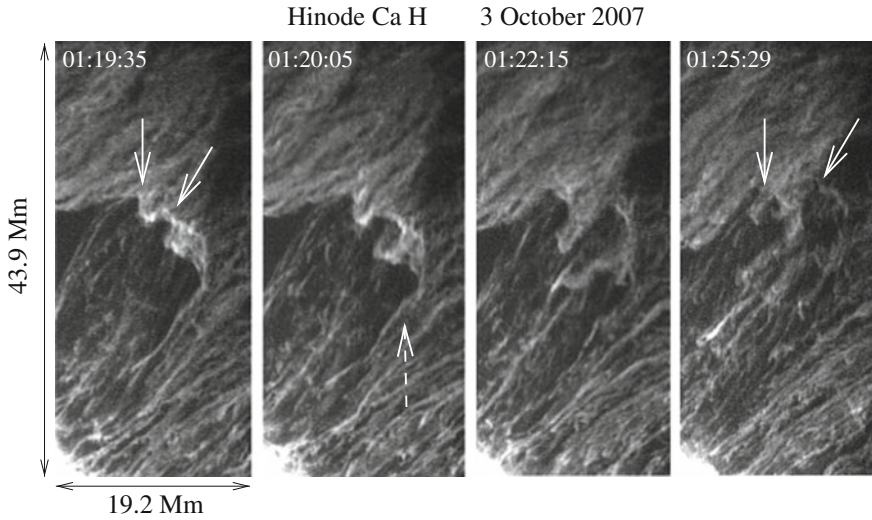
One must bear in mind that there are several important differences between the KH (both linear and explosive branches) and RT instabilities. The main feature of the RT instability is the development of a *series of self-similar plumes*, characterized by the specific wavelength, that corresponds to the distance between family “members.” The KH instability, especially in its nonlinear explosive phase is characterized by the dominance of a *single plume*, breaking through the prominence body. Another typical example of this is shown in Fig. 20.16.

The growth rates of such single disturbances, as well as their dimensions, significantly exceed those formed by the RT instability. Their energy content as well is much higher than the energy content of individual plumes in the RT case. We believe that under some extreme conditions, an explosive phase of the KH instability may be responsible for triggering CMEs associated with quiescent prominences.

It is important, that the observation of prominence dynamics offers one of the most efficient and reliable diagnostic tools. This is provided by the fact that the details of the prominence dynamics is easy to distinguish and analyze them using directly measurable parameters. It is interesting that determination of prominence plasma  $\beta$  from the dynamics of plumes is also possible (Hillier et al. 2012).



**Fig. 20.16** One of November 30, 2006 prominence cavities, partially blocked by the bright gable (shown by *thick yellow arrows*). The linear growth of a single plume lasted over 10 min. At about UT 01:40:06, it started to accelerate taking the form of a post-explosion mushroom cap (denoted by *red arrows*)



**Fig. 20.17** Two-bubble competition captured by Hinode on September 3, 2007. Bubbles 1 and 2 eventually merge destroying the third neighbor bubble 3. See details in text

### 20.5.2 Two-Bubble Competition

Neighboring bubbles being at close vicinity must inevitably interact. Competition between the neighboring bubbles is natural process and can also serve as a diagnostic tool. Example of such an event is shown in Fig. 20.17. One can see in fact three neighboring bubbles, but their life history shows that interaction between two of them (marked by solid arrows, 1 and 2) turns out to be dominant and eventually destroys the lower bubble (marked by dashed arrow, 3). The measured (average) velocities of bubbles 1 and 2 are, respectively,  $u^{(1)} \simeq 5.1$  and  $u^{(2)} \simeq 14.8 \text{ km s}^{-1}$ . The merging time,  $\tau = 5 \text{ min } 54 \text{ s}$ .

Theoretical merger time is

$$\tau_{\text{merg}} = \frac{\Delta u}{0.1Ag} \quad (20.25)$$

where  $\Delta u$  is the velocity difference of the neighboring bubbles,  $A$  is an Atwood number (20.9), and  $g$  is the gravitational constant. Using measured difference of velocities,  $\Delta u = 9.7 \text{ km s}^{-1}$ , for  $A = 0.9$ , we get for the merging time  $\tau = 6 \text{ min } 33 \text{ s}$  which is reasonably close to observed time.

## 20.6 Greenhouse-Like Effect

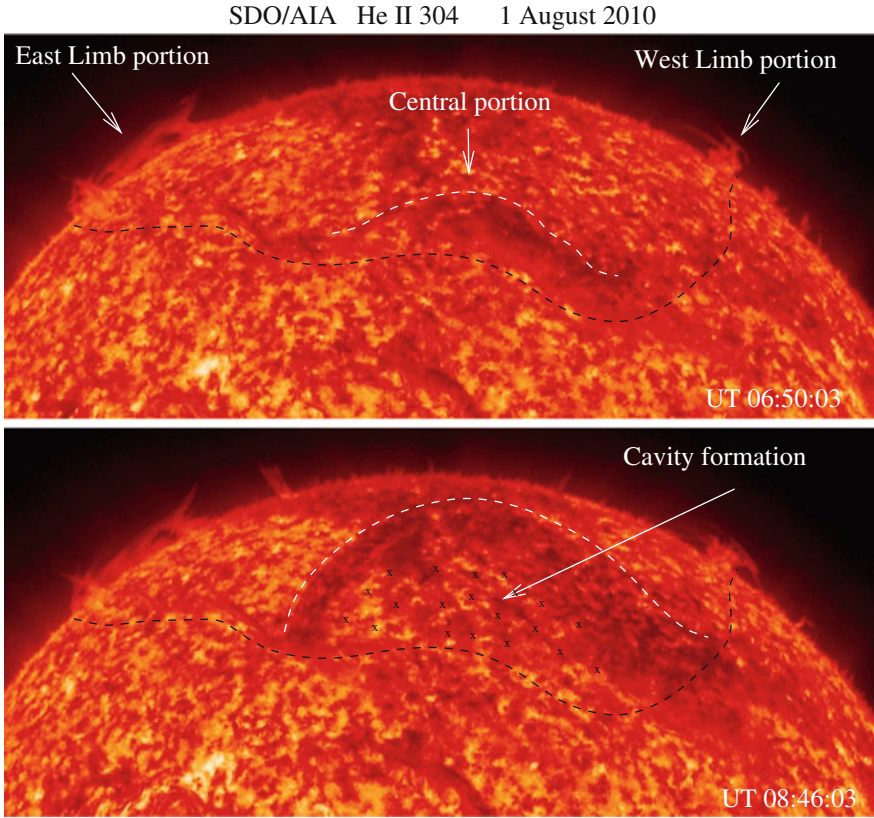
Unlike previous observations limited by the two-dimensional view of the prominence projection on the sky, new space missions opened the opportunity to observe the central portion of prominence body, located on the disk, in high resolution and contrast. These observations give unprecedented information on the prominence nature and dynamics.

Figure 20.18 shows the prominence body stretched across the disk at two instances of time: in its initial raising phase at UT 06:50:03 (top), and at UT 08:46:03, when prominence material is high enough to create a huge cavity underneath (bottom, dotted area, see also Fig. 20.3). Formation of cavities under the prominence body filled by the coronal plasma is an integral part of the three-dimensional helical structure of the prominence.

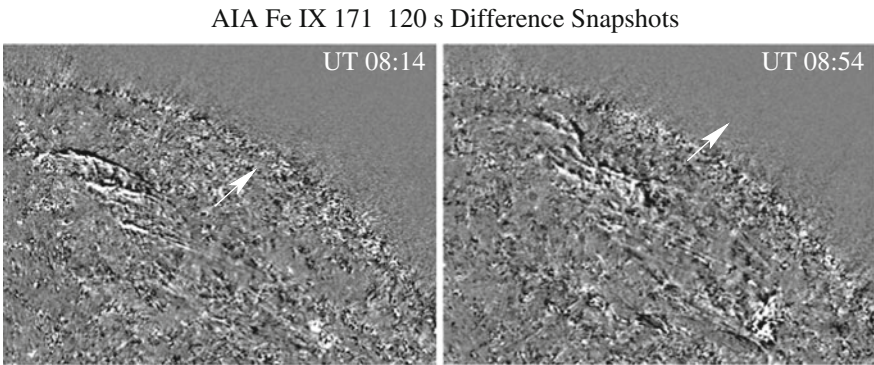
To reveal the true helical structure of the prominence body, it is useful to make a difference movie subtracting images taken at different time intervals. Figure 20.19 shows examples extracted from the movie made in the AIA 171 Å with 120 s difference between the consequent images. The fragments of two snapshots are shown at UT 08:14:13 and UT 08:54:13. At UT 08:14:13 the prominence has been already lifted high enough to leave underneath a well-developed cavity.

Strongly curved prominence body clearly shows a well-preserved three-dimensional helical structure. Raising higher, the prominence solenoid grows farther with enhanced twist of its solenoidal body (cf. a sketch shown in Fig. 20.12a).

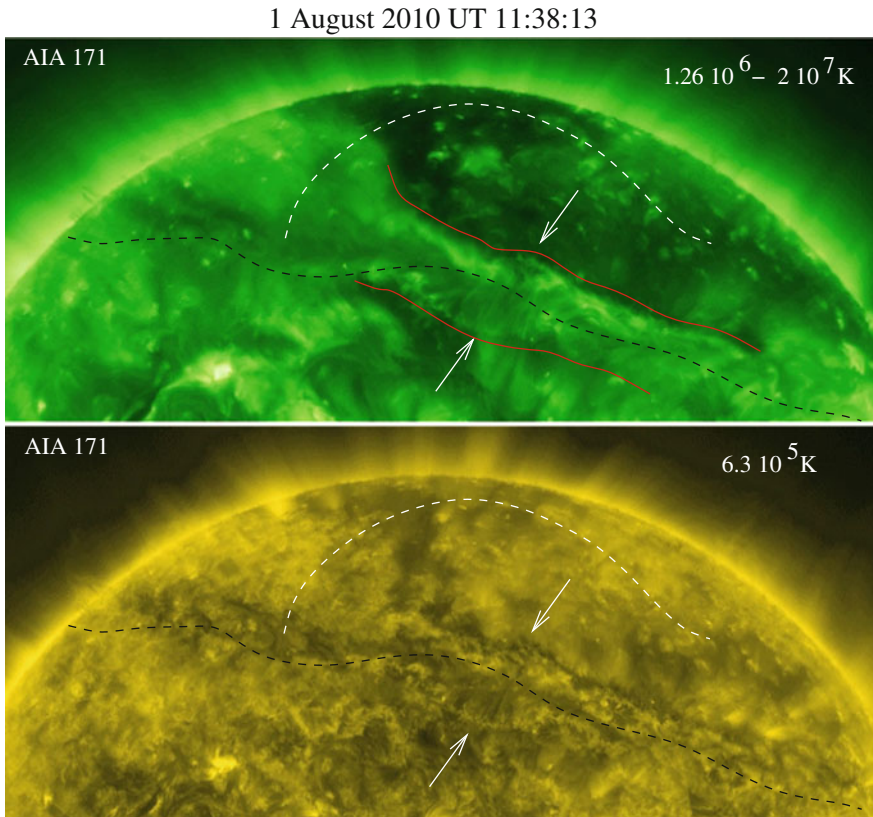
At about UT 11:38:13 the prominence disappears from 171 wavelength (Fig. 20.20 bottom), which means that plasma with temperatures around  $6.3 \times 10^5 \text{ K}$  is replaced by the plasma having much higher temperatures. This is seen in the top panel of



**Fig. 20.18** Snapshots of August 1, 2010 prominence at two instances of time: in its initial raising phase at UT 06:50:03 (*top*), and at UT 08:46:03, when prominence material is high enough to create a huge cavity underneath (*bottom, dotted area*)



**Fig. 20.19** Three-dimensional picture of the prominence clearly exhibiting a solenoidal filamentary structure. The snapshots are obtained from AIA 171 Å movie made with 120 s difference between the consequent frames



**Fig. 20.20** Greenhouse-like effect: A curved prominence body moving upward (white dashed curves) leaves behind a cavity which is quickly filled by the surrounding coronal plasma. But the prominence body acts as a lid to captured plasma whose temperature quickly raises. Top panel shows a million degree plasma under cavity (red lines), while cooler, 171 Å plasma fills the entire disk more or less evenly (bottom). Black dashed line is a polarity inversion line. The white dashed line shows earlier location of lifted prominence

Fig. 20.20. Here, in a huge cavity left behind, the plasma, concentrated *under* the prominence body, has the temperature in the range of  $1.26 \times 10^6 - 2 \times 10^7 \text{ K}$ . Thus, the prominence body covering the cavity works as a lid over the boiling substance.

In other words, when the space where cavity is formed, gets quickly filled by the surrounding coronal plasma, the prominence body acting as a lid, and producing the effect similar to greenhouse effect, leads to significant increase of the temperature of the captured plasma. Note that a compact coronal loop arcades overlying the polarity inversion line (black dashed line in Fig. 20.18) are clearly seen in whole range of temperatures from  $6.5 \times 10^5$  to  $1.26 \times 10^6 - 2 \times 10^7 \text{ K}$ .

Concluding this chapter we note again that high-resolution and high-cadence data from satellites allow to study the dynamics of quiescent prominences and, in particular, to identify manifestation of fundamental plasma instabilities. Data compiled

in movies of several hours duration show both slow processes as well as short-lived events and their possible long-term recurrences. Many processes occurring at different stages of prominence evolution are found to be common for all studied cases. Having universal character, these processes can be related to fundamental plasma instabilities. One can combine the observational evidence and theory to identify these instabilities and perform quantitative analysis.

A fundamental puzzle associated with the dynamic stability of quiescent prominences suspended in rarefied coronal plasma seems to be only natural occurrence. If we consider, however, only the part of the prominence projected on the sky when observed at the limb, this puzzle can hardly be solved. On the other hand, if we look at the problem as being part of the global structure of the prominence body stretched along the entire latitude over the polarity inversion line, we immediately come to a simple solution. Indeed, in accordance with well-known facts from basic plasma physics, a three-dimensional magnetic field configurations with small aspect ratios ( $R/L \ll 1$ ) are intrinsically unstable with respect to screw pinch instabilities, and, to survive, must wind into a helical shape with pitch angle determined by the aspect ratio, and magnetic field components.

Once the helical shape is acquired, the screw pinch configuration is dynamically stable and long lived as long as a safety factor  $q < 1$ . Most importantly, a skewed helical structure in a gravitational field is subject to kinking. The process of skewing leads to formation of prominence cavities under the prominence body which are quickly filled by hot coronal plasma. This creates the illusion of levitation of a heavy prominence material above the rarefied coronal plasma. In other words, formation of kinks observed as underprominence cavity formation is only natural occurrence. The maximum height of a kink is, again, determined by a safety factor: the smaller the safety factor, the “taller” the kink grows. Note this process does not contradict previous models of prominences based on arcades of three-dimensional magnetic field supporting prominence material.

Process of cavity formation and raising motion of prominence body is also associated with phenomenon similar to greenhouse effect: when the space where cavity is formed, gets quickly filled by the surrounding coronal plasma, the prominence body “sitting” over the cavity holds additional energy coming from below acting as a stopper and leading to farther increase of the temperature of underlying, already hot plasma.

## References

- T.E. Berger et al., *Astrophys. J.* **676**, L89 (2008)  
 T.E. Berger et al., *Astrophys. J.* **716**, 1288 (2010)  
 C.E. Brennen, *Cavitation and Cavity Dynamics* (Oxford University Press, Oxford, 1995)  
 J. Carlyle et al., *Astrophys. J.* **782**, 87 (2014)  
 S. Chandrasekhar, *Hydrodynamic and Hydromagnetic Stability* (Dover Publications Inc., New York, 1981)  
 B. Coppi, M.N. Rosenbluth, R. Sudan, *Ann. Phys.* **55**, 201 (1969)

- P. De Bruyne, A.W. Hood, *Sol. Phys.* **147**, 97 (1993)  
A.Z. Dolginov, V.M. Ostryakov, *Astron. Zh.* **57**, 1302 (1980)  
M. Druckmüller et al., *Astrophys. J.* **785**, 14 (2014)  
J. Dudík et al., *Astrophys. J.* **761**, 9 (2012)  
L. Feng, B. Inhester, W.Q. Gan, *Astrophys. J.* **774**, 141 (2013)  
B.H. Fong, O.A. Hurricane, S.C. Cowley, *Sol. Phys.* **201**, 93 (2001)  
J.-P. Franc, J.-M. Michel, *Fundamentals of Cavitation* (Kluwer, Boston, 2004)  
A. Hillier, R. Hillier, D. Tripathi, *Astrophys. J.* **761**, 106 (2012)  
B.B. Kadomtsev, in *Reviews of Plasma Physics*, ed. by M.A. Leontovich (Consultants Bureau, New York, 1966), p. 153  
R. Kippenhahn, A. Schlueter, *Z. Astrophys.* **43**, 36 (1957)  
M.D. Kruskal, R.M. Kulsrud, *Phys. of Fluids* **1**, 265 (1958)  
M. Kuperus, M. Raadu, *Astron. Astrophys.* **31**, 189 (1974)  
M. Kuperus, *Sol. Phys.* **169**, 349 (1996)  
X. Li et al., *Astrophys. J.* **752**, L22 (2012)  
B.C. Low, *Astrophys. J.* (1993)  
B.C. Low, G.J.D. Petrie, *Astrophys. J.* **626**, 551 (2005)  
D.H. Mackay, A.A. van Ballegoijen, *Sol. Phys.* **260**, 321 (2009)  
T. Magara, *Astrophys. J.* **549**, 608 (2001)  
R. Matsumoto, T. Tajima, K. Shibata, M. Kasisig, *Astrophys. J.* **414**, 357 (1993)  
Y. Ohman, *Sol. Phys.* **23**, 134 (1972)  
M.S. Plesset, *J. Appl. Mech.* **16**, 277 (1949)  
E.R. Priest, *Dynamics and Structure of Quiescent Solar Prominences* (Kluwer, Dordrecht, 1988)  
L. Rayleigh, *Proc. Lond. Math. Soc.* **14**, 170 (1883)  
L. Rayleigh, *Philos. Mag.* **34**, 94 (1917)  
K. Rothschild, J.C. Pecker, W.O. Roberts, *Astrophys. J.* **121**, 224 (1955)  
D. Rust, A. Kumar, *Sol. Phys.* **155**, 69 (1994)  
M.P. Ryutova, *Sov. Phys. JETP* **67**(8), 1594 (1988)  
M.P. Ryutova, T.D. Tarbell, *Astrophys. J.* **541**, L29 (2000)  
M.P. Ryutova, *J. Geophys. Res.* **111**, A09102 (2006)  
M.P. Ryutova et al., *Sol. Phys.* **267**, 75 (2010)  
T. Sakurai, *PASJ* **28**, 177 (1976)  
A.B. Severny, V.L. Khokhlova, *Publ. Crime. Astrophys. Obs.* **10**, 9 (1953)  
V.D. Shafranov, *At. Energy* **30**, 38 (1956)  
H.R. Strauss, D.W. Longcope, *Sol. Phys.* **149**, 63 (1994)  
E. Tandberg-Hanssen, *The Nature of Solar Prominences* (Kluwer, Dordrecht, 1995)  
G.I. Taylor, *Proc. R. Soc. Lond. Ser. A* **201**, 192 (1950)  
A. van Ballegoijen, P. Martens, *Astrophys. J.* **361**, 283 (1990)  
B. Vrsnak, V. Ruzdjak, R. Brajsa, A. Dzubur, *Sol. Phys.* **116**, 45 (1988)



# Index

## A

- Abrikosov vortices, 36
- Absence of emission, 348
- Absorbed energy, 52
- Absorbed fraction, 214
- Absorbing regions, 218
- Absorption coefficient, 212
- Absorption of angular momentum, 256
- Absorption of momentum, 255
- Absorption of the momentum, 244
- Accelerating mass flow, 399
- Acceleration, 528
- Acceleration of jets, 347
- Accumulate energy, 426
- Accumulated energy, 156
- Accumulation of energy, 53
- Accuracy of MHD code, 234
- Acoustic branch, 360
- Acoustic component, 358
- Acoustic noise, 141
- Acoustic opacity, 209, 214
- Acoustic streaming, 241
- Acoustic wave packet, 163
- Acoustic wave-trains, 154
- Active filament, 14
- Active latitudes, 11
- Added mass, 41
- Added-mass effect, 312
- Additional energy, 402
- Additional heating, 331
- Adiabatic approach, 206
- Adiabatic excitation, 82
- Advection, 12
- After-shock heating, 333
- Alfvén mode, 170
- Alfvén Resonance, 72
- Alfvén velocity, 48
- Alfvén waves, 256
- Alfvén branch, 360
- Alfvén shocks, 361
- Along the gravity, 370
- Alteration of the travel time, 169
- Ambipolar diffusion, 275
- Amorphous, 398
- Amorphous structure, 374
- Amplitude of generated flow, 248, 253
- Amplitude of mass flows, 256
- Amplitude of the echo, 503
- Amplitude of the shock, 359
- Analytical solution, 199, 247
- Anaxagoras, 2
- Angle of collision, 328
- Angle of propagation, 46
- Angular dependence, 167
- Angular momentum, 244, 254
- Anomalous dispersion, 102
- Anomalous resonance, 72
- Anti-Stokes satellites, 187
- Anticorrelation, 295
- Aperiodic, 323
- Apex of the emission, 381
- Arbitrarily magnetized plasma, 351
- Arc element, 121
- Arc-like flows, 408
- Archimedes force, 41
- Archimedian force, 211
- Artificial viscosity, 234, 262
- Ascending flux tube, 468
- Ascending motion, 523, 525
- Aspect ratio, 426
- Asymptotes, 312
- Asymptotic behavior, 79
- Asymptotic methods, 416
- Attracting centers, 340

- Averaged equations, 197  
 Averages, 43  
 Averaging scale, 197  
 Axial flows, 450  
 Axisymmetric modes, 145  
 Axisymmetric oscillations, 54  
 Azimuthal current, 257  
 Azimuthal harmonic, 53  
 Azimuthal orders, 212
- B**
- Background intensity, 383  
 Back-reaction, 359, 417, 482, 498  
 Balance, 289  
 Barometric, 28  
 Base of the fork, 460  
 Base of the solar wind, 368  
 Beam-particle interactions, 403  
 Beat wave, 186  
 Behind shock temperature, 367  
 Behind-shock brightening, 462  
 Behind-shock flows, 342  
 Behind-shock heating, 337, 342, 462  
 Bernoulli effect, 26  
 Bernoulli's equation, 301  
 Bessel function, 50  
 Bidirectional jets, 344  
 Bifurcate, 481, 489  
 Bifurcation, 418  
 Bifurcation point, 101, 276  
 Bipolar pore, 401  
 Bipolar sunspots, 6  
 Bisector, 306  
 Bisector of collision angle, 308, 442  
 Blast wave, 493  
 Body force, 356  
 Border line, 499  
 Bottom of the fast wind, 371  
 Boundary between, 410  
 Boundary conditions, 50, 356  
 Boundary layer, 242  
 Boundary value problem, 79, 131  
 Bow shock, 312, 318, 455  
 Bow shock formation, 464  
 Brünt-Väisälä frequency, 286  
 Braid period, 380, 391  
 Braidlike behavior, 374  
 Brake Ohm's law, 413  
 Branching, 32, 434, 451  
 Branching points, 436  
 Breaking, 300  
 Bright filaments, 433  
 Bright point, 30, 280, 442  
 Bright soliton, 273, 287  
 Bright transients, 325  
 Bright walls, 31, 434  
 Brightening, 222, 376  
 Brightening of splitting region, 440  
 Broad distribution, 139  
 Broad distribution function, 147, 151  
 Bulbs, 520  
 Bulk viscosity, 248  
 Bullwhip effect, 83  
 Buoyancy force, 282, 320, 466
- C**
- C-class, 479  
 Ca II emission, 21  
 Ca II K, 14  
 Ca II K-line, 279  
 Calcium plages, 21  
 Cancellation, 340  
 Capacitance, 396  
 Capacitive reactance, 411  
 Cascade of shock waves, 334  
 Cascade of shocks, 308, 353  
 Cascades, 154  
 Catastrophic growth, 63  
 Cauchy problem, 47  
 Cavity apex, 525  
 Cavity formation, 521  
 Cavity/prominence interface, 533  
 Cell interior, 340  
 Chaotic conglomerate, 488  
 Chaotic state, 480  
 Character of nonlinearity, 92  
 Characteristic frequency, 361  
 Characteristic time scales, 385  
 Cherenkov condition, 46, 149  
 Chirality, 449  
 Chromosphere, 13, 255, 423  
 Chromospheric bright points, 123  
 Chromospheric flare, 299, 493  
 Chromospheric mottles, 25  
 Chromospheric oscillations, 381  
 Circuit currents, 396  
 Circuit equation, 409  
 Circular cylinder, 245  
 Circularly polarized, 254  
 Classes of explosive events, 344  
 Climatological heat flux, 182  
 Closed set, 229  
 Closed system, 198, 225  
 Closure, 224

- Clouds of energy, 137, 151, 164
  - Cloudy corona, 138
  - Clusters, 492
  - Coefficient of nonlinearity, 272, 356
  - Coherent, 378
  - Collapse, 292, 525
  - Collapse in soliton gases, 392
  - Collective phenomena, 40, 137
  - Collimated flows, 403
  - Collimated mass upflows, 521
  - Collimated plasma flows, 397, 428
  - Collinear, 146, 311
  - Collision angle, 319
  - Collision layer, 301
  - Collision of neighboring shocks, 345
  - Collision rate, 311
  - Collisional, 405
  - Collisionless plasmas, 502
  - Combination frequency, 186
  - Combined dissipative coefficient, 406
  - Common magnetic field, 429
  - Compact active region, 486
  - Compact bipoles, 288
  - Complete absorption, 129
  - Complex  $z$ -plane, 62
  - Complex arguments, 71
  - Complex plane, 71
  - Complex quantity, 95
  - Components of regularities, 490
  - Compressibility, 51
  - Compression, 196
  - Compressional shock heating, 237
  - Computed map, 177
  - Concave form, 328
  - Concentrated cumulative energy, 363
  - Concentration of energy, 392
  - Condition for steepening, 227
  - Confined in loops, 353
  - Conservation laws, 270
  - Conservative system, 270
  - Conserved quantities, 181
  - Continuous fragmentation, 308
  - Convective cell, 7
  - Convective heat flux, 186
  - Convective motions, 250
  - Converging shock fronts, 329
  - Converging supergranules, 340
  - Conversion of magnetic energy, 319
  - Cool down, 426
  - Cooler interior, 447
  - Corkscrew motions, 439
  - Corona, 255, 423
  - Coronal bright points, 123
  - Coronal cavities, 518
  - Coronal dissipation region, 396
  - Coronal flares, 396
  - Coronal hole, 123, 355
  - Coronal jets, 386
  - Coronal loop arcades, 539
  - Coronal loop formation, 296
  - Coronal loop regimes, 418
  - Coronal mass ejection (CME), 480, 514
  - Coronal radiative transients, 385
  - Correlation, 385
  - Correlation function, 200
  - Correlation length, 185
  - Coupling, 327
  - Covariance, 182, 183
  - Crack, 86
  - Critical angle, 332
  - Critical energy level, 491
  - Critical incident angle, 333
  - Critical parameters, 491
  - Critical radius, 253, 427, 443
  - Critical reflection angle, 332
  - Critical value, 63, 424
  - Critical wavelength, 530
  - Critical wavenumber, 208
  - Critically damped oscillations, 418
  - Cross-field shear, 497
  - Cross section, 404
  - Cubic nonlinearity, 390
  - Current carrying systems, 396
  - Current drive, 244, 256, 403
  - Current drive rate, 417
  - Current sheets, 303
  - Currents of air, 242
  - Curved solenoid, 479
  - Curved surface, 328
  - Cyclotron frequency, 73
  - Cylindrical coordinates, 65
  - Cylindrical focusing, 334
  - Cylindrical helices, 437
  - Cylindrical surface, 132
- D**
- Damping length, 117, 154
  - Damping rate, 46, 49, 109, 149, 202, 533
  - Damping time, 143
  - Dark and bright filaments, 9
  - Dark cores, 434
  - Dark filaments, 268
  - Dark penumbral filaments, 433
  - Dark soliton, 287
  - Dark, negative soliton, 273

- Dark-cored filaments, 445
  - Decay of the bow shock, 475
  - Decay phase, 400, 426, 456
  - Decaying regime, 500
  - Deficiency, 498
  - Deficiency of MMFs, 296
  - Deficit of MMFs, 291
  - Deficit of outgoing power, 212
  - Degrees of freedom, 313
  - Delay times, 470
  - Demarcation line, 384
  - Democritus, 2
  - Dense conglomerate, 37, 137, 193, 221
  - Dense plasma jets, 332
  - Density contours, 260
  - Density of jet, 333
  - Density threshold, 424
  - Depth dependence, 182
  - Destruction, 376
  - Detachment, 270
  - Detection points, 174
  - Developing flare, 493
  - Diagnostic facilities, 505
  - Diagnostic goals, 104, 219, 423, 429
  - Diagnostic tool, 286, 323, 506, 535
  - Diagnostics, 504
  - Dielectric function, 102
  - Difference images, 353
  - Difference movie, 537
  - Diffuse boundary layer, 108
  - Diffuse-field, 23
  - Diffused boundary, 272
  - Diffusion, 203
  - Diffusion coefficient, 251
  - Diffusion velocity, 302
  - Diffusive broadening, 251
  - Diffusive dissolution, 243
  - Diffusive regime, 253
  - Diffusive vanishing, 265
  - Dimming, 376
  - Dipole, 4
  - Dipole mode, 51
  - Direct measurements, 321
  - Direction of energy transport, 354
  - Direction of propagation, 172
  - Directly measurable, 380
  - Directly observable, 113
  - Directly observable quantities, 477
  - Directly observed, 99, 297, 450
  - Disbalance, 289
  - Discord of organ, 241
  - Discrepancies in the maps, 177
  - Discrete, 375
  - Discrete frequency spectrum, 81
  - Dispersion coefficient, 272
  - Dispersion effects, 228
  - Dispersion of the wave, 230
  - Dispersion relation, 46, 148, 199
  - Dispersive media, 96
  - Dispersive stretching, 273
  - Displacement vector, 145
  - Disruption of prominences, 516
  - Disruption of the circuit, 421
  - Dissipation of Alfvén waves, 406
  - Dissipation of energy, 318
  - Dissipation rate, 120, 473
  - Dissipation region, 397
  - Dissipative coefficient, 284
  - Dissipative instabilities, 103
  - Dissipative losses, 272
  - Dissipative processes, 108
  - Dissipative stresses, 410
  - Dissipative term, 132
  - Dissolution, 263
  - Dissolved, 81
  - Dissolving, 251
  - Distribution function, 43, 140
  - Distribution of energy input, 126
  - Dive, 450
  - Divergence-free, 197
  - Dominant heating, 332
  - Dominant process, 388
  - Doppler shifted lines, 341
  - Dopplergram, 12, 190, 292
  - Double integration, 162
  - Double structure, 457
  - Double-humped spectrum, 344
  - Downflows, 134
  - Downstream, 116
  - Downward, 254
  - Downward motion, 320
  - Downward shock, 344
  - Drag force, 316, 468
  - Drift, 517
  - Drifting transients, 459
  - Driving emf, 411
  - Duration, 249
  - Dynamic equation, 232
  - Dynamic systems, 491
  - Dynamically stable, 480
  - Dynamically stable kink, 91
- E**
- E.m.f., 497
  - Echo amplitude saturates, 504

- Echo effects, 395
- Echo observations, 506
- Eckart flows, 242
- Eclipses, 1
- Eddy fluxes, 182, 185
- Edge detect procedure, 84
- Effective distance, 188
- Effective radius, 272
- Effective timescale, 253
- Effective viscosity, 252
- Effects of gravity, 180
- Efficient tool, 430
- Eikonal, 119, 128, 406
- Elasticity, 45
- Electric current distributions, 446
- Electric currents, 428
- Electrodynamic equations, 409
- Electromagnetic coupling, 20, 396
- Electromagnetic stresses, 497
- Electromechanical coupling, 339
- Electron component, 257
- Electron heating rate, 74
- Electron inertia, 74
- Electron–ion collision frequency, 404
- Elemental current filaments, 425
- Elemental filament, 427
- Elemental loop, 497
- Elevated temperature, 279
- Emergence, 376
- Emerging phase, 268
- Emission source, 174
- Emitted acoustic power, 189
- Emitted power, 191
- Emitting regions, 117
- Energetically, 12
- Energetically open circuit, 410
- Energetically open oscillator, 419
- Energetically open systems, 101, 267
- Energetically open turbulence, 392
- Energies of different signs, 115
- Energy analysis, 105, 315
- Energy avalanche, 334
- Energy balance, 446
- Energy build up, 385
- Energy build up process, 363
- Energy consideration, 45
- Energy content, 110, 341, 535
- Energy density, 54, 110, 160
- Energy deposition, 161
- Energy dissipation, 162
- Energy distribution, 331
- Energy equation, 273
- Energy escape channels, 123
- Energy extraction, 384
- Energy flow, 498
- Energy flux, 111, 182
- Energy inflow, 491
- Energy input, 154
- Energy loss, 292
- Energy per unit length, 160
- Energy production, 373
- Energy production region, 496
- Energy release, 122
- Energy supply, 349
- Energy transfer, 52
- Energy transfer scenario, 150
- Enhanced absorption, 193
- Enhanced brightening, 436, 492
- Enhanced emission, 292, 304
- Enhanced plasma flows, 337
- Enhanced twist, 537
- Enhanced up-flows, 293
- Enhancement factor, 208, 217, 483
- Enhancement of dissipation, 202
- Enhancement of particle fluxes, 489
- Ensemble of flux tubes, 42
- Ensemble of spins, 501
- Enthalpy, 332
- Entropy, 195
- Entropy equation, 223
- Entropy inhomogeneities, 195
- Entry of helical perturbations, 445
- Equation of motion, 314
- Equation of state, 205
- Equidistant, 190
- Equilibrating, 250
- Equivalence, 409
- Equivalent displacement, 189
- Equivalent LRC, 409
- Equivalent mutual resistance, 413
- Escape channels, 122
- Established flow system, 401
- Established flows, 427
- Evershed flow, 9, 268, 433
- Evolution of coronal structures, 398
- Evolution of Current Systems, 418
- Evolution of flux tube, 243, 259
- Evolution of shock, 306, 343
- Evolution of the eigenfunction, 76
- Evolutionary equation, 95, 273, 390
- Evolutionary soliton, 282
- Excess emission, 268
- Excess of energy, 498
- Excess of energy supply, 417
- Excess of the emission, 278
- Exchange energy, 64

- Expansion in powers, 62
- Explicit expression, 160
- Explosion time, 274
- Explosive events, 326, 327
- Explosive growth, 274, 292, 534
- Explosive instability, 101, 115, 344, 420, 534, 535
- Explosive phase, 283
- Explosive time, 426, 501
- Exponential growth, 362
- Exponentially damping wave, 78
- Extended brightening, 293
- External magnetic field, 357
- Extinction, 127, 143
- Extrapolations, 368
- Extreme fine structure, 122
- Extremum, 126
  
- F**
- $\delta$ -function, 64, 164
- Families of MMFs, 294
- Family of loops, 416
- Fan-like distribution, 461
- Fast, 358
- Fast and slow variables, 390
- Fast growth, 282
- Fast magnetosonic waves, 55
- Fast solar wind, 351
- Fast wind, 368
- Feedback, 397, 498
- Few undulations, 297
- Fibrills, 14
- Field aligned shear flows, 107
- Field of forces, 249, 250
- Field reversal, 444
- Field-aligned current, 437
- Filamentary ray-like structures, 355
- Filamentary structure, 480
- Filamentary structure of sunspot umbra, 23
- Filamentary structure of umbrae, 441
- Filamentation process, 259, 497
- Final velocity, 468
- Finger-like plumes, 532
- Finite amplitude, 139
- Finite amplitude wave, 225
- Finite curvature, 316
- Finite dispersion, 232
- Finite gyroradius, 73
- Finite-amplitude, 92
- Finite-amplitude wave, 142
- First harmonics, 169
- First resonance, 89
  
- Fixed characteristics, 355
- Flare knots, 301
- Flares, 1, 385
- Flexibility, 501
- Flow maps, 295
- Fluctuating part, 183, 200, 229, 230
- Flux conservation, 80
- Flux density, 30
- Flux displacement, 66
- Flux emergence, 280
- Flux reduction, 338
- Flux tube interior, 94
- Flux tube oscillations, 39
- Following sunspot, 5
- Forced Van der Pol equation, 498
- Forcing term, 189
- Forerunner, 403
- Form of the wave packet, 163
- Form-factor, 90
- Formation of a moat, 290
- Formation of the EUV structures, 427
- Fourier harmonics, 186
- Fourier sine and cosine transforms, 171
- Fourier transformation, 199
- Fragmentation, 49, 241, 304
- Fragmentation process, 243
- Frequency detuning, 75
- Frequency of events, 311
- Frequency ratio, 504
- Frequency shift, 149, 188
- Friction, 316
- Friction force, 312
- Frictional force, 467
- Frozen flux, 223
- Frozen in magnetic field, 247
- Frozen-in, 112
- Functional relations, 481
- Fundamental equation, 95
- Fundamental scale, 509
- Future site of pore formation, 408
- Fuzzy emission, 374
  
- G**
- G-band, 29, 280
- Gas discharge filaments, 34
- Gauss's theorem, 27
- Generalized skin depth, 118, 132, 410
- Generated currents, 403
- Generated flows, 338
- Generated twist, 439
- Generating function, 447
- Generation of currents, 377

Generation of electric currents, 244, 396  
 Generation threshold, 417, 500  
 Geometrical acoustics, 119, 169  
 Geometry of the collision, 311  
 Geometry of the problem, 168  
 Giant active region, 219  
 GOES plots, 488  
 Gradient, 246  
 Gradient acceleration, 351, 362  
 Gradient of the eikonal, 121  
 Gradients of mass flows, 173  
 Gradual decay, 283  
 Granular, 12  
 Gravity, 27  
 Greenhouse, 513  
 Greenhouse-Like Effect, 537  
 Group velocity, 170  
 Growing shock front, 84  
 Growth rate, 109, 418, 529  
 Guderley's effect, 334  
 Gulf points, 81  
 Gyrofrequency, 201  
 Gyroradius, 74

## H

$H_\alpha$  surges, 400  
 $H \alpha$ , 14  
 Hankel function, 50  
 Harvey's cartoon, 269  
 He II, 14  
 Head-on collision, 329  
 Heat flux, 184  
 HEAT regime, 338  
 Heat the corona, 387  
 HEAT-JET, 333  
 HEAT-JET regime, 338  
 Heated area, 126  
 Heating power, 78  
 Heaviside step function, 411  
 Hedgerow, Loop-kind, Twirl, Fan, 514  
 Height dependence, 406  
 Height of energy release, 118, 120  
 Height of shock formation, 358  
 Helical instabilities, 437  
 Helical motions, 403, 515  
 Helical structure, 521  
 Helices, 437  
 Helicity injection, 495  
 Helioseismic data, 186  
 Helioseismology effects, 177  
 Helmholtz resonator, 242  
 High  $\beta$  reconnection, 299

High altitude regions, 11  
 High altitudes, 428  
 High birthrate, 346  
 High frequency waves, 164  
 High plasma beta, 328  
 High quality resonator, 418  
 High-energy particles, 301  
 High-energy proton, 479  
 High-velocity events, 99  
 Higher modes, 445  
 Higher-order terms, 51  
 Hodograph, 62  
 Hollow temperature profiles, 448  
 Homogeneous waveguide, 390  
 Homologous microflares, 505  
 Horizontal magnetic field, 172  
 Hotter walls, 447  
 Hydrodynamic cumulation, 328  
 Hydrodynamic instabilities, 130  
 Hydromagnetic activity, 349  
 Hydrostatic equilibrium, 27

## I

Idealized whip, 86  
 Imaginary correction, 49  
 Impulsive phenomena, 428  
 Inborn magnetic fields, 32  
 Inclination, 8, 434  
 Incoherent, 191  
 Incoming, 211  
 Inconsistent, 270  
 Independent solitons, 233  
 Independent variables, 148  
 Individual flares, 482  
 Individual flux tubes, 435  
 Induced coronal flow, 423  
 Induced emf, 415  
 Induced motions, 245  
 Induced power, 403  
 Inductance, 396  
 Inductive circuit, 396  
 Inductive reactance, 411  
 Inertia, 312, 528  
 Infer, 189, 445  
 Inference, 392  
 Initial phase, 281  
 Injected current, 421  
 Inner foot, 268  
 Inner plasma flows, 245  
 Instability, 513  
 Instability growth rates, 113  
 Integro-differential equation, 97, 431

Intensity, 186  
 Intensity inhomogeneities, 433  
 Intensity variation, 381  
 Interaction force, 159  
 Interaction terms, 262  
 Interconnection, 409  
 Interference, 186  
 Intermittent emission, 134  
 Intermittent magnetic structures, 352  
 Intermittent thin streamers, 368  
 Internal structure, 206  
 Interpolation curves, 216  
 Interpolation formula, 215  
 Inverse damping rate, 78, 118  
 Inverse pitch, 447  
 Inverse plasma beta, 173  
 Inverse pressure scale-height, 81  
 Inverse slowing down time, 535  
 Inversion procedure, 182  
 Inverted flow and temperature, 183  
 Ion collision time, 201  
 Ion heating rate, 74  
 Ion temperatures, 74  
 Ion viscosity, 131  
 Irregular pattern, 384  
 Irreversible heating, 74  
 Isotherms, 28  
 Isotropic distribution, 205  
 Isotropic nature, 379

## J

JET regime, 338  
 Jet velocity, 333  
 Jets, 326  
 Joule heating, 448

## K

KdV equation, 232  
 KdV-Burgers equation, 221  
 Kelvin-Helmholtz, 513  
 Kelvin-Helmholtz instability, 99, 271  
 Key element, 296  
 Key factors, 408  
 KH rolls, 101  
 Kinematic viscosity, 74  
 Kinetic coefficients, 255  
 Kinetic energy, 236, 315  
 Kinetic losses, 71  
 Kink oscillations, 42, 112  
 Kink solitons, 96  
 Kinked helical shape, 437

Kitten paw, 397  
 Knots, 381  
 Kruskal-Shafranov, 24, 521  
 Kruskal-Shafranov current, 444  
 Kruskal-Shafranov limit, 444

## L

Laboratory experiment, 33  
 Laboratory plasma, 32, 409  
 Lagrangian planes, 224  
 Landau damping rates, 152  
 Landau resonance, 45, 46  
 Laplace inversion, 76  
 Laplace transform, 76  
 Large local gradients, 193  
 Large scales, 417  
 Large wave packet, 155  
 Larmor radius, 257  
 Lateral extension, 471  
 Lateral jets, 442, 443  
 Lateral motion, 293  
 Lax-Wendroff scheme, 234  
 Lazy motions, 377  
 Leading sunspot, 5  
 Least squares approximation, 216  
 Left-handed, 438  
 Level of fluctuations, 198  
 Level of inhomogeneities, 233  
 Life history, 537  
 Lifetime, 12, 195, 434  
 Lifetime distribution, 31  
 Lifetime of transients, 473  
 Light bridges, 238  
 Limb, 517  
 Limited portion, 365, 443  
 Limiting case, 238  
 Limiting value, 424  
 Line profiles of SUMER, 341  
 Line-tied, 450  
 Linear corrections, 174  
 Linear KH instability, 533  
 Linear oscillations, 49  
 Linear resonance, 144  
 Linearized MHD equations, 50  
 Linearized set, 56  
 Local helioseismology, 167  
 Local inhomogeneities, 177  
 Local reconnections, 265  
 Localized bright regions, 134  
 Localized transients, 377  
 Location of energy input, 156  
 Log-normal distribution, 31



- Logarithmic derivatives, 50
- Long wave, 196
- Long-lasting explosive events, 347
- Longevity, 522
- Longitudinal electric current, 498
- Longitudinal inhomogeneity, 69
- Longitudinal resonances, 80
- Lorentz force, 446
- Loss of energy by NEWs, 105
- Loss of radial equilibrium, 81
- Low altitudes, 428
- Low wavenumbers, 209
- Lundquist field, 449
  
- M**
- Mach number, 330, 362
- Macroscopic effect, 467
- Macroscopic equations, 41
- Macroscopic force, 44
- Macroscopic quantum phenomena, 35
- Macroscopic velocity, 158
- Magnetic body, 4
- Magnetic carpet, 8
- Magnetic cluster, 222
- Magnetic diffusivity, 131
- Magnetic energy, 237
- Magnetic energy avalanche, 370
- Magnetic energy flux, 182
- Magnetic field clusters, 368
- Magnetic field parallel to gravity, 529
- Magnetic field reversal, 450
- Magnetic field transverse to gravity, 530
- Magnetic filling factor, 6, 150, 380
- Magnetic flux changes, 365
- Magnetic knots, 22
- Magnetic loop arcades, 352
- Magnetic reconnection, 299
- Magnetic shear, 21, 495
- Magnetic signal, 434
- Magnetic skeleton, 1
- Magnetic status, 167
- Magnetic status of plasma, 354
- Magnetic stresses, 243
- Magnetic surface, 119
- Magnetic tension, 306, 466
- Magnetogram, 7
- Magnetosonic streaming, 241
- Maintenance, 40
- Major forces, 467
- Mass flows, 326
- Mass of substance, 225
- Matching, 216
- Matching point, 70
- Maximum absorption, 122
- Maximum dissipation, 116
- Maximum energy input, 53
- Maximum radius, 529
- Maxwell equations, 26
- M-class, 479
- MDFs, 289
- Measurable, 90
- Measurable parameters, 397
- Measure of the shock velocity, 341
- Measured times, 176
- Mechanical stressing, 429
- Memory, 283, 502
- Memory device, 502
- Memory of the system, 157
- Merging, 263, 340, 376, 434
- Method of characteristics, 355
- Mezogranular, 12
- MHD approximation, 26, 200
- MHD shocks, 334
- Microjets, 455
- Microscales, 417
- Migrate, 11
- Million degree radiative transients, 384
- Minimum critical radius, 253
- Mixed polarity plage, 10, 373, 388
- Moat, 267
- Moat region, 450
- Model parameters, 178
- Moderate level, 204
- Modified sound speed, 231
- Modulated MKdV soliton, 390
- Modulated oscillations, 419
- Modulation instabilities, 389
- Modulation period, 384
- Modus operandi, 496
- Molecular transport, 208
- Momentum, 254
- Momentum balance, 403
- Momentum flux, 44
- Morphological effects, 151, 388
- Morphology of a heated area, 129
- Motionless, 456, 472
- Mottles, 22, 505
- Mounder minimum, 6
- Moving magnetic features (MMFs), 267
- Multi-spiky, 75
- Multicomponent configurations, 450
- Multiple azimuthal modes, 51
- Multiple branching, 436, 443
- Multiple flares, 508
- Multiple flows, 327

- Multiple reconnection processes, 308, 443
- Multiple shocks, 473
- Multistep process, 322
- Multithreaded loop arcades, 479
- Multiwavelength, 290
- Multiwavelength observations, 395
- Multiwired, 439
- Mushroom cap, 521
- Mutual inductance, 410, 413
- Mysterious magnetic features, 270
  
- N**
- Narrow distribution, 139
- Narrow resonances, 88
- Nature of MMFs, 296
- Nature of NEWs, 105
- Navier–Stokes equations, 527
- Near-polar latitudes, 517
- Negative definite, 231
- Negative dispersion, 288
- Negative energy kink, 286
- Negative energy waves (NEWs), 99, 101, 271, 533
- Net flow of power, 212
- Net force, 313
- Network elements, 375
- Network granules, 8
- Neutral lines, 300
- New-born kink, 277
- Newborn flux tube, 243, 262
- Next generation bipole, 322
- Non-conservative systems, 12
- Non-gravity situation, 313
- Non-oscillatory, 40
- Non-slinky flares, 483
- Nonadiabatic, 210
- Noncollinear, 306, 311
- Noncollinear flux tubes, 367
- Noncollinearity, 28, 48
- Nonconformity, 287
- Nonconservative systems, 267
- Nonconvoluted times, 186
- Noninductive current drive, 403
- Nonlinear, 139
- Nonlinear distortions, 356
- Nonlinear equation, 226, 232
- Nonlinear frequency shift, 142
- Nonlinear kink oscillations, 389
- Nonlinear processes, 306
- Nonlinear regime, 144
- Nonlinear unsteady processes, 413
- Nonmagnetic environment, 305
  
- Nonmagnetic spacing, 441
- Nonpaired, 268
- Nonreciprocity, 182
- Nonresonant, 153
- Nonstationary solution, 390
- Nonuniformities, 176
- Normal dispersion, 102
- Normalization, 43
- Normalizing constants, 234
- N-soliton solution, 390
- Nuclear resonance diagnostics, 502
- Number of collisions, 311
- Numerical simulations, 257
- Numerical solution, 28
- Nyquist criterion, 63
  
- O**
- Oblique shocks, 443
- Observable, 127, 137, 344
- Observable morphological effects, 122
- Observation of a scale invariance, 491
- Observational signatures, 306
- Observational spectroscopy, 193
- Observationally detectable, 450
- Observed delay times, 470
- Observed regularities, 214, 486
- Observed shock–shock interaction, 345
- Observed signatures, 346, 442
- Observed timescales, 303
- Observed values, 285
- Ocean tomography, 182
- Ohmic dissipation, 202
- Ohmic losses, 78
- Ongoing reconnection, 441, 492
- Onset of absorption, 214
- Open structures, 399, 401
- Opening angles, 469
- Opposite parity properties, 172
- Opposite polarity remnants, 517
- Optical depth, 189
- Orientation and magnitude, 173
- Origin of spicules, 256
- Oscillating “energy” channel, 391
- Oscillation period, 322
- Oscillations of thin filaments, 532
- Oscillatory, 40
- Oscillatory pattern, 383, 533
- Oscillatory regime, 322
- Outcome, 487
- Outer foot, 268
- Outflow, 491
- Outflow velocities, 284

- Outgoing, 211
- Outgoing waves, 58
- Overdamped oscillations, 418
- Overpass the skin depth, 502
- Overturning, 225
  
- P**
- Pancakes, 381
- Parabolic equation, 133
- Parameter range, 162
- Parameter studies, 477
- Parental bright points, 456
- Parity of Negative and Positive Energy Waves , 113
- Parity properties, 171
- Parity property, 176
- Partial energy release, 421
- Partial or total cancellation, 310
- Partial vacuum, 25
- Partial wave analysis, 211
- Patchy brightenings, 123
- Patchy character, 126
- Patchy EUV emission, 389
- Path length, 218
- Peak time, 495
- Penumbrae, 9
- Penumbral jets, 14
- Perforated, 375
- Period of the oscillations, 321
- Periodically flaring, 395
- Periodically flaring coronal loops, 418
- Peripheral filaments, 442
- Perturbation, 147, 230
- Perturbation theory, 416
- Petchcheck's mechanism, 301
- Phase memory of particles, 502
- Phase mixing, 117
- Phase shifted, 438
- Phase transition, 491
- Phase velocity, 44, 59
- Phase-mix to zero, 503
- Phase-mixing, 75
- Phenomenology, 385
- Photospheric driver, 397, 496
- Photospheric filigree, 25
- Photospheric reconnections, 305
- Physical reason, 194
- Piecewise model, 319
- Piercing plasma flow, 399
- Pinned, 80
- Pitch, 437, 522
- Pitch of the helical configuration, 438
- Plages, 7
- Plane of motion, 459
- Plasma beta, 202, 234
- Plasma echoes, 479, 501
- Plasma heating, 318
- Plasma instabilities, 15
- Plasma particles, 247
- Plasma streaming, 244, 460
- Plasma turbulence, 117, 392
- Plato, 2
- P-mode fluctuations, 187
- P-mode ridges, 190, 213
- Poincare limit cycle, 419, 499
- Polar, 11
- Polar plumes, 12, 17
- Polarity inversion, 492
- Polarity inversion line, 517
- Polarity reversal, 5
- Poles of the function, 77
- Ponderomotive force, 244, 246
- Population of MMFs, 290
- Pores, 9
- Positive definite, 228
- Positive dispersion, 273, 288
- Post-flare cooling regime, 426
- Post-reconnection processes, 124, 351
- Post-reconnection products, 299, 306, 325
- Post-reconnection shocks, 336, 350, 385
- Post-ridge downflows, 294
- Potential energy, 315, 468
- Potential well, 321
- Power balance, 416
- Power dissipated, 406
- Power law, 330, 367
- Power spectra, 190
- Power spectrum, 213
- Power-law, 125
- Poynting flux, 410
- Practical use, 191
- Pre-flare, 483
- Pre-flare stage, 491
- Pre-shock velocity, 365
- Precursors, 363, 381, 479
- Predictability, 500
- Predictability criteria, 482
- Predictability tools, 113
- Predicted positions, 504
- Prediction, 423
- Preliminary accumulation, 488
- Preshock plasma, 331
- Pressure equilibrium, 42
- Probability, 311
- Probability distribution, 90

- Probability distribution functions, 31  
 Probing inhomogeneities, 215  
 Prominences, 1  
 Prominence cavities, 514  
 Prominence shadow, 517  
 Propagation velocity, 281  
 Proper motion, 408, 460  
 Pure jet formation, 332  
 Pythagoras, 1
- Q**
- Qualitative behavior, 129  
 Quantitative analysis, 381  
 Quantitative analysis, 211, 246, 274, 286,  
 328, 379, 414, 422  
 Quantitative estimates, 178, 252, 361, 365,  
 404  
 Quartz wind, 242  
 Quasi-longitudinal, 55  
 Quasi-simple wave, 356  
 Quasilinear, 532  
 Quasiperiodic driving force, 413  
 Quiescent prominences, 14, 15, 513  
 Quiet sun, 6  
 Quiet sun region, 213
- R**
- Radial eigenfunction, 75  
 Radial inhomogeneity, 69  
 Radial scale length, 77  
 Radially inhomogeneous, 58  
 Radially outward, 354, 370, 433  
 Radiated energy flux, 54  
 Radiated wave, 110  
 Radiation of negative-energy waves, 115  
 Radiative cooling time, 446  
 Radiative damping, 52, 110, 152  
 Radiative damping rate, 52  
 Radiative heat flux, 446  
 Radiative transients, 363  
 Radio occultation, 355  
 Radius of curvature, 314  
 Raman spectroscopy, 186  
 Raman spectroscopy of p-modes, 167  
 Random character, 387  
 Random functions, 228  
 Random parameters, 41  
 Random phases, 154  
 Random quantities, 224  
 Range of current densities, 407  
 Range of frequencies, 104  
 Rapidly damping, 61  
 Rarefied, 383  
 Rarefied ensemble, 37, 137, 146  
 Rate, 386  
 Ray trajectory, 119, 406  
 Rayleigh equation, 247  
 Rayleigh–Plesset equation, 526  
 Rayleigh–Taylor, 513  
 Reactance, 411  
 Real part, 162  
 Reappearance, 156  
 Reciprocal travel times, 183  
 Reconnecting flux tubes, 335  
 Reconnection, 49, 124  
 Reconnection of filaments, 441  
 Reconnection outcome, 303  
 Reconnection rate, 302  
 Reconstruction, 177  
 Recurrence, 520, 525  
 Recurrent flares, 501, 507  
 Recurrent nature, 529  
 Recycling time, 334, 370  
 Redistribution of electric currents, 261  
 Redistribution of the temperature, 277  
 Redshift ridges, 477  
 Reduced absorption, 218  
 Reduction, 327  
 Redundant, 411  
 Reflected shocks, 330  
 Reflection point, 169  
 Regions of the shock formation, 319  
 Regular lattice, 36  
 Regular oscillations, 384  
 Rejoining, 300  
 Relative motions, 211  
 Relaxation period, 482  
 Relaxation regime, 395  
 Released thermal energy, 473  
 Reliable diagnostics, 502  
 Remnant active regions, 6  
 Remnants, 309  
 Repercussions, 320  
 Repetitive bursts, 507  
 Repetitive explosive events, 340  
 Resistance, 396, 411  
 Resistive character, 429  
 Resistive coupling, 416  
 Resistive instability, 302  
 Resistive loads, 497  
 Resistive stresses, 412  
 Resonance condition, 46  
 Resonance frequencies, 89  
 Resonance layer, 246  
 Resonance point, 72

- Resonance structure formations, 80
- Resonant, 153
- Resonant absorption, 106, 138
- Resonant damping, 72
- Resonant denominator, 46
- Resonant excitation, 64
- Resonant flux tubes, 151
- Resonant interaction, 388
- Resonant layer, 69
- Resonant scattering, 53
- Restoring magnetic force, 307
- Restriction, 234
- Reversal, 449
- Reversed chirality, 450
- Reversible process, 502
- Reynolds number, 117
- Reynolds stresses, 243
- Riemann equation, 356
- Riemannian coordinates, 355
- Right-handed, 438
- Ripples, 521
- Rippling mode, 521, 534
- Rotational, 254
- Rotational mass flows, 244
- Rotational motions, 515
- Running waves, 83
  
- S**
- ∩-shaped flux tubes, 319
- ∩-shaped kink, 270
- ∪-shaped flux tubes, 317
- ∪-shaped kink, 270
- Safety factor, 24, 438, 521
- Saturated, 366
- Saturation, 209, 215
- Saturation limit, 416
- Sausage mode, 55, 145
- Sausage oscillations, 111
- Sawtooth character, 365
- Sawtooth shock, 235, 405
- Scale height, 28
- Scale-invariant, 482
- Scaling, 33
- Scattering, 138
- Scattering centers, 188
- Scattering cross section, 144
- Scattering of flux tubes, 307
- Scenarios of the evolution, 273
- Schrödinger equation, 390
- Screw-pinch instability, 24, 516
- Screw-type motion, 437
- Sea-serpent, 269
- Searching for unknown resonances, 502
- Second harmonics, 169
- Second-order spatial echo, 503
- Secondary waves, 51, 106
- Secular equation, 82
- Self-consistently, 225
- Self-excited oscillations, 417
- Self-focused structures, 391
- Self-focusing, 329, 344, 390
- Self-modulation, 390
- Self-organized, 479
- Self-organized structures, 392
- Self-similar, 480
- Self-similarity, 530
- Self-similarity of solution, 313
- Selforganization, 33
- Semi-spherical cavity, 523
- Sensitivity, 60
- Separate filament, 406
- Separation, 278, 285
- Sequence of energy transfer, 141
- Sequences of flares, 488
- Series of echoes, 505
- Series of plumes, 521
- Series of reconnection, 340, 402
- Set of parameters, 148
- Shallow soliton, 283
- Sharp boundary, 60
- Sharp discontinuity, 87
- Sharp inhomogeneity, 56
- Sharp loop, 86
- Sharp temperature jump, 349
- Shear Alfvén waves, 116
- Shear flow instabilities, 100, 271
- Shear flows, 175
- Shear viscosity, 248
- Shock amplitudes, 387
- Shock formation, 84, 309
- Shock front, 493
- Shock profile, 460
- Shock signatures, 341
- Shock velocity, 469
- Shock waves, 82
- Shock–shock interaction, 341
- Shock-related dissipation, 473
- Shocklike form, 273
- Shocklike regime, 276
- Shocks, 221
- Short wave packet, 155
- Short-living UV flashes, 381
- Shortening and straightening, 306
- Shorter-lived MMFs, 268
- Shredding of the magnetic field, 279

- Shredding the flux tubes, 308
- Shrinking, 308
- Sign of dispersion, 273
- Signs of the precursors, 489
- Similarity, 530
- Simple waves, 228
- Single plume, 535
- Single-valued solution, 109
- Singular point, 69
- Singularities, 58, 79
- Singularity, 247
- Sink of wave power, 212
- Sinusoidal pulse, 358
- Skewed shape, 522
- Skewing, 450
- Skin effect, 405
- Slab oscillations, 96
- Slender, 61
- Slingshot effect, 306
- Slingshot outcome, 357
- Slinky, 479
- Sloshing mode, 210
- Slow evolution, 282
- Slow magnetoacoustic mode, 170
- Slow magnetosonic waves, 55
- Slow MHD waves, 358
- Slow solar wind, 10
- Slow variables, 430
- Slow wind, 368
- Slowing down time, 404
- Slowly drifting, 456
- Slowly varying envelope, 158
- Slowly varying function, 159, 273
- Small sunspot, 219
- Small-scale flux tubes, 7
- Solar cycle, 5
- Solar interior, 4
- Solar radii, 368
- Solenoidal shape, 521
- Solitary kink, 284
- Solitary Sausage Wave, 96
- Solitary wave, 91
- Soliton formation, 232
- Soliton gas, 390
- Soliton parameters, 274
- Soliton-like kinks, 276
- Solitons, 221
- Sound barrier, 86
- Source of emf, 411
- Source region, 397
- Sources and sinks, 187
- Space objects, 409
- Space-time, 438
- Space-time cuts, 39, 290, 375
- Spacetime tracks, 378
- Spatial damping rate, 205, 257
- Spatial distribution of mass flows, 175
- Spatial echo, 502
- Spatial variations, 196
- Spatiotemporal, 516
- Spatiotemporal echoes, 502
- Spatiotemporal periodicity, 395
- Specific frequency, 40
- Spectral density, 90, 200
- Spectropolarimetric observations, 477
- Spherical harmonic, 219
- Spheromak, 33
- Spicules, 14, 375
- Spikes, 521
- Spin echo, 501
- Split the averages, 223
- Splitting, 340, 434
- Splitting processes, 376
- Splitting regime, 243
- Spontaneous, 501
- Sporadic events, 374
- Sporadic microflares, 379
- Spreading of energy input region, 156, 164
- Squeezed volume, 393
- Stability, 513
- Stability boundary, 445
- Stabilization, 282, 285
- Stable regime, 424
- Stable solitary wave, 276
- Stable soliton, 293
- Stagnation, 127
- Standoff distance, 462
- Stationary value, 499
- Stationary vortices, 253
- Statistical properties, 220, 222
- Statistical properties of MMFs, 295
- Steady character of the fast wind, 370
- Steady energy input, 370
- Steady-state reconnection, 301
- Steepening, 225
- Step by step process, 491
- Stepwise, 60
- Stochastic field lines, 117
- Stokes, 187
- Straight segments, 315
- Stratified atmosphere, 169, 286, 360
- Stream function, 245
- Streamline, 245, 471
- Stretched variables, 92

- Striking effects, 48
  - Strong damping, 128
  - Strong local brightenings, 238
  - Strong nonlinear regime, 532
  - Strong stratification, 306
  - Strongest absorption, 134
  - Structure dimensions, 427
  - Structure of atmosphere, 189
  - Structure of medium, 220
  - Sub-Alfvénic, 533
  - Subsurface, 178
  - Subsurface flow, 177
  - Subsurface layers, 169, 191
  - Subsurface motions, 427
  - Subsurface velocity field, 178
  - Subtle oscillations, 395
  - SUMER slit, 337
  - SUMER spectra, 336
  - Sunspot dimension, 209
  - Sunspot umbra, 9, 433, 435
  - Sunspots, 1
  - Superconductivity, 35
  - Superfluidity, 35
  - Supergranular, 12
  - Supergranular geometry, 177
  - Supergranular vertex, 346
  - Supergranules, 336
  - Supernova remnant, 34
  - Supersonic, 322, 464
  - Supersonic jets, 353
  - Suppression, 530
  - Surface driver, 396
  - Surface tension, 527
  - Sweet-Parker, 301
  - Swing, 84
  - Symmetry of the fluctuations, 198
  - Symmetry properties, 176
  - Synchronize, 488
  - Synchronous, 439
  - Synchronous lighting, 505
  - System evolution, 499
  - Systematic outflow, 267
- T**
- Tangential discontinuity, 101
  - Tangential motion, 242
  - Temperature diagnostics, 504
  - Temperature distribution, 276
  - Temperature inhomogeneities, 184
  - Temperature jump, 81, 87
  - Temperature minimum, 18, 330
  - Temporal brightening, 91
  - Temporal echo, 502
  - Temporal second-order echo, 503
  - Temporal variability, 39, 375, 525
  - Temporal variation, 161
  - Tendency to self-organization, 393
  - Terminal velocity, 525
  - Thermal conductivity, 78
  - Thermal energy, 237
  - Thermal evolution, 463
  - Thermal losses, 233
  - Thermal noise, 116
  - Thermal velocity, 404
  - Thermodynamic properties, 360
  - Thick flux tubes, 252
  - Third-order echo, 503
  - Three-dimensional helical structure, 537
  - Three-dimensional simulation, 275
  - Three-wave processes, 115
  - Time delays, 462
  - Time of establishing, 249
  - Time of establishing of viscous flow, 250
  - Time series, 280
  - Time-distance analysis, 167
  - Time-distance tomography, 167
  - Timescale for the steepening, 234
  - Tokamak, 32, 403
  - Topographical studies, 220
  - Topological effects, 118
  - Toroidal currents, 403
  - Torsional Alfvén waves, 76
  - Torsional oscillations, 55
  - Total damping rate, 207
  - Total energy flux, 124, 367
  - Total energy transfer, 140
  - Total flux, 23
  - Total number of collisions, 311
  - Total power flux, 134
  - Total pressure perturbation, 65
  - Total replacement, 368
  - Transiently heated, 456
  - Transition, 252, 283
  - Transition region, 13, 122, 326, 408
  - Transonic, 467
  - Transport equations, 404
  - Transonic motion, 316
  - Transverse oscillations, 376
  - Trapped protons, 490
  - Traveling soliton, 271
  - Triggering mechanism, 327, 386
  - Triple integral, 162
  - True location, 156

True microjet, 465  
 Tube waves, 55  
 Turbulent pumping, 25  
 Turbulent stressing, 409  
 Turbulent velocities, 219  
 Turbulent viscosity, 208  
 Turnout time, 251  
 Twisted configuration, 434  
 Twisted flux tubes, 23  
 Twisting motion, 437  
 Two-bubble competition, 536, 537  
 Type I MMFs, 268  
 Type I\* MMFs, 269  
 Type II MMFs, 268  
 Type III MMFs, 269  
 Type IV MMFs, 269  
 Types of axisymmetric modes, 55  
 Types of MMFs, 287

## U

Umbra, 194  
 Umbra/penumbra boundary, 292  
 Umbral dots, 436  
 Unaccounted energy, 100  
 Unbalanced process, 396  
 Uncombed, 8  
 Uncombed system, 433  
 Underdamped oscillations, 418  
 Uneven emission, 276  
 Uneven shock front, 329  
 Unification, 287  
 Unified basis, 290, 495  
 Unify, 486  
 Unipolar features, 289  
 Unipolar magnetic flux tubes, 123  
 Unipolar plages, 11, 373  
 Unipolar regions, 388  
 Universal character, 540  
 Unshifted line, 341  
 Unstable mode, 525  
 Unstable perturbations, 104  
 Unstable structures, 401  
 Unsteady wave packets, 151  
 Upstream, 104, 116  
 Upward, 254  
 Upward acting forces, 468

## V

Validity of soliton solution, 274  
 Van der Pol equation, 419

Variation, 471  
 Various contributions, 176  
 Various instabilities, 134  
 Varying envelope, 157  
 Velocity gradients, 179  
 Velocity of a shock, 366  
 Velocity perturbations, 57  
 Velocity potential, 50, 70, 259  
 Velocity shear maps, 179  
 Velocity vectors, 260  
 Vertex, 327  
 Vertical temperature, 87  
 Vertically upward, 370  
 Vertices, 339  
 Vibrating plate, 242  
 Viewing angles, 459  
 Violation of the equivalence, 297  
 Violent mass ejections, 91  
 Viscosity, 242, 527  
 Viscous dissipation, 202, 206  
 Viscous friction, 211  
 Viscous losses, 78, 130, 233  
 Volt-ampere characteristic, 416  
 Voltage-dependent, 413  
 Volume force, 41, 48, 146  
 Vortex core, 36  
 Vortex part, 194, 246

## W

Wave extinction, 126  
 Wave front, 227  
 Wave momentum, 405  
 Wave train, 243  
 Wave-particle interactions, 403  
 Wave-induced currents, 428  
 Wavy surfaces, 357  
 Weak constraint, 232  
 Weak dissipation, 131  
 Weak nonlinear regime, 532  
 Weak shocks, 233  
 Weakly nonlinear, 405  
 Weakly nonlinear oscillations, 91  
 Weakly nonlinear waves, 69  
 Well defined boundaries, 353  
 Well organized coherent structures, 376  
 Whip cracker, 86  
 Width of a soliton, 281  
 Width of dark cores, 434  
 Width of elemental loop, 410  
 Width of the boundary layer, 259  
 Widths of umbral filaments, 441



Wings of  $H\alpha$ , [290](#)  
Work of the gravity force, [317](#)

**X**

X-class flares, [479](#)  
X-ray bright points, [375](#)

X-type neutral points, [300](#)  
X17 class flare, [487](#)

**Y**

Y-shaped fork, [465](#)  
Yellow dwarfs, [3](#)